UNIVERSIDAD COMPLUTENSE DE MADRID
FACULTAD DE CIENCIAS QUÍMICAS

TESIS DOCTORAL

Multivalent [60]Fullerene Hexakis-adducts for Biomedical Applications

Hexaaductos Multivalentes de [60]Fullereno para Aplicaciones Biomédicas

MEMORIA PARA OPTAR AL GRADO DE DOCTOR

PRESENTADA POR

Jennifer Patino Alonso

DIRIGIDA POR

Nazario Martín León
Beatriz María Illescas Martínez
Justo Enrique Cabrera González

Madrid

© Jennifer Patino Alonso, 2025

UNIVERSIDAD COMPLUTENSE DE MADRID

FACULTAD DE CIENCIAS QUÍMICAS

TESIS DOCTORAL

Multivalent [60]Fullerene Hexakis-adducts for Biomedical Applications

Hexaaductos Multivalentes de [60]Fullereno para Aplicaciones Biomédicas

Jennifer Patino Alonso

Madrid, 2025

Directores:

Prof. Nazario Martín León

Prof. Beatriz María Illescas Martínez

Dr. Justo Enrique Cabrera González

UNIVERSIDAD COMPLUTENSE DE MADRID

FACULTAD DE CIENCIAS QUÍMICAS

TESIS DOCTORAL

Multivalent [60]Fullerene Hexakis-adducts for Biomedical Applications

Hexaaductos Multivalentes de [60]Fullereno para Aplicaciones Biomédicas

MEMORIA PARA OPTAR AL GRADO DE DOCTORA EN QUÍMICA ORGÁNICA presentada por

Jennifer Patino Alonso

DIRECTORES

Prof. Nazario Martín León

Prof. Beatriz María Illescas Martínez

Dr. Justo Enrique Cabrera González

A mi hermana

AGRADECIMIENTOS

Cinco años han pasado desde que decidí embarcarme en la que sería la mejor y más atrevida experiencia de mi vida. Cinco años en los cuales no solo he aprendido como química y crecido como persona, sino que también han estado llenos de momentos, gente y recuerdos que no podré olvidar.

En primer lugar, me gustaría agradecer a la Universidad Complutense de Madrid y, en particular, a la Facultad de Ciencias Químicas, por proporcionarme el espacio académico y personal adecuado para llevar a cabo esta tesis. También quiero reconocer al Departamento de Química Orgánica su apoyo constante y dedicación a la investigación que han sido clave durante todo este proceso.

Asimismo, quiero agradecer a todos los proyectos que han permitido financiar esta tesis: PR65/19-22339 (FULLSTOP VIRUS): Nanoformas Biocompatibles Basadas en Glicofullerenos como Agentes Antivirales; PR38/21-30370 (REACT-ANTICIPA UCM): Anticipación y Prevención de COVID-19 en la Comunidad de Madrid; PID2020-115120GB-I00 (ORCHESTRACA): De la Multivalencia en Moléculas a la Organización de Nanomateriales: Modificación Química de Fullerenos y Nanopuntos de Carbono para Aplicaciones Biomédicas y (bio)sensado.

Dar las gracias también a todos los colaboradores que han participado en estas investigaciones, aportando su granito de arena: a Ángeles Canales, por sus estudios de RMN; a Iván López, por sus estudios con células y en microscopía confocal; a Rafael Delgado, por sus estudios de transinfección; a Javier Rojo, por proporcionarnos los carbohidratos necesarios; a Santi Nonell, por sus estudios fotofísicos; a Jesús Jiménez Barbero, por sus estudios con galectinas; y a Rosario Núñez, Mª José Ruiz y Mª Carmen Ruiz, por ayudarnos con el proyecto de los clústers de boro. Por supuesto, a Lola, Elena, Ángel y Marga, del Servicio de Resonancia Magnética Nuclear de la facultad, cuya ayuda y paciencia han sido requisito indispensable para poder sacar adelante este trabajo.

Gracias a mis directores de tesis por haberme dado la oportunidad y haber depositado su confianza en mí para llevar a cabo esta tesis doctoral. Nazario, me has enseñado que la ciencia también se puede construir con pasión, generosidad y compromiso. Tu dedicación hace que todos nosotros queramos sacar nuestra mejor versión y ser, por lo menos, un 1% de lo buen científico y persona que eres. Beti, eres un ejemplo de fuerza, decisión y claridad. Tu manera de enfrentar los retos, siempre con resolución y determinación, ha sido una guía constante para mí durante esta tesis. Por último, pero no menos importante, Justo. Cuesta creer que dos personas con nuestro carácter hayan congeniado tan bien. Gracias por preocuparte por mí desde el minuto cero y haber luchado para conseguir cada logro que nos hemos marcado. Espero que tu primera doctoranda no quede en el olvido, porque para mí has sido un jefe de 10.

También quiero expresar mi gratitud a Graça Neves, Ermelinda Maçôas y Carla Santos, de la Universidad de Aveiro y el Instituto Superior Técnico de Lisboa, por acogerme durante tres meses y permitirme usar sus instalaciones para ampliar las posibles aplicaciones de nuestras moléculas. Tampoco me olvido de Patrizia, Nina y Luís, por hacerme sentir como en casa cuando estaba lejos de ella. Obrigada!

Durante todos estos años he tenido la suerte de conocer a personas maravillosas que han dejado una huella imborrable en mi vida. Cada uno de vosotros ha aportado algo único y especial en este camino. He tenido la suerte de encontrar a mis compañeros de laboratorio, quienes se convirtieron en amigos y confidentes en los días buenos y en los malos. Gracias por las charlas interminables, el apoyo incondicional y por compartir conmigo la pasión por la ciencia.

Siempre recordaré los primeros meses, en los que únicamente éramos Chus, Justo, Manu, Patri, Juan y yo contra el mundo. Chus, gracias por inspirarnos a todos cada día, por sacarnos una sonrisa con cada anécdota y por poder contar contigo cuando se necesita. Manu, no tengo palabras para describir lo importante que has sido para mí desde el primer día. Gracias por ser mi hermano y cuidarme, por escucharme y por estar ahí siempre que te he necesitado. Patri, no puedo estar más orgullosa de ti. Eres un ejemplo para todos y una científica de los pies a la cabeza. Juan, el favorito en la sombra, eres siempre un soplo de aire fresco. Tu alegría y forma de ver la vida hacen que los días malos no sean tan malos y los problemas no sean tan grandes.

El team bio nunca hubiera sido lo mismo sin Gema y Natalia. Gracias por confiar en mí y uniros a esta aventura. Gema, hemos estado codo con codo desde el principio. Gracias por ser mi gran apoyo desde el primer momento y estar ahí siempre que te he necesitado, no solo por ser mi compañera de glicofullerenos, sino también mi amiga. Natalia, me podré perder tu aventura, pero quiero que sepas que siempre vas a poder contar conmigo cuando lo necesites, aunque sé que eres más que capaz de llegar todo lo lejos que quieras.

Por supuesto, a los dos chicos que nos revolucionaron a todos cuando aparecieron. Arturín, me has enseñado lo que es una amistad de verdad, a valorarla y a cuidarla cada día. Nunca me cansaré de decirte lo agradecida que estoy de que estés en mi vida. Y sí, te quiero. Sergio, tu locura me alimenta el alma. Eres inspiración, siempre con una sonrisa y dispuesto a animarnos a todos. No cambies nunca, porque eres pura magia.

No me puedo olvidar de Jesusín, quien no daba un duro por su carrera científica y se va a convertir en un referente para todos. No puedo estar más orgullosa de ti. Gracias por ponerme los pies en la tierra siempre que es necesario. Por supuesto, tampoco me puedo olvidar de Jaime. Ojalá algún día tener la energía y la confianza que tienes en ti mismo. Que no se te agote nunca. Valeria, dejo en tus manos el poner firmes a las bestias. No dudo ni por un segundo que vas a conseguir todo lo que te propongas. Recuerda siempre: two towers. Alex, confío en que compartirás el cobre de las click

con los demás. Sé que, con lo bien amueblada que tienes la cabeza, cualquier obstáculo que encuentres lo vas a superar con creces.

A las nuevas promesas que toman el relevo que nosotros dejamos y vienen pisando tan fuerte que acabarán haciendo ruido: Marina, Gonzalo, Paula, Víctor, Jaime e Ibai. A las personas de IMDEA que, aunque estén en la tierra prometida, también se les recuerda: Jesús, Javi, Diego, Lorenzo, Jorge y Abbas. Por supuesto, a nuestros fotofísicos favoritos, los cuales te alegran los días siempre que les visitas: Antonio, Carlos y Sergio.

Salvo, Agus, José, Laura, Mª Ángeles, David y todos los miembros del grupo: gracias por haberme ayudado siempre que lo he necesitado y por formar parte de muchos de los momentos compartidos, tanto dentro como fuera del laboratorio. Sergio, Jon, Andrea, Román, Vero, Dani, Ya Jie, Tamara, Lucía, Marcos, Cristina, Manu y toda la gente del departamento que, desde el primer día, me acogieron como una más. Gracias por todos los recuerdos. A mis tutoras de la Autónoma de TFG y TFM, María Antonia Mendiola y Ana Mª Martín Castro, quienes dejaron rienda suelta a mi imaginación para que descubriera lo que era ser investigadora.

A Jorge, quien me ha acompañado durante el grado, el máster y hasta el doctorado. Gracias por ayudarme en todo momento; creo que sin ti no hubiera llegado hasta aquí. Parece que fue ayer cuando nos quedábamos horas en los pasillos de la facultad, y ahora pisarla se siente hasta extraño. Estoy muy orgullosa de ti y de hasta dónde has llegado. Por todas las risas, los momentos y los recuerdos. Sé el tremendo futuro que te espera, porque es lo que te mereces.

A mi familia, por aguantarme tanto en los días malos como en los buenos, por toda la paciencia que tienen y por quererme tal y como soy. A mis padres, quienes ya me dejaban experimentar en el bar lo que era mezclar cualquier cosa que me encontrara para hacer pócimas al estilo Harry Potter. Pero, sobre todo, a mi hermana: mi inspiración para estudiar química, la que siempre está dispuesta a hacer cualquier locura y mi mejor amiga. La alumna nunca superará a la maestra.

Y, aunque esto no sea muy frecuente, me voy a dar las gracias a mí, porque creo que también me lo merezco. Estos cinco años no solo han sido un aprendizaje a nivel científico; he aprendido de la vida, de las personas y de las experiencias. Estoy tremendamente orgullosa de la persona en la que me he convertido, de haber conseguido todo lo que me he propuesto y de haber llegado hasta aquí con la cabeza bien alta. Jenni, te lo mereces. Que nada ni nadie te quite nunca ese brillo que tienes.

Table of Contents

ABBREVIATIONS **1**
SUMMARY **7**
RESUMEN **15**
INTRODUCTION **23**
Nanomaterials and nanoscience 23
Carbon: the backbone of modern chemistry 25
[60-I_h]fullerene: structure, electronic properties and applications 27
1. CHAPTER 1 ..... **33**
1.1. Background **33**
1.1.1. Exohedral functionalization of [60]fullerene 33
1.1.2. Multiaddition reactions and addition patterns 36
1.1.3. [60]Fullerene derivatives for biomedical applications 39
1.1.3.1. Anticancer and photodynamic therapy applications 41
1.1.3.2. Contrast agents and bioimaging applications 43
1.1.3.3. Drugs and gene delivery applications 45
1.1.4. Multivalency: principles and features 47
1.1.4.1. Multivalent systems based on [60]fullerene 49
1.2. Objectives **57**
1.3. Results and discussion **59**
1.3.1. Synthesis of C_{60}-fullerene monoadducts 59
1.3.2. Synthesis of C_{60}-fullerene hexakis-adducts 61
1.3.3. Synthesis of glycofullerenes 65
1.3.3.1. Symmetric glycofullerenes 66
1.3.3.2. Asymmetric glycofullerenes and tridecafullerenes 70
1.3.4. Glycofullerenes biological studies 77
1.3.5. Boron-rich nanostructures based on [60]fullerene 85
1.3.6. Boron nanostructures biological studies 93
1.4. Conclusions **97**
2. CHAPTER 2 ..... **101**
2.1. Background **101**
2.1.1. The pigments of life 101
2.1.2. Structural, electronic and optical characteristics of porphyrins 102
2.1.3. Organic synthesis and coordination chemistry 104

2.1.4. Porphyrinoid-carbon nanostructure conjugates for biomedical applications 107
2.2. Objectives 113
2.3. Results and discussion 115
2.3.1. Glycoporphyrins 115
2.3.1.1. Synthesis of glycofullerenes 115
2.3.1.2. Synthesis of glycoporphyrins 117
2.3.1.3. Photophysical properties 122
2.3.1.4. Biological studies 124
2.3.2. Glycocorroles 127
2.3.2.1. Synthesis of corroles 127
2.3.2.2. Synthesis of glycofullerenes 130
2.3.2.3. Synthesis of glycocorroles 132
2.3.2.4. Photophysical properties 135
2.3.2.5. Biological studies 137
2.4. Conclusions 139
3. CHAPTER 3 143
3.1. Background 143
3.1.1. Polycyclic aromatic hydrocarbons 143
3.1.2. Main features of molecular nanographenes 144
3.1.3. Nanographenes for biomedical applications 148
3.2. Objectives 153
3.3. Results and discussion 155
3.3.1. Synthesis of a molecular nanographene 155
3.3.2. Synthesis of glycofullerenes 157
3.3.3. Glycofullerene-HBC derivatives 160
3.3.4. Photophysical properties 166
3.4. Conclusions 169
EXPERIMENTAL SECTION 173
APPENDIX 1. Chapter 1 247
APPENDIX 2. Chapter 2 253
APPENDIX 3. Chapter 3 263
REFERENCES 267

ABBREVIATIONS

2D	Bidimensional
Abs	Absorption
ACE2	Angiotensin-converting Enzyme 2
AFM	Atomic Force Microscopy
a-PDT	Antimicrobial Photodynamic Therapy
Ar	Aromatic
BNCT	Boron Neutron Capture Therapy
BTK	Bruton's Tyrosine Kinase
CDs	Carbon Dots
ConA	Concanavalin A
COSAN	Cobaltabisdicarbollide
COSY	COrrelated SpectroscopY
CRD	Carbohydrate Recognition Domain
CTV	Cyclotriveratrylene
CuAAC	Copper-catalyzed Azide-alkyne Cycloaddition
D	Diffusion Coefficient
DBPP	Dibenzo[fg,ij]phenanthro-[9,10,1,2,3-pqrst]pentaphene
DBU	1,8-Diazabicyclo[5.4.0]undec-7-ene
DCs	Dendritic Cells
DC-SIGN	Dendritic Cell-specific ICAM-3 Grabbing Non-integrin
DDQ	2,3-Dichloro-5,6-dicyano-1,4-benzoquinone
DEPT	Distortionless Enhancement by Polarization Transfer
DHE	Dihydroethidium, 2,7-diamino-10-ethyl-9-phenyl-9,10-dihydrophenanthridine
DLS	Dynamic Light Scattering
DMA	Dimethylantracene
DMAP	4-Dimethylaminopyridine
DMF	*N*,*N*-Dimethylformamide
DMSO	Dimethyl Sulfoxide
DNA	Deoxyribonucleic Acid
DODAB	Dimethyldioctadecylammonium Bromide
DOSY	Diffusion-Ordered SpectroscopY
DSPE-mPEG5000	Distearoylphosphatidylethanolamine-polyethylene glycol 5000
Em	Emission
ESI	Electrospray Ionization
FimH	Type 1 Fimbrin D-mannose Specific Adhesin
FT-IR	Fourier Transform Infrared Spectroscopy
Fuc	Fucose
Gal	Galactose
Gal-3	Galectin-3
Gal-3 FL	Galectin-3 Full Length
GlcNAc	*N*-Acetylglucosamine
Glu	Glucose
GLUT	Glucose Transporter

HBC	Hexa-*peri*-hexabenzocoronene
HPLC	High Performance Liquid Chromatography
HSQC	Heteronuclear Single Quantum Coherence
IC_{50}	Half-maximum Inhibitory Concentration
IPR	Isolated Pentagon Rule
ISC	Intersystem Crossing
ITC	Isothermal Titration Calorimetry
K_D	Dissociation Constant
LUMO	Lowest Unoccupied Molecular Orbital
MALDI-ToF	Matrix-Assisted Laser Desorption/Ionization-Time-of-Flight
Man	Mannose
MEFs	Mouse Embryonic Fibroblasts
MFI	Mean Fluorescence Intensity
MRI	Magnetic Resonance Imaging
MW	Molecular Weight
NaAsc	Sodium Ascorbate
NIR	Near-Infrared
NMR	Nuclear Magnetic Resonance
PAHs	Polycyclic Aromatic Hydrocarbons
PDT	Photodynamic Therapy
PEG	Polyethylen Glycol
PFG	^{1}H NMR Pulsed-fieldgradient
PPQ-*b*-PS	Poly(phenylquinoline)-*block*-polystyrene
PS	Photosensitizer
PTT	Photothermal Therapy
PVP	Polyvinylpyrrolidone
py	Pyridine
r.t.	Room Temperature
R_H	Hydrodynamic Radius
RNA	Ribonucleic Acid
ROS	Reactive Oxygen Species
RSL	Ralstonia Solanacearum Lectin
SEC	Size Exclusion Chromatography
SEM	Scanning Electron Microscopy
S_N2	Bimolecular Nucleophilic Substitution
S_NAr	Nucleophilic Aromatic Substitution
SPAAC	Strain-Promoted Azide-Alkyne Cycloaddition
STM	Scanning Tunneling Microscopy
SWCNT	Single-walled Carbon Nanotubes
TBAF	Tetrabutylammonium Fluoride
***t*Bu**	*Tert*-butyl
TEG	Triethylen Glycol
TEM	Transmission Electron Microscopy
TFA	Trifluoroacetic Acid
THF	Tetrahydrofuran

TLC	Thin Layer Chromatography
TMS	Trimethylsilyl
TPP	Tetraphenylporphyrin
UV-Vis	Ultraviolet-visible
WT	Wild Type
δ	Chemical Shift
ε	Molar Absorption Coefficient
λ	Wavelength
μW	Microwave
ν	Stretching Vibration
Φ_F	Emission Quantum Yield
Φ_Δ	Singlet Oxygen Quantum Yield

Summary

SUMMARY

Chapter 1

[60]fullerene is the third carbon allotrope with exceptional electron-accepting properties and a highly strained π-system. Due to its unique structure, this carbon-based nanostructure readily undergoes exohedral functionalization through addition reactions that relieve strain and expand its utility in materials science and biomedicine. Among these, cycloaddition reactions such as the **Bingel-Hirsch [2+1] cyclopropanation** and **Prato [3+2] cycloaddition** have emerged as key methods to incorporate functional moieties onto the fullerene sphere. However, pristine **[60]fullerene** is highly hydrophobic and insoluble in aqueous media, which limits its direct use in biological systems. The covalent exohedral functionalization has enabled the development of **water-soluble fullerene derivatives** with promising applications in anticancer therapy, drug delivery, photodynamic therapy, bioimaging and gene delivery, among others. The multivalent presentation of bioactive ligands on the fullerene scaffold mimics the architecture of several pathogens, affording remarkable biological applications. These findings underscore the potential of **glycofullerenes** targeting lectin-mediated pathways.

Overall, this chapter highlights the potential of **[60]fullerene** derivatives as multifunctional nanoplatforms for advanced **biomedical applications**. The synthesis of monoadducts and hexakis-adducts of [60]fullerene was successfully achieved *via* Bingel-Hirsch reactions under kinetic and thermodynamic control, respectively. The strategic incorporation of terminal alkyne functionalities into the fullerene framework enabled subsequent modular diversification through **copper(I)-catalyzed azide-alkyne cycloaddition** reactions. This reaction is a versatile tool that enables the efficient and selective coupling of molecular fragments under mild conditions, facilitating the synthesis of complex conjugates in a single step. This highly efficient and orthogonal approach allowed for the precise attachment of hydrophilic carbohydrates and boron-rich clusters, expanding the chemical potential utility of these nanoconjugates in bioactive environments.

Biological evaluations demonstrated that glycofullerenes functionalized with mono-, di- and trisaccharides exhibited potent antiviral activity by targeting C-type lectins such as **DC-SIGN** (Dendritic Cell-Specific ICAM-3 Grabbing Non-integrin), which is implicated in **SARS-CoV-2** trans-infection. Monosaccharide-functionalized fullerenes achieved moderate inhibition (~59%), while disaccharide and trisaccharide derivatives reached 93-95% inhibition. **Tridecafullerenes**, consisting of 13 fullerene units and 120 carbohydrate moieties, showed an exceptional multivalent effect, reducing viral transfer to negligible levels (0.0001% infected cells). NMR titrations of the DC-SIGN carbohydrate recognition domain in the presence of glycofullerenes revealed significant chemical shift perturbations, thus confirming affinity binding within the canonical binding site. Galactose-functionalized glycofullerenes also

exhibited strong interactions with **Galectin-3**, enhancing binding affinity from millimolar (monovalent ligands) to low micromolar (multivalent systems) as measured by ITC.

Additionally, boron-rich fullerene nanostructures incorporating $[B_{12}H_{12}]^{2-}$ and **COSAN** clusters hold promises as candidates for **Boron Neutron Capture Therapy** due to their high boron content. Despite their insolubility in aqueous media, encapsulation in fluorescently labeled liposomes has allowed its cell internalization and their monitoring by confocal microscopy.

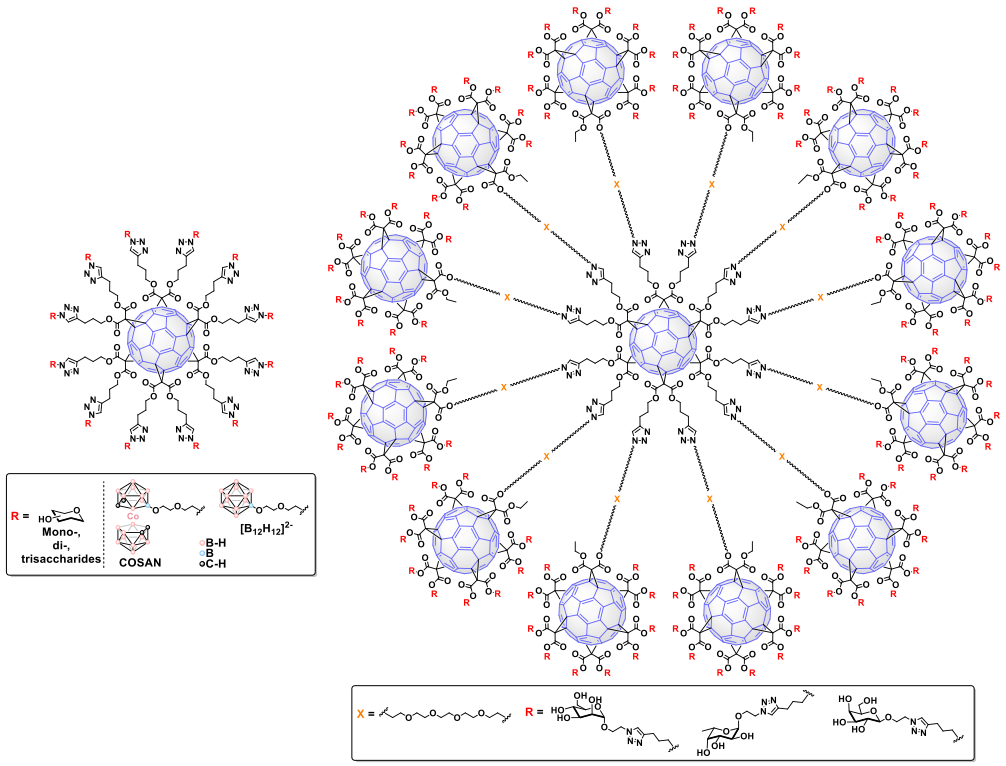

Chapter 2

Porphyrins play key roles in nature, including heme in hemoglobin and chlorophyll in photosynthesis. Their unique structural and photophysical properties, including intense absorption and strong **fluorescence emission**, have positioned them as excellent candidates for photodynamic therapy, bioimaging and anticancer strategies. However, challenges such as hydrophobicity, aggregation and limited photostability have driven the development of new conjugates like those based on **carbon nanostructures**. These hybrids exhibit improved solubility, stability and cellular internalization, enabling their use as **photosensitizers**.

One of the main drawbacks to evaluate the cellular internalization of **glycofullerenes** is their **lack of intrinsic fluorescence**, which prevents monitoring by techniques such as confocal microscopy. To address this limitation, *Chapter 2* focuses on coupling

fluorescent platforms, including porphyrins and corroles, to glycofullerenes functionalized with different carbohydrates. Both porphyrinoid scaffolds were first modified with terminal alkynes and subsequently conjugated to glycofullerenes *via* a click reaction.

Asymmetric **mannose-functionalized glycofullerenes** were covalently attached to **Zn(II) porphyrin scaffolds** through click chemistry reactions, yielding tetra- and octa-substituted glycoporphyrins (**52a-c** and **53a-c**) decorated with up to 80 carbohydrate units *per* molecule. Photophysical studies demonstrated characteristic Soret absorption (~436 nm) and **fluorescence emission**, with minor quenching in intensity due to the bound glycofullerenes. Importantly, reactive oxygen species evaluation revealed **superoxide anion generation** (Type I photosensitizers), highlighting their potential for treating hypoxic tumors.

Biological assays demonstrated potent antiviral activity against **SARS-CoV-2** trans-infection *via* DC-SIGN receptor inhibition. At 1 μM concentration, compound **52b** exhibited **90% inhibition**, while **53b** achieved 61% inhibition. The fluorescence emission of the molecules allowed to see their interaction with the receptor by confocal microscopy as well as the selective receptor-mediated internalization of **52b** in Jurkat cells modified with DC-SIGN. Moreover, flow cytometry showed dose-dependent competition between **52b** and SARS-CoV-2 spike protein for DC-SIGN binding. Additional NMR experiments and molecular dynamics simulations confirmed high-affinity interaction (K_D ~ 1.26 μM) of the product with the canonical carbohydrate recognition site.

Building on the glucose uptake pathways exploited by cancer cells, **glucose-functionalized glycofullerenes** were conjugated to **Ga(III) corrole scaffolds** *via* click chemistry. This approach resulted in one derivative bearing a single glycofullerene unit (**64**) and another incorporating three glycofullerenes (**65**). Photophysical characterization revealed a prominent Soret band at ~425 nm and two emission peaks at ~610 and ~660 nm. While compound **64** exhibited a **high singlet oxygen quantum yield**, this value was markedly reduced in **65**, likely due to quenching effects from the increased number of glycofullerene units. Cytotoxicity and phototoxicity assays in HeLa cells demonstrated that glycocorrole **64** was **non-toxic** in the absence of light but triggered substantial cell death under blue light irradiation, even at submicromolar concentrations. Confocal microscopy confirmed enhanced cellular uptake of **64** compared to its parent corrole, suggesting glucose-receptor mediated internalization. In contrast, **65** showed diminished phototoxicity, consistent with its lower capacity for ROS generation.

Building on these concepts, this chapter describes the design and synthesis of biocompatible **glycofullerene-porphyrinoid** conjugates with tailored carbohydrate valency and fluorescence emission, paving the way for their application in **antiviral therapy** and **cancer phototherapy**.

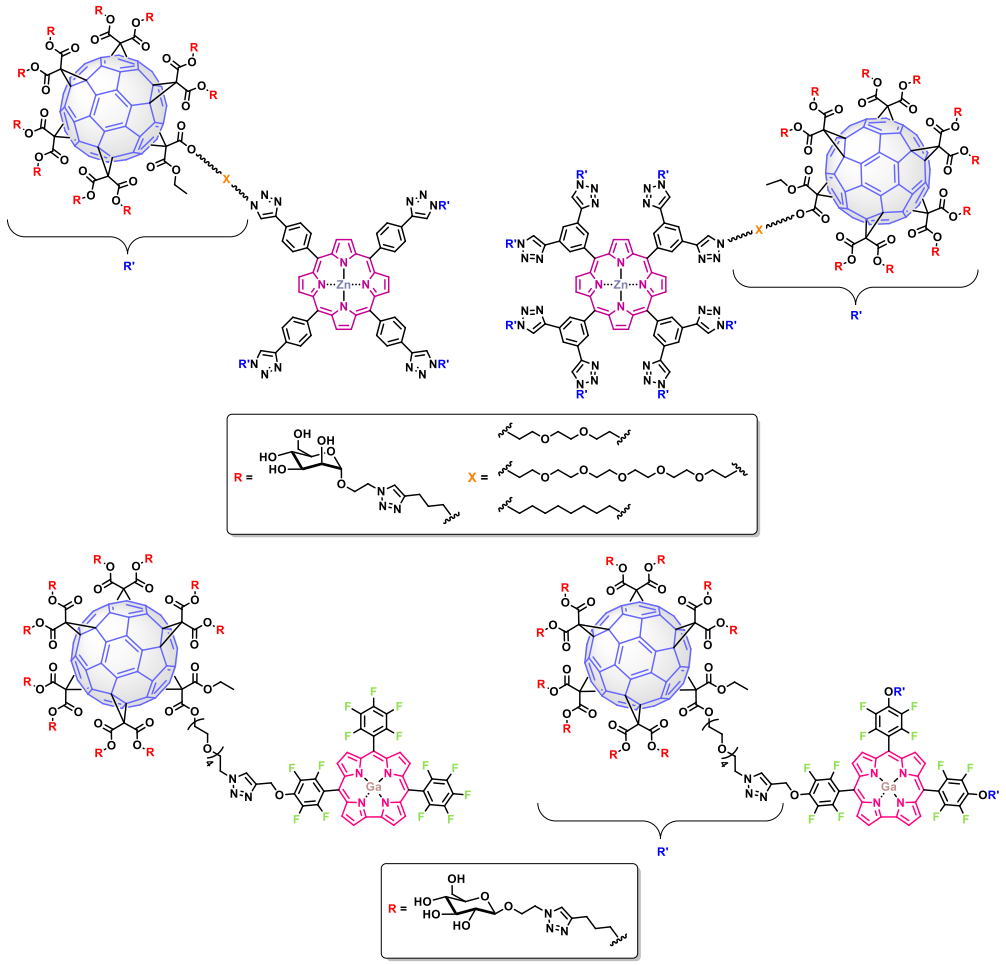

Chapter 3

Molecular nanographenes, monodisperse graphene fragments, exhibit strong light absorption, tunable optoelectronic properties and efficient reactive oxygen species generation. These features position nanographenes as promising candidates for photodynamic therapy, bioimaging and theranostics. However, their **poor aqueous solubility** and tendency to aggregate remain key challenges for biological applications. To address these limitations, strategies involving the introduction of different substituents and curvature to the nanographene core have been employed, reducing aggregation and enhancing solubility. Recent advances include the development of warped nanographenes functionalized with polyether chains and charged nanographene derivatives for improved water dispersibility and biocompatibility, demonstrating potent anticancer effects.

In *Chapter 3*, **water-soluble nanographene** derivatives based on hexa-*peri*-hexabenzocoronene (HBC) were synthesized *via* a multi-step strategy involving Sonogashira cross-coupling, Diels-Alder cycloaddition and Scholl cyclodehydrogenation. The terminal alkyne introduced in the nanographene scaffold

allowed for further click reactions with **glycofullerenes**, yielding amphiphilic conjugates **80a-b**, each bearing two HBC units, and **81**, which incorporates a single HBC moiety.

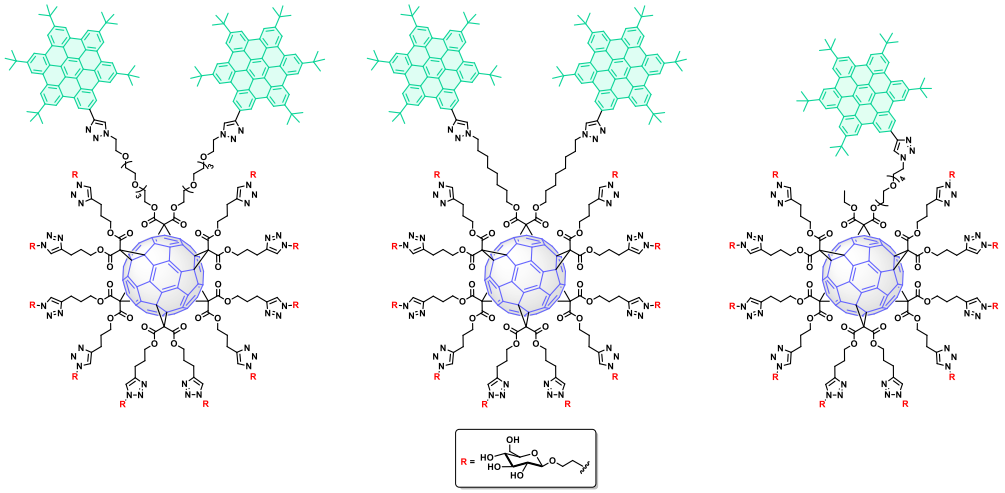

Dynamic light scattering and transmission electron microscopy revealed that these conjugates self-assemble in aqueous media into nanostructures ranging from **quasi-spherical aggregates to elongated fibrillar assemblies**, depending on the number of HBC units *per* molecule.

Photophysical characterization showed that the conjugates retained the characteristic absorption profile of the HBC core. Fluorescence emission was observed in DMSO, while it was almost completely quenched in water, probably attributed to aggregation-induced non-radiative relaxation processes. Despite this, all compounds exhibited **high singlet oxygen quantum yields** ($\Phi_\Delta > 50\%$) in DMSO, highlighting their potential as Type II photosensitizers.

Together, these findings demonstrate the potential of glycofullerene-HBC conjugates as amphiphilic nanoplatforms combining reactive oxygen species generation, fluorescence imaging capability and self-assembly properties, paving the way for their use in PDT and bioimaging applications.

Resumen

RESUMEN

Capítulo 1

El **[60]fullereno** es la tercera forma alotrópica del carbono, caracterizada por sus excepcionales propiedades aceptoras de electrones y un sistema π altamente tensionado. Debido a su estructura única, la superficie del C_{60} puede funcionalizarse mediante reacciones de adición que alivian esta tensión. Esta estrategia conduce a una amplia gama de derivados con utilidad en ciencia de materiales y biomedicina. Entre estas reacciones, las cicloadiciones como la **ciclopropanación de Bingel-Hirsch [2+1]** y la **cicloadición de Prato [3+2]**, han surgido como métodos clave para incorporar grupos funcionales sobre la superficie esférica del fullereno. Sin embargo, el **[60]fullereno** es hidrofóbico e insoluble en medios acuosos, lo que limita su uso directo en sistemas biológicos. Por ello, la funcionalización covalente ha permitido el desarrollo de **derivados de fullereno solubles en agua** con resultados prometedores en terapia anticancerígena, liberación de fármacos, terapia fotodinámica, bioimagen y terapia génica, entre otras. La presentación multivalente de ligandos bioactivos sobre el fullereno permite imitar la superficie de diversos patógenos, lo que posibilita nuevas aplicaciones biológicas. Estos hallazgos subrayan el potencial que tienen los **glicofullerenos** en el diseño de sistemas con afinidad por lectinas.

En conjunto, este capítulo resalta el potencial de los derivados de **[60]fullereno** como nanoplataformas multifuncionales para **aplicaciones biomédicas**. La síntesis de monoaductos y hexaaductos de [60]fullereno se logró mediante reacciones de Bingel-Hirsch bajo control cinético y termodinámico, respectivamente. La incorporación estratégica de grupos alquino terminales sobre la estructura del fullereno, permite posteriores reacciones de **cicloadición azida-alquino catalizadas por cobre(I)**. Esta reacción es una herramienta versátil que permite unir fragmentos moleculares de forma eficiente, selectiva y en condiciones suaves, facilitando la síntesis de sistemas complejos en una única etapa. Este enfoque ortogonal y altamente eficiente permitió la incorporación de carbohidratos hidrófilos y sistemas ricos en boro, ampliando la potencial utilidad de estos nanoconjugados en entornos bioactivos.

Los ensayos biológicos demostraron que los glicofullerenos funcionalizados con mono-, di- y trisacáridos exhibieron una potente actividad antiviral, atribuida a su afinidad por lectinas tipo C como el receptor **DC-SIGN** (Dendritic Cell-Specific ICAM-3 Grabbing Non-integrin). Los fullerenos funcionalizados con monosacáridos lograron una inhibición moderada de la trans-infección del SARS-CoV-2 (~59%), mientras que los derivados con disacáridos y trisacáridos alcanzaron inhibiciones del 93-95%. Los **tridecafullerenos**, compuestos formados por 13 unidades de fullereno y 120 carbohidratos, mostraron un efecto multivalente excepcional, reduciendo la transferencia viral a niveles mínimos (0,0001% de células infectadas). Los ensayos por RMN sobre la interacción de los glicofullerenos con el dominio de reconocimiento de carbohidratos del DC-SIGN revelaron perturbaciones químicas significativas.

Estas perturbaciones señalan la región de interacción, coincidiendo con el sitio canónico del receptor. Por otro lado, glicofullerenos funcionalizados con galactosa también exhibieron fuertes interacciones con la **Galectina-3**, mejorando la afinidad de unión de valores milimolares (ligandos monovalentes) a valores submicromolares (sistemas multivalentes), según las mediciones por ITC.

Además, se prepararon nanoestructuras de fullereno ricas en boro incorporando los clústers **$[B_{12}H_{12}]^{2-}$** y **COSAN**. Estos híbridos se estudian como prometedores candidatos para la **Terapia de Captura de Neutrones por Boro** gracias a su elevado contenido en boro. A pesar de su baja solubilidad en medios acuosos, la encapsulación en liposomas con marcadores fluorescentes ha permitido estudiar su internalización en células y su monitorización mediante microscopía confocal.

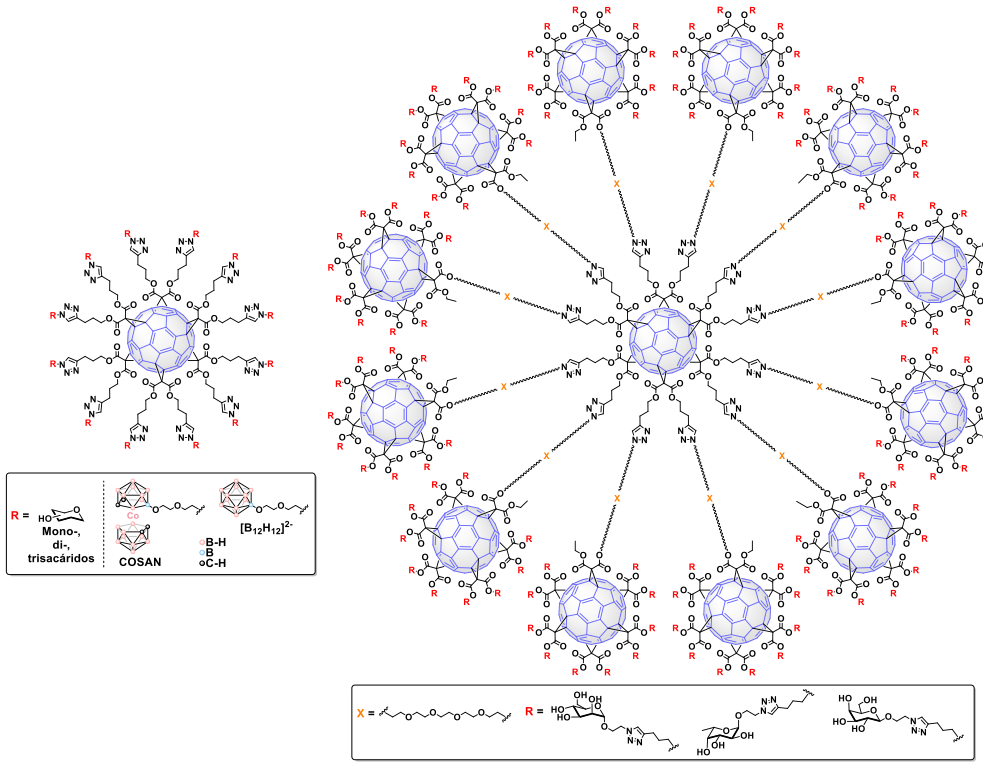

Capítulo 2

Las **porfirinas** desempeñan papeles clave en la naturaleza, con ejemplos destacados como el grupo hemo en la hemoglobina y la clorofila en la fotosíntesis. Sus propiedades estructurales y fotofísicas únicas, que incluyen una intensa absorción y una fuerte emisión de fluorescencia, las han posicionado como excelentes candidatas en áreas como la **terapia fotodinámica** y en bioimagen. Sin embargo, desafíos como la **hidrofobicidad**, la agregación y su limitada fotoestabilidad han impulsado el desarrollo de nuevos conjugados como los basados en **nanoestructuras de carbono**. Estos híbridos presentan una mejor solubilidad, estabilidad e internalización celular, lo que permite su uso como **fotosensibilizadores**.

Uno de los principales desafíos en la síntesis de glicofullerenos y en la evaluación de su internalización en sistemas biológicos es la falta de fluorescencia, lo que impide su seguimiento mediante técnicas como la microscopía confocal. Para abordar esta limitación, el *Capítulo 2* se centra en el acoplamiento de plataformas fluorescentes, como porfirinas y corroles, a glicofullerenos funcionalizados con diversos carbohidratos. Ambos porfirinoides fueron modificados previamente con grupos alquino terminales y posteriormente conjugados a los glicofullerenos mediante reacciones de tipo click.

Los **glicofullerenos asimétricos funcionalizados con manosa** se unieron covalentemente a **porfirinas de Zn(II)** mediante reacciones de click, dando lugar a glicoporfirinas tetra- y octa-sustituidas (**52a-c** y **53a-c**) decoradas con hasta 80 unidades de carbohidratos por molécula. Los estudios fotofísicos mostraron la característica absorción en la banda de Soret (~436 nm) y **emisión de fluorescencia**, con una leve disminución en la intensidad debido a la presencia de los glicofullerenos. Además, la evaluación de la formación de especies reactivas de oxígeno reveló la generación de **aniones superóxido** (fotosensibilizadores de Tipo I), destacando su potencial para el tratamiento de tumores hipóxicos.

Los **ensayos biológicos** mostraron una potente actividad antiviral contra la trans-infección del **SARS-CoV-2** mediada por el receptor DC-SIGN. A una concentración de 1 μM, el compuesto **52b** mostró una **inhibición del 90%**, mientras que **53b** alcanzó un 61%. La emisión fluorescente de las moléculas permitió confirmar su interacción con el receptor mediante microscopía confocal, así como la internalización de **52b** en células Jurkat modificadas con DC-SIGN. Además, la citometría de flujo evidenció una competencia dosis-dependiente entre **52b** y la proteína spike del SARS-CoV-2 por la unión al DC-SIGN. Experimentos adicionales de RMN y simulaciones de dinámica molecular confirmaron una alta afinidad (K_D ~ 1.26 μM) de los productos con el sitio canónico de reconocimiento de carbohidratos del receptor.

Aprovechando las rutas de captación de glucosa utilizadas por las células cancerígenas, se sintetizaron **glicofullerenos funcionalizados con glucosa** conjugados a **corroles de Ga(III)** mediante reacciones tipo click, obteniéndose un derivado con una única unidad de glicofullereno (**64**) y otro con tres unidades (**65**). La caracterización fotofísica mostró una prominente banda Soret a ~425 nm y dos máximos de emisión a ~610 y ~660 nm. Mientras que el compuesto **64** presentó un alto rendimiento cuántico de producción de **oxígeno singlete**, este valor se redujo notablemente en **65**, probablemente debido al mayor número de unidades de glicofullereno. Los ensayos de citotoxicidad y fototoxicidad en células HeLa demostraron que el conjugado glicofullereno-corrol **64 no** era **tóxico** en ausencia de luz, pero bajo irradiación con luz azul desencadenaba la muerte celular, incluso a concentraciones submicromolares. La microscopía confocal confirmó una mayor internalización celular de **64** en comparación con el corrol de partida, sugiriendo un

mecanismo de internalización mediado por glucosa. Sin embargo, **65** mostró una fototoxicidad reducida, consistente con su menor capacidad para generar especies reactivas de oxígeno.

Basándonos en estos conceptos, este capítulo describe el diseño y la síntesis de conjugados de **glicofullereno-porfirinoides** biocompatibles con diferente número de carbohidratos y emisión fluorescente, abriendo el camino para su aplicación en **terapia antiviral** y **fototerapia contra el cáncer**.

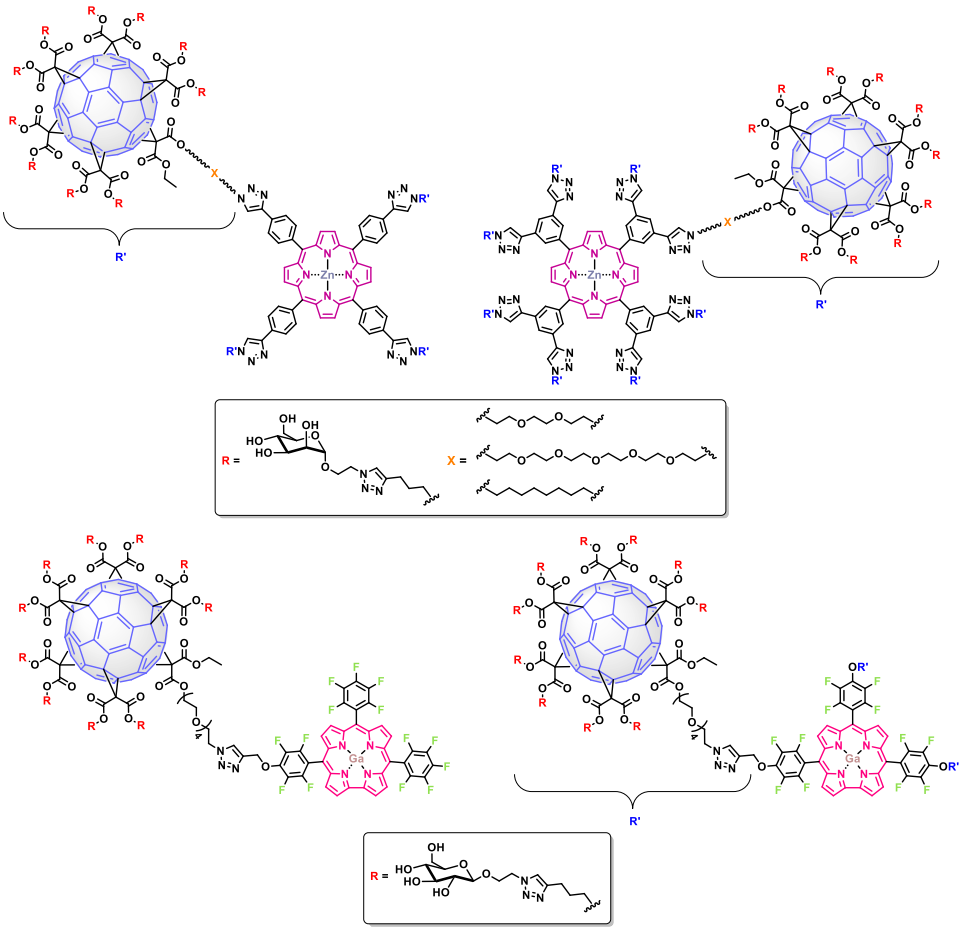

Capítulo 3

Los **nanografenos moleculares**, fragmentos monodispersos de grafeno, presentan una intensa absorción de luz, propiedades optoelectrónicas modulables y una eficiente generación de especies reactivas de oxígeno. Estas características posicionan a los nanografenos como candidatos prometedores para terapia fotodinámica, bioimagen y aplicaciones teranósticas. Sin embargo, su **baja solubilidad en medios acuosos** y la tendencia a agregarse siguen siendo desafíos clave para su uso en aplicaciones biológicas. Para superar estas limitaciones, se han empleado estrategias como la introducción de diferentes sustituyentes y la inducción de curvatura en el nanografeno,

lo que reduce la agregación y mejora la solubilidad. Los avances más recientes incluyen el desarrollo de nanografenos curvados funcionalizados con cadenas de poliéter y derivados iónicos para una mayor solubilidad en agua y biocompatibilidad, demostrando potentes efectos anticancerígenos.

En el *Capítulo 3* se describe la síntesis de **nanografenos solubles en agua** basados en el hexa-*peri*-hexabenzocoroneno (HBC) mediante una estrategia que incluye acoplamientos cruzados de Sonogashira, cicloadición de Diels-Alder y ciclodeshidrogenación de Scholl. El alquino terminal introducido en el HBC permitió realizar reacciones tipo click con **glicofullerenos**, dando lugar a los conjugados anfifílicos **80a-b**, los cuales contienen dos unidades de HBC, y **81**, al cual se incorporó un único HBC.

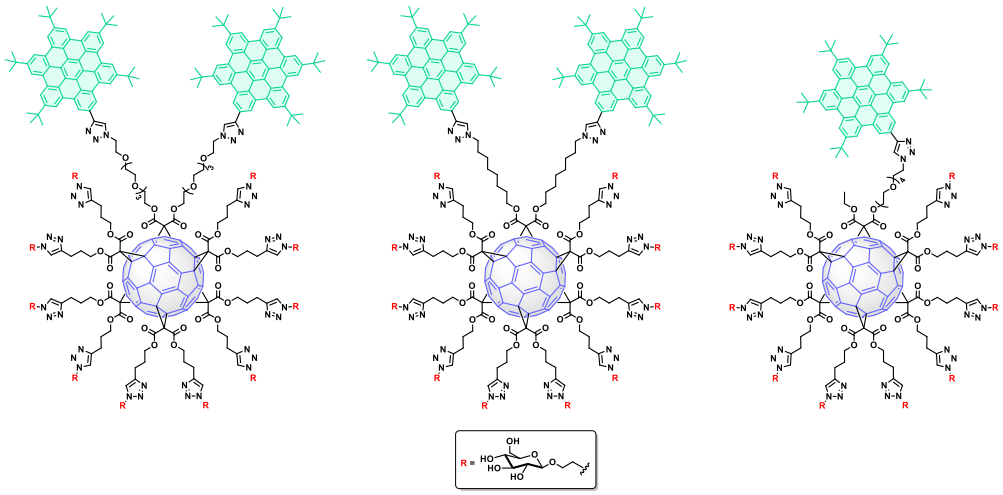

Los estudios de dispersión dinámica de luz y microscopía electrónica de transmisión revelaron que estos conjugados se autoensamblan en medios acuosos formando nanoestructuras que van desde **agregados cuasi-esféricos** hasta **ensamblajes alargados tipo fibra**, dependiendo del número de unidades HBC por molécula.

La caracterización fotofísica mostró que los conjugados conservan el perfil de absorción característico del HBC. Se observó emisión de fluorescencia en DMSO, mientras que en agua esta se encontraba casi completamente apagada, probablemente debido a procesos de relajación no radiativos inducidos por la agregación. A pesar de ello, todos los compuestos exhibieron **elevados rendimientos cuánticos de producción de oxígeno singlete** ($\Phi_\Delta > 50\%$) en DMSO, lo que destaca su potencial como fotosensibilizadores tipo II.

En conjunto, estos hallazgos demuestran el potencial de los conjugados glicofullereno-HBC como nanoplataformas anfifílicas que combinan generación de especies reactivas de oxígeno, emisión fluorescente y autoensamblaje, abriendo el camino para su uso en terapia fotodinámica y aplicaciones en bioimagen.

Introduction

INTRODUCTION

Nanomaterials and nanoscience

Materials at the nanoscale, ranging from 1 to 100 nanometers, exhibit physical, chemical and biological properties that differ drastically from their macroscopic counterparts (Figure 1). They have demonstrated unique and surprising behaviors, such as enhanced electrical conductivity, unusual optical properties, increased chemical reactivity and changes in mechanical strength. These distinctive characteristics have made nanoscience one of the most dynamic and promising areas of modern research.[1]

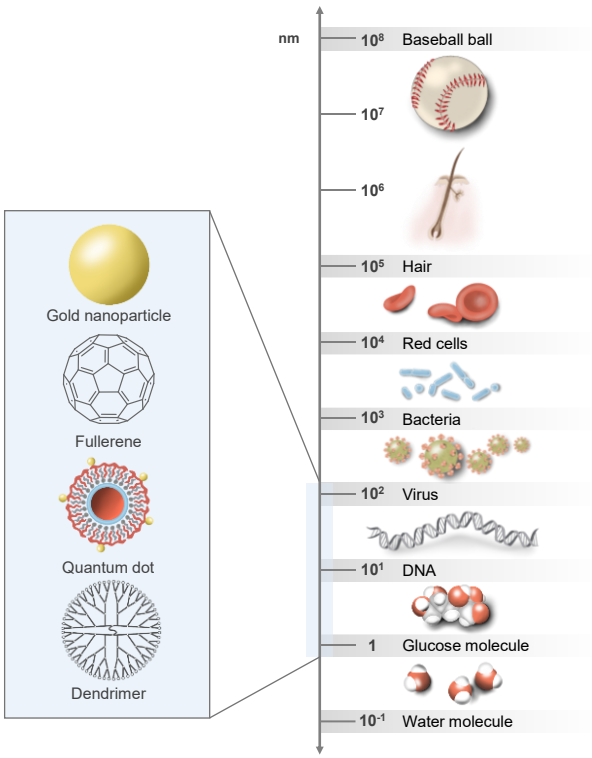

Figure 1. Comparison of different sizes of nanoparticles and biomolecules.

In 1959, physicist Richard Feynman presented a revolutionary vision in his talk *There's Plenty of Room at the Bottom*.[2] He envisioned the possibility of manipulating atoms and molecules to build tailored structures and devices. While Feynman spoke in conceptual terms, his ideas became an intellectual catalyst for the subsequent development of tools and theories.

[1] a) S. Bayda, M. Adeel, T. Tuccinardi, M. Cordani, F. Rizzolio, *Molecules* **2020**, *25*, 112. b) G. A. Mansoori, T. A. F. Soelaiman, *J. ASTM Int.* **2005**, *2*, 1.
[2] R. P. Feynman, *Eng. Sci.* **1960**, *23*, 22.

Practical progress toward the nanoscale took a major leap in the 1980s with the invention of the Scanning Tunneling Microscope (STM) by Gerd Binnig and Heinrich Rohrer, who received the Nobel Prize in Physics in 1986 for this achievement.[3] This technique made possible to observe and manipulate individual atoms for the first time, marking the beginning of experimental nanoscience.

Since then, nanoscience has advanced rapidly, driven by the integration of physics, chemistry, biology and engineering. Today, research at the nanoscale has led to innovations in fields such as medicine, with the development of nanoparticles for drug delivery;[4] electronics, with smaller and faster transistors;[5] and energy, with more efficient solar cells.[6]

Nanomaterials can be classified based on several criteria, with structural composition and dimensionality being the main ones.[7]

According to their structural composition, nanomaterials can be divided into different categories: organic nanomaterials, composed of organic molecules such as polymers, dendrimers and liposomes, widely used in biomedical applications due to their biocompatibility;[8] inorganic nanomaterials, which include metallic nanoparticles (e.g., gold, silver or iron oxide) and non-metallic ones (e.g., silica or ceramics), known for their mechanical, optical and catalytic properties and biomedical applications;[9] carbon-based nanomaterials, such as carbon nanotubes, fullerenes and graphene, renowned for their exceptional strength, conductivity, and versatility;[10] and composites or hybrids, which combine organic and inorganic materials to achieve specific and synergistic properties, making them ideal for advanced applications in energy, the environment and technology, among others.[11]

Regarding the classification based on their dimensionality, four categories can be found: zero-dimensional nanomaterials where all three dimensions are confined to the nanoscale; one-dimensional nanomaterials that present one dimension outside the

[3] G. Binnig, H. Rohrer, C. Gerber, E. Weibel, *Phys. Rev. Lett.* **1982**, *49*, 57.
[4] M. J. Mitchell, M. M. Billingsley, R. M. Haley, M. E. Wechsler, N. A. Peppas, R. Langer, *Nat. Rev. Drug. Discov.* **2021**, *20*, 101.
[5] Z. He, Z. Zhang, S. Bi, *Mater. Res. Express* **2020**, *7*, 012004.
[6] a) A. A. İnada, S. Arman, B. Safaei, *J. Energy Storage*, **2022**, *55*, 105661. b) N. Martín, *Adv. Energy Mater.* **2017**, *7*, 1601102.
[7] B. Mekuye, B. Abera, *Nano Select* **2023**, *4*, 486.
[8] a) C. C. Lee, J. A. MacKay, J. M. J. Fréchet, F. C. Szoka, *Nat. Biotechnol*. **2005**, *12*, 1517. b) K. J. Harrington, S. Mohammadtaghi, P. S. Uster, D. Glass, A. M. Peters, R. G. Vile, J. S. Stewart, *Clin. Cancer Res.* **2001**, *7*, 243.
[9] a) B. Klębowski, J. Depciuch, M. Parlińska-Wojtan, J. Baran, *Int. J. Mol. Sci.* **2018**, *19*, 4031. b) G. Singh, J. L. Z. Ddungu, N. Licciardello, R. Bergmann, L. De Cola, H. Stephan, *Faraday Discuss.* **2020**, *222*, 362.
[10] a) A. Muñoz, D. Sigwalt, B. M. Illescas, J. Luczkowiak, L. Rodríguez-Pérez, I. Nierengarten, M. Holler, J. S. Remy, K. Buffet, S. P. Vincent, J. Rojo, R. Delgado, J.-F. Nierengarten, N. Martín, *Nat. Chem.* **2016**, *8*, 50. b) M. Sbacchi, M. Mamone, L. Morbiato, P. Gobbo, G. Filippini, M. Prato, *ChemCatChem* **2023**, *15*, e202300667.
[11] a) S. Merino, C. Martín, K. Kostarelos, M. Prato, E. Vázquez, *ACS Nano* **2015**, *9*, 4686. b) S. Bolisetty, R. Mezzenga, *Nat. Nanotechnol.* **2016**, *11*, 365.

nanoscale, while the other two dimensions are confined; two-dimensional nanomaterials that have plate-like shapes with two dimensions outside the nanometer range, but one is at the nanoscale; and three-dimensional nanomaterials where no dimension is strictly confined to the nanoscale, but its internal structure is made up of individual blocks at the nanometer scale.

The methods for obtaining these nanomaterials depend mainly on the material and the applications to be given. However, over the past decades, chemical methods for their fabrication have significantly advanced, enabling precise control over their size, shape, and consequently, their properties.

In general, the methods used for the synthesis of nanomaterials can be classified based on two approaches: top-down and bottom-up.[12] The top-down approach allows obtaining nanomaterials from large-scale materials by reducing their size to the nanoscale. Alternatively, bottom-up approach involves the synthesis of nanomaterials from simple precursors, such as atoms or molecules, through controlled reactions where their self-assembly allows the creation of nanostructures (Figure 2).

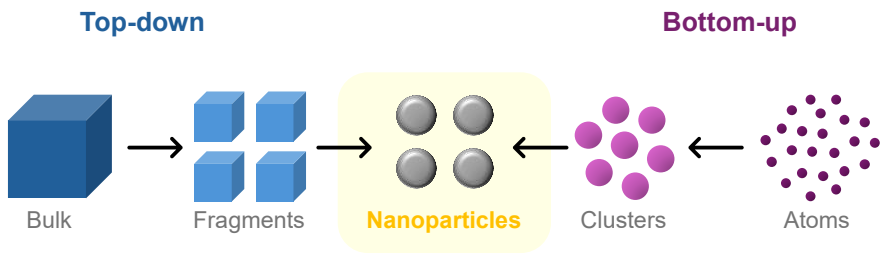

Figure 2. Scheme of the synthesis of nanoparticles *via* top-down and bottom-up approaches.

The future prospects of nanoscience and nanomaterials promise revolutionary transformations across multiple fields. In medicine, the development of targeted nanoparticles will enable more effective treatments and precise diagnostics, while in energy, nanomaterials will enhance the efficiency of batteries, solar panels and energy storage systems. Additionally, their integration with technologies such as artificial intelligence will accelerate the design of innovative materials, while environmental applications, including water purification and carbon capture, will help mitigate climate change.

Carbon: the backbone of modern chemistry

Carbon, the sixth element on the periodic table and the second most abundant element in the human body, forms the basis of the chemistry of life. Its use dates back to prehistoric times when it was used as fuel and to create black pigments in cave paintings. However, it was not until 17th century when it was identified as an element.

[12] N. Abid, A. M. Khan, S. Shujait, K. Chaudhary, M. Ikram, M. Imran, J. Haider, M. Khan, Q. Khan, M. Maqbool, *Adv. Colloid Interface Sci.* **2022**, *300*, 102597.

Shortly after, in 1789, Antoine Lavoisier included it in the list of essential chemical elements in his textbook *Traité Élémentaire de Chimie*.[13]

Its tetravalence and ability to form stable bonds with a wide range of elements, including itself, make carbon the basis of organic chemistry and a key component of living and nonliving matter. Carbon's versatility not only defines its chemical diversity, but also underscores its importance for life, technology and future innovation.

One of the most fascinating characteristics of this element is its ability to form different structures, known as allotropes. Until 1985, only two allotropes of carbon were known, graphite and diamond. However, that year marked the discovery of the third allotropic form of carbon: fullerenes.[14] Since then, other carbon nanoforms have emerged, such as carbon nanotubes in 1991 by Sumio Iijima,[15] carbon nanodots in 2004 by Xiaoyou Xu,[16] or graphene, also discovered in 2004 by Andre Geim and Konstantin Novoselov,[17] among others (Figure 3). The latter allowed its discoverers to win the Nobel Prize in Physics in 2010 *for groundbreaking experiments regarding the two-dimensional material graphene*.

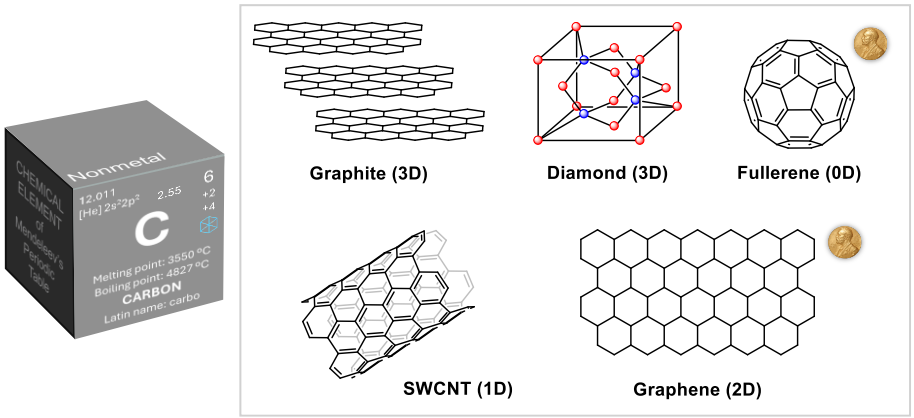

Figure 3. Chemical structures of the main carbon nanoforms.

Carbon has been crucial to humanity's development from ancient times, powering early energy use and technologies, to its central role in the Industrial Revolution. Today, its importance extends into the future, with carbon nanomaterials heralding a new technological era. These materials promise to revolutionize fields such as electronics, renewable energy and medicine, proving the key for tomorrow's innovations.

[13] A.-L. de Lavoisier, Ed. *Traité Élémentaire de Chimie*, Chez Cuchet, Paris, **1789**.
[14] H. W. Kroto, J. R. Heath, S. C. O'Brien, R. F. Curl, R. E. Smalley, *Nature* **1985**, *318*, 162.
[15] S. Iijima, *Nature* **1991**, *354*, 56.
[16] X. Xu, R. Ray, Y. Gu, H. J. Ploehn, L. Gearheart, K. Raker, W. A. Scrivens, *J. Am. Chem. Soc.* **2004**, *126*, 12736.
[17] K. S. Novoselov, A. K. Geim, S. V. Morozov, D. Jiang, Y. Zhang, S. V. Dubonos, I. V. Grigorieva, A. A. Fisov, *Science* **2004**, *306*, 666.

Besides [60]fullerene, which will be the central focus of this doctoral thesis, there are a wide variety of carbon-based nanomaterials known to date, and all of them have unique properties and diverse applications,[18] some examples are: **carbon nanotubes**, that exhibit photoluminescent properties and have demonstrated applications as multifunctional coating materials, hydrogen storage or chemical sensors;[19] **graphene** presents high thermal and electrical conductivity, transparency and a substantial specific surface area, making it suitable for applications in batteries, sensors or transistors;[20] **carbon quantum dots**, discovered during the separation and purification of single-walled carbon nanotubes, are also notable for their fluorescence, low toxicity and biocompatibility, so these structures found applications in nanomedicine, photocatalysts or optoelectronics.[21]

[60-I_h]fullerene: structure, electronic properties and applications

In 1985, while conducting experiments to study the formation of long carbon chains in space, the formation of a stable carbon cluster consisting on 60 carbon atoms was discovered.[14] These studies revealed by mass spectrometry, a major mass peak of 720 corresponding to C_{60} and, to a lesser extent, the one corresponding to C_{70}. This finding led to Robert F. Curl, Jr., Sir Harold W. Kroto and Richard E. Smalley being awarded with the Nobel Prize in Chemistry in 1996 *for their discovery of fullerenes*.

The most intensively studied fullerene is the soccer-ball shaped C_{60} ([60-I_h]fullerene) and it was the first example of zero-dimensional carbon nanoform. The 60 carbon atoms in the molecule are positioned at the vertices of a truncated icosahedron, formed by 12 pentagonal and 20 hexagonal faces in a corannulene-type fashion. The pentagons are responsible for providing curvature to the molecule. This construction satisfies Euler's theorem which states that for the closure of a spherical network of *n* hexagons, 12 pentagons are required (Figure 4).

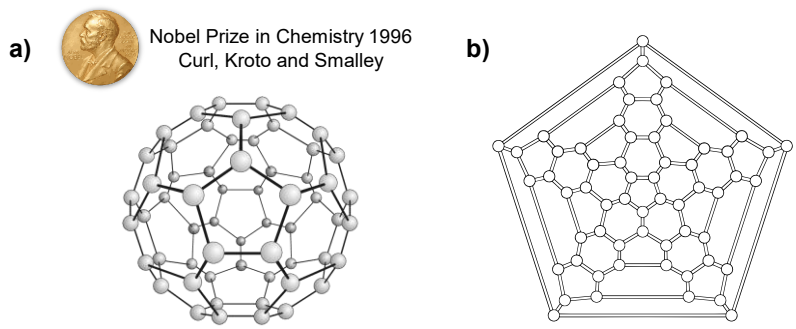

Figure 4. a) [60-I_h]fullerene structure and b) planar embeddings referring to C_{60} (Euler's theorem).

[18] G. Speranza, *Carbon* **2019**, *5*, 84.
[19] M. F. L. De Volder, S. H. Tawfick, R. H. Baughman, A. J. Hart, *Science* **2013**, *339*, 535.
[20] A. K. Worku, D. W. Ayele, *Results Chem.* **2023**, *5*, 100971.
[21] Y. Wang, A. Hu, *J. Mater. Chem. C* **2014**, *2*, 6921.

Despite all the possible isomers that could be constructed with 60 carbon atoms, only the spherical shape of C_{60} is formed. The stability of this geometry was justified in 1987 by H. Kroto through the isolated pentagon rule (IPR).[22] This rule establishes that a structure where pentagons are completely surrounded by hexagons is more stable than the one with two or more pentagons fused. The deviation from planarity introduces significant strain energy, while the presence of fused pentagons in non-IPR fullerenes leads to greater strain instability due to enforced bond angles. In the case of C_{60}, since all the pentagons are isolated, all the carbon atoms are equivalent, and the strain energy is uniformly distributed. Moreover, this C_{60} conformation avoids resonance destabilization due to pentalene-type 8-π-electron system, which do not satisfy the Hückel rule for aromaticity.[23]

In spite of being a completely conjugated and unsaturated carbon network, the presence of pentagons in the structure introduces curvature to the molecule and causes pyramidalization of carbon atoms. The pure *p* character of the π-orbitals is only possible in strictly planar systems. As a result, deviation from planarity means that the π-orbitals do not have a purely *p* character nor do the σ-orbitals. Consequently, the hybridization of carbon atoms falls between sp^3 and sp^2, more specifically $sp^{2.27}$.[24]

Another important aspect in the structure of C_{60} is the presence of two types of bonds: those located between two hexagons ([6,6]-bonds) and bonds between a pentagon and a hexagon ([5,6]-bonds). Through theoretical calculations and experimental investigations, it was concluded that the [6,6]-bonds were shorter (1.36 Å) than the [5,6]-bonds (1.47 Å) (Figure 5a).[25] The difference in bond lengths can be explained by the symmetry of the molecule and the occupation of the π-orbitals. To achieve the lowest Kekulé energy structure, the double bonds in the C_{60} molecule are located in the hexagonal rings, while no double bonds are in pentagons. For this reason, each hexagon of the structure exhibits the character of a cyclohexatriene while each pentagon resembles a [5]radialene (Figure 5b).[23,24]

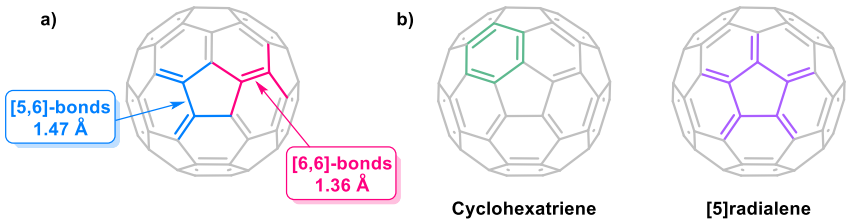

Figure 5. a) Bond types and lengths in C_{60} and b) cyclohexatriene and [5]radialene subunits in C_{60}.

[22] H. W. Kroto, *Nature* **1987**, *329*, 529.
[23] M. Bühl, A. Hirsch, *Chem. Rev.* **2001**, *101*, 1153.
[24] A. Hirsch, Principles of Fullerene Reactivity. In *Fullerenes and Related Structures*. Topics in Current Chemistry, vol. 199, A. Hirsch Ed. Springer-Verlag Berlin, Heidelberg, **1999**, pp. 1-65.
[25] S. Liu, Y. J. Lu, M. M. Kappes, J. A. Ibers, *Science* **1991**, *254*, 408.

The production of fullerene on a usable scale did not arrive until 1990, when Krätschmer, Huffman and coworkers developed a method that consists on the vaporization of graphite rods by resistive heating in a helium atmosphere.[26] Several methods have been reported for the production of C_{60}, such as contact-arc vaporization[27], solar generators,[28] combustion[29] or pyrolysis of hydrocarbons.[30] However, these approaches have the disadvantage of poor control of the reaction, resulting in the formation of C_{60} along with impurities such as C_{70} and even larger fullerenes. Consequently, bottom-up methods based on classical chemical reactions are currently being explored, allowing for precise control over the reaction.[31]

Fullerene-based materials have found numerous applications in materials science and biomedicine. Their outstanding electron-accepting capabilities have been utilized in organic fotovoltaics.[6b] However, one of the most exploited fields for the use of these derivatives has focused on the synthesis of molecules with biological properties. Therefore, several fullerene-based compounds have been developed with applications like antioxidants, antimicrobials, antivirals or anticancer agents, among others.[32] Our research group is at the forefront of synthesizing fullerene derivatives for biological applications. Hence, this thesis focuses on the development of molecules aimed at their application in this area.[10a,33]

[26] W. Krätschmer, L. D. Lamb, K. Fostiropoulos, D. R. Huffman, *Nature* **1990**, *347*, 354.
[27] R. E. Haufler, J. Conceicao, L. P. F. Chibante, Y. Chai, N. E. Byrne, S. Flanagan, M. M. Haley, S. C. O'Brien, C. Pan, Z. Xiao, W. E. Billups, M. A. Ciufolini, R. H. Hauge, J. L. Margrave, L. J. Wilson, R. F. Curl, R. E. Smalley, *J. Phys. Chem.* **1990**, *94*, 8634.
[28] a) L. P. F. Chibante, A. Thess, J. M. Alford, M. D. Diener, R. E. Smalley, *J. Phys. Chem.* **1993**, *97*, 8696. b) C. L. Fields, J. R. Pitts, M. J. Hale, C. Bingham, A. Lewandowski, D. E. King, *J. Phys. Chem.* **1993**, *97*, 8701.
[29] J. B. Howard, J. T. McKinnon, M. E. Johnson, Y. Makarovsky, A. L. Lafleur, *J. Phys. Chem.* **1992**, *96*, 6657.
[30] R. Taylor, G. J. Langley, H. W. Kroto, D. R. M. Walton, *Nature* **1993**, *366*, 728.
[31] M. Mojica, J. A. Alonso, F. Méndez, *J. Phys. Org. Chem.* **2013**, *26*, 526.
[32] E. Castro, A. Hernández-García, G. Zavala, L. Echegoyen, *J. Mater. Chem. B* **2017**, *5*, 6523.
[33] a) B. M. Illescas, J. Rojo, R. Delgado, N. Martín, *J. Am. Chem. Soc.* **2017**, *139*, 6018. b) B. M. Illescas, A. Pérez-Sánchez, A. Mallo, A. Martín-Domenech, I. Rodríguez-Crespo, N. Martín, *J. Mater. Chem. B* **2020**, *8*, 4505. c) J. Patino-Alonso, J. Cabrera-González, J. Merino, G. Nieto-Ortiz, F. Lasala, J. Katati, C. H. Bezerra da Cruz, A. K. Monnappa, P. Mateos-Gil, A. Canales, I. López-Montero, B. M. Illescas, R. Delgado, N. Martín, *Small* **2024**, *20*, 2307045.

Chapter 1

1. CHAPTER 1

1.1. Background

1.1.1. Exohedral functionalization of [60]fullerene

[60]Fullerene is an unsaturated molecule entirely formed by carbon atoms which acts as an electron-deficient olefin. Therefore, the main chemical transformations that can be carried out in its exohedral skeleton, and the most studied by far, are addition reactions. However, a wide variety of reactions have been carried out on this singular molecule, including hydrogenations, transition metal complex formation or reactions with electrophiles, among others (Figure 1.1).[34]

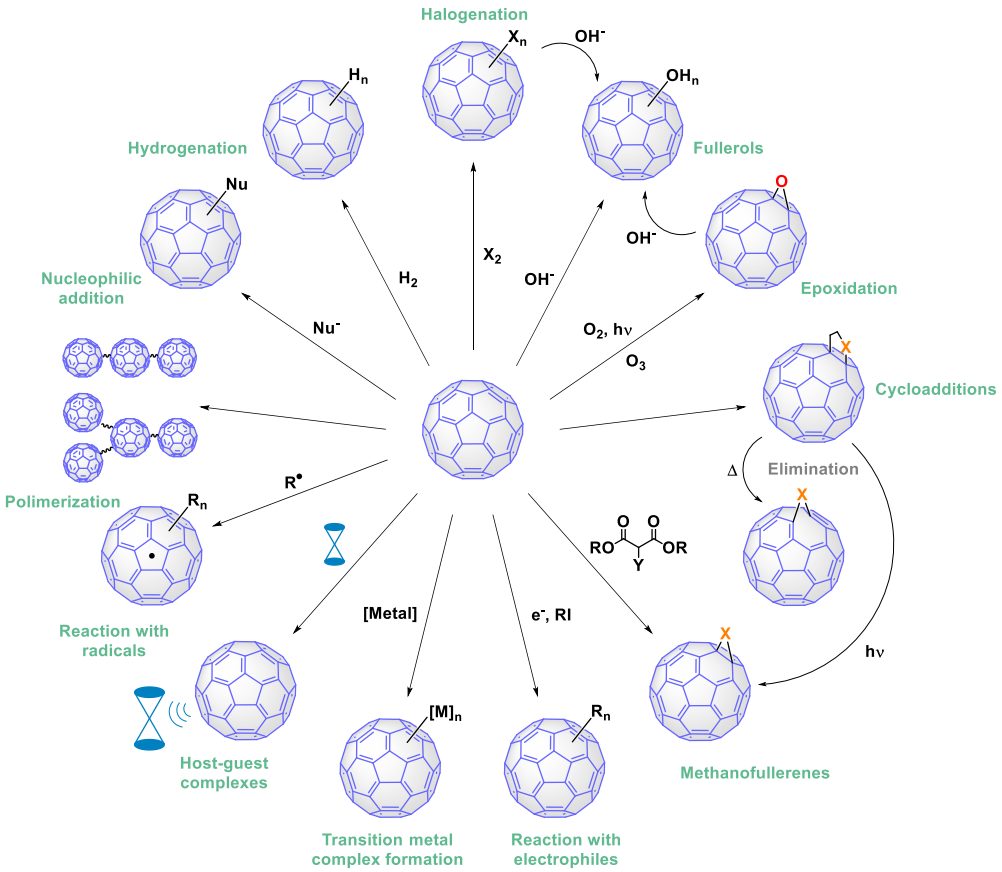

Figure 1.1. Most representative reactivity with C_{60}.

The driving force for [60]fullerene functionalization is the release of strain in the structure. The regioselectivity of the nucleophilic additions is governed by the requirement to minimize the number of double bonds at the [5,6]-positions of the molecule. Therefore, in most cases, additions take place in positions 1,2.[35] However,

[34] a) R. Taylor, D. R. M. Walton, *Nature* **1993**, *363*, 685. b) A. Hirsch, M. Brettreich, Eds. *Fullerenes: Chemistry and Reactions*, Wiley-VCH Verlag GmbH & Co. KGaA, Weinheim, **2005**.
[35] D. A. Dixon, N. Matsuzawa, T. Fukunaga, F. N. Tebbe, *J. Phys. Chem.* **1992**, *96*, 6107.

on some occasions and due to the steric hindrance of the substituents, 1,4-additions can take place. This implies the presence of a doble bond in a five-membered ring to have the lowest Kekulé energy in the structure, which is unfavorable since it represents a gain of 8.5 kcal/mol. This is why this addition is only preferred for sterically demanding addends (Scheme 1.1).[24]

Fullerene C_{60} can experience nucleophilic additions with carbon, nitrogen, phosphorus and oxygen nucleophiles. The initial attack of a nucleophile on C_{60} leads to the formation of the intermediate $Nu_nC_{60}^{n-}$ which can be stabilized by the addition of electrophiles E^+ such as protons or carbocations, the addition of neutral electrophiles EX like alkyl halides or by oxidation.[36]

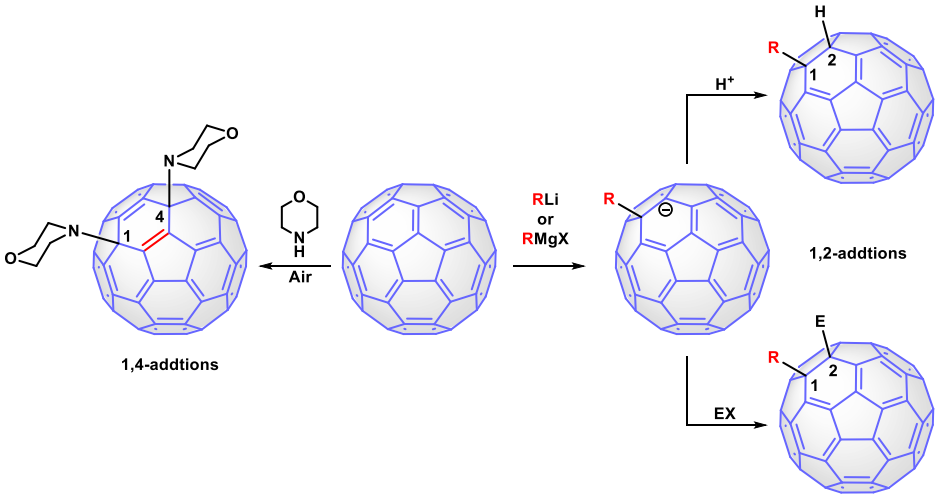

Scheme 1.1. Common examples of nucleophilic additions to C_{60}.

Among the nucleophilic additions to fullerene, a considerable number of transformations occur *via* cycloaddition reactions. These reactions result in the formation of a three-, four-, five- or six-membered ring on the external surface of the fullerene framework. Depending on the type of cycloaddition, one side of the newly formed ring also becomes an integral part of the fullerene cage.

One of the most widely employed strategies for conducting [2+1] cycloadditions and synthesizing methanofullerenes is the well-established Bingel reaction.[37] Initially, this reaction was performed using pre-synthesized bromomalonates and NaH as the base. This methodology enabled the efficient preparation of fullerene adducts under mild conditions and with high yields.

However, the concurrent formation of dibromomalonates made purification processes complicated in most cases.

[36] a) A. Hirsch, *Synthesis* **1995**, *8*, 895. b) G. Schick, K.-D. Kampe, A. Hirsch, *J. Chem. Soc. Chem. Commun.* **1995**, *19*, 2023.
[37] C. Bingel, *Chem. Ber.* **1993**, *126*, 1957.

To address this challenge, A. Hirsch introduced an improved approach involving the *in situ* generation of bromomalonates using CBr_4 as the halogenating agent and DBU as the base (Scheme 1.2).[38] This approach successfully prevented the formation of dibromomalonates while ensuring the correct progression of the reaction. As a result, this refined methodology is known as the Bingel-Hirsch cyclopropanation.

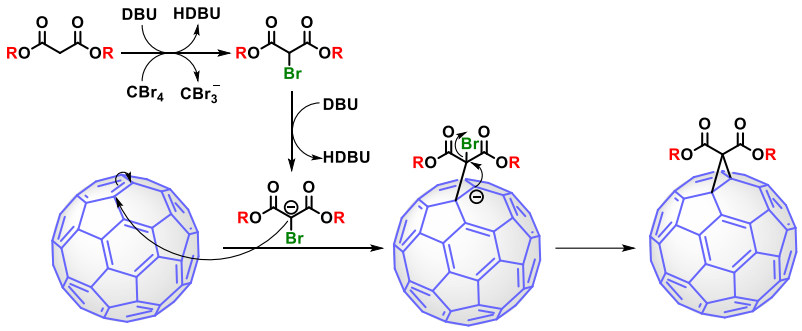

Scheme 1.2. Proposed mechanism for Bingel-Hirsch cyclopropanation reaction.

Due to the availability of malonates with very diverse structures, the Bingel-Hirsch reaction is widely used for the functionalization of the fullerene sphere in targeted syntheses of new compounds with useful properties.

Another important example of cycloaddition, in this case [3+2], is the so-called Prato reaction.[39] It is a 1,3-dipolar reaction between azomethine ylides and one of the double bonds of the fullerene. These ylides are generated *in situ* in the reaction medium by the condensation of an aldehyde or a ketone with an amino acid or an amino ester (Scheme 1.3). In the reaction, a five-membered ring containing a nitrogen in the structure is formed. These types of derivatives are known as fulleropyrrolidines.

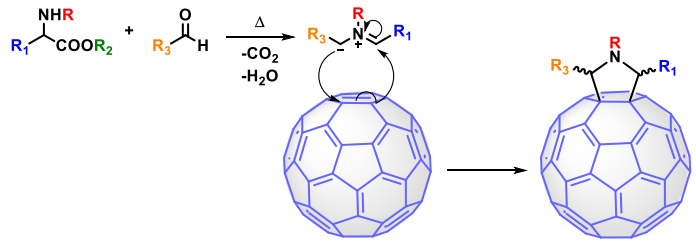

Scheme 1.3. General mechanism proposed for Prato reaction.

Other examples of cycloadditions are [2+2] for the formation of four-membered rings,[34] [4+2] for the formation of six-membered rings[40] and [8+2].[41]

[38] X. Camps, A. Hirsch, *J. Chem. Soc. Perkin Trans.* 1 **1997**, *11*, 1595.
[39] M. Maggini, G. Scorrano, M. Prato, *J. Am. Chem. Soc.* **1993**, *115*, 9798.
[40] N. Martín, J. L. Segura, F. Wudl, New Concepts in Diels-Alder Cycloadditions to Fullerenes. In *Fullerenes: From Synthesis to Optoelectronic Properties*, D. M. Guldi, N. Martín, Eds. Kluwer Academic Publishers, Dordrecht, **2002**, vol. 4. pp. 81-120.
[41] E. Beer, M. Feuerer, A. Knorr, A. Mirlach, J. Daub, *Angew. Chem. Int. Ed. Engl.* **1994**, *33*, 1087.

1.1.2. Multiaddition reactions and addition patterns

The addition of substituents to the fullerene sphere follows certain substitution patterns (Figure 1.2). A single substituent preferentially attaches at the [6,6]-bond, as previously described. However, the remaining [6,6] positions are not identical and introducing more appendages to the structure leads to the formation of different regioisomers. These positions, relative to the first substituent, are classified as *cis*-n (n = 1 – 3), *equatorial* (*e*) and *trans*-n (n = 1 – 4).[42]

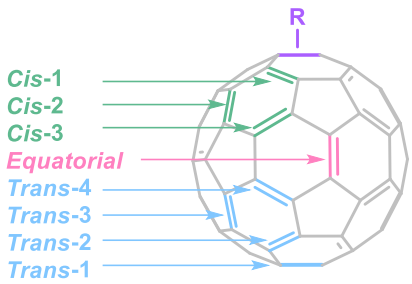

Figure 1.2. Labeled positional relationship between [6,6]-bonds.

Cis positions are adjacent to the first substituent, which makes this configuration the least stable due to the repulsion between the functional groups. On the other hand, *trans* positions are on the opposite side of the fullerene. In this case, steric hindrance is minimal due to the distance between the substituents. The *equatorial* positions are distributed along the fullerene equator. One might assume, for steric reasons, that the first regioisomer formed during the addition of successive substituents would adopt a *trans* configuration. However, the most favored positions are the equatorial ones because the LUMO and LUMO+1 orbitals exhibit the highest orbital coefficient. Therefore, theoretical predictions suggest that successive additions will primarily occur at *equatorial* positions, followed by the next most favored site with higher orbital coefficients such as *trans*-3.[43] However, Hirsch *et al.* studied the successive addition of ethyl malonate to C_{60} identifying a mixture of five isomers in varying proportions, which they successfully isolated using HPLC.[44] Their study revealed that successive cyclopropanations with the *equatorial* bis-adduct led to the regioselective formation of additional polyadducts at *equatorial* positions. Despite this, the lack of control over regioselectivity at the initial stages of the reaction remains a challenge in directing the process toward the desired products.

The most effective method for controlling multiple additions is the tether-directed remote multifunctionalization methodology introduced by Diederich in 1994.[45] By controlling the length and geometry of the tether, either *equatorial*, *cis* or *trans* structures can be almost exclusively obtained.

In the synthesis of bis-adducts, Nierengarten *et al.* reported that modifying the rigidity of the bridge between malonates directs the formation of adducts at the *cis*-2 (**1.1**) and

[42] R. Caballero, P. de la Cruz, F. Langa, Basic Principles of the Chemical Reactivity of Fullerenes, In *Fullerenes: Principles and Applications*, F. Langa, J.-F. Nierengarten, Eds. 2nd ed. The Royal Society of Chemistry, Cambridge, **2011**, ch. 3, pp. 66-124.
[43] A. Hirsch, I. Lamparth, T. Grösser, *J. Am. Chem. Soc.* **1994**, *116*, 9385.
[44] A. Hirsch, I. Lamparth, H. R. Karfunkel, *Angew. Chem. Int. Ed. Engl.* **1994**, *33*, 437.
[45] L. Isaacs, R. F. Haldimann, F. Diederich, *Angew. Chem. Int. Ed. Engl.* **1994**, *33*, 2339.

trans-3 (**1.2**) positions (Figure 1.3).[46] Similarly, Hirsch *et al.* demonstrated that introducing a porphyrin spacer between the malonates imparts sufficient rigidity and appropriate length to enable the selective synthesis of the *trans*-2 isomer (**1.3**) as the sole reaction product (Figure 1.3).[47] Good regioselectivities have also been achieved by using spacers derived from xylene[48] and crown ethers.[49]

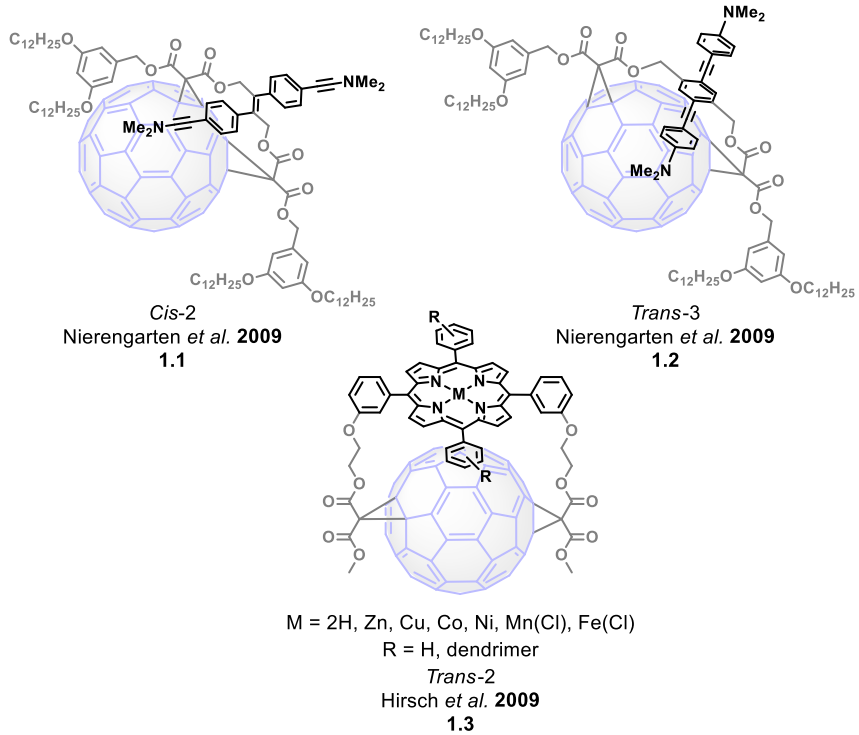

Figure 1.3. Fullerene bis-adducts with different addition patterns.

A similar approach is employed for the regioselective synthesis of tris-adducts using tripodal tethers. Thus, Torres *et al.* reported the synthesis of a tris-adduct with an *e*,*e*,*e* addition pattern (**1.4**) by using a subphthalocyanine containing three malonates (Figure 1.4).[50] A comparable approach but using more flexible tethers was described by Hirsch and coworkers.[51] Unexpectedly, the synthesis of tris-adducts with a *trans*, *trans*, *trans* addition pattern (**1.5**) has also been achieved using a cyclotriveratrylene

[46] T. M. Figueira-Duarte, V. Lloveras, J. Vidal-Gancedo, B. Delavaux-Nicot, C. Duhayon, J. Veciana, C. Rovira, J.-F. Nierengarten, *Eur. J. Org. Chem.* **2009**, *2009*, 5779.
[47] F. Spänig, M. Ruppert, J. Dannhäuser, A. Hirsch, D. M. Guldi, *J. Am. Chem. Soc.* **2009**, *131*, 9378.
[48] a) J.-F. Nierengarten, V. Gramlich, F. Cardullo, F. Diederich, *Angew. Chem. Int. Ed. Engl.* **1996**, *35*, 2101. b) J.-F. Nierengarten, T. Habicher, R. Kessinger, F. Cardullo, F. Diederich, V. Gramlich, J.-P. Gisselbrecht, C. Boudon, M. Gross, *Helv. Chim. Acta* **1997**, *80*, 2238.
[49] a) J.-P. Bourgeois, L. Echegoyen, M. Fibbioli, E. Pretsch, F. Diederich, *Angew. Chem. Int. Ed.* **1998**, *37*, 2118. b) J.-P. Bourgeois, P. Seiler, M. Fibbioli, E. Pretsch, F. Diederich, L. Echegoyen, *Helv. Chim. Acta* **1999**, *82*, 1572.
[50] D. González-Rodríguez, E. Carbonell, G. de Miguel-Rojas, C. Atienza-Castellanos, D. M. Guldi, T. Torres, *J. Am. Chem. Soc.* **2010**, *132*, 16488.
[51] N. Chronakis, A. Hirsch, *Chem. Commun.* **2005**, 3709.

(CTV) tether (Figure 1.4).[52] This regioisomer is formed due to the strong interaction between the electron-rich aromatic rings of the CTV moiety and the electron-deficient fullerene surface, which is more pronounced than in the *e*,*e*,*e* tris-adducts. More recently, Nierengarten *et al.* prepared tris-adducts using malonates constructed around a silicon atom, where the influence of the length of the spacer determines the formation of the isomer of interest.[53]

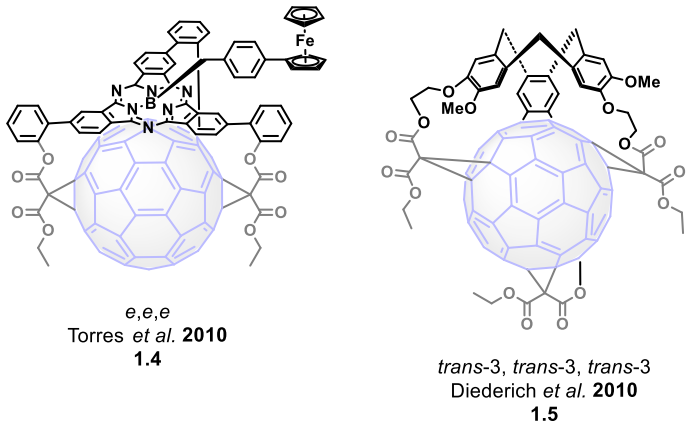

e,*e*,*e*
Torres *et al.* **2010**
1.4

trans-3, *trans*-3, *trans*-3
Diederich *et al.* **2010**
1.5

Figure 1.4. Fullerene tris-adducts with different addition patterns.

Hexakis-adducts are distinguished by the presence of six substituents on the fullerene sphere, arranged in an octahedral addition pattern, resulting in species with T_h symmetry. Substituents have preference for being placed in *equatorial* positions, leading to the exclusive formation of *e*-isomers. However, obtaining these adducts using only pristine fullerene or monoadducts is a challenge due to the formation of different isomers in the early stages of the reaction. To overcome this issue, tethers can be employed, as in the previous cases. Thus, hexakis-adducts with a [3:3][54] or [3:2:1][55] (**1.6**) substitution patterns have been described, where all substituents are located in the *equatorial* positions (Figure 1.5).

The synthesis of hexakis-adducts was achieved without the use of linkers thanks to the use of activation templates such as 9,10-dimethylanthracene (DMA)[56] or CBr_4 (Figure 1.5).[57] DMA generates multi-adducts through Diels-Alder cycloadditions reversible at room temperature with an *e* substitution pattern. Subsequently, the malonates replace the DMA positions through irreversible reactions such as cyclopropanations to finally form the hexakis-adduct with the desired geometry. The

[52] A. Kraszewska, P. Rivera-Fuentes, G. Rapenne, J. Crassous, A. G. Petrovic, J. L. Alonso-Gómez, E. Huerta, F. Diederich, C. Thilgen, *Eur. J. Org. Chem.* **2010**, *2010*, 4402.
[53] F. Schillinger, U. Hahn, S. Guerra, T. M. N. Trinh, D. Sigwalt, M. Holler, I. Nierengarten, J.-F. Nierengarten, *Helv. Chim. Acta* **2023**, *106*, e202300026.
[54] F. Beuerle, A. Hirsch, *Chem. Eur. J.* **2009**, *15*, 7447.
[55] M. Wachter, L. Jurkiewicz, A. Hirsch, *Chem. Eur. J.* **2021**, *27*, 7677.
[56] I. Lamparth, C. Maichle-Mossmer, A. Hirsch, *Angew. Chem. Int. Ed. Engl.* **1995**, *34*, 1607.
[57] a) H. Li, A. Kitaygorodskiy, R. A. Carino, Y.-P. Sun, *Org. Lett.* **2005**, *7*, 859. b) H. Li, S. A. Haque, A. Kitaygorodskiy, M. J. Meziani, M. Torres-Castillo, Y.-P. Sun, *Org. Lett.* **2006**, *8*, 5641.

same goes for CBr_4. Bromination of the malonate occurs first thus generating a large excess of CBr_3^- anions capable of giving rise to reversible addition reactions onto the double bonds of C_{60}. The use of templates is the method used today for the synthesis of these adducts, which allows subsequent modifications to the malonates introduced into the fullerene.

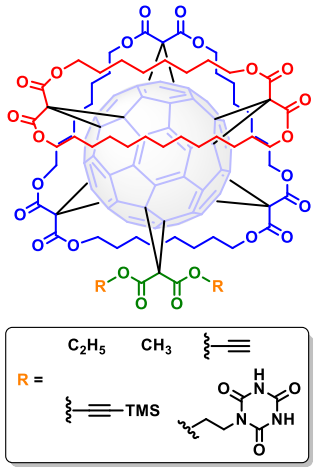

Hirsch *et al.* **2021**
1.6

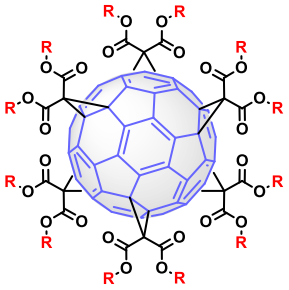

T_h-symmetry hexakis-adduct using template-directed methods

Figure 1.5. Fullerene hexakis-adducts structures.

1.1.3. [60]Fullerene derivatives for biomedical applications

Over the years, there has been a lot of research regarding the biological properties of C_{60}. Pristine fullerene is highly hydrophobic and mainly soluble in aromatic hydrocarbons, halogenated solvents or CS_2, among others. Since organic solvents can be disruptive to biological systems, this poses a problem for its application in biology due to the low solubility in aqueous media. For this reason, various aqueous solubilization techniques are employed to overcome this limitation, such as encapsulation in special carriers, suspensions or chemical functionalization. Both encapsulation and suspension formation using co-solvents are methods that allow the direct use of pristine fullerene.

Encapsulation involves the formation of complexes using different compounds (Figure 1.6). Cyclodextrins[58] or calixarenes[59] are the most commonly used, though polymers such as polyvinylpyrrolidone (PVP)[60] and artificial membranes like Triton X-100 or dimethyldioctadecylammonium bromide (DODAB) can also be employed.[61] The formation of colloidal systems has also been reported through the use of

[58] T. Andersson, K. Nilsson, M. Sundahl, G. Westman, O. Wennerström, *J. Chem. Soc. Chem. Commun.* **1992**, 604.
[59] J. L. Atwood, G. A. Koutsantonis, C. L. Raston, *Nature* **1994**, *368*, 229.
[60] Y. N. Yamakoshi, T. Yagami, K. Fukuhara, S. Sueyoshi, N. Miyata, *J. Chem. Soc. Chem. Commun.* **1994**, 517.
[61] H. Hungerbuehler, D. M. Guldi, K. D. Asmus, *J. Am. Chem. Soc.* **1993**, *115*, 3386.

ammonium halides,[62] as well as the use of co-polymers such as poly(phenylquinoline)-*block*-polystyrene (PPQ-*b*-PS)[63] or the combination of lipid membranes with fullerene.[64]

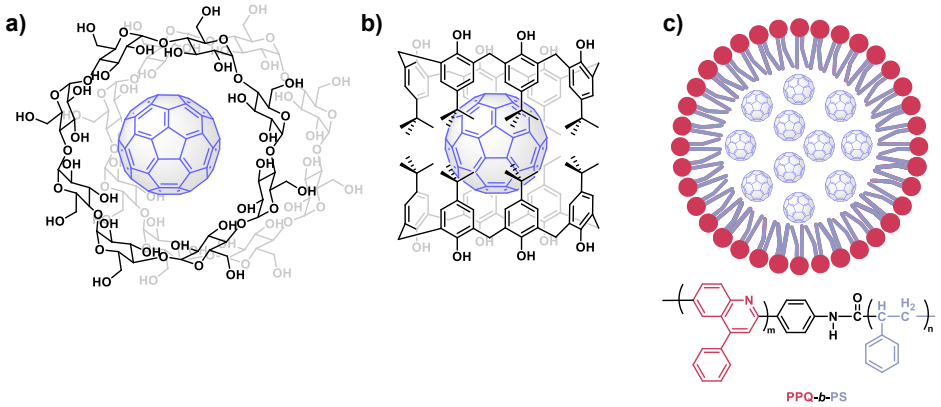

Figure 1.6. Schematic illustration of [60]fullerene complexes with: a) γ-cyclodextrins, b) calix[6]arene and c) co-polymers such as PPQ-*b*-PS.

The formation of suspensions has been employed to directly harness the potential applications of pristine fullerene. This process involves the use of apolar organic solvents such as benzene, followed by a gradual increase in polarity until a stable suspension in water is achieved.[65] Additionally, sonication of C_{60} in toluene/water mixtures has been explored, allowing the toluene to evaporate and resulting in stable colloidal dispersions.[66] However, the use of toxic organic solvents like benzene and toluene should be avoided to ensure compatibility with biological applications. Consequently, more recent studies have reported the formation of suspensions using only tetrahydrofuran (THF) and water, providing a safer alternative.[67]

The most common approach to achieve solubility in aqueous media is the surface functionalization of fullerene to introduce hydrophilic appendages. However, the introduction of a single hydrophilic unit is often not enough to ensure water solubility, probably due to aggregation phenomena. Usually, the hydrophobic part tends to stay together while the hydrophilic part remains outside the aggregate.

Fullerene derivatives have been widely used in biological applications over the years.[10a,33] In this section, we will focus on those fields in which fullerene hexakis-adducts have had a relevant impact.

---

[62] N. O. Mchedlov-Petrossyan, V. K. Klochkov, G. V. Andrievsky, *J. Chem. Soc. Faraday Trans.* **1997**, *93*, 4343.
[63] S. A. Jenekhe, X. L. Chen, *Science* **1998**, *279*, 1903.
[64] M. Hetzer, S. Bayerl, X. Camps, O. Vostrowsky, A. Hirsch, T. M. Bayerl, *Adv. Mater.* **1997**, *9*, 913.
[65] W. A. Scrivens, J. M. Tour, K. E. Creek, L. Pirisi, *J. Am. Chem. Soc.* **1994**, *116*, 4517.
[66] G. V. Andrievsky, M. V. Kosevich, O. M. Vovk, V. S. Shelkovsky, L. A. Vashchenko, *J. Chem. Soc. Chem. Commun.* **1995**, 1281.
[67] S. Deguchi, R. G. Alargova, K. Tsujii, *Langmuir* **2001**, *17*, 6013.

1.1.3.1. Anticancer and photodynamic therapy applications

One of the main possible applications of [60]fullerene is in photodynamic therapy (PDT), particularly for cancer treatment. The enhanced selectivity of sugar-fullerene derivatives toward cancer cells can significantly improve treatment efficiency while reducing side effects. This tumor-selective cytotoxicity is likely due to the increased expression of GLUT (glucose transporters) in different types of cancer cells.[68] C_{60}-glycoconjugated derivatives, which feature one or more glucose units attached to the fullerene, may exhibit higher specificity for cancer cells over healthy ones.

Monofunctionalized glycofullerene derivatives, containing one or two carbohydrate units, have been widely studied as photosensitizers for PDT.[69] However, there are only a few reported examples of hexa-substituted glycofullerenes being explored as anticancer agents.

Serda *et al.* investigated glycofullerenes functionalized with D-glucosamine fragments (**1.7** and **1.8**) as nonreceptor inhibitors of tyrosine kinases, enzymes involved in regulating cell growth, proliferation, differentiation, adhesion, migration and apoptosis, particularly in pancreatic cancer (Figure 1.7a).[70] Cellular studies revealed that glycofullerenes are non-toxic and do not affect the cell cycle in pancreatic cancer cells. However, they disrupt the redox balance by increasing reactive oxygen species (ROS) production, which in turn activates autophagy. This response plays a crucial role in influencing cell viability and enhances drug synergy in combined treatments. Additionally, studies highlighted their low toxicity in the absence of light, but upon irradiation with blue or green light, they generate ROS, leading to cell death through phototoxicity (Figure 1.7a).[71]

In a related study, authors also reported a glycine derivative for the inhibition of BTK protein (**1.9**), a key regulator in the signal transduction of the B-cell antigen receptor, with significant implications for the treatment of certain blood cancers (Figure 1.7b).[72] The enzymatic and cellular studies revealed strong inhibition of the BTK protein in the micromolar range.

[68] P.-B. Ancey, C. Contat, E. Meylan, *FEBS J* **2018**, *285*, 2926.
[69] L. Tanzi, M. Terreni, Y. Zhang, *Eur. J. Med. Chem.* **2022**, *230*, 114104.
[70] M. Serda, K. Malarz, A. Mrozek-Wilczkiewicz, M. Wojtyniak, R. Musioł, S. A. Curley, *Sci. Rep.* **2020**, *10*, 260.
[71] M. Serda, M. J. Ware, J. M. Newton, S. Sachdeva, M. Krzykawska-Serda, L. Nguyen, J. Law, A. O. Anderson, S. A. Curley, L. J Wilson, S. J. Corr, *Nanomedicine* **2018**, *13*, 2981.
[72] K. Malarz, J. Korzuch, T. D. Marforio, K. Balin, M. Calvaresi, A. Mrozek-Wilczkiewicz, R. Musiol, M. Serda, *Int. J. Nanomedicine* **2023**, *18*, 1709.

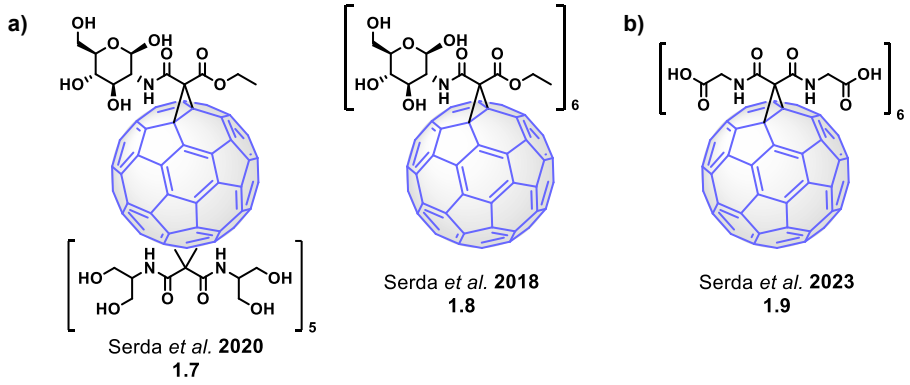

Figure 1.7. a) D-glucosamine derivatives for tyrosine kinase inhibition and b) glycofullerene for BTK kinase inhibition.

Rancan *et al.* explored the synthesis of photosensitizers conjugated with 2, 6 and 12 pyropheophorbide-A units for their use in PDT (Figure 1.8).[73] Their findings indicated that the derivative containing six pyropheophorbide-A units exhibited the highest therapeutic potential, demonstrating cytotoxic effects even at the lowest tested concentrations.

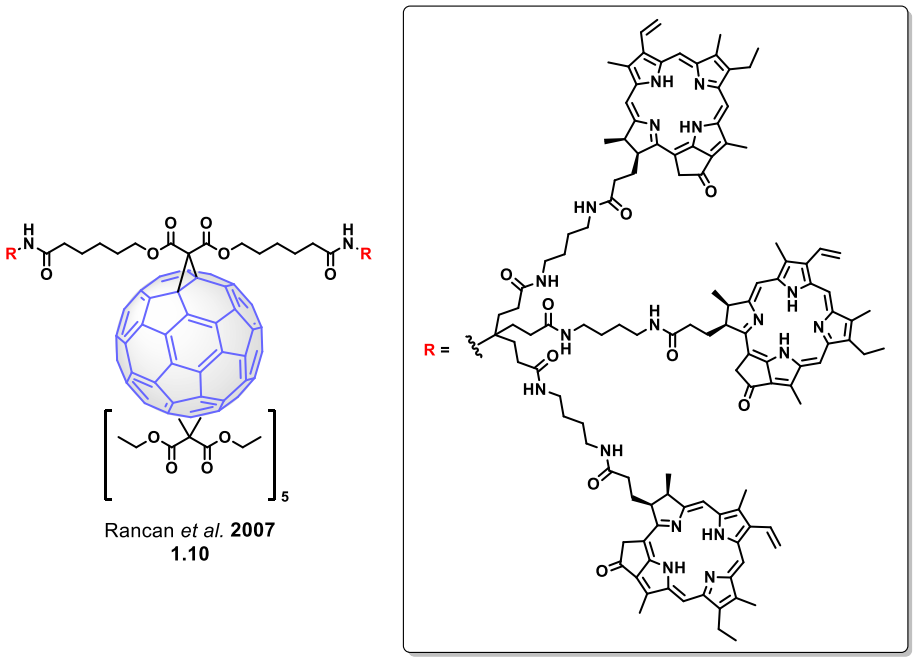

Figure 1.8. [60]fullerene hexakis-adduct conjugated with pyropheophorbide-A.

[73] F. Rancan, M. Helmreich, A. Mölich, N. Jux, A. Hirsch, B. Röder, F. Böhm, *Photochem. Photobiol.* **2007**, *83*, 1330.

1.1.3.2. Contrast agents and bioimaging applications

Gadolinium (Gd^{3+}) is the primary component of the most efficient contrast agents. However, elemental gadolinium and its salts are highly toxic, and even when administered as chelates, they can lead to severe progressive diseases such as nephrogenic systemic fibrosis. Encapsulating gadolinium within an inert structure like fullerenes presents a promising strategy to mitigate toxicity concerns.

Endohedral metallofullerenes are a class of functionalized fullerenes capable of encapsulating (metal) atoms, molecules or clusters inside the cage. The development of water-soluble derivatives has been crucial for their application in medicine. In these compounds, the fullerene cage acts as a protective barrier, shielding the encapsulated metal from chemical or enzymatic interactions in the body and preventing its unintended release.

Bolskar *et al.* developed water-soluble $Gd@C_{60}$ derivatives, specifically $Gd@C_{60}[C(COOH)_2]_{10}$, demonstrating the first metallofullerene-based MRI contrast agent with a biodistribution comparable to clinically approved agents.[74] However, C_{80} and C_{82} derivatives are more commonly used for this purpose, as they provide significantly stronger magnetic resonance contrast than traditional gadolinium chelates.[75]

The use of [60]fullerene hexakis-adducts as potential contrast agents is scarcely documented in the literature. In 2021, Krishnan *et al.* reported the first example of a hexa-substituted fullerene derivative containing two chelated gadolinium ions (Figure 1.9a). However, the molecule did not effectively generate radiosensitization. Despite this, numerous alternative strategies could be explored in the future to enhance the radiosensitization of these constructs through innovative chemical modifications.[76] Zhang *et al.* reported water-soluble hexakis-adducts based on polyethylene glycol chains and Gd^{3+} endohedral metallofullerenes (Figure 1.9b).[77] The compounds demonstrated their efficiency as MRI contrast agents with higher T_1 relaxivity and enhanced imaging contrast compared to the well-established gadodiamide.

[74] R. D. Bolskar, A. F. Benedetto, L. O. Husebo, R. E. Price, E. F. Jackson, S. Wallace, L. J. Wilson, J. M. Alford, *J. Am. Chem. Soc.* **2003**, *125*, 5471.
[75] a) P. P. Fatouros, F. D. Corwin, Z.-J. Chen, W. C. Broaddus, J. L. Tatum, B. Kettenmann, Z. Ge, H. W. Gibson, J. L. Russ, A. P. Leonard, J. C. Duchamp, H. C. Dorn, *Radiology* **2006**, *240*, 756. b) M. Mikawa, H. Kato, M. Okumura, M. Narazaki, Y. Kanazawa, N. Miwa, H. Shinohara, *Bioconjugate Chem.* **2001**, *12*, 510.
[76] J. B.-K. Kim, Y. Mackeyev, S. Raghuram, S. H. Cho, S. Krishnan, *Int. J. Radiat. Biol.* **2021**, *97*, 1129.
[77] Y. Li, R. Biswas, W. P. Kopcha, T. Dubroca, L. Abella, Y. Sun, R. A. Crichton, C. Rathnam, L. Yang, Y.-W. Yeh, K. Kundu, A. Rodríguez-Fortea, J. M. Poblet, K.-B. Lee, S. Hill, J. Zhang, *Angew. Chem. Int. Ed.* **2023**, *62*, e202211704.

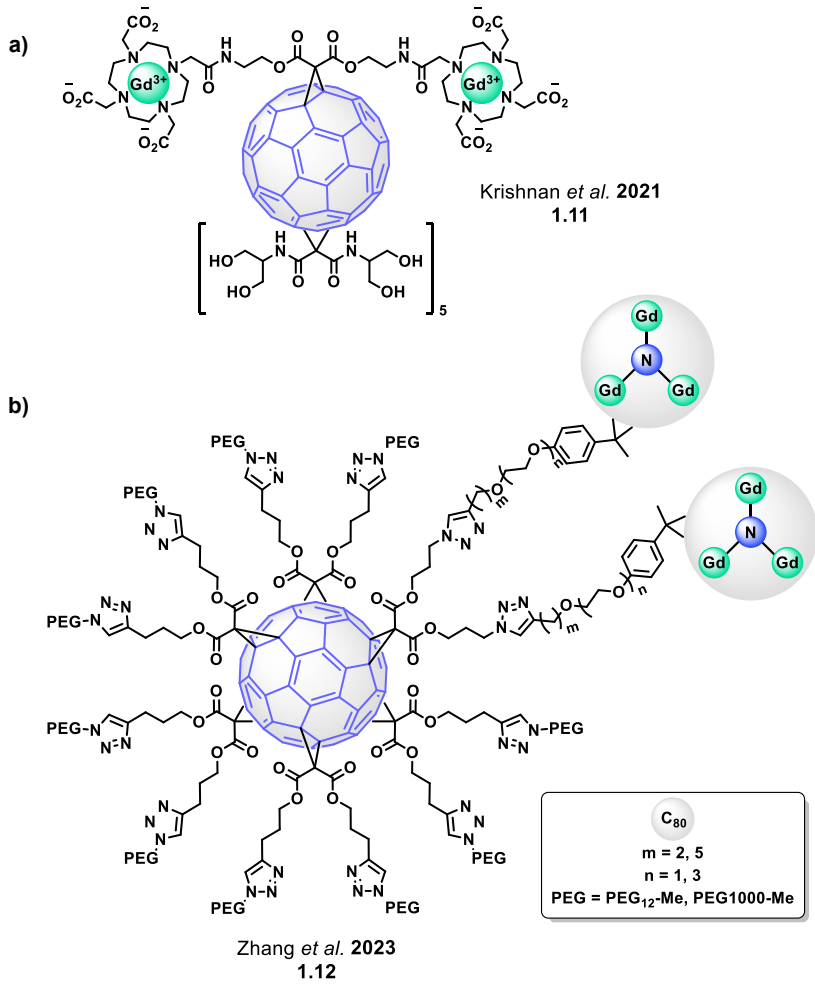

Figure 1.9. a) Fullerene hexakis-adduct with two chelated gadolinium ions and b) hexakis-adducts based on polyethylene glycol chains and Gd^{3+} endohedral metallofullerenes.

In order to synthesize fluorescent probes for bioimaging, Serda *et al.* reported two hexakis-adducts with coumarin (**1.13**) and sulfocyanine (**1.14**) derivatives in the structure as the fluorophores (Figure 1.10).[78] The click reaction between the starting hexakis-adduct and the fluorophores was performed *in situ* in the cell media and the compounds were successfully localized in the MCF-7 breast cancer cell line using fluorescent microscopy.

[78] M. Serda, K. Malarz, J. Korzuch, M. Szubka, M. Zubko, R. Musioł, *ACS Biomater. Sci. Eng.* **2022**, *8*, 3450.

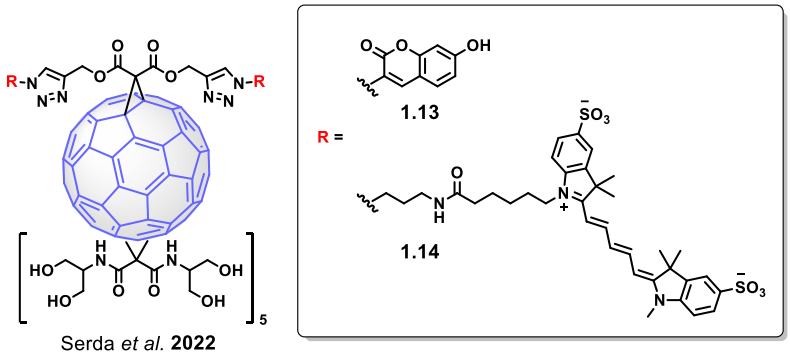

Figure 1.10. [60]Fullerene hexakis-adduct conjugated with fluorophores.

1.1.3.3. Drugs and gene delivery applications

The development of advanced therapies has led to the need for efficient systems for the targeted delivery of drugs and genetic material. These technologies allow the transport of therapeutic molecules in a controlled and specific manner, optimizing their efficacy and reducing side effects. In the case of drug delivery, intelligent systems enable the controlled release of drugs into specific tissues or cells, improving treatments for cancer, neurodegenerative diseases and viral infections. On the other hand, gene delivery facilitates the introduction of DNA, RNA or gene-editing tools into cells, paving the way for innovative gene therapies for hereditary and acquired health conditions.

The conjugation of fullerenes with well-established drug molecules has been a representative strategy to impart fullerene-specific properties. Doxorubicin and paclitaxel (Taxol®) are hydrophobic anticancer drugs for the treatment of a variety of tumors. For paclitaxel, Wilson and coworkers synthesized a covalent conjugate with C_{60} for a lipophilic slow-release system to enhance therapeutic efficacy. Their results suggested that the conjugate activity was similar to free paclitaxel for anticancer applications.[79] Similar to this, Sun and coworkers prepared conjugates of fullerene with doxorubicin. The results suggested comparable antineoplastic activities of the conjugate with those of free doxorubicin against the human breast cancer cells.[80]

To improve drug transport and solve the problem of hydrophobicity, Hirsch and coworkers reported the synthesis of amphiphilic fullerene hexakis-adducts, called buckysomes (**1.15**), that self-assemble in aqueous solution to form spherical vesicles.[81] Later, Conyers *et al.* reported the use of these buckysomes as nanocarriers for the transport of hydrophobic molecules (Figure 1.11). Paclitaxel was introduced

[79] T. Y. Zakharian, A. Seryshev, B. Sitharaman, B. E. Gilbert, V. Knight, L. J. Wilson, *J. Am. Chem. Soc.* **2005**, *127*, 12508.
[80] F. Lu, A. Haque S.-T. Yang, P. G. Luo, L. Gu, A. Kitaygorodskiy, H. Li, S. Lacher, Y.-P. Sun, *J. Phys. Chem. C* **2009**, *113*, 17768.
[81] M. Brettreich, S. Burghardt, C. Böttcher, T. Bayerl, S. Bayerl, A. Hirsch, *Angew. Chem. Int. Ed.* **2000**, *39*, 1845. b) S. Burghardt, A. Hirsch, B. Schade, K. Ludwig, C. Böttcher, *Angew. Chem. Int. Ed.* **2005**, *44*, 2976.

into the buckysomes, and preliminary results demonstrated suppression of MCF-7 breast cancer cell growth.[82]

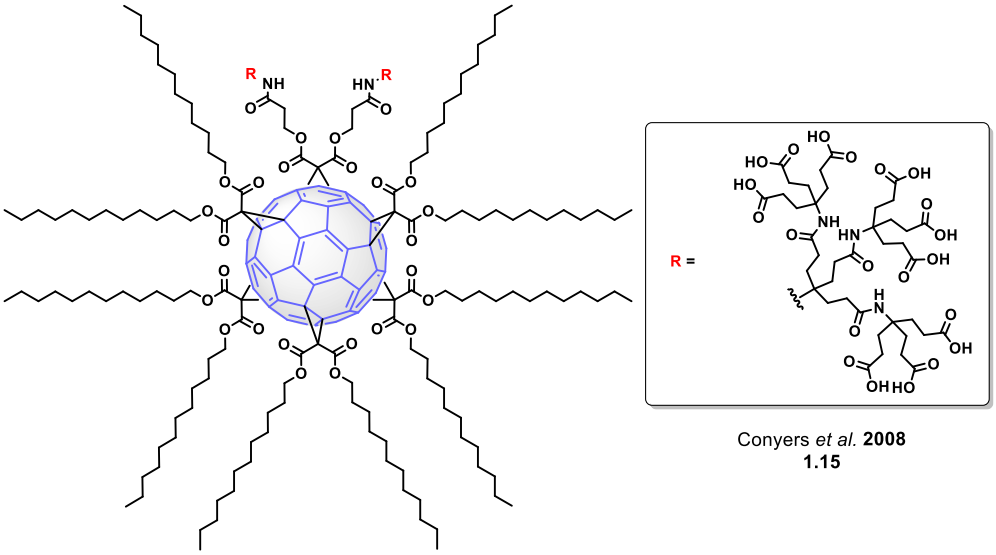

Figure 1.11. Buckysome structure for the encapsulation of paclitaxel.

The treatment of genetic diseases is based on cellular delivery of foreign nucleic acids. Viral methods take advantage of the ability of viruses to inject their genetic code inside a host cell, but the risks of a high immune response are possible. Alternatively, the nonviral approach is based on the use of cationic systems to complex and deliver genetic material.

Nakamura *et al.* pioneered the potential use of fullerene derivatives as carriers for gene delivery based on polycationic nanostructures (**1.16**).[83] However, they initially found that fullerene hexakis-adducts were completely inactive as gene-delivery agents.[84] Later, Nierengarten *et al.* revealed that this inactivity was due to their limited DNA condensation capacity, attributed to the low number of protonable amino groups. Similar to dendritic vectors, increasing the generation number enhances efficiency (**1.17** - **1.19**). The globular structure of fullerene hexakis-adducts makes them well-suited for gene delivery, even from the second generation onwards. The presence of enough amino groups in higher generations ensures efficient DNA delivery while maintaining low toxicity (Figure 1.12).[85]

[82] R. Partha, L. R. Mitchell, J. L. Lyon, P. P. Joshi, J. L. Conyers, *ACS Nano* **2008**, *2*, 1950.
[83] H. Isobe, W. Nakanishi, N. Tomita, S. Jinno, H. Okayama, E. Nakamura, *Chem. Asian. J.* **2006**, *1*, 167.
[84] E. Nakamura, H. Isobe, N. Tomita, M. Sawamura, S. Jinno, H. Okayama, *Angew. Chem. Int. Ed.* **2000**, *39*, 4254.
[85] D. Sigwalt, M. Holler, J. Iehl, J.-F. Nierengarten, M. Nothisen, E. Morin, J.-S. Remy, *Chem. Commun.* **2011**, *47*, 4640.

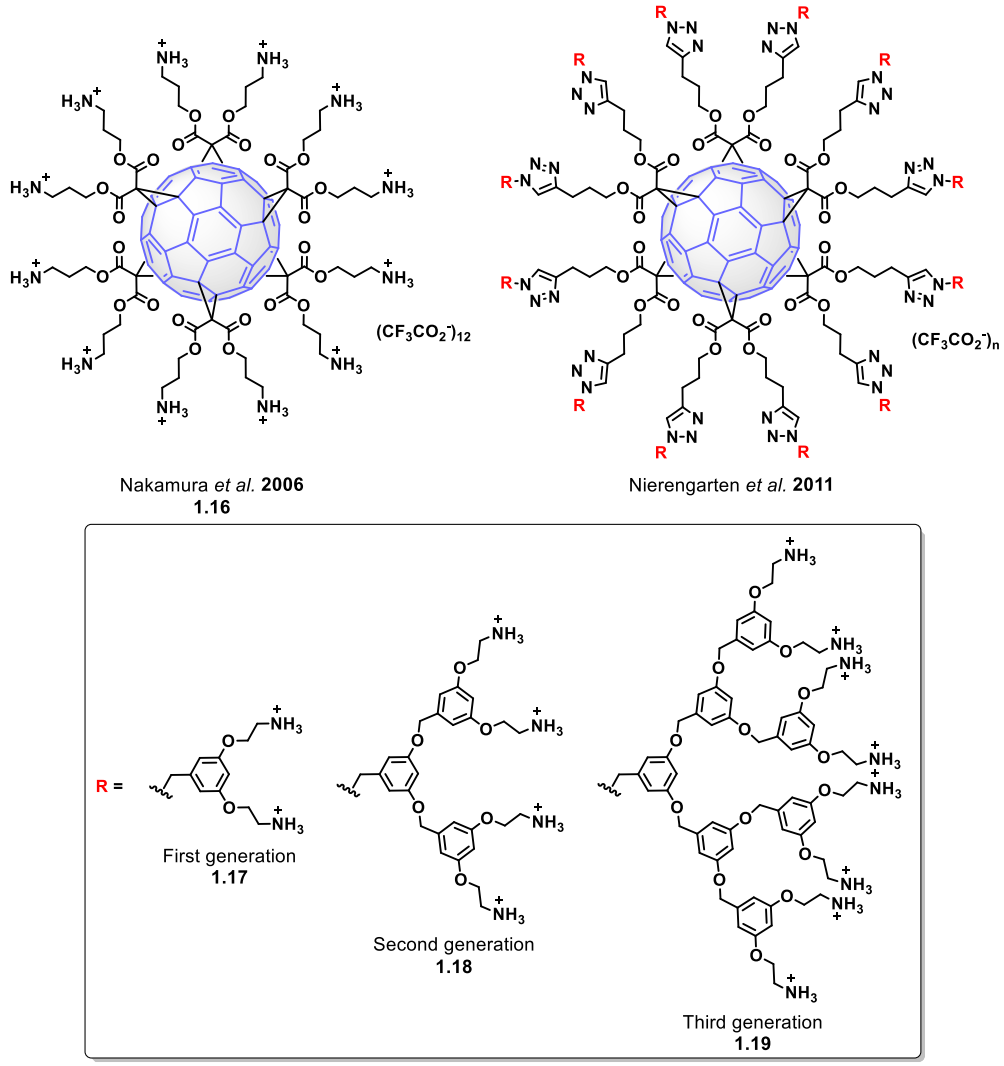

Figure 1.12. Polycationic [60]fullerene hexakis-adducts for DNA delivery.

More recently, Martín *et al.* reported the synthesis of fullerene hexakis-adducts containing 12, 24, 36 and even tridecafullerenes with 120 positive charges in their structure. These derivatives can efficiently and dose-dependently associate with plasmid DNA, forming stable complexes. This association allows mammalian cells to internalize these complexes and release the plasmid into the cytoplasm while maintaining its functional properties.[33b]

1.1.4. Multivalency: principles and features

The surface of most mammalian cells is covered by a dense layer of carbohydrates conjugated mainly to proteins and lipids, called glycocalyx. These conjugates are involved in numerous biological processes of cell adhesion and recognition through

interaction with their corresponding receptors.[86] However, this interaction has very low affinity and nature, to solve it, resorts to the multivalent presentation of carbohydrates and receptors. Multivalency is a phenomenon that occurs in nature that involves strong yet reversible non-covalent interactions between ligands and receptors.[87] Unlike monovalent interactions, where a single binding site determines affinity and specificity, multivalent interactions enhance the stability and efficacy of the binding process. This phenomenon is similar to how Velcro works: numerous flexible hooks interact with a filamentous surface, forming a network of weak interactions that together create a strong and stable connection (Figure 1.13).[88]

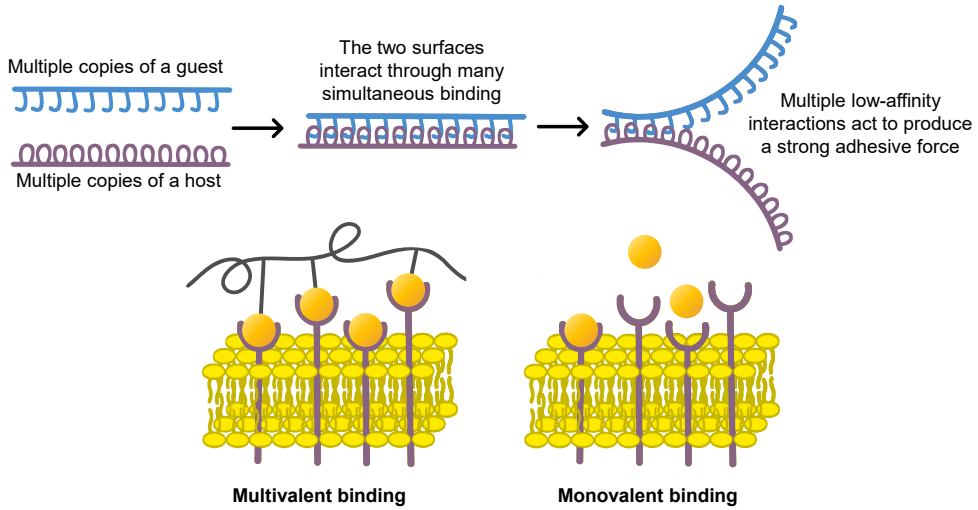

Figure 1.13. Multivalent interaction between a host and a guest (adapted from reference 88).

However, designing these systems is complex as multiple factors come into play, including the scaffold, size, linker, ligand density or mechanical properties.[89] These parameters must be considered when constructing a multivalent ligand using models and theoretical studies.

Small scaffolds can be considered a better design because they can penetrate and diffuse through biological membranes. However, if they are too small, like cyclodextrins[90] or calixarenes,[91] they can accommodate only a limited number of ligands, reducing the multivalent effect and resulting in low affinity. In contrast, dendrimers can serve as an excellent example of a well-optimized multivalent system.[92]

[86] T. Feizi, *Curr. Opin. Struct. Biol.* **1993**, *3*, 701.
[87] S. Bhatia, L. Cuellar-Camacho, R. Haag, *J. Am. Chem. Soc.* **2016**, *138*, 8654.
[88] C. S. Mahon, D. A. Fulton, *Nat. Chem.* **2014**, *6*, 665.
[89] A. K. Bakshi, T. Haider, R. Tiwari, V. Soni, *Drug Deliv. and Transl. Res.* **2022**, *12*, 2335.
[90] M. Adeli, M. Kalantari, Z. Zarnega, R. Kabiri, *RSC Adv.* **2012**, *2*, 2756.
[91] F. Sansone, L. Baldini, A. Casnatia, R. Ungaro, *New J. Chem.* **2010**, *34*, 2715.
[92] J. Khandare, M. Calderón, N. M. Dagia, R. Haag, *Chem. Soc. Rev.* **2012**, *41*, 2824.

The valency refers to the number of ligands that interact with a receptor. A high valency enhances multivalent interactions, strengthening the overall binding. This parameter can be tuned by adjusting the length or diameter of the scaffold to accommodate more ligands.

Linkers that connect ligands to central scaffolds play a crucial role in molecular design. Their length and flexibility significantly impact the entropy of the system. If a linker is too short or rigid, it may introduce steric strain, restrict flexibility and lower conformational entropy, which can weaken binding efficiency. Conversely, if a linker is too long or highly flexible, it may adopt multiple conformations or extend in different directions, leading to an excess of entropy and reducing the binding affinity. To minimize entropy loss and optimize binding, the linker should maintain an optimal balance of rigidity and flexibility within the system.

Another key factor is the ligand density, which refers to the number of ligands per molecule relative to the available side chains or functional groups in the system. Optimal density maximizes the number of functional binding sites, enhancing interaction efficiency. However, excessive density can lead to steric hindrance, obstructing receptor binding and reducing overall effectiveness.

As an example of carbon nanostructure for the design of multivalent systems and the influence of these parameters, Martín *et al.* reported the synthesis of fullerene-carbohydrate derivatives containing either 12 or 36 carbohydrate units.[33a] The derivative with 12 carbohydrates exhibited antiviral activity in an Ebola pseudotyped infection model within the low micromolar range. In contrast, the 36-unit derivative showed a loss of activity, probably due to steric congestion of sugars at the surface of the fullerene. However, extending the spacer length in the latter significantly enhanced its inhibitory activity, restoring it to the low micromolar range.

1.1.4.1. Multivalent systems based on [60]fullerene

An important example of multivalency phenomenon is the interaction and adhesion of pathogens to host cells in the initial stages of the infection process. In this context, hexa-substituted glycofullerenes have attracted much attention as a biocompatible carbon nanoplatform for the multivalent presentation of carbohydrates. The singular spherical distribution of the carbohydrate residues due to the 3D-structure of fullerene gave rise to unprecedented globular ligands with remarkable biological properties.

The applications of C_{60} as a multivalent platform have been particularly notable in three areas like enzyme inhibition, antibacterials and antivirals.

Enzyme inhibition

High valency iminosugar-fullerene conjugates (**1.20**) have demonstrated enhanced binding to glycosidase enzymes compared to their monovalent counterparts. Nierengarten *et al.* synthesized various glycoconjugates containing 36, 108 and 120

iminocarbohydrate units and evaluated their inhibitory effects on glycosidases (Figure 1.14).[93] Their findings revealed that multivalent ligand architectures dramatically enhance inhibitory potency, reaching up to a million-fold increase compared to the monovalent counterpart.

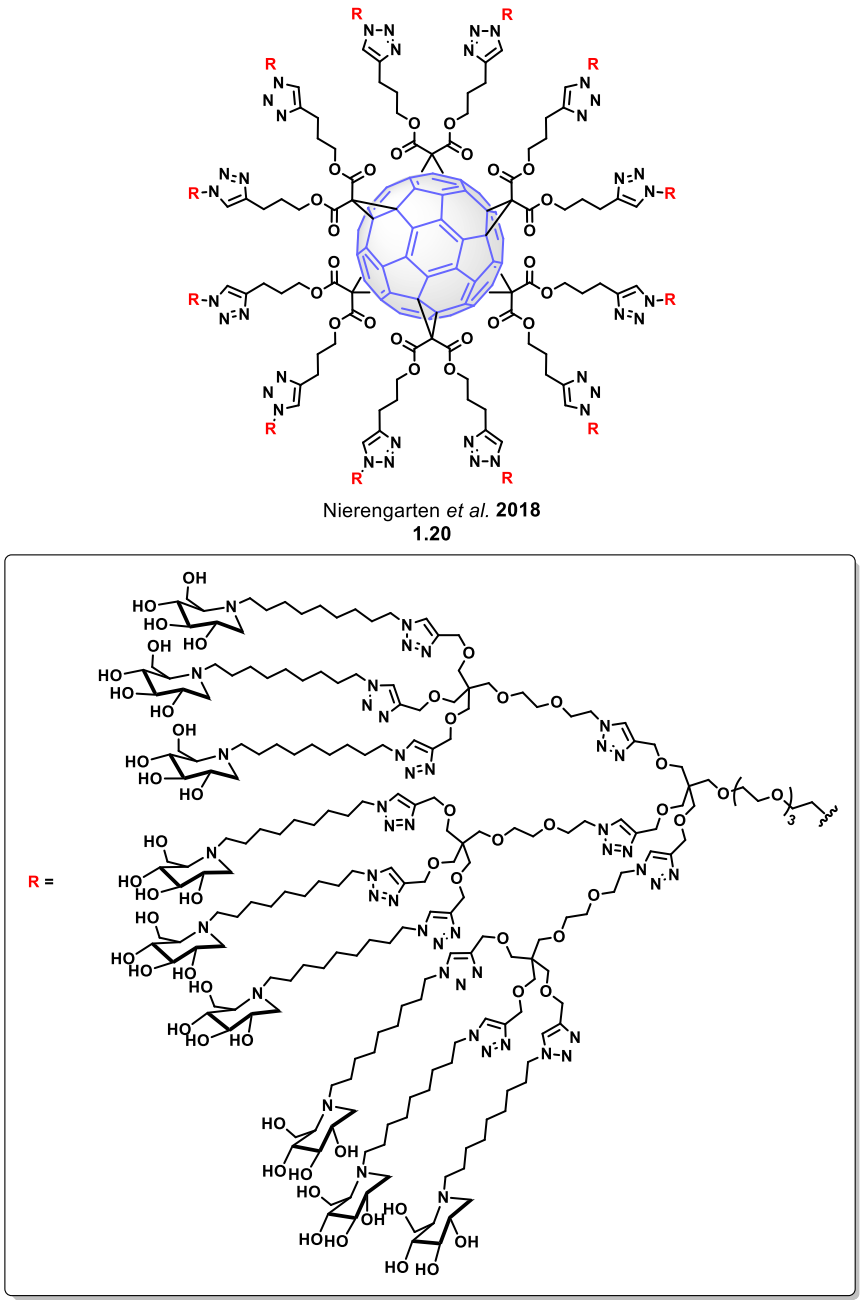

Figure 1.14. High valency iminosugar-fullerene conjugates.

[93] J.-F. Nierengarten, J. P. Schneider, T. M. N. Trinh, A. Joosten, M. Holler, M. L. Lepage, A. Bodlenner, M. I. García-Moreno, C. Ortiz-Mellet, P. Compain, *Chem. Eur. J.* **2018**, *24*, 2483.

Vincent *et al.* found an unexpected multivalent effect in glycosyltransferase enzyme inhibition. Fullerene sugar balls containing mannose, heptose or octose derivatives (**1.21 - 1.23**) were tested as inhibitors of heptosyltransferase WaaC, showing inhibition in the low micromolar range, whereas their monomeric glycoside counterparts exhibited significantly weaker inhibition, ranging from high micromolar to low millimolar levels (Figure 1.15).[94] The average affinity of a single glycoside towards WaaC increased notably when presented in a multivalent format. However, due to the complexity of both the enzyme and the fullerenes, a specific binding mode could not be determined. In a later study, they clarified that the multivalent carbohydrate presentation enhances inhibition because the 3D-structure of WaaC display two recognition sites: one for the so-called "acceptor", to which a sugar unit located in the "donor" binding site will be transferred.[95] The observed multivalent inhibition likely results from the strengthened affinity of ligands for the accessible acceptor pocket, with aggregation playing a contributing but not primary role in enzyme inhibition.

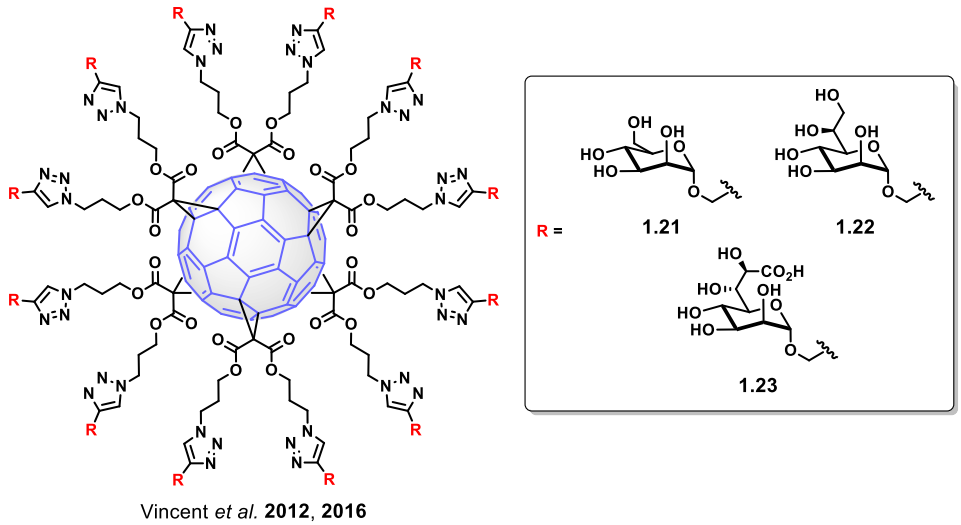

Figure 1.15. Fullerene sugar balls containing mannose, heptose or octose derivatives.

Antibacterial applications

The emerging resistance of most pathogenic bacteria to clinically relevant antibiotics urges the scientific community to find a new class of drugs or new mode of actions to treat infectious diseases. Bacterial adhesion to cell surface tissues is one of the very first steps of the infective process and is often mediated by carbohydrate-protein interactions. The multivalent presentation of carbohydrates is generally an essential point for achieving high affinity interactions with lectin proteins on the cells membrane. The first examples of multivalent [60]fullerene molecules for antibacterial

[94] M. Durka, K. Buffet, J. Iehl, M. Holler, J.-F. Nierengarten, S. P. Vincent, *Chem. Eur. J.* **2012**, *18*, 641.
[95] A. Tikad, H. Fu, C. M. Sevrain, S. Laurent, J.-F. Nierengarten, S. P. Vincent, *Chem. Eur. J.* **2016**, *22*, 13147.

applications were based on the synthesis of glycofullerenes functionalized with mannose and galactose derivatives. These glycoconjugates were tested with three different lectins: ConA (**1.24**),[96] FimH (**1.25**),[97] and LecA (**1.26**) (Figure 1.16).[98] In all cases, the fullerene derivatives exhibited greater affinity for the lectins compared to the reference monomers, highlighting the significance of the multivalent effect.

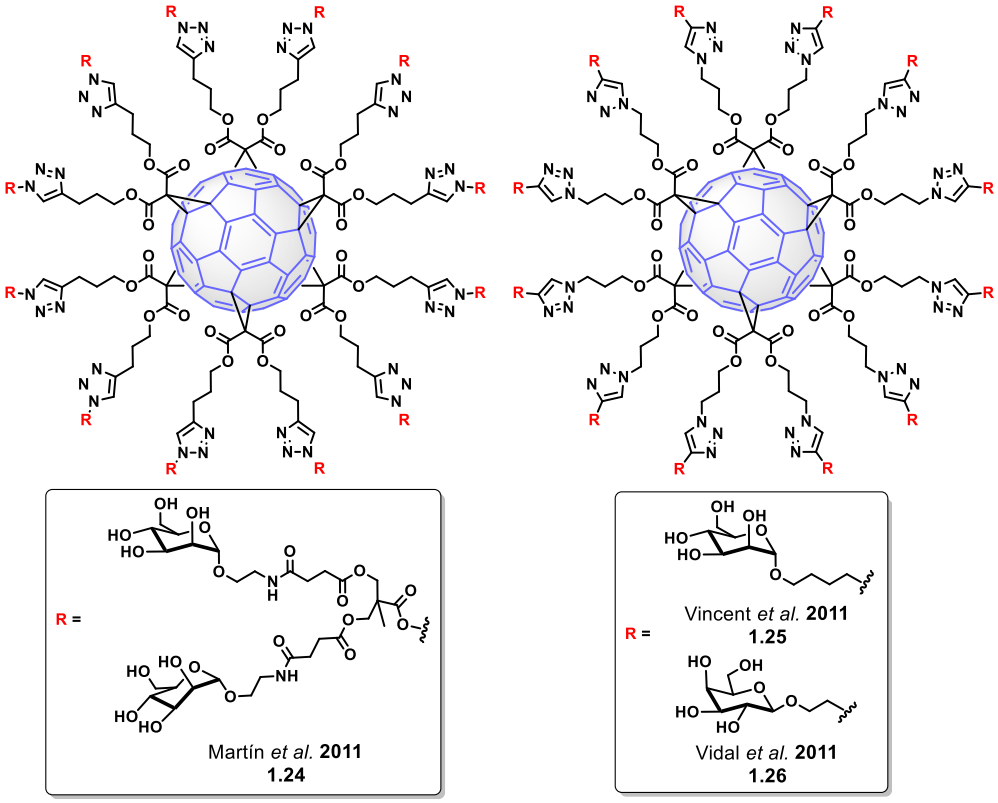

Figure 1.16. Examples of [60]fullerene hexakis-adducts for antibacterial applications.

More recently, Vincent's group reported the preparation of a series of fucofullerenes (**1.27** - **1.29**) containing up to 24 fucose residues which could be used against two fucose-specific lectins namely LecB and RSL (Figure 1.17).[99] In these studies it was seen that increasing the length between the central core and the carbohydrate, as well as increasing the valency of the glycofullerene, both enhance the binding affinity.

[96] M. Sánchez-Navarro, A. Muñoz, B. M. Illescas, J. Rojo, N. Martín, *Chem. Eur. J.* **2011**, *17*, 766.
[97] M. Durka, K. Buffet, J. Iehl, M. Holler, J.-F. Nierengarten, J. Taganna, J. Bouckaert, S. P. Vincent, *Chem. Commun.* **2011**, *47*, 1321.
[98] S. Cecioni, V. Oerthel, J. Iehl, M. Holler, D. Goyard, J.-P. Praly, A. Imberty, J.-F. Nierengarten, S. Vidal, *Chem. Eur. J.* **2011**, *17*, 3252.
[99] K. Buffet, E. Gillon, M. Holler, J.-F. Nierengarten, A. Imberty, S. P. Vincent, *Org. Biomol. Chem.* **2015**, *13*, 6482.

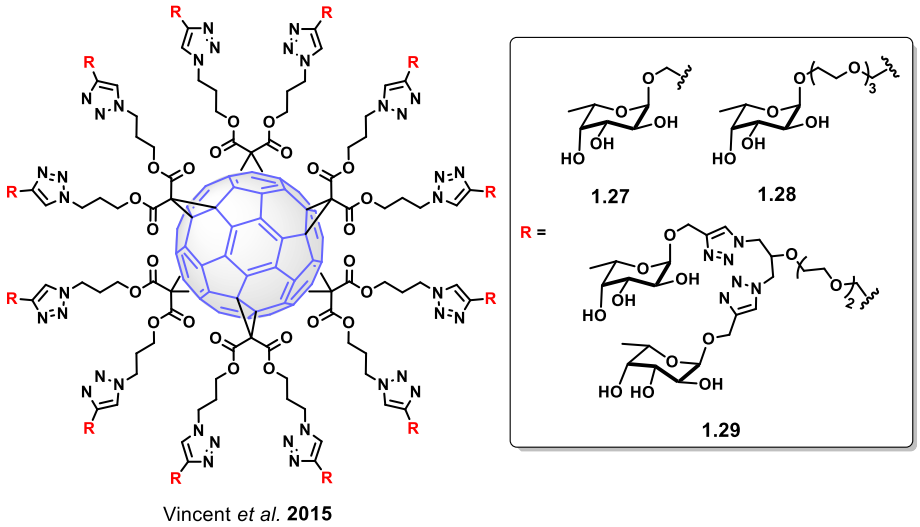

Figure 1.17. Fucofullerenes for antibacterial applications.

Antiviral applications

Glycofullerenes have been extensively exploited for antiviral applications because the globular disposition of the carbohydrates can mimic the surface of the pathogens and interfere with the infectious process blocking the corresponding cell-surface receptor.

Dendritic cells (DCs) play a vital role in initiating pathogen-specific immune responses. These pathogens are detected by receptors such as C-type lectins found on the surface of DCs.[100,101] One such lectin is DC-SIGN (dendritic cell-specific ICAM-3 grabbing non-integrin), which contains a Carbohydrate Recognition Domain (CRD) that specifically binds to *N*-linked high-mannose oligosaccharides and branched fucosylated structures (Figure 1.18). The CRD is connected to the transmembrane region by a neck domain composed of seven complete and one incomplete tandem repeat, which is essential for oligomerization and carbohydrate specificity. Additionally, a cytoplasmic tail is present. DC-SIGN serves as a receptor for various viruses, including HIV, Ebola, cytomegalovirus, hepatitis C virus and Dengue virus. Therefore, designing glycomimetics with multivalent mannose presentation offers a promising approach to blocking the CRDs of DC-SIGN.

[100] Y. v. Kooyk, T. B. H. Geijtenbeek, *Nat. Rev. Immunol.* **2003**, *3*, 697.
[101] G. Tabarani, M. Thépaut, D. Stroebel, C. Ebel, C. Vivès, P. Vachette, D. Durand, F. Fieschi, *J. Biol. Chem.* **2009**, *284*, 21229.

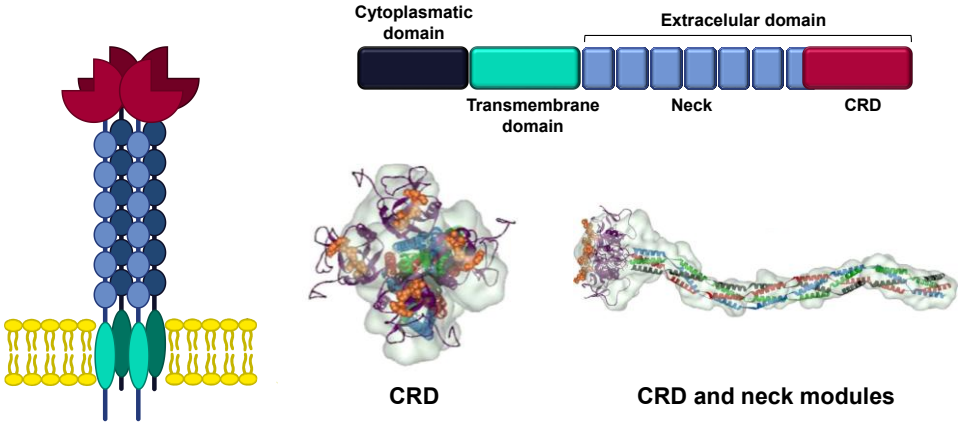

Figure 1.18. DC-SIGN structure (adapted from references 100 and 101).

Highly multivalent glycofullerenes, commonly known as *sugar balls* or tridecafullerenes, were prepared simultaneously by Martín and Nierengarten groups containing 120 carbohydrates and 13 fullerenes units per molecule following a copper-catalyzed azide-alkyne cycloaddition (CuAAC) click-chemistry methodology (Figure 1.19).[10a] The biological assays were carried out using mannose (**1.31** - **1.32**) and galactose (**1.30**) as carbohydrates. The results demonstrated that the mannose derivatives exhibited very strong inhibition of cell infection by Ebola-pseudotyped viral particles, with half-maximum inhibitory concentration (IC_{50}) values in the subnanomolar range, while the galactose derivative was unable to inhibit the infection process.

A comparable approach was employed to synthesize glycofullerenes containing 360 carbohydrate units per molecule using mannose disaccharides.[102] The synthesis utilized a strain-promoted azide-alkyne cycloaddition (SPAAC) strategy, integrating cyclooctynes into the structure. These molecules were evaluated for their ability to inhibit Zika and Dengue viruses, demonstrating the most potent inhibitory activity in the picomolar range.

In a complementary strategy, Martín *et al.* developed the synthesis of multivalent tryptophan and tyrosine hexakis-adducts for the inhibition of HIV.[103] In this case, the molecules interacted with the peripheral carbohydrates of the virus rather than with the cellular receptor, exhibiting anti-HIV-1 activity at low micromolar range.

[102] J. Ramos-Soriano, J. J. Reina, B. M. Illescas, N. de la Cruz, L. Rodríguez-Pérez, F. Lasala, J. Rojo, R. Delgado, N. Martín, *J. Am. Chem. Soc.* **2019**, *141*, 15403.
[103] M. Ruiz-Santaquiteria, B. M. Illescas, R. Abdelnabi, A. Boonen, A. Mills, O. Martí-Marí, S. Noppen, J. Neyts, D. Schols, F. Gago, A. San-Félix, M.-J. Camarasa, N. Martín, *Chem. Eur. J.* **2021**, *27*, 10700.

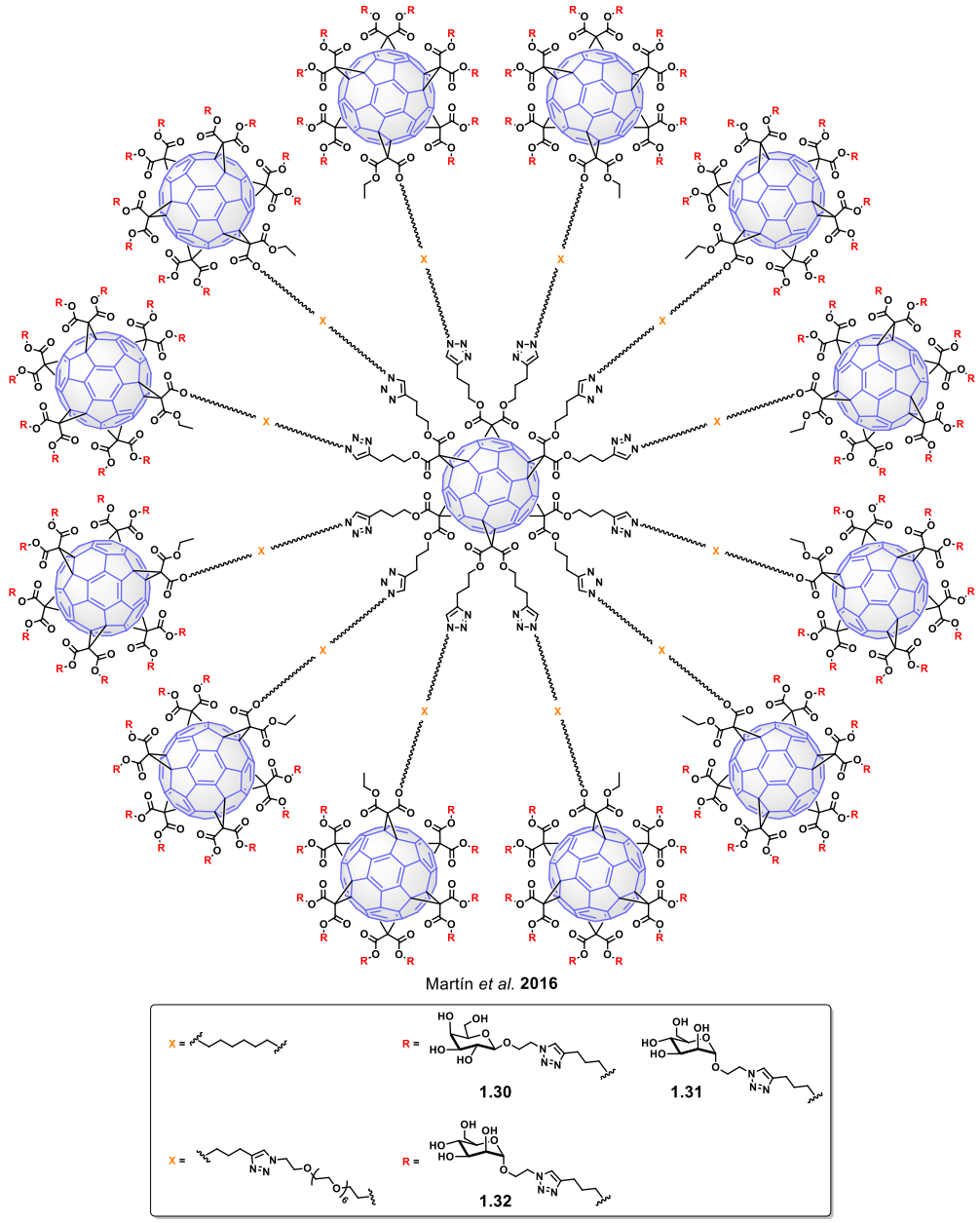

Figure 1.19. Tridecafullerenes containing 120 carbohydrate units for the inhibition of Ebola virus.

1.2. Objectives

This chapter focuses on the synthesis of [60]fullerene hexakis-adducts derivatives for their subsequent functionalization with different substituents such as carbohydrates and boron clusters. For this purpose, the design of different malonates will be carried out to covalently attach them to the fullerene core and synthesize both symmetrical and asymmetrical scaffolds using the Bingel-Hirsch cyclopropanation reaction. These appendages will contain terminal alkynes, which are prone to react through CuAAC reaction with azide-terminated carbohydrates or boron clusters. The synthesis of asymmetric hexakis-adducts will allow further functionalization of the molecules for the synthesis of tridecafullerenes, which will contain 120 carbohydrate units and 13 fullerene units per molecule.

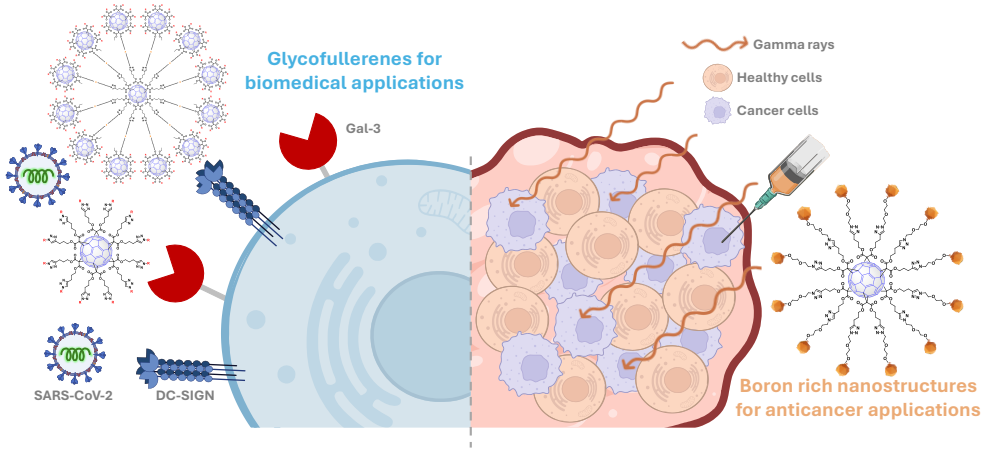

Once the structural characterization of the products has been carried out, their biological properties as virus inhibitors or as potential anticancer agents will be evaluated. Moreover, the interaction of various glycofullerenes with lectins will be investigated using techniques such as NMR experiments.

1.3. Results and discussion

1.3.1. Synthesis of C_{60}-fullerene monoadducts

The functionalization of [60]fullerene to produce molecules soluble in organic solvents can be achieved through the incorporation of polar groups on its structure using the Bingel-Hirsch cyclopropanation reaction. To this end, both symmetrical and asymmetrical malonates were synthesized *via* esterification with alcohols. The alcohols used in this process are either commercially available such as 4-pentyn-1-ol or synthesized in the laboratory through the Appel reaction (Scheme 1.4).

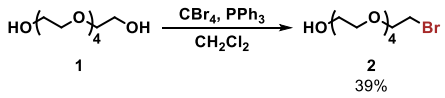

Scheme 1.4. General procedure for the synthesis of compound **2**.

After alcohol **2** was prepared, the corresponding esterification reactions were performed using malonyl chloride **3** for symmetrical malonates or ethyl malonyl chloride **4** for asymmetrical ones (Scheme 1.5). Symmetrical malonates are generally employed for its functionalization with small molecules, whereas asymmetrical malonates serve as anchoring points for the synthesis of more complex molecules, as will be discussed later. Accordingly, malonates **6-7** were synthesized in good yields.

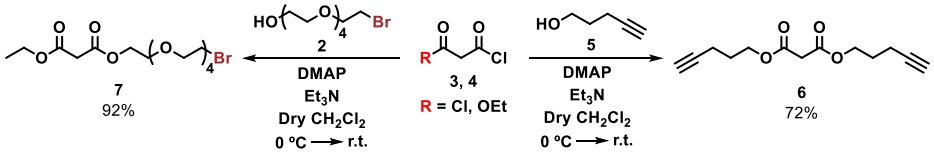

Scheme 1.5. Synthesis of malonates from the respective alcohol derivatives.

The cycloaddition of malonates onto C_{60} was carried out by Bingel-Hirsch reaction under kinetic control conditions. This means that, at low temperature, monitoring the reaction with thin layer chromatography (TLC) and using excess of fullerene, the reaction can be directed towards the formation of the monoadduct. The reaction was performed in the presence of I_2 as the halogenating agent, DBU as non-nucleophilic base and toluene as solvent. Once the reaction was complete, it was quenched with $Na_2S_2O_3$ to remove unreacted I_2. Following this methodology, the synthesis of the monoadduct **8** was carried out (Scheme 1.6).

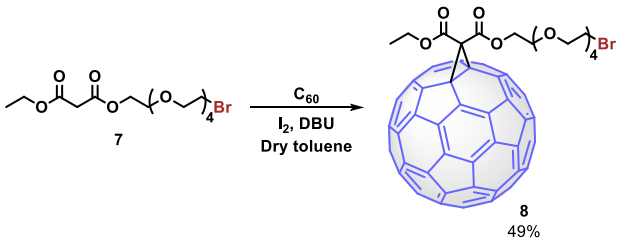

Scheme 1.6. General procedure for the synthesis of monoadduct **8**.

The presence of bromine at the end of the malonate chain acts as a reactive position that will allow further functionalization of the molecule. The synthesized monoadduct was purified by column chromatography and characterized by the standard techniques: NMR, FT-IR and mass spectrometry.

^{1}H NMR is a straightforward method to corroborate that the reaction has been successful. If the spectrum of monoadduct **8** is compared with the starting malonate **7**, the disappearance of the singlet at ~3 ppm, corresponding to the protons of the alpha position to both carbonyl groups, is observed (Figure 1.20). This occurs due to cyclopropane formation during the reaction that led to a quaternary carbon.

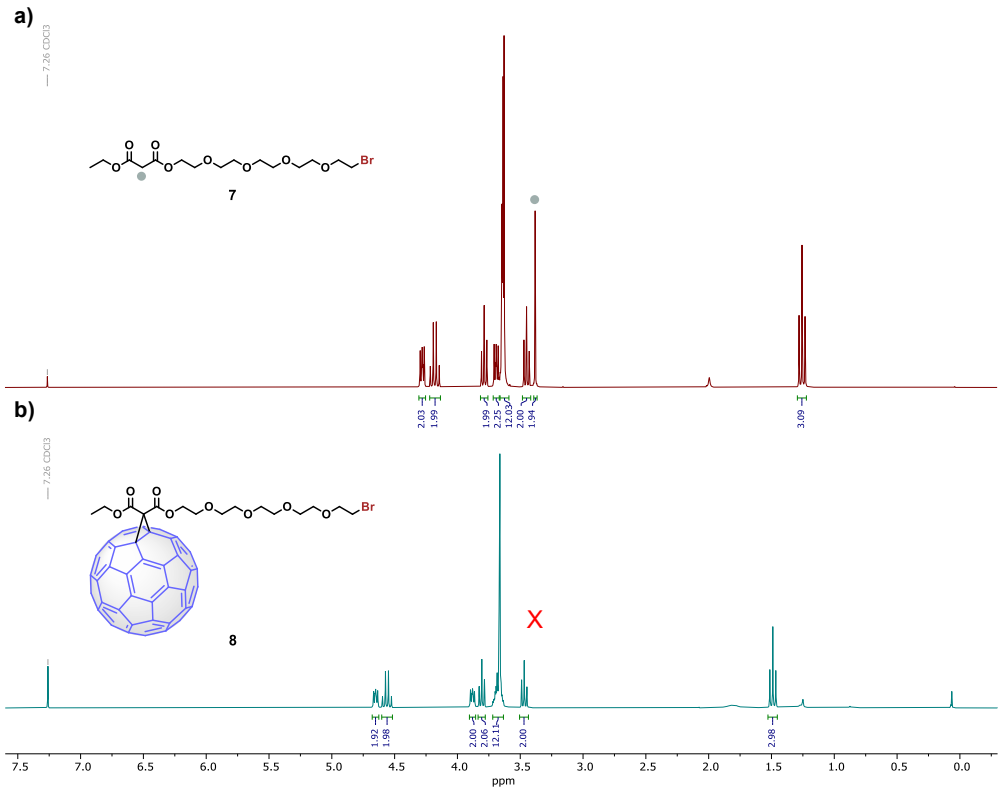

Figure 1.20. ^{1}H NMR spectra of: a) compound **7** and b) compound **8** ($CDCl_3$, 300 MHz).

The presence of C_{60} in the molecule can be observed in the ^{13}C NMR spectrum. Due to the C_{2v} symmetry of the monoadduct, in the aromatic region, between 139 – 146 ppm, 15 signals appear (compared to the only signal observed for the pristine fullerene) corresponding to the sp^2 carbons of the fullerene as well as the signal at ~72 ppm of the sp^3 carbons formed during the reaction. Another characteristic resonances from the malonate are the carbonyls over ~160 ppm, the adjacent carbons to the carbonyl groups at ~66 – 64 ppm, the alpha carbon to both carbonyl groups at ~52 ppm, the *C*H$_2$-Br at ~30 ppm and the methyl group at ~14 ppm (Figure 1.21).

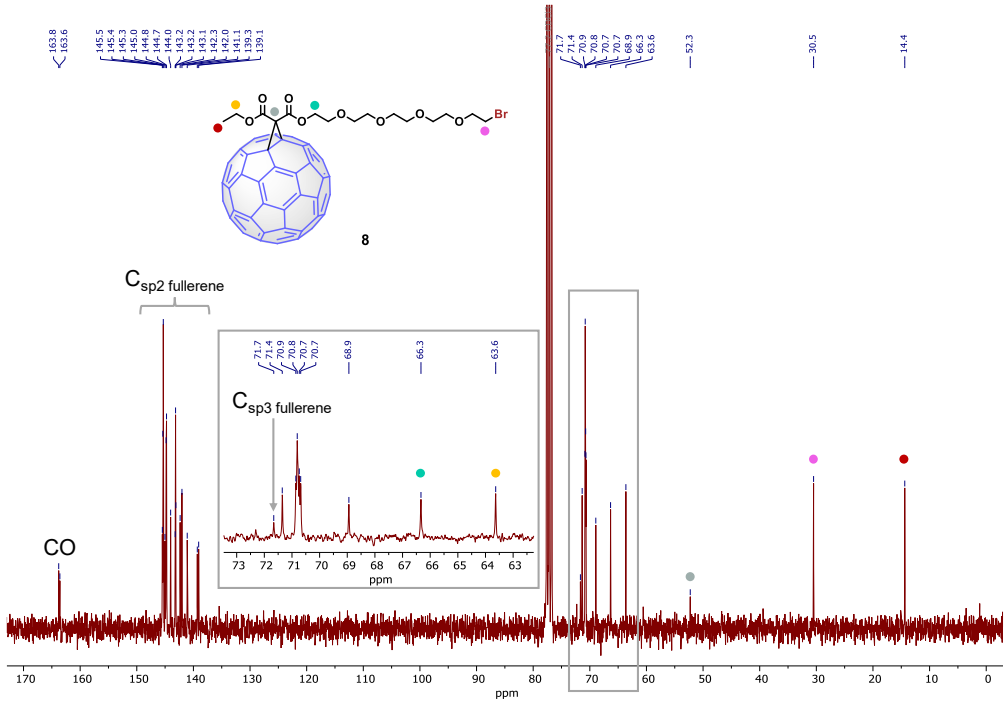

Figure 1.21. ^{13}C NMR spectrum of compound **8** ($CDCl_3$, 75 MHz).

In the mass spectrum, the peak corresponding to $[M]^+$ is observed. Regarding the IR spectrum, the characteristic bands to highlight are the C-H stretching around 2920 cm^{-1} and the C=O stretching of the carbonyl groups of the malonate around 1744 cm^{-1} (Appendix 1, Figure AP1.1a). Monoadduct **8** was obtained in moderate yield and showed greater solubility in organic solvents such as CH_2Cl_2 or $CHCl_3$ compared to the starting C_{60}, which facilitates handling and characterization.

1.3.2. Synthesis of C_{60}-fullerene hexakis-adducts

The covalent attachment of additional malonates to monoadducts or pristine [60]fullerene allows the formation of hexakis-adducts. These adducts represent the maximum possible degree of substitution in the fullerene molecule, comprising six addends. Based on the characteristics of the malonates, these adducts can be categorized as either symmetrical or asymmetrical.

In the case of symmetrical hexa-substituted adducts, all six malonate moieties are identical, exhibiting an A_{12} substitution pattern, with pristine [60]fullerene serving as the starting material. Conversely, asymmetric adducts adopt a [5:1] structural configuration characterized by an $A_{10}B$ substitution pattern, where one position is occupied by the asymmetric unit, while the remaining five are substituted with a different malonate. The synthesis of these asymmetric adducts typically employs monoadducts, such as the described above, as starting materials. The primary distinction between these two types lays in their reactivity: symmetrical adducts exhibit uniform single-type reactivity, whereas asymmetric adducts enable the

incorporation of diverse functionalities with varying reactivity in a straightforward manner, providing that the chemical compatibility is maintained.

The formation of these compounds is achieved through the Bingel-Hirsch cyclopropanation reaction. Unlike the synthesis of monoadducts, where precise control of the conditions is required to obtain the monosubstituted product, hexakis-adducts formation is performed under thermodynamically controlled conditions. By employing an excess of the malonate, using CBr_4 as the halogenating agent and maintaining a reaction time of 72 hours, the reaction is directed almost exclusively toward the formation of the desired products. The choice of CBr_4 instead of I_2, as used in the previous section, is due to its dual role as both the halogenating agent and the template for obtaining products with T_h-symmetry.[104]

Employing compound **8** and malonate **6** in the presence of CBr_4 and DBU, a new asymmetric hexakis-adduct (**9**) containing ten terminal alkynes and one bromine was successfully synthesized, and it is suitable for conducting further click chemistry reactions (Scheme 1.6).

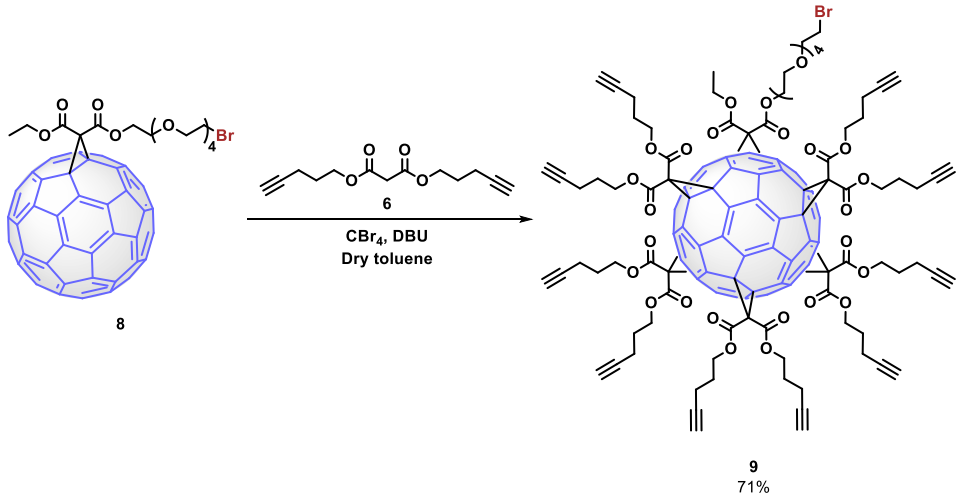

Scheme 1.6. General procedure for the synthesis of asymmetric hexakis-adduct **9**.

The characterization of compound **9** was carried out with conventional techniques used in organic chemistry. However, it was not possible to achieve the mass spectra due to the high level of fragmentation.[102]

In the ^{1}H NMR spectrum (Figure 1.22), it can be observed how the complexity of the signals increases due to the high degree of functionalization of the molecule. However, this complexity together with the appearance of the new signals corresponding to the malonate of alkynes indicates the possible formation of the hexakis-adduct.

[104] J.-F. Nierengarten, *Chem. Commun.* **2017**, *53*, 11855.

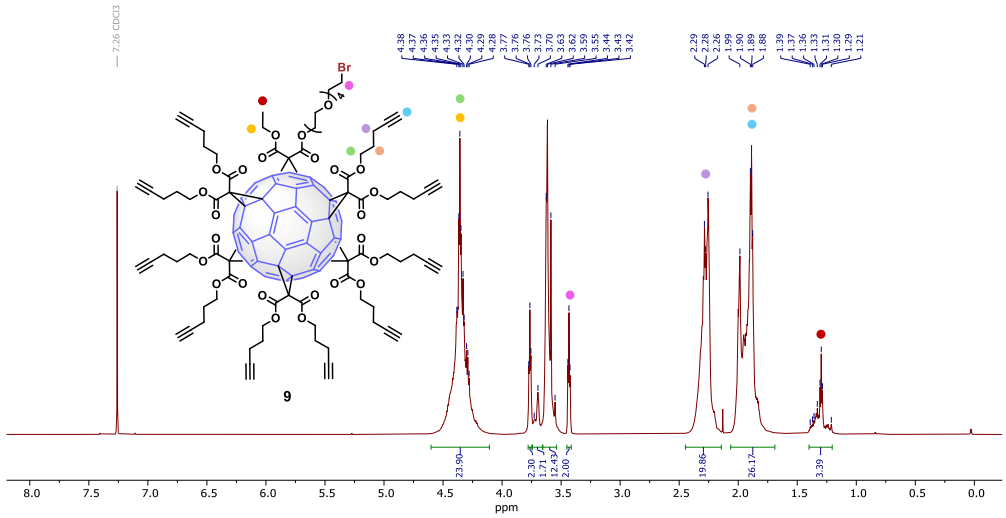

Figure 1.22. ^{1}H NMR spectrum of compound **9** ($CDCl_3$, 700 MHz).

The appropriate technique to corroborate the correct functionalization of the desired product is ^{13}C NMR spectroscopy (Figure 1.23). The most significant observation in the hexakis-adduct spectrum, when compared to the monoadduct (Figure 1.21), is the decrease in the number of signals from the *C*(sp^2) of the fullerene. While fifteen signals are observed in the monoadduct, in the case of the hexakis-adduct this number is reduced to two due to the high symmetry of the molecule. The two types of malonates present in the molecule can also be distinguished using this technique. In the new introduced malonates, the terminal alkynes are detected at ~82 ppm and ~78 ppm while in polyethylene glycol malonate the *C*H$_2$-Br signal remains characteristic at ~30 ppm. In both cases, the quaternary carbons adjacent to the carbonyl groups are identified at ~45 ppm and ~39 ppm. With the help of experiments such as DEPT-135 and 2D experiments like Heteronuclear Single Quantum Coherence (HSQC), the complete assignment of each proton and carbon can be achieved.

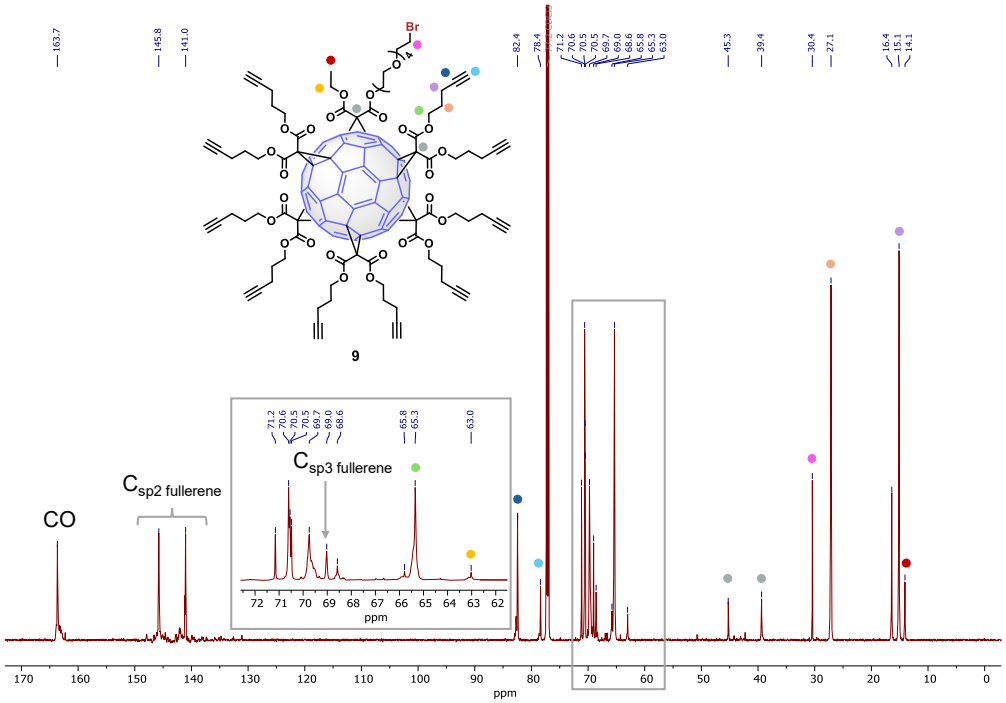

Figure 1.23. ^{13}C NMR spectrum of compound **9** ($CDCl_3$, 176 MHz).

The FT-IR remains unchanged in comparison with monoadducts, except for the appearance of a new stretching band at 3293 cm^{-1} corresponding to the stretching vibration of the terminal C-H bond of the alkyne groups (Appendix 1, Figure AP1.1b).

The synthesis of a symmetric hexakis-adduct was also carried out using the methodology described in the literature.[97] This is similar to the asymmetric adducts but varying the equivalents of malonate **6** used and using pristine [60]fullerene as the starting material (Scheme 1.7).

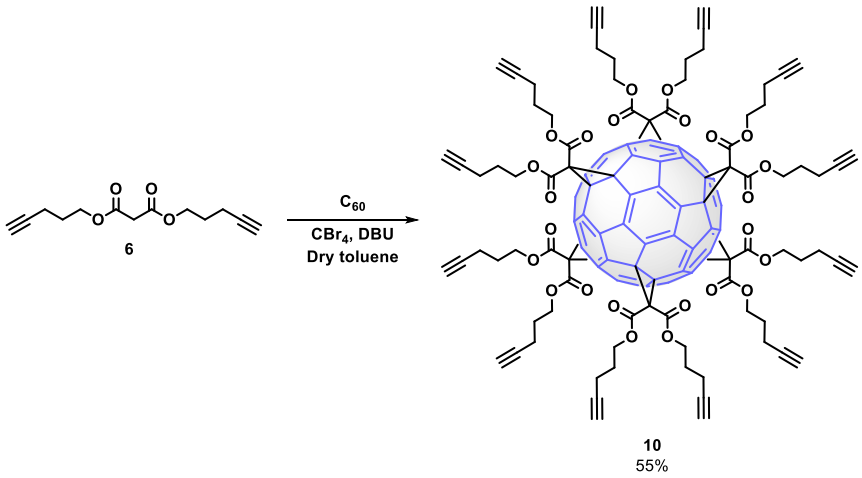

Scheme 1.7. General procedure for the synthesis of compound **10**.

The characterization of compound **10** is practically identical to the asymmetric hexakis-adduct except for the lack of the signals corresponding to polyethylene glycol malonate. Figure 1.24 highlights the most representative signals of this compound for its characterization.

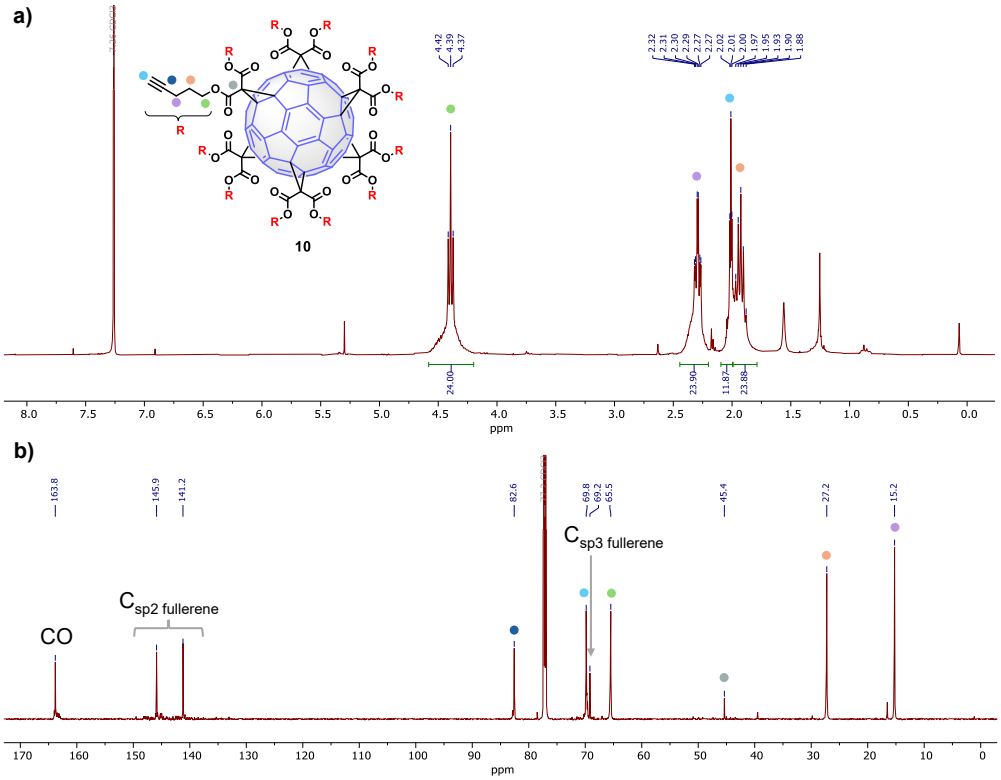

Figure 1.24. a) ^{1}H NMR spectrum ($CDCl_3$, 300 MHz) and b) ^{13}C NMR spectrum ($CDCl_3$, 176 MHz) of compound **10**.

1.3.3. Synthesis of glycofullerenes

The synthesized fullerene hexakis-adducts can be further functionalized through CuAAC, a 1,3-dipolar cycloaddition reaction that occurs between a terminal alkyne group and a compound containing an azide group, leading to the formation of triazole rings. The first click reaction was reported by Huisgen[105] but it required high temperatures, long reaction times and showed poor regiospecificity due to the high stability of alkynes. Later, Medal[106] and Sharpless,[107] by using Cu(I) catalysts, managed to solve these problems since Cu(I) is capable of activating alkyne groups and acting as a template for the formation of a single regioisomer. This reaction is known nowadays as copper-catalyzed azide-alkyne cycloaddition and allowed

[105] R. Huisgen, *Angew. Chem. Int. Ed.* **1963**, *2*, 565.
[106] C. W. Tornøe, C. Christensen, M. Meldal, *J. Org. Chem.* **2002**, *67*, 3057.
[107] V. V. Rostovtsev, L. G. Green, V. V. Fokin, K. B. Sharpless, *Angew. Chem. Int. Ed.* **2002**, *41*, 2596.

Bertozzi, Meldal and Sharpless to obtain the Nobel Prize in Chemistry in 2022 *for the development of click chemistry and bioorthogonal chemistry.*

Through theoretical calculations and kinetic studies, two mechanisms for the click reaction have been proposed. One of the pathways is a slow process catalyzed by a mononuclear copper specie and the other pathway is a more kinetically favored route promoted by the formation of dinuclear copper species (Scheme 1.8).[108,109]

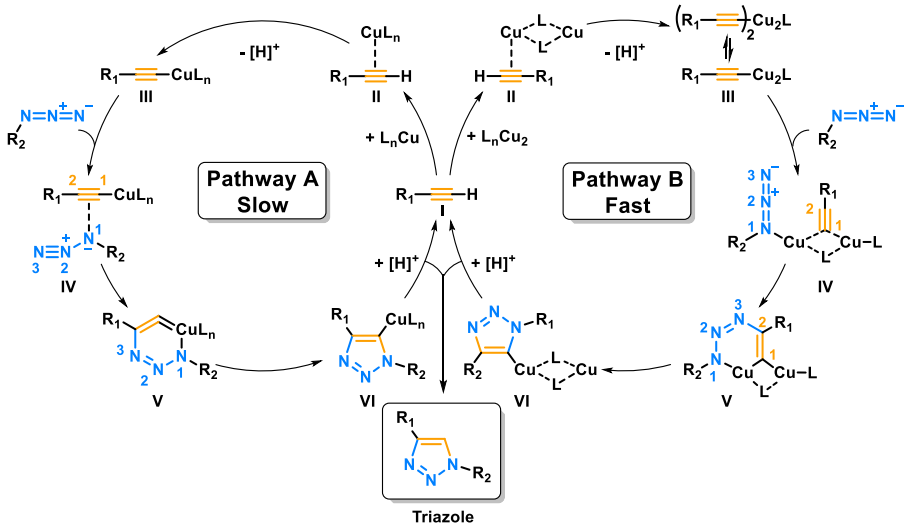

Scheme 1.8. Proposed mechanisms for the CuAAC reaction (adapted from reference 108).

In both cases the catalytic cycle starts with the coordination of the Cu(I) species to the alkyne **I** (**II**), followed by the deprotonation of the alkyne and the formation of a Cu-acetylide intermediate (**III**). Subsequently, the organic azide is incorporated into the cycle and coordinates with the Cu(I) complex (**IV**), followed by the addition of N-3 from the azide to C-2 of the alkyne, resulting in the formation of a Cu(III) metallacycle (**V**). The last step involves the contraction of the six-membered ring to form the triazolyl-copper derivative (**VI**) which releases the triazole *via* protolysis, thereby completing the catalytic cycle.

Then, the described hexakis-adducts can be functionalized with species containing a terminal azide group. This section focuses on the incorporation of carbohydrates to synthesize highly water-soluble structures with biological applications.

1.3.3.1. Symmetric glycofullerenes

The use of derivative **10** containing twelve terminal alkynes allows the synthesis of symmetrical glycofullerenes. The click reaction was carried out using different carbohydrates derived from galactose, mannose, fucose and *N*-acetylglucosamine, all of them containing an azide-terminated linker (Figure 1.25).

[108] N. Z. Fantoni, A. H. El-Sagheer, T. Brown, *Chem. Rev.* **2021**, *121*, 7122.
[109] L. Jin, D. R. Tolentino, M. Melaimi, G. Bertrand, *Sci. Adv.* **2015**, *1*, e1500304.

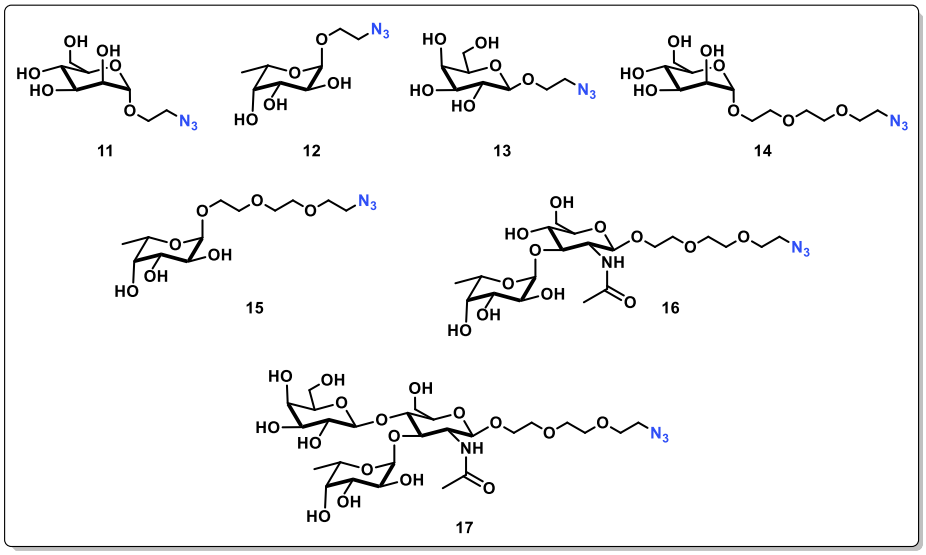

Figure 1.25. Structure of the different carbohydrates used.

The reactions were carried out using $CuBr{\cdot}SMe_2$ as the catalyst, sodium ascorbate and a wire of metallic copper. The purpose of these last two reagents is to prevent the formation of Cu(II) species which would hinder the progress of the reaction. The presence of Cu(0) would result in a comproportionation between the two species, while sodium ascorbate would function as a reducing agent for the Cu(II). Together, these processes facilitate the regeneration of Cu(I). The reactions were carried out using DMSO as the solvent to ensure the solubility of both the starting and final products. An important factor to consider is the reaction concentration, which is maintained at a highly concentrated level (~1.5 mL/250 mg of hexakis-adduct) to ensure optimal reaction progress and to enhance yields. With all of this in mind and using the explained methodology, it was possible to synthesize glycofullerenes **18**-**24** (Scheme 1.9).

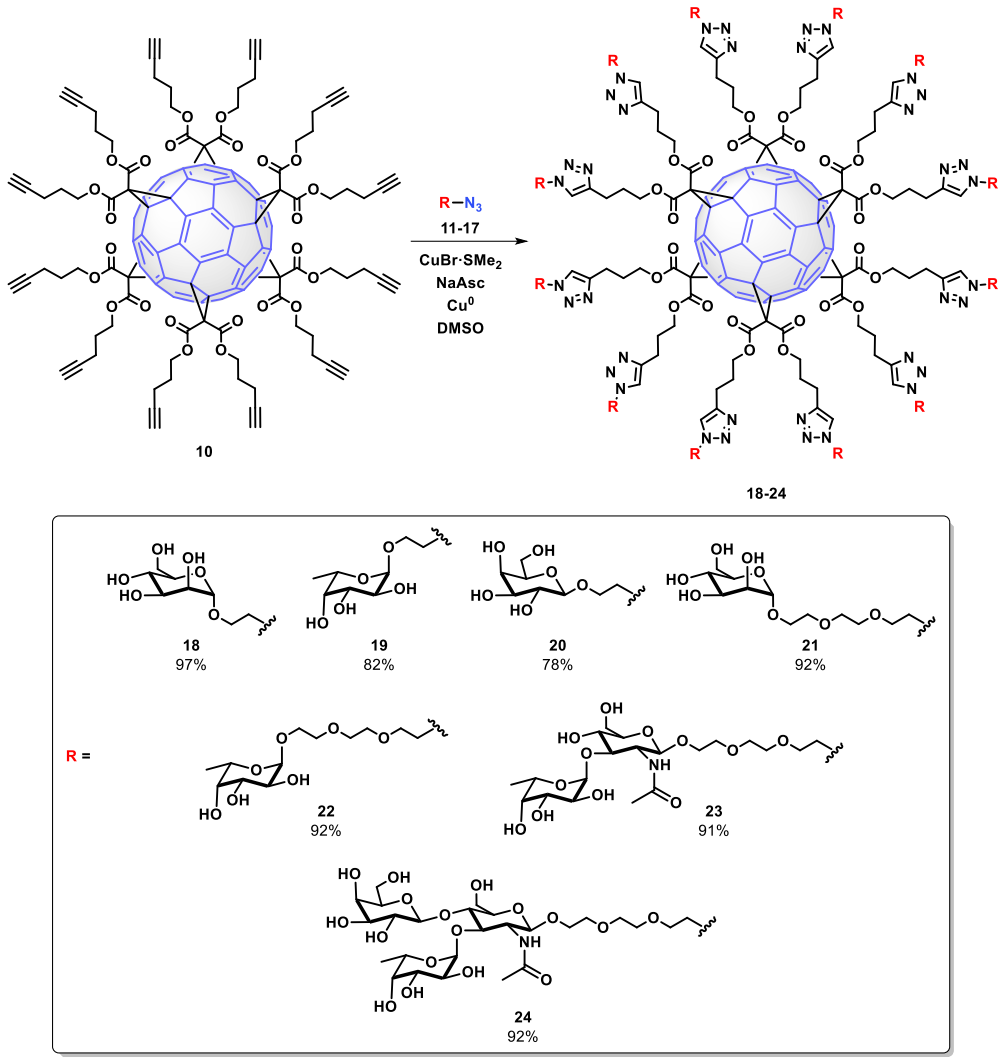

Scheme 1.9. General procedure for the synthesis of glycofullerenes **18-24**.

Since copper is cytotoxic and these products are intended for biological applications, any excess of remaining copper was removed using a copper scavenger resin known as QuadraSil® Mercaptopropyl. This resin contains terminal thiol groups capable of chelating free copper in the reaction medium, which can then be eliminated with filtration.

As the final products are only soluble in DMSO or H_2O, the purification method for these compounds consists on their precipitation in methanol. This approach also facilitates the removal of the excess of carbohydrates used in the reaction, as these are soluble in methanol. The synthesized glycofullerenes **18-24** were afforded in high yields and are completely soluble in H_2O.

The characterization of these compounds can be carried out using conventional techniques, however, ^{13}C NMR serves as the definitive method to confirm that the

reaction worked successfully. For a better understanding, the characterization of compound **18** will be explained as a representative example.

In the ^{13}C NMR and DEPT-135 spectra (Figure 1.26), all the signals of the molecule can be identified. The first evidence indicating the correct functionalization of the alkynes is the disappearance of their characteristic resonances at ~80 ppm and the emergence of two signals at ~146 ppm and ~122 ppm corresponding to the new triazole rings formed during the click reaction. The signals attributed to the carbohydrate can also be distinguished, with the most representative being the anomeric carbon at ~99 ppm and those corresponding to the CH_2-N at ~49 ppm. Moreover, it can be observed the resonances of the sp^2 carbons of the fullerene at ~145 ppm and ~141 ppm, the sp^3 carbons of the fullerene at ~69 ppm and the alpha-carbon adjacent to both carbonyl groups at ~46 ppm.

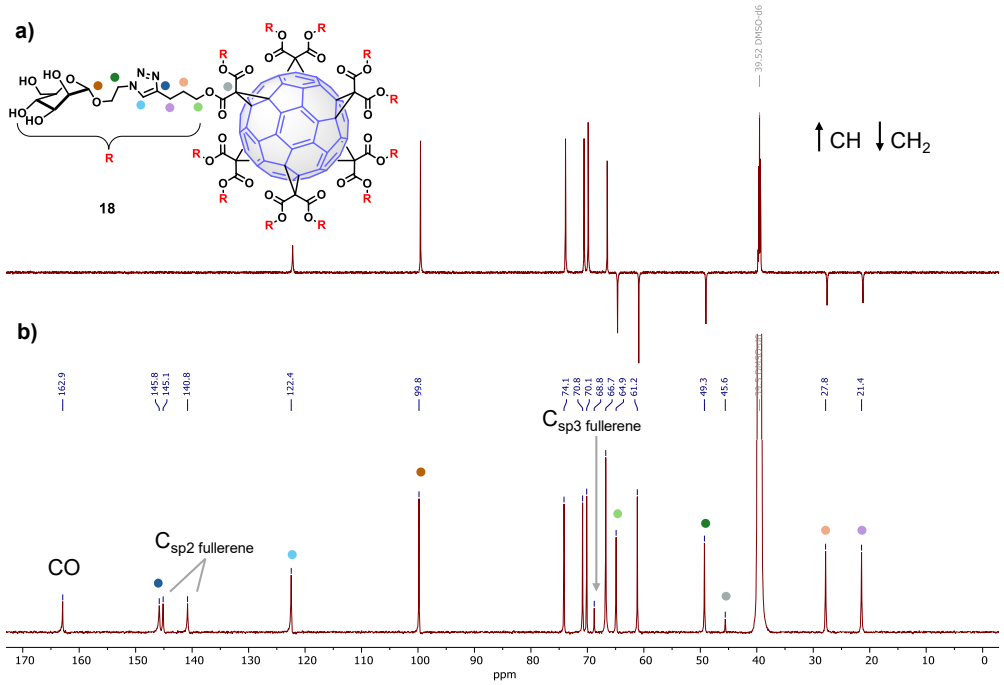

Figure 1.26. a) DEPT-135 and b) ^{13}C NMR spectra of compound **18** (DMSO-d_6, 176 MHz).

The ^{1}H NMR spectrum (Figure 1.27) is useful due to the appearance of the characteristic proton signals from triazole rings at ~8 ppm, providing clear evidence of the success of the reaction. However, as can be seen, the rest of the signals are quite complex, making it challenging to discern even the multiplicity of the peaks. This complexity arises from the intricate structure of the molecule, the presence of carbohydrates and the tendency of these systems to aggregate. With the help of techniques such as HSQC, once all the carbon signals are assigned, it is possible to elucidate and characterize the glycofullerenes correctly by ^{1}H NMR.

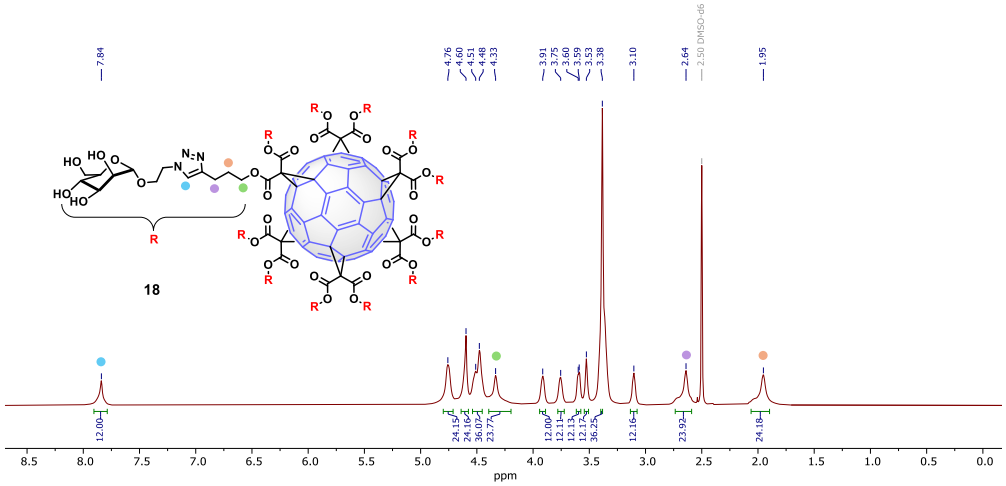

Figure 1.27. ^{1}H NMR spectrum of compound **18** (DMSO-d_6, 700 MHz).

These compounds can be further characterized by FT-IR, where the appearance of a band around 3340 cm^{-1} confirms the presence of OH groups from carbohydrates (Appendix 1, Figure AP1.2a).

1.3.3.2. Asymmetric glycofullerenes and tridecafullerenes

The symmetric fullerene hexakis-adduct described in the previous section, obtained from six identical malonates to bear twelve alkynes, only have one functionality. The introduction of an asymmetric unit allows the synthesis of glycofullerenes in which the structure can be further functionalized. The synthesis of these structures enables the construction of larger molecules such as the well-known tridecafullerenes or *sugar balls* that will be seen throughout this chapter.

The synthesis of asymmetric glycofullerenes follows the same procedure and principles as for the symmetric ones, using azide derivatives of mannose (**11**), fucose (**12**) and galactose (**13**) as carbohydrates (Scheme 1.10). The main difference is the use of hexakis-adduct **9**, which contains ten terminal alkynes and a polyethylene glycol malonate.

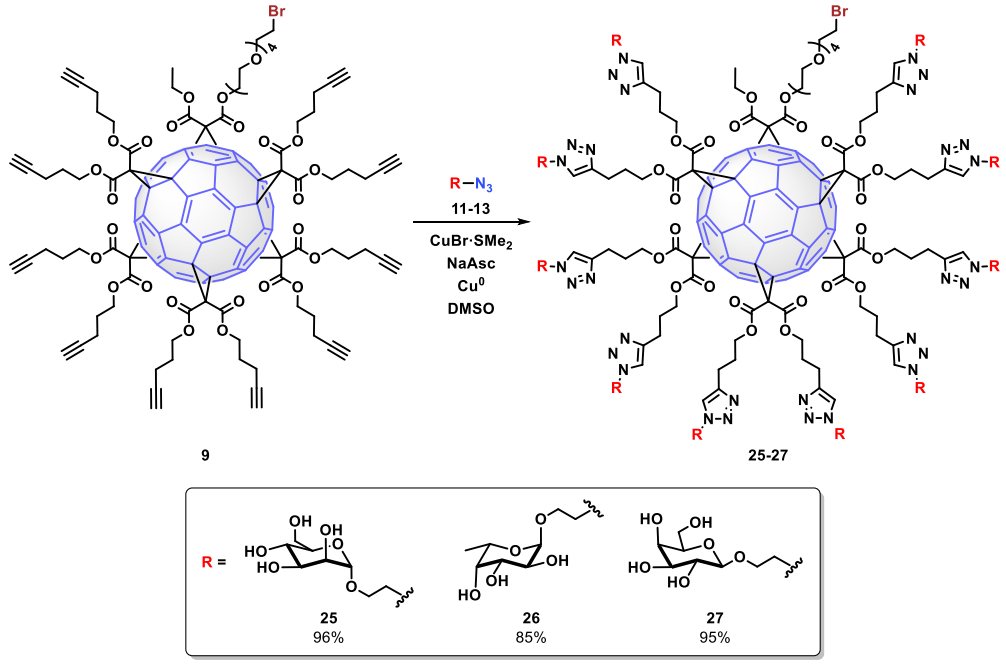

Scheme 1.10. General procedure for the synthesis of glycofullerenes **25**-**27**.

Once the click reaction was carried out, compounds **25**-**27** were purified by precipitation in methanol and obtained in excellent yield. The good outcome of the reaction was checked by common spectroscopic techniques. For a better understanding, the characterization of glycofullerene **27** will be used as an example.

First of all, ^{13}C NMR spectrum (Figure 1.28) shows the appearance of new triazole ring signals at ~146 ppm and ~124 ppm. The two sp^2 carbon signals of the fullerene can also be identified at ~145 and ~141 ppm and the anomeric carbon of the galactose appears at ~103 ppm. From the carbohydrate, it is also observed the CH_2-N signal at ~50 ppm, as well as the carbons of the alkyl chain identified at ~27 ppm and ~22 ppm. As for asymmetric malonate, the most characteristic signals that can be observed are the CH_2-Br at ~32 ppm and the methyl group at ~14 ppm.

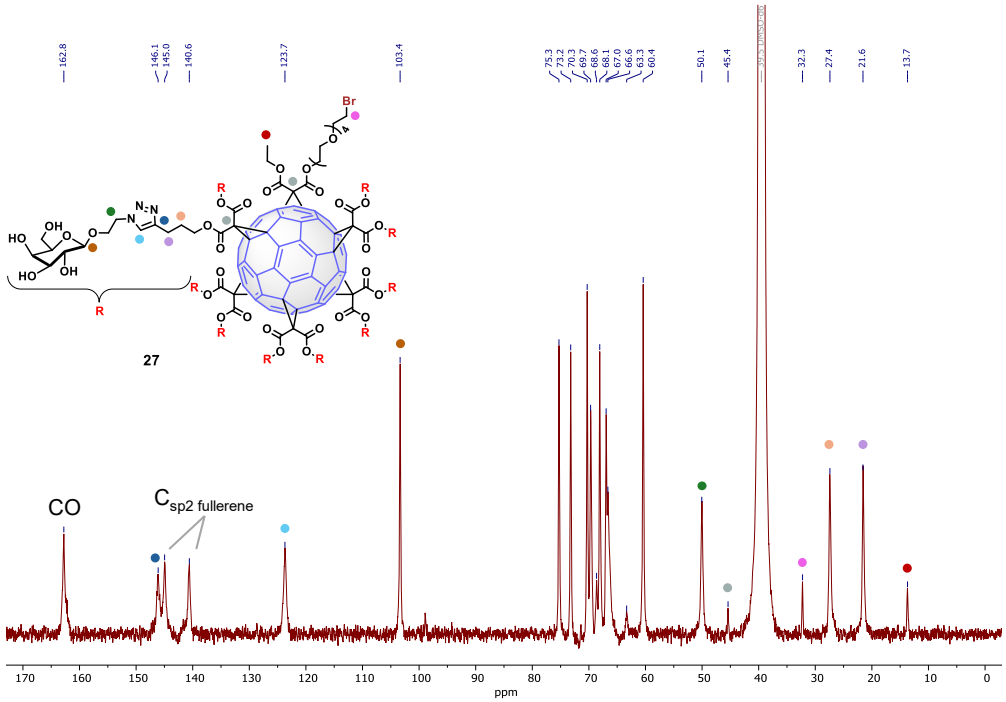

Figure 1.28. ^{13}C NMR spectrum of compound **27** (DMSO-d_6, 176 MHz).

In the ^{1}H NMR spectrum, the most characteristic signal appears at ~8 ppm corresponding to the protons of the triazoles. Due to the complexity of the spectrum signals, once all the carbon signals have been identified, the rest of the resonances can be assigned with the help of 2D NMR experiments (Figure 1.29).

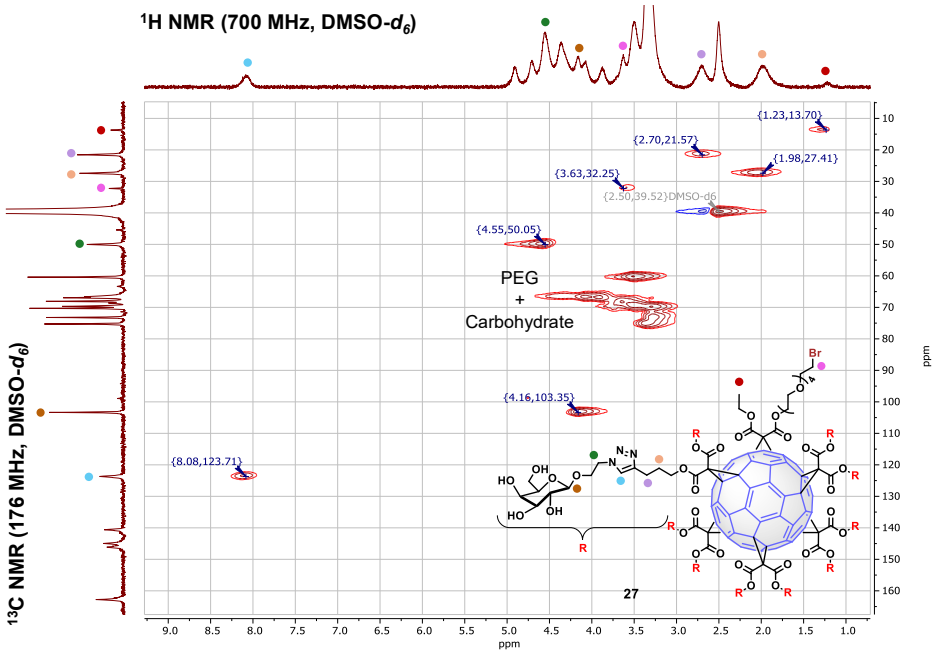

Figure 1.29. ^{1}H-^{13}C HSQC NMR spectrum of compound **27** (DMSO-d_6, 176 MHz).

The presence of bromine in the structure allows further reactions to be carried out on the glycofullerene without affecting the rest of the components of the molecule. If bimolecular nucleophilic substitution reactions (S_N2) are carried out and the bromine is replaced by an azide group, it is obtained a glycofullerene that can undergo a further click reaction. This is the basis of the synthesis of tridecafullerenes, the covalent union of an asymmetric glycofullerene such as compounds **25**-**27**, correctly functionalized, with a hexakis-adduct containing terminal alkynes such as compound **10**.

Carrying out the reaction in the microwave for 1.5 h, using sodium azide as nucleophile and DMSO-d_6 as solvent, compounds **28**-**30** were synthesized with moderate to high yields (Scheme 1.11). The use of DMSO-d_6 is due to the solubility of glycofullerene, but also to monitor the progress of the reaction by NMR.

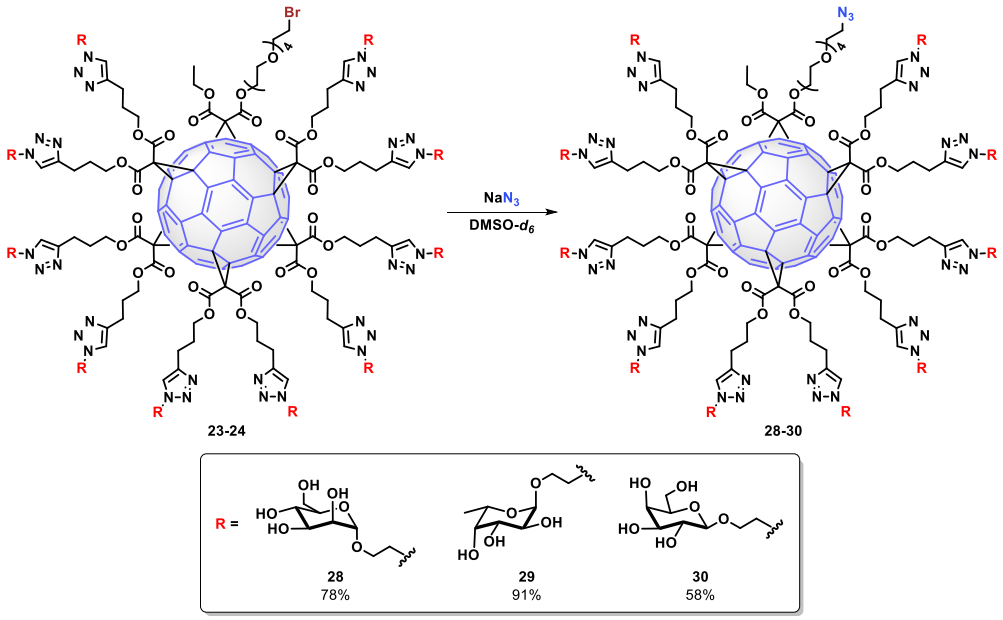

Scheme 1.11. General procedure for the synthesis of compounds **28**-**30**.

Due to the high polarity of these compounds, the excess of sodium azide cannot be removed by conventional methods such as liquid-liquid extraction. Size exclusion chromatography (SEC) is used to purify these glycofullerenes using Sephadex G-25 and H_2O/CH_3OH 9:1 as the mobile phase. In this way, glycofullerenes, having a much higher molecular weight than sodium azide, can be separated without problems and the DMSO that had been used for the reaction can also be removed.

Since the only structural modification is the substitution of bromine to azide, the only change observed in the ^{13}C NMR spectrum is the disappearance of the CH_2-Br signal from starting glycofullerenes **25**-**27** and the appearance of a new one corresponding to CH_2-N_3 at ~50 ppm in compounds **28**-**30**. Figure 1.30 shows the ^{13}C NMR of compounds **27** and **30** as a representative example.

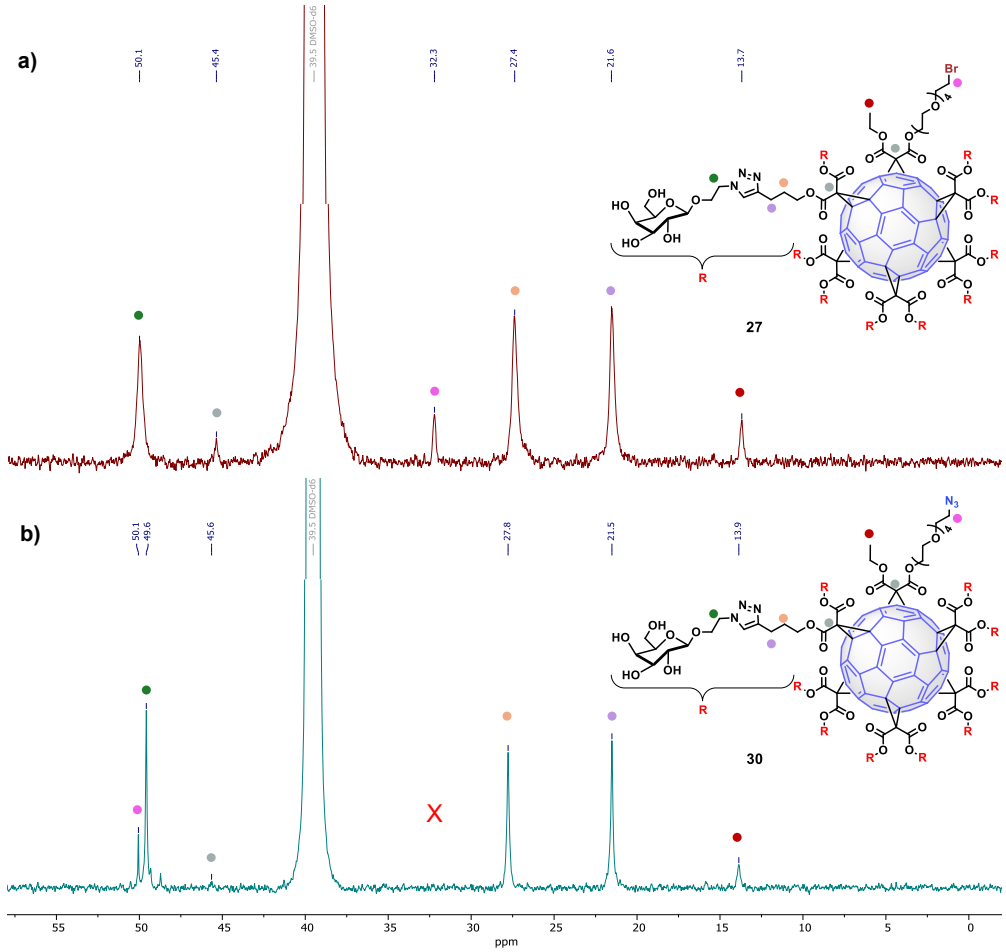

Figure 1.30. Partial ^{13}C NMR spectra (DMSO-d_6, 176 MHz) of: a) compound **27** and b) compound **30**.

A similar observation is made in ^{1}H NMR, where the only noticeable change is the shift of the CH_2-N_3 signal. However, due to signal complexity, their confirmation requires 2D experiments such as ^{1}H-^{13}C HSQC. Nonetheless, in the infrared spectrum a notable difference is observed in comparison with compound **27**, which is the appearance of the characteristic stretching band of the azide group at 2113 cm^{-1} (Figure 1.31).

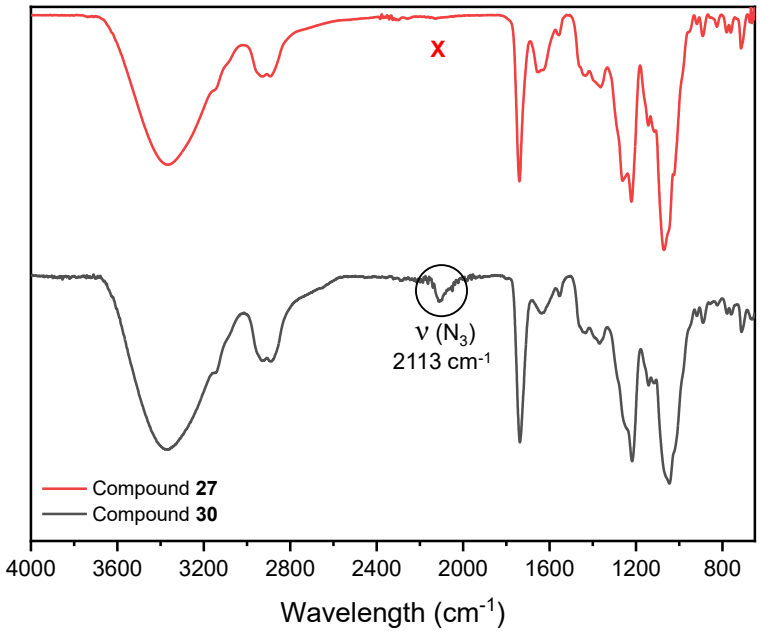

Figure 1.31. FT-IR of **27** (**red**) and **30** (**dark grey**).

Compounds **28**-**30**, having a terminal azide group, can react at this focal position *via* CuAAC with symmetrical hexakis-adduct **10**. Through this reaction, twelve glycofullerenes are introduced into the terminal alkyne groups enabling the synthesis of compounds **31**-**33** (Scheme 1.12). The final molecules are formed by thirteen units of [60]fullerene and contain 120 carbohydrates.

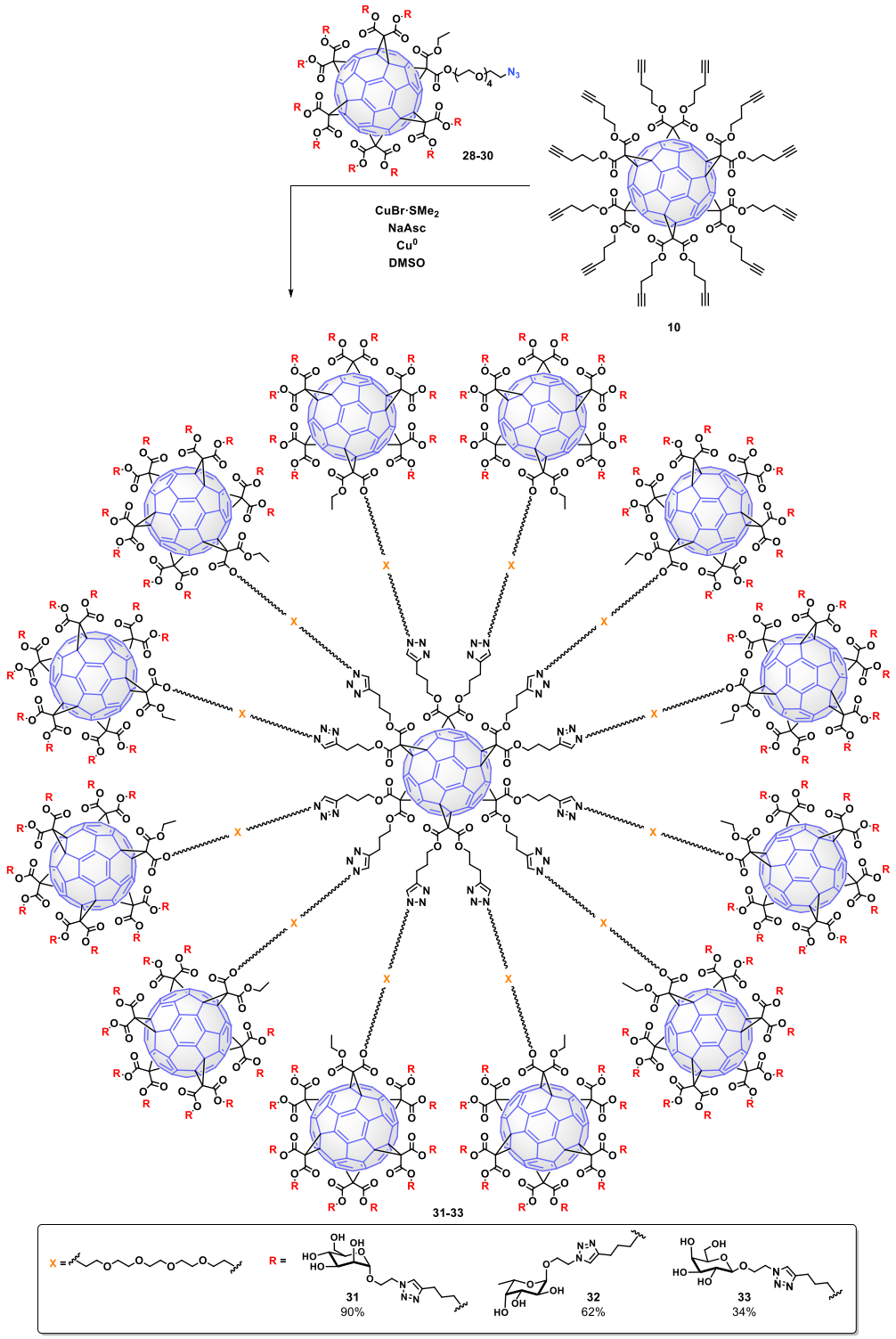

Scheme 1.12. General procedure for the synthesis of compounds **31-33**.

Purification of compounds **31-33** was carried out by SEC. In this case, Sephadex G-50 was used due to the high molecular weight of the product, using H_2O/CH_3OH 9:1 as the mobile phase.

The characterization of these compounds is similar to that of the glycofullerenes previously described. With compound **33** as an example, ^{1}H NMR spectrum shows the signal corresponding to triazoles at ~8 ppm. Again, ^{13}C NMR is the technique that allows us to check the correct functionalization and purification of the compound. The main differences detected when spectra of compounds **10**, **30** and **33** are compared, is the disappearance of the terminal alkynes of the symmetrical hexakis-adduct at ~80 ppm as well as the downfield shift of the CH_2-N_3 signal from the starting glycofullerene **30** at ~50 ppm. To corroborate the latter, 2D experiments such as ^{1}H-^{13}C HSQC are used to verify it. This indicates that the click reaction has worked successfully due to the correct transformation of the azide groups into CH_2-N (Figure 1.32a). FT-IR experiments also demonstrate the disappearance of the azide band at 2113 cm^{-1} due to the formation of the new triazole rings (Figure 1.32b).

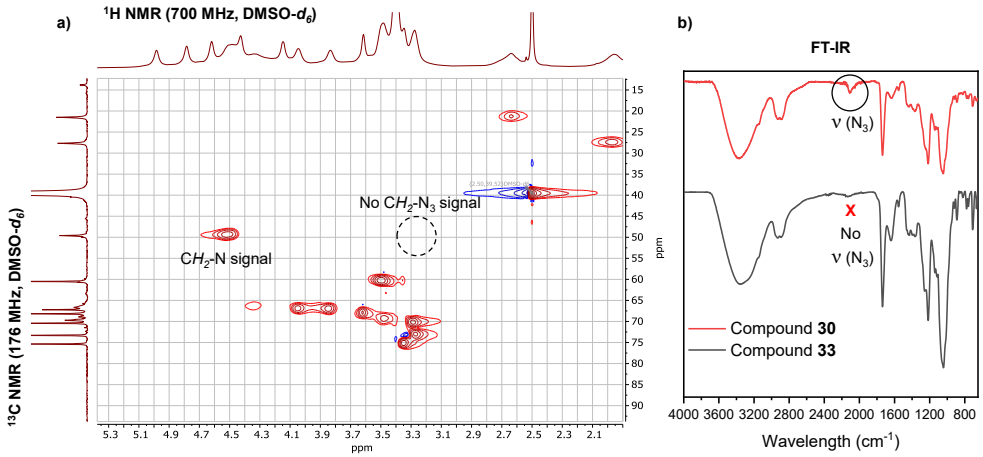

Figure 1.32. a) ^{1}H-^{13}C HSQC NMR spectrum of compound **33** (DMSO-d_6, 176 MHz) and b) FT-IR of compounds **30** and **33**.

1.3.4. Glycofullerenes biological studies

Both the symmetric glycofullerenes and tridecafullerenes synthesized in this chapter have been used for different biological studies such as the inhibition of SARS-CoV-2 trans-infection and galectin binding assays.

Interaction with DC-SIGN receptor and inhibition of SARS-CoV-2 trans-infection

Angiotensin-converting enzyme 2 (ACE2) is recognized as the primary receptor for the SARS-CoV-2 spike protein and facilitates viral entry into host cells. Although earlier studies indicated widespread expression of ACE2 in lungs, vascular system and other organs, more recent findings suggest that ACE2 is actually expressed at very

low levels.[110] This implies that SARS-CoV-2 may also exploit alternative receptors to infect certain human cells.

One such alternative is the family of C-type lectin receptors, particularly DC-SIGN. As previously discussed, DC-SIGN can recognize *N*-linked high-mannose oligosaccharides, which account for roughly one-third of the *N*-glycans on the SARS-CoV-2 spike protein. This makes the competitive inhibition of virus-receptor interactions using glycomimetics a promising strategy in antiviral therapy.

To evaluate the potential of the synthesized glycofullerenes as inhibitors of SARS-CoV-2 trans-infection, competition assays were conducted in collaboration with Dr. Rafael Delgado from the Instituto de Investigación del Hospital 12 de Octubre (Imas12).

The assays were conducted with all synthesized glycofullerenes, excluding those bearing galactose residues (**20** and **33**), as galactose is not recognized by DC-SIGN. The experiments utilized Jurkat cells, a T-lymphocyte cell line that do not express ACE2 in their membrane, therefore, the DC-SIGN lectin would be the only surface molecule capable of interacting with the SARS-CoV-2 glycoprotein (Figure 1.33). These cells were incubated with SARS-CoV-2 pseudovirus in the presence or absence (control) of glycofullerenes at a concentration of 1 μM.

Following incubation, the culture medium was removed, the cells were thoroughly washed, and then co-cultured with VeroE6 cells. These cells are highly susceptible to viral infection by SARS-CoV-2 due to their expression of key viral receptors. If the DC-SIGN receptor on Jurkat cells successfully captures the virus, it facilitates its transfer to VeroE6 cells, leading to infection.

Therefore, in the presence of the virus alone, 100% trans-infection to VeroE6 cells is expected. However, this level of infection should be significantly reduced in the presence of glycofullerenes, which are designed to competitively inhibit viral binding to DC-SIGN, thereby preventing viral transfer to the VeroE6 cells.

[110] a) J. Liu, F. Lu, Y. Chen, E. Plow, J. Qin, *J. Biol. Chem.* **2022**, *298*, 101710. b) M. Thépaut, J. Luczkowiak, C. Vivès, N. Labiod, I. Bally, F. Lasala, Y. Grimoire, D. Fenel, S. Sattin, N. Thielens, G. Schoehn, A. Bernardi, R. Delgado, F. Fieschi, *PLoS Pathog.* **2021**, *17*, e1009576.

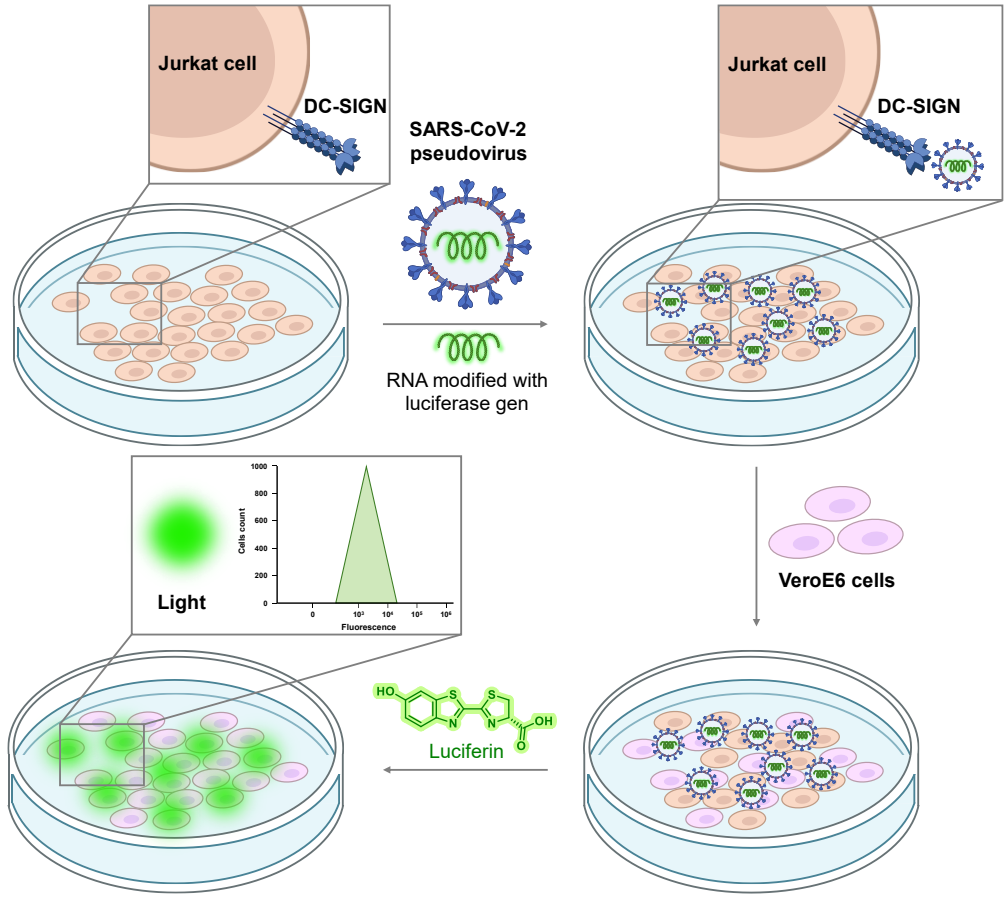

Figure 1.33. General scheme of how the trans-infection process mediated by DC-SIGN is evaluated.

The selection of carbohydrates was based on the fact that DC-SIGN receptor recognizes both fucose and mannose, with a higher selectivity for fucose.[111] Previous studies have also highlighted the essential role of fucose in mediating interactions with DC-SIGN. Additionally, trisaccharide **24**, known as Lewis-X, is a natural ligand of DC-SIGN and exhibits greater affinity and specificity compared to other oligosaccharide structures.[112] For these reasons, derivatives of these carbohydrates were chosen, along with disaccharide **23** as an intermediate between the monosaccharides and Lewis-X. This disaccharide shares structural similarity with Lewis-X but lacks the galactose moiety. Moreover, multivalent systems based on Lewis-X remain largely unexplored, providing an opportunity to establish the foundation for evaluating their inhibitory potential against DC-SIGN.

[111] Y. Guo, H. Feinberg, E. Conroy, D. A. Mitchell, R. Alvarez, O. Blixt, M. E. Taylor, W. I. Weis, K. Drickamer, *Nat. Struct. Mol. Biol.* **2004**, *11*, 591.
[112] B. J. Appelmelk, I. v. Die, S. J. v. Vliet, C. M. J. E. Vandenbroucke-Grauls, T. B. H. Geijtenbeek, Y. v. Kooyk, *J. Immunol.* **2003**, *170*, 1635.

Figure 1.34 illustrates the percentage of SARS-CoV-2 trans-infection observed in the presence of various glycofullerenes. Compounds based on monosaccharides (**18**-**19**, **21**-**22**) demonstrated a maximum inhibition of 59%. For the mannose derivatives (**18** and **21**), the length of the spacer between the carbohydrate and the fullerene had little effect on the level of inhibition. In contrast, for the fucose derivatives (**19** and **22**), while the shorter linker had no significant impact, increasing the linker length led to a 59% reduction in trans-infection.

More pronounced effects were observed with compounds **23** and **24**, which are functionalized with disaccharides and trisaccharides, respectively. These structures achieved 93% and 95% inhibition, clearly outperforming the monosaccharide-based glycofullerenes.

The most striking results were obtained with the tridecafullerenes (**31** and **32**), which exhibit a strong multivalent effect. These compounds showed just a 0.0001% of cells infected, effectively blocking viral transfer to target cells.

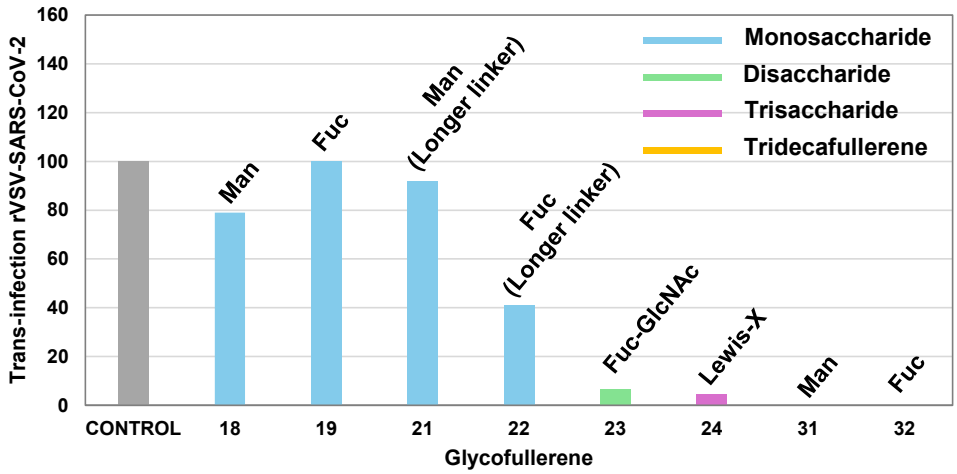

Figure 1.34. Trans-infection of SARS-CoV-2 in the presence or not (control) of 1 μM of monosaccharides **18**-**19** and **21**-**22**, disaccharide **23** and trisaccharide **24** functionalized glycofullerenes and tridecafullenes **31**-**32**.

Considering the above, the results indicate that the Lewis-X derivative **24** exhibits the highest inhibitory activity among the symmetric glycofullerenes. However, the disaccharide derivative **23** demonstrates a comparable inhibitory effect to **24**, while being significantly more accessible from a synthetic viewpoint. Additionally, tridecafullerenes **31** and **32** underscore the critical role of multivalency in these systems, as even with fucose and mannose monosaccharides they are able to almost completely block trans-infection.

The interaction between compounds **23** or **24** and the CRD of DC-SIGN was studied by NMR spectroscopy, in collaboration with Prof. María Ángeles Canales from Universidad Complutense de Madrid. The CRD was overexpressed in *E. coli* using

$^{15}NH_4Cl$ to achieve isotopic labeling of the protein. This ^{15}N-labeled CRD enabled the acquisition of ^{1}H-^{15}N HSQC spectra, which detects the amide protons of individual amino acids. Since these signals are highly sensitive to environmental changes, monitoring chemical shift perturbations upon addition of ligands provides detailed information on the binding interactions between the compounds and the CRD. ^{1}H-^{15}N HSQC experiment of DC-SIGN CRD was acquired in the absence and in the presence of **23** or **24** (protein:ligand ratio 1:0.5).

In the presence of compound **24** that bears twelve Lewis-X trisaccharide motifs, the chemical shift perturbations observed along the DC-SIGN protein sequence are represented in Figure 1.35a. The most significantly affected amide signals correspond to residues E120, E127 and C142 (Figure 1.35b). These three residues are located within the canonical carbohydrate-binding site of DC-SIGN, as illustrated in the 3D-structural model shown in Figure 1.35c.

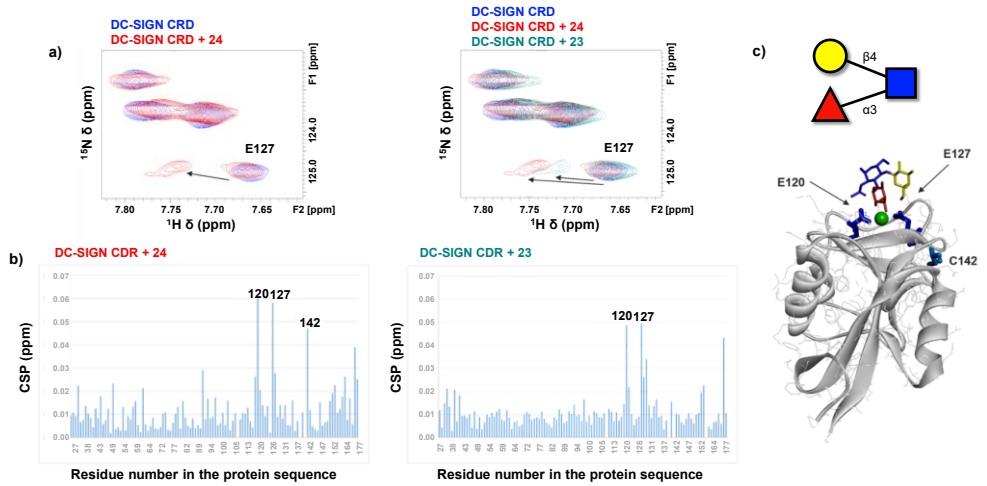

Figure 1.35. a) Left panel, expansion of the ^{1}H-^{15}N HSQC spectra of CRD-DC SIGN in the absence (**blue color**) and in the presence of **24** (**red color**) showing one of the signals with higher chemical shift perturbation. Right panel, comparison of the change in chemical shift of E127 in the presence of **23** and **24**, b) representation of the chemical shift perturbations detected in DC-SIGN signals upon addition of compounds **23** and **24** and c) 3D model of Lewis-X DC-SIGN interaction built based on X-ray structures.

It is important to note that two distinct sets of resonances are observed, one corresponding to the free protein (**blue color**) and the other to the ligand-bound form (**red color**). This behavior is characteristic of a slow exchange regime in NMR titrations, which is typically indicative of tight binding affinity between the ligand and specific amino acids from the protein.

The same experiment was conducted with compound **23**, that bears twelve peripheral disaccharides, and it showed fewer chemical shift perturbations. The most affected residues are located within the canonical carbohydrate-binding site, similar to those perturbed by **24**, indicating that both compounds target the same region of the protein.

The greater degree of perturbation caused by compound **24** may be attributed to additional interactions between the CRD and the Lewis-X trisaccharide motif present in **24**, compared to the simpler disaccharide unit in **23**.

These results show that glycofullerenes are potent inhibitors of DC-SIGN-mediated SARS-CoV-2 trans-infection. While monosaccharide-functionalized fullerenes exhibited moderate inhibition, compounds bearing multiple disaccharide and Lewis-X trisaccharide motifs achieved over 93% inhibition, with tridecafullerenes nearly abolishing viral transfer. NMR spectroscopy confirmed that these compounds bind specifically to the CRD of DC-SIGN, with significant chemical shift perturbations in key residues (E120, E127 and C142) located within the canonical binding site. These findings support a competitive binding mechanism and identify multivalent glycofullerenes as promising antiviral agents targeting DC-SIGN to prevent SARS-CoV-2 dissemination.

Galectin-binding properties of galactose glycofullerenes

Galectins are a family of lectins that specifically recognize β-galactosidases and play key roles in various biological processes, including tissue regeneration, cancer progression and host defense against pathogens.[113] Given the critical importance of galectin-glycan interactions, targeting galectins represents a promising strategy for therapeutic intervention in a range of diseases.

Therefore, the interactions of galactose-decorated compounds **20** and **33** with galectin-3, a protein involved in numerous biological processes, were evaluated, with particular emphasis on the multivalent binding effect exhibited by these molecules.[114] These studies were conducted in collaboration with Jesús Jiménez Barbero from CIC bioGUNE.

The assays were conducted using both the full-length chimeric galectin-3 (Gal-3 FL) and its isolated CRD (Gal-3). Preliminary results indicated that compound **20** exhibited non-specific interactions with Gal-3, occurring outside the carbohydrate-binding site. As a result, all subsequent experiments were performed using compound **33**.

The interaction of tridecafullerene **33** with both Gal-3 FL and Gal-3 was investigated. NMR studies revealed a reduction in signal intensity, as monitored by ^{1}H-^{15}N HSQC experiments, suggesting the formation of high-molecular-weight complexes, likely resulting from interactions between **33** and the galectins (Figure 1.36a). Upon addition of 24 equivalents of **33**, Gal-3 CRD exhibited a 28% signal intensity loss, whereas Gal-3 FL showed a more pronounced reduction of 47%, indicating stronger interaction in the full-length form. Moreover, detailed analysis of each ^{1}H-^{15}N cross-peak revealed a distinctive response from the *N*-terminal domain of Gal-3 FL. In

[113] G. A. Rabinovich, M. A. Toscano, S. S. Jackson, G. R. Vasta, *Curr. Opin. Struct. Biol*. **2007**, *17*, 513.
[114] J. Dumic, S. Dabelic, M. Flögel, *Biochim. Biophys. Acta - Gen. Subj.* **2006**, *1769*, 616.

comparison to residues within the CRD, the signal intensity of amino acids in the *N*-terminal tail showed a significantly greater reduction. This observation indicates that the *N*-terminal region is notably restricted upon binding to **33**. These results support a binding mechanism driven by cross-linking, likely facilitated by protein oligomerization (Figure 1.36c).

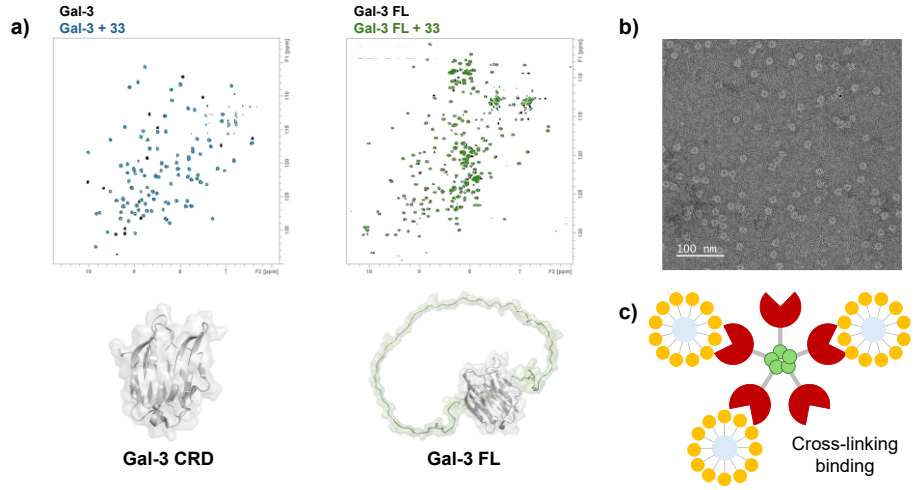

Figure 1.36. a) ^{1}H-^{15}N HSQC spectra of Gal-3 CRD and Gal-3 FL in the absence (**black**) and in the presence (**blue**/**green**) of compound **33**, b) TEM images of **33**:Gal-3 FL at 1:30 molar ratio and c) schematic representation of cross-linking on ligand binding.

To further characterize this interaction, isothermal titration calorimetry (ITC) was conducted (Figure 1.37). As a reference, the binding of Gal-3 FL to free galactose was evaluated, showing a weak affinity with a dissociation constant (K_D) of 4 mM. In contrast, compound **33** exhibited a dramatically improved binding affinity of 2.7 μM, approximately 1,400 times stronger, likely due to multivalent interactions. On a per-galactose basis, each unit on the glycofullerene scaffold is 12 times more potent than the monovalent ligand, highlighting the powerful impact of multivalency on binding strength. ITC analysis of Gal-3 CRD with **33** revealed minimal binding, underscoring the importance of cross-linking effects enabled by Gal-3 FL's oligomerization, as also supported by NMR data. These findings suggest that the enhanced affinity is primarily driven by protein cross-linking, rather than simple statistical rebinding.

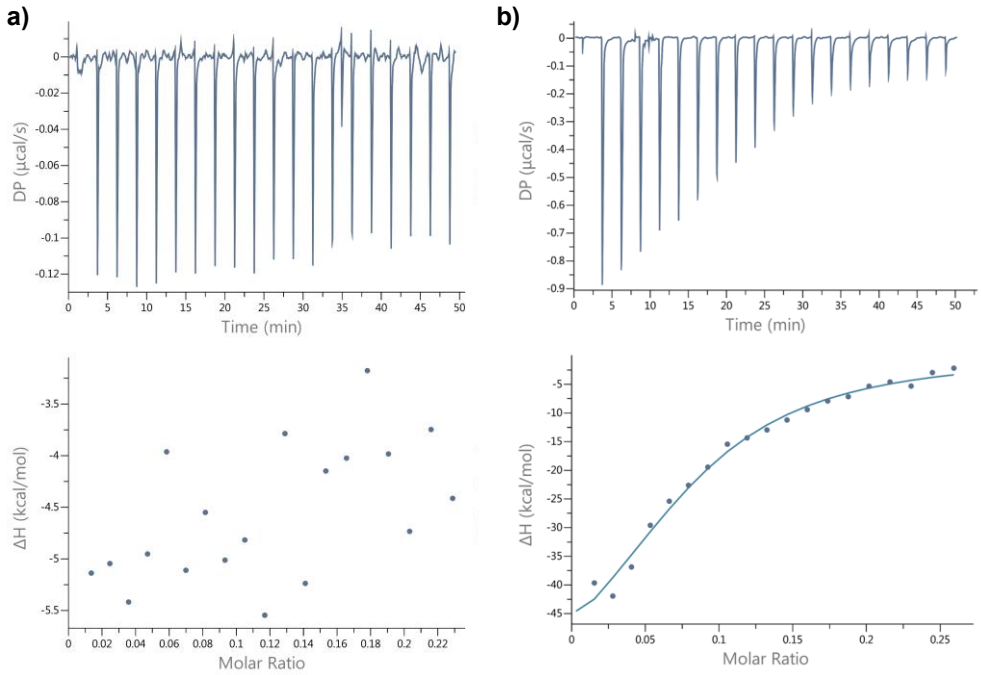

Figure 1.37. ITC profiles (heat of injection and binding isotherm) for the interaction of **33** with: a) Gal-3 CRD and b) Gal-3 FL.

To gain insight into the nature of these high-molecular-weight assemblies, transmission electron microscopy (TEM) was employed. The TEM images revealed a dense distribution of glycofullerene particles suggesting the formation of aggregates or multivalent assemblies (Figure 1.36b). Importantly, no such structures were detected in the absence of Gal-3 FL, confirming the formation of mixed complexes between the lectin and glycofullerene **33**.

The potential of compound **33** to function as a Gal-3 inhibitor was also explored by flow cytometry (Figure 1.38a). Gal-3 is known to bind and cross-link glycoprotein receptors on Jurkat T cells. The ability of **33** to inhibit this interaction was assessed by evaluating Gal-3 binding to cell surface glycans. A progressive decrease in mean fluorescence intensity (MFI) was observed with increasing concentrations of **33**, demonstrating its capacity to effectively block Gal-3 binding to the Jurkat cell surface (Figure 1.38b and 1.38c).

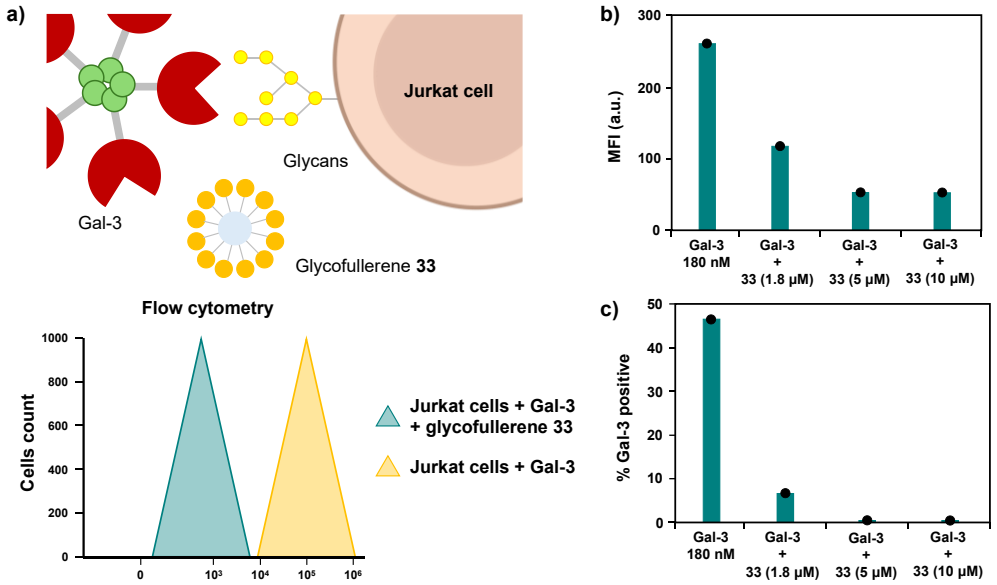

Figure 1.38. a) General scheme of the binding experiment between Gal-3 and Jurkat cells, b) MFI in the presence of increasing amounts of **33** and c) % of Jurkat cells linked to Gal-3 at different concentrations of **33**.

This study demonstrates that glycofullerene **33**, functionalized with galactose residues, exhibits high-affinity binding to Gal-3, particularly its full-length form (Gal-3 FL), through a mechanism driven by multivalent cross-linking interactions. NMR spectroscopy and ITC data revealed that compound **33** forms large molecular assemblies with Gal-3 FL, resulting in significantly enhanced binding affinity (K_D = 2.7 µM) compared to free galactose, confirming the strong contribution of multivalency. The reduced signal intensities observed in the *N*-terminal domain of Gal-3 FL further suggest a key role for this region in glycofullerene-mediated clustering. TEM microscopy supported the formation of supramolecular complexes, while flow cytometry confirmed that compound **33** effectively inhibits Gal-3 binding to cell surface glycans on Jurkat T cells. Together, these findings highlight the potential of galactose-functionalized glycofullerenes as potent multivalent inhibitors of Gal-3, with possible applications in the modulation of galectin-mediated cellular processes in inflammation, cancer and immune response.

1.3.5. Boron-rich nanostructures based on [60]fullerene

Boron hydrides are compounds with the general formula $[B_mH_n]^{x-}$ that are not found in nature. In these molecules, boron self-assembles analogously to carbon-based systems, yet instead of adopting ring or chain configurations, boron atoms occupy vertices of polyhedral structures.[115]

[115] a) R. N. Grimes, Ed. *Carboranes*, 3rd ed. Academic Press, Inc. New York, **2016**. b) N. S. Hosmane, Ed. *Boron Science: New Technologies and Applications*, 1st ed. Taylor & Francis Group, Boca Raton, **2011**.

These 3D-aromatic clusters adopt deltahedral frameworks composed of triangular faces, where their structural integrity is maintained through three-center two-electron (3c-2e) bonds.[116] This aromaticity is used to describe their exceptional thermal and oxidative stability, which made them exceptional candidates in materials science.[117]

The most representative boron cluster is the highly symmetrical icosahedral *closo*-dodecaborate anion $[B_{12}H_{12}]^{2-}$.[118] However, chemistry of boron clusters has been mostly focused on carboranes, where one or more B-H vertices are replaced by the isoelectronic CH^+ group.[115,119] A related family of compounds, known as metallacarboranes, emerged when a metal atom is incorporated as a structural vertex. The most studied are those composed of two dicarbollide units linked by a central metal atom. These metals can be transition or lanthanide elements, with the most notable examples being cobalt- and iron-based metallacarboranes, commonly known as COSAN and FESAN, respectively (Figure 1.39).

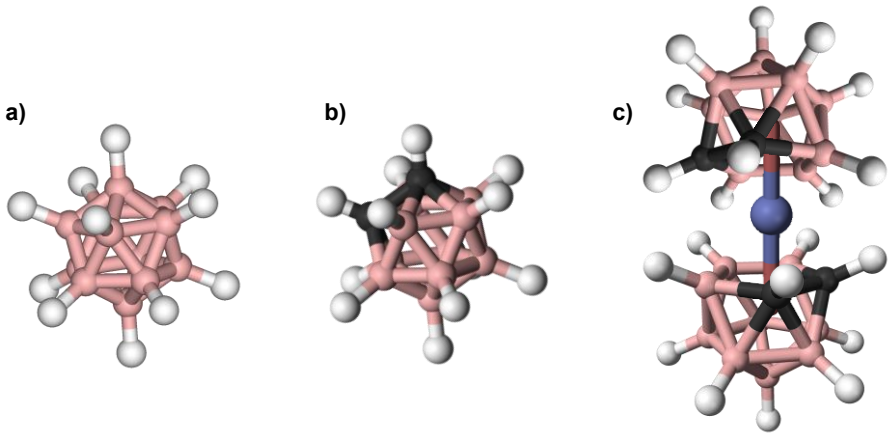

Figure 1.39. 3D representation of: a) dodecaborate anion $[B_{12}H_{12}]^{2-}$, b) *orto*-carborane and c) metallacarborane COSAN.

As mentioned, borohydride, carborane and metallacarborane clusters are not naturally occurring and are entirely abiotic.[120] In addition, these nonnatural B-H groups can interact differently with biomolecules compared to organic compounds. These properties, combined with their good stability and bioavailability, make boron clusters

[116] a) J. Poater, M. Solà, C. Viñas, F. Teixidor, *Angew. Chem. Int. Ed.* **2014**, *53*, 12191. b) O. El Bakouri, D. W. Szczepanik, K. Jorner, R. Ayub, P. Bultinck, M. Solà, H. Ottosson, *J. Am. Chem. Soc.* **2022**, *144*, 8560.
[117] a) R. Núñez, M. Tarrés, A. Ferrer-Ugalde, F. F. de Biani, F. Teixidor, *Chem. Rev.* **2016**, *116*, 14307. b) R. Núñez, I. Romero, F. Teixidor, C. Viñas, *Chem. Soc. Rev.* **2016**, *45*, 5147.
[118] L. Wang, Y. Jiang, S. Duttwyler, F. Lin, Y. Zhang, *Coord. Chem. Rev.* **2024**, *516*, 215974.
[119] D. Olid, R. Núñez, C. Viñas, F. Teixidor, *Chem. Soc. Rev.* **2013**, *42*, 3318.
[120] a) F. Teixidor, R. Núñez, C. Viñas, *Molecules* **2023**, *28*, 4449. b) E. Hey-Hawkins, C. Viñas, Eds. *Boron-Based Compounds: Potential and Emerging Applications in Medicine*, 1st ed. John Wiley & Sons Ltd. New Jersey, **2016**.

excellent candidates in drug development,[121] e.g. antimicrobial agents, biosensors, bioimaging agents and drug carriers, among others.[122]

One of the most studied biological applications is cancer treatment using Boron Neutron Capture Therapy (BNCT). BNCT involves introducing ^{10}B-enriched compounds to the tumor, followed by external neutron irradiation, which induces ^{10}B fission. This nuclear reaction releases high-energy alpha particles that destroy those boron-loaded cells (Figure 1.40).[123] This therapy requires some features, such as an appropriate concentration of boron in the tumoral tissue, low toxicity of the molecules and selective accumulation in the tumoral cells.[124] Then, the preparation of biocompatible boron rich systems is the key for an effective BNCT treatment. The more boron atoms contained in a cell, the more probability of neutron impact, resulting in an improved effectiveness.

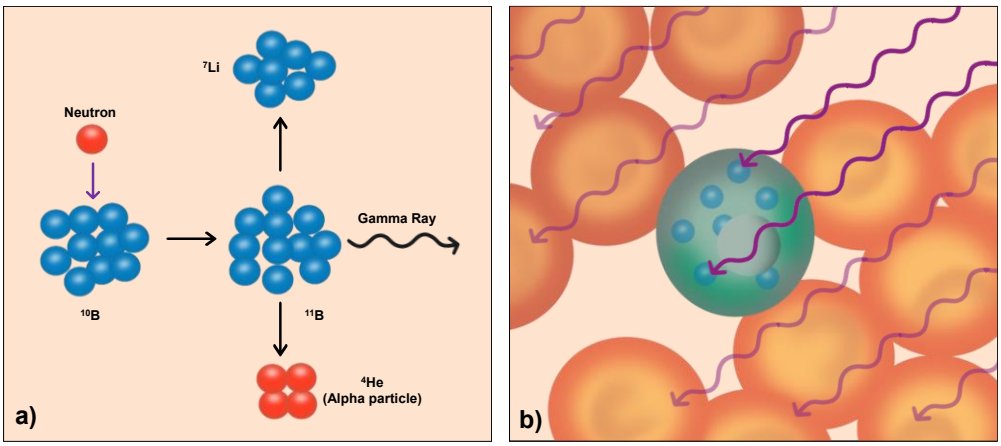

Figure 1.40. Scheme of BNCT technique: a) disintegration mechanism of ^{10}B and b) irradiation of cells with neutrons (adapted from reference 124b).

Some useful derivatives of these clusters are the oxonium ring-containing metallacarboranes and $[B_{12}H_{12}]^{2-}$. These compounds demonstrated high versatility for the incorporation of boron clusters into other scaffolds.[125] The presence of a dioxane ring in their structure enables ring-opening reactions with nucleophiles. When these

[121] a) A. Marfavi, P. Kavianpour, L. M. Rendina, *Nat. Rev. Chem.* **2022**, *6*, 486. b) M. Gozzi, B. Schwarze, E. Hey-Hawkins, *ChemMedChem* **2021**, *16*, 1533.
[122] a) K. Fink, M. Uchman, *Coord. Chem. Rev.* **2021**, *431*, 213684. b) A. Ferrer-Ugalde, S. Sandoval, K. R. Pulagam, A. Muñoz-Juan, A. Laromaine, J. Llop, G. Tobias, R. Núñez, *ACS Appl. Nano Mater.* **2021**, *4*, 1613. c) Z. Yinghuai, A. T. Peng, K. Carpenter, J. A. Maguire, N. S. Hosmane, M. Takagaki, *J. Am. Chem. Soc.* **2005**, *127*, 9875.
[123] a) M. F. Hawthorne, *Mol. Med. Today* **1998**, *4*, 174. b) M. Lamba, A. Goswami, A. Bandyopadhyay, *Chem. Commun.* **2021**, *57*, 827.
[124] a) R. F. Barth, P. Mi, W. Yang, *Cancer Commun.* **2018**, *38*, 1. b) R. F. Barth, Z. Zhang, T. Liu, *Cancer Commun.* **2018**, *38*, 36.
[125] a) A. A. Druzina, A. V. Shmalko, I. B. Sivaev, V. I. Bregadze, *Russ. Chem. Rev.* **2021**, *90*, 785. b) A. A. Semioshkin, I. B. Sivaev, V. I. Bregadze, *Dalton Trans.* **2008**, 977.

reactions are performed using sodium azide, an azide group can be introduced into the structure, allowing its use in click chemistry reactions (Scheme 1.13).

Therefore, throughout this section, boron-rich nanostructures will be synthesized using fullerene as a biocompatible platform which allows the incorporation of twelve boron cluster units per molecule. To achieve this, dioxane-containing boron clusters were used as starting materials derived from metallacarborane COSAN (**34**) and $[B_{12}H_{12}]^{2-}$ *closo*-dodecaborate (**35**). These compounds were provided by the research group of Rosario Núñez from ICMAB-CSIC.

Compounds **34** and **35** were treated with sodium azide, resulting in dioxane ring opening and the incorporation of an azide group into the structure (Scheme 1.13).

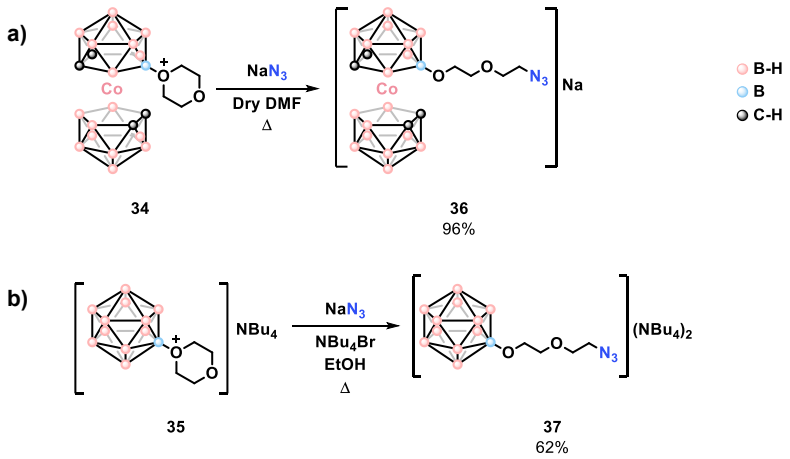

Scheme 1.13. General procedures for the synthesis of: a) compound **36** and b) compound **37**.

Compounds **36** and **37** can undergo CuAAC reactions with symmetrical hexakis-adduct **10** (Scheme 1.14). This process allows the incorporation of twelve boron cluster units per fullerene molecule, resulting in a total of 216 boron atoms for the COSAN derivative (**38**) and 144 boron atoms for dodecaborate derivative (**39**).

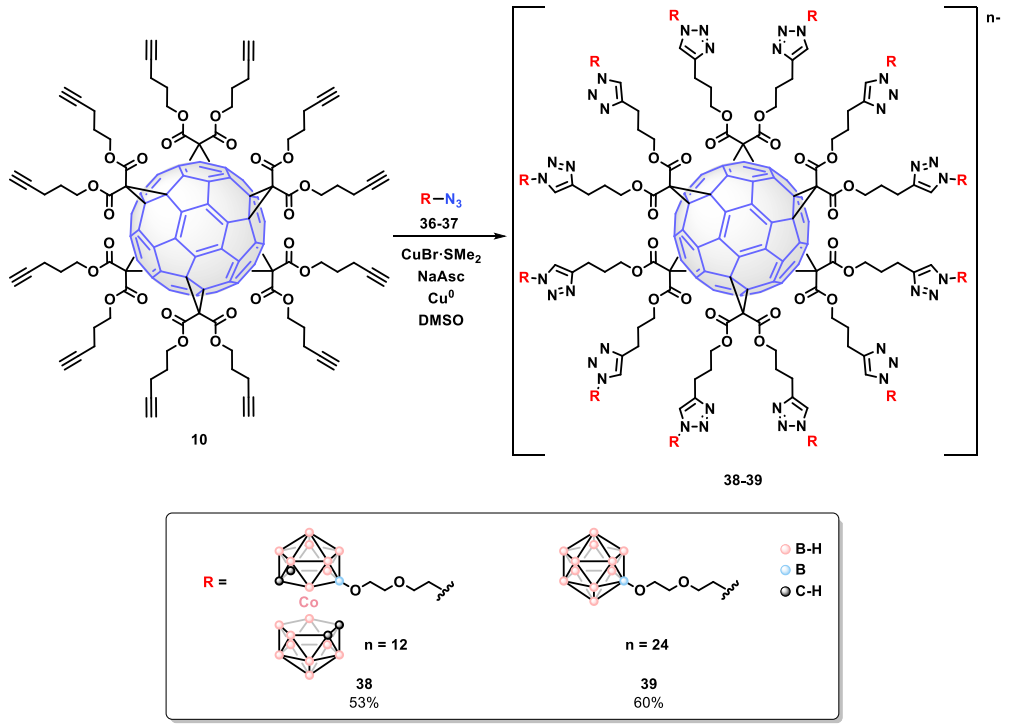

Scheme 1.14. General procedure for the synthesis of compounds **38** and **39**.

As with the previous glycofullerenes, once the reaction was completed, it was treated with QuadraSil® Mercaptopropyl to remove copper residues. Compound **38** was purified by column chromatography, while **39** was precipitated in water using a saturated aqueous solution of [NBu_4]Br. Both products were obtained with moderate yield.

The characterization of **38** and **39** was carried out using standard organic chemistry techniques such as NMR and FT-IR.

^{11}B NMR and ^{11}B{^{1}H} NMR spectra confirm the presence of boron in the target molecules (Figure 1.41). In the ^{11}B NMR spectra, resonances appear as doublets due to the coupling of ^{11}B and ^{1}H nuclei, except for those corresponding to the *B*-O vertices. In contrast, in ^{11}B{^{1}H} NMR all the signals appear as singlets due to the ^{1}H decoupling. When compared, it is possible to identify the substituted *B*-O vertices as the most downfield-shifted signals at ~23.3 ppm for **38** and at ~6.6 ppm for **39**.

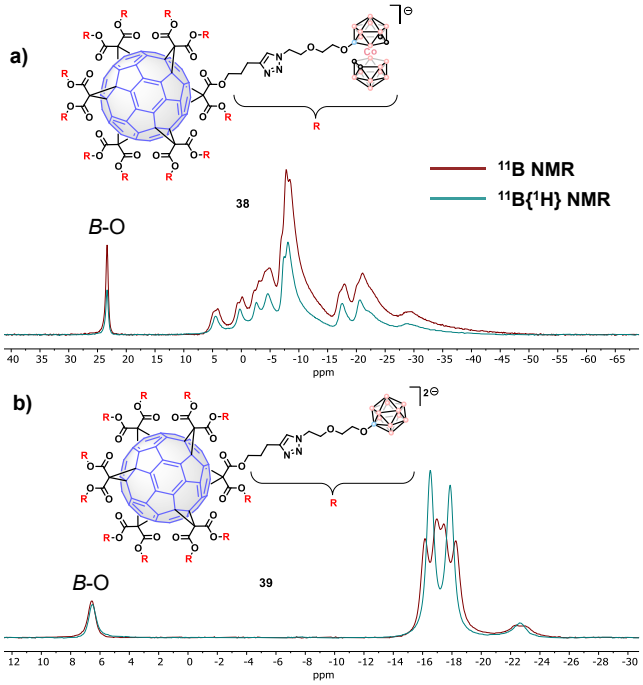

Figure 1.41. ^{11}B NMR and ^{11}B{^{1}H} NMR spectra (acetone-d_6, 160 MHz) of: a) compound **38** and b) compound **39**.

In the ^{1}H NMR spectra (Figure 1.42), it is worth highlighting the presence of a signal at ~8 ppm corresponding to the C*H* of the new triazole rings, confirming the successful click reaction. For **38**, a relevant signal appears at ~4.19 ppm corresponding to the protons of the cluster carbons (C$_C$-*H*) and those found at ~4.55 ppm attributed to the methylene groups adjacent to the triazole rings (CH_2-N). The latter can also be observed at ~4.57 ppm for **39**. Additionally, both compounds exhibit a broad band in the baseline in the range of ~3.50 – 0.50 ppm corresponding to the B-*H* protons of both clusters.

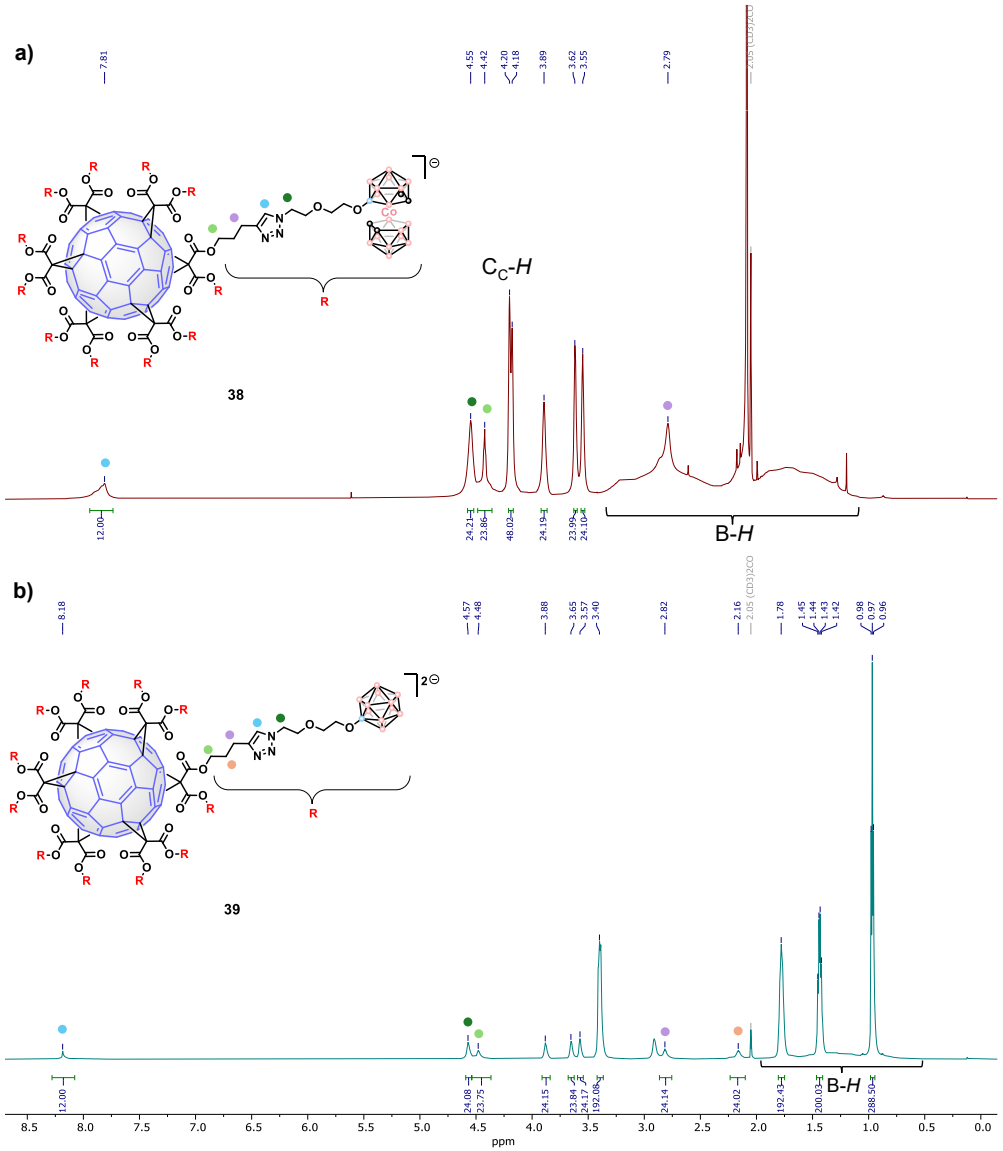

Figure 1.42. ^{1}H NMR spectra (acetone-d_6, 700 MHz) of: a) compound **38** and b) compound **39**.

In the ^{13}C NMR spectra (Figure 1.43), the disappearance of the alkyne signals from the starting hexakis-adduct (**10**) at ~80 ppm is observed, along with the appearance of two new signals at ~147 ppm and ~123 ppm, which correspond to the carbons of the newly formed triazole rings. These evidences confirm the successful functionalization of the fullerene with the clusters. The characteristic resonances of the hexakis-adduct of C_{60} are identified at ~147 ppm and ~142 ppm for the sp^2 carbons, and at ~69 ppm for the sp^3 carbons. For compound **38**, signals from the *C*$_C$-H appear at ~55 ppm and ~47 ppm. Additionally, the carbonyls of the malonates are detected at ~164 ppm, while the alkyl chains are observed at ~68 ppm, ~29 ppm and ~23 ppm.

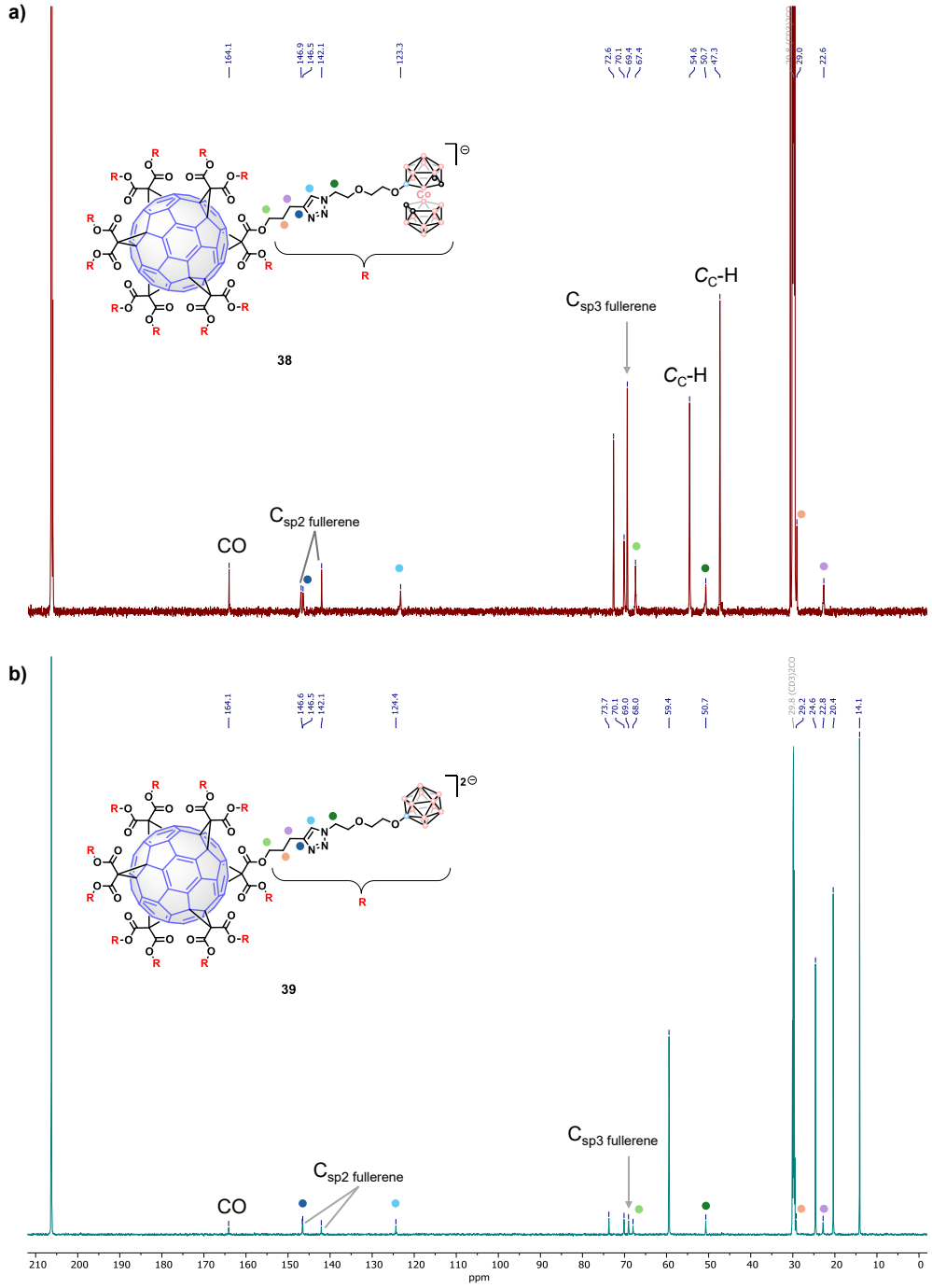

Figure 1.43. ^{13}C NMR spectra (acetone-d_6, 176 MHz) of: a) compound **38** and b) compound **39**.

These compounds can be further characterized by FT-IR where the band corresponding to the B-H stretching vibrations at ~2500 cm^{-1} as well as the C=O stretching vibrations at ~1735 cm^{-1} are identified (Appendix 1, Figure AP1.6).

Additionally, the number of COSAN units in compound **38** has been estimated using a method previously described by Kim *et al.*, based on the UV-Vis spectra.[126] This estimation involves the comparison of the molar absorptivity (ε_λ) of the COSAN cluster in compound **36** (which contains only one COSAN unit) and in compound **38** (which contains twelve COSAN units), with both spectra recorded in the same solvent and at the same concentration. To perform this estimation, Gaussian curve deconvolution of the UV-Vis spectra of **36** and **38** will first be required, in order to identify the absorption bands attributed to the contribution of COSAN moieties.

Figure 1.44 represents the deconvolutions of the UV-Vis spectra of **36** and **38** as well as the experimental curves.

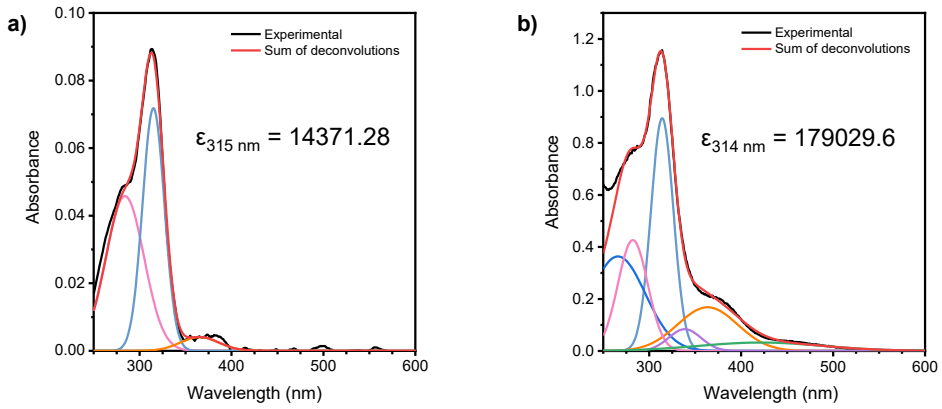

Figure 1.44. UV-Vis spectra (CH_3CN, $5 \cdot 10^{-6}$ M) of: a) compound **36** and b) compound **38** and their corresponding deconvolutions.

For compound **36**, the deconvolution revealed absorption maxima at 284 nm (**pink**), 315 nm (**blue**) and 365 nm (**orange**) (Figure 1.44a). For compound **38** (Figure 1.44b), several absorption bands unequivocally attributed to the COSAN cluster can be identified, with the curve centered at 314 nm (**blue**) standing out.[126b]

Taking as reference the aforementioned COSAN absorption at ~315 nm, the ε_λ for **36** and **38** have been compared. Hence, the ratio ε_{314}(**38**)/ε_{315}(**36**) results in 12.5 clusters per molecule, which is consistent with the expected value.

1.3.6. Boron nanostructures biological studies

The biological response of compounds **38** and **39** was evaluated in both healthy and cancerous cells to assess their cytotoxicity and cellular internalization. Since neither compounds are soluble enough in aqueous media, both were encapsulated in liposomes acting as biocompatible nanocarriers, with rhodamine A incorporated as a

[126] a) C. Kim, I. Jung, *J. Organomet. Chem.* **2000**, *599*, 208. b) J. Cabrera-González, V. Sánchez-Arderiu, C. Viñas, T. Parella, F. Teixidor, R. Núñez, *Inorg. Chem.* **2016**, *55*, 11630.

fluorescent marker to enable visualization by confocal microscopy (Appendix 1, Liposomes preparation).

The assays with healthy cells were conducted in collaboration with Prof. Iván López from Universidad Complutense de Madrid using mouse embryonic fibroblasts (MEFs). MEFs were labeled with Lysotracker Green, a lysosomal dye. The compounds were tested at various concentrations, showing no cytotoxicity up to the highest tested dose of 26 µg boron/mL (Figures 1.45a and 1.45b). After confirming the lack of toxicity, cellular internalization was assessed. MEFs were incubated with both compounds encapsulated at concentrations of 2.1 and 10 µg boron/mL for up to 72 hours, with imaging performed at 0, 2, 24 and 48 hours (Figure 1.45c). In both cases, successful internalization of the liposomes was observed, likely through endocytic uptake, as suggested by the colocalization patterns (**purple**).

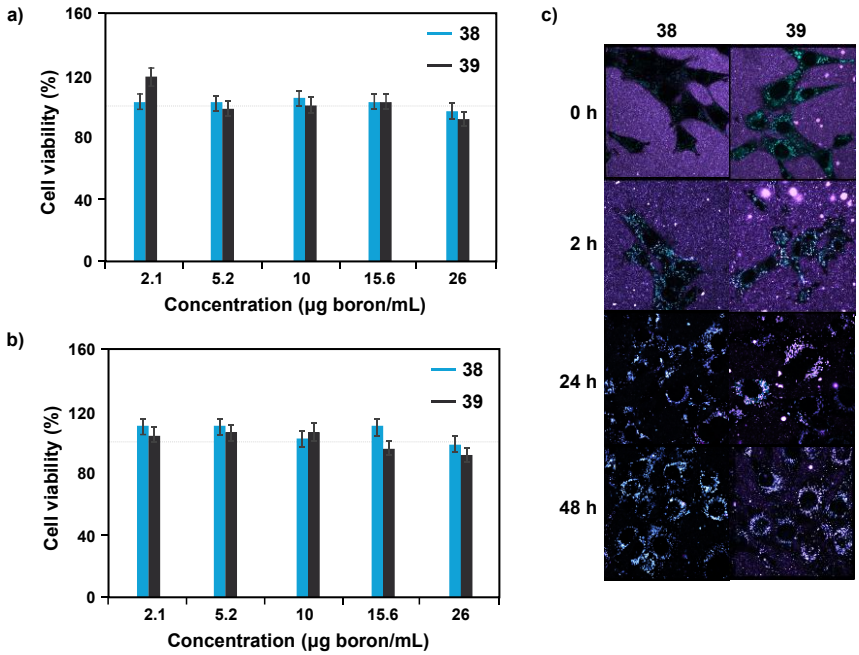

Figure 1.45. a) Cell viability after 24 h, b) cell viability after 48 h and c) confocal microscopy images at 10 µg boron/mL at different periods of time.

Building on the positive results obtained with healthy cells, further studies were carried out using cancer cells, in collaboration with M. José Ruiz, PhD and M. Carmen Ruiz, PhD from the Inmunología Molecular research group at Universidad de Granada. The assays were conducted using the Cal33 cell line, derived from head and neck carcinoma. Cytotoxicity was assessed over a 48-hour period at varying concentrations. The results showed that both the control liposomes and derivatives **38** and **39** exhibited no significant cytotoxicity, with only a slight decrease in cell viability observed at concentrations starting from 26 µg/mL (Figure 1.46).

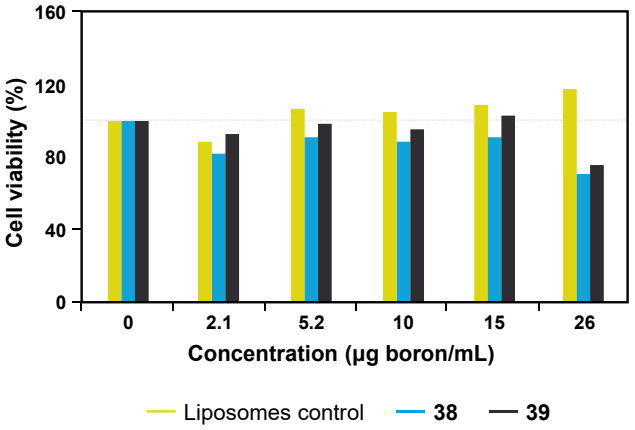

Figure 1.46. Viability of Cal33 cells treated with compounds **38**, **39** and control liposomes at different concentrations.

The cellular uptake of the compounds was investigated using confocal microscopy with a concentration of 10 µg/mL. Short-term incubation experiments confirmed the internalization of the compounds within 2 hours. To visualize intracellular localization, control cells were pre-treated with Lysotracker Green.

Preliminary results indicate that compounds **38** and **39** enter cells primarily through an endocytic pathway. Their co-localization with lysosomes confirms successful cellular internalization and suggests a possible degradative route within the lysosomal compartment (Figure 1.47). This information is crucial for understanding the compounds' intracellular fate and should be considered when assessing their potential therapeutic efficacy.

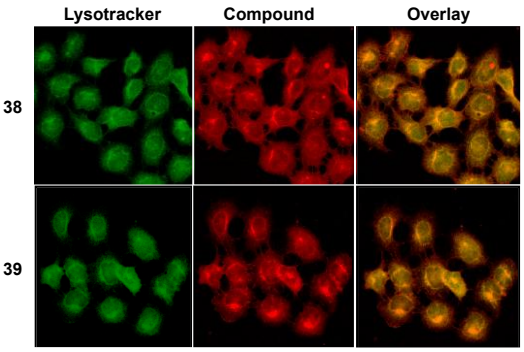

Figure 1.47. Fluorescence images of Cal33 cells incubated for 2 h with 10 µg/mL of compounds **38** and **39**.

1.4. Conclusions

In conclusion, this chapter presents the successful synthesis of glycofullerenes functionalized with various carbohydrates, yielding structures bearing either 12 or 120 carbohydrate units totally soluble in aqueous media. The [60]fullerene core was functionalized through Bingel-Hirsch cyclopropanation, enabling the introduction of up to six malonate units. When identical malonates were used, symmetrical hexakis-adducts were obtained. Alternatively, an asymmetrical [5:1] substitution pattern was achieved by first introducing a single brominated malonate (monoadduct), followed by a second cyclopropanation to install five additional malonates.

The resulting hexakis-adducts, containing terminal alkynes, were further functionalized *via* CuAAC with azido-functionalized carbohydrates, yielding the target glycofullerenes. In the case of asymmetric hexakis-adducts, the remaining terminal bromine served as a reactive site for additional modification, enabling the synthesis of tridecafullerenes.

Both the 12-unit glycofullerenes and tridecafullerenes were evaluated as inhibitors of SARS-CoV-2 trans-infection by targeting the DC-SIGN receptor. The results demonstrated that both the type of carbohydrate and chain length significantly influenced inhibitory activity. Monosaccharide-functionalized derivatives showed modest inhibition, whereas disaccharide (compound **23**) and especially trisaccharide (compound **24**) derivatives exhibited enhanced activity. The best inhibition results, approaching complete blockage of trans-infection were achieved with tridecafullerenes **31** and **32** with just a 0.0001% of cells infected.

Furthermore, the interaction of compounds **23** and **24** with the CRD of DC-SIGN was investigated *via* ^{1}H-^{15}N HSQC NMR, revealing more substantial chemical shift perturbations for compound **24**, in agreement with its superior performance in trans-infection assays.

In addition, galactose-containing derivatives **20** and **33** were tested for their interaction with galectins. Compound **33** showed high-affinity interaction to Gal-3 FL, with a K_D approximately 1,400 times higher than that of monovalent galactose, making it a promising candidate as a galectin inhibitor.

Finally, this chapter also described the first example of hybrids that combine anionic boron clusters and fullerene. These nanostructures included the functionalization of symmetrical hexakis-adducts with twelve boron COSAN or *closo*-dodecaborate clusters. Although these derivatives were not water-soluble, their encapsulation in fluorescently labeled liposomes enabled biological studies in healthy and cancer cells. Their cellular internalization was confirmed *via* confocal microscopy and none of the hybrids showed cytotoxicity. The high-boron content of these nanostructures and the first biological results support their potential as anticancer agents in BNCT.

Chapter 2

2. CHAPTER 2

2.1. Background

2.1.1. The pigments of life

Porphyrins – from Greek πορφύρα, *porphura*, "purple" – are intensely colored compounds considered as the pigments of life (Figure 2.1). Their most well-known role is the encapsulation of iron in heme (**2.1**), the active site of hemoglobin in red blood cells, which is responsible for transporting oxygen from the lungs to the tissues and carbon dioxide from the tissues to the lungs. However, porphyrins are also found in other bioinorganic systems involved in metabolic processes, such as vitamin B12 (**2.2**), which contains cobalt and has a cherry-red color, or cofactor F430 (**2.3**), which is a yellow nickel-containing macrocycle. Even more fundamentally, oxygen-breathing life would not exist without porphyrins. In plants, magnesium-complexed porphyrins are key components in photosynthesis (**2.4**). These are found in chlorophyll, which converts light energy into chemical energy and also produces molecular oxygen.[127]

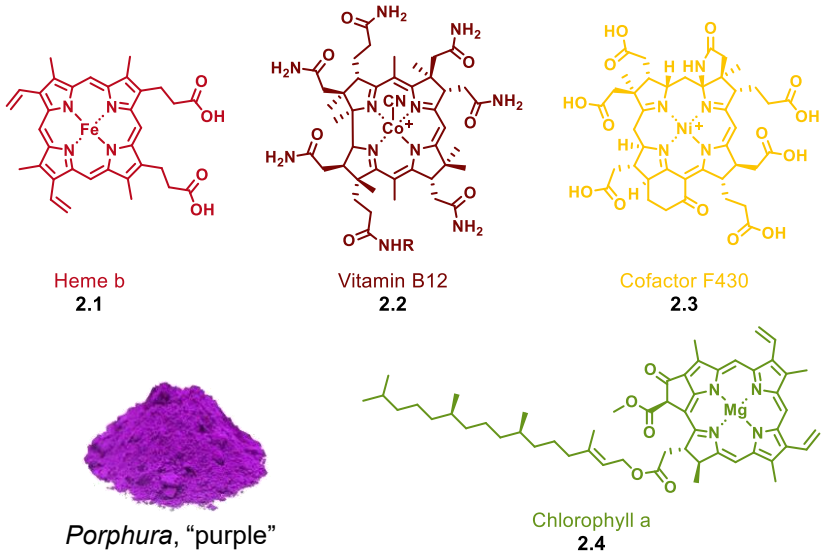

Figure 2.1. Examples of porphyrins present in organisms.

The importance of porphyrins has been highlighted by the awarding of multiple Nobel Prizes. Since the mid-20th century, progress in synthetic techniques have enabled the total synthesis of tetrapyrroles and broadened the scope of metal coordination across the periodic table. These advancements have paved the way for contemporary

[127] M. O. Senge, N. N. Sergeeva, K. J. Hale, *Chem. Soc. Rev.* **2021**, *50*, 4730.

applications of porphyrins in fields such as medicine, catalysis, materials science and photovoltaics.[128]

2.1.2. Structural, electronic and optical characteristics of porphyrins

Structurally, porphyrins consist of four pyrrole rings linked by methine bridges, forming a cyclic, highly conjugated macrocycle. The first structural model was proposed by Küster in 1912[129] and later confirmed by Fischer in 1929 through his successful synthesis of heme.[130] This achievement earned Fischer the Nobel Prize in Chemistry (1930) *for his research into the constitution of haemin and chlorophyll and especially for his synthesis of haemin*.

The structure of the porphyrin parent compound consists of 24 atoms, with the nitrogen atoms from the pyrrole rings forming the central coordination site for metal binding (Figure 2.2). Within this framework, three types of carbon atoms are distinguished: the α-carbons (C_α) and β-carbons (C_β) of the pyrrole rings, and the meso-carbons (C_m) that connect the pyrrole rings. The inner nitrogen atoms can accept or donate protons, leading to the formation of dianionic or dicationic species. Furthermore, metal ions can readily coordinate to the central core, yielding metalloporphyrin complexes.[131]

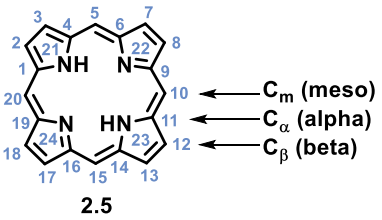

2.5

Figure 2.2. Nomenclature and atom numbering.

The porphyrin macrocycle contains 22 π-electrons, though only 18 of them contribute to its aromatic character (**2.6**). While Hückel's rule is applicable to monocyclic systems, the aromaticity of porphyrins can be interpreted through the annulene model. According to this model, the porphyrin ring is considered a derivative of the neutral [18]annulene system (**2.7**).[131] By following the pathway outlined in Figure 2.3a (**purple**), an 18-electron monocyclic conjugated system emerges, where the remaining four π-electrons are localized in bonds that display stronger double-bond character and do not participate in the delocalized aromatic system.

[128] a) H. Huang, W. Song, J. Rieffel, J. F. Lovell, *Front. Phys.* **2015**, *3*, 1. b) J. López-Andarias, S. H. Mejías, T. Sakurai, W. Matsuda, S. Seki, F. Feixas, S. Osuna, C. Atienza, N. Martín, A. L. Cortajarena, *Adv. Funct. Mater.* **2018**, *28*, 1704031. c) M. Wolf, C. Villegas, O. Trukhina, J. L. Delgado, T. Torres, N. Martín, T. Clark, D. M. Guldi, *J. Am. Chem. Soc.* **2017**, *139*, 17474. d) L. Moreira, J. Calbo, J. Aragó, B. M. Illescas, I. Nierengarten, B. Delavaux-Nicot, E. Ortí, N. Martín, J.-F. Nierengarten, *J. Am. Chem. Soc.* **2016**, *138*, 15359. e) D. Arteaga, R. Cotta, A. Ortíz, B. Insuasty, N. Martín, L. Echegoyen, *Dyes Pigm.* **2015**, *112*, 127. f) G. Bottari, G. de la Torre, D. M. Guldi, T. Torres, *Coord. Chem. Rev.* **2021**, *428*, 213605.

[129] W. Küster, *Ber. Dtsch. Chem. Ges.* **1912**, *45*, 1935.

[130] H. Fischer, K. Zeile, *Justus Liebigs Ann. Chem.* **1929**, *468*, 98.

[131] P. J. Brothers, M. O. Senge, Eds. *Fundamentals of Porphyrin Chemistry: A 21st Century Approach*, 1st ed. John Wiley & Sons Ltd. New Jersey, **2022**.

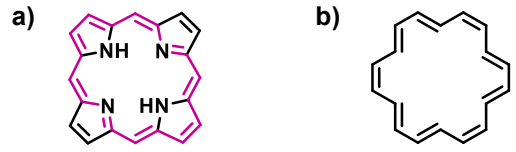

18 π-electron system
2.6

[18]annulene
2.7

Figure 2.3. a) The parent porphyrin aromatic system and b) [18]annulene system.

Porphyrins possess remarkable optical properties due to their highly conjugated π-system, which makes them intensely colored and fluorescent chromophores. Their UV-Vis absorption spectrum features two distinct regions: the intense Soret band (also known as the B band), located in the near-UV range (~400-450 nm), and the weaker Q-bands, which span the visible range (~500-700 nm) (Figure 2.4). These absorption features arise from $\pi \rightarrow \pi^*$ electronic transitions: the Soret band corresponds to a transition from the ground state to the second excited state ($S_0 \rightarrow S_2$), while the Q-bands represent transitions to the first excited state ($S_0 \rightarrow S_1$). Free-base porphyrins exhibit four Q-bands due to their inherent asymmetric structure. However, when the porphyrin core is metal-coordinated, symmetry increases, resulting in a simplified Q-band pattern. Additionally, porphyrins emit fluorescence typically in the 600-750 nm region, with their emission characteristics being highly sensitive to the chemical environment.[132]

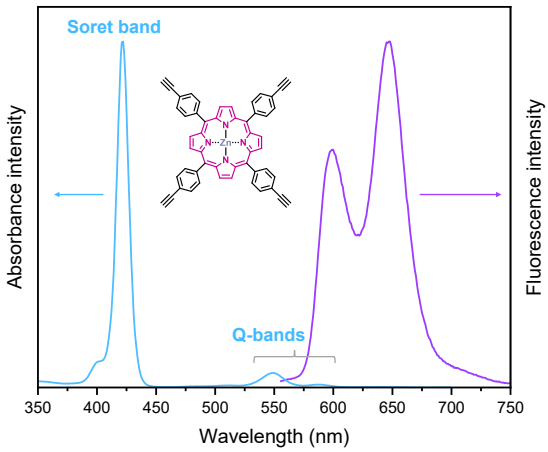

Figure 2.4. Example of the absorption and emission spectrum of a Zn(II) metalloporphyrin in DMSO.

The porphyrin family extends far beyond the parent porphyrin compound, encompassing a wide range of derivatives formed through modification, substitution, rearrangement, insertion, or removal of atoms within the tetrapyrrolic macrocycle

[132] a) M. Gouterman, *J. Mol. Spectrosc*. **1961**, *6*, 138. b) A. K. Mandal, M. Taniguchi, J. R. Diers, D. M. Niedzwiedzki, C. Kirmaier, J. S. Lindsey, D. F. Bocian, D. Holten, *J. Phys. Chem. A* **2016**, *120*, 9719.

(Figure 2.5).[131] Notable examples include chlorins and corroles, which have found diverse applications, most prominently as photosensitizers.

Chlorins and bacteriochlorins are porphyrinoids characterized by the partial reduction of double bonds in their pyrrole rings. This structural change induces a red shift in their absorption spectra, extending into the near-infrared region, an advantage that enhances tissue penetration and improves their effectiveness as photosensitizers.[133]

Corroles are often described as contracted porphyrins, comprised of four pyrrole units connected by three methine bridges, which results in a direct pyrrole-pyrrole linkage. Their cavity contains three "pyrrole-type" and one "pyridine-type" nitrogen atoms. This structural feature enables corroles to coordinate with metal ions in higher oxidation states.[134]

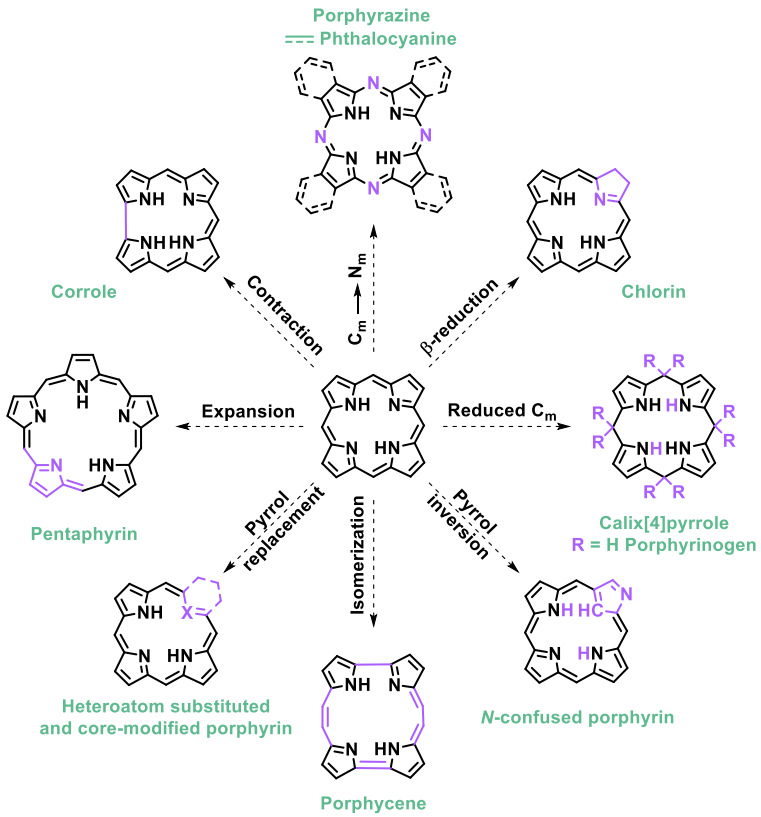

Figure 2.5. Main members of the porphyrin family (adapted from reference 131).

2.1.3. Organic synthesis and coordination chemistry

Symmetrical porphyrins with four identical substituents at the *meso* positions are among the most thoroughly investigated and widely utilized porphyrin derivatives, with *meso*-tetraphenylporphyrin (H_2TPP) serving as a well-known example. These

[133] B. Pucelik, A. Sułek, J. M. Dąbrowski, *Coord. Chem. Rev.* **2020**, *416*, 213340.
[134] I. Aviv-Harel, Z. Gross, *Chem. Eur. J.* **2009**, *15*, 8382.

compounds can be synthesized using two main strategies: the Adler-Longo method, first reported by Adler, Longo and collaborators in 1964,[135] or the more recent Lindsey method.[136]

The Adler-Longo approach involves heating equimolar amounts of pyrrole and an aldehyde in propionic acid, followed by filtration. This technique is well-suited for aldehydes stable under acidic and high-temperature conditions, and it remains effective for large-scale synthesis when the porphyrin product readily crystallizes. In contrast, the Lindsey method employs milder conditions, typically reacting pyrrole with an aldehyde in CH_2Cl_2 using trifluoroacetic acid (TFA) or $BF_3 \cdot Et_2O$ as catalysts at room temperature. This methodology works very well for a broad range of aldehydes due to the mild conditions, and its versatility has made this strategy the standard method for C_m-substituted porphyrins.

A key structural modification in porphyrins involves deprotonating the inner nitrogen atoms at positions 21 and 23 to generate a tetradentate ligand capable of coordinating a wide array of metal ions (Figure 2.6).[137] One of the main challenges in their synthesis lies in identifying a solvent system that can dissolve both the porphyrin and the metal salt. The classical Adler-Longo protocol addresses this by using metal acetates, halides, hydroxides, or carbonates in refluxing DMF, with the final product precipitated upon water addition. Variations of this method include reactions in chlorinated solvents with alcohols with an excess of metal salt. Recently, greener alternatives such as mechanochemical and ultrasound-assisted methods have emerged to promote sustainable metalloporphyrin synthesis.[138]

[135] a) A. D. Adler, F. R. Longo, W. Shergalis, *J. Am. Chem. Soc.* **1964**, *86*, 3145. b) A. D. Adler, F. R. Longo, J. D. Finarelli, J. Goldmacher, J. Assour, L. Korsakoff, *J. Org. Chem*. **1967**, *32*, 476.
[136] a) J. S. Lindsey, H. C. Hsu, I. C. Schreiman, *Tetrahedron Lett.* **1986**, *27*, 4969. b) J. S. Lindsey, *Acc. Chem. Res.* **2010**, *43*, 300.
[137] J. W. Buchler, Synthesis and Properties of Metalloporphyrins. In *The Porphyrins: Structure and Synthesis, Part A*, D. Dolphin, Ed. Academic Press, Inc. New York, **1978**, ch. 10, pp. 389-483.
[138] C. Gomes, M. Peixoto, M. Pineiro, *Molecules* **2021**, *26*, 6652.

a)

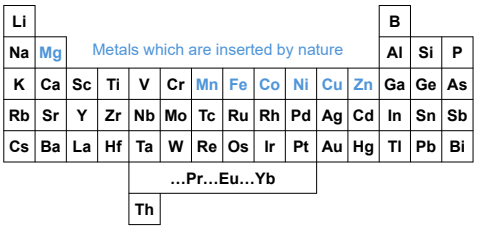

b)

SELECTED SYSTEMS TO PREPARE METALLOPORPHYRINS

Metalating system	T (ºC)	Scope of metals inserted
MX_mL_n/HOAc	100	Zn, Cu, Ni, Co, Fe, Mn, Ag, In, V, Hg, Tl, Sn, Pt, Rh, Ir
MX_m/Py	115 – 185	Mg, Ca, Sr, Ba, Zn, Cd, Hg, Si, Ge, Sn, Pb, Ag, Au, Tl, As, Sb, Bi, Sc, P
$M(acac)_n$/solvent	180 – 240	Mn, Fe, Co, Ni, Cu, Zn, Al, Sc, Ga, In, Cr, Mo, Ti, V, Zr, Hf, Eu, Pr, Yb, Y, Th
MX_m/PhOH	180 – 240	Ta, Mo, W, Re, Os (X = O, OPh, acac, Cl)
MCl_m/PhCN	191	Nb, Cr, Mo, W, Pd, Pt, Zr, In
MCl_m/DMF	153	Zn, Cu, Ni, Co, Fe, Mn, V, Hg, Cd, Pb, Sn, Mg, Ba, Ca, Pb, Ag, Rh, In, As, Sb, Tl, Bi, Cr
MR_m/solvent	25 – 200	Mg, Al, Ti
$MX_m(CO)_n$/solvent	80 – 200	Cr, Mo, Mn, Tc, Re, Fe, Ru, Co, Rh, Ir, Ni, Os
$M(OR)_n$/solvent	25 – 80	Li, Na, K, Rb, Cs, Mg, Ca, Sr, Ba

Figure 2.6. a) Periodic table of metalloporphyrins and b) metalating systems to prepare metalloporphyrins (adapted from reference 138).

Until 1999, the synthesis of corroles was stuck due to the lack of direct and precise methods for their synthesis. However, in that year, Gross *et al.* working on the synthesis of porphyrin analogues reported the first direct synthesis of corroles.[139] Later, Gryko *et al.* refined the synthetic methods and developed methodologies based on the types of aldehydes used.[140]

Since then, *meso*-substituted A_3-corroles have garnered significant interest among researchers, leading to the development of various synthetic approaches. Lee *et al.* introduced a two-step method: first, a TFA-catalyzed reaction of an aldehyde with pyrrole to generate a tetrapyrrane (**2.8**) intermediate, followed by its purification and subsequent oxidation with 2,3-dichloro-5,6-dicyano-1,4-benzoquinone (DDQ) to afford the desired corrole (**2.9**).[141]

To avoid the need for the tetrapyrrane purification, Gryko *et al.* developed an optimized one-pot synthesis of corroles (Scheme 2.1). This method involves initially reacting pyrrole with an aldehyde in the presence of TFA for a defined period of time, followed directly by the addition of DDQ to complete the oxidation step. The optimal reaction conditions depend on the reactivity of the aldehyde, which determines both the required amount of pyrrole and reaction time.[140]

For highly reactive aldehydes, an excess of pyrrole (1.5 mmol per mmol of aldehyde) is added, and the reaction proceeded within minutes. In the case of moderately reactive aldehydes, the pyrrole ratio is increased to 3 mmol per mmol of aldehyde and the

[139] Z. Gross, N. Galili, I. Saltsman, *Angew. Chem. Int. Ed.* **1999**, *38*, 1427.
[140] a) D. T. Gryko, B. Koszarna, *Org. Biomol. Chem.* **2003**, *1*, 350. b) R. Orłowski, D. Gryko, D. T. Gryko, *Chem. Rev.* **2017**, *117*, 3102.
[141] J.-W. Ka, W.-S. Cho, C.-H. Lee, *Tetrahedron Lett.* **2000**, *41*, 8121.

reaction time extended to several hours. For sterically hindered aldehydes, the amount of pyrrole is further increased to 5 mmol per mmol of aldehyde and the reaction required overnight stirring to reach completion.[140]

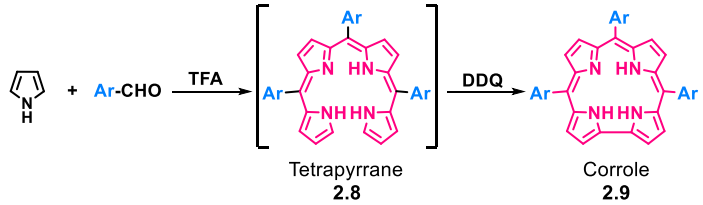

Scheme 2.1. General procedure for the synthesis of corroles in a one-pot process.

2.1.4. Porphyrinoid-carbon nanostructure conjugates for biomedical applications

Porphyrins have demonstrated enormous potential in biomedical applications thanks to their unique photophysical properties, particularly in photodynamic therapy (PDT) and imaging.[142] However, their limited solubility in aqueous media, tendency to aggregate, and moderate photophysical stability have driven the search for strategies to improve their performance in biological environments. In this context, carbon nanostructures have emerged as ideal platforms for porphyrin functionalization, offering significant improvements in solubility, stability and cellular transport capacity.[143]

PDT is a minimally invasive therapeutic modality that combines the action of a photosensitizer (PS), appropriate light wavelength and molecular oxygen to induce localized damage. This renders PDT a promising approach against cancer and microbial infections.[144] The process begins with the administration of the photosensitizer which preferentially accumulates in affected tissues. Upon irradiation with appropriate light, the photosensitizer is excited (PS*) from its ground state to an excited singlet state, from where it can undergo intersystem conversion to a longer-lived triplet state. In this state, it can transfer energy to molecular oxygen present in tissues, generating singlet oxygen (type II PDT) or other reactive oxygen species (ROS) (type I PDT) which cause oxidative damage (Figure 2.7).

[142] a) A. Akbar, S. Khan, T. Chatterjee, M. Ghosh, *J. Photochem. Photobiol. B* **2023**, *248*, 112796. b) T. W. Liu, E. Huynh, T. D. MacDonald, G. Zheng. Porphyrins for Imaging, Photodynamic Therapy, and Photothermal Therapy. In *Cancer Theranostics*, X. Chen, S. Wong, Eds. 1st ed. Academic Press, Inc. New York, **2014**, ch. 14, pp. 229-254.
[143] X.-T. Yu, S.-Y. Sui, Y.-X. He, C.-H. Yu, Q. Peng, *Biomater. Adv.* **2022**, *135*, 212725.
[144] a) F. Akhtar, L. Misba, A. U Khan, *Drug Discov. Today* **2024**, *29*, 104099. b) X. Wang, J. Peng, C. Menga, F. Feng, *Chem. Sci.* **2024**, *15*, 12234.

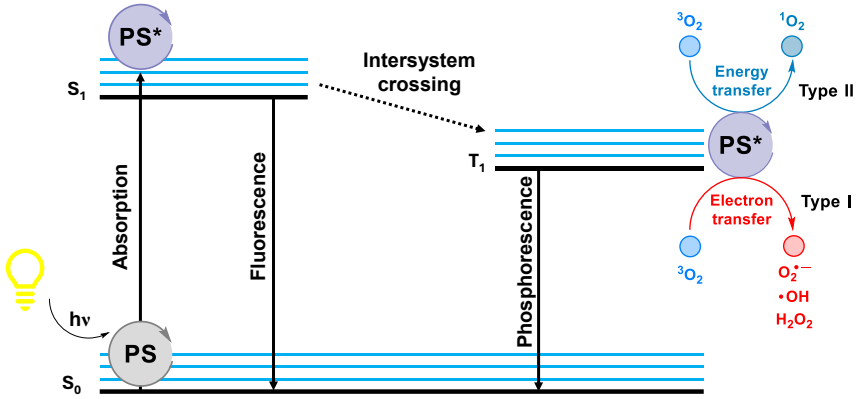

Figure 2.7. Jablonski diagram and the two classic types of photodynamic therapy.

The low oxygen levels in solid tumors present a significant challenge for the effectiveness of photodynamic therapy. To address this, nanoplatforms capable of generating O_2 *in situ* within tumor tissues have been developed. Sahu *et al.* designed a system consisting of a pluronic-coated graphene oxide carrier, incorporating hemin as a hydrogen peroxide (H_2O_2) decomposing catalyst and chlorin Ce6 as a photosensitizer (**2.10**).[145] Both active components were co-encapsulated through hydrophobic π-π interactions. These nanoparticles exhibited excellent colloidal stability, efficient cellular uptake by breast cancer (MCF-7) cells, and no cytotoxicity in the absence of light. In the presence of endogenous H_2O_2, hemin catalyzes oxygen generation, significantly boosting ROS production upon light exposure (Figure 2.8). Additionally, the use of graphene oxide conjugated with folic or hyaluronic acids as carriers based on hydrophobic π-π interactions for the transport of photosensitizers has also been reported.[146]

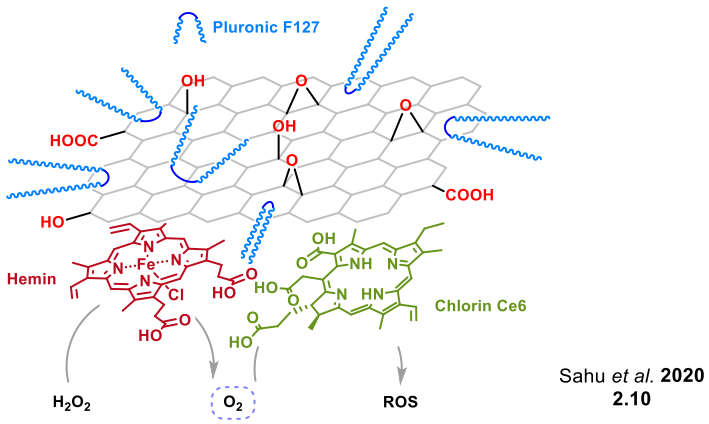

Figure 2.8. Pluronic-coated graphene oxide with hemin and chlorin Ce6.

[145] A. Sahu, K. Min, J. Jeon, H. S. Yang, G. Tae, *J. Control. Release* **2020**, *326*, 442.
[146] a) P. Huang, C. Xu, J. Lin, C. Wang, X. Wang, C. Zhang, X. Zhou, S. Guo, D. Cui, *Theranostics* **2011**, *1*, 240. b) F. Li, S.-J. Park, D. Ling, W. Park, J. Y. Han, K. Nab, K. Char, *J. Mater. Chem. B* **2013**, *1*, 1678.

Santos *et al*. have extensively explored the functionalization of nanomaterials with porphyrins and corroles to enhance their performance in biomedical applications (Figure 2.9).[147] The resulting nanoconjugates have shown effective cellular uptake, making them promising platforms for bioimaging due to their fluorescence, as well as for PDT. In some cases, the systems have also demonstrated potential for photothermal therapy, thus supporting a multimodal therapeutic approach.

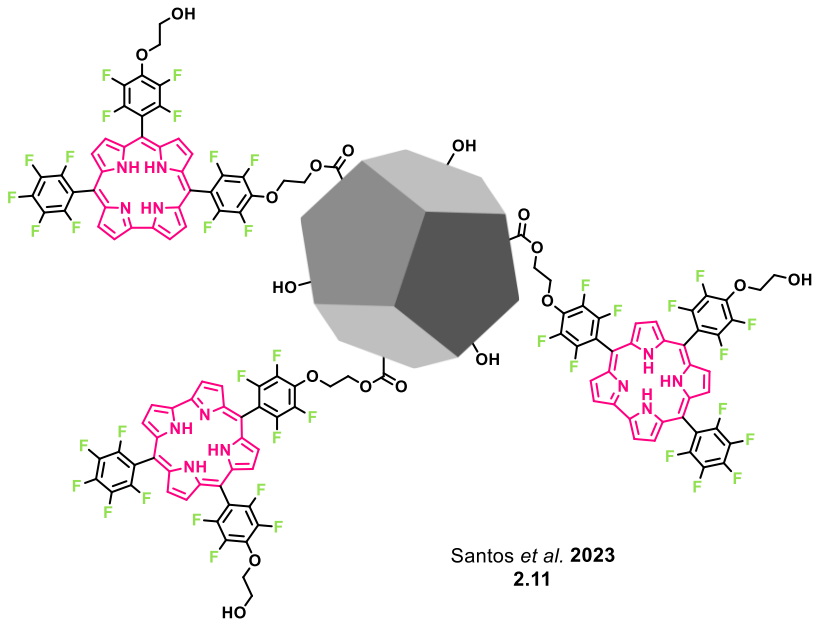

Figure 2.9. Nanodiamonds-corrole hybrids.

Other porphyrin-carbon nanoconjugates such as graphene quantum dots and carbon dots (CDs) have also been explored as ROS generators. Magaela *et al.* reported the development of biotin-decorated nitrogen-doped graphene quantum dots covalently linked to Sn(IV) porphyrins (Figure 2.10a).[148] The presence of the heavy Sn(IV) atom promotes intersystem crossing to the triplet state, thereby enhancing PDT efficiency. The hybrid material demonstrated superior cellular uptake compared to the individual porphyrin or graphene quantum dots. Tests conducted on MCF-7 breast cancer cells revealed minimal dark toxicity, while irradiation with a 625 nm light induced significant phototoxicity, leading to a reduction in cancer cells viability. Similarly, Beack *et al.* synthesized carbon dots conjugated with chlorin Ce6 and hyaluronate for

[147] a) C. I. M. Santos, M. Cicuéndez, G. Gonçalves, L. Rodríguez-Pérez, M. T. Portolés, M. A. F. Faustino, M. A. Herranz, M. G. P. M. S. Neves, J. M. G. Martinho, E. M. S. Maçôas, N. Martín, *J. Mater. Chem. B* **2023**, *11*, 675. b) C. I. M. Santos, L. Rodríguez-Pérez, G. Gonçalves, S. N. Pinto, M. Melle-Franco, P. A. A. P. Marques, M. A. F. Faustino, M. A. Herranz, N. Martín, M. G. P. M. S. Neves, J. M. G. Martinho, E. M. S. Maçôas, *Carbon* **2020**, *166*, 164. c) C. I. M. Santos, L. Rodríguez-Pérez, G. Gonçalves, C. J. Dias, F. Monteiro, M. A. F. Faustino, S. I. Vieira, L. A. Helguero, M. A. Herranz, N. Martín, M. G. P. M. S. Neves, J. M. G. Martinho, E. M. S. Maçôas, *ACS Appl. Nano Mater*. **2021**, *4*, 13079.
[148] N. B. Magaela, R. Matshitse, B. Babu, M. Managa, E. Prinsloo, T. Nyokong, *Polyhedron* **2022**, *213*, 115624.

melanoma skin cancer treatment (Figure 2.10b).[149] Their findings showed that the conjugates produced greater singlet oxygen generation in aqueous media compared to chlorin Ce6 itself. Moreover, laser irradiation following topical application resulted in the complete suppression of melanoma tumors.

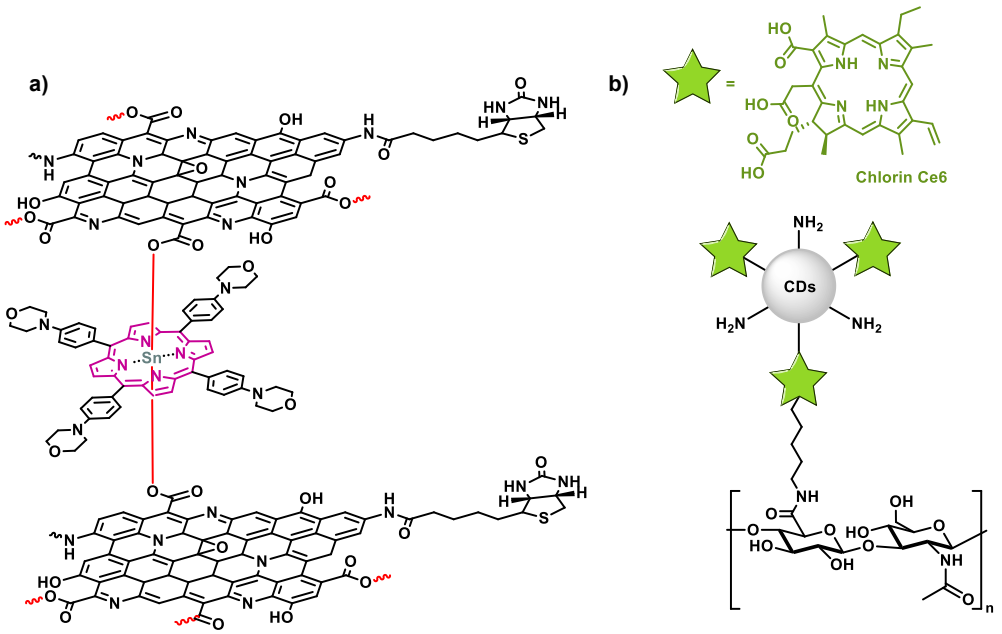

Figure 2.10. a) Graphene quantum dots covalently linked to Sn(IV) porphyrins and b) carbon dots conjugated with chlorin Ce6 and hyaluronate.

Antimicrobial photodynamic therapy (a-PDT) is an emerging therapeutic approach which combines the use of photosensitizing molecules with visible light to produce ROS that oxidatively damage microbial cells.[150] Sah *et al.* designed and evaluated a nanocomposite based on single-walled carbon nanotubes (SWCNTs) conjugated with porphyrins against *Staphylococcus aureus* (Figure 2.11a).[151] The nanocomposite exhibited significant antibacterial activity under visible light irradiation, attributed to the generation of ROS that damage bacterial cell membranes. Bacterial survival after exposure to the conjugate and visible light was evaluated, showing a significant decrease in bacterial viability with longer exposure times and higher conjugate concentrations. Additionally, experiments demonstrated that the antimicrobial effect depends on both the presence of the conjugate and light activation, ruling out toxicity

[149] S. Beack, W. H. Kong, H. S. Jung, I. H. Do, S. Han, H. Kim, K. S. Kim, S. H. Yun, S. K. Hahn, *Acta Biomater.* **2015**, *26*, 295.
[150] R. Youf, M. Müller, A. Balasini, F. Thétiot, M. Müller, A. Hascoët, U. Jonas, H. Schönherr, G. Lemercier, T. Montier, T. Le Gall, *Pharmaceutics* **2021**, *13*, 1995.
[151] U. Sah, K. Sharma, N. Chaudhri, M. Sankar, P. Gopinath, *Colloids Surf. B Biointerfaces* **2018**, *162*, 108.

in the absence of light. A similar strategy was employed by Durantini *et al.* in the synthesis of porphyrin-fullerene C_{60} dyads (Figure 2.11b).[152] The incorporation of cationic groups significantly enhances the amphiphilic character of the photosensitizer. This amphiphilicity may facilitate the penetration or accumulation of the dyads in membranes, thereby improving photosensitization efficiency.

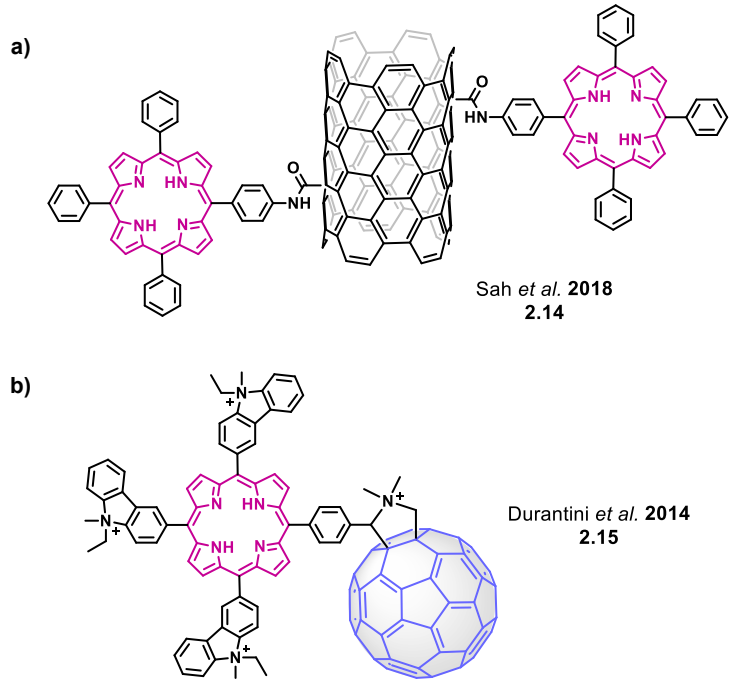

Figure 2.11. a) Single-walled carbon nanotubes conjugated with porphyrins and b) C_{60}-porphyrin dyad for ROS generation.

[152] M. B. Ballatore, M. B. Spesia, M. E. Milanesio, E. N. Durantini, *Eur. J. Med. Chem.* **2014**, *83*, 685.

2.2. Objectives

The primary goal of this chapter is the synthesis of multivalent systems based on glycofullerenes anchored to fluorescent and biocompatible platforms. Porphyrin and corrole derivatives were selected as the core scaffolds, as their chemical versatility allows the incorporation of varying numbers of substituents. Herein, glycofullerene-decorated porphyrin and corrole nanostructures will be prepared in order to investigate the effect of carbohydrate valency on biological behavior. Depending on the type of carbohydrate, the resulting molecules can serve different purposes: mannose-functionalized systems aim to inhibit viruses such as SARS-CoV-2 by blocking DC-SIGN receptor, while glucose-containing compounds will be designed to preferentially accumulate in cancer cells and induce cell death through ROS generation.

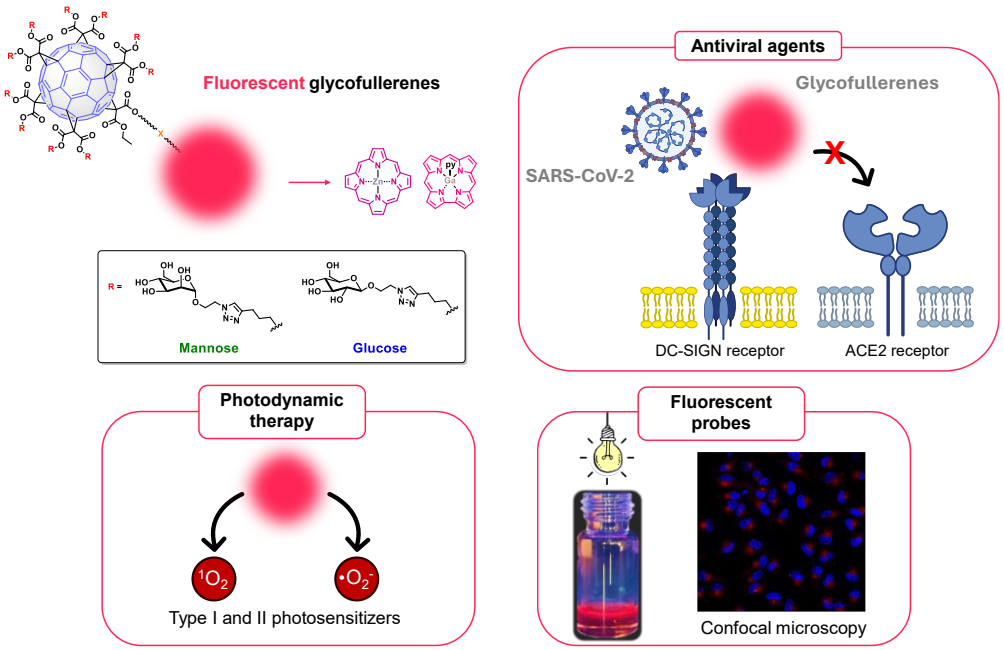

Additionally, the intrinsic fluorescence of porphyrinoid platforms will be harnessed to monitor their interaction with receptors and cellular uptake using confocal microscopy. The final compounds will be thoroughly characterized, including analysis of their photophysical properties, determination of diffusion coefficients and hydrodynamic radii, as well as the evaluation of their cytotoxicity and biocompatibility.

2.3. Results and discussion

2.3.1. Glycoporphyrins

2.3.1.1. Synthesis of glycofullerenes

This section describes the synthesis of three asymmetric [5:1] mannose-derived glycofullerenes. They differ in the linker in the asymmetric branch to attach them to the central scaffold. Two of them are polyethylene glycol derivatives with different chain lengths, and one of them is an alkyl chain.

As illustrated in Scheme 2.2, the synthetic route starts with the preparation of monobrominated alcohols *via* Appel reaction, yielding compounds **42** and **43**. These intermediates as well as 8-bromo-1-octanol (**44**) then undergo a condensation reaction with ethyl malonyl chloride **4** to synthesize the corresponding malonates **45a-c**.

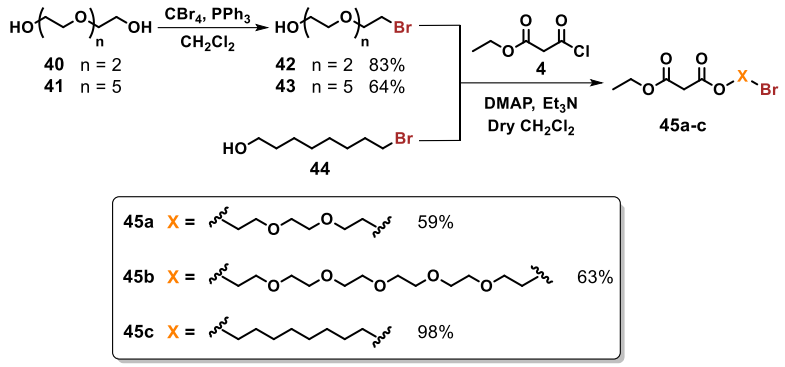

Scheme 2.2. Synthetic methodology for the preparation of malonates **45a-c**.

Subsequently, two Bingel-Hirsch cyclopropanation reactions were carried out to afford asymmetric hexakis-adducts **47a-c** bearing ten terminal alkyne groups and a single asymmetric arm with a terminal bromine atom. In the following step, a CuAAC reaction was performed between the terminal alkynes and 2-azidoethyl α-D-mannopyranoside (**11**) resulting in the formation of glycofullerenes **48a-c**. The final transformation involves a S_N2 of the terminal bromine for an azide group, using sodium azide under microwave irradiation to yield compounds **49a-c** (Scheme 2.3).

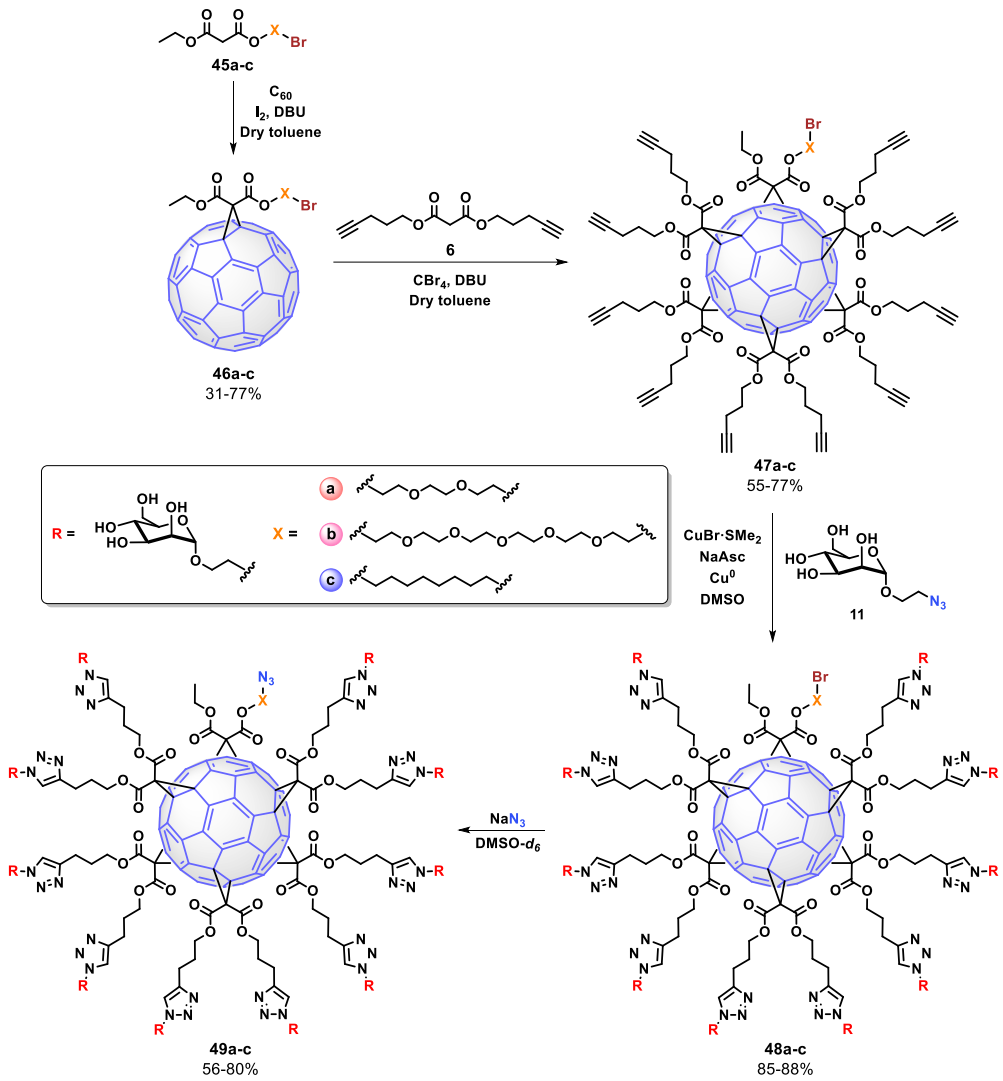

Scheme 2.3. Synthetic pathway to obtain azide-substituted glycofullerenes **49a-c**.

Purification of glycofullerenes **49a-c** was carried out using SEC Sephadex G-25 (H_2O/CH_3OH 9:1). The products were obtained in moderate to high yields and are completely soluble in aqueous media.

The characterization by NMR and FT-IR confirmed the structures of glycofullerenes **49a-c**. For a better understanding, the characterization of glycofullerene **49a** will be used as an example.

In the ^{1}H NMR spectrum (Figure 2.12a), the appearance of the signal at ~8 ppm corresponding to the C*H* of the triazoles formed during the click reaction can be detected, confirming that the reaction has occurred successfully. In the ^{13}C NMR spectrum (Figure 2.12b), the triazole resonances can also be observed at ~146 ppm and ~122 ppm, as well as two signature signals corresponding to the sp^2 carbons of

the fullerene at ~145 and ~141 ppm. The anomeric carbon of mannose at ~99 ppm confirms the presence of the carbohydrate in the molecule, while the peak at ~50 ppm indicates that the exchange of bromine to azide has occurred successfully. Other characteristic signals are the quaternary carbons of the malonates at ~45 ppm, as well as the carbons of the alkyl chain at ~28 ppm and ~21 ppm and methyl group at ~14 ppm.

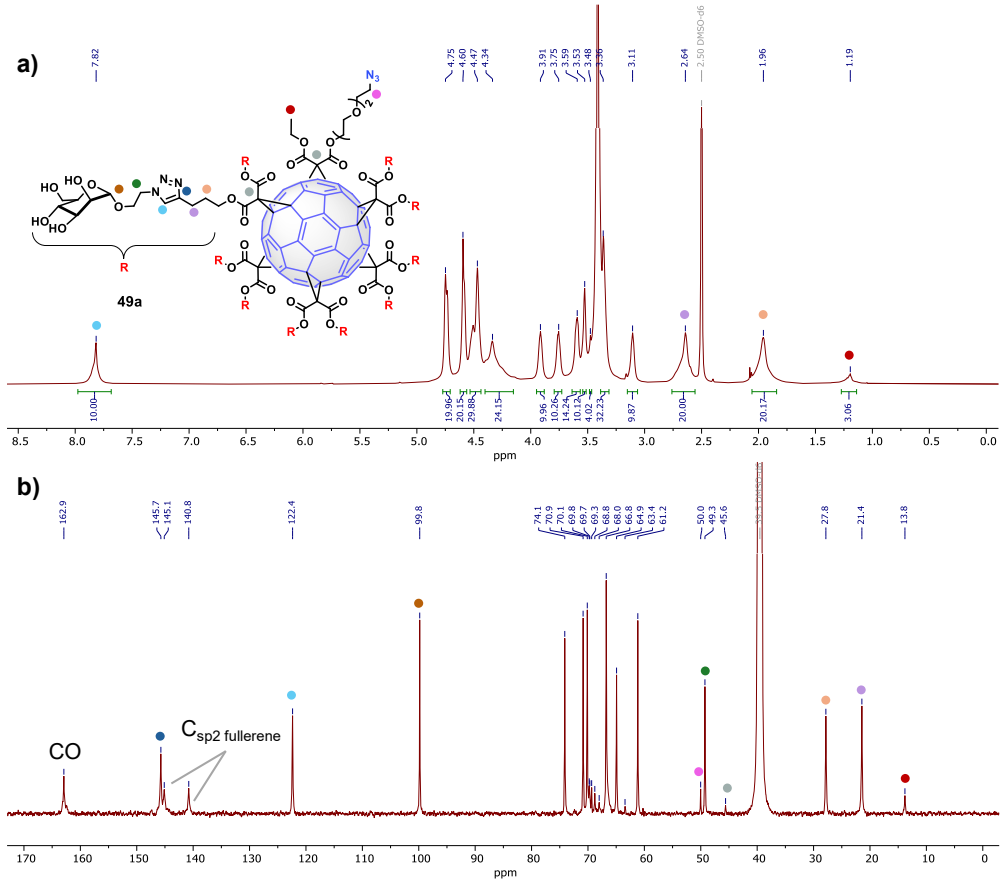

Figure 2.12. a) ^{1}H NMR spectrum (DMSO-d_6, 700 MHz) and b) ^{13}C NMR spectrum (DMSO-d_6, 176 MHz) of compound **49a**.

As the last synthetic step to get glycofullerene **49a** involves the replacement of a bromine atom by an azido group, FT-IR was useful due to the appearance of the azido band at 2112 cm^{-1} (Appendix 2, Figure AP2.1a).

2.3.1.2. Synthesis of glycoporphyrins

The synthesis of the target molecules, termed glycoporphyrins, involves the covalent bonding of glycofullerenes to porphyrin platforms. These porphyrins possess either four or eight alkynes in their structure, enabling 40 or 80 carbohydrate units per molecule. This will allow the analysis of the multivalency and the influence of having a higher valency in the molecules when interacting with receptors such as DC-SIGN.

The porphyrins used (**50** and **51**) were previously synthesized in the laboratory following the described methodology,[153] and the bonding between the terminal azide groups of glycofullerenes **49a-c** and the terminal alkynes of the porphyrins was carried out through a CuAAC reaction (Scheme 2.4).

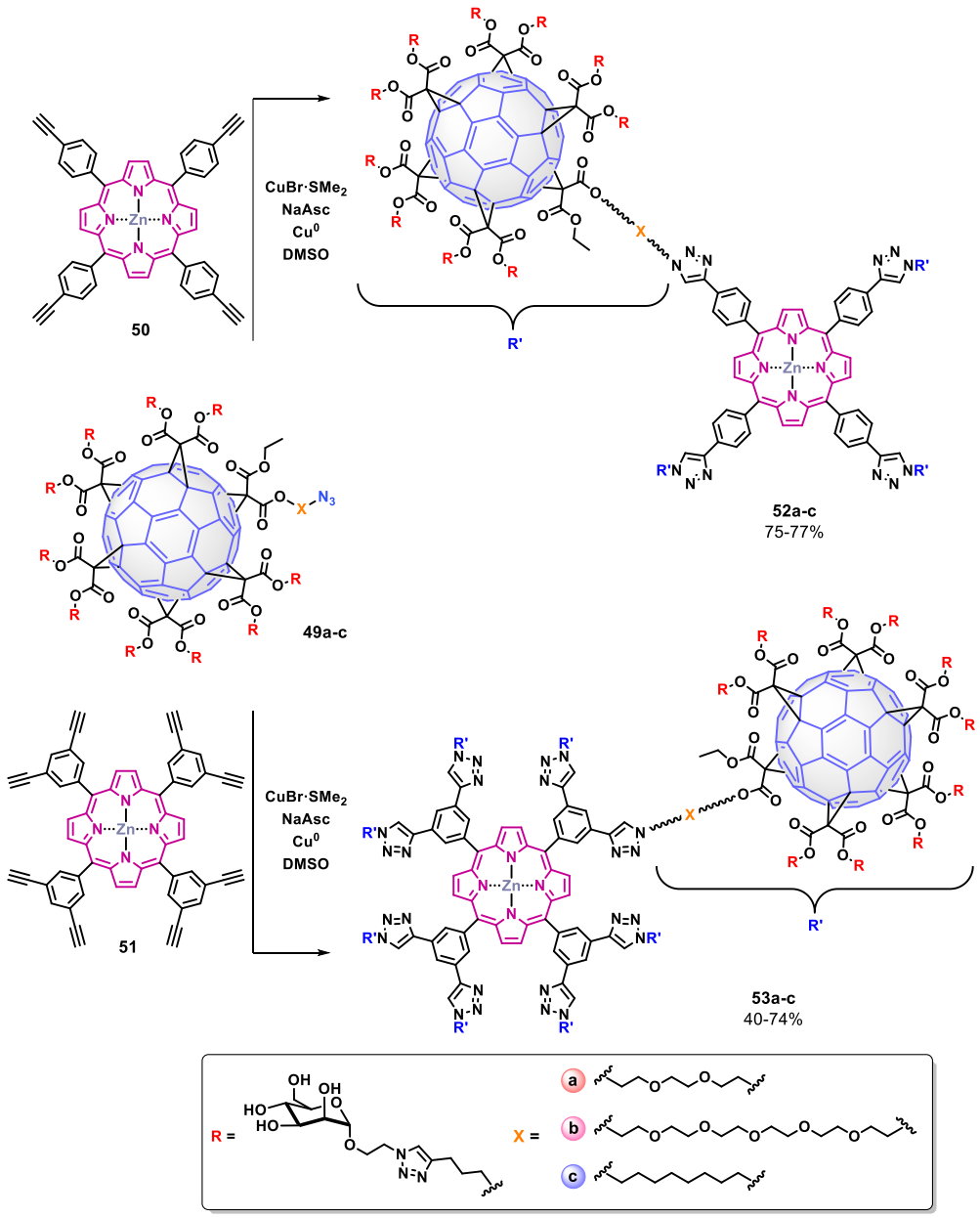

Scheme 2.4. General procedure for the synthesis of glycoporphyrins **52a-c** and **53a-c**.

[153] a) A. R. McDonald, N. Franssen, G. P. M. v. Klink, G. v. Koten, *J. Organomet. Chem.* **2009**, *694*, 2153. b) S. M. Aly, H. Guernon, B. Guérin, P. D. Harvey, *J. Porphyr. Phthalocyanines* **2011**, *15*, 871.

The purification of these compounds was performed using SEC on Sephadex G-50 (H_2O/CH_3OH 9:1), yielding glycoporphyrins **52a-c** and **53a-c** in moderate to high yields. These compounds exhibit full solubility in aqueous media, except for **53c**. For the latter, despite the high number of carbohydrates, the hydrophobic nature of the eight alkyl chains appears to be the key factor determining its reduced water solubility. In terms of appearance, glycoporphyrins display markedly different colors compared to the precursor glycofullerenes. Tetra-substituted glycoporphyrins exhibit a green color, while the octa-substituted variants, with a higher number of glycofullerenes, show a brownish color more reminiscent of the starting glycofullerene materials.

The characterization was carried out using standard spectroscopic techniques such as NMR and FT-IR. For a better understanding, the characterization of glycoporphyrin **52a** will be detailed.

In the ^{1}H NMR spectrum, the main difference with the starting glycofullerene is the appearance of signals in the aromatic region due to the porphyrin core in the structure (Figure 2.13). This suggests the correct functionalization of the molecules.

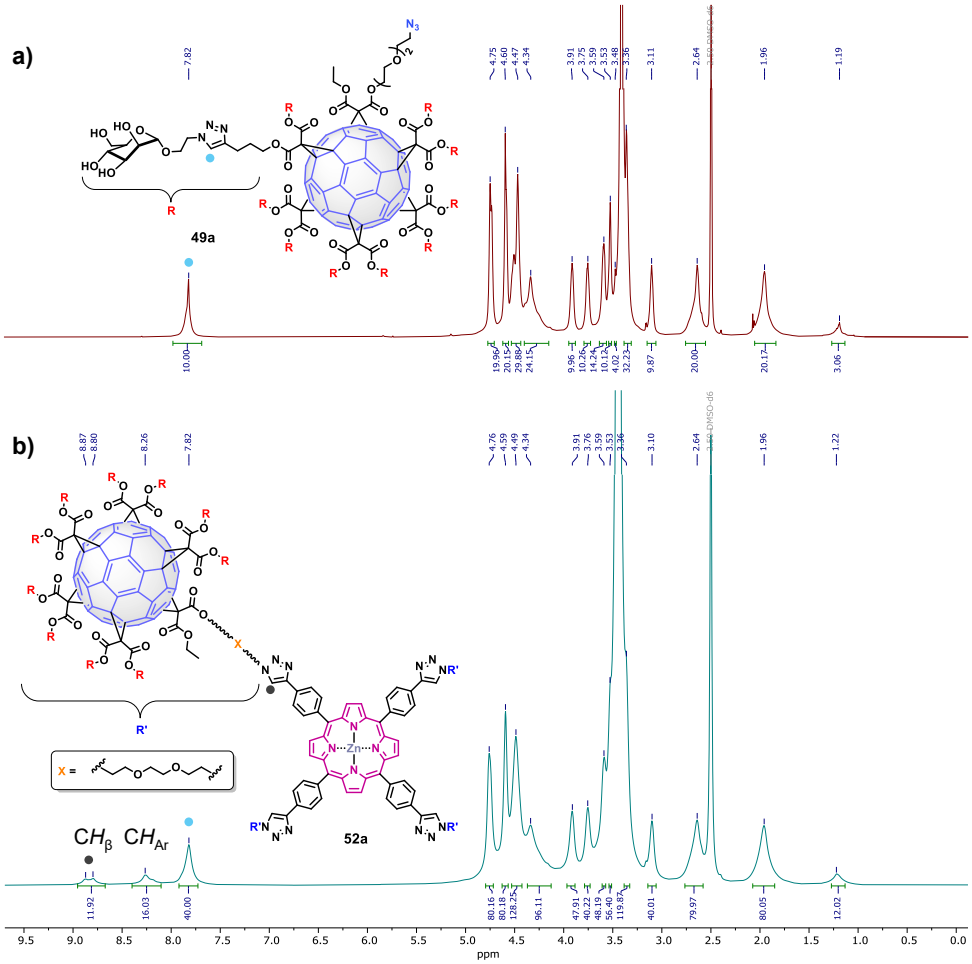

Figure 2.13. ^{1}H NMR spectra (DMSO-d_6, 700 MHz) of: a) **49a** and b) **52a**.

As previously seen, ^{13}C NMR provides the most reliable confirmation of successful functionalization (Figure 2.14). The incorporation of the porphyrin moiety is observed in the aromatic region of the spectrum (~150 – 120 ppm), where small signals attributed to the porphyrin are present (Figure 2.14c). The absence of signals in the alkyne region at ~90 ppm confirms that the functionalization has proceeded to completion, so the porphyrin unit is now fully integrated into the system. Furthermore, the disappearance of the CH_2-N_3 resonance at ~50 ppm verifies the success of the click reaction and the absence of unreacted glycofullerene. The remaining signals associated with the glycofullerene, including the typical signals at ~145 ppm and ~141 ppm for the Csp^2 of fullerene, remain unchanged, indicating that this part of the molecule was not altered during the reaction.

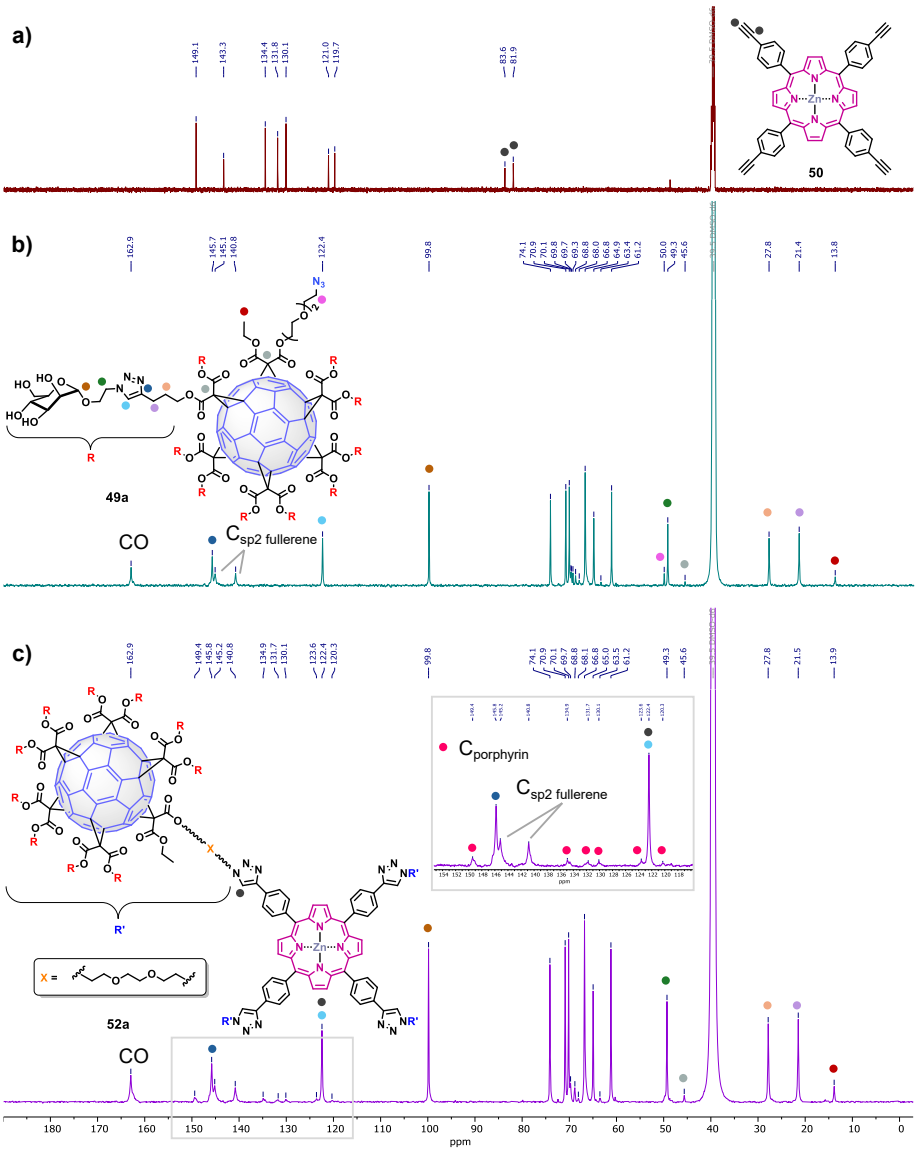

Figure 2.14. ^{13}C NMR spectra (DMSO-d_6, 176 MHz) of: a) **50**, b) **49a** and c) **52a**.

Due to the transformation of the CH_2-N_3 group into CH_2-N, FT-IR is especially useful for observing the disappearance of the azido band at 2108 cm^{-1} in the final compound (Appendix 2, Figure AP2.1a and Figure AP2.2a).

The molecular size of glycoporphyrins was estimated by dynamic light scattering (DLS), which revealed an increase in hydrodynamic diameter from approximately 4 nm for the tetra-substituted porphyrins to around 6 nm for the octa-substituted analogues (Appendix 2, Figure AP2.5). Figure 2.15 shows an example of the curves obtained after measurement for compounds **52b** and **53b**.

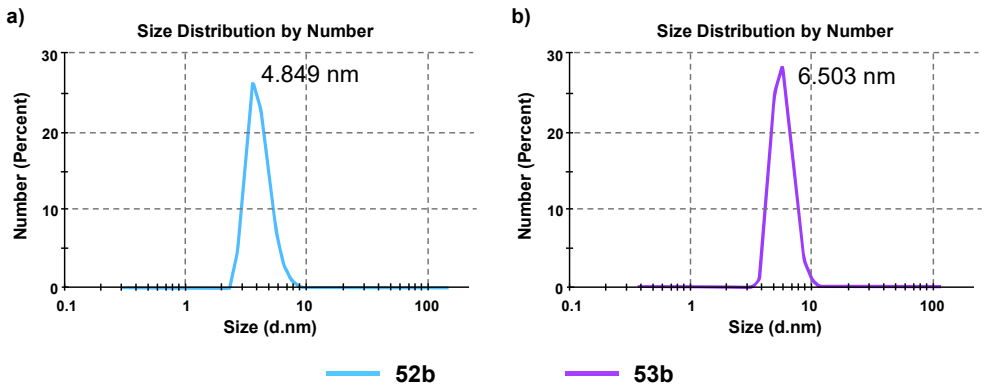

Figure 2.15. Dynamic Light Scattering (DLS) measurements (H_2O, $1 \cdot 10^{-5}$ M) in number % of: a) **52b** and b) **53b**.

Additionally, and as a proof of concept, the hydrodynamic radii of molecules **52b** and **53b** was calculated using Diffusion-Ordered SpectroscopY (DOSY) NMR experiments (Appendix 2, Figures AP2.7-AP2.9). This technique allows to know the diffusion coefficient (D) and the estimation of the hydrodynamic radius (R_H) according to the Stokes-Einstein equation, assuming a spherical shape.[154] Molecular weights (MW), D and R_H values are shown in Table 2.1. Additionally, D was determined for the previously described symmetric glycofullerene **18** to compare it with the glycoporphyrins. Glycofullerene **18**, that contains only one central fullerene, shows a R_H value of 11.4 Å in agreement with the result obtained by ^{1}H NMR pulsed-fieldgradient (PFG) diffusion experiments.[155] When glycofullerenes are arranged around the porphyrin core, there is an increase in the overall size with a R_H value of 22.9 and 45.6 Å. These results show a remarkable correlation between D and MW, which is also an indication of the correct functionalization of the starting porphyrins.

[154] K. F. Morris, C. S. Johnson Jr, *J. Am. Chem. Soc.* **1992**, *114*, 3139.
[155] O. Engström, A. Muñoz, B. M. Illescas, N. Martín, R. Ribeiro-Viana, J. Rojo, G. Widmalm, *Org. Biomol. Chem.* **2015**, *13*, 8750.

Table 2.1. Diffusion coefficients determined by 2D-DOSY (700 MHz, ~2 mg·mL^{-1} in D_2O) and hydrodynamic radii.

Compound	Molecular Weight (MW, g·mol^{-1})	Diffusion coefficient (D, m^2·s^{-1})	Hydrodynamic radii (R_H, Å)
18	5116.77	$2.14 \cdot 10^{-10}$	11.4
52b	19988.94	$1.07 \cdot 10^{-10}$	22.9
53b	39298.37	$5.37 \cdot 10^{-11}$	45.6

2.3.1.3. Photophysical properties

The photophysical characterization of glycoporphyrin conjugates **52a-c** and **53a-c** was performed in collaboration with Prof. Santiago Nonell from Universitat Ramon Llull. The measurements were carried out in water at room temperature and in DMSO for precursors **50** and **51** as they are not soluble in aqueous media (data summarized in Table 2.2 and Appendix 2, Figure AP2.12). Due to the similarity across all measurements and to facilitate clearer interpretation, the graphs will present only the results obtained for compounds **52b** and **53b**.

Table 2.2. Photophysical properties of glycoporphyrins **52a-c** and **53a-c** and their precursors **50** and **51**.

Comp.	Solvent	Soret (nm) (ε/10^3 M^{-1} cm^{-1})	Q-bands (nm) (ε/10^3 M^{-1} cm^{-1})	λ_{em}^{max} (nm)	Φ_F (%)[a]
50	DMSO	431 (523.9)	562 (19.2) 603 (10.7)	610 663	4.7
51	DMSO	431 (804.2)	562 (30.6) 603 (10.6)	606 660	2.7
52a	Water	436 (445.5)	566 (31.0) 608 (20.6)	612 666	1.6
52b	Water	437 (403.0)	566 (26.9) 607 (18.8)	610 661	1.3
52c	Water	437 (382.9)	567 (25.8) 608 (15.5)	610 659	0.7
53a	Water	435 (716.0)	564 (38.3) 605 (13.0)	604 655	2.0
53b	Water	434 (726.8)	564 (40.6) 605 (15.2)	604 656	3.0
53c	Water	435 (720.2)	563 (48.3) 604 (22.3)	603 654	1.3

[a]Fluorescence quantum yields (Φ_F) were measured by the reference method using a tetraphenylporphyrin solution in toluene (Φ_F = 0.11) as reference.

Glycoporphyrins exhibit an absorption spectrum characteristic of porphyrins, with a prominent Soret band centered at ~436 nm and two weaker Q-bands in the 560-600 nm range (Figure 2.16a). A broad absorption band is also observed below 350 nm, corresponding to the glycofullerene unit.[156] The fact that the spectra of compounds

[156] J. Ramos-Soriano, A. Pérez-Sánchez, S. Ramírez-Barroso, B. M. Illescas, K. Azmani, A. Rodríguez-Fortea, J. M. Poblet, C. Hally, S. Nonell, D. García-Fresnadillo, J. Rojo, N. Martín, *Angew. Chem. Int. Ed.* **2021**, *60*, 16109.

52a-c and **53a-c** closely resemble to those of the parent compounds **50** and **51** indicates that there is minimal or no electronic communication between the porphyrin core and the glycofullerene fragment.

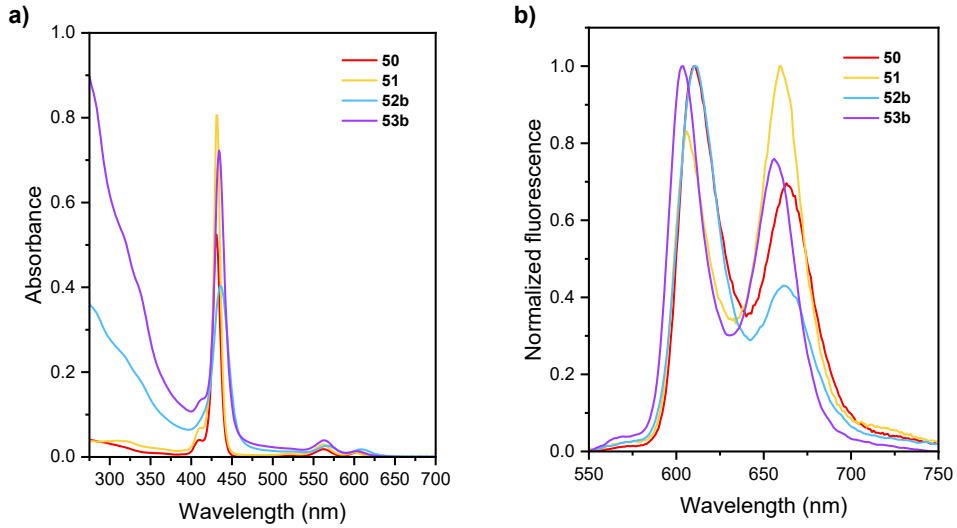

Figure 2.16. a) Absorption spectra of **50**-**51** (DMSO, $1 \cdot 10^{-6}$ M), **52b** and **53b** (H_2O, $1 \cdot 10^{-6}$ M) and b) emission spectra of **50**-**51** (DMSO, $2.5 \cdot 10^{-7}$ M for **50** and $1.25 \cdot 10^{-7}$ M for **51**, λ_{exc} = 431 nm), **52b** and **53b** (H_2O, $5 \cdot 10^{-7}$ M, λ_{exc} = 436 nm).

Similar to the starting porphyrins **50** and **51**, glycoporphyrin derivatives display two emission peaks at approximately ~564 nm and ~606 nm, indicating that the glycofullerene moiety does not contribute to the fluorescence emission of the final compounds (Figure 2.16b). As for the fluorescence quantum yield (Φ_F), a slight decrease is observed in the glycoporphyrins compared to their precursors, likely attributed to quenching effects induced by the attached fullerene units.

As outlined in the introduction, porphyrins are known for their ability to generate ROS. To evaluate this property, the singlet oxygen quantum yield (Φ_Δ) was measured. However, none of the tested compounds produced detectable amounts of singlet oxygen.

Consequently, the generation of alternative ROS was investigated using dihydroethidium (DHE, 2,7-diamino-10-ethyl-9-phenyl-9,10-dihydrophenanthridine) as superoxide radical anions fluorescent probe. In fact, these studies reveal that the molecules produced superoxide radical anions, indicative of a Type I ROS generation mechanism (Figure 2.17). Unlike Type II photosensitizers, that rely on singlet oxygen production, Type I photosensitizers are less dependent on oxygen availability and engage in electron-transfer processes, leading to the formation of superoxide radicals. These can trigger superoxide dismutase-mediated catalytic cascades, ultimately producing hydroxyl radicals (·OH), the most cytotoxic ROS in biological systems. Given that solid tumors often exhibit hypoxia due to poor vascularization and high

oxygen consumption, Type I photosensitizers are particularly promising for the treatment of hypoxic tumors.[157] Therefore, these compounds can be considered as candidates for future PDT studies in anticancer applications.

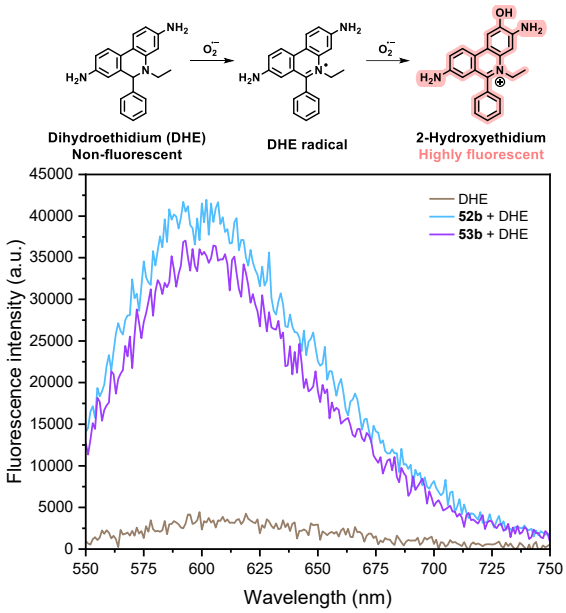

Figure 2.17. Detection of superoxide anion in compounds **52b** and **53b** using DHE after irradiating for 10 minutes at 10 kHz (λ_{exc} = 532 nm).

2.3.1.4. Biological studies

Among the eight synthesized glycoporphyrins, the hexaethylene glycol derivatives **52b** and **53b** were selected to assess their antiviral activity against the SARS-CoV-2 trans-infection process, in collaboration with Dr. Rafael Delgado (Hospital Universitario 12 de Octubre).

Cytotoxicity tests conducted at concentrations ranging from 0.01 to 10 μM indicated that the compounds start to exhibit cytotoxic effects at 10 μM (Figure 2.18a). Consequently, assays were performed at a concentration of 1 μM, which does not affect cell viability.

The trans-infection assays were carried out following a methodology similar to that discussed in *Chapter 1* but in this case using the real virus. Both compounds demonstrated significant inhibitory effects in DC-SIGN-expressing cells: **52b** achieved 90% inhibition, while **53b** reached 61% (Figure 2.18b). These results indicate that increasing the number of carbohydrate moieties does not necessarily enhance the antiviral efficacy of the molecules. Given the superior performance of **52b**, further studies focused on this nanostructure were performed to explore its therapeutic potential.

[157] M. Li, Y. Xu, X. Peng, J. S. Kim, *Acc. Chem. Res.* **2022**, *55*, 3253.

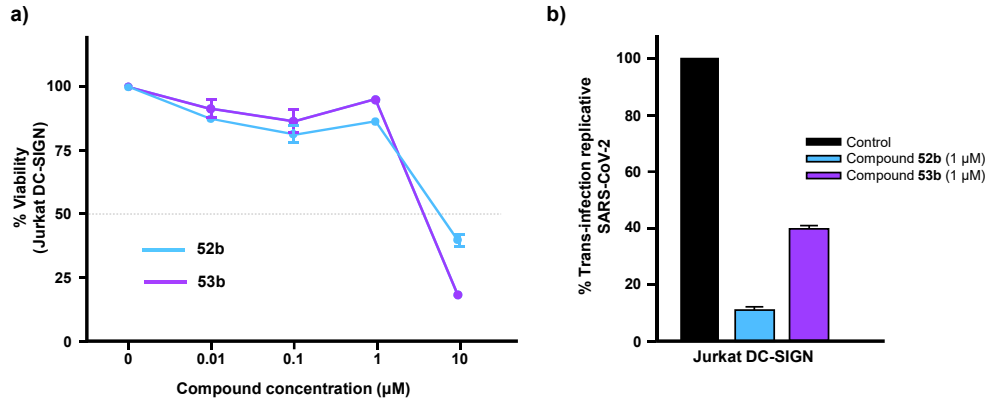

Figure 2.18. a) Viability of Jurkat cells treated with compounds **52b** and **53b** at different concentrations and b) trans-infection of SARS-CoV-2 in the presence or not (control) of 1 µM of compounds **52b** or **53b**.

Flow cytometry was employed to investigate the interaction between DC-SIGN lectin and the SARS-CoV-2 S-protein, both in the absence and presence of **52b**. To track this interaction, fluorescent beads (trans-fluorospheres) peripherally decorated with the soluble trimeric SARS-CoV-2 S-protein (Figure 2.19a) were employed. The addition of **52b** to Jurkat-DC-SIGN cells progressively reduced the fluorescence signal, dropping to 40% at 1 µM and to 20% at 10 µM showing the competition between compound **52b** and the virus for the receptor (Figure 2.19b).

Both, the trans-infection and binding experiments, consistently indicate that glycoporphyrin **52b** is a potent and specific inhibitor of the interaction between SARS-CoV-2 and DC-SIGN lectin.

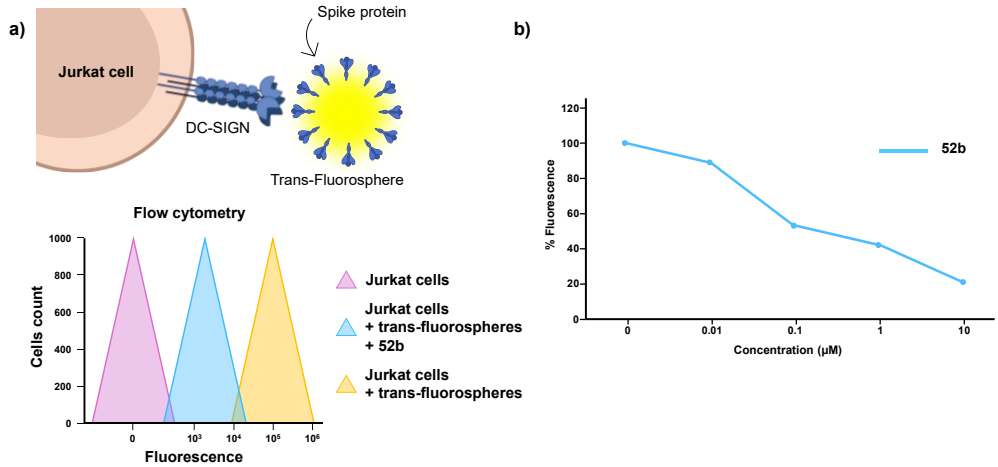

Figure 2.19. a) Scheme of the binding experiment with trans-fluorospheres coated with SARS-CoV-2 spike protein and DC-SIGN-expressing Jurkat cells and b) % of fluorescence in the presence of increasing amounts of compound **52b**.

The intrinsic fluorescence of the porphyrin core allowed to trace glycoporphyrin within the cells using confocal fluorescence microscopy. The trials were carried out in collaboration with Prof. Iván López (Universidad Complutense de Madrid). Based on previous cell viability studies, both wild-type (WT) Jurkat cells and DC-SIGN-expressing Jurkat cells were incubated with **52b** at a concentration of 1 μM to prevent cytotoxic effects.

When DC-SIGN-Jurkat cells were incubated with **52b** at 37 °C (Figure 2.20a), an increasing red fluorescence signal was detected both on the cell membrane and inside the cells as internalization progressed. In contrast, WT Jurkat cells incubated under similar conditions (37 °C, 1 μM) displayed only a faint background signal when imaged using the same acquisition settings, indicating a significantly lower level of uptake compared to the DC-SIGN-expressing cells (Figure 2.20b).

Since temperature significantly influences endocytosis, additional experiments were conducted at 4 °C (Figure 2.20c). Under these conditions, endocytosis is minimal, resulting in the absence of intracellular labeling; however, fluorescence was detected at the cell periphery. These findings suggest that **52b** undergoes selective uptake, initially binding to the lectin surface receptor *via* carbohydrate-protein interactions.

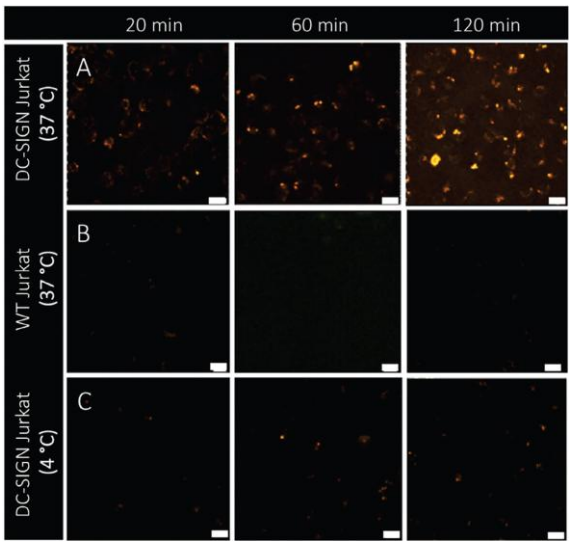

Figure 2.20. Confocal fluorescence micrographs of Jurkat cells incubated with 1 μM of glycoporphyrin **52b**: a) DC-SIGN-expressing Jurkat cells at 37 °C, b) WT Jurkat cells at 37 °C and c) DC-SIGN expressing Jurkat cells at 4 °C. Scale bars: 10 μm.

The specific interaction between **52b** and the DC-SIGN receptor was confirmed through ^{1}H-^{15}N HSQC NMR experiments, where the addition of **52b** to the DC-SIGN CRD caused noticeable perturbations in the protein signals. These residues are situated in regions that also showed changes in previously reported NMR titrations of DC-SIGN with Lewis-X and mannose, confirming that **52b** interacts with the

canonical carbohydrate-binding site (Figure 2.21a).[158] This interaction was also confirmed by molecular dynamic simulations using compound **18**, a symmetric mannose glycofullerene, for simplicity, where the strongest binding affinity was observed at the canonical binding site (highlighted in **red**), followed by adjacent surrounding amino acids (highlighted in **green**) (Figure 2.21b). Furthermore, the dissociation constant (K_D) of **52b** with the CRD of the protein was determined to be approximately 1.26 ± 0.11 μM. The low K_D value obtained indicates that **52b** effectively competes with the SARS-CoV-2 spike protein for binding to DC-SIGN. This competitive interaction is further supported by the fact that the spike protein binds to DC-SIGN with a higher K_D in the range of 5-10 μM.[159]

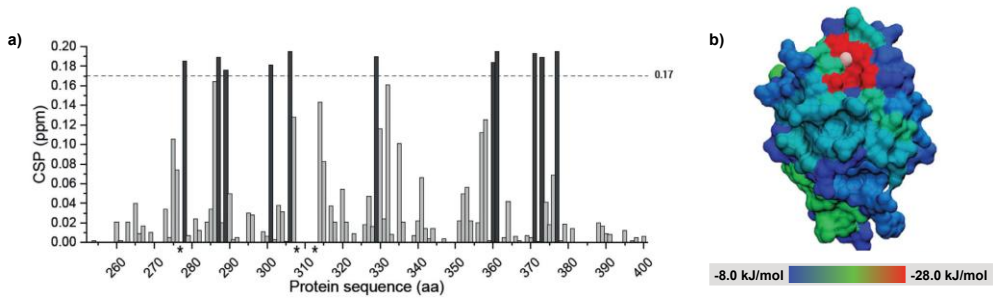

Figure 2.21. a) Chemical shift perturbation for each residue of protein. Signals that disappear in the presence of **52b** are marked with an asterisk and b) front view of the CRD protein surface, with a color scale indicating the mannose binding free energy at each amino acid residue, as determined by molecular docking assays. Ca^{2+} ion is highlighted in pink.

2.3.2. Glycocorroles

2.3.2.1. Synthesis of corroles

All the work carried out on the synthesis of corroles, their characterization and the measurement of their properties was carried out in collaboration with the groups of Ermelinda Maçôas, PhD (Instituto Superior Técnico, Lisboa) and Prof. Maria da Graça de Pinho Morgado Silva Neves (Universidade de Aveiro).

Scheme 2.5 shows the synthetic route to the target corroles. The methodology developed by Gryko was employed, using pentafluorobenzaldehyde (**55**), pyrrole (**54**), TFA as the catalytic acid and DDQ as the oxidizing agent for the formation of the tetrapyrrolic core.[140] Following isolation and purification *via* column chromatography, the free-base corrole **56** was afforded. This compound was subsequently complexed with Ga(III) by refluxing with $GaCl_3$ in pyridine.[160] The

[158] a) K. Pederson, D. A. Mitchell, J. H. Prestegard, *Biochemistry* **2014**, *53*, 5700. b) J. Aretz, H. Baukmann, E. Shanina, J. Hanske, R. Wawrzinek, V. A. Zapol'skii, P. H. Seeberger, D. E. Kaufmann, C. Rademacher, *Angew. Chem. Int. Ed.* **2017**, *56*, 7292.
[159] M. Thépaut, J. Luczkowiak, C. Vivès, N. Labiod, I. Bally, F. Lasala, Y. Grimoire, D. Fenel, S. Sattin, N. Thielens, G. Schoehn, A. Bernardi, R. Delgado, F. Fieschi, *PLoS Pathog.* **2021**, *17*, e1009576.
[160] J. Bendix, I. J. Dmochowski, H. B. Gray, A. Mahammed, L. Simkhovich, Z. Gross, *Angew. Chem. Int. Ed.* **2000**, *39*, 4048.

resulting metallocorrole **57** presents a pyridine ligand coordinated to the gallium. Then, the substitution of the *para*-position fluorine atoms was achieved through an nucleophilic aromatic substitution (S_NAr) reaction, employing propargyl alcohol (**58**) as the nucleophile. By adjusting the equivalents of propargyl alcohol and tuning the reaction conditions, either the monosubstituted (**59**) or trisubstituted (**60**) corrole derivatives were selectively obtained. Specifically, treating the fluorinated corrole **57** with a slight excess of propargyl alcohol in DMSO at 100 ºC for 3 hours in the presence of K_2CO_3 afforded the monosubstituted corrole **59** as an inseparable mixture of regioisomers **59a** and **59b** in a 2:1 ratio. In contrast, using a large excess of propargyl alcohol in refluxing THF for 1 hour and NaH as the base led to the formation of the trisubstituted corrole **60**. Both reactions provided the desired products ranging from low to moderate yields.

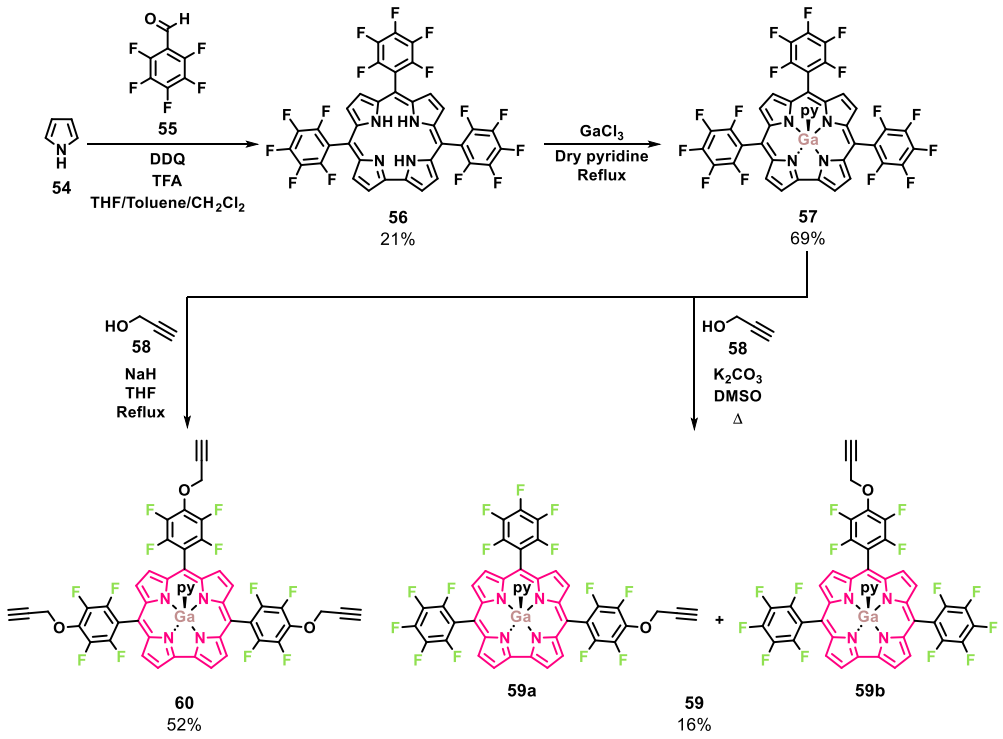

Scheme 2.5. General procedure for the synthesis of corroles **59** and **60**.

Characterization of products **59** and **60** was carried out by the common techniques: NMR, FT-IR and mass spectrometry. For a better understanding, the characterization of **59** will be detailed as a representative example.

The incorporation of propargyl alcohol into the molecule can be confirmed by ^{1}H NMR, where two doublets at ~5.20 ppm, corresponding to the CH_2 group of the propargyl moiety are observed, each associated with one of the isomers (Figure 2.22). Additionally, two triplets appear at ~2.86 ppm, attributed to the terminal alkyne proton, which couples with the adjacent CH_2 group. The integration of these signals

reveals a 2:1 ratio between the two isomers, with **59a** predominating due to the presence of two equivalent reactive positions. The remaining signals in the spectrum correspond to the *β*-pyrrolic protons in the aromatic region, along with resonances at ~6.65 ppm, ~5.85 ppm and ~2.88 ppm, which are assigned to the pyridine ligand bound to gallium.

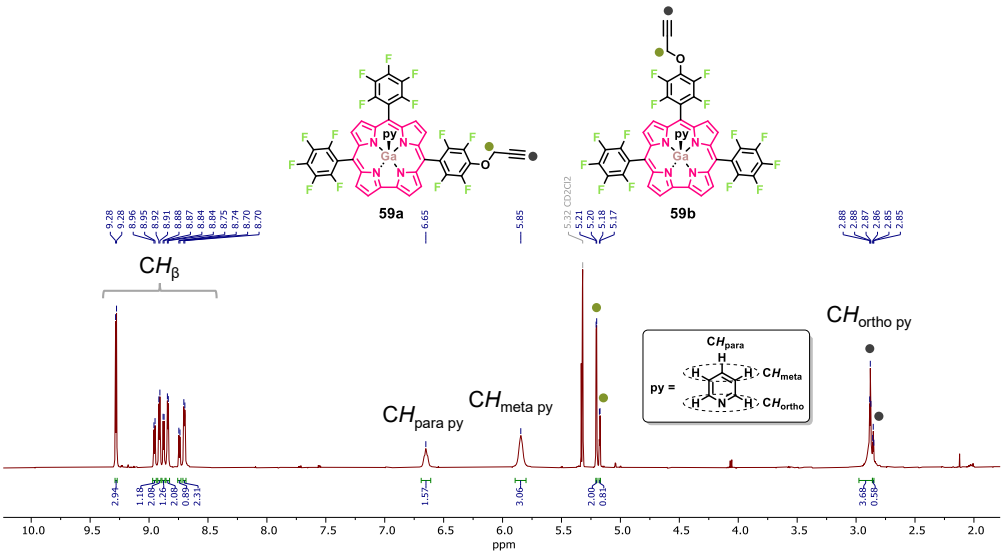

Figure 2.22. ^{1}H NMR spectrum of compound **59** (CD_2Cl_2, 500 MHz).

$^{19}F\{^{1}H\}$ NMR shows the molecule's asymmetry, confirming the incorporation of propargyl alcohol into them (Figure 2.23b). This is evidenced by the splitting of the signals due to the presence of the two isomers. Their assignment was carried out using $^{19}F\{^{1}H\}$-$^{19}F\{^{1}H\}$ COSY experiments (Figure 2.23a).

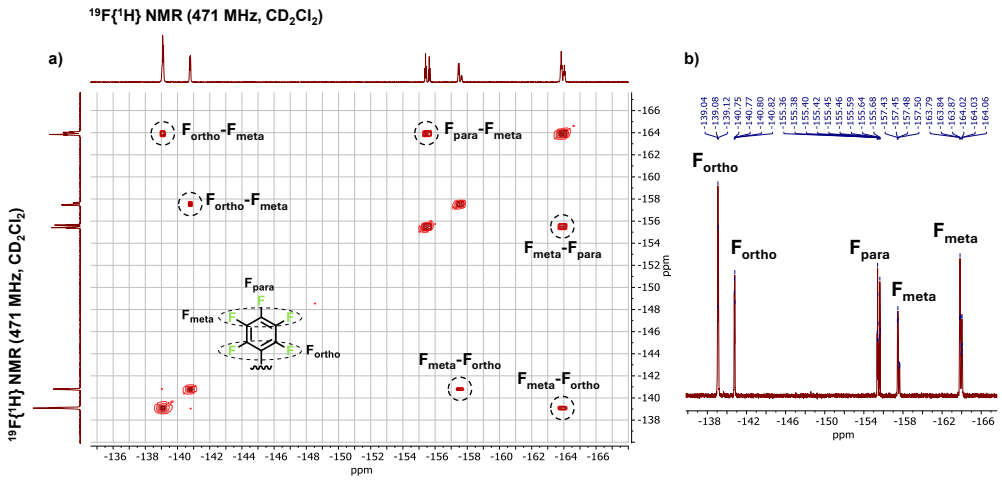

Figure 2.23. a) $^{19}F\{^{1}H\}$-$^{19}F\{^{1}H\}$ COSY NMR and b) $^{19}F\{^{1}H\}$ NMR spectra of compound **59** (CD_2Cl_2, 471 MHz).

The FT-IR shows a stretching band at 3306 cm^{-1} corresponding to the alkynes and 1491 cm^{-1} corresponding to the C=N from the pyrrol rings (Appendix 2, Figure AP2.3a) while MALDI-ToF experiments showed the expecting mass with the loss of the pyridine ligand.

2.3.2.2. Synthesis of glycofullerenes

The synthesis of the glycofullerene of interest for the functionalization of corroles was carried out with the methodology described in *Chapter 1*. To do this, and with compound **9** as the asymmetric hexakis-adduct, a click reaction was carried out using 2-azidoethyl β-D-glucopyranoside (**61**) as the carbohydrate (Scheme 2.6). The crude was treated with QuadraSil® Mercaptopropyl to remove any copper residues and compound **62** was isolated by precipitation in methanol with high yield. The bromine atom was then replaced in a S_N2 by azide using NaN_3 and DMSO-d_6 as solvent under microwave irradiation. The crude product was purified by SEC on Sephadex G-25 (H_2O/CH_3OH 9:1), and the glucose-decorated compound **63** was obtained in high yield.

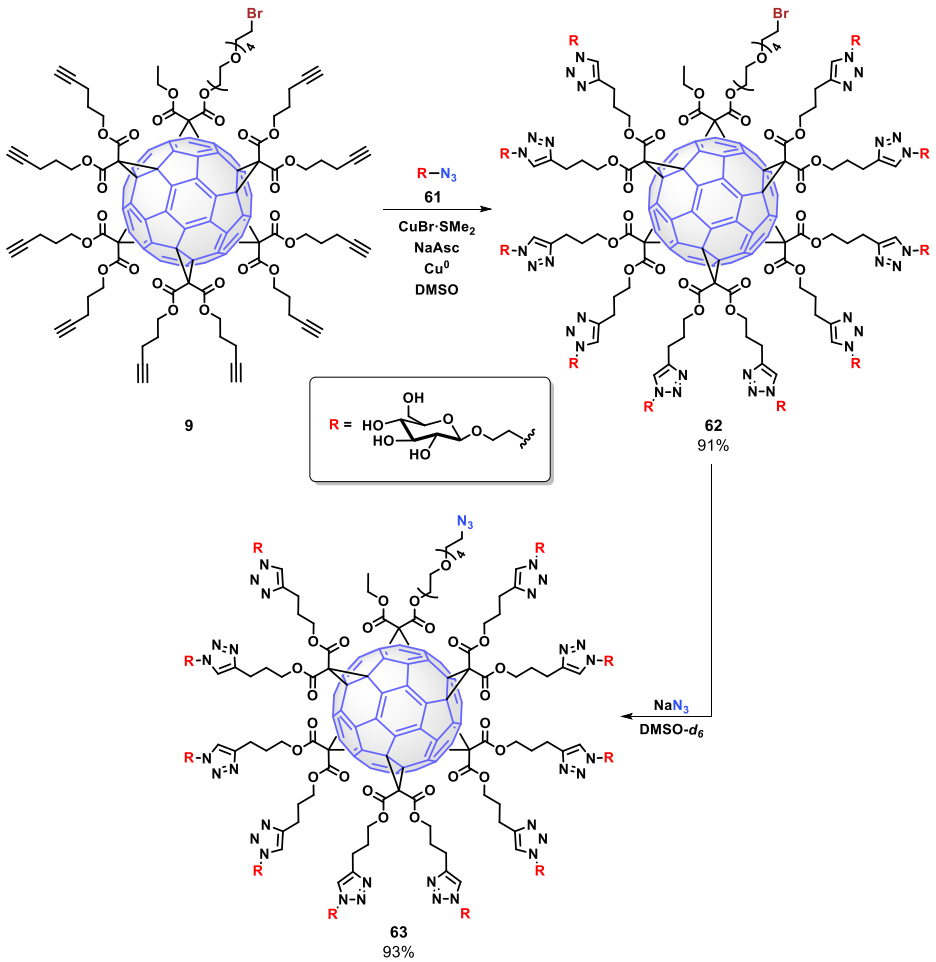

Scheme 2.6. General procedure for the synthesis of compound **63**.

The characterization of compound **63** was carried out using NMR and FT-IR.

The ^{1}H NMR spectrum serves to confirm the appearance of a new signal at ~8 ppm corresponding to the C*H* from newly formed triazole rings, indicating the good overcome of the reaction (Figure 2.24a). The most relevant NMR information was revealed by ^{13}C NMR where the appearance of triazole ring signals at ~146 ppm and ~123 ppm can be observed (Figure 2.24b). The two sp^2 carbon signals of the fullerene can also be identified at ~145 and ~141 ppm and the anomeric carbon of the glucose appears at ~103 ppm. At ~50 ppm, the *C*H$_2$-N signal from the carbohydrate chain can also be observed as well as the *C*H$_2$-N$_3$ formed during de S$_N$2. Other characteristic resonances are quaternary carbons of the malonates at ~46 ppm, the carbons of the alkyl chain identified at ~28 ppm and ~21 ppm and the methyl group at ~14 ppm.

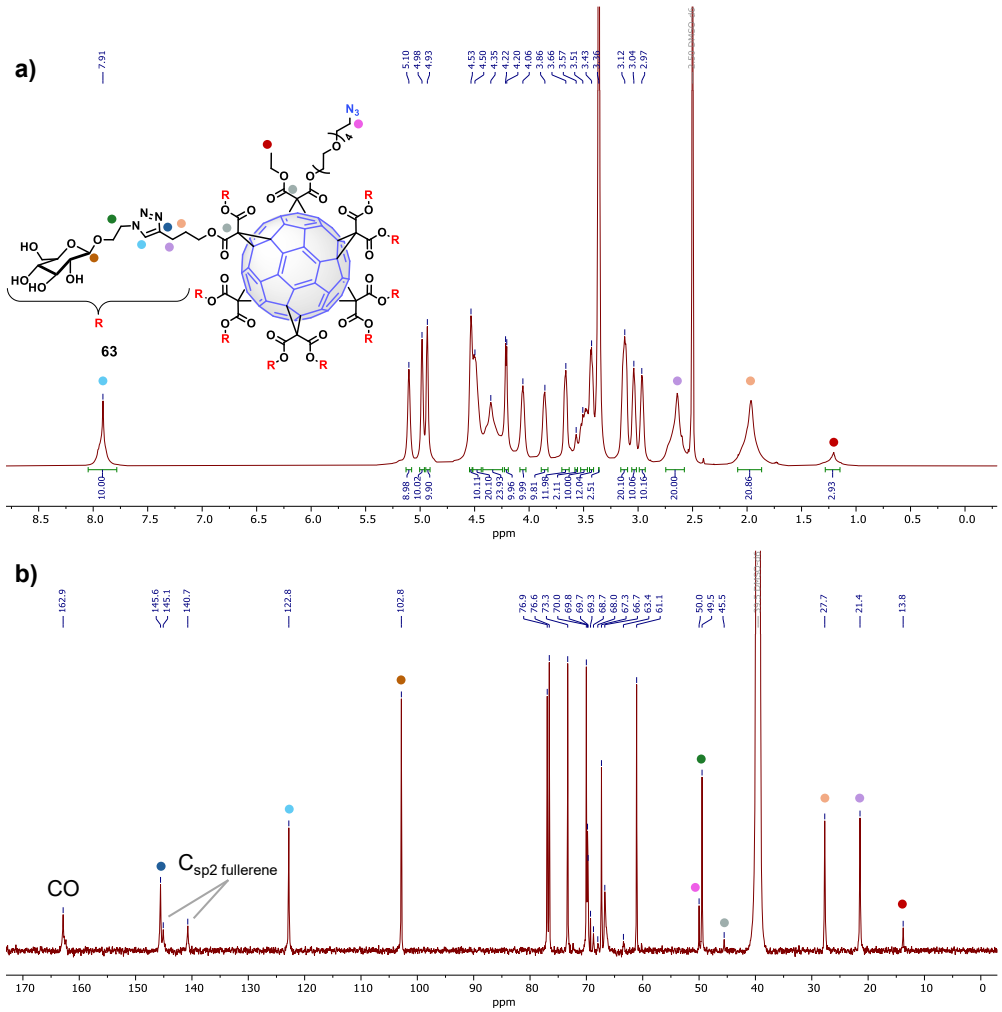

Figure 2.24. a) ^{1}H NMR (DMSO-d_6, 700 MHz) and b) ^{13}C NMR (DMSO-d_6, 176 MHz) spectra of compound **63**.

FT-IR experiments show the characteristic azide band at 2108 cm^{-1} which indicates the presence of the azide group in the molecule after the S_N2 reaction (Appendix 2, Figure AP2.4a).

2.3.2.3. Synthesis of glycocorroles

As explained in *Chapter 1*, cancer cells commonly exhibit elevated glucose uptake compared to healthy cells. The synthesized glycofullerenes contain glucose in their structure, so they shall pass through the cells' GLUT channels. By anchoring them to the previously synthesized corroles, known for their ability to generate ROS, a dual-function system was obtained to selectively target and destroy cancer cells. To investigate the effect of glycosylation density, two glycocorroles bearing different numbers of carbohydrate moieties were synthesized.

The strategy to obtain the desired molecules consists of a click reaction between the terminal azide group of glycofullerene **63** and the alkynes of the corroles **59** and **60** (Scheme 2.7). In this way, the monosubstituted (**64**) and trisubstituted (**65**) glycocorroles were synthesized in high yield.

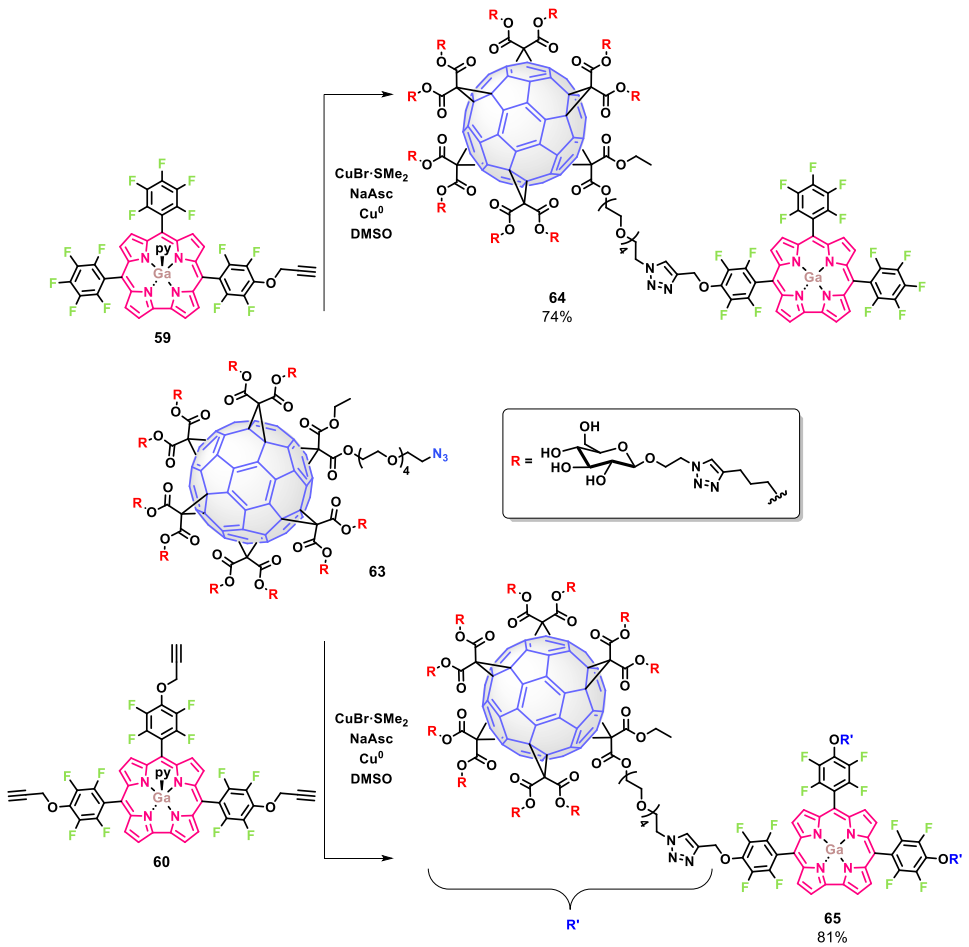

Scheme 2.7. General procedure for the synthesis of compounds **64** and **65**.

The products were purified by SEC with Sephadex G-50 (H_2O/CH_3OH 9:1), and violet solids completely soluble in aqueous medium were isolated.

The synthesized glycocorroles were characterized by NMR and FT-IR. For a better understanding, the characterization of compound **65** will be detailed.

The incorporation of the corrole moiety into the molecule was confirmed by both ^{1}H NMR and $^{19}F\{^{1}H\}$ NMR. In the ^{1}H NMR spectrum (Figure 2.25a) new signals appear in the aromatic region corresponding to the *β*-pyrrolic protons of the corrole. Additionally, a new signal at ~8.50 ppm, integrating for three protons, is attributed to the three triazole rings formed during the click reaction between the corrole and the glycofullerene. Furthermore, a resonance corresponding to the C*H*$_2$ coming from the propargyl group previously introduced in the corrole can be observed at ~5.66 ppm. The presence of the pyridine ligand cannot be confirmed because none of its signals are observed in the spectrum and due to its lability, its loss is assumed when carrying out the reaction. The $^{19}F\{^{1}H\}$ NMR spectrum (Figure 2.25b) further supports the presence of the corrole unit, displaying two signals that correspond to the ortho and meta fluorine atoms on the corrole's aromatic rings.

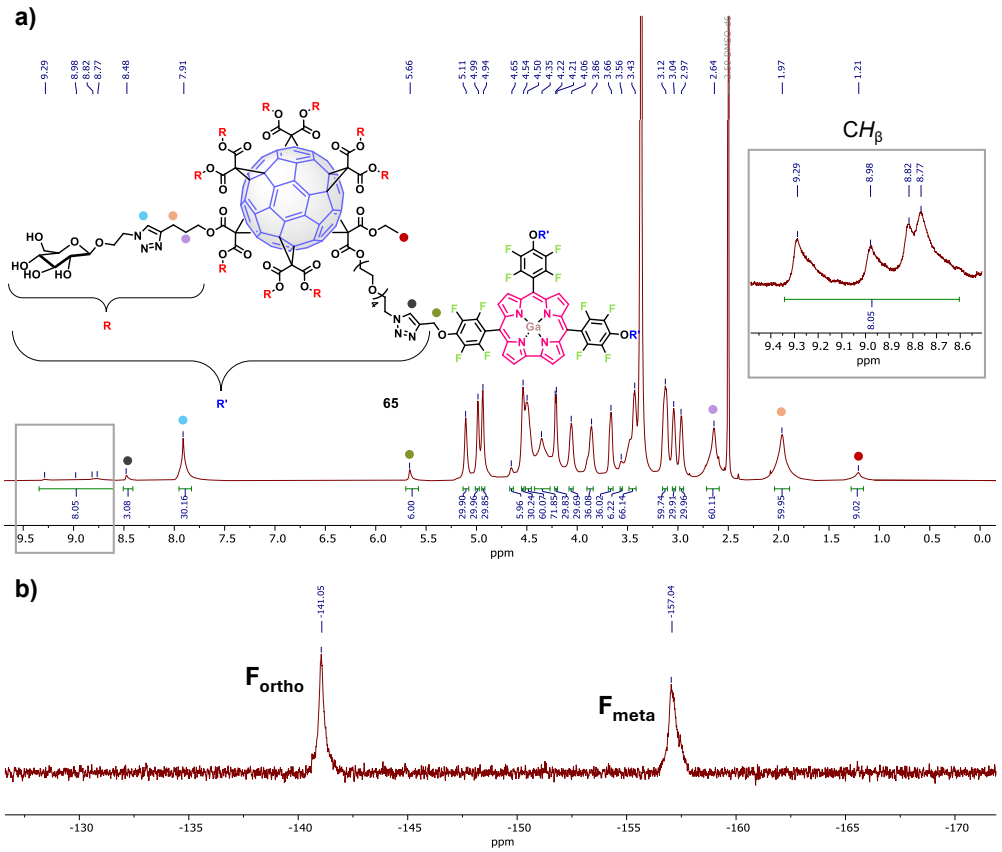

Figure 2.25. a) ^{1}H NMR (DMSO-d_6, 700 MHz) and b) $^{19}F\{^{1}H\}$ NMR (DMSO-d_6, 471 MHz) spectra of compound **65**.

^{13}C NMR spectrum confirms the good outcome of the reaction evidenced by the emergence of a signal at ~126 ppm corresponding to the newly formed triazole rings (Figure 2.26). Although the resonances from the corrole core are challenging to assign, two new peaks at ~142 and ~137 ppm can be attributed to it. Additionally, the disappearance of the CH_2-N_3 signal at ~50 ppm supports the proper functionalization of the glycofullerene. All other signals remain consistent with those of the starting glycofullerene, indicating that the rest of the structure remains unaltered.

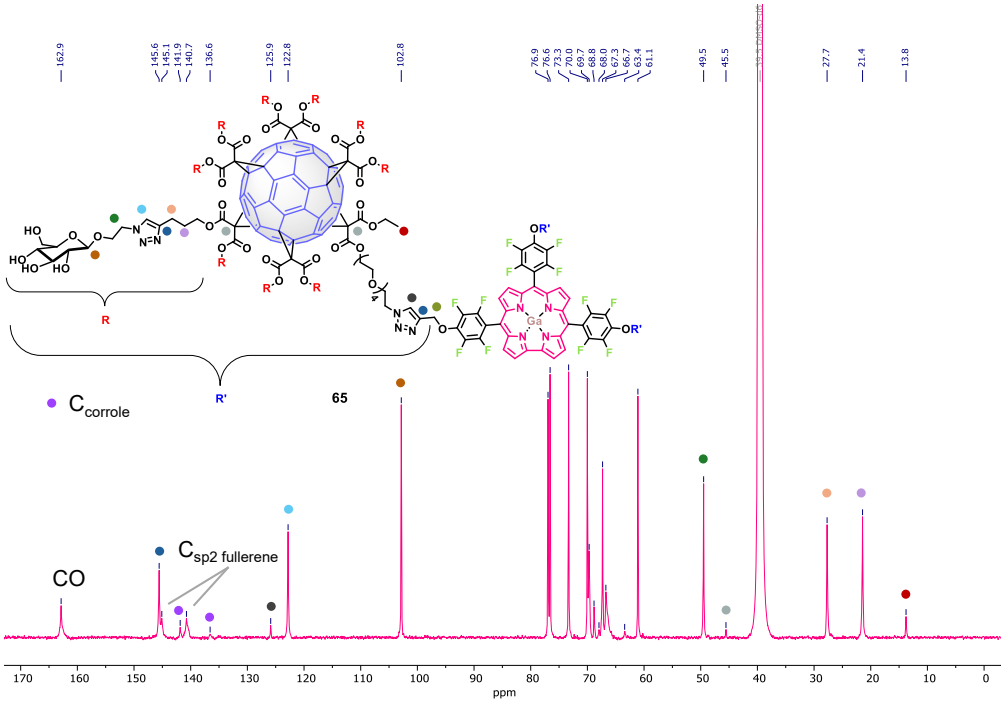

Figure 2.26. ^{13}C NMR spectrum of compound **65** (DMSO-d_6, 176 MHz).

FT-IR again confirms the disappearance of the azido group after the click reaction due to the disappearance of the band at 2108 cm^{-1} (Appendix 2, Figure AP2.4b).

Additionally, the hydrodynamic radii and diameter of the molecules were calculated using DOSY (data summarized in Table 2.3) and DLS.

Both techniques reveal an increase in molecular size that correlates with the number of glycofullerene units incorporated into the structure (Appendix 2, Figure AP2.6 and Figures AP2.10-AP2.11). The monosubstituted glycocorrole (**64**) exhibits an approximate diameter of 7 nm, whereas the trisubstituted counterpart (**65**) reaches about 8 nm. When compared to the symmetrical glycofullerene (**18**), the size increase is evident, reflecting the higher degree of functionalization.

Table 2.3. Diffusion coefficients determined by 2D-DOSY (700 MHz, ~2 mg·mL^{-1} in D_2O) and hydrodynamic radii.

Compound	Molecular Weight (g/mol)	Diffusion coefficient (D, $m^2 \cdot s^{-1}$)	Hydrodynamic radii (R_H, Å)
18	5116.77	$2.14 \cdot 10^{-10}$	11.4
64	5658.70	$6.30 \cdot 10^{-11}$	38.9
65	15249.75	$5.82 \cdot 10^{-11}$	42.1

2.3.2.4. Photophysical properties

The photophysical characterization of the glycofullerene-corrole conjugates **64** and **65** was performed in water, DMF and DMSO at room temperature and the spectra of their precursors **59** and **60** were evaluated in DMSO and DMF (data summarized in Table 2.4 and Appendix 2, Figure AP2.13 and Figure AP2.14).

Table 2.4. Photophysical properties of glycofullerene-corrole conjugates **64** and **65** and their precursors **59** and **60**.

Comp.	Solvent	Soret (nm) (ε/10^3 M^{-1} cm^{-1})	Q-bands (nm) (ε/10^3 M^{-1} cm^{-1})	λ_{em}^{max} (nm)	Φ_F (%)[a]	Φ_Δ (%)[b]
59	DMF	423 (228.7)	574 (17.7) 598 (24.6)	605 660	8.9	60
	DMSO	425 (219.9)	575 (17.7) 599 (20.1)	608 665	7.8	-
60	DMF	424 (231.5)	574 (17.6) 600 (23.9)	608 663	9.9	65
	DMSO	427 (231.7)	576 (18.7) 603 (22.8)	612 666	8.7	-
64	DMF	424 (212.6)	575 (15.6) 599 (20.3)	609 661	2.3	61
	DMSO	426 (207.2)	576 (16.6) 601 (19.9)	610 668	1.6	-
	Water	423 (114.0)	574 (8.2) 595 (12.2)	606 657	-	-
65	DMF	425 (215.3)	576 (17.1) 602 (25.4)	611 666	1.2	30
	DMSO	427 (244.5)	577 (20.3) 604 (26.5)	612 666	1.4	-
	Water	425 (222.1)	576 (22.9) 598 (29.0)	606 660	-	-

[a]Fluorescence quantum yields (Φ_F) were measured by the reference method using a cresyl violet perchlorate solution in methanol (Φ_F = 0.54) as reference.
[b]Singlet oxygen quantum yields (Φ_Δ) were determined with TPP in DMF (Φ_Δ = 0.65) as reference.

To facilitate comparison, the UV-Vis spectra in DMSO were analyzed for all referenced compounds, as no significant spectral differences were observed among the solvents used. All compounds display the characteristic corrole absorption profile, featuring a prominent Soret band around ~425 nm and several weaker Q-bands between 570-600 nm (Figure 2.27a). For conjugates **64** and **65**, the absorption spectra are primarily dominated by the corrole unit, with no substantial shifts observed upon conjugation with the glycofullerene, indicating minimal electronic interaction

between the two moieties in the ground state. Below 350 nm, a broad absorption band attributed to the glycofullerene becomes evident, extending into the ultraviolet region.

The parent corroles **59** and **60**, as well as their glycofullerene-conjugated derivatives **64** and **65**, exhibit fluorescence emission peaks at ~610 nm and ~660 nm, which are characteristic of the corrole core (Figure 2.27b). The glycofullerene units do not contribute to the emission spectra of the conjugates. This confirms that the fluorescence properties are primarily governed by the corrole moiety.

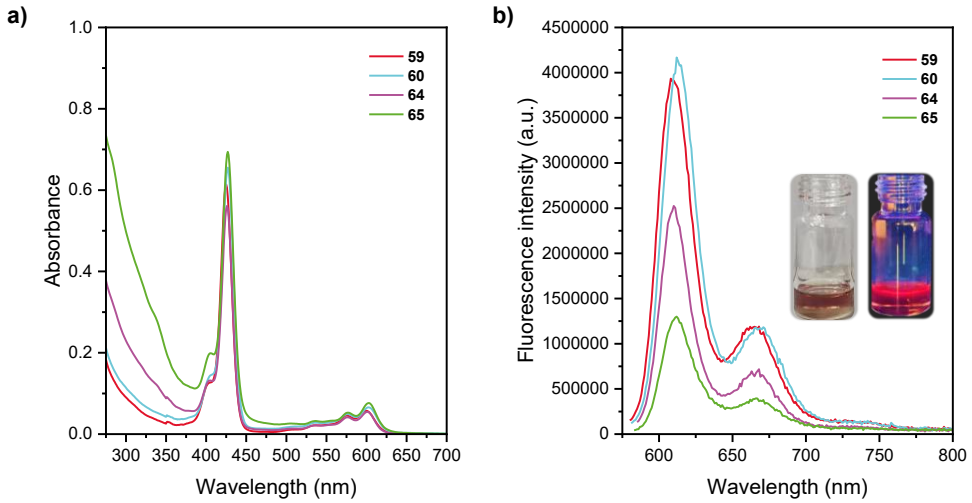

Figure 2.27. a) Absorption spectra of **59**, **60**, **64** and **65** (DMSO, $5 \cdot 10^{-6}$ M) and b) emission spectra of **59**, **60**, **64** and **65** (DMSO, $5 \cdot 10^{-6}$ M, λ_{exc} = 575 nm); inset picture of compound **64** in DMSO in the presence (right) or absence (left) of 365 nm UV-light irradiation.

The singlet oxygen quantum yield (Φ_Δ) in DMF remains high for conjugate **64**, which contains a single glycofullerene unit, showing values comparable to the parent corrole **59**, near ~60%. However, conjugate **65**, where three glycofullerene units are attached to the central corrole, exhibits a Φ_Δ value reduced by about half of that observed for the starting corrole **60**. This decrease may result from the high local concentration of glycofullerenes surrounding the corrole core. While fullerenes are known to generate ROS under irradiation, they can also act as radical scavengers in the ground state.[161] An alternative explanation is that the simultaneous attachment of three glycofullerenes may interfere with the heavy atom effect provided by Ga(III). As a relatively heavy atom, Ga(III) promotes intersystem crossing to the triplet state, from

[161] a) C. N. McEwen, R. G. McKay, B. S. Larsen, *J. Am. Chem. Soc.* **1992**, *114*, 4412. b) C.-W. Lee, Y.-H. Su, Y.-C. Chiang, I.-T. Lee, S.-Y. Li, H.-C. Lee, L.-F. Hsu, Y.-L. Yan, H.-Y. Li, M.-C. Chen, K.-T. Peng, C.-H. Lai, *Biomolecules* **2020**, *10*, 514. c) M. R. Hamblin, *Photochem. Photobiol. Sci.* **2018**, *17*, 1515.

which singlet oxygen is produced.[162] A disruption in this effect could explain the reduced Φ_{Δ}.

In terms of fluorescence quantum yield (Φ_F), the starting corroles **59** and **60** exhibit significantly higher values compared to their glycofullerene conjugates, likely due to quenching effects introduced by the fullerene units, also observed in the fluorescence intensity. Additionally, Φ_F could not be determined in water, as the very low emission of compounds **64** and **65** in this solvent prevented accurate measurement. The impact of this reduced fluorescence on confocal microscopy results will be discussed in the following section.

2.3.2.5. Biological studies

The potential of conjugates **64** and **65** as photosensitizers was evaluated using HeLa cells. Cytotoxicity was first assessed under dark conditions across a concentration range from 0 to 20 μM (Figure 2.28a). Under these conditions, compound **64** exhibited no cytotoxic effects even at concentrations above 10 μM. In contrast, compound **65** showed noticeable cytotoxicity at 20 μM, prompting the use of 10 μM as the working concentration for all subsequent phototoxicity assays.

Phototoxicity was evaluated across a concentration range below 10 μM under blue light irradiation (420 nm) at energy doses of 1, 5 and 10 J/cm^2 for 100, 500 and 1000 seconds of exposure (Appendix 2, Figure AP2.15). Except for compound **65**, all tested compounds exhibited a clear and dose-dependent reduction in cell viability, even at the lowest concentrations (Figure 2.28b). The weak phototoxic effect observed for compound **65** is consistent with its lower singlet oxygen quantum yield. Among all tested molecules, corroles **59** and **60**, along with glycocorrole **64**, demonstrated the most potent photosensitizing activity.

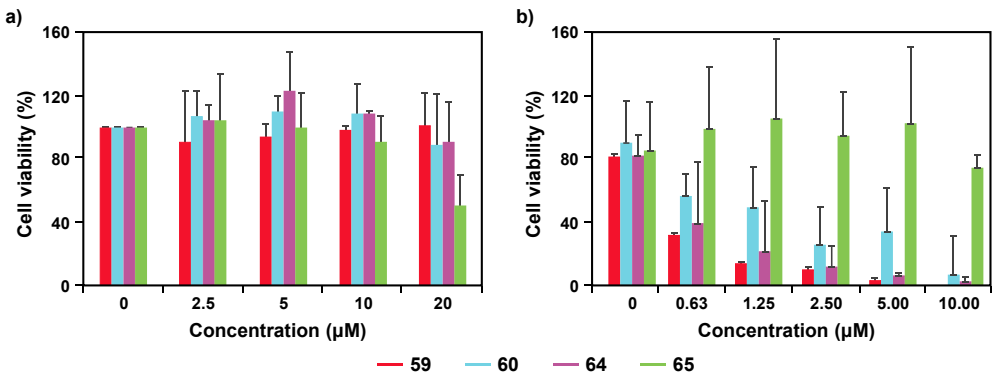

Figure 2.28. Viability of HeLa cells in the presence of compounds **59**, **60**, **64** and **65** at different concentrations: a) under non-irradiated conditions and b) after irradiation for 500 s with a fluence of 5 J/cm^2 and an irradiance of 10 mW/cm^2 at 420 nm.

[162] a) A. Mahammed, Z. Gross, *Coord. Chem. Rev.* **2019**, *379*, 121. b) H. Saigusa, T. Azumi, M. Sumitani, K. Yoshihara, *J. Chem. Phys.* **1980**, *72*, 1713.

The cellular uptake and distribution of the compounds were examined in HeLa cells using confocal and multiphoton fluorescence microscopy (Figure 2.29). The images clearly show intracellular fluorescence from corroles **59** and **60**, as well as from conjugate **64**, all predominantly localized in the cytoplasmic compartment. The absence of overlap between the red fluorescence of the compounds and the blue nuclear stain indicates that none of these compounds accumulate in the cell nucleus. The average intracellular fluorescence intensity of corrole **59** and its corresponding glycofullerene conjugate **64** was found to be comparable. In contrast, the emission from corrole **60** was lower, and that of conjugate **65** was barely distinguishable from the autofluorescence observed in the control cells. Given that conjugate **64** has a lower fluorescence quantum yield than corrole **59**, the observation of similar fluorescence intensity inside cells suggests that **64** is taken up more efficiently by the cells than the parent corrole. This indicates that the incorporation of a single glucose-functionalized glycofullerene into the structure not only preserves photosensitizing efficiency and enhances its water solubility but also improves the cellular delivery, making compound **64** a promising candidate for photodynamic therapy applications where glycofullerene acts as targeting moiety for glucose-avid cancer cells.

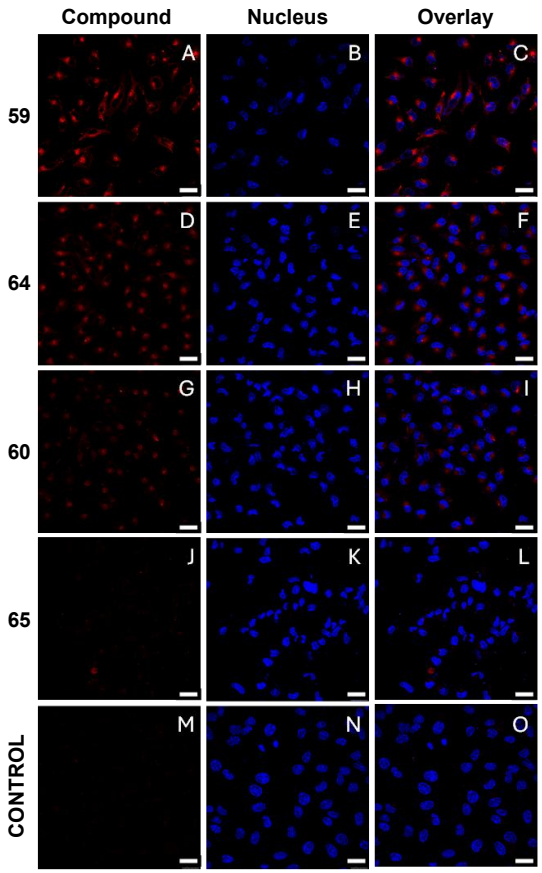

Figure 2.29. Fluorescence images of HeLa cells incubated overnight with 10 μM of each compound (**59**, **60**, **64** and **65**). Scale bars: 25 μm.

2.4. Conclusions

Glycofullerenes inherently lack fluorescence, limiting the ability to track their cellular interaction and internalization. To address this limitation, *Chapter 2* focused on the synthesis of fluorescent glycofullerenes by incorporating porphyrinoid scaffolds. These not only confer fluorescence emission, but also introduce the capacity of ROS generation, expanding their potential application to include anticancer therapy.

To achieve this, a series of asymmetric mannose-functionalized glycofullerenes were designed for recognition by DC-SIGN receptor. The asymmetric branch of each glycofullerene included three distinct malonates: two bearing PEG chains of varying lengths and one containing an alkyl chain. These glycofullerenes were conjugated to either a tetra- or octa-substituted porphyrin, enabling investigation of multivalency effects on biological activity. Photophysical characterization revealed that all derivatives are fluorescent, making them suitable as fluorescent probes. ROS generation studies showed no singlet oxygen production; however, the compounds efficiently generated superoxide anions, a type of ROS that is especially relevant under low-oxygen conditions. This finding supports their promise as photosensitizers in PDT, particularly for hypoxic tumors.

Two derivatives, **52b** and **53b**, were selected for further biological evaluation. Both were found to be non-cytotoxic and demonstrated potent SARS-CoV-2 trans-infection inhibition *via* DC-SIGN blocking, achieving 90% inhibition with **52b** and 61% with **53b**. The interaction of compound **52b** with DC-SIGN was further explored using confocal fluorescence microscopy, where localization at both the cell surface and interior was observed. Additionally, ^{1}H-^{15}N HSQC NMR experiments confirmed that **52b** binds at the canonical carbohydrate-recognition site, a result that was also supported by molecular dynamics simulations.

By modifying the carbohydrate moiety to include glucose, a new glycofullerene has been synthesized with the potential for enhanced selectivity to cancer cells. This glycofullerene was conjugated to two different corrole derivatives, one monosubstituted and the other trisubstituted with terminal alkyne groups. Photophysical studies confirmed that both conjugates are fluorescent, although the fluorescence intensity decreases as more glycofullerene units are incorporated into the structure. Importantly, both compounds were found to be capable of generating singlet oxygen, identifying them as promising candidates for PDT.

Biological evaluations revealed that these glycofullerene-containing corrole hybrids are non-cytotoxic in the dark, yet exhibit significant phototoxicity upon irradiation. Notably, conjugate **64** demonstrated potent activity at concentrations below 1 μM. Confocal microscopy also confirmed the internalization of the conjugates into cancer cells. Finally, it is worth noting that despite compound **64** having a lower fluorescence quantum yield than its precursor **59**, the comparable intracellular fluorescence signal suggests that **64** is internalized more efficiently, revealing the importance of the

glucose-functionalized glycofullerene for the cellular uptake of the compound, enhancing its potential utility in cancer-targeted phototherapy.

Chapter 3

3. CHAPTER 3

3.1. Background

3.1.1. Polycyclic aromatic hydrocarbons

One of the most significant carbon allotropes is graphene, a single layer of sp^2-hybridized carbon atoms arranged in a honeycomb lattice of benzene rings. Discovered in 2004 by K. Novoselov and A. Geim, their pioneering work on this two-dimensional material awarded them the Nobel Prize in Physics in 2010.[17] Graphene exhibits a zero bandgap between its conduction and valence bands, classifying it as a semimetal with extraordinary properties, including exceptionally high charge-carrier mobility. However, its lack of a bandgap poses limitations for use in semiconductors and optoelectronic devices, and strategies such as doping or chemical functionalization are used to tailor its properties.[163] Today, graphene finds application across a wide spectrum of fields, including electronics, energy storage and biomedicine, among others.[164]

In this context, nanoscale graphene derivatives exhibit electronic quantum confinement, enabling the formation of discrete energy levels between the conduction and valence bands, thereby producing semiconductors with exceptional optical properties. These derivatives fall under the broad category of polycyclic aromatic hydrocarbons (PAHs), graphene fragments composed of two or more fused aromatic rings, ranging from simple structures like naphthalene to larger, complex systems made entirely of sp^2-hybridized carbon and hydrogen atoms (Figure 3.1).

A notable subgroup within PAHs are nanographenes, which have attracted significant attention in the scientific community due to their tunable optoelectronic properties. These properties can be precisely modulated through traditional organic synthesis, making nanographenes highly adaptable for a wide range of targeted applications.[165]

---

[163] a) J. M. Englert, C. Dotzer, G. Yang, M. Schmid, C. Papp, J. M. Gottfried, H.-P. Steinrück, E. Spiecker, F. Hauke, A. Hirsch, *Nat. Chem.* **2011**, *3*, 279. b) A. Criado, M. Melchionna, S. Marchesan, M. Prato, *Angew. Chem. Int. Ed.* 2**015**, *54*, 10734. c) V. Georgakilas, J. N. Tiwari, K. C. Kemp, J. A. Perman, A. B. Bourlinos, K. S. Kim, R. Zboril, *Chem. Rev.* **2016**, *116*, 5464. d) L. Rodríguez-Pérez, M. Á. Herranz, N. Martín, *Chem. Commun.* **2013**, *49,* 3721. e) K. Dirian, M. Á. Herranz, G. Katsukis, J. Malig, L. Rodríguez-Pérez, C. Romero-Nieto, V. Strauss, N. Martín, D. M. Guldi, *Chem. Sci.* **2013**, *4*, 4335. f) G. Bottari, M. Á. Herranz, L. Wibmer, M. Volland, L. Rodríguez-Pérez, D. M. Guldi, A. Hirsch, N. Martín, F. D'Souza, T. Torres, *Chem. Soc. Rev.* **2017**, *46*, 4464.

[164] a) J. Wu, H. Lin, D. J. Moss, K. P. Loh, B. Jia, *Nat. Rev. Chem.* **2023**, *7*, 162. b) F. Bonaccorso, L. Colombo, G. Yu, M. Stoller, V. Tozzini, A. C. Ferrari, R. S. Ruoff, V. Pellegrini, *Science* **2015**, *347*, 1246501. c) J. Li, H. Zeng, Z. Zeng, Y. Zeng, T. Xie, *ACS Biomater. Sci. Eng*. **2021**, *7*, 5363.

[165] a) P. Izquierdo-García, J. M. Fernández-García, N. Martin, *J. Am. Chem. Soc*. **2024**, *146*, 32222. b) N. Martín, C. Nuckolls, Eds. *Molecular Nanographenes: Synthesis, Properties, and Applications*, 1st ed. Wiley-VCH GmbH, Weinheim, **2025**.

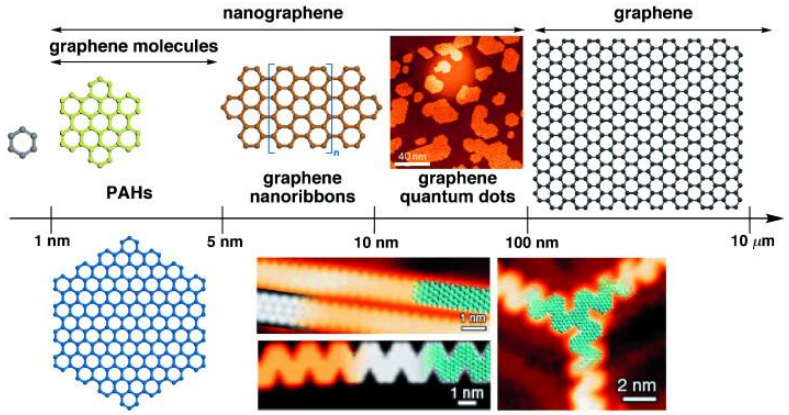

Figure 3.1. Different sizes and shapes: from benzene to graphene (adapted from reference 166).

However, the use of these materials in biomedical applications remains a largely unexplored frontier, as challenges like their limited solubility in aqueous media continue to hinder their full potential.

3.1.2. Main features of molecular nanographenes

Molecular nanographenes are monodisperse graphene fragments with sizes ranging from 1 to 100 nm.[166] Over the past decade, there has been a surge of interest in these structures with the synthesis of increasingly sophisticated architectures with remarkable optoelectronic properties.[167]

Hexa-*peri*-hexabenzocoronene (HBC) was described for the first time by Halleux in 1958, and was considered the largest fully characterized polyaromatic hydrocarbon for many years (Figure 3.2a).[168] A notable milestone came in 2002 when Müllen *et al.* reported one of the largest nanographene structures to date comprising 222 carbon atoms (Figure 3.2b).[169] This breakthrough demonstrated the significant potential of organic chemistry to produce large graphene-derived molecules.

[166] L. Chen, Y. Hernández, X. Feng, K. Müllen, *Angew. Chem. Int. Ed.* **2012**, *51*, 7640.
[167] Z. Liu, S. Fu, X. Liu, A. Narita, P. Samori, M. Bonn, H. I. Wang, *Adv. Sci*. **2022**, *9*, 2106055.
[168] A. Halleux, R. H. Martin, G. S. D. King, *Helv. Chim. Acta* **1958**, *41*, 1177.
[169] C. D. Simpson, J. D. Brand, A. J. Berresheim, L. Przybilla, H. J. Räder, K. Müllen, *Chem. Eur. J.* **2002**, *8*, 1424.

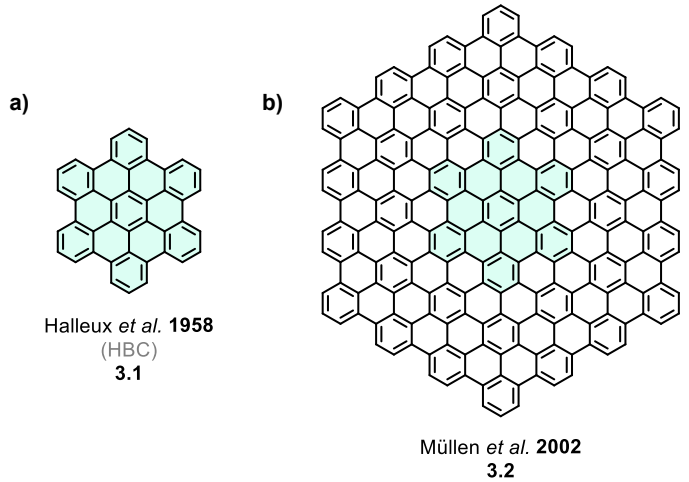

Figure 3.2. a) Hexa-*peri*-hexabenzocoronene and b) nanographene composed of 222 carbon atoms.

Bottom-up synthesis of nanographenes enables the production of monodisperse molecular graphene fragments. The general approach involves synthesizing polyarene-like structures followed by the formation of multiple carbon-carbon bonds, leading to graphitization of the system. Polyarene-like structures are obtained through π-extension from simpler precursors. One of the reactions that stands out for the formation of polyarenes is the Diels-Alder cycloaddition.[170]

Diels-Alder cycloaddition in these systems is based on the reaction between aromatic alkynes (**3.3**) as dienophiles and tetraphenylcyclopentadienones (**3.4**) as dienes, yielding hexaarylbenzenes (**3.5**), as represented in Scheme 3.1. The [4+2] cycloaddition results in the formation of a new benzene ring decorated with six functionalized aryl groups. The reaction proceeds with the extrusion of carbon monoxide *via* chelotropic elimination after the formation of the six-membered ring, leading to the aromatization of the central benzene core.

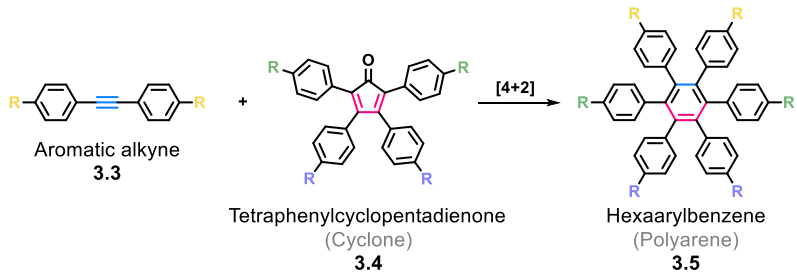

Scheme 3.1. Diels-Alder cycloaddition for the synthesis of polyarenes.

[170] S. Ito, M. Wehmeier, J. D. Brand, C. Kübel, R. Epsch, J. P. Rabe, K. Müllen, *Chem. Eur. J.* **2000**, *6*, 4327.

The most widely used graphitization reaction for molecular nanographenes is the Scholl oxidation, first described by Roland Scholl in 1910.[171,172] This reaction involves cyclodehydrogenation through double aryl C-H activation, resulting in the formation of multiple C-C covalent bonds.[173] Typically, the oxidation is carried out using Lewis acids such as $FeCl_3$ or $AlCl_3$, or with oxidizing agents such as DDQ or *para*-chloranil in the presence of Brønsted acids.

However, controlling the Scholl reaction can be challenging due to potential issues such as rearrangements, unexpected cyclizations or undesired functionalization that may arise under oxidation conditions.

Wu *et al.* reported that applying different Scholl reaction conditions to the same polyarene (**3.6**) can lead to distinct mechanisms and yield different products (Scheme 3.2).[174] Specifically, when the reaction was conducted using $FeCl_3$, the graphitization process resulted in the formation of six six-membered rings (**3.7**). In contrast, using DDQ as the reagent led to the formation of two eight-membered rings (**3.8**).

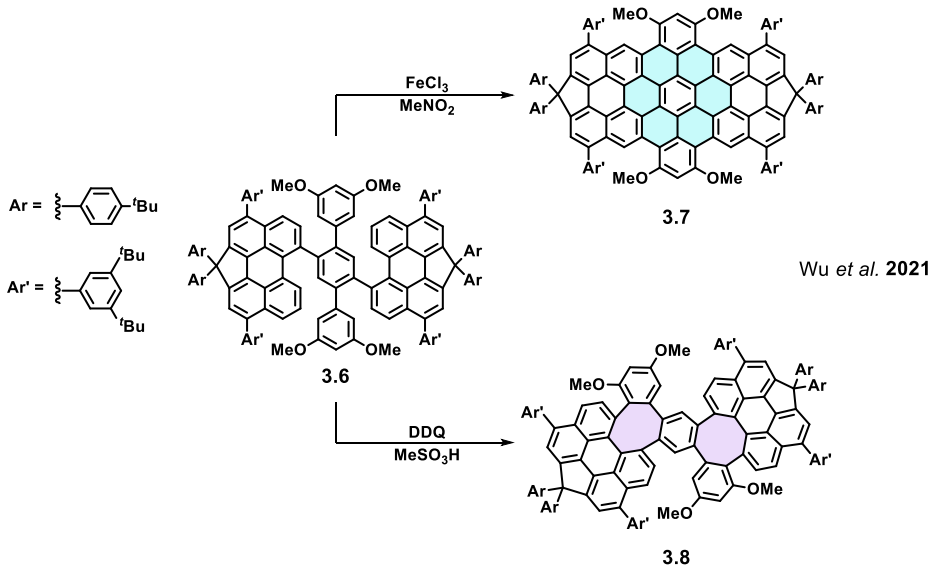

Scheme 3.2. Example of the formation of different rings depending on the reaction conditions.

Mastalerz *et al.* reported the cyclization of a pentacene-based structure (Scheme 3.3).[175] When the Scholl reaction was carried out in the presence of $FeCl_3$, it resulted

[171] a) R. Scholl, J. Mansfeld, *Ber. Dtsch. Chem. Ges*. **1910**, *43*, 1734. b) R. Scholl, C. Seer, *Justus Liebigs Ann. Chem*. **1912**, *394*, 111.
[172] R. S. Jassas, E. U. Mughal, A. Sadiq, R. I. Alsantali, M. M. Al-Rooqi, N. Naeem, Z. Moussa, S. A. Ahmed, *RSC Adv*. **2021**, *11*, 32158.
[173] a) M. Grzybowski, K. Skonieczny, H. Butenschön, D. T. Gryko, *Angew. Chem. Int. Ed*. **2013**, *52*, 9900. b) M. Grzybowski, B. Sadowski, H. Butenschön, D. T. Gryko, *Angew. Chem. Int. Ed*. **2020**, *59*, 2998.
[174] Y. Zou, Y. Han, S. Wu, X. Hou, C. H. E. Chow, J. Wu, *Angew. Chem. Int. Ed.* **2021**, *60*, 17654.
[175] X. Yang, M. Hoffmann, F. Rominger, T. Kirschbaum, A. Dreuw, M. Mastalerz, *Angew. Chem. Int. Ed.* **2019**, *58*, 10650.

in the formation of two new five-membered rings (**3.10**). However, performing the same reaction with DDQ and triflic acid not only led to the formation of the two five-membered rings but also resulted in the incorporation of two triflate groups into the structure (**3.11**).

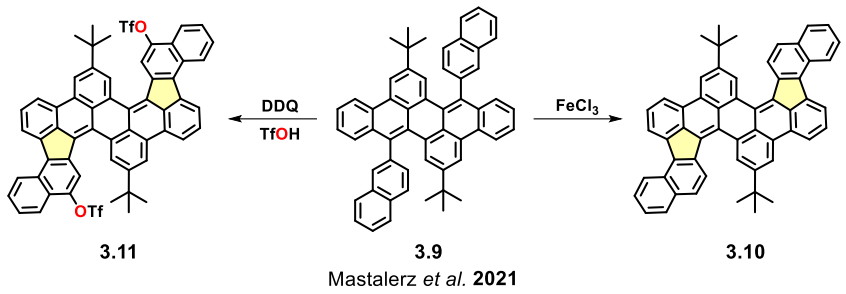

Scheme 3.3. Example of incorporation of heteroatoms in the structure.

As an example of rearrangements, Sugiura *et al.* reported an unexpected ketone in the synthesis of tetrabenzo[a,d,j,m]coronene (**3.14**) formed by the rearrangement reaction of one phenyl group (**3.13**), without observing the graphitization of the system (Scheme 3.4).[176]

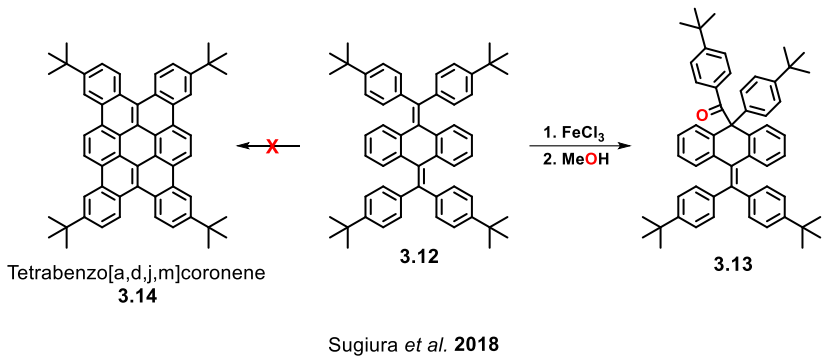

Scheme 3.4. Example of rearrangements in Scholl reaction.

In a recent example, our group demonstrated that the Scholl reaction is also controlled by the electronic effects on the starting substrate (Scheme 3.5).[177] Thus, anthracene-based polyphenylenes lead to spiro nanographenes under Scholl conditions (**3.18**). In contrast, an electron-deficient anthracene substrate affords a helically arranged molecular nanographene formed by two orthogonal dibenzo[fg,ij]phenanthro-[9,10,1,2,3-pqrst]pentaphene (DBPP) moieties linked through an octafluoroanthracene core (**3.17**).

[176] F. Ko, K. Hirabayashi, T. Shimizu, K.-I. Sugiura, *Tetrahedron* **2018**, *59*, 4251.
[177] P. Izquierdo-García, J. M. Fernández-García, J. Perles, I. Fernández, N. Martín, *Angew. Chem. Int. Ed.* **2023**, *61*, e202215655.

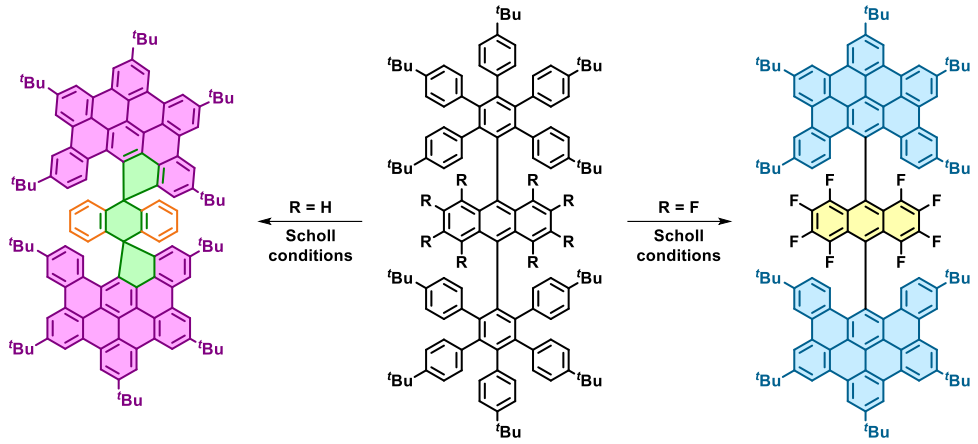

Scheme 3.5. Scholl oxidation of **3.15** and **3.16** leads to the formation of spironanographene *syn* **3.18** or helical nanographene **3.17** depending on the electronic features of the starting polyphenylene.

3.1.3. Nanographenes for biomedical applications

The biological applications of nanographenes are limited by their tendency to aggregate and their poor water solubility. To overcome these challenges, structural modifications can be introduced, namely adding lateral substituents or inducing twists or curvature to reduce aggregation. Despite these issues, nanographenes exhibit strong light absorption and efficient reactive oxygen species production, making them highly promising candidates for developing new photosensitizers for PDT.

There are relatively few reports in the literature focusing on the synthesis of water-soluble nanographenes for biological applications. Herein, we highlight some significant recent examples.

In 2018, Itami *et al.* reported the synthesis of a warped nanographene by incorporating five- and seven-membered rings into the structure (**3.19**), creating a flexible conformation that reduces aggregation (Figure 3.3).[178] To enhance solubility, the molecule was functionalized at the periphery with tetraethylene glycol (TEG) chains, enabling dissolution in a wide range of solvents, including non-polar, polar aprotic and polar protic solvents such as water. The resulting nanographene exhibited green-yellow fluorescence, demonstrated good photostability and showed low cytotoxicity. Experiments with HeLa cells confirmed cellular internalization, and the compound was capable of inducing cell death upon light irradiation.

[178] H.-A. Lin, Y. Sato, Y. Segawa, T. Nishihara, N. Sugimoto, L. T. Scott, T. Higashiyama, K. Itami, *Angew. Chem. Int. Ed.* **2018**, *57*, 2874.

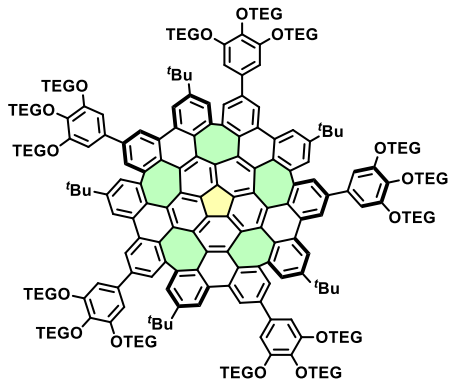

Itami *et al.* **2018**
3.19

Figure 3.3. Warped nanographene with tetraethylene glycol chains.

Building on the C_{222} nanographene synthesized by Müllen, Tan *et al.* developed a derivative featuring carboxylic acid groups at the periphery (**3.20**), which imparted aqueous solubility (Figure 3.4).[179] The molecule exhibited high ROS production and strong optical absorption in the near-infrared region. *In vitro* and *in vivo* studies of **3.20** demonstrated its excellent biocompatibility, photostability and remarkable photodynamic and photothermal properties. Notably, experiments conducted on HepG2 liver tumor-bearing mice showed an impressive 96% tumor regression following laser irradiation.

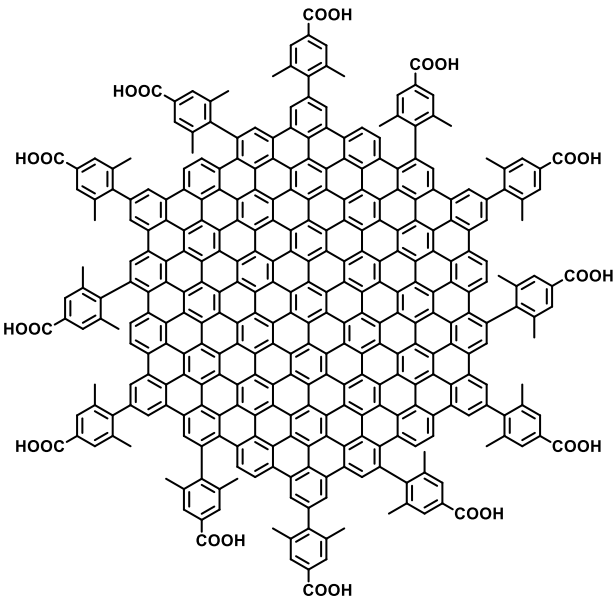

Tan *et al.* **2024**
3.20

Figure 3.4. Carboxylated nanographene based on C_{222}.

Charged nanographene structures can significantly enhance water solubility. In this context, An *et al.* reported a heteroatom-doped cationic nanographene (**3.21**) that

[179] X.-H. Ma, X. Gao, J.-Y. Chen, M. Cao, Q. Dai, Z.-K. Jia, Y.-B. Zhou, X.-J. Zhao, C. Chu, G. Liu, Y.-Z. Tan, *J. Am. Chem. Soc.* **2024**, *146*, 2411.

demonstrated excellent membrane permeability, biocompatibility and efficient ROS production (Figure 3.5).[180] This behavior was attributed to the formation of an electron-donor architecture, capable of inducing intersystem crossing (ISC) through charge recombination. The compound exhibited pronounced ROS generation, which was evaluated in HeLa cells. Upon irradiation with a 630 nm laser, the treated cells displayed 80% cell death, highlighting the molecule strong photosensitization potential for PDT.

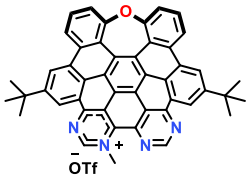

An *et al.* **2024**
3.21

Figure 3.5. Charged nanographene for anticancer applications.

These derivatives can be utilized not only for ROS production but also for applications that leverage their near-infrared (NIR) emission. For instance, Narita *et al.* investigated nanographene-based polymer nanoparticles as NIR-emissive neuronal tracers (Figure 3.6a).[181] These nanoparticles demonstrated high photostability and low cytotoxicity, making them suitable for real-time neuronal tracing with potential applications in neurobiology, particularly for mapping brain connectivity. Similarly, Shen *et al.* reported the use of a dication of hexapyrrolohexaazacoronene for NIR-II photothermal therapy (PTT) (Figure 3.7b).[182] The molecule was encapsulated in DSPE-mPEG5000, forming water-soluble nanoparticles that exhibited excellent photothermal stability, good biocompatibility, strong photoacoustic signals and outstanding PTT performance. In cancer cell assays, laser irradiation resulted in 80% cell damage, highlighting the therapeutic potential of these nanoparticles.

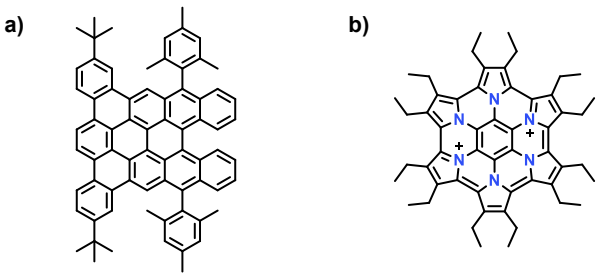

Narita *et al.* **2024**
3.22

Shen *et al.* **2024**
3.23

Figure 3.6. a) Nanographene for neuronal tracing and b) charged hexapyrrolohexaazacoronene for photothermal therapy.

[180] R. Li, B. Ma, M. Li, D. Wang, P. Liu, P. An, *Chem. Sci.* **2024**, *15*, 11408.
[181] H. Zhao, L. Guillaud, M. F. Emily, X. Xu, L. Moshniaha, H. Hanayama, R. Kabe, M. Terenzio, A. Narita, *ACS Nano* **2024**, *18*, 34730.
[182] C. Zhao, C. Qu, Y. Hu, F. Wu, S. Liu, F. Cai, Y. Chen, Y. Qiu, Z. Shen, *Adv. Healthcare Mater.* **2024**, *13*, 2402545.

Although the number of examples in literature is limited, these recent investigations clearly demonstrate the powerful potential of these molecules in biomedicine. The development of future nanographene-derived compounds could significantly impact therapeutic approaches.

3.2. Objectives

Given the promising potential of nanographenes in biomedical applications, particularly as generators of reactive oxygen species, the primary objective of this chapter is the synthesis of water-soluble hexa-*peri*-hexabenzocoronene (HBC) derivatives. To achieve this, an HBC derivative bearing a terminal alkyne group will be designed and subsequently conjugated to a glycofullerene *via* click chemistry. This strategy will lead to amphiphilic structures, with the glycofullerene acting as the hydrophilic domain and the HBC core as the hydrophobic segment.

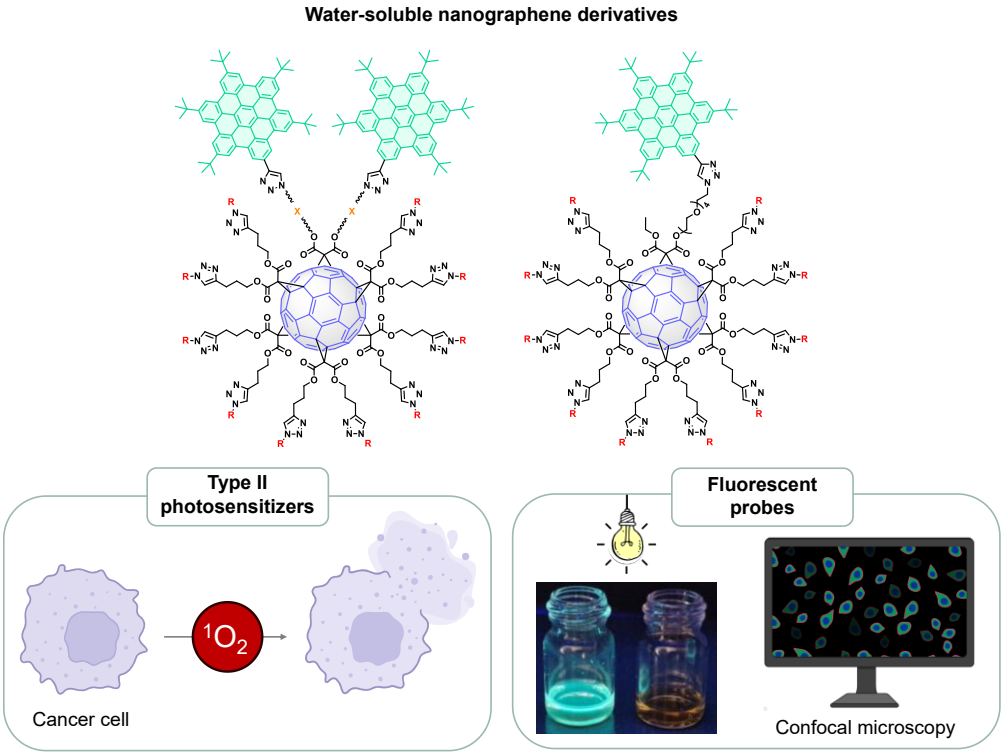

These hybrid molecules are expected to self-assemble into aggregates, which will be characterized using techniques such as DLS, TEM, AFM and SEM. Additionally, a full photophysical characterization will be conducted to evaluate their potential as fluorescent probes or photosensitizers for future anticancer therapies.

3.3. Results and discussion

3.3.1. Synthesis of a molecular nanographene

The synthetic strategy to obtain the target molecular nanographene starts with a Sonogashira cross-coupling reaction between 4-(*tert*-butyl)phenylacetylene (**66**) and 1,4-diiodobenzene (**67**), yielding compound **68** (Scheme 3.6). This was followed by a [4+2] Diels-Alder cycloaddition using cyclopentadienone **69** (previously synthesized in the laboratory[170,183]) as the diene, which extends the π-system and forms polyarene **70**.

The resulting polyarene undergoes graphitization *via* Scholl cyclodehydrogenation to afford compound **71**. To introduce a reactive triple bond suitable for subsequent CuAAC reactions, compound **71** is subjected to a second Sonogashira cross-coupling with trimethylsilylacetylene (**72**), giving intermediate **73**. Finally, TBAF-mediated deprotection of the terminal alkyne affords the desired nanographene **74**. This compound was synthesized using a previously reported methodology with minor modifications.[184]

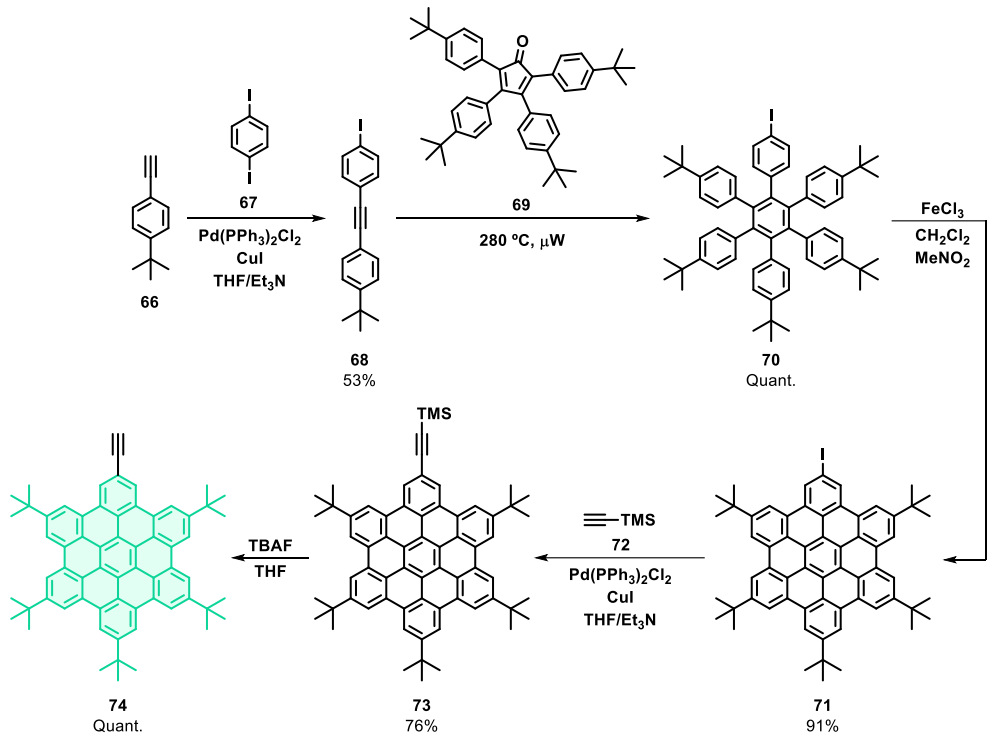

Scheme 3.6. General procedure for the synthesis of nanographene **74**.

[183] D. Lungerich, J. F. Hitzenberger, M. Marcia, F. Hampel, T. Drewello, N. Jux, *Angew. Chem. Int. Ed.* **2014**, *53*, 12231.
[184] F. A. Murphy, S. M. Draper, *J. Org. Chem.* **2010**, *75*, 1862.

The characterization of nanographene **74** was carried out by conventional techniques in organic chemistry such as NMR.

By comparing the ^{13}C NMR spectra of compounds **71**, **73** and **74**, the functionalization of the HBC core with an alkyne group and its subsequent deprotection can be clearly tracked. In Figure 3.7a, the *C*-I signal in compound **71** appears at ~94 ppm. Upon performing the Sonogashira cross-coupling reaction to obtain compound **73**, this signal disappears, and two new resonances emerge at ~108 ppm and ~95 ppm, corresponding to the alkyne carbons (Figure 3.7b). Additionally, a peak at ~0.7 ppm is observed, attributed to the methyl groups of the TMS.

After TMS deprotection, this methyl signal disappears, and the alkyne carbon signals shift to ~86 ppm and ~78 ppm, confirming the formation of the free terminal alkyne in compound **74** (Figure 3.7c).

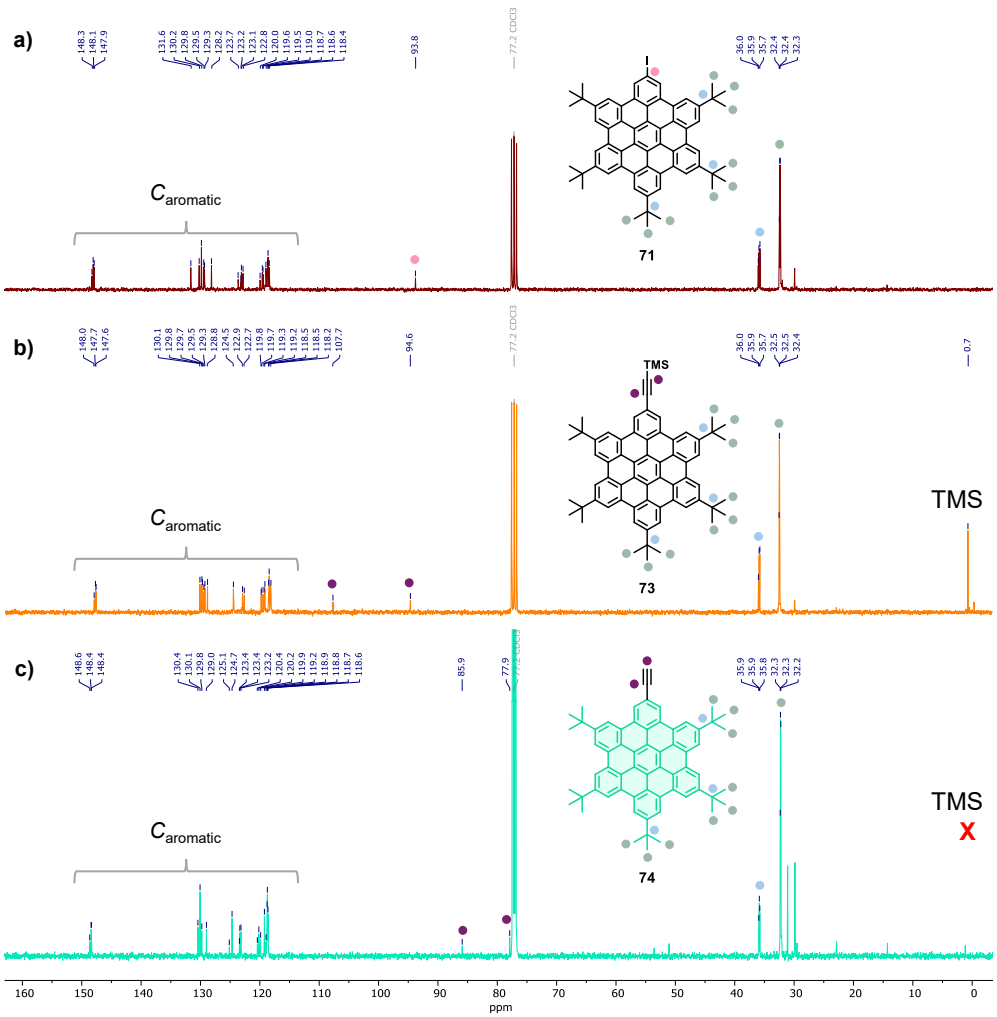

Figure 3.7. ^{13}C NMR spectra of: a) **71** ($CDCl_3$, 75 MHz), b) **73** ($CDCl_3$, 75 MHz) and c) **74** ($CDCl_3$, 126 MHz).

3.3.2. Synthesis of glycofullerenes

For the synthesis of the desired products, three different asymmetric glycofullerenes were designed. One of them contains one terminal bromine and corresponds to compound **63** previously synthesized in *Chapter 2*. The other two glycofullerenes contain two terminal bromines on the asymmetric branch, which enables the introduction of two HBC units *per* molecule.

As can be seen in Scheme 3.7, the synthesis of hexakis-adducts **77a-b** follows the aforementioned procedure. First, the synthesis of the symmetric malonates takes place by condensation between malonyl chloride (**3**) and the monobrominated alcohols **2** and **44**. Next, two consecutive Bingel-Hirsch cyclopropanations were performed, firstly anchoring one unit of malonates **75a-b** to C_{60}, followed by the functionalization with malonate **6** in the five remaining positions. Hexakis-adducts **77a-b** were obtained with good yields.

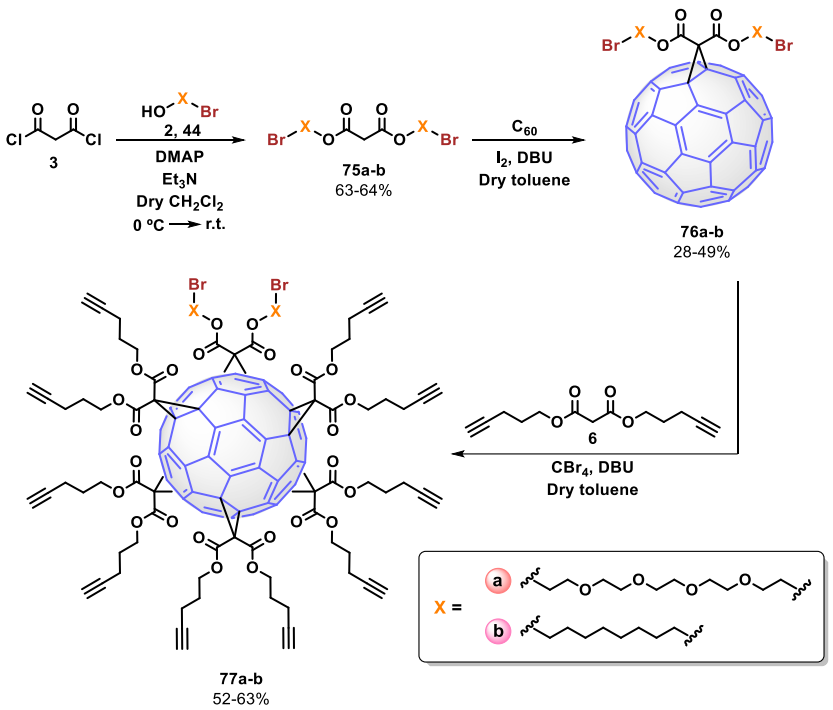

Scheme 3.7. General procedure for the synthesis of asymmetric hexakis-adducts **77a-b**.

The characterization of compounds **77a-b** was carried out with standard spectroscopy techniques used in organic chemistry such as NMR and FT-IR. For a better understanding, the characterization of compound **77a** will be explained as a representative example.

The ^{1}H NMR spectrum (Figure 3.8a) reveals a high degree of signal complexity, with most resonances appearing as multiplets, reflecting the extensive functionalization of the molecule. A multiplet centered at ~4.39 ppm corresponds to the OC*H*$_2$ groups

adjacent to the carbonyl moieties, while the region between 3.90 – 3.40 ppm displays signals attributed to the polyethylene glycol chains. In the aliphatic region (2.50 – 1.80 ppm), signals from the C*H*$_2$ groups of alkyl chains of the malonate units are observed as well as the terminal C*H* group from the alkynes.

The ^{13}C NMR spectrum (Figure 3.8b), supported by DEPT-135 and HSQC experiments, enabled the full structural assignment of the molecule. Two signals at ~164 ppm correspond to the carbonyl carbons of the two different malonates. The sp^2 carbons of the fullerene cage are observed at ~146 ppm and ~141 ppm, confirming the success of the reaction and the formation of the hexakis-adduct with the expected geometry.

Signals around ~83 ppm and ~78 ppm are attributed to the alkyne carbons of the malonates introduced in the second Bingel reaction, indicating their successful incorporation. The sp^3 carbon of the fullerene appears at ~69 ppm, while the O*C*H$_2$ groups adjacent to the carbonyls resonate at ~66 ppm. The quaternary carbons in alpha to carbonyl groups are observed at ~45 ppm and ~40 ppm, the *C*H$_2$-Br signal appears at ~30 ppm and the aliphatic *C*H$_2$ groups of the alkyl chains are located at ~17 ppm and ~15 ppm.

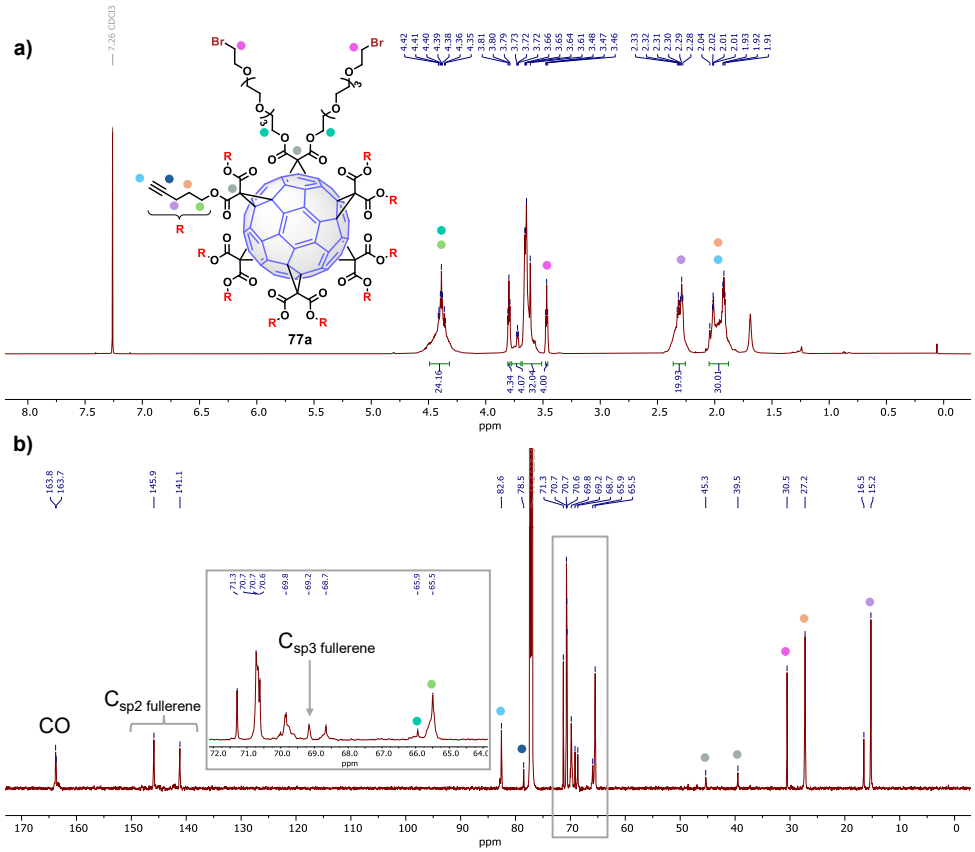

Figure 3.8. a) ^{1}H NMR ($CDCl_3$, 700 MHz) and b) ^{13}C NMR ($CDCl_3$, 176 MHz) spectra of **77a**.

The next step involves the functionalization of the terminal alkynes on hexakis-adducts **77a-b** using glucose derivative **61**, leading to the synthesis of glycofullerenes **78a-b**. This was followed by the substitution of the bromine atom with an azide group, yielding the final compounds **79a-b** (Scheme 3.8).

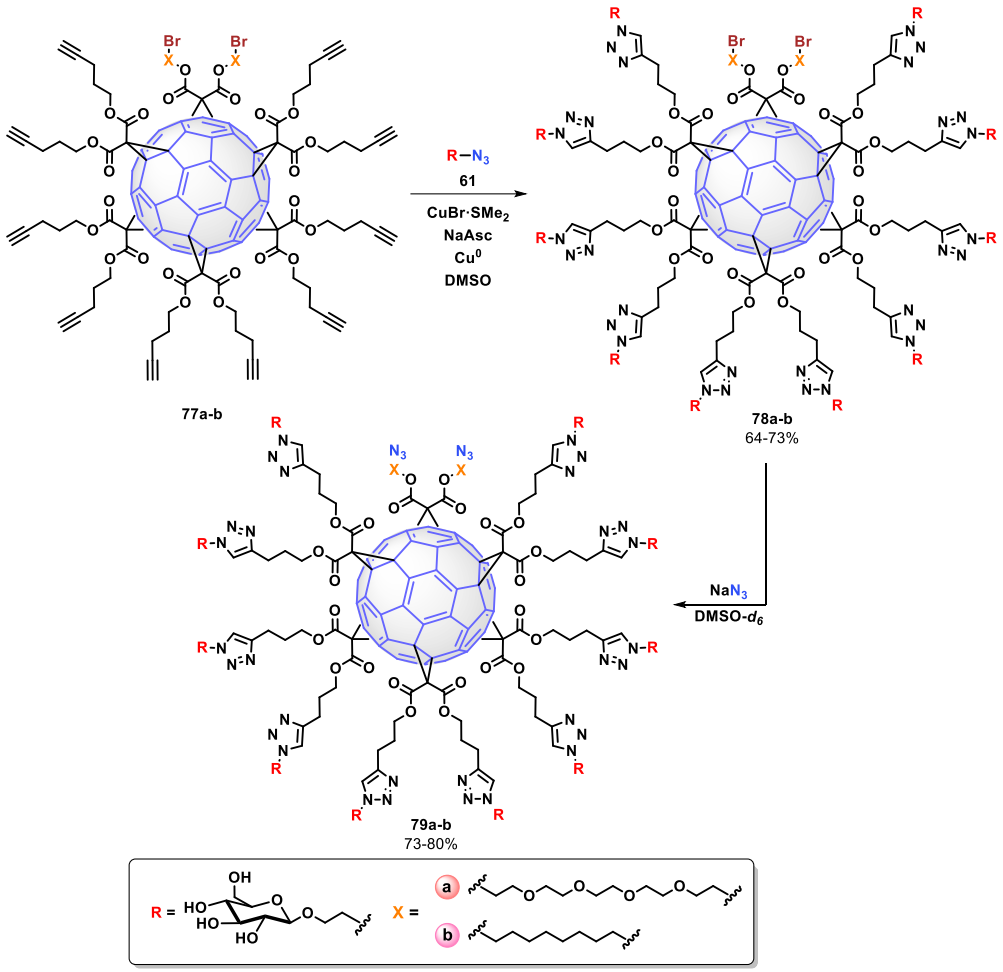

Scheme 3.8. General procedure for the synthesis of asymmetric glycofullerenes **79a-b**.

After the purification of compounds **79a-b** using SEC Sephadex G-25 and H_2O/CH_3OH 9:1 as the mobile phase, the characterization was checked by NMR and FT-IR.

With compound **78a** as an example, the ^{1}H NMR spectrum confirms the success of the click reaction through the appearance of a signal at ~8 ppm, corresponding to the triazole rings (Figure 3.9a). In the ^{13}C NMR spectrum, new signals emerge at approximately ~146 ppm and ~124 ppm, also attributed to the triazole carbons (Figure 3.9b). The two sp^2 carbons of the fullerene are observed at ~145 ppm and ~141 ppm, while the anomeric carbon of the glucose appears at ~103 ppm. Additional signals include the CH_2-N group from the carbohydrates at ~50 ppm and the alkyl chain

carbons at ~27 ppm and ~22 ppm. For the asymmetric malonate moiety, the characteristic *C*H_2-Br signal is present at ~32 ppm and the quaternary carbons of the malonates at ~45 ppm.

The subsequent bromine-to-azide substitution can be monitored by both ^{13}C NMR and FT-IR. In the ^{13}C NMR, the *C*H_2-Br signal at ~32 ppm disappears, while a new *C*H_2-N_3 signal emerges at ~50 ppm in compound **79a** (Figure 3.9c). In the FT-IR spectrum (Figure 3.9d), the incorporation of the azide group is evidenced by the appearance of a band at 2105 cm^{-1} corresponding to the N_3 stretching vibration.

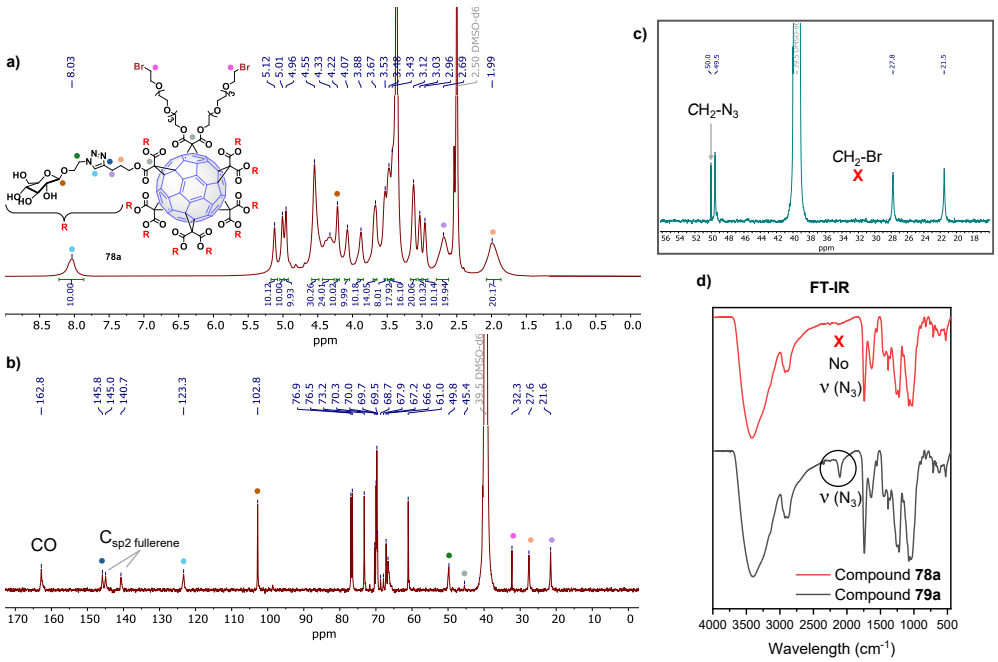

Figure 3.9. a) ^{1}H NMR spectrum (DMSO-d_6, 700 MHz) of **78a**, b) ^{13}C NMR spectrum (DMSO-d_6, 176 MHz) of **78a**, c) partial ^{13}C NMR spectrum (DMSO-d_6, 176 MHz) of **79a** and d) FT-IR spectrum of **78a** and **79a**.

3.3.3. Glycofullerene-HBC derivatives

To functionalize the alkyne group present in nanographene **74**, a click-type reaction was performed using glycofullerenes **79a-b** and glycofullerene **63** previously synthesized in *Chapter 2* (Scheme 3.9). Due to the poor solubility of compound **74** in polar solvents, the reaction could not be conducted in DMSO as in previous cases. Instead, a DMSO/CH_2Cl_2 mixture (1:3) was used, providing a medium in which both the nanographene and the glycofullerenes were readily soluble. In this way, the synthesis of three derivatives containing one or two HBCs in the structure was achieved.

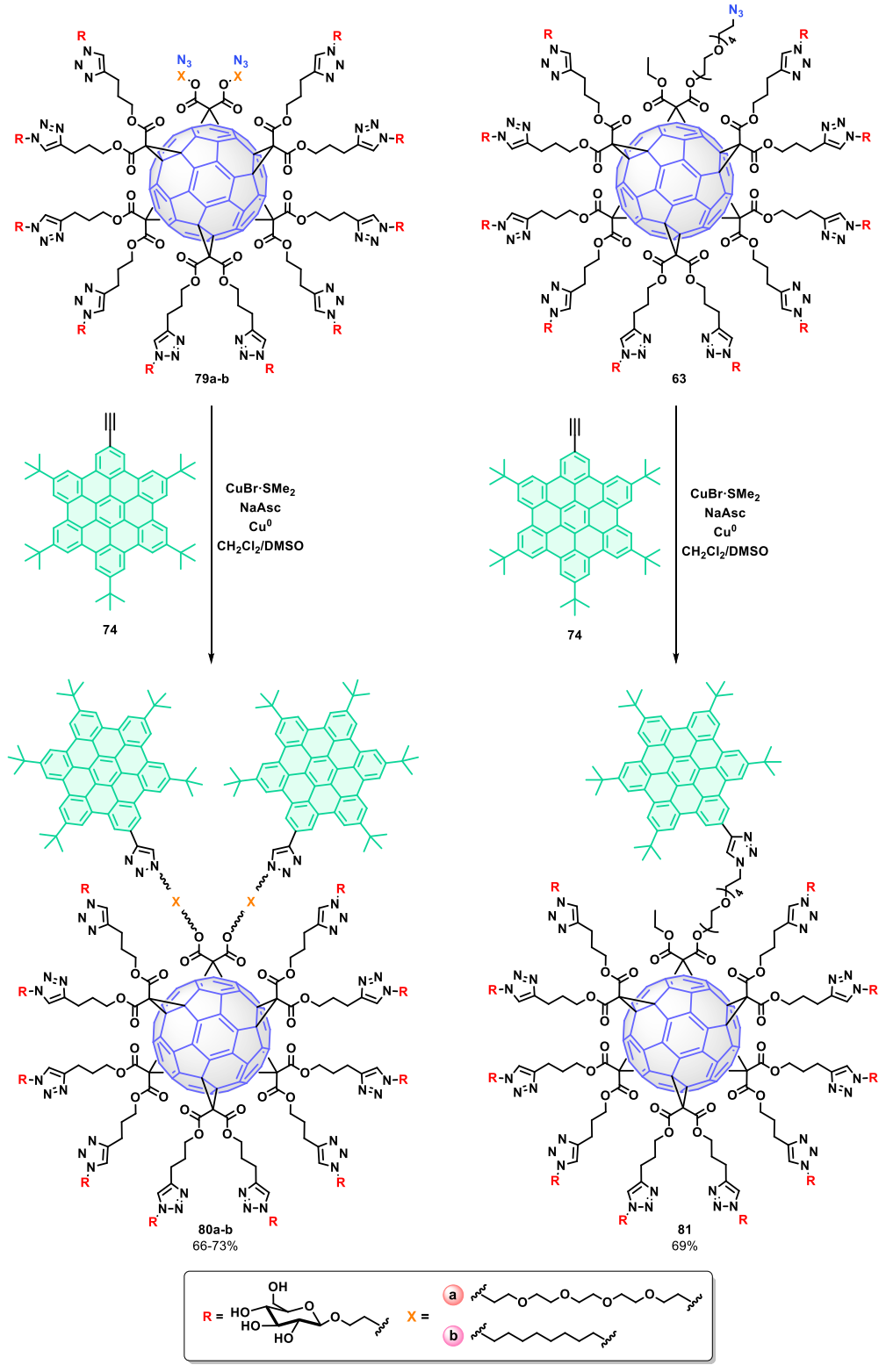

Scheme 3.9. General procedure for the synthesis of HBC derivatives **80a-b** and **81**.

Purification of compounds **80a-b** and **81** was carried out by SEC Sephadex G-50 using H_2O/CH_3OH 9:1 as mobile phase to obtain the desired products with moderate to high yields. These compounds exhibit a strong tendency to aggregate, which makes them insoluble in water when stored in the solid state. For instance, compound **80b** is entirely insoluble in H_2O after a first drying cycle. However, if it is first dissolved in DMSO followed by the addition of water and subsequent removal of DMSO, the compound becomes fully soluble in the aqueous medium.

The characterization of these nanostructures can be carried out using standard spectroscopic techniques such as NMR and FT-IR. Compound **81** will be used as a representative example.

The ^{1}H NMR shows a signal pattern typical of glycofullerenes, where the most distinctive signal is that of triazoles at ~8 ppm (Figure 3.10). Since it contains an HBC unit, a multiplet of signals can be distinguished in the aromatic region at ~10 – 8 ppm, corresponding to the aromatic C*H* of the structure. Furthermore, three signals that did not appear in the starting glycofullerene can be distinguished above ~1.8 ppm, corresponding to the *tert*-butyl groups of the HBC moiety.

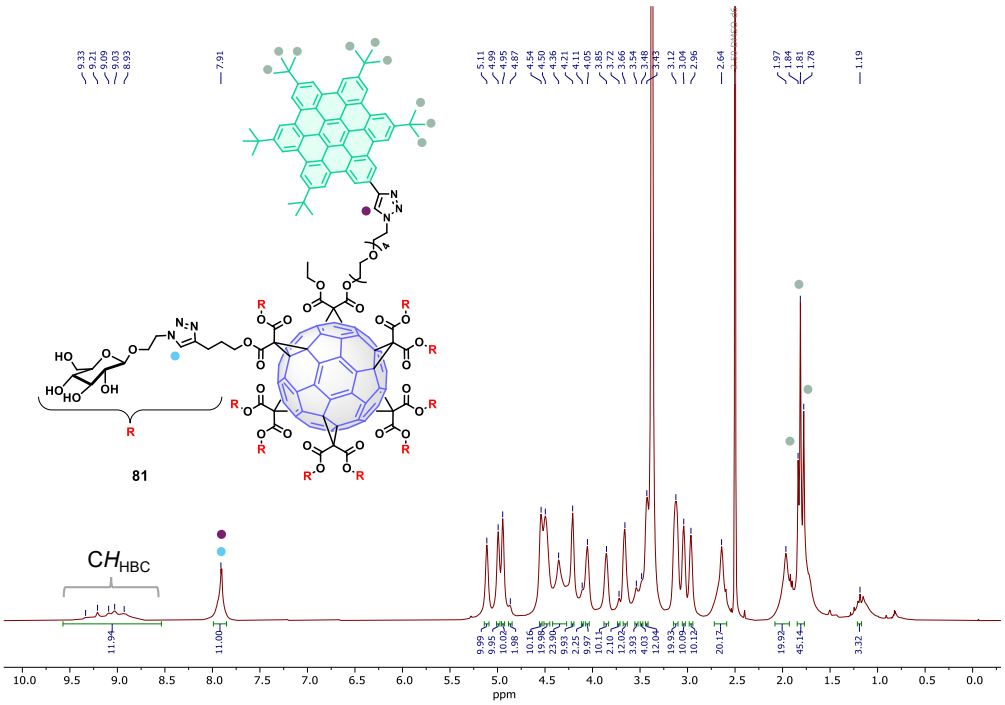

Figure 3.10. ^{1}H NMR spectrum (DMSO-d_6, 700 MHz) of compound **81**.

Moreover, ^{13}C NMR is the appropriate technique to corroborate the correct functionalization and purification of compound **81** (Figure 3.11). In the aromatic region, the appearance of new signals corresponding to the carbons of the HBC moiety can be seen, while in the aliphatic region, the signals corresponding to the *tert*-butyl groups can be distinguished at ~36 ppm and ~32 ppm. As for the fullerene, at ~146

and ~142 ppm, the signals of the sp^2 carbons are detected, as well as the triazoles at ~123 ppm. The rest of the signals remain unchanged compared to the spectrum of the starting glycofullerene **63**.

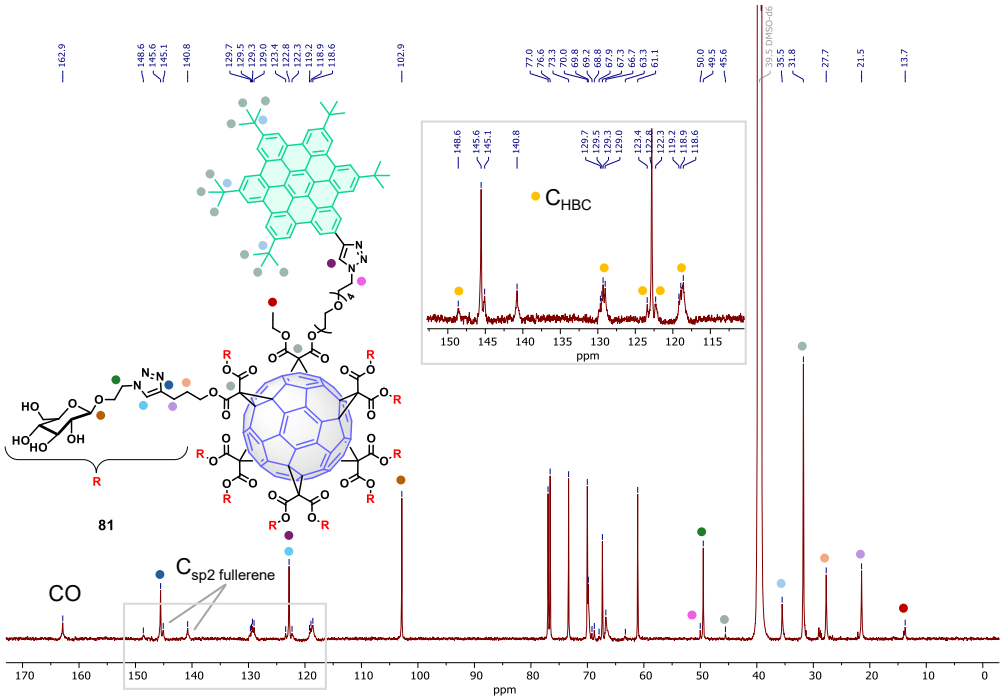

Figure 3.11. ^{13}C NMR spectrum (DMSO-d_6, 176 MHz) of compound **81**.

To further confirm the structure, HSQC NMR was used (Figure 3.12a). These experiments revealed that the signal at ~50 ppm corresponds to the CH_2-N group formed during the click reaction, rather than the CH_2-N_3 group, which would indicate the presence of unreacted glycofullerene. FT-IR also demonstrate the disappearance of the azide band at 2105 cm^{-1} due to the formation of the new triazole ring (Figure 3.12b).

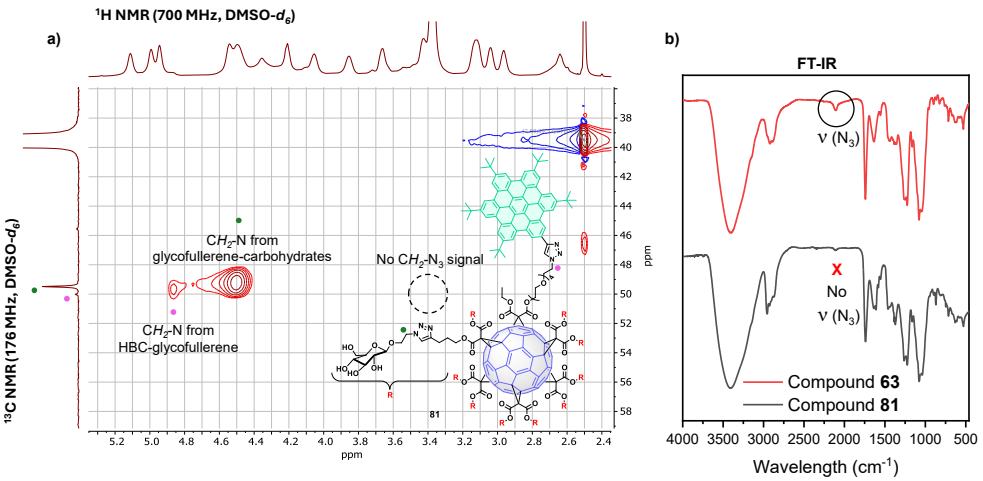

Figure 3.12. a) ^{1}H-^{13}C HSQC NMR spectrum (DMSO-d_6, 176 MHz) and b) FT-IR spectrum of compound **81**.

The hydrodynamic radius average for the final materials has been estimated by DLS measurements in water and DMSO (Figure 3.13). In the case of compound **80b**, since it is insoluble in H_2O, the measurement was carried out in a H_2O/DMSO 99:1 mixture. When measurements were performed in aqueous medium, an increase in hydrodynamic radii was observed (Figure 3.13a). This is attributed to an increased hydrophobic character due to the additional HBC unit. As a result, compound **81** exhibits a hydrodynamic radius of 6.5 nm, while compounds **80a** and **80b** show hydrodynamic radii of 10.1 nm and 15.7 nm, respectively.

In contrast, when the same measurements were conducted in DMSO the hydrodynamic radii decreased significantly to ~2 nm (Figure 3.13b). This behavior underscores the strong aggregation tendency of these molecules in aqueous environments, driven by their amphiphilic nature, with HBC moieties acting as the hydrophobic domains and the glycofullerene unit serving as the hydrophilic component.

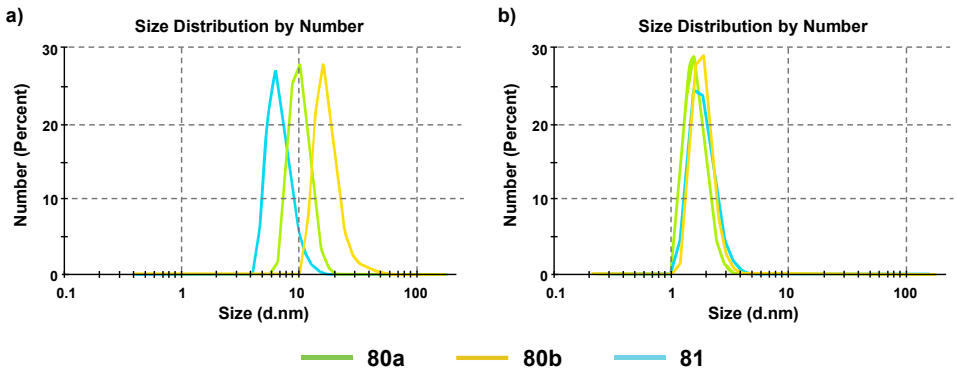

Figure 3.13. DLS measurements in number % of compounds **80a-b** and **81** in: a) H_2O ($1 \cdot 10^{-5}$ M) and b) DMSO ($1 \cdot 10^{-5}$ M).

Transmission electron microscopy (TEM), atomic force microscopy (AFM) and scanning electron microscopy (SEM) were employed to analyze the morphology and size distribution of **80a-b** and **81** (Appendix 3, Figure AP3.2).

TEM micrographs confirmed that compound **80a** exhibits quasi-spherical morphologies with an average particle size of approximately 5.1 ± 0.7 nm (Figure 3.14a). AFM analysis complemented these results by revealing vertical dimensions ranging from ~5 – 6 nm for **80a** (Figure 3.14d) and ~2 – 3 nm for **81** (Appendix 3, Figure AP3.2b). In the case of compound **80b**, height measurements could not be obtained by AFM, as the sample showed an almost complete absence of spherical particles and was predominantly composed of aggregates with a chain-like structure (Figure 3.14e). Compound **81** showed exclusively quasi-spherical structures (Appendix 3, Figure AP3.2b), whereas compounds **80a** displayed a combination of spherical and elongated assemblies, suggesting their ability to form fibrous aggregates (Figure 3.14d). These findings were further supported by SEM images: compound **81** mainly displayed amorphous aggregates (Figure 3.14b), while **80a-b** additionally featured needle-like structures characteristic of linear, fiber-like assemblies (Figure 3.14c and Appendix 3, Figure AP3.2c).

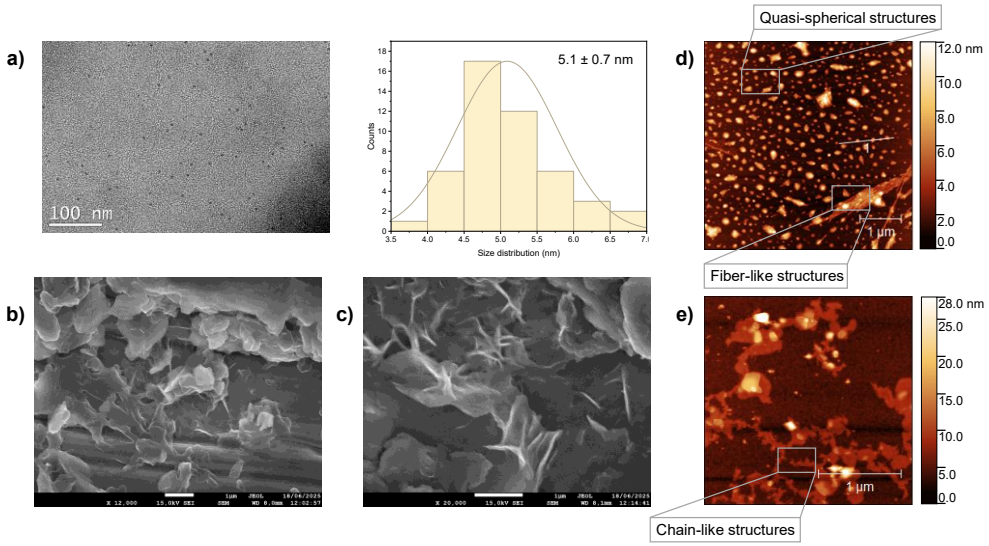

Figure 3.14. a) Representative TEM image and size histogram with a curve fit of the data using a Gaussian of **80a**, b) SEM image of **81**, c) SEM image of **80a**, d) AFM image of **80a** and e) AFM image of **80b**.

All these findings align with the increasing hydrophobic character of the compounds as the number of HBC units rises. For compound **80b**, the pronounced aggregation behavior corresponds with its lack of solubility in pure aqueous media, while remaining soluble in DMSO/H_2O mixtures.

3.3.4. Photophysical properties

The photophysical characterization of compounds **80a** and **81** was carried out in water and DMSO. In the case of compound **80b**, the characterization was limited to DMSO due to its lack of water solubility. For the starting nanographene **74**, the measurements were carried out in CH_2Cl_2 due to the lack of solubility of this compound in both DMSO and H_2O. The spectroscopic properties of these compounds are summarized in Table 3.1.

Table 3.1. Photophysical properties of compounds **74**, **80a**-**b** and **81**.

Comp.	Solvent	λ_{abs}^{max} (nm) ($\varepsilon/10^3$ M^{-1} cm^{-1})	λ_{em}^{max}(nm)	Φ_F (%)[a]	Φ_Δ (%)[b]
74	CH_2Cl_2	331 (24.6), 345 (65.1), 362 (154.9), 393 (43.6)	450, 459, 469, 480, 489, 499, 524, 534, 563, 574	5.7	73
80a	DMSO	346 (shoulder), 363 (211.4), 394 (69.3)	450, 458, 469, 480, 489, 498, 523, 534, 563, 575	3.7	63
	Water	356 (175.6), 399 (59.3)	-	-	-
80b	DMSO	346 (shoulder), 363 (240.6), 394 (77.9)	450, 458, 469, 480, 490, 499, 524, 534, 563, 573	4.9	60
81	DMSO	347 (115.4), 363 (188.5), 393 (61.3)	451, 458, 469, 480, 489, 499, 524, 534, 563, 575	3.6	55
	Water	357 (92.8), 396 (29.2)	-	-	-

[a]Fluorescence quantum yields (Φ_F) measured using a quinine sulfate solution in H_2SO_4 0.5M (Φ_F = 0.55) as reference.
[b]Singlet oxygen quantum yields (Φ_Δ) were determined using phenalenone in DMSO and CH_2Cl_2 (Φ_Δ = 0.95) as reference.

All derivatives display an absorption profile similar to starting nanographene **74** in DMSO, with three bands in the visible region at ~346, 363 and 394 nm (Figure 3.15a). The absorption spectra are primarily dominated by the nanographene unit, with no substantial shifts observed upon conjugation with the glycofullerene, indicating minimal electronic interaction between the two moieties in the ground state. In addition, under ~320 nm, the contribution of glycofullerene is observed as a broad band extending into the ultraviolet region.

Spectra recorded in water show a blue shift in the absorption maximum, accompanied by a broadening of the bands, where only two bands can be distinguished at ~356 and ~399 nm (Figure 3.15b). This phenomenon could be associated with the aggregation of molecules in an aqueous medium, which causes changes in the electronic environment and molecular packing of the conjugated system.

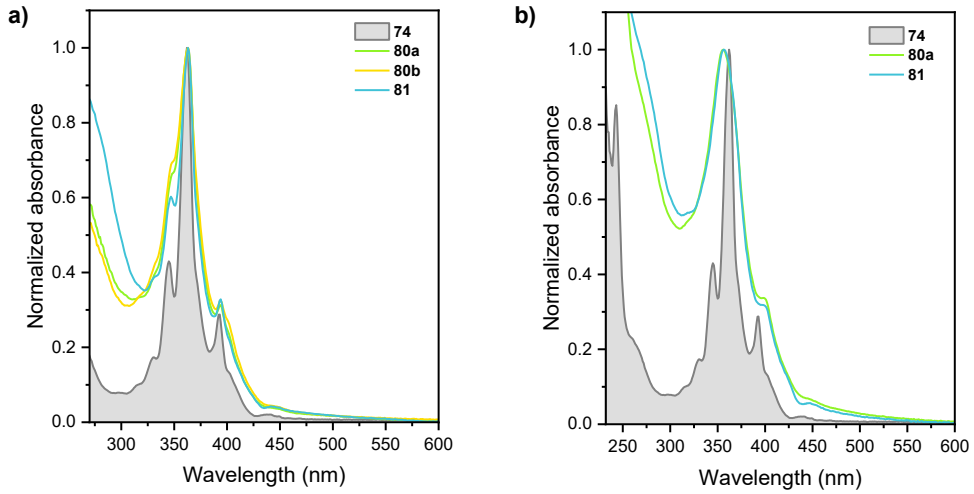

Figure 3.15. UV-Vis absorption spectra of compounds **74**, **80a-b** and **81** in: a) DMSO for **80a-b** and **81** ($1 \cdot 10^{-6}$ M) and in CH_2Cl_2 for **74** ($1 \cdot 10^{-6}$ M) and b) H_2O for **80a** and **81** ($1 \cdot 10^{-6}$ M) and in CH_2Cl_2 for **74** ($1 \cdot 10^{-6}$ M).

Emission spectra in DMSO also maintain a band pattern similar to nanographene **74**, demonstrating the ability of these molecules to have fluorescent properties (Figure 3.16a). However, a particular behavior is observed in the spectra recorded in water, where fluorescence is almost quenched (Figure 3.16b). This phenomenon suggests that, in aqueous media, self-aggregation processes or intermolecular interactions are favored, promoting non-radiative relaxation pathways that effectively suppress the fluorescent emission. In contrast, in DMSO, where the system remains mostly dispersed and stable, the fluorescence maintains the same emission profile as the initial nanographene, demonstrating the preservation of its optical properties. This difference is clearly evident when solutions of the compounds in DMSO and H_2O are exposed to ultraviolet light: while the compounds, initially brown in color, show green emission in DMSO, no fluorescent emission is observed when dissolved in H_2O.

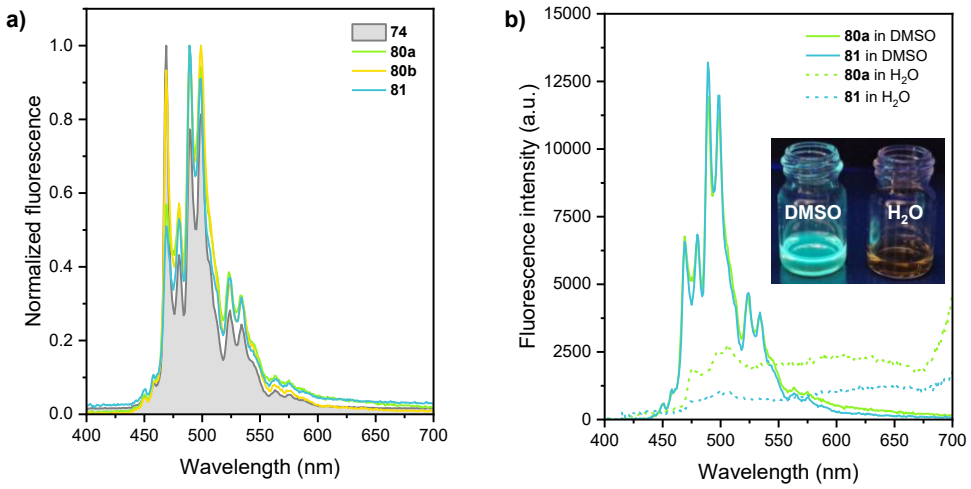

Figure 3.16. a) Emission spectra of compounds **80a** ($1 \cdot 10^{-6}$ M, λ_{exc} = 363 nm), **80b** and **81** ($7.5 \cdot 10^{-7}$ M, λ_{exc} = 363 nm) in DMSO and in CH_2Cl_2 for **74** ($7.5 \cdot 10^{-7}$ M, λ_{exc} = 363 nm) and b) comparison between the emission spectra in H_2O and DMSO for **80a** ($1 \cdot 10^{-6}$ M, $\lambda_{exc\ DMSO}$ = 363 nm and $\lambda_{exc\ water}$ = 356 nm) and **81** ($7.5 \cdot 10^{-7}$ M, $\lambda_{exc\ DMSO}$ = 363 nm and $\lambda_{exc\ water}$ = 356 nm); inset picture of compound **81** under 365 nm UV-light.

The singlet oxygen quantum yield (Φ_Δ) in DMSO decreases slightly in the conjugated products compared to the starting nanographene, but remains relatively high, with values exceeding 50%. This reduction can be attributed to the known ability of fullerene derivatives to act as radical scavengers in the ground state.[161]

In contrast to the significant drop in fluorescence quantum yield (Φ_F) observed for porphyrinoid conjugates discussed in *Chapter 2*, the HBC-based derivatives demonstrate that the presence of glycofullerenes does not substantially impact Φ_F. In fact, the glycofullerene conjugates show comparable Φ_F values to the unmodified nanographene when measured in DMSO.

The synthesized derivatives, combining water solubility, fluorescence emission and the ability to generate ROS, represent promising candidates for biomedical applications. Their fluorescence makes them potentially useful as probes in bioimaging by confocal microscopy, while their efficient singlet oxygen production suggests possible cytotoxic effects relevant to oncological settings. Although cellular or *in vivo* studies have not yet been conducted, these fundamental properties open an interesting avenue for future evaluation as theranostic agents in biological environments.

3.4. Conclusions

Chapter 3 focuses on the development of new water-soluble HBC derivatives tailored for biological applications, particularly PDT. While nanographene derivatives are widely explored for optoelectronic purposes, their limited solubility in aqueous media has hindered their use in biomedical fields.

To address this limitation, three HBC derivatives functionalized with glycofullerenes were designed to enhance water solubility. The strategy involved synthesizing a nanographene (**74**) bearing a terminal alkyne, which enables conjugation *via* click chemistry with azide-terminated glycofullerenes. Glucose was chosen as the carbohydrate unit to increase selectivity toward cancer cells. Depending on the structure of the malonates used in the asymmetric branch of the hexakis-adduct, glycofullerenes bearing either one or two HBC units were obtained.

DLS measurements revealed that particle sizes in aqueous media were significantly larger than in DMSO, likely due to aggregation driven by the amphiphilic nature of the molecules. This effect was more pronounced in derivatives containing two HBC moieties. AFM confirmed this trend: compound **81** displayed only quasi-spherical particles, while compound **80a** showed both spherical and thread-like aggregates. For compound **80b**, only elongated structures were detected. SEM further supported these observations, showing amorphous aggregates and fine, needle-like features consistent with fibrous assemblies.

Photophysical characterization revealed typical HBC absorption bands. Fluorescence emission was observed exclusively in DMSO, while it was quenched in water, likely due to aggregation. Importantly, all compounds exhibited singlet oxygen quantum yields above 50%, underscoring their potential for future biological evaluations and PDT-based therapeutic applications.

Experimental Section

EXPERIMENTAL SECTION

Unless otherwise noted, all materials including solvents were obtained from commercial suppliers and used without further purification. All work-up and purification procedures were carried out with HPLC-grade solvents in air. Flash chromatography was performed using Scharlab silica gel (230-400 mesh, 0.040-0.063 mm) and size exclusion chromatography was performed using gel filtration Sephadex G-25 or G-50 purchased from Cytiva. Analytical thin layer chromatography (TLC) was performed using E. Merck silica gel 60 F_{254} precoated plates (0.25 mm). The developed chromatogram was analyzed by UV lamp (λ = 254 or 365 nm) or charring with potassium permanganate as development reagent.

Compounds **11**,[185] **12**,[186] **13**,[187] **14**,[188] **50**,[153a] **51**[153b] and **61**[189] were prepared according to previously reported procedures. The procedures for the synthesis of compounds **2**,[190] **7**,[191] **18**,[192] **68**,[184] **69**,[170,183] **70**,[184] **71**,[184] **73**[184] and **74**[184] were modified from the previously reported. Carbohydrates **15** and **16** were provided by Dr. Javier Rojo's group while carbohydrate **17** was provided by Asparia Glycomics.

Microwave reactions were performed in an Anton-Parr Monowave 300 microwave or in an Anton-Parr Monowave 400 microwave reactor.

NMR experiments were performed on a Bruker AVIII HD 300 MHz BACS-60 (^{1}H: 300 MHz, ^{13}C: 75 MHz), Bruker NEO 500 MHz (^{1}H: 500 MHz, ^{13}C: 126 MHz, ^{19}F: 471 MHz, ^{11}B: 160 MHz) and Bruker AVIII 700MHz (^{1}H: 700 MHz, ^{13}C: 176 MHz). Coupling constants (*J*) are expressed in Hertz (Hz) and chemical shifts (δ) in parts per million (ppm) relative to the solvent. For referencing NMR spectra, the residual solvent signal ($CDCl_3$ δ 7.26 ppm for ^{1}H and δ 77.16 ppm for ^{13}C, Methylene Chloride-d_2 δ 5.32 ppm for ^{1}H and δ 54.00 ppm for ^{13}C, DMSO-d_6 δ 2.50 ppm for ^{1}H and δ 39.52 ppm for ^{13}C and Acetone-d_6 δ 2.05 ppm for ^{1}H and δ 29.84 ppm for ^{13}C) was used. Data are reported as follows: chemical shift, multiplicity (s = singlet, br s = broad singlet, d = doublet, t = triplet, td = triplet of doublets, tt = triplet of triplets, q = quartet, p = pentet, m = multiplet), coupling constant (Hz) and integration.

---

[185] a) E. Arce, P. M. Nieto, V. Díaz, R. G. Castro, A. Bernad, J. Rojo, *Bioconjug Chem* **2003**, *14*, 817. b) T. K. Lindhorst, S. Kötter, U. Krallmann-Wenzel, S. Ehlers, *J. Chem. Soc. Perkin Trans. 1* **2001**, 823.
[186] J. Geng, G. Mantovani, L. Tao, J. Nicolas, G. Chen, R. Wallis, D. A. Mitchell, B. R. G. Johnson, S. D. Evans, D. M. Haddleton, *J. Am. Chem. Soc.* **2007**, *129*, 15156.
[187] H. Tamiaki, A. Shinkai, Y. Kataoka, *J. Photochem. Photobiol. A Chem.* **2009**, *207*, 115.
[188] O. Otman, P. Boullanger, D. Lafont, T. Hamaide, *Macromol. Chem. Phys.* **2008**, *209*, 2410.
[189] V. Yarlagadda, M. M. Konai, G. B. Manjunath, C. Ghosh, J. Haldar, *J. Antibiot.* **2015**, *68*, 302.
[190] G. Tao, T. Ji, N. Wang, G. Yang, X. Lei, W. Zheng, R. Liu, X. Xu, L. Yang, G.-Q. Yin, X. Liao, X. Li, H.-M. Ding, X. Ding, J. Xu, H.-B. Yang, G. Chen, *ACS Macro Lett.* **2020**, *9*, 61.
[191] T. M. N. Trinh, M. Holler, J. P. Schneider, M. I. García-Moreno, J. M. García-Fernández, A. Bodlenner, P. Compain, C. Ortiz-Mellet, J.-F. Nierengarten, *J. Mater. Chem. B* **2017**, *5*, 6546.
[192] J.-F. Nierengarten, J. Iehl, V. Oerthel, M. Holler, B. M. Illescas, A. Muñoz, N. Martín, J. Rojo, M. Sánchez-Navarro, S. Cecioni, S. Vidal, K. Buffet, M. Durka, S. P. Vincent, *Chem. Commun.* **2010**, *46*, 3860.

Infrared spectra were recorded on a FT-IR Nicolet iS50 equipped with a KBr beamsplitter or Spectrum 3™ FT-IR spectrometers. In all cases it was used KBr for water-soluble compounds or dissolved in the proper solvent when possible.

MALDI-ToF matrices were trans-2-[3-(4-*tert*-butylphenyl)-2-methyl-2-propenylidene]-malononitrile (DCTB) or 1,8-dihidroxi-9,10-dihydroanthracen-9-ona (dithranol) and mass analysis were performed in a Bruker Ultraflex II using an LTB MNL 106 laser source. Electrospray ionization (ESI) was performed in a Bruker IMPACT II spectrometer. The ionization conditions were the same for low-resolution as well as high-resolution experiments. The HR spectra were acquired at a resolution of 100,000.

The UV-vis absorption spectra were recorded with a JASCO V-540 spectrophotometer or a Varian Cary 5000 UV-Vis-NIR spectrophotometer. Emission spectra were acquired on a Horiba Jobin Yvon Fluorolog 3-22 spectrofluorimeter equipped with a 450 W xenon lamp, in a PicoQuant FluoTime 300 fluorescence spectrophotometer or Horiba FluoroLog 3 spectrophotometer equipped with a high-pressure Xenon lamp and a Hamamatsu R928P photomultiplier tube. Samples were dissolved in HPLC grade solvents, and a 0.5 cm or 1.0 cm optical path length quartz cells were used.

Hydrodynamic diameter measurements were acquired on a Dynamic Light Scattering (DLS) Zetasizer Nano ZS Zen 3600 (Malvern), working with an He-Ne laser operating at $\lambda = 633$ nm. The samples were recorded with a scattering angle of 173º. Measurements were made in a 1.0 cm path-length quartz cell. Solution samples were filtered through nylon Acrodisc syringe filters (Pall Life Sciences) with a 0.2 μm pore size.

TEM micrographs were obtained using a JEOL 2100 microscope, operating at 120 kV. The samples were dispersed in water with a few drops of ethanol (to facilitate the dispersion), sonicated and the resulting suspension was dropped onto a holey carbon copper grid (200 mesh) allowing the solvent to evaporate.

AFM images were acquired under ambient conditions using SPM Nanoscope IIIa multimode working on tapping mode with a TESPSS tip (Veeco) at a working frequency of ~235 kHz. The samples were prepared by drop casting from H_2O solutions on a freshly cleaved mica surface and were dried under ambient conditions.

SEM images were obtained using a JEOL JSM 7600F microscope working at 15 kV. The samples were prepared by drop casting from H_2O solutions on a gold surface and metallized with carbon in a Sputter Coater in high vacuum.

Chapter 1

Compound 2[190]

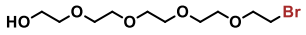

Triphenylphosphine (808 mg, 3.08 mmol) dissolved in dry CH_2Cl_2 (2 mL) was added dropwise to a solution of pentaethylene glycol (**1**) (2.00 g, 8.39 mmol) and CBr_4 (929 mg, 2.80 mmol) in dry CH_2Cl_2 (25 mL) at 0 ºC under argon atmosphere. After 30 min, the mixture was allowed to warm slowly to room temperature and stirred for 3 hours. Then, the crude was evaporated to dryness and purified by column chromatography (SiO_2, AcOEt) to afford **2** as a light-yellow oil (346 mg, 39%).

^{1}H NMR (300 MHz, $CDCl_3$) δ (ppm) = 3.79 (t, $^3J_{H,H}$ = 6.3 Hz, 2H; OC*H*$_2$CH$_2$Br), 3.73 – 3.68 (m, 2H; HOC*H*$_2$CH$_2$O), 3.67 – 3.62 (m, 12H; C*H*$_2$O), 3.61 – 3.56 (m, 2H; HOCH$_2$C*H*$_2$O), 3.45 (t, $^3J_{H,H}$ = 6.3 Hz, 2H; C*H*$_2$Br), 2.94 (br s, 1H; O*H*).

^{13}C NMR (75 MHz, $CDCl_3$) δ (ppm) = 72.7 (HOCH$_2$*C*H$_2$O), 71.3 (O*C*H$_2$CH$_2$Br), 70.7, 70.6, 70.4 (*C*H$_2$O), 61.8 (HO*C*H$_2$CH$_2$O), 30.4 (*C*H$_2$Br).

Compound 6[193]

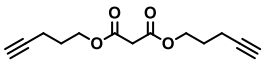

Malonyl chloride (**3**) (1.79 mL, 17.80 mmol) was added dropwise to a solution of 4-pentyn-1-ol (**5**) (3.41 mL, 35.70 mmol), Et_3N (5 mL, 36.10 mmol) and DMAP (0.109 mg, 0.89 mmol) in dry CH_2Cl_2 (50 mL) at 0 ºC under argon atmosphere. After 30 min, the mixture was allowed to warm slowly to room temperature and stirred overnight. Then, the solution was washed with HCl 1M (2 x 50 mL), Na_2CO_3 (2 x 50 mL) and brine (50 mL). The organic layer was dried over anh. $MgSO_4$, filtered and concentrated. The resulting crude was purified by column chromatography (SiO_2, Hexane/AcOEt 1:2) to afford **6** as a yellow oil (3.04 g, 72%).

^{1}H NMR (300 MHz, $CDCl_3$) δ (ppm) = 4.25 (t, $^3J_{H,H}$ = 6.3 Hz, 4H; COOC*H*$_2$CH$_2$CH$_2$), 3.38 (s, 2H; COC*H*$_2$CO), 2.29 (td, $^3J_{H,H}$ = 7.0 Hz, $^4J_{H,H}$ = 2.7 Hz, 4H; COOCH$_2$CH$_2$C*H*$_2$), 1.97 (t, $^4J_{H,H}$ = 2.7 Hz, 2H; C≡C*H*), 1.87 (p, $^3J_{H,H}$ = 6.6 Hz, 4H; COOCH$_2$C*H*$_2$CH$_2$).

^{13}C NMR (75 MHz, $CDCl_3$) δ (ppm) = 166.5 (*C*O), 82.8 (*C*≡CH), 69.3 (C≡*C*H), 64.0 (COO*C*H$_2$CH$_2$CH$_2$), 41.5 (CO*C*H$_2$CO), 27.4 (COOCH$_2$*C*H$_2$CH$_2$), 15.1 (COOCH$_2$CH$_2$*C*H$_2$).

[193] Y. Min, F. Leng, B. F. Machado, P. Lecante, P. Roblin, H. Martínez, T. Theussl, A. Casu, A. Falqui, M. Barcenilla, S. Coco, B. M. Illescas, N. Martín, M. R. Axet, P. Serp, *Eur. J. Inorg. Chem.* **2020**, *2020*, 4069.

Compound 7[191]

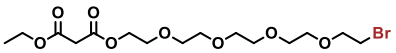

Ethyl malonyl chloride (**4**) (0.13 mL, 1.04 mmol) was added dropwise to a solution of **2** (346 mg, 1.15 mmol), Et_3N (0.16 mL, 1.15 mmol) and DMAP (6.4 mg, 0.052 mmol) in dry CH_2Cl_2 (10 mL) at 0 ºC under argon atmosphere. After 30 min, the mixture was allowed to warm slowly to room temperature and stirred overnight. Then, the solution was washed with HCl 1M (20 mL) and brine (20 mL). The organic layer was dried over anh. $MgSO_4$, filtered and concentrated. The resulting crude was purified by column chromatography (SiO_2, AcOEt) to afford **7** as a colourless oil (402 mg, 92%).

^{1}H NMR (300 MHz, $CDCl_3$) δ (ppm) = 4.30 – 4.25 (m, 2H; COOCH_2CH$_2$O), 4.18 (q, $^3J_{H,H}$ = 7.1 Hz, 2H; CH_2CH$_3$), 3.78 (t, $^3J_{H,H}$ = 6.3 Hz, 2H; OCH_2CH$_2$Br), 3.71 – 3.67 (m, 2H; COOCH$_2$CH_2O), 3.66 – 3.59 (m, 12H; CH_2O), 3.45 (t, $^3J_{H,H}$ = 6.3 Hz, 2H; CH_2Br), 3.38 (s, 2H; COCH_2CO), 1.26 (t, $^3J_{H,H}$ = 7.1 Hz, 3H; CH_3).

^{13}C NMR (75 MHz, $CDCl_3$) δ (ppm) = 166.7, 166.5 (*C*O), 71.3 (O*C*H$_2$CH$_2$Br), 70.7, 70.6 (*C*H$_2$O), 68.9 (COOCH$_2$*C*H$_2$O), 64.6 (COO*C*H$_2$CH$_2$O), 61.6 (*C*H$_2$CH$_3$), 41.6 (CO*C*H$_2$CO), 30.4 (*C*H$_2$Br), 14.1 (*C*H$_3$).

Compound 8[191]

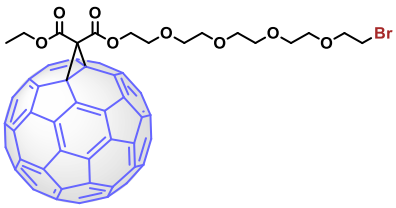

DBU (0.34 mL, 2.28 mmol) was added dropwise to a solution of **7** (377 mg, 0.91 mmol), [60]fullerene (1.31 g, 1.82 mmol) and I_2 (810 mg, 3.19 mmol) in dry toluene (500 mL) under argon at 0 ºC. The reaction mixture was then allowed to warm gradually to room temperature and stirred for 3 hours. After that time, the reaction mixture was washed with sat. $Na_2S_2O_3$ (100 mL), HCl 0.5 M (2 x 100 mL), water (100 mL) and brine (100 mL). The organic layer was dried over anh. $MgSO_4$, filtered and concentrated under vacuum. The crude was purified by column chromatography (SiO_2, CS_2 → Toluene/Acetone 10:1) to afford **8** as a dark brown solid (500 mg, 49%).

^{1}H NMR (300 MHz, $CDCl_3$) δ (ppm) = 4.68 – 4.63 (m, 2H; COOCH_2CH$_2$O), 4.56 (q, $^3J_{H,H}$ = 7.2 Hz, 2H; CH_2CH$_3$), 3.90 – 3.86 (m, 2H; COOCH$_2$CH_2O), 3.81 (t, $^3J_{H,H}$ = 6.3 Hz, 2H; OCH_2CH$_2$Br), 3.72 – 3.63 (m, 12H; CH_2O), 3.47 (t, $^3J_{H,H}$ = 6.3 Hz, 2H; CH_2Br), 1.49 (t, $^3J_{H,H}$ = 7.2 Hz, 3H; CH_3).

^{13}C NMR (75 MHz, $CDCl_3$) δ (ppm) = 163.8, 163.6 (*C*O), 145.5, 145.4, 145.3, 145.0, 144.8, 144.0, 143.2, 143.1, 142.3, 142.0, 141.1, 139.3, 139.1 ($C_{sp2\ fullerene}$), 71.7

($C_{sp3\ fullerene}$), 71.4 (O*C*H$_2$CH$_2$Br), 70.9, 70.8, 70.7 (*C*H$_2$O), 68.9 (COOCH$_2$*C*H$_2$O), 66.3 (COO*C*H$_2$CH$_2$O), 63.6 (*C*H$_2$CH$_3$), 52.3 ($C_{q\ bridge}$), 30.5 (*C*H$_2$Br), 14.4 (*C*H$_3$).

Compound 9

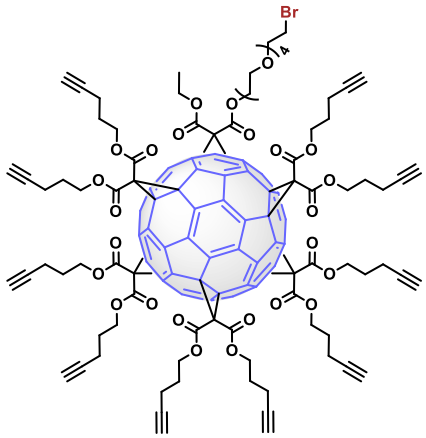

DBU (1.35 mL, 9.00 mmol) was added dropwise to a solution of **8** (510 mg, 0.45 mmol), **6** (1.06 g, 4.50 mmol) and CBr_4 (11.94 g, 36.00 mmol) in dry toluene (165 mL) under argon atmosphere. The mixture was stirred at room temperature for 72 h. After that time, the reaction mixture was washed with sat. $Na_2S_2O_3$ (100 mL), HCl 1 M (2 x 100 mL), water (100 mL) and brine (100 mL). The organic layer was dried over anh. $MgSO_4$, filtered and concentrated under vacuum. The crude was purified by column chromatography (SiO_2, DCM → DCM/Acetone 100:1 → 50:1 → 20:1) to afford **9** as a dark red solid (737 mg, 71%).

^{1}H NMR (700 MHz, $CDCl_3$) δ (ppm) = 4.60 – 4.11 (m, 24H; COOC*H*$_2$), 3.76 (t, $^3J_{H,H}$ = 6.3 Hz, 2H; OC*H*$_2$CH$_2$Br), 3.74 – 3.66 (m, 2H; COOCH$_2$C*H*$_2$O), 3.65 – 3.54 (m, 12H; C*H*$_2$O$_{PEG}$), 3.43 (t, $^3J_{H,H}$ = 6.3 Hz, 2H; C*H*$_2$Br), 2.45 – 2.14 (m, 20H; COOCH$_2$CH$_2$C*H*$_2$), 2.06 – 1.59 (m, 30H; COOCH$_2$C*H*$_2$CH$_2$ and C≡C*H*), 1.40 – 1.20 (m, 3H; C*H*$_3$).

^{13}C NMR (176 MHz, $CDCl_3$) δ (ppm) = 163.7 (*C*O), 145.8, 141.0 ($C_{sp2\ fullerene}$), 82.5 (*C*≡CH), 78.4 (C≡*C*H), 71.2 (O*C*H$_2$CH$_2$Br), 70.6, 70.5 (*C*H$_2$O$_{PEG}$), 69.8 (C≡*C*H), 69.0 ($C_{sp3\ fullerene}$), 68.6 (COOCH$_2$*C*H$_2$O), 65.8 (COO*C*H$_2$CH$_2$O), 65.4 (COO*C*H$_2$CH$_2$CH$_2$), 63.0 (*C*H$_2$CH$_3$), 45.3, 39.4 ($C_{q\ bridge}$), 30.4 (*C*H$_2$Br), 27.1 (COOCH$_2$*C*H$_2$CH$_2$), 16.4, 15.1 (COOCH$_2$CH$_2$*C*H$_2$), 14.1 (*C*H$_3$).

FTIR-ATR (ν cm^{-1}): 3293 (C≡C-H), 2958 (C-H), 1739 (C=O).

Compound 10[97]

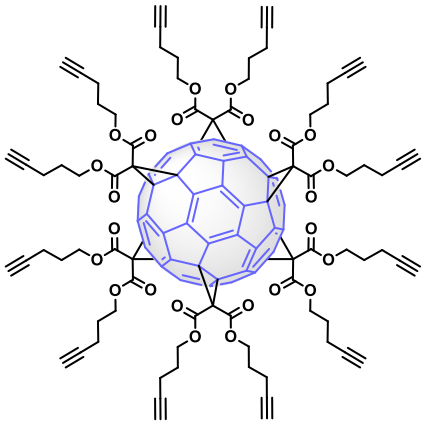

DBU (0.63 mL, 4.22 mmol) was added dropwise to a solution of [60]fullerene (152 mg, 0.21 mmol), **6** (500 mg, 2.11 mmol) and CBr_4 (7.00 g, 21.10 mmol) in dry toluene (375 mL) under argon atmosphere. The mixture was stirred at room temperature for 72 h. After that time, the reaction mixture was washed with sat. $Na_2S_2O_3$ (100 mL), HCl 1 M (2 x 100 mL), water (100 mL) and brine (100 mL). The organic layer was dried over anh. $MgSO_4$, filtered and concentrated under vacuum. The crude was purified by column chromatography (SiO_2, DCM → DCM/AcOEt 98:2) affording **10** as a dark red solid (247 mg, 55%).

^{1}H NMR (300 MHz, $CDCl_3$) δ (ppm) = 4.39 (t, $^3J_{H,H}$ = 6.3 Hz, 24H; COOC*H*$_2$CH$_2$CH$_2$), 2.29 (td, $^3J_{H,H}$ = 6.9 Hz, $^4J_{H,H}$ = 2.7 Hz, 24H; COOCH$_2$CH$_2$C*H*$_2$), 1.97 (t, $^4J_{H,H}$ = 2.6 Hz, 12H; C≡C*H*), 1.87 (p, $^3J_{H,H}$ = 6.5 Hz, 24H; COOCH$_2$C*H*$_2$CH$_2$).

^{13}C NMR (75 MHz, $CDCl_3$) δ (ppm) = 163.8 (*C*O), 145.9, 141.3 ($C_{sp2\ fullerene}$), 82.6 (*C*≡CH), 69.8 (C≡*C*H), 69.2 ($C_{sp3\ fullerene}$), 65.5 (COO*C*H$_2$CH$_2$CH$_2$), 37.1 ($C_{q\ bridge}$), 27.3 (COOCH$_2$*C*H$_2$CH$_2$), 15.3 (COOCH$_2$CH$_2$*C*H$_2$).

Compound 18[192]

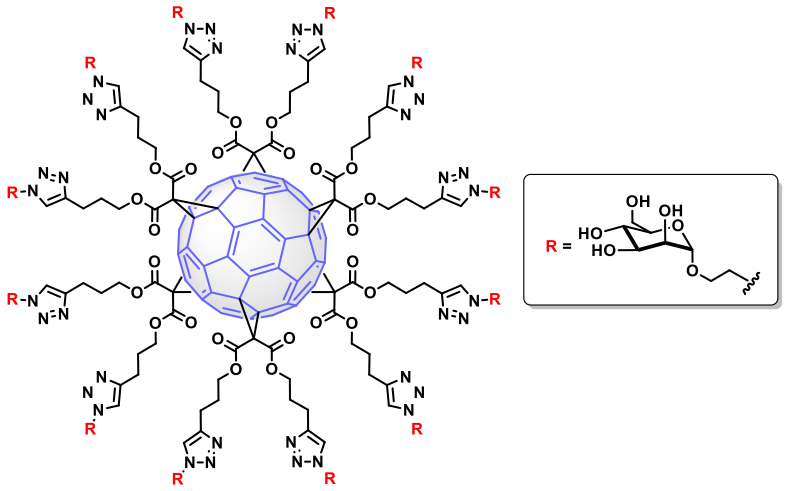

A mixture of 2-azidoethyl α-D-mannopyranoside (**11**) (189 mg, 0.76 mmol), **10** (101 mg, 0.047 mmol), $CuBr{\cdot}S(CH_3)_2$ (78 mg, 0.38 mmol), sodium ascorbate (151 mg, 0.76 mmol) and a piece of copper metal wire in DMSO (1 mL) was deoxygenated and kept under argon with vigorous stirring for 72 h. The crude reaction was filtered through a QuadraSil® Mercaptopropyl column. CH_3OH was added to the mixture and the precipitate was centrifuged and extensively washed with CH_3OH, then dried under high vacuum to afford **18** as a brown solid (210 mg, 97%).

^{1}H NMR (700 MHz, DMSO-*d*$_6$) δ (ppm) = 7.84 (s, 12H; C*H*$_{triazole}$), 4.76 (s, 24H; O*H*), 4.64 – 4.58 (m, 24H; C*H*$_{1man}$ and O*H*), 4.54 – 4.45 (m, 36H; OCH$_2$C*H*$_2$N$_{man}$ and O*H*), 4.39 – 4.20 (m, 24H; COOC*H*$_2$CH$_2$CH$_2$), 3.94 – 3.89 (m, 12H; OC*H*$_2$CH$_2$N$_{man}$), 3.78 – 3.72 (m, 12H; OC*H*$_2$CH$_2$N$_{man}$), 3.62 – 3.58 (m, 12H; C*H*$_2$OH$_{man}$), 3.54 – 3.51 (m, 12H; C*H*$_{man}$), 3.40 – 3.38 (m, 36H; C*H*$_{man}$ and C*H*$_2$OH$_{man}$ overlaps with water), 3.13 – 3.07 (m, 12H; C*H*$_{man}$), 2.74 – 2.59 (m, 24H; COOCH$_2$CH$_2$C*H*$_2$), 2.06 – 1.90 (m, 24H; COOCH$_2$C*H*$_2$CH$_2$).

^{13}C NMR (176 MHz, DMSO-*d*$_6$) δ (ppm) = 162.9 (*C*O), 145.8 (*C*$_{triazole}$), 145.1, 140.8 (*C*$_{sp2\ fullerene}$), 122.5 (*C*H$_{triazole}$), 99.8 (*C*H$_{1man}$), 74.1 (*C*H$_{man}$), 70.9 (*C*H$_{man}$), 70.1 (*C*H$_{man}$), 68.9 (*C*$_{sp3\ fullerene}$), 66.8 (COO*C*H$_2$CH$_2$CH$_2$ and *C*H$_{man}$), 64.9 (O*C*H$_2$CH$_2$N$_{man}$), 61.2 (*C*H$_2$OH$_{man}$), 49.3 (OCH$_2$*C*H$_2$N$_{man}$), 45.6 (*C*$_{q\ bridge}$), 27.8 (COOCH$_2$*C*H$_2$CH$_2$), 21.5 (COOCH$_2$CH$_2$*C*H$_2$).

FTIR-ATR (ν cm^{-1}): 3340 (OH), 2930 (C-H), 1738 (C=O).

Compound 19

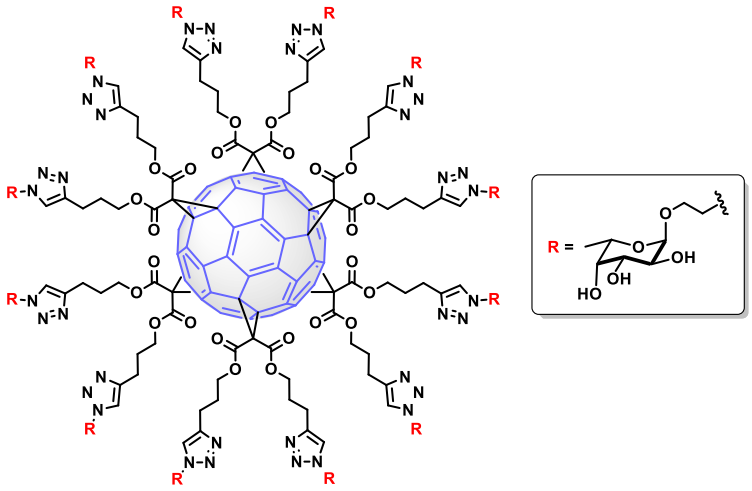

A mixture of 2-azidoethyl α-L-fucopyranoside (**12**) (196 mg, 0.84 mmol), **10** (112 mg, 0.052 mmol), $CuBr{\cdot}S(CH_3)_2$ (86 mg, 0.42 mmol), sodium ascorbate (166 mg, 0.84 mmol) and a piece of copper metal wire in DMSO (1 mL) was deoxygenated and kept under argon with vigorous stirring for 72 h. The crude reaction was filtered through a QuadraSil® Mercaptopropyl column. CH_3OH was added to the mixture and the precipitate was centrifuged and extensively washed with CH_3OH, then dried under high vacuum to afford **19** as a brown solid (210 mg, 82%).

^{1}H NMR (700 MHz, DMSO-d_6) δ (ppm) = 7.96 (s, 12H; CH_{triazole}), 4.65 – 4.60 (m, 12H; C$H_{1\text{fuc}}$), 4.56 – 4.44 (m, 48H; OCH$_2$CH_2N$_{\text{fuc}}$ and O*H*), 4.33 (s, 12H; O*H*), 4.42 – 4.38 (m, 24H; COOCH_2CH$_2$CH$_2$), 3.91 – 3.82 (m, 12H; OCH_2CH$_2$N$_{\text{fuc}}$), 3.76 – 3.66 (m, 12H; OCH_2CH$_2$N$_{\text{fuc}}$), 3.55 – 3.50 (m, 12H; CH_{fuc}), 3.49 – 3.44 (m, 12H; CH_{fuc}), 3.37 (m, 24H; CH_{fuc} overlaps with water), 2.76 – 2.58 (m, 24H; COOCH$_2$CH$_2$CH_2), 2.05 – 1.87 (m, 24H; COOCH$_2$CH_2CH$_2$), 0.97 (d, $^3J_{H,H}$ = 6.7 Hz, 36H; CH_3).

^{13}C NMR (176 MHz, DMSO-d_6) δ (ppm) = 162.9 (*C*O), 145.7 (C_{triazole}), 145.1, 140.8 ($C_{\text{sp2 fullerene}}$), 122.8 (*C*H$_{\text{triazole}}$), 99.0 (*C*H$_{1\text{fuc}}$), 71.5, 69.6 (*C*H$_{\text{fuc}}$), 68.8 ($C_{\text{sp3 fullerene}}$), 67.9 (*C*H$_{\text{fuc}}$), 66.6 (COO*C*H$_2$CH$_2$CH$_2$), 66.1 (*C*H$_{\text{fuc}}$), 65.7 (O*C*H$_2$CH$_2$N$_{\text{fuc}}$), 49.5 (OCH$_2$*C*H$_2$N$_{\text{fuc}}$), 45.5 ($C_{\text{q bridge}}$), 27.8 (COOCH$_2$*C*H$_2$CH$_2$), 21.5 (COOCH$_2$CH$_2$*C*H$_2$), 16.4 (*C*H$_3$).

FTIR-ATR (ν cm^{-1}): 3361 (OH), 2933 (C-H), 1738 (C=O).

Compound 20[97]

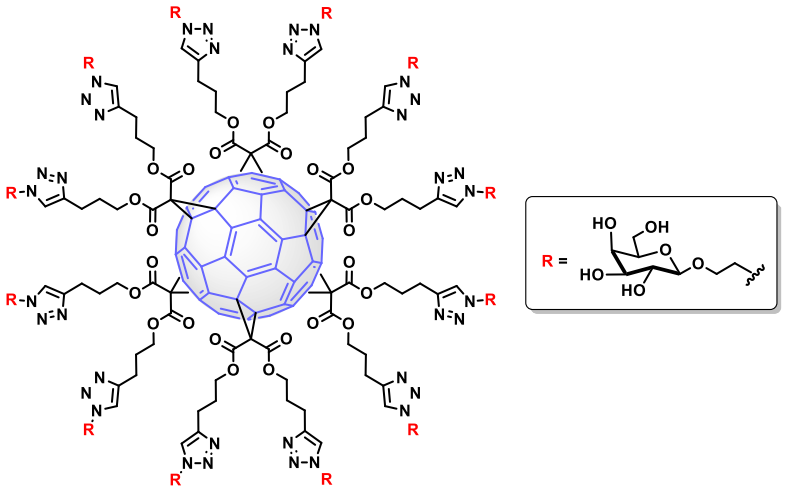

A mixture of 2-azidoethyl β-D-galactopyranoside (**13**) (99 mg, 0.40 mmol), **10** (53 mg, 0.025 mmol), $CuBr{\cdot}S(CH_3)_2$ (41 mg, 0.20 mmol), sodium ascorbate (79 mg, 0.40 mmol) and a piece of copper metal wire in DMSO (1 mL) was deoxygenated and kept under argon with vigorous stirring for 72 h. The crude reaction was filtered through a QuadraSil® Mercaptopropyl column. CH_3OH was added to the mixture and the precipitate was centrifuged and extensively washed with CH_3OH, then dried under high vacuum to afford **20** as a brown solid (99 mg, 78%).

^{1}H NMR (700 MHz, DMSO-d_6) δ (ppm) = 8.04 (s, 12H; C$H_{triazole}$), 4.98 (s, 12H; O*H*), 4.78 (s, 12H; O*H*), 4.62 (s, 12H; O*H*), 4.58 – 4.47 (m, 24H; $OCH_2CH_2N_{gal}$), 4.43 (s, 12H; O*H*), 4.38 – 4.19 (m, 24H; $COOCH_2CH_2CH_2$), 4.18 – 4.11 (m, 12H; CH_{1gal}), 4.09 – 4.00 (m, 12H; $OCH_2CH_2N_{gal}$), 3.91 – 3.80 (m, 12H; $OCH_2CH_2N_{gal}$), 3.64 – 3.57 (m, 12H; CH_{gal}), 3.52 – 3.46 (m, 24H; CH_2OH_{gal} overlaps with water), 3.31 – 3.20 (m, 36H; CH_{gal} overlaps with water), 2.78 – 2.59 (m, 24H; $COOCH_2CH_2CH_2$), 2.06 – 1.83 (m, 24H; $COOCH_2CH_2CH_2$).

^{13}C NMR (176 MHz, DMSO-d_6) δ (ppm) = 162.9 (*C*O), 146.0 ($C_{triazole}$), 145.0, 140.8 ($C_{sp2\ fullerene}$), 123.5 (C$H_{triazole}$), 103.5 (CH_{1gal}), 75.4, 73.3, 70.4 (CH_{gal}), 68.8 ($C_{sp3\ fullerene}$), 68.2 (CH_{gal}), 67.1 ($OCH_2CH_2N_{gal}$), 66.7 ($COOCH_2CH_2CH_2$), 60.5 (CH_2OH_{gal}), 49.9 ($OCH_2CH_2N_{gal}$), 45.6 ($C_{q\ bridge}$), 27.6 ($COOCH_2CH_2CH_2$), 21.6 ($COOCH_2CH_2CH_2$).

FTIR-ATR (ν cm^{-1}): 3409 (OH), 2923 (C-H), 1739 (C=O).

Compound 21

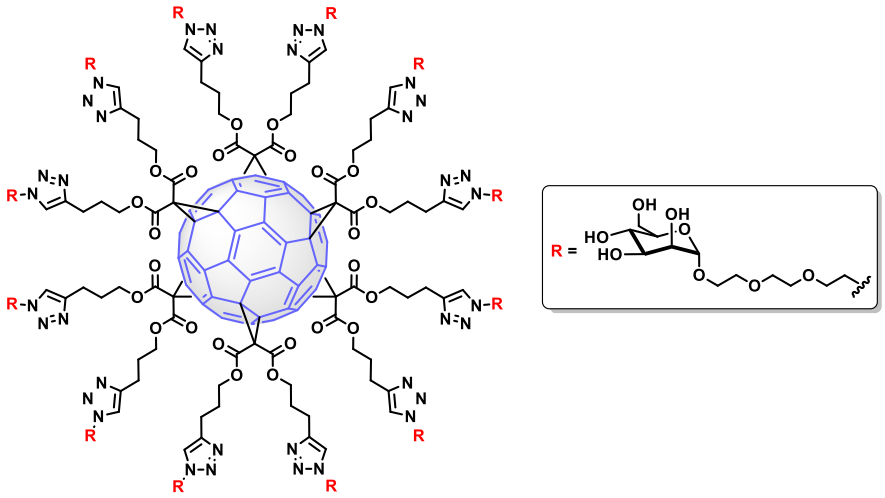

A mixture of **14** (113 mg, 0.33 mmol), **10** (51 mg, 0.024 mmol), $CuBr{\cdot}S(CH_3)_2$ (39 mg, 0.19 mmol), sodium ascorbate (75 mg, 0.38 mmol) and a piece of copper metal wire in DMSO (1 mL) was deoxygenated and kept under argon with vigorous stirring for 72 h. The crude reaction was filtered through a QuadraSil® Mercaptopropyl column and purified by size-exclusion chromatography (Sephadex G-25 H_2O/CH_3OH 9:1) to afford **21** as a brown sticky solid (136 mg, 92%).

^{1}H NMR (700 MHz, DMSO-d_6) δ (ppm) = 7.85 (s, 12H; C$H_{triazole}$), 4.78 – 4.68 (m, 24H; O*H*), 4.64 – 4.60 (m, 12H; CH_{1man}), 4.57 (m, 12H; O*H*), 4.49 – 4.41 (m, 36H; $OCH_2CH_2N_{man}$ and O*H*), 4.38 – 4.12 (m, 24H; $COOCH_2CH_2CH_2$), 3.82 – 3.75 (m, 24H; $OCH_2CH_2N_{man}$), 3.67 – 3.62 (m, 24H; OCH_2 and CH_2OH_{man}), 3.60 – 3.57 (m, 12H; CH_{man}), 3.52 – 3.46 (m, 72H; OCH_2), 3.46 – 3.42 (m, 36H; OCH_2, CH_2OH_{man} and CH_{man}), 3.34 – 3.38 (m, 24H; CH_{man}), 2.76 – 2.58 (m, 24H; $COOCH_2CH_2CH_2$), 2.07 – 1.84 (m, 24H; $COOCH_2CH_2CH_2$).

^{13}C NMR (176 MHz, DMSO-d_6) δ (ppm) = 162.8 (*C*O), 145.6 ($C_{triazole}$), 145.1, 140.8 ($C_{sp2\ fullerene}$), 122.5 (*C*H$_{triazole}$), 100.0 (*C*H$_{1man}$), 73.9, 71.0, 70.3 (*C*H$_{man}$), 69.7, 69.6, 69.5 (OCH_2), 68.8 (OCH_2 and $C_{sp3\ fullerene}$), 67.0 (*C*H$_{man}$), 66.6 ($COOCH_2CH_2CH_2$), 65.7 ($OCH_2CH_2N_{man}$), 61.3 (CH_2OH_{man}), 49.4 ($OCH_2CH_2N_{man}$), 45.6 ($C_{q\ bridge}$), 27.8 ($COOCH_2CH_2CH_2$), 21.4 ($COOCH_2CH_2CH_2$).

FTIR-ATR (ν cm^{-1}): 3393 (OH), 2923 (C-H), 1742 (C=O).

Compound 22

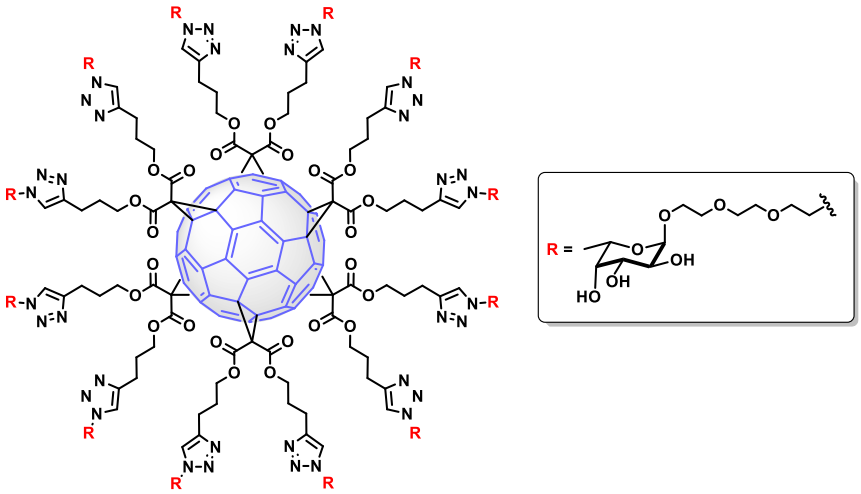

A mixture of **15** (108 mg, 0.33 mmol), **10** (51 mg, 0.024 mmol), CuBr·S(CH_3)$_2$ (39 mg, 0.19 mmol), sodium ascorbate (75 mg, 0.38 mmol) and a piece of copper metal wire in DMSO (1 mL) was deoxygenated and kept under argon with vigorous stirring for 72 h. The crude reaction was filtered through a QuadraSil® Mercaptopropyl column and purified by size-exclusion chromatography (Sephadex G-25 H_2O/CH_3OH 9:1) to afford **22** as a brown sticky solid (132 mg, 92%).

^{1}H NMR (700 MHz, DMSO-d_6) δ (ppm) = 7.85 (s, 12H; C$H_{triazole}$), 4.61 – 4.58 (m, 12H; CH_{1fuc}), 4.50 (m, 12H; O*H*), 4.48 – 4.43 (m, 24H; OCH$_2$CH_2N$_{fuc}$), 4.40 (s, 24H; O*H*), 4.37 – 4.05 (m, 24H; COOCH_2CH$_2$CH$_2$), 3.82 – 3.74 (m, 36H; OCH_2 and CH_{fuc}), 3.62 – 3.58 (m, 12H; CH_{fuc}), 3.53 – 3.42 (m, 120H; OCH_2 and CH_{fuc}), 2.79 – 2.55 (m, 24H; COOCH$_2$CH$_2$CH_2), 2.08 – 1.84 (m, 24H; COOCH$_2$CH_2CH$_2$), 1.04 (d, $^3J_{H,H}$ = 6.4 Hz, 36H; CH_3).

^{13}C NMR (176 MHz, DMSO-d_6) δ (ppm) = 162.8 (*C*O), 145.6 ($C_{triazole}$), 145.1, 140.8 ($C_{sp2\ fullerene}$), 122.5 (*C*H$_{triazole}$), 99.3 (*C*H$_{1fuc}$), 71.6, 69.8 (*C*H$_{fuc}$), 69.6 (*C*H$_{fuc}$ and O*C*H$_2$), 68.8 (O*C*H$_2$ and $C_{sp3\ fullerene}$), 68.0 (*C*H$_{fuc}$), 66.6 (COO*C*H$_2$CH$_2$CH$_2$), 65.9 (*C*H$_{fuc}$), 65.7 (O*C*H$_2$CH$_2$N$_{fuc}$), 49.4 (OCH$_2$*C*H$_2$N$_{fuc}$), 45.6 ($C_{q\ bridge}$), 27.8 (COOCH$_2$*C*H$_2$CH$_2$), 21.4 (COOCH$_2$CH$_2$*C*H$_2$), 16.5 (*C*H$_3$).

FTIR-ATR (ν cm^{-1}): 3413 (OH), 2915 (C-H), 1743 (C=O).

Compound 23

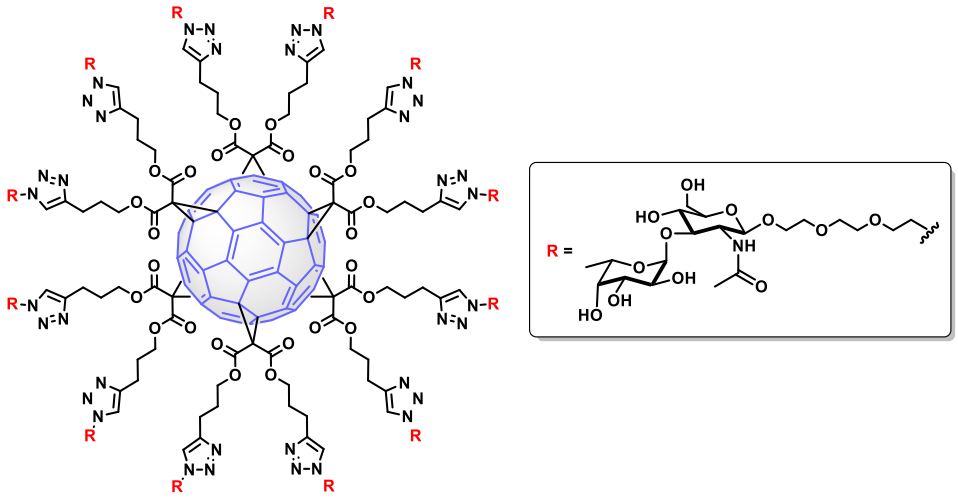

A mixture of **16** (45 mg, 0.086 mmol), **10** (14 mg, 6.6 µmol), $CuBr{\cdot}S(CH_3)_2$ (11 mg, 0.053 mmol), sodium ascorbate (22 mg, 0.11 mmol) and a piece of copper metal wire in DMSO (1 mL) was deoxygenated and kept under argon with vigorous stirring for 72 h. The crude reaction was filtered through a QuadraSil® Mercaptopropyl column. CH_3OH was added to the mixture and the precipitate was centrifuged and extensively washed with CH_3OH, then dried under high vacuum to afford **23** as a brown solid (50 mg, 91%).

^{1}H NMR (700 MHz, DMSO-d_6) δ (ppm) = 7.93 – 7.74 (m, 24H; C$H_{triazole}$ and N*H*), 4.81 (m, 12H; O*H*), 4.77 – 4.72 (m, 12H; CH_1), 4.63 – 4.56 (m, 24H; O*H*), 4.54 – 4.19 (m, 84H; OCH_2CH_2N, CH_1, $COOCH_2CH_2CH_2$ and O*H*), 4.16 – 4.12 (m, 12H; C*H*), 3.81 – 3.75 (m, 36H; C*H* and OCH_2), 3.69 – 3.66 (m, 12H; CH_2OH), 3.54 – 3.43 (m, 156H; OCH_2, C*H* and CH_2OH), 3.22 – 3.19 (m, 12H; C*H*), 3.18 – 3.15 (m, 12H; C*H*), 2.74 – 2.58 (m, 24H; $COOCH_2CH_2CH_2$), 2.06 – 1.89 (m, 24H; $COOCH_2CH_2CH_2$), 1.77 (s, 36H; $CH_{3\ amide}$), 1.03 (d, $^3J_{H,H}$ = 6.7 Hz, 36H; $CH_{3\ fuc}$).

^{13}C NMR (176 MHz, DMSO-d_6) δ (ppm) = 170.1 (CO_{amide}), 162.8 ($CO_{malonate}$), 145.5 ($C_{triazole}$), 145.0, 140.8 ($C_{sp2\ fullerene}$), 122.3 ($CH_{triazole}$), 100.5, 100.0 (CH_1), 81.9, 76.7, 71.7, 70.8, 69.8 (*C*H), 69.7, 69.6, 69.5 (CH_2O), 69.0 (*C*H), 68.8 ($C_{sp3\ fullerene}$ and CH_2O), 68.2 (*C*H), 67.9 (CH_2O), 66.5 (*C*H and $COOCH_2CH_2CH_2$), 60.8 (CH_2OH), 54.5 (*C*H), 49.3 (OCH_2CH_2N), 45.6 ($C_{q\ bridge}$), 27.7 ($COOCH_2CH_2CH_2$), 23.0 ($CH_{3\ amide}$), 21.4 ($COOCH_2CH_2CH_2$), 16.4 ($CH_{3\ fuc}$).

FTIR (KBr) (ν cm^{-1}): 3393 (OH), 2933 (C-H), 1743 (C=O).

Compound 24

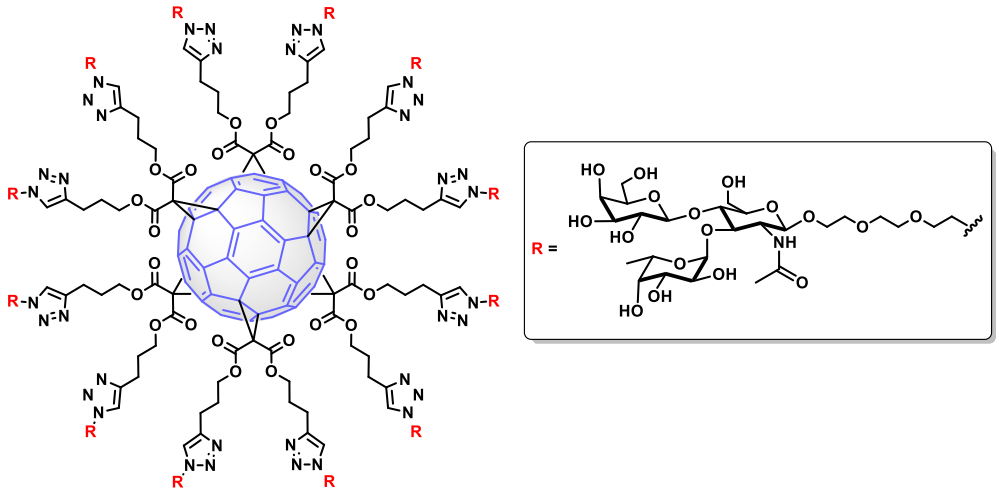

A mixture of **17** (126 mg, 0.18 mmol), **10** (30 mg, 0.014 mmol), $CuBr{\cdot}S(CH_3)_2$ (23 mg, 0.11 mmol), sodium ascorbate (44 mg, 0.22 mmol) and a piece of copper metal wire in DMSO (1 mL) was deoxygenated and kept under argon with vigorous stirring for 72 h. The crude reaction was filtered through a QuadraSil® Mercaptopropyl column. CH_3OH was added to the mixture and the precipitate was centrifuged and extensively washed with CH_3OH, then dried under high vacuum to afford **24** as a brown solid (134 mg, 92%).

^{1}H NMR (700 MHz, DMSO-d_6) δ (ppm) = 7.94 (s, 12H; N*H*), 7.84 (s, 12H; CH_{triazole}), 4.99 (m, 12H; O*H*), 4.84 – 4.80 (m, 12H; CH_1), 4.75 – 4.71 (m, 24H; O*H*), 4.70 – 4.66 (m, 12H; C*H*), 4.53 – 4.37 (m, 60H; OCH_2CH_2N, CH_1 and O*H*), 4.35 – 4.15 (m, 60H; CH_1, $COOCH_2CH_2CH_2$ and O*H*), 4.10 (m, 12H; O*H*), 3.79 – 3.75 (m, 36H; CH_2OH and OCH_2), 3.71 – 3.67 (m, 12H; CH_2OH), 3.66 – 3.63 (m, 24H; C*H*), 3.62 – 3.58 (m, 24H; C*H*), 3.54 – 3.51 (m, 24H; C*H* and CH_2OH), 3.50 – 3.41 (m, 108H; C*H* and OCH_2), 3.39 (m, 24H; CH_2OH and C*H* overlaps with water), 3.29 – 3.25 (m, 24H; C*H*), 3.24 – 3.21 (m, 24H; C*H*), 2.76 – 2.57 (m, 24H; $COOCH_2CH_2CH_2$), 2.05 – 1.87 (m, 24H; $COOCH_2CH_2CH_2$), 1.77 (s, 36H; $CH_{3\ \text{amide}}$), 0.99 (d, $^3J_{H,H}$ = 5.7 Hz, 36H; $CH_{3\ \text{fuc}}$).

^{13}C NMR (176 MHz, DMSO-d_6) δ (ppm) = 170.0 (CO_{amide}), 162.8 (CO_{malonate}), 145.7 (C_{triazole}), 145.0, 140.7 ($C_{\text{sp2 fullerene}}$), 122.5 (CH_{triazole}), 102.2, 100.4, 98.9 (CH_1), 76.0, 75.5, 74.7, 73.7, 73.5, 71.7, 70.8 (*C*H), 69.7, 69.6 (CH_2O), 69.4 (CH_2O and *C*H), 68.8 ($C_{\text{sp3 fullerene}}$ and CH_2O), 68.3 (*C*H), 67.9 (CH_2O), 67.4 (*C*H), 66.6 ($COOCH_2CH_2CH_2$), 65.8 (*C*H), 59.9, 59.4 (CH_2OH), 55.2 (*C*H), 49.3 (OCH_2CH_2N), 45.6 ($C_{\text{q bridge}}$), 27.8 ($COOCH_2CH_2CH_2$), 23.0 ($CH_{3\ \text{amide}}$), 21.4 ($COOCH_2CH_2CH_2$), 16.4 ($CH_{3\ \text{fuc}}$).

FTIR (KBr) (ν cm^{-1}): 3402 (OH), 2932 (C-H), 1742 (C=O).

Compound 25

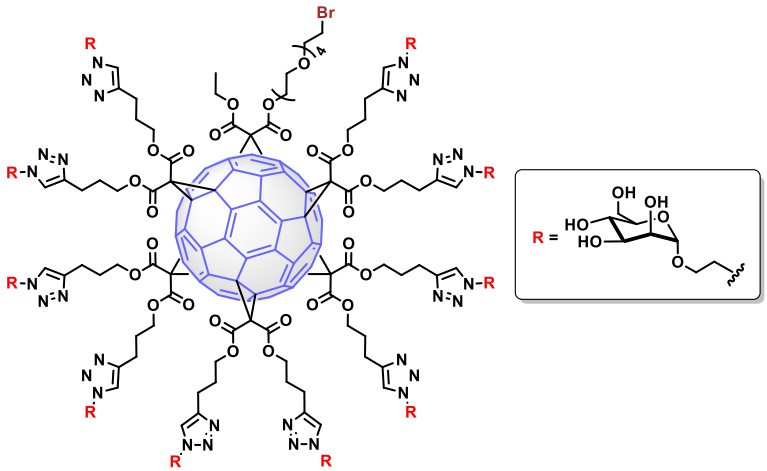

A mixture of 2-azidoethyl α-D-mannopyranoside (**11**) (583 mg, 2.34 mmol), **9** (300 mg, 0.13 mmol), $CuBr{\cdot}S(CH_3)_2$ (134 mg, 0.65 mmol), sodium ascorbate (194 mg, 0.98 mmol) and a piece of copper metal wire in DMSO (1.5 mL) was deoxygenated and kept under argon with vigorous stirring for 72 h. The crude reaction was filtered through a QuadraSil® Mercaptopropyl column. CH_3OH was added to the mixture and the precipitate was centrifuged and extensively washed with CH_3OH, then dried under high vacuum to afford **25** as an orange solid (597 mg, 96%).

^{1}H NMR (700 MHz, DMSO-*d*$_6$) δ (ppm) = 7.99 (s, 10H; C*H*$_{triazole}$), 4.75 (s, 20H; O*H*), 4.63 – 4.44 (m, 50H; C*H*$_{1man}$, $OCH_2CH_2N_{man}$ and O*H*), 4.38 – 4.16 (m, 24H; CH_2CH_3, $COOCH_2CH_2O$ and $COOCH_2CH_2CH_2$), 3.98 – 3.89 (m, 10H; $OCH_2CH_2N_{man}$), 3.82 – 3.74 (m, 10H; $OCH_2CH_2N_{man}$), 3.71 – 3.66 (m, 4H; CH_2O_{PEG}), 3.62 – 3.57 (m, 10H; CH_2OH_{man}), 3.54 – 3.41 (m, 54H; CH_2OH_{man}, CH_2Br, CH_2O_{PEG} and C*H*$_{man}$ overlaps with water), 3.15 – 3.06 (m, 10H; C*H*$_{man}$), 2.82 – 2.61 (m, 20H; $COOCH_2CH_2CH_2$), 2.11 – 1.86 (m, 20H; $COOCH_2CH_2CH_2$), 1.28 – 1.14 (m, 3H; CH_3).

^{13}C NMR (176 MHz, DMSO-*d*$_6$) δ (ppm) = 162.8 (*C*O), 146.2 (*C*$_{triazole}$), 145.0, 140.7 (*C*$_{sp2\ fullerene}$), 123.2 (*C*H$_{triazole}$), 99.7 (*C*H$_{1man}$), 74.1, 70.8 (*C*H$_{man}$), 70.3 (CH_2O_{PEG}), 70.0 (*C*H$_{man}$), 69.7, 69.5 (CH_2O_{PEG}), 68.7 (*C*$_{sp3\ fullerene}$), 67.9 ($COOCH_2CH_2O$), 66.9 ($COOCH_2CH_2CH_2$ and *C*H$_{man}$), 64.7 ($OCH_2CH_2N_{man}$), 63.4 (CH_2CH_3), 61.1 (CH_2OH_{man}), 49.7 ($OCH_2CH_2N_{man}$), 45.5 (*C*$_{q\ bridge}$), 32.3 (CH_2Br), 27.6 ($COOCH_2CH_2CH_2$), 21.5 ($COOCH_2CH_2CH_2$), 13.8 (CH_3).

FTIR-ATR (ν cm^{-1}): 3389 (OH), 2928 (C-H), 1736 (C=O).

Compound 26

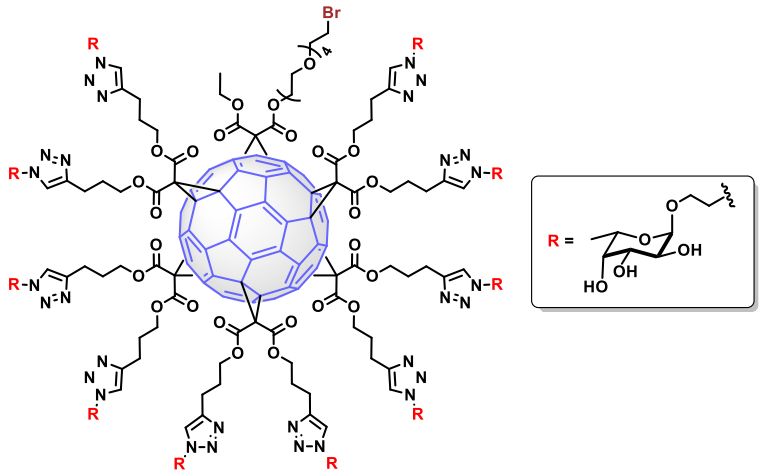

A mixture of 2-azidoethyl α-D-fucopyranoside (**12**) (374 mg, 1.61 mmol), **9** (206 mg, 0.89 mmol), $CuBr{\cdot}S(CH_3)_2$ (92 mg, 0.45 mmol), sodium ascorbate (133 mg, 0.67 mmol) and a piece of copper metal wire in DMSO (1.5 mL) was deoxygenated and kept under argon with vigorous stirring for 72 h. The crude reaction was filtered through a QuadraSil® Mercaptopropyl column. CH_3OH was added to the mixture and the precipitate was centrifuged and extensively washed with CH_3OH, then dried under high vacuum to afford **26** as an orange solid (353 mg, 85%).

^{1}H NMR (700 MHz, DMSO-d_6) δ (ppm) = 8.11 (s, 10H; CH_{triazole}), 4.67 – 4.61 (m, 10H; C$H_{1\text{fuc}}$), 4.60 – 4.45 (m, 40H; OCH$_2$CH_2N$_{\text{fuc}}$ and OH), 4.43 (s, 10H; OH), 4.36 – 4.11 (m, 24H; CH_2CH$_3$, COOCH_2CH$_2$O and COOCH_2CH$_2$CH$_2$), 3.93 – 3.83 (m, 10H; OCH_2CH$_2$N$_{\text{fuc}}$), 3.75 – 3.66 (m, 12H; OCH_2CH$_2$N$_{\text{fuc}}$ and CH_2O$_{\text{PEG}}$), 3.57 – 3.43 (m, 56H; CH_{fuc}, CH_2O$_{\text{PEG}}$ and CH_2Br overlaps with water), 2.85 – 2.62 (m, 20H; COOCH$_2$CH$_2$CH_2), 2.11 – 1.86 (m, 20H; COOCH$_2$CH_2CH$_2$), 1.27 – 1.16 (m, 3H; CH_3), 1.06 – 0.89 (m, 30H; C$H_{3\text{ fuc}}$).

^{13}C NMR (176 MHz, DMSO-d_6) δ (ppm) = 162.9 (*C*O), 146.1 (C_{triazole}), 145.0, 140.6 ($C_{\text{sp2 fullerene}}$), 123.6 (*C*H$_{\text{triazole}}$), 99.0 (*C*H$_{1\text{fuc}}$), 71.5 (*C*H$_{\text{fuc}}$), 70.4, 69.8 (*C*H$_2$O$_{\text{PEG}}$), 69.5 (*C*H$_{\text{fuc}}$), 68.7 ($C_{\text{sp3 fullerene}}$), 67.8 (*C*H$_{\text{fuc}}$), 66.6 (COO*C*H$_2$CH$_2$O and COO*C*H$_2$CH$_2$CH$_2$), 66.1 (*C*H$_{\text{fuc}}$), 65.5 (O*C*H$_2$CH$_2$N$_{\text{fuc}}$), 63.4 (*C*H$_2$CH$_3$), 50.0 (OCH$_2$*C*H$_2$N$_{\text{fuc}}$), 45.5 ($C_{\text{q bridge}}$), 32.3 (*C*H$_2$Br), 27.6 (COOCH$_2$*C*H$_2$CH$_2$), 21.6 (COOCH$_2$CH$_2$*C*H$_2$), 16.5 (*C*H$_{3\text{ fuc}}$), 13.8 (*C*H$_3$).

FTIR-ATR (ν cm^{-1}): 3385 (OH), 2932 (C-H), 1738 (C=O).

Compound 27

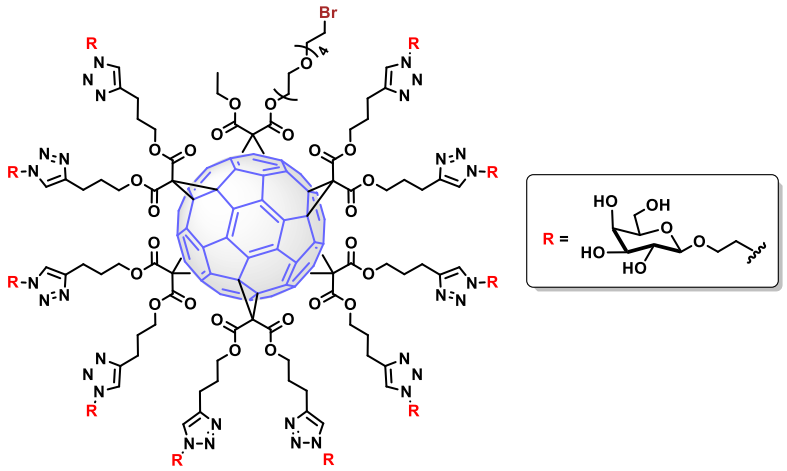

A mixture of 2-azidoethyl β-D-galactopyranoside (**13**) (391 mg, 1.57 mmol), **9** (202 mg, 0.087 mmol), $CuBr{\cdot}S(CH_3)_2$ (91 mg, 0.44 mmol), sodium ascorbate (129 mg, 0.65 mmol) and a piece of copper metal wire in DMSO (1.5 mL) was deoxygenated and kept under argon with vigorous stirring for 72 h. The crude reaction was filtered through a QuadraSil® Mercaptopropyl column. CH_3OH was added to the mixture and the precipitate was centrifuged and extensively washed with CH_3OH, then dried under high vacuum to afford **27** as an orange solid (396 mg, 95%).

^{1}H NMR (700 MHz, DMSO-*d*$_6$) δ (ppm) = 8.03 (s, 10H; C*H*$_{triazole}$), 4.95 (s, 10H; O*H*), 4.74 (s, 10H; O*H*), 4.61 – 4.47 (m, 30H; $OCH_2CH_2N_{gal}$ and O*H*), 4.43 – 4.25 (m, 34H; CH_2CH_3, $COOCH_2CH_2O$, $COOCH_2CH_2CH_2$ and O*H*), 4.18 – 4.12 (m, 10H; C*H*$_{1gal}$), 4.08 – 4.00 (m, 10H; $OCH_2CH_2N_{gal}$), 3.89 – 3.80 (m, 10H; $OCH_2CH_2N_{gal}$), 3.68 – 3.59 (m, 14H; CH_2Br, CH_2O_{PEG} and C*H*$_{gal}$), 3.53 – 3.44 (m, 34H; CH_2OH_{gal} and CH_2O_{PEG}), 3.31 – 3.22 (m, 30H; C*H*$_{gal}$ overlaps with water), 2.76 – 2.58 (m, 20H; $COOCH_2CH_2CH_2$), 2.09 – 1.86 (m, 20H; $COOCH_2CH_2CH_2$), 1.28 – 1.13 (m, 3H; CH_3).

^{13}C NMR (176 MHz, DMSO-*d*$_6$) δ (ppm) = 162.7 (*C*O), 144.8 (*C*$_{triazole}$ and *C*$_{sp2\ fullerene}$), 140.5 (*C*$_{sp2\ fullerene}$), 123.5 (*C*H$_{triazole}$), 103.2 (*C*H$_{1gal}$), 75.2, 73.1, 70.2 (*C*H$_{gal}$), 69.6, 69.4 (CH_2O_{PEG}), 68.5 (*C*$_{sp3\ fullerene}$), 68.0 (*C*H$_{gal}$), 66.9 ($OCH_2CH_2N_{gal}$), 66.5 ($COOCH_2CH_2O$ and $COOCH_2CH_2CH_2$), 63.2 (CH_2CH_3), 60.3 (CH_2OH_{gal}), 49.6 ($OCH_2CH_2N_{gal}$), 45.3 (*C*$_{q\ bridge}$), 32.1 (CH_2Br), 27.4 ($COOCH_2CH_2CH_2$), 21.4 ($COOCH_2CH_2CH_2$), 13.6 (CH_3).

FTIR-ATR (ν cm^{-1}): 3359 (OH), 2928 (C-H), 1740 (C=O).

Compound 28

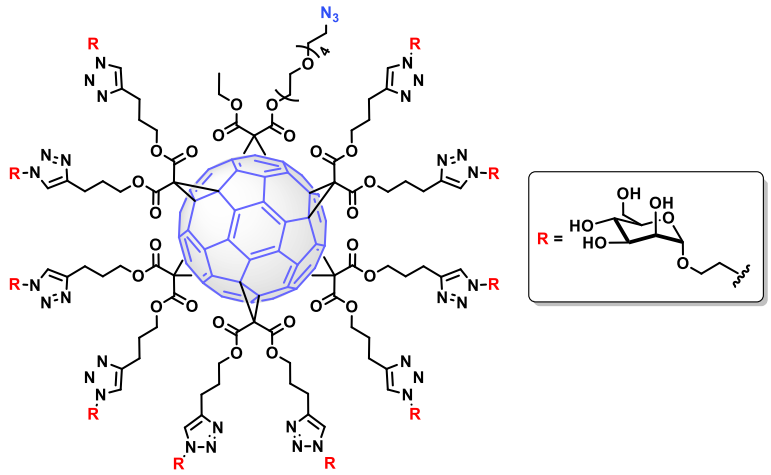

A mixture of **25** (121 mg, 0.025 mmol) and NaN_3 (16 mg, 0.25 mmol) in DMSO-*d*$_6$ (0.8 mL) was heated for 90 min at 55 ºC under microwave irradiation. The crude was purified by size-exclusion chromatography (Sephadex G-25 H_2O/CH_3OH 9:1) to afford **28** as a brown glassy solid (93 mg, 78%).

^{1}H NMR (700 MHz, DMSO-*d*$_6$) δ (ppm) = 7.82 (s, 10H; C*H*$_{triazole}$), 4.75 (s, 20H; O*H*), 4.62 – 4.57 (m, 20H; C*H*$_{1man}$ and O*H*), 4.53 – 4.45 (m, 30H; OCH$_2$C*H*$_2$N$_{man}$ and O*H*), 4.41 – 4.20 (m, 24H; C*H*$_2$CH$_3$, COOC*H*$_2$CH$_2$O and COOC*H*$_2$CH$_2$CH$_2$), 3.94 – 3.89 (m, 10H; OC*H*$_2$CH$_2$N$_{man}$), 3.79 – 3.73 (m, 10H; OC*H*$_2$CH$_2$N$_{man}$), 3.62 – 3.56 (m, 14H; C*H*$_2$OH$_{man}$ and C*H*$_2$O$_{PEG}$), 3.54 – 3.42 (m, 32H; C*H*$_2$O$_{PEG}$, C*H*$_{man}$ and C*H*$_2$OH$_{man}$ overlaps with water), 3.37 – 3.32 (m, 22H; C*H*$_{man}$ and C*H*$_2$N$_3$), 3.15 – 3.07 (m, 10H; C*H*$_{man}$), 2.75 – 2.59 (m, 20H; COOCH$_2$CH$_2$C*H*$_2$), 2.05 – 1.89 (m, 20H; COOCH$_2$C*H*$_2$CH$_2$), 1.27 – 1.16 (m, 3H; C*H*$_3$).

^{13}C NMR (176 MHz, DMSO-*d*$_6$) δ (ppm) = 162.9 (*C*O), 145.7 (*C*$_{triazole}$), 145.2, 140.8 (C$_{sp2\ fullerene}$), 122.3 (*C*H$_{triazole}$), 99.8 (*C*H$_{1man}$), 74.1, 70.9, 70.1 (*C*H$_{man}$), 69.8, 69.7, 69.3 (*C*H$_2$O$_{PEG}$), 68.8 (C$_{sp3\ fullerene}$), 68.0 (COO*C*H$_2$CH$_2$O), 66.8 (COO*C*H$_2$CH$_2$CH$_2$ and *C*H$_{man}$), 64.9 (O*C*H$_2$CH$_2$N$_{man}$), 63.4 (*C*H$_2$CH$_3$), 61.2 (*C*H$_2$OH$_{man}$), 50.0 (*C*H$_2$N$_3$), 49.3 (OCH$_2$*C*H$_2$N$_{man}$), 45.6 (*C*$_{q\ bridge}$), 27.8 (COOCH$_2$*C*H$_2$CH$_2$), 21.4 (COOCH$_2$CH$_2$*C*H$_2$), 13.8 (*C*H$_3$).

FTIR-ATR (ν cm^{-1}): 3372 (OH), 2927 (C-H), 2105 (N_3), 1739 (C=O).

Compound 29

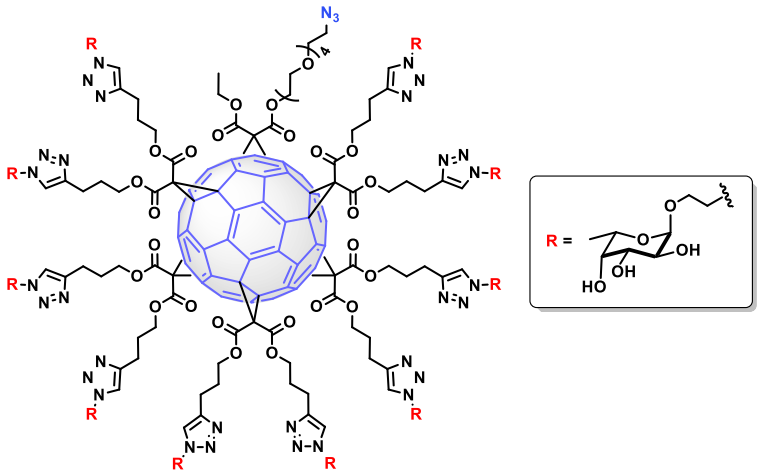

A mixture of **26** (150 mg, 0.032 mmol) and NaN_3 (21 mg, 0.32 mmol) in DMSO-d_6 (0.8 mL) was heated for 90 min at 55 ºC under microwave irradiation. The crude was purified by size-exclusion chromatography (Sephadex G-25 H_2O/CH_3OH 9:1) to afford **29** as a brown glassy solid (139 mg, 91%).

^{1}H NMR (700 MHz, DMSO-d_6) δ (ppm) = 7.92 (s, 10H; C$H_{triazole}$), 4.64 – 4.60 (m, 10H; CH_{1fuc}), 4.56 – 4.45 (m, 40H; OCH$_2$CH_2N$_{fuc}$ and O*H*), 4.42 (s, 10H; O*H*), 4.37 – 4.16 (m, 24H; CH_2CH$_3$, COOCH_2CH$_2$O and COOCH_2CH$_2$CH$_2$), 3.88 – 3.82 (m, 10H; OCH_2CH$_2$N$_{fuc}$), 3.72 – 3.67 (m, 10H; OCH_2CH$_2$N$_{fuc}$), 3.57 – 3.43 (m, 2H; CH_2O$_{PEG}$), 3.53 – 3.51 (m, 10H; CH_{fuc}), 3.49 – 3.44 (m, 24H; CH_{fuc} and CH_2O$_{PEG}$), 3.38 – 3.34 (m, 22H; CH_{fuc} and CH_2N$_3$), 2.72 – 2.56 (m, 20H; COOCH$_2$CH$_2$CH_2), 2.04 – 1.87 (m, 20H; COOCH$_2$CH_2CH$_2$), 1.25 – 1.16 (m, 3H; CH_3), 0.97 (d, $^3J_{H,H}$ = 6.1 Hz, 30H; CH_3).

^{13}C NMR (176 MHz, DMSO-d_6) δ (ppm) = 162.9 (*C*O), 145.7 (*C*$_{triazole}$), 145.1, 140.8 (*C*$_{sp2\ fullerene}$), 122.7 (*C*H$_{triazole}$), 99.0 (*C*H$_{1fuc}$), 71.6 (*C*H$_{fuc}$), 69.9, 69.7 (*C*H$_2$O$_{PEG}$), 69.6 (*C*H$_{fuc}$), 69.3 (*C*H$_2$O$_{PEG}$), 68.8 (*C*$_{sp3\ fullerene}$), 67.9 (*C*H$_{fuc}$), 66.7 (COO*C*H$_2$CH$_2$O and COO*C*H$_2$CH$_2$CH$_2$), 66.1 (*C*H$_{fuc}$), 65.8 (O*C*H$_2$CH$_2$N$_{fuc}$), 63.5 (*C*H$_2$CH$_3$), 50.0 (*C*H$_2$N$_3$), 49.4 (OCH$_2$*C*H$_2$N$_{fuc}$), 45.6 (*C*$_{q\ bridge}$), 27.9 (COOCH$_2$*C*H$_2$CH$_2$), 21.5 (COOCH$_2$CH$_2$*C*H$_2$), 16.5 (*C*H$_{3\ fuc}$), 13.8 (*C*H$_3$).

FTIR-ATR (ν cm^{-1}): 3382 (OH), 2934 (C-H), 2107 (N_3), 1739 (C=O).

Compound 30

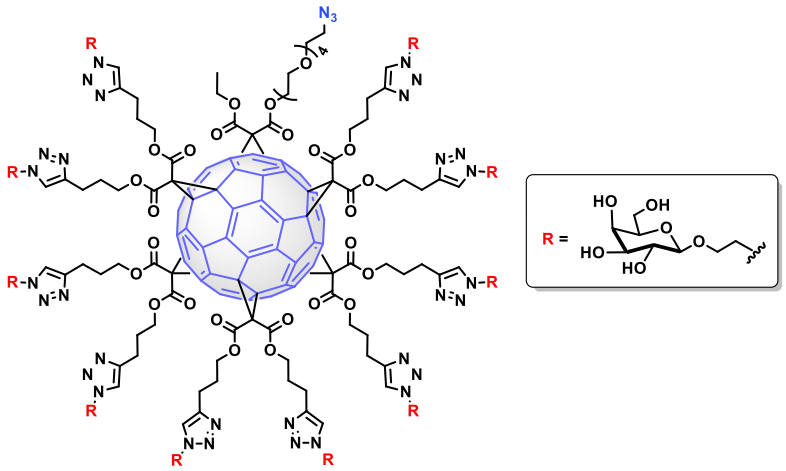

A mixture of **27** (150 mg, 0.031 mmol) and NaN_3 (20 mg, 0.31 mmol) in DMSO-d_6 (0.8 mL) was heated for 90 min at 55 ºC under microwave irradiation. The crude was purified by size-exclusion chromatography (Sephadex G-25 H_2O/CH_3OH 9:1) to afford **30** as a brown glassy solid (85 mg, 58%).

^{1}H NMR (700 MHz, DMSO-d_6) δ (ppm) = 7.91 (s, 10H; C$H_{triazole}$), 4.99 (s, 10H; O*H*), 4.78 (s, 10H; O*H*), 4.64 (s, 10H; O*H*), 4.55 – 4.45 (m, 20H; OCH$_2$C*H*$_2$N$_{gal}$), 4.43 (s, 10H; O*H*), 4.39 – 4.19 (m, 24H; C*H*$_2$CH$_3$, COOC*H*$_2$CH$_2$O and COOC*H*$_2$CH$_2$CH$_2$), 4.14 (d, $^3J_{H,H}$ = 7.4 Hz, 10H; C*H*$_{1gal}$), 4.07 – 4.01 (m, 10H; OC*H*$_2$CH$_2$N$_{gal}$), 3.87 – 3.79 (m, 10H; OC*H*$_2$CH$_2$N$_{gal}$), 3.63 – 3.60 (m, 10H; C*H*$_{gal}$), 3.53 – 3.44 (m, 36H; C*H*$_2$OH$_{gal}$ and C*H*$_2$O$_{PEG}$), 3.37 – 3.33 (m, 12H; C*H*$_{gal}$ and C*H*$_2$N$_3$), 3.31 – 3.23 (m, 20H; C*H*$_{gal}$), 2.76 – 2.56 (m, 20H; COOCH$_2$CH$_2$C*H*$_2$), 2.09 – 1.85 (m, 20H; COOCH$_2$C*H*$_2$CH$_2$), 1.28 – 1.13 (m, 3H; C*H*$_3$).

^{13}C NMR (176 MHz, DMSO-d_6) δ (ppm) = 163.0 (*C*O), 145.7 (*C*$_{triazole}$), 145.2, 140.9 (*C*$_{sp2\ fullerene}$), 122.9 (*C*H$_{triazole}$), 103.5 (*C*H$_{1gal}$), 75.4, 73.4, 70.5 (*C*H$_{gal}$), 69.9, 69.8 (*C*H$_2$O$_{PEG}$), 69.0 (*C*$_{sp3\ fullerene}$), 68.2 (*C*H$_{gal}$), 67.3 (O*C*H$_2$CH$_2$N$_{gal}$), 66.8 (COO*C*H$_2$CH$_2$O and COO*C*H$_2$CH$_2$CH$_2$), 63.5 (*C*H$_2$CH$_3$), 60.6 (*C*H$_2$OH$_{gal}$), 50.1 (*C*H$_2$N$_3$), 49.6 (OCH$_2$*C*H$_2$N$_{gal}$), 45.6 (*C*$_{q\ bridge}$), 27.8 (COOCH$_2$*C*H$_2$CH$_2$), 21.5 (COOCH$_2$CH$_2$*C*H$_2$), 13.9 (*C*H$_3$).

FTIR-ATR (ν cm^{-1}): 3373 (OH), 2927 (C-H), 2113 (N_3), 1738 (C=O).

Compound 31

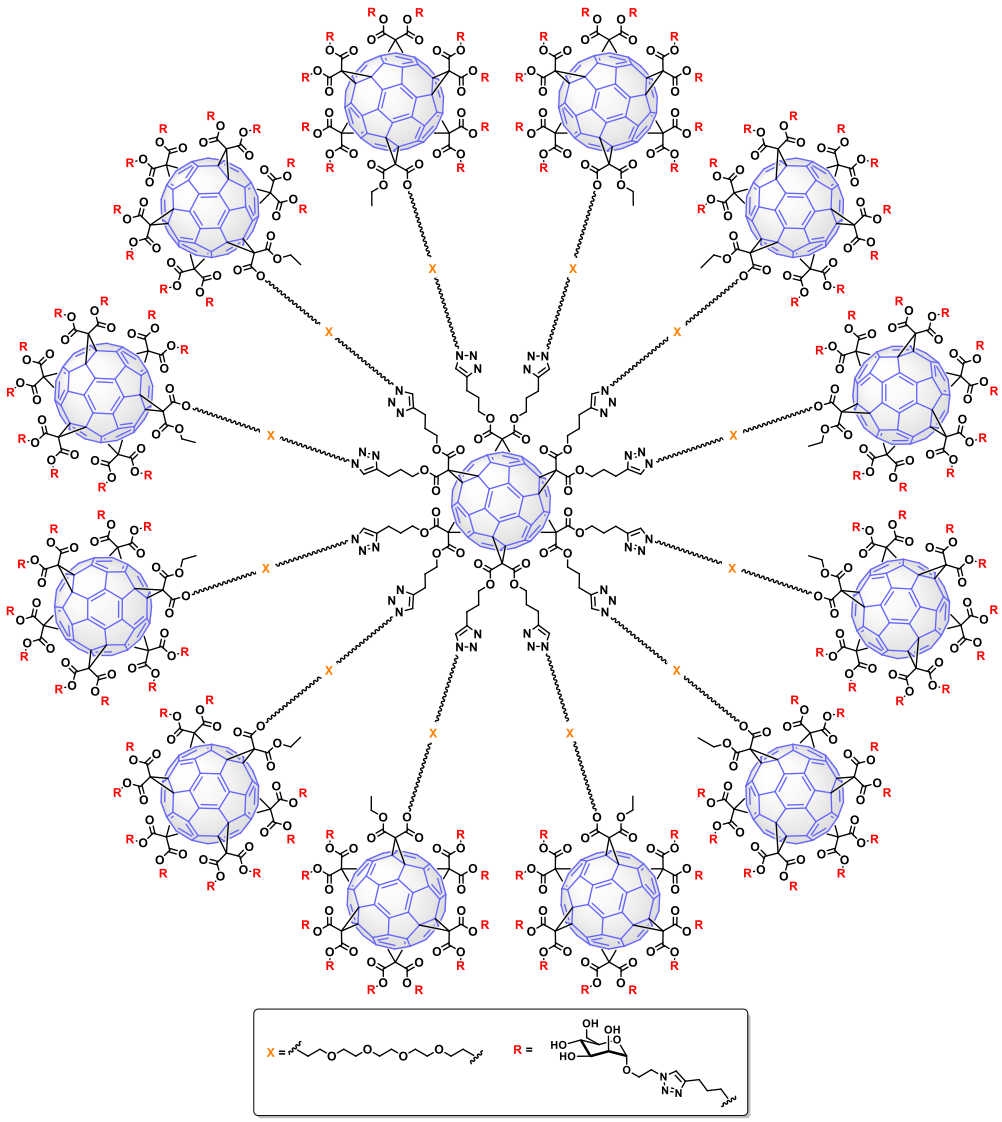

A mixture of **28** (181 mg, 0.038 mmol), **10** (5 mg, 2.4 μmol), $CuBr{\cdot}S(CH_3)_2$ (60 mg, 0.29 mmol), sodium ascorbate (109 mg, 0.55 mmol) and a piece of copper metal wire in DMSO (1.5 mL) was deoxygenated and kept under argon with vigorous stirring for 72 h. The crude reaction was filtered through a QuadraSil® Mercaptopropyl column and purified by size-exclusion chromatography (Sephadex G-50 H_2O/CH_3OH 9:1) to afford **31** as a brown solid (127 mg, 90%).

^{1}H NMR (700 MHz, DMSO-d_6) δ (ppm) = 7.82 (s, 132H; C$H_{triazole}$), 4.73 (s, 240H; O*H*), 4.63 – 4.56 (m, 240H; CH_{1man} and O*H*), 4.53 – 4.42 (m, 384H; OCH_2CH_2N and O*H*), 4.38 – 4.10 (m, 312H; CH_2CH_3, $COOCH_2CH_2O$ and $COOCH_2CH_2CH_2$), 3.94 – 3.88 (m, 120H; $OCH_2CH_2N_{man}$), 3.79 – 3.72 (m, 144H; $OCH_2CH_2N_{man}$ and CH_2O_{PEG}), 3.61 – 3.58 (m, 120H; CH_2OH_{man}), 3.56 – 3.46 (m, 288H; CH_2O_{PEG} and

C*H*$_{man}$), 3.44 – 3.37 (m, 360H; C*H*$_2$OH$_{man}$ and C*H*$_{man}$ overlaps with water) 3.14 – 3.07 (m, 120H; C*H*$_{man}$), 2.78 – 2.57 (m, 264H; COOCH$_2$CH$_2$C*H*$_2$), 2.11 – 1.80 (m, 264H; COOCH$_2$C*H*$_2$CH$_2$), 1.30 – 1.12 (m, 36H; C*H*$_3$).

^{13}C NMR (176 MHz, DMSO-d_6) δ (ppm) = 162.9 (*C*O), 145.6 ($C_{triazole}$), 145.1, 140.6 ($C_{sp2\ fullerene}$), 122.3 (*C*H$_{triazole}$), 99.8 (*C*H$_{1man}$), 74.1, 70.8, 70.1 (*C*H$_{man}$), 69.7 (*C*H$_2$O$_{PEG}$), 68.7 ($C_{sp3\ fullerene}$), 66.7 (COO*C*H$_2$CH$_2$O, COO*C*H$_2$CH$_2$CH$_2$ and *C*H$_{man}$), 64.9 (O*C*H$_2$CH$_2$N$_{man}$), 63.3 (*C*H$_2$CH$_3$), 61.1 (*C*H$_2$OH$_{man}$), 49.2 (OCH$_2$*C*H$_2$N), 45.4 ($C_{q\ bridge}$), 27.8 (COOCH$_2$*C*H$_2$CH$_2$), 21.4 (COOCH$_2$CH$_2$*C*H$_2$), 13.7 (*C*H$_3$).

FTIR (KBr) (ν cm^{-1}): 3404 (OH), 2927 (C-H), 1740 (C=O).

Compound 32

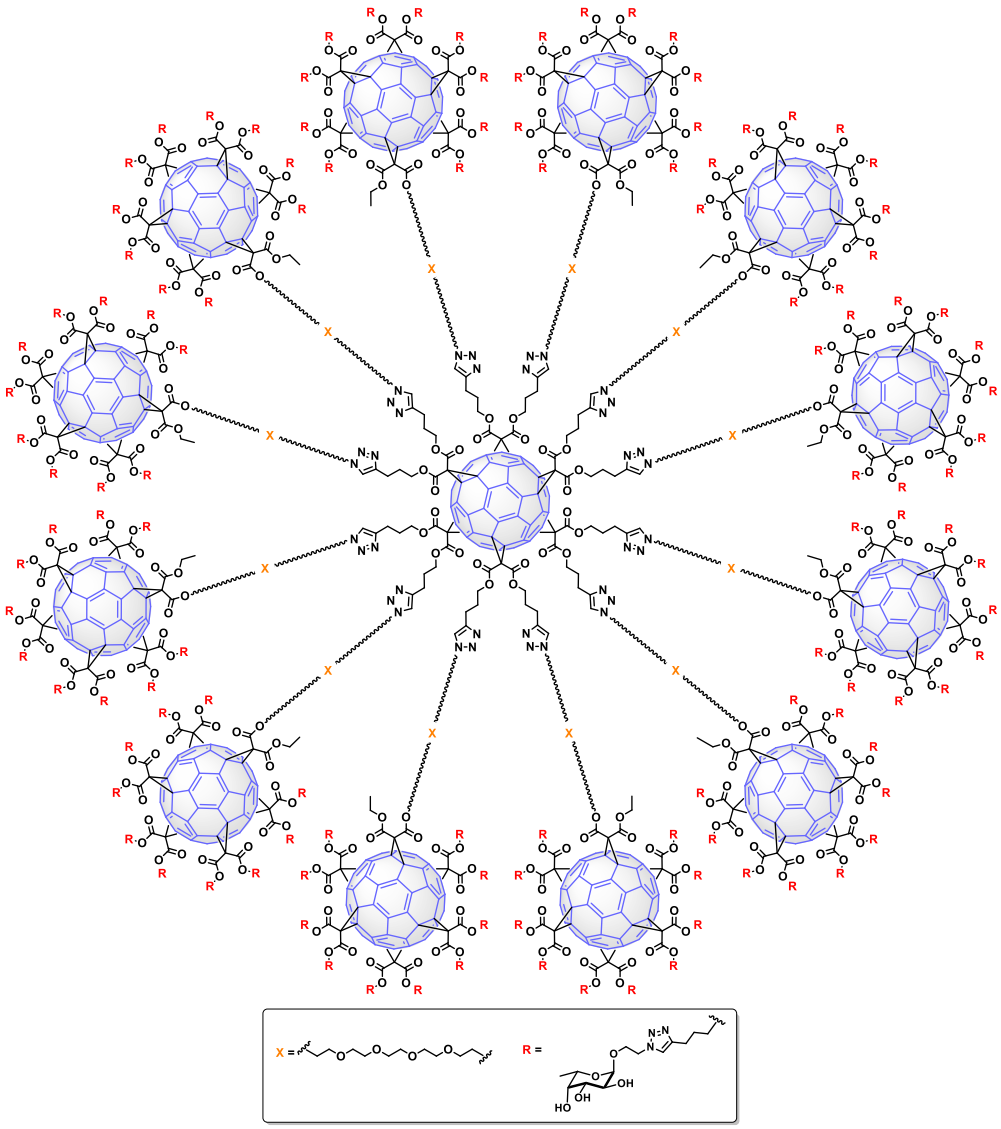

A mixture of **29** (139 mg, 0.030 mmol), **10** (4 mg, 1.9 µmol), $CuBr{\cdot}S(CH_3)_2$ (47 mg, 0.23 mmol), sodium ascorbate (85 mg, 0.43 mmol) and a piece of copper metal wire in DMSO (1.5 mL) was deoxygenated and kept under argon with vigorous stirring for 72 h. The crude reaction was filtered through a QuadraSil® Mercaptopropyl column and purified by size-exclusion chromatography (Sephadex G-50 H_2O/CH_3OH 9:1) to afford **32** as a brown solid (67 mg, 62%).

^{1}H NMR (700 MHz, DMSO-d_6) δ (ppm) = 7.95 (s, 132H; C$H_{triazole}$), 4.64 – 4.60 (m, 120H; CH_{1fuc}), 4.57 – 4.41 (m, 624H; OCH_2CH_2N and O*H*), 4.37 – 4.14 (m, 312H; CH_2CH_3, $COOCH_2CH_2O$ and $COOCH_2CH_2CH_2$), 3.88 – 3.82 (m, 120H; $OCH_2CH_2N_{fuc}$), 3.73 – 3.66 (m, 144H; $OCH_2CH_2N_{fuc}$ and CH_2O_{PEG}), 3.55 – 3.48 (m, 408H; CH_{fuc} and CH_2O_{PEG} overlaps with water), 3.38 – 3.35 (m, 240H; CH_{fuc} overlaps

with water), 2.78 – 2.56 (m, 264H; $COOCH_2CH_2CH_2$), 2.04 – 1.81 (m, 264H; $COOCH_2CH_2CH_2$), 1.25 – 1.15 (m, 36H; CH_3), 1.00 – 0.92 (m, 360H; $CH_{3\ fuc}$).

^{13}C NMR (176 MHz, DMSO-d_6) δ (ppm) = 162.9 (*C*O), 145.8 ($C_{triazole}$), 145.1, 140.8 ($C_{sp2\ fullerene}$), 122.9 ($CH_{triazole}$), 99.0 (CH_{1fuc}), 71.6 (CH_{fuc}), 69.8 (CH_2O_{PEG}), 69.6 (CH_{fuc}), 68.8 ($C_{sp3\ fullerene}$), 67.9 (CH_{fuc}), 66.6 ($COOCH_2CH_2O$ and $COOCH_2CH_2CH_2$), 66.1 (CH_{fuc}), 65.7 ($OCH_2CH_2N_{fuc}$), 63.5 (CH_2CH_3), 49.5 (OCH_2CH_2N), 45.6 ($C_{q\ bridge}$), 27.8 ($COOCH_2CH_2CH_2$), 21.5 ($COOCH_2CH_2CH_2$), 16.5 ($CH_{3\ fuc}$), 13.8 (CH_3).

FTIR-ATR (ν cm^{-1}): 3382 (OH), 2934 (C-H), 1738 (C=O).

Compound 33

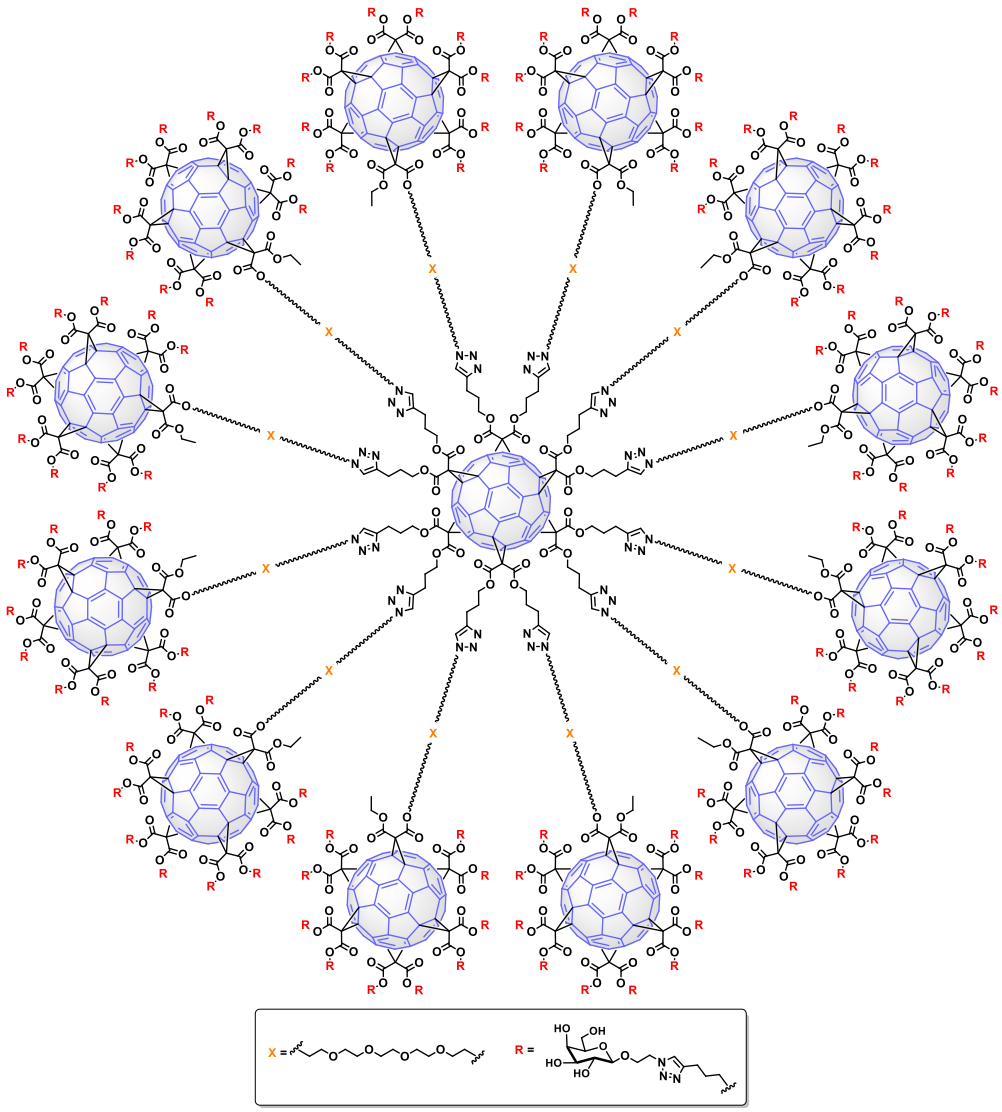

A mixture of **30** (143 mg, 0.030 mmol), **10** (4 mg, 1.9 µmol), $CuBr{\cdot}S(CH_3)_2$ (47 mg, 0.23 mmol), sodium ascorbate (85 mg, 0.43 mmol) and a piece of copper metal wire in DMSO (1.5 mL) was deoxygenated and kept under argon with vigorous stirring for 72 h. The crude reaction was filtered through a QuadraSil® Mercaptopropyl column and purified by size-exclusion chromatography (Sephadex G-50 H_2O/CH_3OH 9:1) to afford **33** as a brown solid (38 mg, 34%).

^{1}H NMR (700 MHz, DMSO-*d*$_6$) δ (ppm) = 7.95 (s, 132H; C*H*$_{triazole}$), 4.98 (s, 120H; O*H*), 4.78 (s, 120H; O*H*), 4.62 (s, 120H; O*H*), 4.59 – 4.46 (m, 264H; OCH_2CH_2N), 4.43 (s, 12H; O*H*), 4.41 – 4.17 (m, 312H; CH_2CH_3, $COOCH_2CH_2O$ and $COOCH_2CH_2CH_2$), 4.17 – 4.11 (m, 120H; C*H*$_{1gal}$), 4.08 – 4.01 (m, 120H; $OCH_2CH_2N_{gal}$), 3.90 – 3.78 (m, 144H; $OCH_2CH_2N_{gal}$ and CH_2O_{PEG}), 3.64 – 3.59 (m,

120H; CH_{gal}), 3.55 – 3.44 (m, 408H; CH_2OH$_{gal}$ and CH_2O$_{PEG}$), 3.36 – 3.33 (m, 120H; CH_{gal}), 3.31 – 3.23 (m, 240H; CH_{gal}), 2.88 – 2.54 (m, 264H; COOCH$_2$CH$_2$CH_2), 2.11 – 1.78 (m, 264H; COOCH$_2$CH_2CH$_2$), 1.27 – 1.15 (m, 36H; CH_3).

^{13}C NMR (176 MHz, DMSO-d_6) δ (ppm) = 162.9 (*C*O), 145.8 ($C_{triazole}$), 145.2, 140.7 ($C_{sp2\ fullerene}$), 123.0 (*C*H$_{triazole}$), 103.5 (*C*H$_{1gal}$), 75.4, 73.3, 70.4 (*C*H$_{gal}$), 69.7 (*C*H$_2$O$_{PEG}$), 68.9 ($C_{sp3\ fullerene}$), 68.2 (*C*H$_{gal}$), 67.2 (O*C*H$_2$CH$_2$N$_{gal}$), 66.7 (COO*C*H$_2$CH$_2$O and COO*C*H$_2$CH$_2$CH$_2$), 63.4 (*C*H$_2$CH$_3$), 60.5 (*C*H$_2$OH$_{gal}$), 50.0 (OCH$_2$*C*H$_2$N), 49.6 (OCH$_2$*C*H$_2$N), 45.6 ($C_{q\ bridge}$), 27.7 (COOCH$_2$*C*H$_2$CH$_2$), 21.5 (COOCH$_2$CH$_2$*C*H$_2$), 13.8 (*C*H$_3$).

FTIR-ATR (ν cm^{-1}): 3354 (OH), 2929 (C-H), 1737 (C=O).

Compound 36[194]

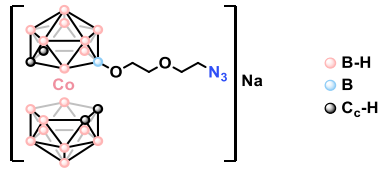

[3,3'-Co(8-C$_4$H$_8$O$_2$-1,2-C$_2$B$_9$H$_{10}$)(1',2'-C$_2$B$_9$H$_{11}$)] (**34**) (300 mg, 0.73 mmol) and NaN$_3$ (380 mg, 5.85 mmol) were dissolved in dry DMF (5 mL) under argon atmosphere and the mixture was stirred at 80 ºC for 16 h. Then, the crude was filtered over celite, evaporated to dryness under vacuum and purified by column chromatography (SiO$_2$, CH$_2$Cl$_2$ → CH$_2$Cl$_2$/MeOH 97:3) to afford **36** as an orange solid (332 mg, 96%).

^{1}H NMR (300 MHz, Acetone-d_6) δ (ppm) = 4.26 (s, 4H; C$_{cluster}$-*H*), 3.67 (t, $^3J_{H,H}$ = 5.0 Hz, 2H; CH_2O), 3.62 – 3.51 (m, 4H; CH_2O), 3.38 (t, $^3J_{H,H}$ = 5.0 Hz, 2H; CH_2N$_3$).

^{13}C NMR (75 MHz, Acetone-d_6) δ (ppm) = 72.6, 70.6, 69.3 (*C*H$_2$O), 55.3 ($C_{cluster}$-H), 51.5 (*C*H$_2$N$_3$), 47.3 ($C_{cluster}$-H).

Compound 37[195]

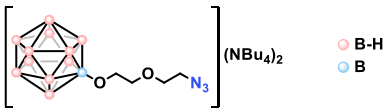

[Bu$_4$N][B$_{12}$H$_{11}$(C$_4$H$_8$O$_2$)] (**35**) (258 mg, 0.55 mmol), [NBu$_4$]Br (203 mg, 0.61 mmol) and NaN$_3$ (143 mg, 2.20 mmol) were dissolved in ethanol 96% (v/v) (8 mL) under argon atmosphere and the mixture was stirred at 80 ºC for 16 h. Then, the crude was concentrated under vacuum, a few drops of water were added, and the precipitate was

[194] B. A. Wojtczak, A. Andrysiak, B. Grüner, Z. J. Lesnikowski, *Chem. Eur. J.* **2008**, *14*, 10675.
[195] A. V. Orlova, N. N. Kondakov, B. G. Kimel, L. O. Kononov, E. G. Kononova, I. B. Sivaev, V. I. Bregadze, *Appl. Organometal. Chem.* **2007**, *21*, 98.

filtered off and washed with water (3 – 4 mL) to afford **37** as a white solid (258 mg, 62%).

**In the ^{1}H NMR spectrum, the integrals in the 0.50 – 2.00 ppm region do not correspond to the actual number of protons, as this range includes signals from B-H protons.*

^{1}H NMR (500 MHz, Acetone-d_6) δ (ppm) = 3.72 (t, $^{3}J_{H,H}$ = 5.0 Hz, 2H; CH_2O), 3.70 – 3.65 (m, 2H; CH_2O), 3.55 (t, $^{3}J_{H,H}$ = 5.8 Hz, 2H; CH_2O), 3.46 – 3.42 (m, 16H; NCH_2CH$_2$CH$_2$CH$_3$), 3.36 (t, $^{3}J_{H,H}$ = 5.8 Hz, 2H; CH_2N$_3$), 1.85 – 1.78 (m, 16H; NCH$_2$CH_2CH$_2$CH$_3$), 1.45 (s, $^{3}J_{H,H}$ = 7.4 Hz, 16H; NCH$_2$CH$_2$CH_2CH$_3$), 0.98 (t, $^{3}J_{H,H}$ = 7.4 Hz, 24H; NCH$_2$CH$_2$CH$_2$CH_3).

^{13}C NMR (126 MHz, Acetone-d_6) δ (ppm) = 73.6, 70.4, 69.0 (*C*H$_2$O), 59.5 (N*C*H$_2$CH$_2$CH$_2$CH$_3$), 51.8 (*C*H$_2$N$_3$), 24.6 (NCH$_2$*C*H$_2$CH$_2$CH$_3$), 20.4 (NCH$_2$CH$_2$*C*H$_2$CH$_3$), 13.9 (NCH$_2$CH$_2$CH$_2$*C*H$_3$).

Compound 38

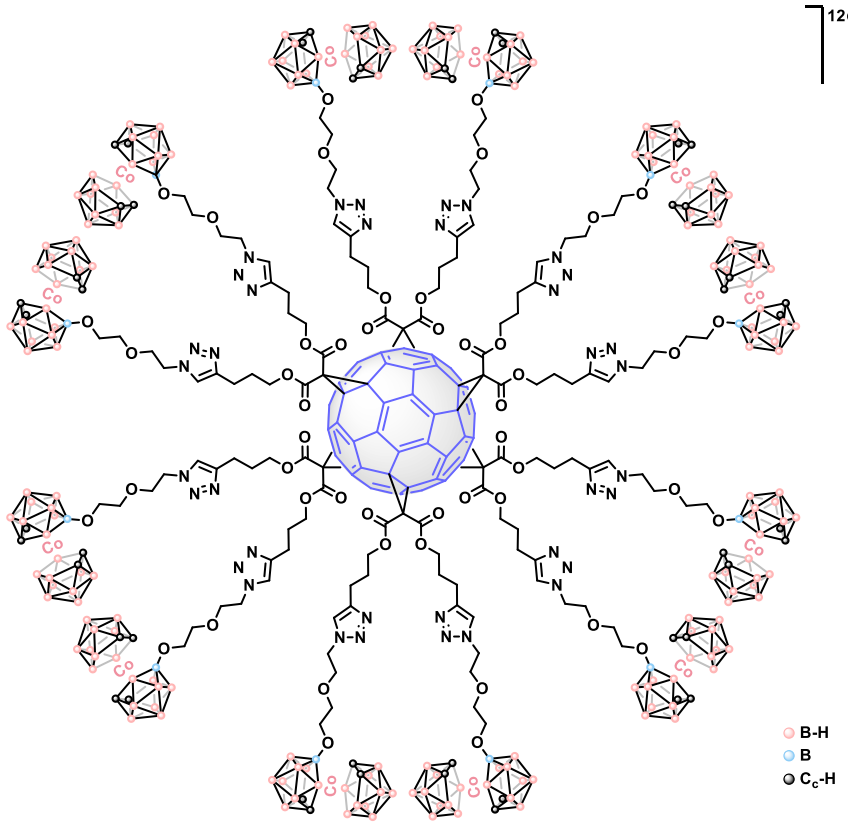

A mixture of **10** (20 mg, 9.4 µmol), **36** (72 mg, 0.15 mmol), CuBr·S(CH$_3$)$_2$ (16 mg, 0.075 mmol), sodium ascorbate (30 mg, 0.15 mmol) and a piece of copper metal wire in DMSO (1 mL) was deoxygenated and kept under argon with vigorous stirring for 72 h. The crude reaction was filtered through a QuadraSil® Mercaptopropyl column

and purified by column chromatography (SiO_2, CH_2Cl_2 → CH_2Cl_2/CH_3CN 3:1 → CH_3CN) to afford **38** as a red glassy solid (39 mg, 53%).

^{1}H NMR (700 MHz, Acetone-d_6) δ (ppm) = 7.82 (s, 12H; C$H_{triazole}$), 4.58 – 4.52 (m, 24H; CH_2N), 4.49 – 4.36 (m, 24H; COOCH_2), 4.21 – 4.17 (m, 48H; $C_{cluster}$-H), 3.92 – 3.87 (s, 24H; CH_2O), 3.63 – 3.60 (m, 24H; CH_2O), 3.56 – 3.53 (s, 24H; CH_2O), 2.79 (m, 24H; $COOCH_2CH_2CH_2$ overlaps with B-H), 2.09 (m, 24H; $COOCH_2CH_2CH_2$ overlaps with B-H).

^{13}C NMR (176 MHz, Acetone-d_6) δ (ppm) = 164.1 (*C*O), 146.9 ($C_{sp2\ fullerene}$), 146.5 ($C_{triazole}$), 142.1 ($C_{sp2\ fullerene}$), 123.3 (*C*H$_{triazole}$), 72.6, 70.1 (*C*H$_2$O), 69.4 (*C*H$_2$O and $C_{sp3\ fullerene}$), 67.4 (COO*C*H$_2$), 54.6 ($C_{cluster}$-H), 50.7 (*C*H$_2$N), 47.3 ($C_{cluster}$-H), 29.0 ($COOCH_2CH_2CH_2$), 22.6 ($COOCH_2CH_2CH_2$).

^{11}B{^{1}H} NMR (160 MHz, Acetone-d_6) δ (ppm) = 23.32 (s, 12B; *B*O), 4.46 (s, 24B; *B*H), 0.21 (s, 24B; *B*H), -2.64 (s, 24B; *B*H), -4.62 (s, 24B; *B*H), -8.12 (s, 36B; *B*H), -17.55 (s, 24B; *B*H), -20.64 (s, 24B; *B*H), -28.79 (s, 24B; *B*H).

^{11}B NMR (160 MHz, Acetone-d_6) δ (ppm) = 23.32 (s, 12B; *B*O), 4.48 (d, $^1J_{B,H}$ = 131.1 Hz, 24B; *B*H), 0.25 (d, $^1J_{B,H}$ = 123.1 Hz, 24B; *B*H), -2.68 (d, $^1J_{B,H}$ = 125.4 Hz, 24B; *B*H), -4.42 (d, $^1J_{B,H}$ = 126.9 Hz, 24B; *B*H), -6.12 – -13.01 (m, 36B; *B*H), -17.49 (d, $^1J_{B,H}$ = 139.3 Hz, 24B; *B*H), -20.60 (d, $^1J_{B,H}$ = 155.6 Hz, 24B; *B*H), -29.16 (d, $^1J_{B,H}$ = 151.6 Hz, 24B; *B*H).

FTIR-ATR (ν cm^{-1}): 2947 (C-H), 2560 (B-H), 1740 (C=O).

Compound 39

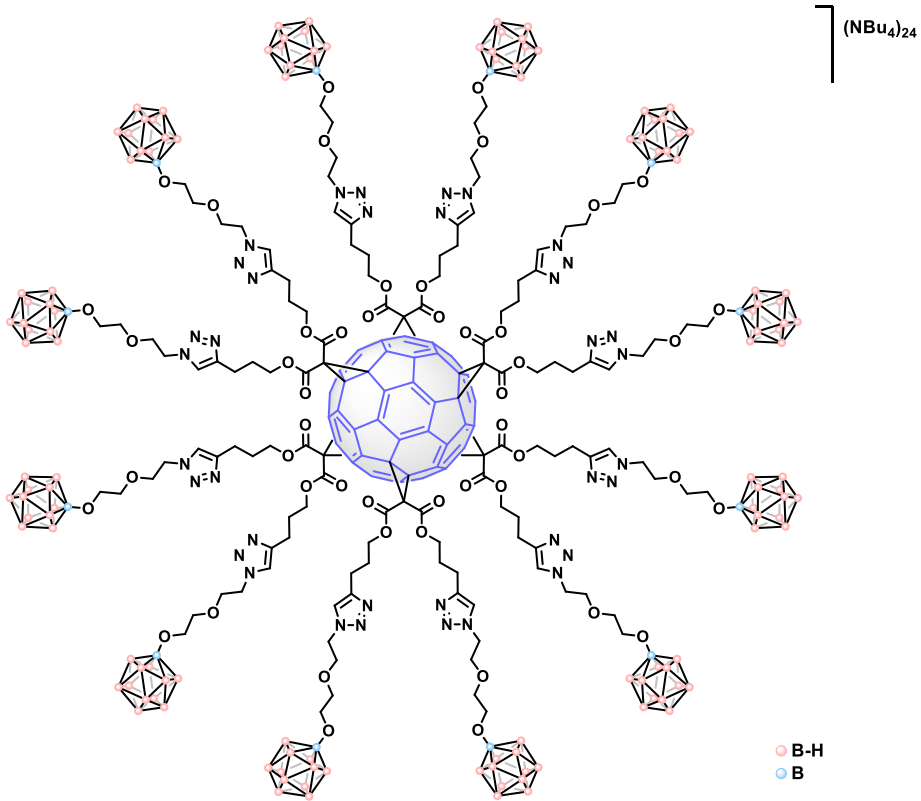

A mixture of **10** (20 mg, 9.6 µmol), **37** (113 mg, 0.15 mmol), $CuBr{\cdot}S(CH_3)_2$ (16 mg, 0.097 mmol), sodium ascorbate (30 mg, 0.15 mmol) and a piece of copper metal wire in DMSO (1 mL) was deoxygenated and kept under argon with vigorous stirring for 72 h. The crude reaction was filtered through a QuadraSil® Mercaptopropyl column. Acetone was first added to the crude to precipitate **37** excess and then, to the filtrate, H_2O and sat. $[NBu_4]Br$ was added and filtered off to afford **39** as an orange solid (65 mg, 60%).

^{1}H NMR (700 MHz, Acetone-*d*$_6$) δ (ppm) = 8.18 (s, 12H; C*H*$_{triazole}$), 4.59 – 4.54 (m, 24H; OCH_2CH_2N), 4.54 – 4.37 (m, 24H; $COOCH_2$), 3.91 – 3.84 (m, 24H; CH_2O), 3.68 – 3.62 (m, 24H; CH_2O), 3.59 – 3.54 (m, 24H; CH_2O), 3.42 – 3.37 (m, 192; $NCH_2CH_2CH_2CH_3$), 2.86 – 2.75 (m, 24H; $COOCH_2CH_2CH_2$), 2.23 – 2.10 (m, 24H; $COOCH_2CH_2CH_2$), 1.80 – 1.75 (m, 192H; $NCH_2CH_2CH_2CH_3$), 1.44 (m, $^3J_{H,H}$ = 7.4 Hz, 192H; $NCH_2CH_2CH_2CH_3$), 0.97 (t, $^3J_{H,H}$ = 7.5 Hz, 288H; $NCH_2CH_2CH_2CH_3$).

^{13}C NMR (176 MHz, Acetone-*d*$_6$) δ (ppm) = 164.1 (*C*O), 146.6 (*C*$_{sp2\ fullerene}$), 146.5 (*C*$_{triazole}$), 142.1 (*C*$_{sp2\ fullerene}$), 124.4 (*C*H$_{triazole}$), 73.7, 70.1 (*C*H_2O), 69.1 (*C*H_2O and C$_{sp3\ fullerene}$), 68.0 ($COOCH_2$), 59.4 ($NCH_2CH_2CH_2CH_3$), 50.7 (OCH_2CH_2N), 29.2 ($COOCH_2CH_2CH_2$), 24.6 ($NCH_2CH_2CH_2CH_3$), 22.8 ($COOCH_2CH_2CH_2$), 20.4 ($NCH_2CH_2CH_2CH_3$), 14.1 ($NCH_2CH_2CH_2CH_3$).

$^{11}B\{^{1}H\}$ NMR (160 MHz, Acetone-d_6) δ (ppm) = 6.51 (s, 12B; *B*O), -16.51 (s, 60B; *B*H), -17.88 (s, 60B; *B*H), -22.64 (s, 12B; *B*H).

^{11}B NMR (160 MHz, Acetone-d_6) δ (ppm) = 6.56 (s, 12B; *B*O), -14.52 – -20.48 (m, 120B; *B*H), -22.69 (d, $^{1}J_{B,H}$ = 96.8 Hz, 12B; *B*H).

FTIR-ATR (ν cm^{-1}): 2960 (C-H), 2468 (B-H), 1740 (C=O).

Chapter 2

Compound 42[196]

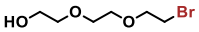

Triphenylphosphine (1.92 g, 7.33 mmol) dissolved in dry CH_2Cl_2 (2 mL) was added dropwise to a solution of triethylene glycol (**40**) (3.00 g, 20.00 mmol) and CBr_4 (2.21 g, 6.66 mmol) in dry CH_2Cl_2 (50 mL) at 0 ºC under argon atmosphere. After 30 min, the mixture was allowed to warm slowly to room temperature and stirred for 3 hours. Then, the crude was evaporated to dryness and purified by column chromatography (SiO_2, Hexane/AcOEt 1:3) to afford **42** as a light-yellow oil (1.18 g, 83%).

^{1}H NMR (300 MHz, $CDCl_3$) δ (ppm) = 3.82 (t, $^3J_{H,H}$ = 6.2 Hz, 2H; OC*H*$_2$CH$_2$Br), 3.76 – 3.72 (m, 2H; HOC*H*$_2$CH$_2$O), 3.71 – 3.67 (m, 4H; C*H*$_2$O), 3.65 – 3.59 (m, 2H; HOCH$_2$C*H*$_2$O), 3.48 (t, $^3J_{H,H}$ = 6.2 Hz, 2H; C*H*$_2$Br), 2.08 (br s, 1H; O*H*).

^{13}C NMR (75 MHz, $CDCl_3$) δ (ppm) = 72.6 (HOCH$_2$*C*H$_2$O), 71.3 (O*C*H$_2$CH$_2$Br), 70.7, 70.5 (*C*H$_2$O), 61.9 (HO*C*H$_2$CH$_2$O), 30.4 (*C*H$_2$Br).

Compound 43[197]

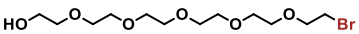

Hexaethylene glycol (**41**) (2.00 g, 7.08 mmol) and triphenylphosphine (929 mg, 3.54 mmol) were dissolved in 25 mL of dry CH_2Cl_2. The solution was purged with argon for 40 min and after that time CBr_4 (1.17 g, 3.54 mmol) was added. The reaction mixture was stirred for 4 h at room temperature. Then, the crude was evaporated to dryness and purified by column chromatography (SiO_2, AcOEt → CH_3Cl/CH_3OH 95:5) to afford **43** as a yellow oil (778 mg, 64%).

^{1}H NMR (300 MHz, $CDCl_3$) δ (ppm) = 3.81 (t, $^3J_{H,H}$ = 6.3 Hz, 2H; OC*H*$_2$CH$_2$Br), 3.74 – 3.70 (m, 2H; HOC*H*$_2$CH$_2$O), 3.69 – 3.64 (m, 16H; C*H*$_2$O), 3.62 – 3.58 (m, 2H; HOCH$_2$C*H*$_2$O), 3.47 (t, $^3J_{H,H}$ = 6.3 Hz, 2H; C*H*$_2$Br), 2.77 (br s, 1H; O*H*).

^{13}C NMR (75 MHz, $CDCl_3$) δ (ppm) = 72.6 (HOCH$_2$*C*H$_2$O), 71.3 (O*C*H$_2$CH$_2$Br), 70.8, 70.7, 70.6, 70.4 (*C*H$_2$O), 61.8 (HO*C*H$_2$CH$_2$O), 30.4 (*C*H$_2$Br).

General procedure for the synthesis of malonates 45a-c

Ethyl malonyl chloride (**4**) (1 eq.) was added dropwise to a solution of the corresponding monobrominated alcohol (1.1 eq.), Et_3N (1.1 eq.) and DMAP (5 mol%) in dry CH_2Cl_2 at 0 ºC under argon atmosphere. After 30 min, the mixture was allowed to warm slowly to room temperature and stirred overnight. Then, the solution was washed with HCl 1M (50 mL) and brine (50 mL). The organic layer was dried over

[196] P.-F. Cao, J. Mangadlao, R. Advincula, *Angew. Chem. Int. Ed.* **2015**, *54*, 5127.
[197] G. Yang, H. Oh, C. Chanthad, Q. Wang, *Chem. Mater.* **2017**, *29*, 9275.

anh. $MgSO_4$, filtered and concentrated under vacuum. The resulting crude was purified by column chromatography under the appropriate conditions.

Compound 45a

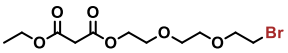

Following the general procedure, using **4** (0.64 mL, 5.04 mmol), **42** (1.18 g, 5.54 mmol), Et_3N (0.77 mL, 5.54 mmol) and DMAP (31 mg, 0.25 mmol) in dry CH_2Cl_2 (50 mL), the crude was purified by column chromatography (SiO_2, Hexane/AcOEt 1:2) to afford **45a** as a light-yellow oil (973 mg, 59%).

^{1}H NMR (300 MHz, $CDCl_3$) δ (ppm) = 4.33 – 4.26 (m, 2H; COOCH_2CH$_2$O), 4.19 (q, $^3J_{H,H}$ = 7.2 Hz, 2H; CH_2CH$_3$), 3.80 (t, $^3J_{H,H}$ = 6.3 Hz, 2H; CH_2CH$_2$Br), 3.74 – 3.69 (m, 2H; COOCH$_2$CH_2O), 3.68 – 3.61 (m, 4H; CH_2O), 3.46 (t, $^3J_{H,H}$ = 6.3 Hz, 2H; CH_2Br), 3.39 (s, 2H; COCH_2CO), 1.27 (t, $^3J_{H,H}$ = 7.2 Hz, 3H; CH_3).

^{13}C NMR (75 MHz, $CDCl_3$) δ (ppm) = 166.7, 166.6 (*C*O), 71.4 (*C*H$_2$CH$_2$Br), 70.7, 70.6 (*C*H$_2$O), 69.1 (COOCH$_2$*C*H$_2$O), 64.6 (COO*C*H$_2$CH$_2$O), 61.7 (*C*H$_2$CH$_3$), 41.6 (CO*C*H$_2$CO), 30.4 (*C*H$_2$Br), 14.2 (*C*H$_3$).

FTIR-ATR (ν cm^{-1}): 2923 (C-H), 1731 (C=O).

ESI: *m/z* calcd for $C_{11}H_{19}BrO_6$: 326.0365, found: 327.0390 $[M+H]^+$.

Compound 45b[33c]

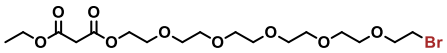

Following the general procedure, using **4** (0.35 mL, 2.77 mmol), **43** (1.05 g, 3.05 mmol), Et_3N (0.42 mL, 3.05 mmol) and DMAP (17 mg, 0.14 mmol) in dry CH_2Cl_2 (25 mL), the crude was purified by column chromatography (SiO_2, AcOEt) to afford **45b** as a yellow oil (799 mg, 63%).

^{1}H NMR (300 MHz, $CDCl_3$) δ (ppm) = 4.24 – 4.19 (m, 2H; COOCH_2CH$_2$O), 4.12 (q, $^3J_{H,H}$ = 7.2 Hz, 2H; CH_2CH$_3$), 3.73 (t, $^3J_{H,H}$ = 6.3 Hz, 2H; CH_2CH$_2$Br), 3.66 – 3.61 (m, 2H; COOCH$_2$CH_2O), 3.61 – 3.64 (m, 16H; CH_2O), 3.39 (t, $^3J_{H,H}$ = 6.3 Hz, 2H; CH_2Br), 3.32 (s, 2H; COCH_2CO), 1.20 (t, $^3J_{H,H}$ = 7.2 Hz, 3H; CH_3).

^{13}C NMR (75 MHz, $CDCl_3$) δ (ppm) = 166.5, 166.3 (*C*O), 71.1 (*C*H$_2$CH$_2$Br), 70.6, 70.5, 70.4 (*C*H$_2$O), 68.8 (COOCH$_2$*C*H$_2$O), 64.5 (COO*C*H$_2$CH$_2$O), 61.4 (*C*H$_2$CH$_3$), 41.4 (CO*C*H$_2$CO), 30.3 (*C*H$_2$Br), 14.0 (*C*H$_3$).

Compound 45c[198]

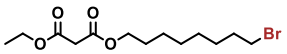

Following the general procedure, using **4** (0.27 mL, 2.10 mmol), 8-bromo-1-octanol (**44**) (483 mg, 2.31 mmol), Et_3N (0.32 mL, 2.31 mmol) and DMAP (13 mg, 0.11 mmol) in dry CH_2Cl_2 (25 mL), the crude was purified by column chromatography (SiO_2, Hexane/AcOEt 1:4) to afford **45c** as a light-yellow oil (666 mg, 98%).

^{1}H NMR (300 MHz, $CDCl_3$) δ (ppm) = 4.19 (q, $^3J_{H,H}$ = 7.2 Hz, 2H; CH_2CH$_3$), 4.12 (t, $^3J_{H,H}$ = 6.7 Hz, 2H; COOCH_2), 3.39 (t, $^3J_{H,H}$ = 6.8 Hz, 2H; CH_2Br), 3.35 (s, 2H; COCH_2CO), 1.83 (p, $^3J_{H,H}$ = 6.9 Hz, 2H; CH_2 linker), 1.70 – 1.57 (m, 2H; CH_2 linker), 1.47 – 1.23 (m, 11H; CH_2 linker and CH_3).

^{13}C NMR (75 MHz, $CDCl_3$) δ (ppm) = 166.8, 166.7 (*C*O), 65.6 (COO*C*H$_2$), 61.6 (*C*H$_2$CH$_3$), 41.8 ($C_{q\ bridge}$), 34.0 (*C*H$_2$Br), 32.8, 29.1, 28.7, 28.5, 28.1, 25.8 (*C*H$_2$ linker), 14.2 (*C*H$_3$).

General procedure for the synthesis of monoadducts 46a-c

DBU (2.5 eq.) was added dropwise to a solution of the corresponding malonate (1 eq.), [60]fullerene (2 eq.) and I_2 (3.5 eq.) in dry toluene (500 mL) under argon at 0 ºC. The reaction mixture was then allowed to warm gradually to room temperature and stirred for 3 hours. After that time, the reaction mixture was washed with sat. $Na_2S_2O_3$ (2 x 100 mL), HCl 0.5 M (2 x 100 mL), water (100 mL) and brine (100 mL). The organic layer was dried over anh. $MgSO_4$, filtered and concentrated under vacuum. The crude was purified by column chromatography under the appropriate conditions.

Compound 46a

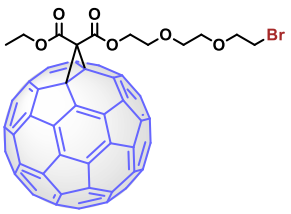

Following the general procedure, using DBU (0.37 mL, 3.83 mmol), **45a** (500 mg, 1.53 mmol), [60]fullerene (2.20 g, 3.06 mmol) and I_2 (1.36 g, 5.36 mmol) in dry toluene (500 mL), the crude was purified by column chromatography (SiO_2, CS_2 → DCM) to afford **46a** as a dark brown solid (401 mg, 31%).

^{1}H NMR (300 MHz, $CDCl_3$) δ (ppm) = 4.69 – 4.63 (m, 2H; COOCH_2CH$_2$O), 4.57 (q, $^3J_{H,H}$ = 7.2 Hz, 2H; CH_2CH$_3$), 3.92 – 3.87 (m, 2H; COOCH$_2$CH_2O), 3.82 (t, $^3J_{H,H}$ = 6.2 Hz, 2H; CH_2CH$_2$Br), 3.74 – 3.64 (m, 4H; CH_2O), 3.48 (t, $^3J_{H,H}$ = 6.2 Hz, 2H; CH_2Br), 1.49 (t, $^3J_{H,H}$ = 7.2 Hz, 3H; CH_3).

[198] P. Piotrowski, J. Pawłowska, J. G. Sadło, R. Bilewicz, A. Kaim, *J. Nanopart. Res.* **2017**, *19*, 161.

^{13}C NMR (75 MHz, $CDCl_3$) δ (ppm) = 163.8, 163.6 (*C*O), 145.5, 145.4, 145.3, 145.0, 144.8, 144.0, 143.2, 143.1, 142.4, 142.3, 142.0, 141.1, 139.3, 139.1 ($C_{sp2\ fullerene}$), 71.7 ($C_{sp3\ fullerene}$), 71.4 (*C*$H_2$$CH_2$Br), 70.8, 70.7 (*C*$H_2$O), 69.1 (COOC$H_2$*C*$H_2$O), 66.3 (COO*C*$H_2$$CH_2$O), 63.6 (*C*$H_2$$CH_3$), 52.3 ($C_{q\ bridge}$), 30.5 (*C*$H_2$Br), 14.4 (*C*$H_3$).

FTIR-ATR (ν cm^{-1}): 2923 (C-H), 1743 (C=O).

MALDI-TOF: *m/z* calcd for $C_{72}H_{21}BrO_6$: 1044.0209, found: 1044.1420 $[M]^+$.

Compound 46b[33c]

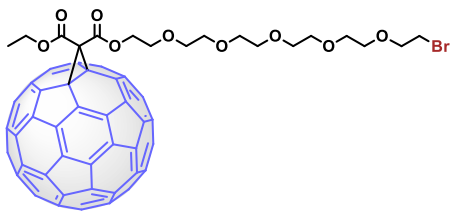

Following the general procedure, using DBU (0.37 mL, 3.83 mmol), **45b** (499 mg, 1.09 mmol), [60]fullerene (1.57 g, 2.18 mmol) and I_2 (970 mg, 3.82 mmol) in dry toluene (500 mL), the crude was purified by column chromatography (SiO_2, CS_2 → Toluene/Acetone 5:1) to afford **46b** as a dark brown solid (637 mg, 50%).

^{1}H NMR (300 MHz, $CDCl_3$) δ (ppm) = 4.67 – 4.61 (m, 2H; COOC*H*$_2$$CH_2$O), 4.55 (q, $^3J_{H,H}$ = 7.1 Hz, 2H; C*H*$_2$$CH_3$), 3.91 – 3.84 (m, 2H; COOCH_2C*H*$_2$O), 3.80 (t, $^3J_{H,H}$ = 6.3 Hz, 2H; C*H*$_2$$CH_2$Br), 3.72 – 3.60 (m, 16H; C*H*$_2$O), 3.46 (t, $^3J_{H,H}$ = 6.3 Hz, 2H; C*H*$_2$Br), 1.48 (t, $^3J_{H,H}$ = 7.1 Hz, 3H; C*H*$_3$).

^{13}C NMR (75 MHz, $CDCl_3$) δ (ppm) = 163.7, 163.5 (*C*O), 145.4, 145.3, 145.0, 144.8, 144.7, 144.0, 143.2, 143.1, 143.0, 142.3, 142.0, 141.0, 139.3, 139.0 ($C_{sp2\ fullerene}$), 71.6 ($C_{sp3\ fullerene}$), 71.3 (*C*$H_2$$CH_2$Br), 70.8, 70.7, 70.6 (*C*H_2O), 68.9 (COOCH_2*C*H_2O), 66.3 (COO*C*$H_2$$CH_2$O), 63.6 (*C*$H_2$$CH_3$), 52.2 ($C_{q\ bridge}$), 30.5 (*C*$H_2$Br), 14.4 (*C*$H_3$).

FTIR-ATR (ν cm^{-1}): 2922 (C-H), 1744 (C=O).

MALDI-TOF: *m/z* calcd for $C_{77}H_{29}BrO_9$: 1176.0995, found: 1176.0993 $[M]^+$.

Compound 46c

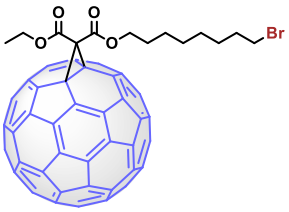

Following the general procedure, using DBU (0.58 mL, 3.88 mmol), **45c** (0.50 g, 1.55 mmol), [60]fullerene (2.23 g, 3.10 mmol) and I_2 (1.38 g, 5.43 mmol) in dry toluene (500 mL), the crude was purified by column chromatography (SiO_2, CS_2 → Toluene) to afford **46c** as a dark brown solid (845 mg, 52%).

^{1}H NMR (300 MHz, $CDCl_3$) δ (ppm) = 4.56 (q, $^{3}J_{H,H}$ = 7.2 Hz, 2H; CH_2CH$_3$), 4.50 (t, $^{3}J_{H,H}$ = 6.6 Hz, 2H; COOCH_2), 3.40 (t, $^{3}J_{H,H}$ = 6.8 Hz, 2H; CH_2Br), 1.92 – 1.78 (m, 4H; C$H_{2\ \text{linker}}$), 1.52 – 1.32 (m, 11H; C$H_{2\ \text{linker}}$ and CH_3).

^{13}C NMR (75 MHz, $CDCl_3$) δ (ppm) = 163.8, 163.7 (*C*O), 145.5, 145.4, 145.3, 145.0, 144.8, 144.7, 144.0, 143.2, 143.1, 143.0, 142.3, 142.0, 141.1, 139.2, 139.1 ($C_{sp2\ \text{fullerene}}$), 71.8 ($C_{sp3\ \text{fullerene}}$), 67.5 (COO*C*H$_2$), 63.6 (*C*H$_2CH_3$), 52.4 ($C_{q\ \text{bridge}}$), 34.1 (*C*H$_2$Br), 32.9, 29.2, 28.8, 28.7, 28.2, 26.0 (*C*H$_{2\ \text{linker}}$), 14.4 (*C*H$_3$).

FTIR-ATR (ν cm^{-1}): 2926 (C-H), 1745 (C=O).

MALDI-TOF: *m/z* calcd for $C_{73}H_{21}BrO_4$: 1040.0623, found: 1040.0589 $[M]^+$.

General procedure for the synthesis of hexakis-adducts 47a-c

DBU (20 eq.) was added dropwise to a solution the corresponding monoadduct (1 eq.), compound **6** (10 eq.) and CBr_4 (80 eq.) in dry toluene under argon atmosphere. The mixture was stirred at room temperature for 72 h. After that time, the reaction mixture was washed with sat. $Na_2S_2O_3$ (100 mL), HCl 1 M (2 x 100 mL), water (100 mL) and brine (100 mL). The organic layer was dried over anh. $MgSO_4$, filtered and concentrated under vacuum. The crude was purified by column chromatography under the appropriate conditions.

Compound 47a

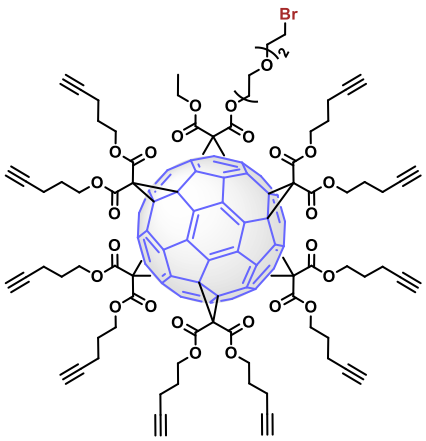

Following the general procedure, using DBU (1.20 mL, 8.00 mmol), **46a** (418 mg, 0.40 mmol), **6** (945 mg, 4.00 mmol) and CBr_4 (10.61 g, 32.00 mmol) in dry toluene (120 mL), the crude was purified by column chromatography (SiO_2, DCM → DCM/Acetone 100:1 → 50:1) to afford **47a** as a red sticky solid (486 mg, 55%).

^{1}H NMR (700 MHz, $CDCl_3$) δ (ppm) = 4.54 – 4.22 (m, 24H; COOCH_2), 3.80 (t, $^{3}J_{H,H}$ = 6.3 Hz, 2H; CH_2CH$_2$Br), 3.74 – 3.56 (m, 6H; COOCH$_2$CH_2O and CH_2O$_{PEG}$), 3.47 (t, $^{3}J_{H,H}$ = 6.3 Hz, 2H; CH_2Br), 2.43 – 2.21 (m, 20H; COOCH$_2$CH$_2$CH_2), 2.11 – 1.74 (m, 30H; COOCH$_2$CH_2CH$_2$ and C≡C*H*), 1.43 – 1.31 (m, 3H; CH_3).

^{13}C NMR (176 MHz, $CDCl_3$) δ (ppm) = 163.8 (*C*O), 145.9, 141.2 ($C_{sp2\ fullerene}$), 82.5 (*C*≡CH), 78.5 (C≡*C*H), 71.4 (*C*$H_2$$CH_2$Br), 70.8, 70.6 (*C*$H_2O_{PEG}$), 69.8 (C≡*C*H), 69.2 ($C_{sp3\ fullerene}$), 68.8 (COOCH$_2$*C*$H_2$O), 65.5 (COO*C*$H_2$$CH_2$O and COO*C*$H_2$$CH_2$$CH_2$), 63.2 (*C*$H_2$$CH_3$), 45.4, 39.5 ($C_{q\ bridge}$), 30.6 (*C*$H_2$Br), 27.3 (COOCH$_2$*C*$H_2$$CH_2$), 16.6, 15.3 (COOCH$_2CH_2$*C*$H_2$), 14.2 (*C*$H_3$).

FTIR-ATR (ν cm^{-1}): 3293 (C≡C-H), 2962 (C-H), 1741 (C=O).

Compound 47b[33c]

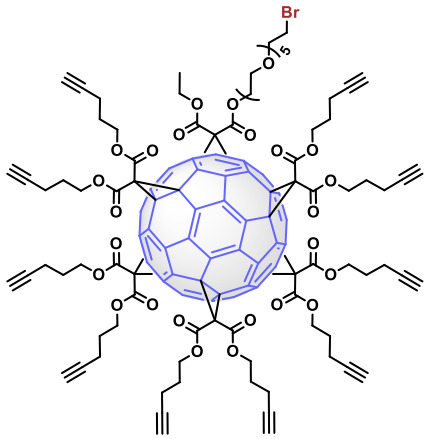

Following the general procedure, using DBU (1.62 mL, 10.80 mmol), **46b** (637 mg, 0.54 mmol), **6** (1.28 mg, 5.40 mmol) and CBr_4 (14.33 g, 43.20 mmol) in dry toluene (120 mL), the crude was purified by column chromatography (SiO_2, DCM → DCM/Acetone 100:1 → 50:1 → 20:1) to afford **47b** as a red sticky solid (682 mg, 54%).

^{1}H NMR (700 MHz, $CDCl_3$) δ (ppm) = 4.52 – 4.20 (m, 24H; COOC*H*$_2$), 3.80 (t, $^{3}J_{H,H}$ = 6.3 Hz, 2H; C*H*$_2$CH$_2$Br), 3.77 – 3.69 (m, 2H; COOCH$_2$C*H*$_2$O), 3.66 – 3.56 (m, 16H; C*H*$_2O_{PEG}$), 3.46 (t, $^{3}J_{H,H}$ = 6.3 Hz, 2H; CH$_2$*H*$_2$Br), 2.44 – 2.17 (m, 20H; COOCH$_2$CH$_2$C*H*$_2$), 2.11 – 1.65 (m, 30H; COOCH$_2$C*H*$_2$CH$_2$ and C≡C*H*), 1.42 – 1.29 (m, 3H; C*H*$_3$).

^{13}C NMR (176 MHz, $CDCl_3$) δ (ppm) = 163.8 (*C*O), 145.9, 141.2 ($C_{sp2\ fullerene}$), 82.6 (*C*≡CH), 78.5 (C≡*C*H), 71.3 (*C*$H_2$$CH_2$Br), 70.7, 70.6 (*C*$H_2O_{PEG}$), 69.8 (C≡*C*H), 69.1 ($C_{sp3\ fullerene}$), 68.7 (COOCH$_2$*C*$H_2$O), 66.0 (COO*C*$H_2$$CH_2$O), 65.5 (COO*C*$H_2$$CH_2$$CH_2$), 63.1 (*C*$H_2$$CH_3$), 45.4, 39.5 ($C_{q\ bridge}$), 30.5 (*C*$H_2$Br), 27.2 (COOCH$_2$*C*$H_2$$CH_2$), 16.5 (COOCH$_2CH_2$*C*$H_2$), 15.2 (COOCH$_2CH_2$*C*$H_2$), 14.2 (*C*$H_3$).

Compound 47c

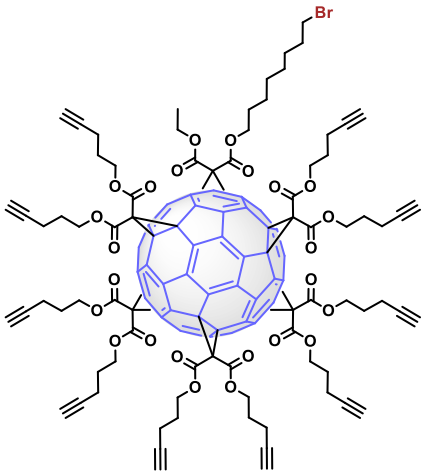

Following the general procedure, using DBU (2.9 mL, 19.40 mmol), **46c** (1.01 g, 0.97 mmol), **6** (2.29 g, 9.70 mmol) and CBr_4 (25.73 g, 77.60 mmol) in dry toluene (300 mL), the crude was purified by column chromatography (SiO_2, Hexane/AcOEt 4:1 → 3:1 → DCM) to afford **47c** as a dark red solid (1.66 g, 77%).

^{1}H NMR (700 MHz, $CDCl_3$) δ (ppm) = 4.62 – 4.13 (m, 24H; $COOCH_2$), 3.42 – 3.38 (m, 2H; CH_2Br), 2.43 – 2.19 (m, 20H; $COOCH_2CH_2CH_2$); 2.09 – 1.80 (m, 30H; $COOCH_2CH_2CH_2$ and $C{\equiv}CH$); 1.78 – 1.67 (m, 2H; $CH_{2\ \text{linker}}$), 1.44 – 1.29 (m, 11H; $CH_{2\ \text{linker}}$ and CH_3).

^{13}C NMR (176 MHz, $CDCl_3$) δ (ppm) = 163.8 (*C*O), 145.9, 141.2 ($C_{sp2\ \text{fullerene}}$), 82.3 (*C*≡CH), 78.5, 69.9 (C≡*C*H), 69.2 ($C_{sp3\ \text{fullerene}}$), 67.1 ($COOCH_2$), 65.5 ($COOCH_2CH_2CH_2$), 63.1 ($CH_2CH_3$), 45.4, 39.5 ($C_{q\ \text{bridge}}$), 34.1 ($CH_2Br$), 32.9, 29.1, 28.7, 28.5, 28.2 ($CH_{2\ \text{linker}}$), 27.3 ($COOCH_2CH_2CH_2$), 25.8 ($CH_{2\ \text{linker}}$), 16.5, 15.3 ($COOCH_2CH_2CH_2$), 14.2 (CH_3).

FTIR-ATR (ν cm^{-1}): 3295 (C≡C-H), 2925 (C-H), 1739 (C=O).

General procedure for the synthesis of glycofullerenes 48a-c

A mixture of the corresponding hexakis-adduct (1 eq.), 2-azidoethyl α-D-mannopyranoside (**11**) (18 eq.), $CuBr{\cdot}S(CH_3)_2$ (5 eq.), sodium ascorbate (7.5 eq.) and a piece of copper metal wire in DMSO (1.5 mL) was deoxygenated and kept under argon with vigorous stirring for 72 h. The crude reaction was filtered through a QuadraSil® Mercaptopropyl column. CH_3OH was added to the mixture and the precipitate was centrifuged, extensively washed with CH_3OH and then dried under high vacuum.

Compound 48a

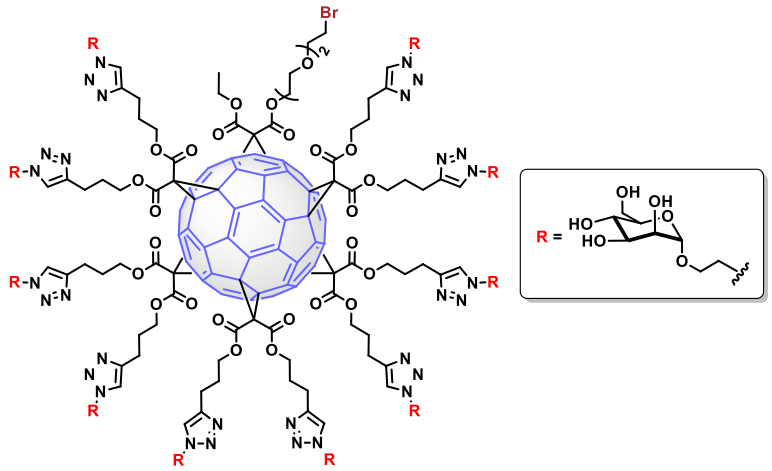

Following the general procedure, using hexakis-adduct **47a** (301 mg, 0.14 mmol), **11** (610 mg, 2.45 mmol), $CuBr{\cdot}S(CH_3)_2$ (144 mg, 0.70 mmol), sodium ascorbate (208 mg, 1.05 mmol) and a piece of copper metal wire in DMSO (1.5 mL), compound **48a** was afforded as an orange solid (659 mg, 88%).

^{1}H NMR (700 MHz, DMSO-d_6) δ (ppm) = 7.88 (s, 10H; C$H_{triazole}$), 4.74 (s, 20H; OH), 4.62 – 4.56 (m, 20H; CH_{1man} and OH), 4.55 – 4.45 (m, 30H; $OCH_2CH_2N_{man}$ and OH), 4.40 – 4.18 (m, 24H; CH_2CH_3, $COOCH_2CH_2O$ and $COOCH_2CH_2CH_2$), 3.95 – 3.88 (m, 10H; $OCH_2CH_2N_{man}$), 3.79 – 3.73 (m, 10H; $OCH_2CH_2N_{man}$), 3.70 – 3.64 (m, 4H; CH_2O_{PEG}), 3.61 – 3.57 (m, 10H; CH_2OH_{man}), 3.54 – 3.50 (m, 12H; CH_{man} and CH_2Br), 3.49 – 3.43 (m, 14H; CH_2OH_{man} and CH_2O_{PEG} overlaps with water), 3.37 – 3.33 (m, 20H; CH_{man}), 3.15 – 3.07 (m, 10H; CH_{man}), 2.77 – 2.58 (m, 20H; $COOCH_2CH_2CH_2$), 2.07 – 1.86 (m, 20H; $COOCH_2CH_2CH_2$), 1.28 – 1.15 (m, 3H; CH_3).

^{13}C NMR (176 MHz, DMSO-d_6) δ (ppm) = 162.8 (CO), 146.0 ($C_{triazole}$), 145.0, 140.7 ($C_{sp2\ fullerene}$), 122.7 (C$H_{triazole}$), 99.8 (CH_{1man}), 74.1, 70.8 (CH_{man}), 70.4 (CH_2O_{PEG}), 70.1 (CH_{man}), 69.6, 69.5 (CH_2O_{PEG}), 68.7 ($C_{sp3\ fullerene}$), 68.0 ($COOCH_2CH_2O$), 66.7 ($COOCH_2CH_2CH_2$ and CH_{man}), 64.8 ($OCH_2CH_2N_{man}$), 63.4 (CH_2CH_3), 61.1 (CH_2OH_{man}), 49.4 ($OCH_2CH_2N_{man}$), 45.5 ($C_{q\ bridge}$), 32.2 (CH_2Br), 27.7 ($COOCH_2CH_2CH_2$), 21.4 ($COOCH_2CH_2CH_2$), 13.8 (CH_3).

FTIR-ATR (ν cm^{-1}): 3375 (OH), 2926 (C-H), 1739 (C=O).

Compound 48b[33c]

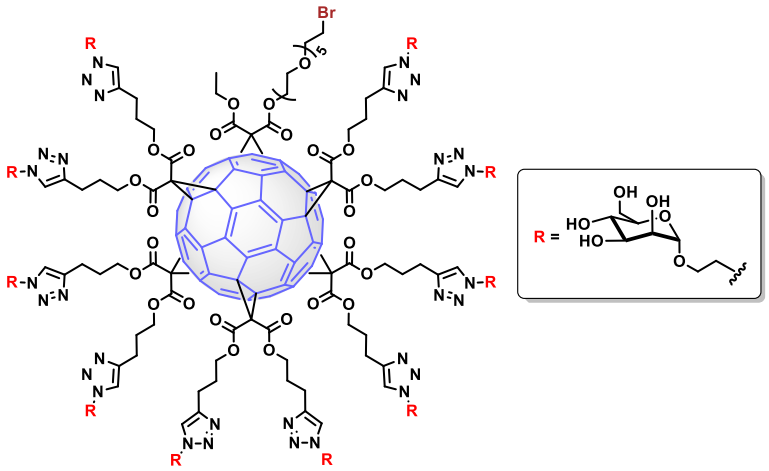

Following the general procedure, using hexakis-adduct **47b** (201 mg, 0.085 mmol), **11** (384 mg, 1.54 mmol), $CuBr{\cdot}S(CH_3)_2$ (88 mg, 0.43 mmol), sodium ascorbate (127 mg, 0.64 mmol) and a piece of copper metal wire in DMSO (1.5 mL), compound **48b** was afforded as an orange solid (350 mg, 85%).

^{1}H NMR (700 MHz, DMSO-d_6) δ (ppm) = 7.99 (s, 10H; C$H_{triazole}$), 4.79 – 4.70 (m, 20H; OH), 4.63 – 4.45 (m, 50H; CH_{1man}, OCH$_2$CH_2N$_{man}$, OH), 4.39 – 4.17 (m, 24H; CH_2CH$_3$, COOCH_2CH$_2$O and COOCH_2CH$_2$CH$_2$), 3.97 – 3.84 (m, 10H; OCH_2CH$_2$N$_{man}$), 3.82 – 3.75 (m, 10H; OCH_2CH$_2$N$_{man}$), 3.71 – 3.67 (m, 4H; CH_2O$_{PEG}$), 3.62 – 3.57 (m, 10H; CH_2OH$_{man}$), 3.53 – 3.38 (m, 58H; CH_2OH$_{man}$, CH_2Br, CH_2O$_{PEG}$ and CH_{man}), 3.15 – 3.05 (m, 10H; CH_{man}), 2.82 – 2.58 (m, 20H; COOCH$_2$CH$_2$CH_2), 2.07 – 1.83 (m, 20H; COOCH$_2$CH_2CH$_2$), 1.28 – 1.14 (m, 3H; CH_3).

^{13}C NMR (176 MHz, DMSO-d_6) δ (ppm) = 162.8 (*C*O), 146.3 ($C_{triazole}$), 145.0, 140.7 ($C_{sp2\ fullerene}$), 123.4 (*C*H$_{triazole}$), 99.8 (*C*H$_{1man}$), 74.1, 70.8 (*C*H$_{man}$), 70.3 (*C*H$_2$O$_{PEG}$), 70.0 (*C*H$_{man}$), 69.8, 69.5 (*C*H$_2$O$_{PEG}$), 68.7 ($C_{sp3\ fullerene}$), 67.9 (COO*C*H$_2$CH$_2$O), 66.7 (COO*C*H$_2$CH$_2$CH$_2$ and *C*H$_{man}$), 64.6 (O*C*H$_2$CH$_2$N$_{man}$), 63.4 (*C*H$_2$CH$_3$), 61.1 (*C*H$_2$OH$_{man}$), 49.9 (OCH$_2$*C*H$_2$N$_{man}$), 45.5 ($C_{q\ bridge}$), 32.3 (*C*H$_2$Br), 27.5 (COOCH$_2$*C*H$_2$CH$_2$), 21.6 (COOCH$_2$CH$_2$*C*H$_2$), 13.8 (*C*H$_3$).

FTIR-ATR (ν cm^{-1}): 3376 (OH), 2928 (C-H), 1738 (C=O).

Compound 48c

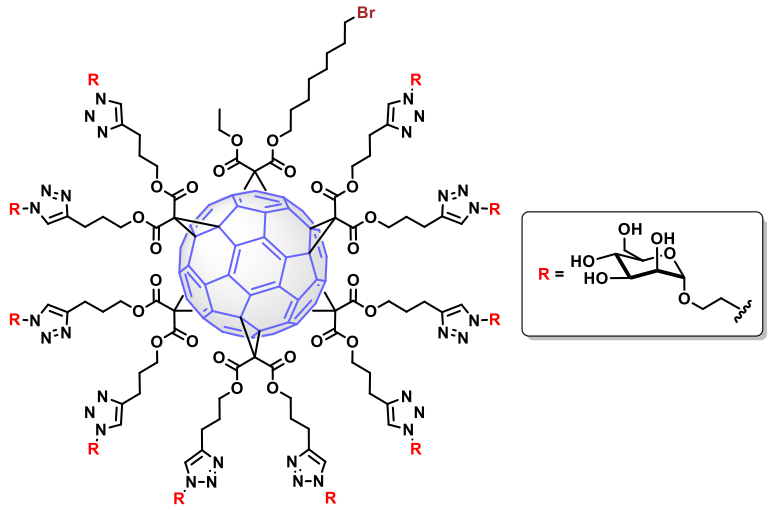

Following the general procedure, using hexakis-adduct **47c** (206 mg, 0.093 mmol), **11** (416 mg, 1.67 mmol), $CuBr{\cdot}S(CH_3)_2$ (97 mg, 0.47 mmol), sodium ascorbate (139 mg, 0.70 mmol) and a piece of copper metal wire in DMSO (1.5 mL), compound **48c** was afforded as an orange solid (366 mg, 84%).

^{1}H NMR (700 MHz, DMSO-d_6) δ (ppm) = 7.96 (s, 10H; C*H*$_{triazole}$), 4.74 (s, 20H; O*H*), 4.61 – 4.44 (m, 50H; C*H*$_{1man}$, $OCH_2CH_2N_{man}$ and O*H*), 4.36 – 4.15 (m, 24H; CH_2CH_3, $COOCH_2$ $_{linker}$ and $COOCH_2CH_2CH_2$), 3.96 – 3.89 (m, 10H; $OCH_2CH_2N_{man}$), 3.81 – 3.74 (m, 10H; $OCH_2CH_2N_{man}$), 3.61 – 3.57 (m, 10H; CH_2OH_{man}), 3.53 – 3.50 (m, 12H; CH_2OH_{man} and CH_2Br), 3.37 – 3.33 (m, 30H; CH_2OH_{man} and C*H*$_{man}$ overlaps with water), 3.13 – 3.05 (m, 10H; C*H*$_{man}$), 2.80 – 2.60 (m, 20H; $COOCH_2CH_2CH_2$), 2.08 – 1.86 (m, 20H; $COOCH_2CH_2CH_2$), 1.77 – 1.69 (m, 2H; CH_2 $_{linker}$), 1.61 – 1.53 (m, 2H; CH_2 $_{linker}$), 1.29 – 1.13 (m, 11H; CH_2 $_{linker}$ and CH_3).

^{13}C NMR (176 MHz, DMSO-d_6) δ (ppm) = 162.7 (*C*O), 146.3 (*C*$_{triazole}$), 144.9, 140.6 (*C*$_{sp2}$ $_{fullerene}$), 123.0 (*C*H$_{triazole}$), 99.7 (*C*H$_{1man}$), 74.0, 70.7, 69.9 (*C*H$_{man}$), 68.6 (*C*$_{sp3}$ $_{fullerene}$), 66.6 ($COOCH_2CH_2CH_2$, *C*H$_{man}$ and $COOCH_2$ $_{linker}$), 64.6 ($OCH_2CH_2N_{man}$), 63.3 (CH_2CH_3), 61.0 (CH_2OH_{man}), 49.5 ($OCH_2CH_2N_{man}$), 45.4 (*C*$_{q\ bridge}$), 35.1 (CH_2Br), 32.1, 28.3 (CH_2 $_{linker}$), 27.5 ($COOCH_2CH_2CH_2$ and *C*H$_2$ $_{linker}$), 25.2 (CH_2 $_{linker}$), 21.4 ($COOCH_2CH_2CH_2$), 13.7 (CH_3).

FTIR-ATR (ν cm^{-1}): 3364 (OH), 2928 (C-H), 1738 (C=O).

General procedure for the synthesis of glycofullerenes 49a-c

A mixture of the corresponding glycofullerene (1 eq.) and NaN_3 (10 eq.) in DMSO-d_6 was heated for 90 min at 55 ºC under microwave irradiation. The crude was purified by size-exclusion chromatography (Sephadex G-25 H_2O/CH_3OH 9:1).

Compound 49a

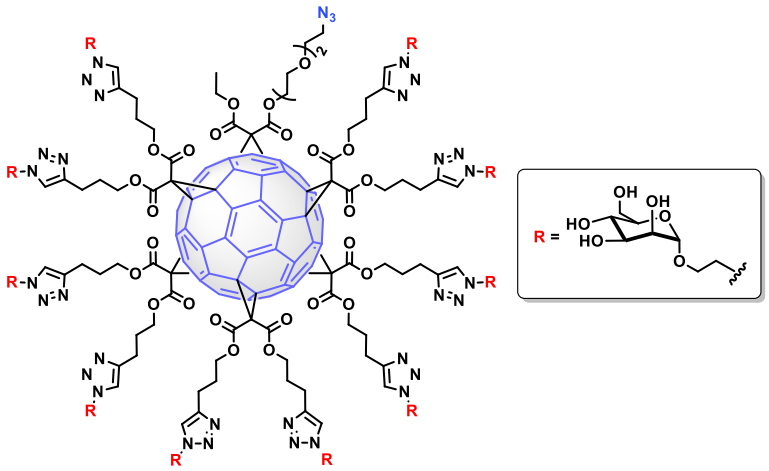

Following the general procedure, using glycofullerene **48a** (303 mg, 0.064 mmol) and NaN_3 (42 mg, 0.64 mmol) in DMSO-d_6 (0.8 mL), compound **49a** was afforded as a brown glassy solid (167 mg, 56%).

^{1}H NMR (700 MHz, DMSO-d_6) δ (ppm) = 7.82 (s, 10H; C$H_{triazole}$), 4.75 (s, 20H; OH), 4.62 – 4.56 (m, 20H; CH_{1man} and OH), 4.53 – 4.44 (m, 30H; OCH$_2$CH_2N$_{man}$ and OH), 4.40 – 4.15 (m, 24H; CH_2CH$_3$, COOCH_2CH$_2$O and COOCH_2CH$_2$CH$_2$), 3.95 – 3.88 (m, 10H; OCH_2CH$_2$N$_{man}$), 3.79 – 3.73 (m, 10H; OCH_2CH$_2$N$_{man}$), 3.64 – 3.57 (m, 14H; CH_2OH$_{man}$ and CH_2O$_{PEG}$), 3.54 – 3.51 (m, 10H; CH_{man}), 3.48 – 3.46 (m, 4H; CH_2O$_{PEG}$), 3.39 – 3.31 (m, 32H; CH_2OH$_{man}$, CH_{man} and CH_2N$_3$), 3.15 – 3.06 (m, 10H; CH_{man}), 2.76 – 2.56 (m, 20H; COOCH$_2$CH$_2$CH_2), 2.06 – 1.84 (m, 20H; COOCH$_2$CH_2CH$_2$), 1.27 – 1.14 (m, 3H; CH_3).

^{13}C NMR (176 MHz, DMSO-d_6) δ (ppm) = 162.9 (*C*O), 145.7 (*C*$_{triazole}$), 145.1, 140.8 (C$_{sp2\ fullerene}$), 122.4 (*C*H$_{triazole}$), 99.8 (*C*H$_{1man}$), 74.1, 70.9, 70.1 (*C*H$_{man}$), 69.7, 69.4 (*C*H$_2$O$_{PEG}$), 68.8 (C$_{sp3\ fullerene}$), 68.0 (COO*C*H$_2$CH$_2$O), 66.8 (COO*C*H$_2$CH$_2$CH$_2$ and *C*H$_{man}$), 64.9 (O*C*H$_2$CH$_2$N$_{man}$), 63.4 (*C*H$_2$CH$_3$), 61.2 (*C*H$_2$OH$_{man}$), 50.0 (*C*H$_2$N$_3$), 49.3 (OCH$_2$*C*H$_2$N$_{man}$), 45.6 (*C*$_{q\ bridge}$), 27.8 (COOCH$_2$*C*H$_2$CH$_2$), 21.4 (COOCH$_2$CH$_2$*C*H$_2$), 13.8 (*C*H$_3$).

FTIR-ATR (ν cm^{-1}): 3357 (OH), 2927 (C-H), 2112 (N_3), 1738 (C=O).

Compound 49b[33c]

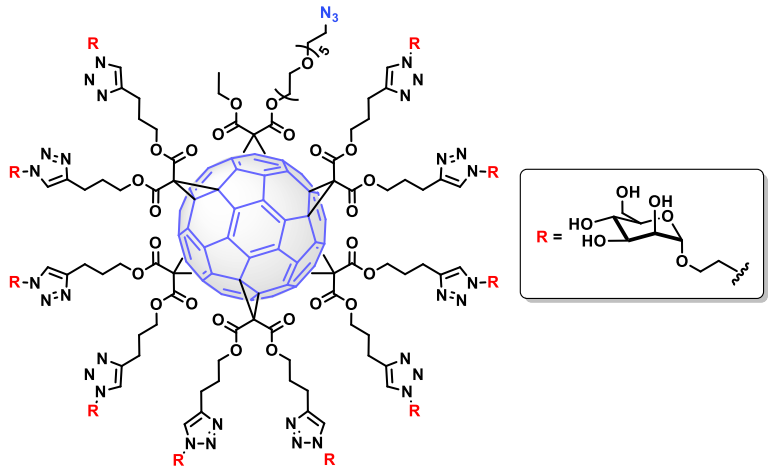

Following the general procedure, using glycofullerene **48b** (327 mg, 0.068 mmol) and NaN_3 (44 mg, 0.68 mmol) in DMSO (1.2 mL), compound **49b** was afforded as a brown glassy solid (221 mg, 68%).

^{1}H NMR (700 MHz, DMSO-d_6) δ (ppm) = 7.82 (s, 10H; C$H_{triazole}$), 4.79 – 4.71 (m, 20H; OH), 4.61 – 4.67 (m, 20H; CH_{1man} and OH), 4.53 – 4.45 (m, 30H; OCH$_2$CH_2N$_{man}$ and OH), 4.40 – 4.22 (m, 24H; CH_2CH$_3$, COOCH_2CH$_2$O and COOCH_2CH$_2$CH$_2$), 3.94 – 3.88 (m, 10H; OCH_2CH$_2$N$_{man}$), 3.80 – 3.69 (m, 12H; OCH_2CH$_2$N$_{man}$ and CH_2O$_{PEG}$), 3.61 – 3.56 (m, 12H; CH_2OH$_{man}$ and CH_2O$_{PEG}$), 3.53 – 3.45 (m, 26H; CH_2O$_{PEG}$ and CH_{man}), 3.40 (m, 10H; CH_2OH$_{man}$ overlaps with water), 3.37 – 3.30 (m, 22H; CH_{man} and CH_2N$_3$), 3.13 – 3.08 (m, 10H; CH_{man}), 2.72 – 2.58 (m, 20H; COOCH$_2$CH$_2$CH_2), 2.04 – 1.90 (m, 20H; COOCH$_2$CH_2CH$_2$), 1.25 – 1.17 (m, 3H; CH_3).

^{13}C NMR (176 MHz, DMSO-d_6) δ (ppm) = 162.9 (*C*O), 145.7 ($C_{triazole}$), 145.1, 140.8 ($C_{sp2\ fullerene}$), 122.4 (*C*H$_{triazole}$), 99.8 (*C*H$_{1man}$), 74.1, 70.9 (*C*H$_{man}$), 70.1 (*C*H$_{man}$ and *C*H$_2$O$_{PEG}$), 69.8, 69.7, 69.3 (*C*H$_2$O$_{PEG}$), 68.8 ($C_{sp3\ fullerene}$), 68.0 (COO*C*H$_2$CH$_2$O), 66.8 (COO*C*H$_2$CH$_2$CH$_2$ and *C*H$_{man}$), 64.9 (O*C*H$_2$CH$_2$N$_{man}$), 63.4 (*C*H$_2$CH$_3$), 61.2 (*C*H$_2$OH$_{man}$), 50.0 (*C*H$_2$N$_3$), 49.3 (OCH$_2$*C*H$_2$N$_{man}$), 45.6 ($C_{q\ bridge}$), 27.8 (COOCH$_2$*C*H$_2$CH$_2$), 21.4 (COOCH$_2$CH$_2$*C*H$_2$), 13.8 (*C*H$_3$).

FTIR-ATR (ν cm^{-1}): 3376 (OH), 2925 (C-H), 2108 (N_3), 1739 (C=O).

Compound 49c

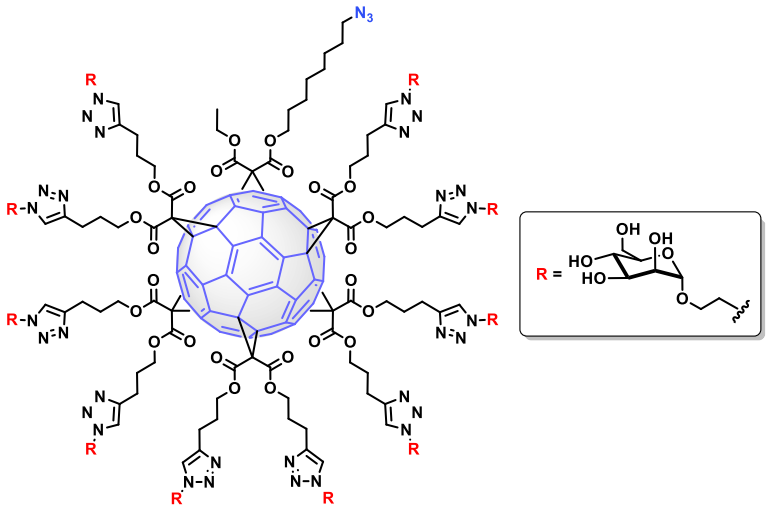

Following the general procedure, using glycofullerene **48c** (106 mg, 0.022 mmol) and NaN_3 (15 mg, 0.22 mmol) in DMSO (1.2 mL), compound **49c** was afforded as a brown glassy solid (125 mg, 80%).

^{1}H NMR (700 MHz, DMSO-d_6) δ (ppm) = 7.80 (s, 10H; C$H_{triazole}$), 4.78 (s, 20H; OH), 4.59 (s, 20H; OH), 4.52 – 4.47 (m, 30H; CH_{1man}, and OCH$_2$CH_2N$_{man}$), 4.36 – 4.15 (m, 24H; CH_2CH$_3$, COOCH_2 $_{linker}$ and COOCH_2CH$_2$CH$_2$), 3.93 – 3.88 (m, 10H; OCH_2CH$_2$N$_{man}$), 3.77 – 3.72 (m, 10H; OCH_2CH$_2$N$_{man}$), 3.60 – 3.57 (m, 10H; CH_2OH$_{man}$), 3.42 – 3.32 (m, 42H; CH_2OH$_{man}$, CH_{man} and CH_2N$_3$ overlaps with water), 3.13 – 3.05 (m, 10H; CH_{man}), 2.73 – 2.57 (m, 20H; COOCH$_2$CH$_2$CH_2), 2.05 – 1.87 (m, 20H; COOCH$_2$CH_2CH$_2$), 1.62 – 1.53 (m, 2H; CH_2 $_{linker}$), 1.51 – 1.43 (m, 2H; CH_2 $_{linker}$), 1.37 – 1.18 (m, 11H; CH_2 $_{linker}$ and CH_3).

^{13}C NMR (176 MHz, DMSO-d_6) δ (ppm) = 163.0 (*C*O), 145.8 ($C_{triazole}$), 145.2, 140.9 (C_{sp2} $_{fullerene}$), 122.4 (*C*H$_{triazole}$), 99.9 (*C*H$_{1man}$), 74.1, 70.9, 70.2 (*C*H$_{man}$), 68.9 (C_{sp3} $_{fullerene}$), 66.8 (COO*C*H$_2$CH$_2$CH$_2$, *C*H$_{man}$ and COO*C*H$_2$ $_{linker}$), 65.0 (OCH$_2$CH$_2$N$_{man}$), 63.5 (*C*H$_2$CH$_3$), 61.2 (*C*H$_2$OH$_{man}$), 50.7 (*C*H$_2$N$_3$), 49.3 (OCH$_2$*C*H$_2$N$_{man}$), 45.7 (C_q $_{bridge}$), 32.6, 28.9, 28.5, 28.3 (*C*H$_2$ $_{linker}$), 27.9 (COOCH$_2$*C*H$_2$CH$_2$), 26.1, 25.4 (*C*H$_2$ $_{linker}$), 21.5 (COOCH$_2$CH$_2$*C*H$_2$), 13.9 (*C*H$_3$).

FTIR-ATR (ν cm^{-1}): 3370 (OH), 2927 (C-H), 2102 (N_3), 1738 (C=O).

General procedure for the synthesis of glycoporphyrins 52a-c

A mixture of the corresponding glycofullerene (6 eq.), porphyrin **50** (1 eq.), CuBr·S(CH$_3$)$_2$ (5 eq.) sodium ascorbate (7.5 eq.) and a piece of copper metal wire in DMSO (1.5 mL) was deoxygenated and kept under argon with vigorous stirring for 72 h. The crude reaction was filtered through a QuadraSil® Mercaptopropyl column and purified by size-exclusion chromatography (Sephadex G-50 H$_2$O/CH$_3$OH 9:1).

Compound 52a

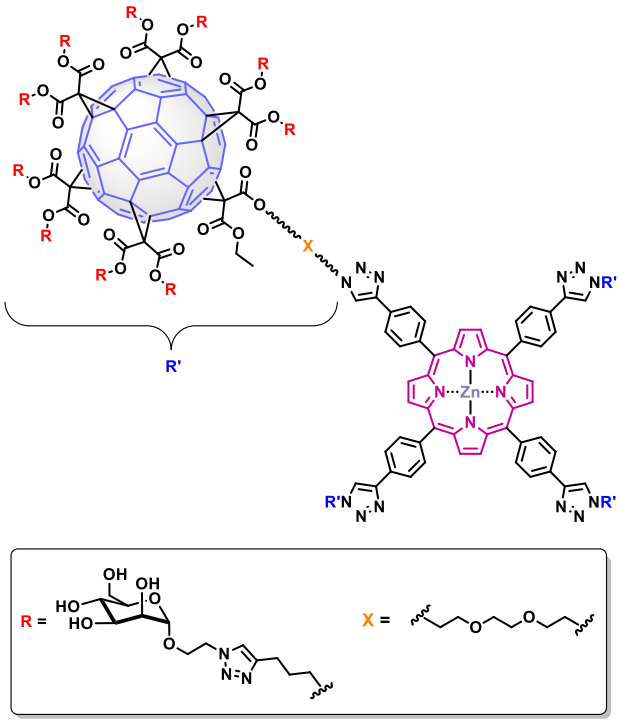

Following the general procedure, using glycofullerene **49a** (181 mg, 0.039 mmol), porphyrin **50** (5 mg, 6.5 μmol), $CuBr{\cdot}S(CH_3)_2$ (6.6 mg, 0.032 mmol), sodium ascorbate (9.6 mg, 0.048 mmol) and a piece of copper metal wire in DMSO, compound **52a** was obtained as a green solid (96 mg, 76%).

^{1}H NMR (700 MHz, DMSO-d_6) δ (ppm) = 8.95 – 8.67 (m, 12H; CH_{triazole} and C$H_{\beta\ \text{porphyrin}}$), 8.40 – 8.10 (m, 16H; CH_{aromatic}), 7.82 (s, 40H; CH_{triazole}), 4.76 (s, 80H; OH), 4.63 – 4.57 (m, 80H; C$H_{1\text{man}}$ and OH), 4.53 – 4.43 (m, 128H; OCH_2CH_2N and OH), 4.37 – 4.13 (m, 96H; CH_2CH_3, $COOCH_2CH_2O$ and $COOCH_2CH_2CH_2$), 3.97 – 3.88 (m, 48H; $OCH_2CH_2N_{\text{man}}$ and CH_2O_{PEG}), 3.79 – 3.73 (m, 40H; $OCH_2CH_2N_{\text{man}}$), 3.61 – 3.57 (m, 48H; CH_2OH_{man} and CH_2O_{PEG}), 3.54 – 3.51 (m, 56H; CH_2O_{PEG} and CH_{man}), 3.38 – 3.33 (m, 120H; CH_2OH_{man} and CH_{man} overlaps with water), 3.14 – 3.06 (m, 40H; CH_{man}), 2.77 – 2.58 (m, 80H; $COOCH_2CH_2CH_2$), 2.07 – 1.85 (m, 80H; $COOCH_2CH_2CH_2$), 1.27 – 1.13 (m, 12H; CH_3).

^{13}C NMR (176 MHz, DMSO-d_6) δ (ppm) = 163.0 (CO), 149.4 ($C_{\alpha\ \text{porphyrin}}$), 145.8 ($C_{\text{triazole}}$), 145.2, 140.8 ($C_{\text{sp2 fullerene}}$), 134.9, 131.7, 130.1, 123.6 ($C_{\text{porphyrin}}$), 122.4 (CH$_{\text{triazole}}$), 120.3 ($C_{\text{porphyrin}}$), 99.8 (CH$_{1\text{man}}$), 74.1, 70.9, 70.2 (CH$_{\text{man}}$), 69.7 (CH_2O_{PEG}), 68.8 ($C_{\text{sp3 fullerene}}$ and CH_2O_{PEG}), 68.1 ($COOCH_2CH_2O$), 66.8 ($COOCH_2CH_2CH_2$ and CH$_{\text{man}}$), 65.0 ($OCH_2CH_2N_{\text{man}}$), 63.5 (CH_2CH_3), 61.2 (CH_2OH_{man}), 49.3 (OCH_2CH_2N), 45.6 ($C_{\text{q bridge}}$), 27.8 ($COOCH_2CH_2CH_2$), 21.5 ($COOCH_2CH_2CH_2$), 13.9 (CH_3).

FTIR-ATR (ν cm^{-1}): 3369 (OH), 2926 (C-H), 1739 (C=O).

Compound 52b[33c]

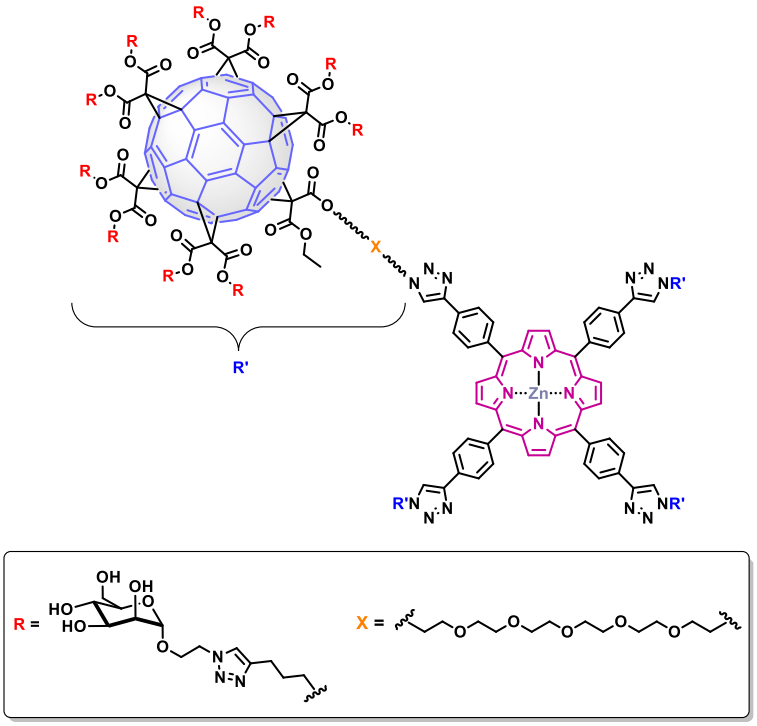

Following the general procedure, using glycofullerene **49b** (111 mg, 0.023 mmol), porphyrin **50** (3.5 mg, 4.5 μmol), $CuBr{\cdot}S(CH_3)_2$ (4.6 mg, 0.023 mmol), sodium ascorbate (6.7 mg, 0.034 mmol) and a piece of copper metal wire in DMSO, compound **52b** was obtained as a green solid (67 mg, 75%).

^{1}H NMR (700 MHz, DMSO-d_6) δ (ppm) = 8.93 – 8.69 (m, 12H; CH_{triazole} and C$H_{\beta\ \text{porphyrin}}$), 8.38 – 8.12 (m, 16H; CH_{aromatic}), 7.82 (s, 40H; CH_{triazole}), 4.79 – 4.72 (m, 80H; OH), 4.62 – 4.57 (m, 80H; C$H_{1\text{man}}$ and OH), 4.53 – 4.44 (m, 128H; OCH_2CH_2N and OH), 4.38 – 4.18 (m, 96H; CH_2CH_3, $COOCH_2CH_2O$ and $COOCH_2CH_2CH_2$), 3.95 – 3.89 (m, 48H; $OCH_2CH_2N_{\text{man}}$ and CH_2O_{PEG}), 3.78 – 3.73 (m, 40H; $OCH_2CH_2N_{\text{man}}$), 3.61 – 3.58 (m, 48H; CH_2OH_{man} and CH_2O_{PEG}), 3.54 – 3.48 (m, 104H; CH_2O_{PEG} and CH_{man}), 3.41 (m, 40H; CH_2OH_{man} overlaps with water), 3.37 – 3.32 (m, 80H; CH_{man}), 3.13 – 3.07 (m, 40H; CH_{man}), 2.76 – 2.59 (m, 80H; $COOCH_2CH_2CH_2$), 2.04 – 1.87 (m, 80H; $COOCH_2CH_2CH_2$), 1.25 – 1.17 (m, 12H; CH_3).

^{13}C NMR (176 MHz, DMSO-d_6) δ (ppm) = 162.9 (*C*O), 149.3 ($C_{\alpha\ \text{porphyrin}}$), 145.7 ($C_{\text{triazole}}$), 145.1, 140.6 ($C_{\text{sp2 fullerene}}$), 135.0, 131.8, 129.9, 123.5 ($C_{\text{porphyrin}}$), 122.4 (CH_{triazole}), 119.7 ($C_{\text{porphyrin}}$), 99.8 (C$H_{1\text{man}}$), 74.1, 70.9, 70.1 (CH_{man}), 69.9 (CH_2O_{PEG}), 68.9 ($C_{\text{sp3 fullerene}}$ and CH_2O_{PEG}), 68.0 ($COOCH_2CH_2O$), 66.8 ($COOCH_2CH_2CH_2$ and CH_{man}), 64.9 ($OCH_2CH_2N_{\text{man}}$), 63.4 (CH_2CH_3), 61.2 (CH_2OH_{man}), 49.3 (OCH_2CH_2N), 45.6 ($C_{\text{q bridge}}$), 27.8 ($COOCH_2CH_2CH_2$), 21.4 ($COOCH_2CH_2CH_2$), 13.8 (CH_3).

FTIR-ATR (ν cm^{-1}): 3361 (OH), 2926 (C-H), 1738 (C=O).

Compound 52c

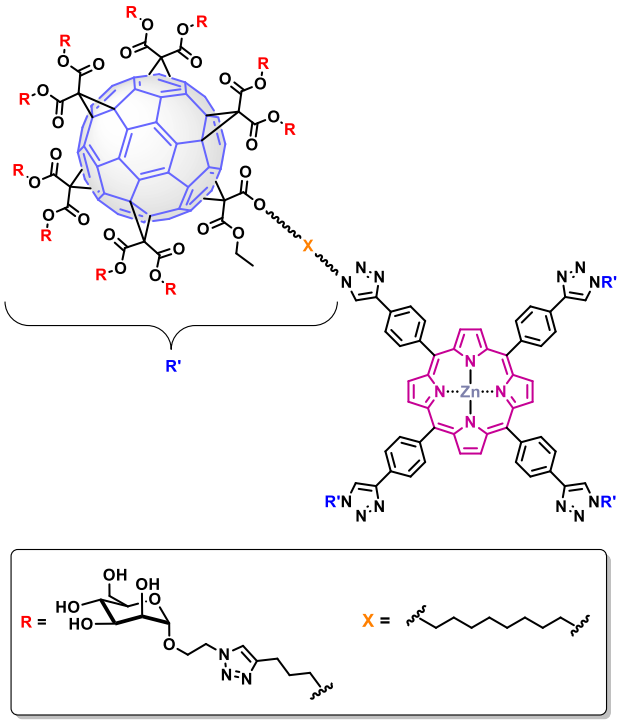

Following the general procedure, using glycofullerene **49c** (176 mg, 0.038 mmol), porphyrin **50** (4.9 mg, 6.3 µmol), $CuBr{\cdot}S(CH_3)_2$ (6.6 mg, 0.032 mmol), sodium ascorbate (9.3 mg, 0.047 mmol) and a piece of copper metal wire in DMSO, compound **52c** was obtained as a green solid (94 mg, 77%).

^{1}H NMR (700 MHz, DMSO-d_6) δ (ppm) = 8.98 – 8.71 (m, 12H; C*H*$_{triazole}$ and C*H*$_{β\ porphyrin}$), 8.36 – 8.16 (m, 16H; C*H*$_{aromatic}$), 7.81 (s, 40H; C*H*$_{triazole}$), 4.76 – 4.71 (m, 80H; O*H*), 4.61 – 4.57 (m, 80H; C*H*$_{1man}$ and O*H*), 4.52 – 4.44 (m, 128H; OCH_2CH_2N and O*H*), 4.37 – 4.20 (m, 96H; CH_2CH_3, $COOCH_2CH_2O$ and $COOCH_2CH_2CH_2$), 3.94 – 3.89 (m, 40H; $OCH_2CH_2N_{man}$), 3.78 – 3.73 (m, 40H; $OCH_2CH_2N_{man}$), 3.61 – 3.58 (m, 40H; CH_2OH_{man}), 3.54 – 3.52 (m, 40H; C*H*$_{man}$), 3.38 – 3.35 (m, 120H; CH_2OH_{man} and C*H*$_{man}$ overlaps with water), 3.14 – 3.07 (m, 40H; C*H*$_{man}$), 2.72 – 2.59 (m, 80H; $COOCH_2CH_2CH_2$), 2.04 – 1.90 (m, 80H; $COOCH_2CH_2CH_2$), 1.72 – 1.49 (m, 16H; C*H*$_{2\ linker}$), 1.33 – 1.21 (m, 44H; C*H*$_{2\ linker}$ and C*H*$_3$).

^{13}C NMR (176 MHz, DMSO-d_6) δ (ppm) = 162.9 (*C*O), 149.3 (*C*$_{α\ porphyrin}$), 145.7 (*C*$_{triazole}$), 145.1, 140.8 (*C*$_{sp2\ fullerene}$), 134.9, 131.7, 130.2, 123.7 (*C*$_{porphyrin}$), 122.3 (*C*H$_{triazole}$), 120.1 (*C*$_{porphyrin}$), 99.8 (*C*H$_{1man}$), 74.1, 70.9, 70.1 (*C*H$_{man}$), 68.8 (*C*$_{sp3\ fullerene}$), 66.8 ($COOCH_2CH_2CH_2$, *C*H$_{man}$ and $COOCH_2$ $_{linker}$), 65.0 ($OCH_2CH_2N_{man}$), 63.5 (CH_2CH_3), 61.2 (CH_2OH_{man}), 49.3 (OCH_2CH_2N), 45.6 (*C*$_{q\ bridge}$), 32.5, 29.9, 28.6

($CH_{2\ linker}$), 27.8 ($COOCH_2CH_2CH_2$ and $CH_{2\ linker}$), 26.0, 25.3 ($CH_{2\ linker}$), 21.4 ($COOCH_2CH_2CH_2$), 13.9 (CH_3).

FTIR-ATR (ν cm^{-1}): 3365 (OH), 2927 (C-H), 1738 (C=O).

General procedure for the synthesis of glycoporphyrins 53a-c

A mixture of the corresponding glycofullerene (10 eq.), porphyrin **51** (1 eq.), $CuBr{\cdot}S(CH_3)_2$ (10 eq.), sodium ascorbate (15 eq.) and a piece of copper metal wire in DMSO was deoxygenated and kept under argon with vigorous stirring for 96 h. The crude reaction was filtered through a QuadraSil® Mercaptopropyl column and purified by size-exclusion chromatography (Sephadex G-50 H_2O/CH_3OH 9:1).

Compound 53a

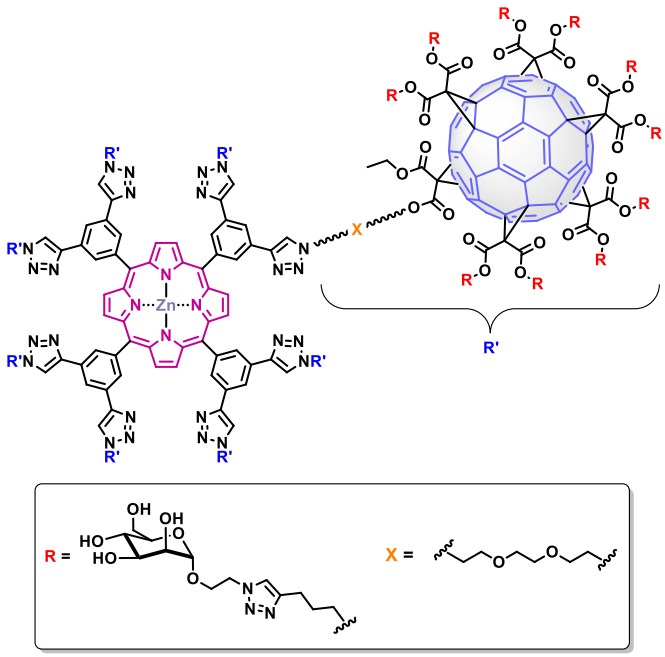

Following the general procedure, using glycofullerene **49a** (258 mg, 0.055 mmol), porphyrin **51** (4.8 mg, 5.5 µmol), $CuBr{\cdot}S(CH_3)_2$ (12 mg, 0.057 mmol), sodium ascorbate (17 mg, 0.086 mmol) and a piece of copper metal wire in DMSO (1.5 mL), compound **53a** was obtained as a maroon solid (85 mg, 40%).

^{1}H NMR (700 MHz, DMSO-d_6) δ (ppm) = 9.24 – 7.54 (m, 108H; $CH_{triazole}$, $CH_{\beta\ porphyrin}$, $CH_{aromatic}$), 4.74 (s, 160H; O*H*), 4.63 – 4.56 (m, 160H; CH_{1man} and O*H*), 4.54 – 4.42 (m, 256H; OCH_2CH_2N and O*H*), 4.39 – 4.08 (m, 192H; CH_2CH_3, $COOCH_2CH_2O$ and $COOCH_2CH_2CH_2$), 3.97 – 3.87 (m, 96H; $OCH_2CH_2N_{man}$ and CH_2O_{PEG}), 3.79 – 3.72 (m, 80H; $OCH_2CH_2N_{man}$), 3.63 – 3.57 (m, 96H; CH_2OH_{man} and CH_2O_{PEG}), 3.56 – 3.50 (m, 112H; CH_2O_{PEG} and CH_{man}), 3.38 – 3.35 (m, 240H; CH_2OH_{man} and CH_{man} overlaps with water), 3.15 – 3.05 (m, 80H; CH_{man}), 2.82 – 2.56

(m, 160H; $COOCH_2CH_2CH_2$), 2.06 – 1.79 (m, 160H; $COOCH_2CH_2CH_2$), 1.29 – 1.14 (m, 24H; CH_3).

^{13}C NMR (176 MHz, DMSO-d_6) δ (ppm) = 162.9 (*C*O), 145.7 ($C_{triazole}$), 145.1, 140.8 ($C_{sp2\ fullerene}$), 122.4 ($CH_{triazole}$), 99.8 (CH_{1man}), 74.1, 70.9, 70.1 (CH_{man}), 69.6 (CH_2O_{PEG}), 68.8 ($C_{sp3\ fullerene}$ and CH_2O_{PEG}), 68.0 ($COOCH_2CH_2O$), 66.6 ($COOCH_2CH_2CH_2$ and CH_{man}), 64.9 ($OCH_2CH_2N_{man}$), 63.5 (CH_2CH_3), 61.2 (CH_2OH_{man}), 49.3 (OCH_2CH_2N), 45.6 ($C_{q\ bridge}$), 27.8 ($COOCH_2CH_2CH_2$), 21.4 ($COOCH_2CH_2CH_2$), 13.8 (CH_3).

FTIR-ATR (ν cm^{-1}): 3357 (OH), 2927 (C-H), 1737 (C=O).

Compound 53b[33c]

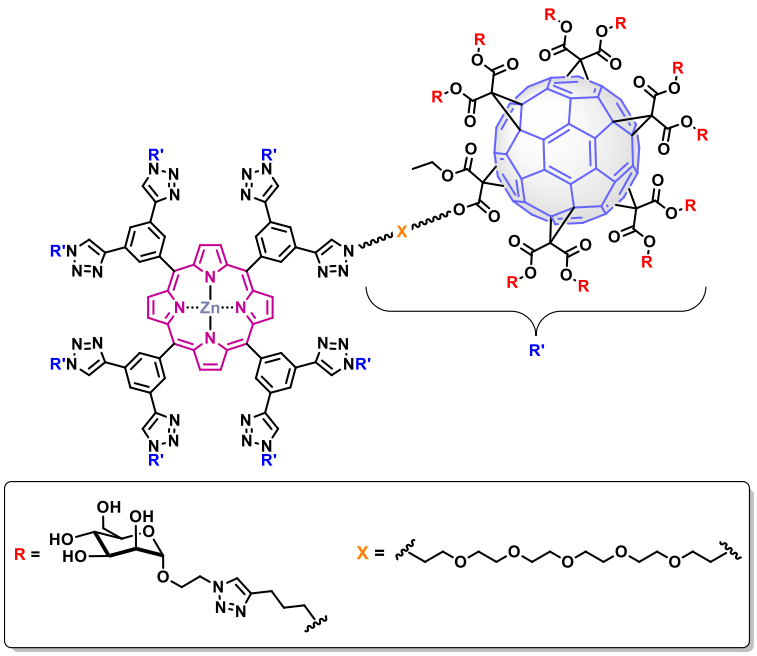

Following the general procedure, using glycofullerene **49b** (206 mg, 0.043 mmol), porphyrin **51** (3.7 mg, 4.3 μmol), $CuBr{\cdot}S(CH_3)_2$ (8.8 mg, 0.043 mmol), sodium ascorbate (13 mg, 0.065 mmol) and a piece of copper metal wire in DMSO (1.5 mL), compound **53b** was obtained as a maroon solid (125 mg, 74%).

^{1}H NMR (700 MHz, DMSO-d_6) δ (ppm) = 9.25 – 7.50 (m, 108H; $CH_{triazole}$, $CH_{\beta\ porphyrin}$, $CH_{aromatic}$), 4.86 – 4.75 (m, 160H; O*H*), 4.64 – 4.44 (m, 416H; CH_{1man}, OCH_2CH_2N and O*H*), 4.40 – 4.13 (m, 192H; CH_2CH_3, $COOCH_2CH_2O$ and $COOCH_2CH_2CH_2$), 3.96 – 3.88 (m, 96H; $OCH_2CH_2N_{man}$ and CH_2O_{PEG}), 3.77 – 3.74 (m, 80H; $OCH_2CH_2N_{man}$), 3.59 – 3.52 (m, 304H; CH_2OH_{man}, CH_2O_{PEG} and CH_{man} overlaps with water), 3.43 – 3.40 (m, 80H; CH_2OH_{man}), 3.39 – 3.33 (m, 160H; CH_{man}), 3.14 – 3.04 (m, 80H; CH_{man}), 2.83 – 2.56 (m, 160H; $COOCH_2CH_2CH_2$), 2.15 – 1.79 (m, 160H; $COOCH_2CH_2CH_2$), 1.27 – 1.09 (m, 24H; CH_3).

^{13}C NMR (176 MHz, DMSO-d_6) δ (ppm) = 163.1 (*C*O), 146.1 ($C_{triazole}$), 145.3, 141.0 ($C_{sp2\ fullerene}$), 122.7 (*C*H$_{triazole}$), 99.9 (*C*H$_{1man}$), 74.1, 71.0, 70.3 (*C*H$_{man}$), 69.9 (*C*H$_2$O$_{PEG}$), 68.8 ($C_{sp3\ fullerene}$ and *C*H$_2$O$_{PEG}$), 68.1 (COO*C*H$_2$CH$_2$O), 66.9 (COOCH$_2$*C*H$_2$CH$_2$ and *C*H$_{man}$), 65.1 (OCH$_2$*C*H$_2$N$_{man}$), 63.7 (*C*H$_2$CH$_3$), 61.3 (*C*H$_2$OH$_{man}$), 49.5 (OCH$_2$*C*H$_2$N), 45.8 ($C_{q\ bridge}$), 28.0 (COOCH$_2$*C*H$_2$CH$_2$), 21.6 (COOCH$_2$CH$_2$*C*H$_2$), 14.0 (*C*H$_3$).

FTIR-ATR (ν cm^{-1}): 3394 (OH), 2928 (C-H), 1738 (C=O).

Compound 53c

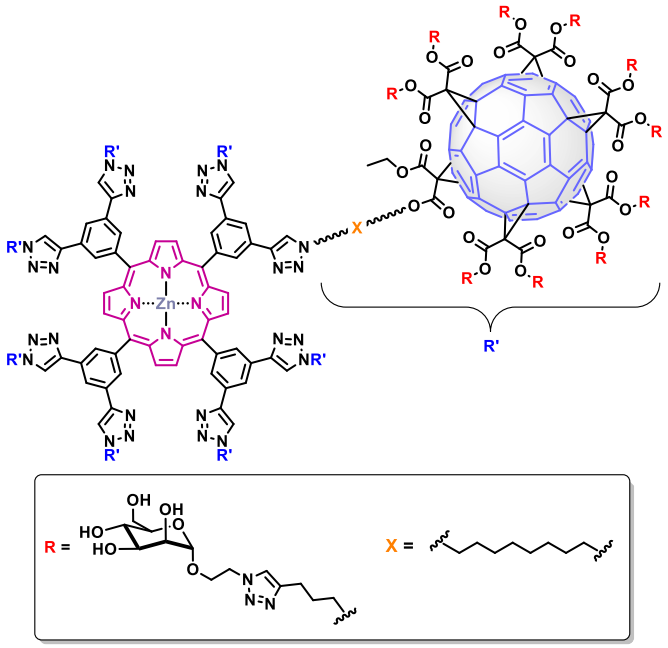

Following the general procedure, using glycofullerene **49c** (221 mg, 0.047 mmol), porphyrin **51** (4 mg, 4.7 μmol), CuBr·S(CH$_3$)$_2$ (10 mg, 0.047 mmol), sodium ascorbate (14 mg, 0.071 mmol) and a piece of copper metal wire in DMSO (1.8 mL), compound **53c** was obtained as a maroon solid (72 mg, 40%).

^{1}H NMR (700 MHz, DMSO-d_6) δ (ppm) = 9.21 – 7.45 (m, 108H; C*H*$_{triazole}$, C*H*$_{β\ porphyrin}$, C*H*$_{aromatic}$), 4.77 (s, 160H; O*H*), 4.62 – 4.57 (m, 160H; C*H*$_{1man}$ and O*H*), 4.54 – 4.44 (m, 256H; OCH$_2$C*H*$_2$N and O*H*), 4.40 – 4.20 (m, 192H; C*H*$_2$CH$_3$, COOC*H*$_2$CH$_2$O and COOC*H*$_2$CH$_2$CH$_2$), 3.94 – 3.88 (m, 80H; OC*H*$_2$CH$_2$N$_{man}$), 3.78 – 3.72 (m, 80H; OC*H*$_2$CH$_2$N$_{man}$), 3.60 – 3.57 (m, 80H; C*H*$_2$OH$_{man}$), 3.53 – 3.51 (m, 80H; C*H*$_{man}$ overlaps with water), 3.38 – 3.31 (m, 240H; C*H*$_2$OH$_{man}$ and C*H*$_{man}$), 3.12 – 3.05 (m, 80H; C*H*$_{man}$), 2.76 – 2.58 (m, 160H; COOCH$_2$CH$_2$C*H*$_2$), 2.05 – 1.85 (m, 160H; COOCH$_2$C*H*$_2$CH$_2$), 1.65 – 1.51 (m, 32H; C*H*$_{2\ linker}$), 1.37 – 1.16 (m, 88H; C*H*$_{2\ linker}$ and C*H*$_3$).

^{13}C NMR (176 MHz, DMSO-d_6) δ (ppm) = 162.9 (*C*O), 145.8 ($C_{triazole}$), 145.1, 140.8 ($C_{sp2\ fullerene}$), 122.4 (*C*H$_{triazole}$), 99.8 (*C*H$_{1man}$), 74.1, 70.9, 70.1 (*C*H$_{man}$), 68.8

($C_{sp3\ fullerene}$), 66.8 ($COOCH_2CH_2CH_2$, CH_{man} and $COOCH_{2\ linker}$), 64.9 ($OCH_2CH_2N_{man}$), 63.5 (CH_2CH_3), 61.2 (CH_2OH_{man}), 49.3 (OCH_2CH_2N), 45.6 ($C_{q\ bridge}$), 32.5, 28.6 ($CH_{2\ linker}$), 27.8 ($COOCH_2CH_2CH_2$ and $CH_{2\ linker}$), 25.5 ($CH_{2\ linker}$), 21.5 ($COOCH_2CH_2CH_2$), 13.9 (CH_3).

FTIR-ATR (ν cm^{-1}): 3363 (OH), 2930 (C-H), 1739 (C=O).

Compound 56[140]

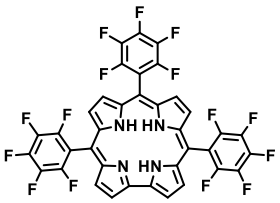

To a mixure of 2,3,4,5,6-pentafluorobenzaldehyde (**55**) (0.24 mL, 2 mmol) and TFA (20 μL) from a pre-prepared solution of TFA (1 mL) in CH_2Cl_2 (10 mL), pyrrol (**54**) (0.21 mL, 3.00 mmol) was added, and the mixture was stirred for 10 minutes. After that time, CH_2Cl_2 (20 mL) and a solution of DDQ in toluene/CH_2Cl_2 (8 mL, 1:1) were added and stirred for further 5 minutes. The reaction mixture was passed by a silica gel plug (SiO_2, Hexane/CH_2Cl_2 3:1) to give corrole **56** contaminated with porphyrin. Subsequent chromatography (SiO_2, Hexane → Hexane/CH_2Cl_2 4:1) afforded compound **56** as a purple solid (255 mg, 21%).

^{1}H NMR (500 MHz, CD_2Cl_2) δ (ppm) = 9.28 (d, $^3J_{H,H}$ = 4.0 Hz, 2H; CH_β), 8.92 (d, $^3J_{H,H}$ = 4.6 Hz, 2H; CH_β), 8.85 (d, $^3J_{H,H}$ = 4.0 Hz, 2H; CH_β), 8.71 (d, $^3J_{H,H}$ = 4.6 Hz, 2H; CH_β).

^{19}F{^{1}H} NMR (471 MHz, CD_2Cl_2) δ (ppm) = -138.54 – -138.53 (m; F_{ortho}), -154.87 (t, $^3J_{F,F}$ = 20.7 Hz; F_{para}), -155.08 (t, $^3J_{F,F}$ = 20.7 Hz; F_{para}), -163.26 – -163.41 (m; F_{meta}), -163.44 – -163.59 (m, F_{meta}).

Compound 57[160]

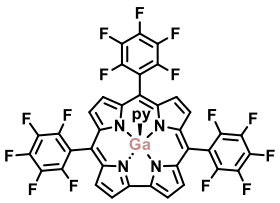

To a solution of **56** (765 mg, 0.96 mmol) in dry pyridine (85 mL), $GaCl_3$ (5.00 g, 28.80 mmol) was added, and the mixture was heated to reflux for 16 h under nitrogen. After that time, the solvent was evaporated and the resulting crude was purified by column chromatography (SiO_2, Hexane/CH_2Cl_2 3:1 → 2:1 → 1:1 → $CHCl_3$) to afford compound **57** as a purple solid (628 mg, 69%).

^{1}H NMR (500 MHz, CD_2Cl_2) δ (ppm) = 9.28 (d, $^{3}J_{H,H}$ = 4.0 Hz, 2H; CH_{β}), 8.92 (d, $^{3}J_{H,H}$ = 4.6 Hz, 2H; CH_{β}), 8.85 (d, $^{3}J_{H,H}$ = 4.0 Hz, 2H; CH_{β}), 8.71 (d, $^{3}J_{H,H}$ = 4.6 Hz, 2H; CH_{β}), 6.63 (tt, $^{3}J_{H,H}$ = 7.6 Hz, $^{4}J_{H,H}$ = 1.7 Hz, 1H; C$H_{\text{para py}}$), 5.85 – 5.80 (m, 2H; C$H_{\text{meta py}}$), 2.89 – 2.86 (m, 2H; C$H_{\text{ortho py}}$).

^{19}F{^{1}H} NMR (471 MHz, CD_2Cl_2) δ (ppm) = -138.54 – -138.53 (m; F_{ortho}), -154.87 (t, $^{3}J_{F,F}$ = 20.7 Hz; F_{para}), -155.08 (t, $^{3}J_{F,F}$ = 20.7 Hz; F_{para}), -163.26 – -163.41 (m; F_{meta}), -163.44 – -163.59 (m; F_{meta}).

Compound 59

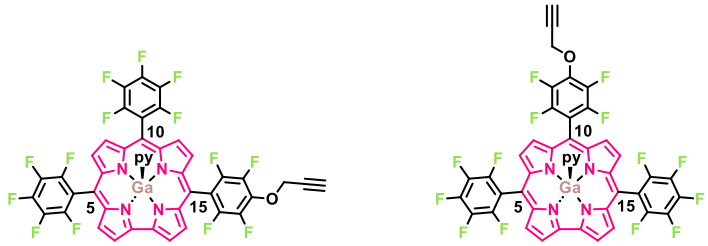

Propargyl alcohol (**58**) (2.2 µL, 0.038 mmol) was added to a solution of **57** (30 mg, 0.032 mmol) and K_2CO_3 (22 mg, 0.16 mmol) in DMSO (5 mL). The mixture was heated at 100 ºC for 3 h. After that time, $CHCl_3$ (100 mL) was added and the organic layer was washed with water (50 mL), dried over anh. $MgSO_4$, filtered and concentrated under vacuum. The resulting crude product was purified by column chromatography (SiO_2, Hexane/AcOEt/pyridine 3:1:0.02) to afford monosubstituted derivatives **59a** and **59b** as a 2:1 mixture of inseparable regioisomers (fuchsia solid, 5 mg, 16%).

^{1}H NMR (500 MHz, CD_2Cl_2) δ (ppm) = 9.28 [d, $^{3}J_{H,H}$ = 4.0 Hz, 3H; CH_{β} (2H, **59a**; 1H, **59b**)], 8.95 (d, $^{3}J_{H,H}$ = 4.6 Hz, 1H; CH_{β}, **59b**), 8.91 (d, $^{3}J_{H,H}$ = 4.3 Hz, 2H; CH_{β}, **59a**), 8.88 (d, $^{3}J_{H,H}$ = 4.0 Hz, 1H; CH_{β}, **59b**), 8.84 (d, $^{3}J_{H,H}$ = 4.0 Hz, 2H; CH_{β}, **59a**), 8.74 (d, $^{3}J_{H,H}$ = 4.6 Hz, 1H; CH_{β}, **59b**), 8.70 (d, $^{3}J_{H,H}$ = 4.3 Hz, 2H; CH_{β}, **59a**), 6.69 – 6.61 [m, 1.5H; C$H_{\text{para py}}$ (1H, **59a**; 0.5H, **59b**)], 5.89 – 5.80 [m, 3H; C$H_{\text{meta py}}$ (2H, **59a**; 1H, **59b**)], 5.20 (d, $^{3}J_{H,H}$ = 2.4 Hz, 2H; OCH_2, **59a**), 5.18 (d, $^{3}J_{H,H}$ = 2.4 Hz, 1H; OCH_2, **59b**), 2.98 – 2.86 [m, 4H; C$H_{\text{ortho py}}$ (2H, **59a**; 1H, **59b**) and C≡C*H*, **59a**], 2.85 (t, $^{3}J_{H,H}$ = 2.4 Hz, 0.5H; C≡C*H*, **59b**).

^{19}F{^{1}H} NMR (471 MHz, CD_2Cl_2) δ (ppm) = -138.86 – -139.33 [m; F_{ortho} (10-F_{ortho}, 15-F_{ortho}, **59a**; 5-F_{ortho}, 15-F_{ortho}, **59b**)], -140.78 [dd, $^{3}J_{F,F}$ = 23.8, 8.9 Hz; F_{ortho}, (5-F_{ortho}, **59a**; 10-F_{ortho}, **59b**)], -155.34 – -155.39 (m; F_{para}, **59a**), -155.64 (t, $^{3}J_{F,F}$ = 20.6 Hz; F_{para}, **59b**), -157.46 (dd, $^{3}J_{F,F}$ = 23.1, 8.6 Hz; 5-F_{meta}, **59a**), -157.64 (dd, $^{3}J_{F,F}$ = 24.0, 8.3 Hz; 10-F_{meta}, **59b**), -163.73 – -163.93 (m; 10-F_{meta} and 15-F_{meta}, **59a**), -164.02 (dd, $^{3}J_{F,F}$ = 25.0, 5.0 Hz; 5-F_{meta} and 15-F_{meta}, **59b**).

MALDI-TOF: *m/z* calcd for $C_{40}H_{11}F_{14}GaN_4O$: 898.0000, found: 898.0750 [M^+].

FTIR-ATR (ν cm^{-1}): 3306 (C≡C-H), 2927 (C-H), 1491 (C=N).

Compound 60

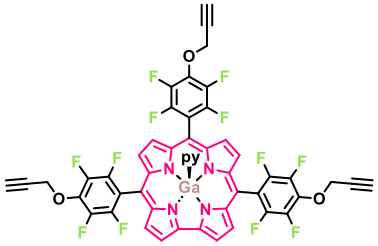

Propargyl alcohol (**58**) (2.6 µL, 0.044 mmol) and NaH (8 mg, 0.33 mmol) were dissolved in dry THF (5 mL) and heated to reflux for 30 min under argon. Then, a solution of **57** (10 mg, 0.011 mmol) in dry THF was added and the mixture was heated to reflux for 1 h. After that time, CH_2Cl_2 (50 mL) was added and the organic layer was washed with water (50 mL), dried over anh. $MgSO_4$, filtered and concentrated under vacuum. The resulting crude was purified by column chromatography (SiO_2, Hexane/AcOEt/pyridine 3:1:0.02) to afford **60** as a fuchsia solid (6 mg, 52%).

^{1}H NMR (500 MHz, CD_2Cl_2) δ (ppm) = 9.27 (d, $^3J_{H,H}$ = 4.0 Hz, 2H; CH_β), 8.94 (d, $^3J_{H,H}$ = 4.5 Hz, 2H; CH_β), 8.86 (d, $^3J_{H,H}$ = 4.0 Hz, 2H; CH_β), 8.72 (d, $^3J_{H,H}$ = 4.5 Hz, 2H; CH_β), 6.70 – 6.63 (m, 1H; C$H_{\text{para py}}$), 5.88 – 5.84 (m, 2H; C$H_{\text{meta py}}$), 5.20 (d, $^3J_{H,H}$ = 2.4 Hz, 4H; OCH_2), 5.18 (d, $^3J_{H,H}$ = 2.4 Hz, 2H; OCH_2), 2.94 (d, $^3J_{H,H}$ = 5.4 Hz, 2H; C$H_{\text{ortho py}}$), 2.87 (t, $^3J_{H,H}$ = 2.4 Hz, 2H; C≡CH), 2.85 (t, $^3J_{H,H}$ = 2.4 Hz, 1H; C≡CH).

^{19}F{^{1}H} NMR (471 MHz, CD_2Cl_2) δ (ppm) = -140.69 – -140.83 (m; F_{ortho}), -157.52 (dd, $^3J_{F,F}$ = 23.6, 8.8 Hz; F_{meta}), -158.71 (dd, $^3J_{F,F}$ = 24.2, 9.0 Hz; F_{meta}).

MALDI-TOF: *m/z* calcd for $C_{51}H_{22}F_{12}GaN_5O_3$: 1049.0787, found: 1049.1874 $[M]^+$.

FTIR-ATR (ν cm^{-1}): 3303 (C≡C-H), 2929 (C-H), 1489 (C=N).

Compound 62

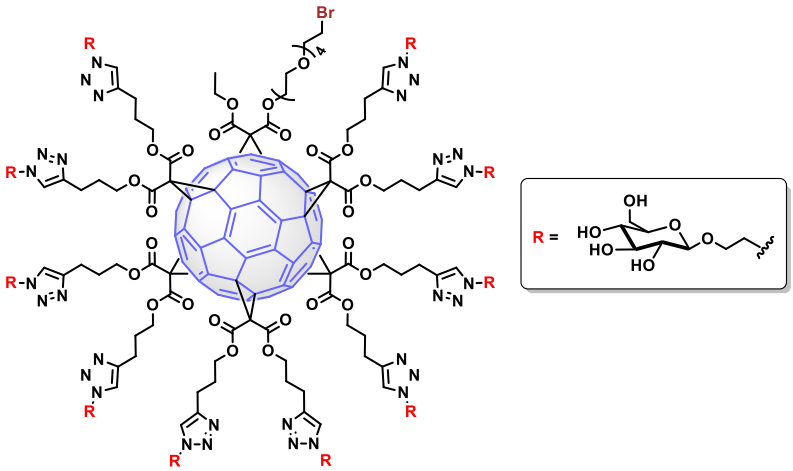

A mixture of **9** (202 mg, 0.088 mmol), 2-azidoethyl β-D-glucopyranoside (**61**) (393 mg, 1.56 mmol), $CuBr{\cdot}S(CH_3)_2$ (91 mg, 0.44 mmol), sodium ascorbate (131 mg, 0.66 mmol) and a piece of copper metal wire in DMSO (1 mL) was deoxygenated and kept under argon with vigorous stirring for 72 h. The crude reaction was filtered through a QuadraSil® Mercaptopropyl column. CH_3OH was added to the mixture and the precipitate was centrifuged and extensively washed with CH_3OH, then dried under high vacuum to afford **62** as a brown solid (386 mg, 91%).

^{1}H NMR (700 MHz, DMSO-*d*$_6$) δ (ppm) = 8.05 (s, 10H; C*H*$_{triazole}$), 5.10 (s, 10H; O*H*), 4.99 (s, 10H; O*H*), 4.94 (s, 10H; O*H*), 4.61 – 4.48 (m, 30H; $OCH_2CH_2N_{glu}$ and O*H*), 4.44 – 4.25 (m, 22H; CH_2CH_3 and $COOCH_2CH_2CH_2$), 4.24 – 4.18 (m, 12H; C*H*$_{1glu}$ and $COOCH_2CH_2O$), 4.11 – 4.05 (m, 10H; $OCH_2CH_2N_{glu}$), 3.93 – 3.85 (m, 10H; $OCH_2CH_2N_{glu}$), 3.70 – 3.64 (m, 12H; CH_2OH_{glu} and CH_2O_{PEG}), 3.56 – 3.53 (m, 4H; CH_2Br and CH_2O_{PEG}), 3.52 – 3.46 (m, 10H; CH_2O_{PEG}), 3.45 – 3.40 (m, 12H; CH_2OH_{glu} and CH_2O_{PEG}), 3.16 – 3.10 (m, 20H; C*H*$_{glu}$), 3.06 – 3.01 (m, 10H; C*H*$_{glu}$), 2.99 – 2.93 (m, 10H; C*H*$_{glu}$), 2.83 – 2.59 (m, 20H; $COOCH_2CH_2CH_2$), 2.10 – 1.84 (m, 20H; $COOCH_2CH_2CH_2$), 1.28 – 1.13 (m, 3H; CH_3).

^{13}C NMR (176 MHz, DMSO-*d*$_6$) δ (ppm) = 162.8 (*C*O), 145.9 (*C*$_{triazole}$), 145.0, 140.7 (*C*$_{sp2\ fullerene}$), 123.5 (*C*H$_{triazole}$), 102.8 (*C*H$_{1glu}$), 76.9, 76.5, 73.2 (*C*H$_{glu}$), 70.3 (CH_2O_{PEG}), 70.0 (*C*H$_{glu}$), 69.7, 69.5 (CH_2O_{PEG}), 68.7 (*C*$_{sp3\ fullerene}$), 67.9 ($COOCH_2CH_2O$), 67.1 ($OCH_2CH_2N_{glu}$), 66.6 ($COOCH_2CH_2CH_2$), 63.3 (CH_2CH_3), 61.0 (CH_2OH_{glu}), 49.9 ($OCH_2CH_2N_{glu}$), 45.5 (*C*$_{q\ bridge}$), 32.2 (CH_2Br), 27.6 ($COOCH_2CH_2CH_2$), 21.5 ($COOCH_2CH_2CH_2$), 13.7 (CH_3).

IR (KBr) (ν cm^{-1}): 3401 (OH), 2920 (C-H), 1741 (C=O).

Compound 63

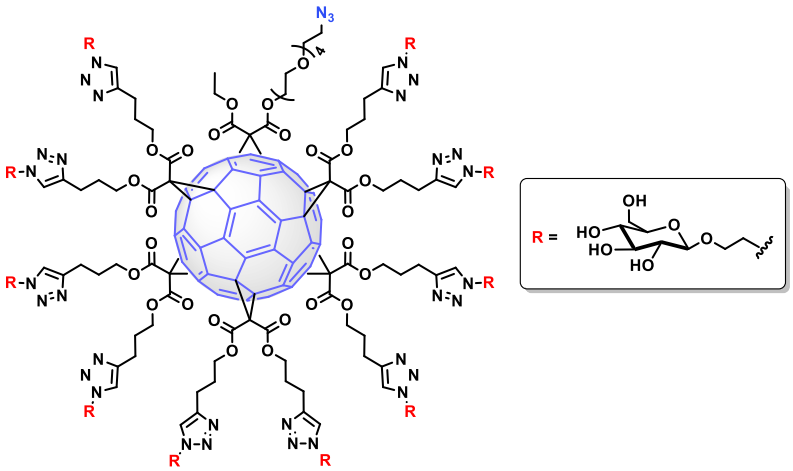

A mixture of **62** (150 mg, 0.031 mmol) and NaN_3 (20 mg, 0.31 mmol) in DMSO-d_6 (0.8 mL) was heated for 90 min at 55 ºC under microwave irradiation. The crude was purified by size-exclusion chromatography (Sephadex G-25 H_2O/CH_3OH 9:1) to afford **63** as a brown glassy solid (138 mg, 93%).

^{1}H NMR (700 MHz, DMSO-d_6) δ (ppm) = 7.91 (s, 10H; C$H_{triazole}$), 5.10 (s, 10H; O*H*), 4.98 (s, 10H; O*H*), 4.93 (s, 10H; O*H*), 4.53 (s, 10H; O*H*), 4.52 – 4.44 (m, 20H; OCH$_2$CH_2N$_{glu}$), 4.42 – 4.24 (m, 24H; CH_2CH$_3$, COOCH_2CH$_2$CH$_2$ and COOCH_2CH$_2$O), 4.21 (d, $^3J_{H,H}$ = 7.7 Hz, 10H; CH_{1glu}), 4.08 – 4.03 (m, 10H; OCH_2CH$_2$N$_{glu}$), 3.89 – 3.83 (m, 10H; OCH_2CH$_2$N$_{glu}$), 3.70 – 3.63 (m, 12H; CH_2OH$_{glu}$ and CH_2O$_{PEG}$), 3.58 – 3.56 (m, 2H; CH_2O$_{PEG}$), 3.53 – 3.46 (m, 10H; CH_2O$_{PEG}$), 3.45 – 3.41 (m, 12H; CH_2OH$_{glu}$ and CH_2O$_{PEG}$), 3.36 (m, 2H; CH_2N$_3$ overlaps with water), 3.16 – 3.10 (m, 20H; CH_{glu}), 3.06 – 3.02 (m, 10H; CH_{glu}), 2.99 – 2.93 (m, 10H; CH_{glu}), 2.75 – 2.58 (m, 20H; COOCH$_2$CH$_2$CH_2), 2.09 – 1.87 (m, 20H; COOCH$_2$CH_2CH$_2$), 1.28 – 1.15 (m, 3H; CH_3).

^{13}C NMR (176 MHz, DMSO-d_6) δ (ppm) = 162.9 (*C*O), 145.6 ($C_{triazole}$), 145.1, 140.7 ($C_{sp2\ fullerene}$), 122.8 (*C*H$_{triazole}$), 102.8 (*C*H$_{1glu}$), 77.0, 76.6, 73.3, 70.0 (*C*H$_{glu}$), 69.8, 69.7, 69.3 (*C*H$_2$O$_{PEG}$), 68.7 ($C_{sp3\ fullerene}$), 68.0 (COO*C*H$_2$CH$_2$O), 67.3 (O*C*H$_2$CH$_2$N$_{glu}$), 66.7 (COO*C*H$_2$CH$_2$CH$_2$), 63.4 (*C*H$_2$CH$_3$), 61.1 (*C*H$_2$OH$_{glu}$), 50.0 (*C*H$_2$N$_3$), 49.5 (OCH$_2$*C*H$_2$N$_{glu}$), 45.6 ($C_{q\ bridge}$), 27.7 (COOCH$_2$*C*H$_2$CH$_2$), 21.4 (COOCH$_2$CH$_2$*C*H$_2$), 13.8 (*C*H$_3$).

IR (KBr) (ν cm^{-1}): 3401 (OH), 2921 (C-H), 2108 (N_3), 1741 (C=O).

Compound 64

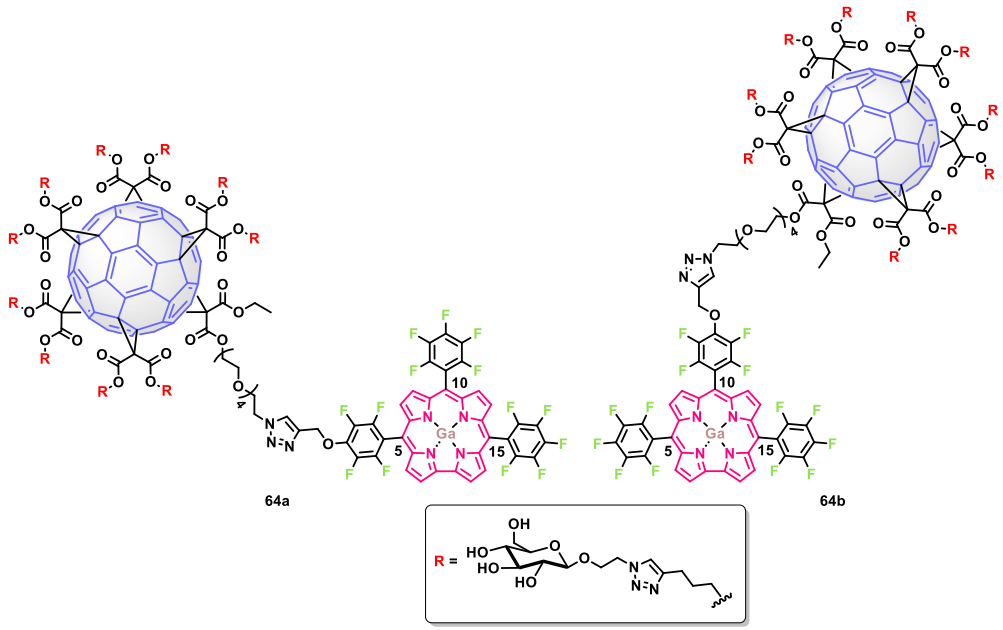

A mixture of glycofullerene **63** (82 mg, 0.018 mmol), corrole **59** (13.4 mg, 0.014 mmol), $CuBr{\cdot}S(CH_3)_2$ (3 mg, 0.014 mmol), sodium ascorbate (4 mg, 0.021 mmol) and a piece of copper metal wire in DMSO (1.5 mL) was deoxygenated and kept under argon with vigorous stirring for 48 h. The crude reaction was filtered through a QuadraSil® Mercaptopropyl column. Then, it was purified by size-exclusion chromatography (Sephadex G-50 H_2O/CH_3OH 9:1) to afford **64** as a violet solid (60 mg, 74%).

The product was obtained as a mixture of isomers indistinguishable by ^{1}H and ^{13}C NMR. For simplicity, only the major isomer (64a**) is referred to.*

^{1}H NMR (700 MHz, DMSO-d_6) δ (ppm) = 9.36 – 8.52 (m, 8H; C$H_{\beta\ corrole}$), 8.48 (s, 1H; C$H_{triazole}$), 7.91 (s, 10H; C$H_{triazole}$), 5.66 (m, 2H; OC$H_{2\ corrole}$), 5.12 (s, 10H; OH), 5.00 (s, 10H; OH), 4.95 (s, 10H; OH), 4.67 – 4.64 (m, 2H; $OCH_2CH_2N_{PEG}$), 4.55 (s, 10H; OH), 4.52 – 4.46 (m, 20H; $OCH_2CH_2N_{glu}$), 4.41 – 4.27 (m, 24H; CH_2CH_3, $COOCH_2CH_2CH_2$ and $COOCH_2CH_2O$), 4.21 (d, $^{3}J_{H,H}$ = 7.7 Hz, 10H; CH_{1glu}), 4.08 – 4.04 (m, 10H; $OCH_2CH_2N_{glu}$), 3.89 – 3.84 (m, 12H; $OCH_2CH_2N_{glu}$ and CH_2O_{PEG}), 3.69 – 3.65 (m, 12H; CH_2OH_{glu} and CH_2O_{PEG}), 3.56 – 3.54 (m, 2H; CH_2O_{PEG}), 3.48 – 3.42 (m, 22H; CH_2OH_{glu} and CH_2O_{PEG}), 3.15 – 3.11 (m, 20H; CH_{glu}), 3.06 – 3.03 (m, 10H; CH_{glu}), 2.98 – 2.95 (m, 10H; CH_{glu}), 2.69 – 2.58 (m, 20H; $COOCH_2CH_2CH_2$), 2.02 – 1.90 (m, 20H; $COOCH_2CH_2CH_2$), 1.25 – 1.15 (m, 3H; CH_3).

^{13}C NMR (176 MHz, DMSO-d_6) δ (ppm) = 162.9 (*C*O), 145.6 (*C*$_{triazole}$), 145.1 (*C*$_{sp2\ fullerene}$), 141.8 (*C*$_{corrole}$), 140.8 (*C*$_{sp2\ fullerene}$), 138.1, 136.7 (*C*$_{corrole}$), 125.9, 122.8 (*C*H$_{triazole}$), 102.9 (*C*H$_{1glu}$), 77.0, 76.6, 73.3, 70.0 (*C*H$_{glu}$), 69.7 (*C*H_2O_{PEG}), 68.9

($C_{sp3\ fullerene}$ and $OCH_{2\ corrole}$), 68.0 ($COOCH_2CH_2O$), 67.4 ($OCH_2CH_2N_{glu}$), 66.8 ($COOCH_2CH_2CH_2$), 63.4 (CH_2CH_3), 61.1 (CH_2OH_{glu}), 49.5 (OCH_2CH_2N), 45.7 ($C_{q\ bridge}$), 27.7 ($COOCH_2CH_2CH_2$), 21.5 ($COOCH_2CH_2CH_2$), 13.8 (CH_3).

$^{19}F\{^1H\}$ NMR (471 MHz, DMSO-d_6) δ (ppm) = -139.27 – -140.25 [m; F_{ortho} (10-F_{ortho}, 15-F_{ortho}, **64a**; 5-F_{ortho}, 15-F_{ortho}, **64b**)], -140.81 – 141.50 [m; F_{ortho} (5-F_{ortho}, **64a**; 10-F_{ortho}, **64b**)], -155.37 – -156.21 (m; F_{para}), -156.59 – -157.60 [(m; F_{meta} (5-F_{meta}, **64a**; 10-F_{meta}, **64b**)], -163.17 – -164.55 [(m; F_{meta} (10-F_{meta} and 15-F_{meta}, **64a**; 5-F_{meta} and 15-F_{meta}, **64b**)].

IR (KBr) (ν cm^{-1}): 3414 (OH), 2926 (C-H), 1740 (C=O).

Compound 65

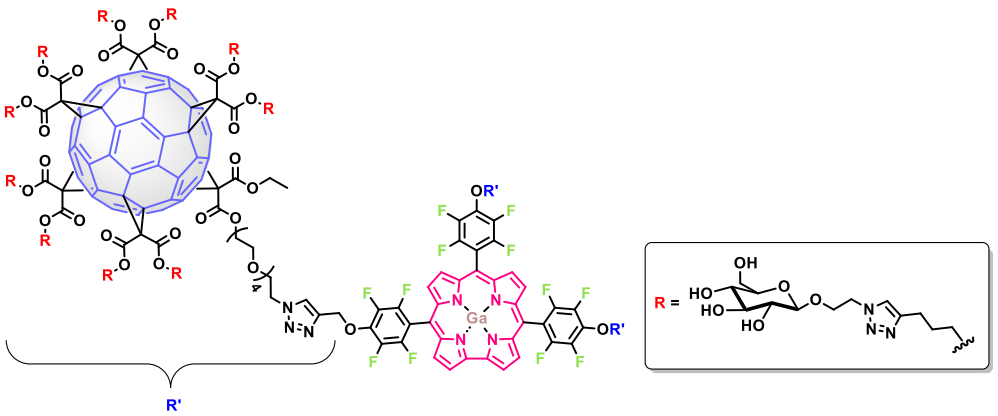

A mixture of glycofullerene **63** (192 mg, 0.040 mmol), corrole **60** (11 mg, 0.011 mmol), $CuBr{\cdot}S(CH_3)_2$ (11 mg, 0.055 mmol), sodium ascorbate (16 mg, 0.083 mmol) and a piece of copper metal wire in DMSO (1.5 mL) was deoxygenated and kept under argon with vigorous stirring for 72 h. The crude reaction was filtered through a QuadraSil® Mercaptopropyl column. Then, it was purified by size-exclusion chromatography (Sephadex G-50 H_2O/CH_3OH 9:1) to afford **65** as a purple solid (137 mg, 81%).

^1H NMR (700 MHz, DMSO-d_6) δ (ppm) = 9.34 – 8.60 (m, 8H; $CH_{\beta\ corrole}$), 8.48 (s, 3H; $CH_{triazole}$), 7.91 (s, 30H; $CH_{triazole}$), 5.66 (s, 6H; $OCH_{2\ corrole}$), 5.11 (s, 30H; O*H*), 4.99 (s, 30H; O*H*), 4.94 (s, 30H; O*H*), 4.67 – 4.63 (m, 6H; $OCH_2CH_2N_{PEG}$), 4.54 (s, 30H; O*H*), 4.51 – 4.45 (m, 60H; $OCH_2CH_2N_{glu}$), 4.42 – 4.27 (m, 72H; CH_2CH_3, $COOCH_2CH_2CH_2$ and $COOCH_2CH_2O$), 4.21 (d, $^3J_{H,H}$ = 8.0 Hz, 30H; CH_{1glu}), 4.08 – 4.04 (m, 30H; $OCH_2CH_2N_{glu}$), 3.90 – 3.84 (m, 36H; $OCH_2CH_2N_{glu}$ and CH_2O_{PEG}), 3.69 – 3.64 (m, 36H; CH_2OH_{glu} and CH_2O_{PEG}), 3.57 – 3.55 (m, 6H; CH_2O_{PEG}), 3.49 – 3.41 (m, 66H; CH_2OH_{glu} and CH_2O_{PEG}), 3.15 – 3.10 (m, 60H; CH_{glu}), 3.06 – 3.02 (m, 30H; CH_{glu}), 2.98 – 2.94 (m, 30H; CH_{glu}), 2.72 – 2.59 (m, 60H; $COOCH_2CH_2CH_2$), 2.04 – 1.89 (m, 60H; $COOCH_2CH_2CH_2$), 1.28 – 1.16 (m, 9H; CH_3).

^{13}C NMR (176 MHz, DMSO-d_6) δ (ppm) = 162.9 (*C*O), 145.6 ($C_{triazole}$), 145.1 ($C_{sp2\ fullerene}$), 141.9 ($C_{corrole}$), 140.8 ($C_{sp2\ fullerene}$), 136.6 ($C_{corrole}$), 125.9, 122.8 (*C*H$_{triazole}$), 102.8 (*C*H$_{1glu}$), 77.0, 76.6, 73.3, 70.0 (*C*H$_{glu}$), 69.7 (*C*H$_2$O$_{PEG}$), 68.8 ($C_{sp3\ fullerene}$), 68.0 (COO*C*H$_2$CH$_2$O), 67.3 (O*C*H$_2$CH$_2$N$_{glu}$ and O*C*H$_{2\ corrole}$), 66.7 (COO*C*H$_2$CH$_2$CH$_2$), 63.4 (*C*H$_2$CH$_3$), 61.1 (*C*H$_2$OH$_{glu}$), 49.5 (OCH$_2$*C*H$_2$N), 45.6 ($C_{q\ bridge}$), 27.7 (COOCH$_2$*C*H$_2$CH$_2$), 21.4 (COOCH$_2$CH$_2$*C*H$_2$), 13.8 (*C*H$_3$).

^{19}F{^{1}H} NMR (471 MHz, DMSO-d_6) δ (ppm) = -139.92 – -142.19 (m; F_{ortho}), -156.21 – -158.23 (m; F_{meta}).

IR (KBr) (ν cm^{-1}): 3392 (OH), 2926 (C-H), 1740 (C=O).

Chapter 3

Compound 68[184]

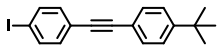

1-(*tert*-butyl)-4-ethynylbenzene (**66**) (350 mg, 2.22 mmol) was added to a solution of 1,4-diiodobenzene (**67**) (1.10 g, 3.33 mmol), $Pd(PPh_3)_2Cl_2$ (15 mg, 0.022 mmol) and CuI (8.4 mg, 0.044 mmol) in a THF (25 mL) and Et_3N (4.5 mL) solution under argon atmosphere. The mixture was stirred at room temperature for 16 h. Then, NH_4Cl (50 mL) and AcOEt (50 mL) were added to the reaction mixture, and the organic layer was separated. The aqueous layer was washed with AcOEt (3 x 40 mL), and the combined organic fractions were washed with brine (50 mL), dried over anh. $MgSO_4$, filtered and concentrated under vacuum. The resulting crude was purified by column chromatography (SiO_2, Hexane) to afford **68** as a white solid (423 mg, 53%).

^{1}H NMR (300 MHz, $CDCl_3$) δ (ppm) = 7.68 (d, $^3J_{H,H}$ = 8.6 Hz, 2H; C*H*), 7.46 (d, $^3J_{H,H}$ = 8.8 Hz, 2H; C*H*), 7.37 (d, $^3J_{H,H}$ = 8.8 Hz, 2H; C*H*), 7.25 (d, $^3J_{H,H}$ = 8.7 Hz, 2H; C*H*), 1.33 [s, 9H; $C(CH_3)_3$].

^{13}C NMR (75 MHz, $CDCl_3$) δ (ppm) = 152.0 (*C*), 137.6, 133.2, 131.5, 125.5 (*C*H), 123.2, 120.0 (*C*), 94.0 (*C*≡C), 91.1 (*C*-I), 88.0 (C≡*C*), 35.0 [*C*$(CH_3)_3$], 31.3 [C(*C*$H_3)_3$].

Compound 70[184]

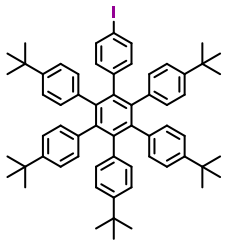

A mixture of compound **68** (50 mg, 0.14 mmol) and 2,3,4,5-tetrakis[4-(*tert*-butyl)phenyl]cyclopenta-2,4-dien-1-one (**69**) (110 mg, 0.18 mmol) was heated for 40 min at 280 ºC under microwave irradiation. The crude was precipitated in cold CH_3OH and filtered affording **70** as a light-brown solid (133 mg, quant.).

^{1}H NMR (300 MHz, $CDCl_3$) δ (ppm) = 7.16 (d, $^3J_{H,H}$ = 8.5 Hz, 2H; C*H*), 6.88 – 6.78 (m, 10H; C*H*), 6.70 – 6.57 (m, 12H; C*H*), 1.14 [s, 16H; $C(CH_3)_3$], 1.10 [s, 27H; $C(CH_3)_3$].

^{13}C NMR (75 MHz, $CDCl_3$) δ (ppm) = 148.0, 147.7, 147.6, 141.0, 140.9, 140.2, 138.7, 137.9, 137.7 (*C*), 135.6, 133.7, 131.2, 131.1, 123.5, 123.2 (*C*H), 90.8 (*C*-I), 34.3, 34.2 [*C*$(CH_3)_3$], 31.4, 31.3 [C(*C*$H_3)_3$].

Compound 71[184]

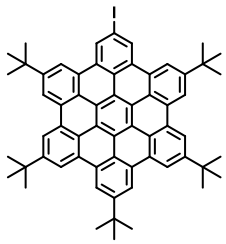

Compound **70** (50 mg, 0.053 mmol) was dissolved in dry DCM (25 mL) and a stream of argon was bubbled through the solution. Then, a solution of $FeCl_3$ (215 mg, 1.33 mmol) in nitromethane (3.6 mL) was added dropwise and the reaction was stirred for 4 h under inert atmosphere. After that time, CH_3OH (20 mL) was added to quench the reaction and evaporated under vacuum. The precipitate was dissolved in DCM and passed through a short plug of silica. The resulting solution was evaporated to dryness affording **71** as a yellow solid (46 mg, 93%)

^{1}H NMR (300 MHz, $CDCl_3$) δ (ppm) = 9.16 (s, 2H; C*H*), 9.07 (s, 2H; C*H*), 8.97 (s, 2H; C*H*), 8.81 (s, 2H; C*H*), 8.60 (s, 2H; C*H*), 8.49 (s, 2H; C*H*), 1.99 [s, 9H; C(C*H*$_3$)$_3$], 1.94 [s, 16H; C(C*H*$_3$)$_3$], 1.81 [s, 16H; C(C*H*$_3$)$_3$].

^{13}C NMR (75 MHz, $CDCl_3$) δ (ppm) = 148.3, 148.1, 147.9, 131.6, 130.2, 129.8, 129.5 (*C*), 129.3 (*C*H) 128.2, 123.5, 123.2, 123.1, 122.8, 120.0, 119.6, 119.5 (*C*), 119.0, 118.7, 118.6, 118.4 (*C*H), 93.8 (*C*-I), 36.0, 35.9, 35.7 [*C*(CH$_3$)$_3$], 32.4, 32.3 [C(*C*H$_3$)$_3$].

Compound 73[184]

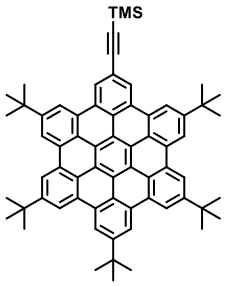

Trimethylsilylacetylene (**72**) (0.013 mL, 0.097 mmol) was added to a solution of **71** (45 mg, 0.048 mmol), $Pd(PPh_3)_2Cl_2$ (2.0 mg, 2.9 μmol) and CuI (0.6 mg, 2.9 μmol) in a THF (15 mL) and Et_3N (6 mL) solution under argon atmosphere. The mixture was stirred at room temperature for 18 h. After that time, the reaction was evaporated to dryness and the resulting crude was purified by column chromatography (SiO_2, Hexane/DCM 3:1) affording **73** as a yellow solid (33 mg, 76%).

^{1}H NMR (300 MHz, $CDCl_3$) δ (ppm) = 9.08 (s, 2H; C*H*), 9.00 (s, 2H; C*H*), 8.92 (s, 2H; C*H*), 8.75 (s, 2H; C*H*), 8.56 (s, 2H; C*H*), 8.42 (s, 2H; C*H*), 2.02 [s, 9H; C(C*H*$_3$)$_3$], 1.97 [s, 16H; C(C*H*$_3$)$_3$], 1.87 [s, 16H; C(C*H*$_3$)$_3$], 0.67 (s, 9H; C*H*$_3$).

^{13}C NMR (75 MHz, $CDCl_3$) δ (ppm) = 148.0, 147.7, 147.6, 130.1, 129.8, 129.7, 129.5, 129.3, 128.8 (*C*), 124.5 (*C*H), 124.4, 123.1, 122.9, 122.7, 119.8, 119.3 (*C*), 119.2, 118.5, 118.2 (*C*H), 107.7 (*C*≡C), 94.6 (C≡*C*), 36.0, 35.9, 35.7 [*C*(CH_3)$_3$], 32.5, 32.4 [C(*C*H_3)$_3$], 0.7 (*C*H_3).

Compound 74[184]

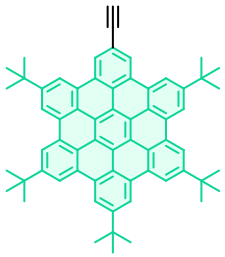

TBAF (0.092 mL, 0.092 mmol) was added to a solution of **73** in DCM (2 mL) and stirred for 16 h. After that time, water (10 mL) and DCM (20 mL) were added and the organic layer was separated and washed with water (10 mL), dried over anh. $MgSO_4$, filtered and concentrated under vacuum affording **74** as a yellow solid (29 mg, quant.).

^{1}H NMR (500 MHz, $CDCl_3$) δ (ppm) = 9.18 (s, 2H; C*H*), 9.12 (s, 2H; C*H*), 9.04 (s, 2H; C*H*), 8.93 (s, 2H; C*H*), 8.75 (s, 2H; C*H*), 8.69 (s, 2H; C*H*), 3.57 (s, 1H; C≡C*H*), 1.93 [s, 9H; C(C*H*$_3$)$_3$], 1.89 [s, 16H; C(C*H*$_3$)$_3$], 1.80 [s, 16H; C(C*H*$_3$)$_3$].

^{13}C NMR (126 MHz, $CDCl_3$) δ (ppm) = 148.6, 148.4, 130.4, 130.1, 129.8, 129.0 (*C*), 124.7 (*C*H), 123.4, 123.2, 120.4, 120.2, 119.9, 119.2 (*C*), 118.8, 118.7, 118.6 (*C*H), 85.9 (*C*≡CH), 77.9 (C≡*C*H), 35.9, 35.8 [*C*(CH_3)$_3$], 32.3, 32.2 [C(*C*H_3)$_3$].

General procedure for the synthesis of malonates 75a-b

Malonyl chloride (**3**) (1 eq.) was added dropwise to a solution of the corresponding monobrominated alcohol (2 eq.), Et_3N (5 eq.) and DMAP (5 mol%) in dry CH_2Cl_2 at 0 ºC under argon atmosphere. After 30 min, the mixture was allowed to warm slowly to room temperature and stirred overnight. Then, the solution was washed with HCl 1M (2 x 50 mL), Na_2CO_3 (2 x 50 mL) and brine (50 mL). The organic layer was dried over anh. $MgSO_4$, filtered and concentrated under vacuum. The resulting crude was purified by column chromatography under the appropriate conditions.

Compound 75a

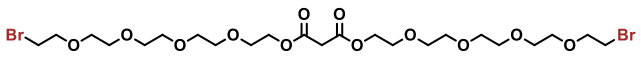

Following the general procedure, using **3** (0.14 mL, 1.47 mmol), **2** (885 mg, 2.94 mmol), Et_3N (1.00 mL, 7.17 mmol) and DMAP (9 mg, 0.074 mmol) in dry CH_2Cl_2 (20 mL), the crude was purified by column chromatography (SiO_2, DCM/CH_3OH 100:5) to afford **75a** as a yellow oil (628 mg, 63%).

^{1}H NMR (300 MHz, $CDCl_3$) δ (ppm) = 4.31 – 4.26 (m, 4H; COOCH_2CH$_2$O), 3.80 (t, $^{3}J_{H,H}$ = 6.3 Hz, 4H; OCH_2CH$_2$Br), 3.72 – 3.68 (m, 4H; COOCH$_2$CH_2O), 3.67 – 3.62 (m, 24H; CH_2O), 3.50 – 3.42 (m, 6H; CH_2Br and COCH_2CO).

^{13}C NMR (75 MHz, $CDCl_3$) δ (ppm) = 166.6 (*C*O), 71.3 (O*C*H$_2$CH$_2$Br), 70.8, 70.7 (*C*H$_2$O), 69.0 (COOCH$_2$*C*H$_2$O), 64.7 (COO*C*H$_2$CH$_2$O), 41.4 (CO*C*H$_2$CO), 30.5 (*C*H$_2$Br).

FTIR-ATR (ν cm^{-1}): 2868 (C-H), 1732 (C=O).

MALDI-TOF: *m/z* calcd for $C_{73}H_{21}BrO_4$: 668.1043, found: 669.1102 $[M+H]^+$.

Compound 75b[199]

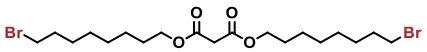

Following the general procedure, using **3** (0.12 mL, 1.20 mmol), 8-bromo-1-octanol (**44**) (0.41 mL, 2.39 mmol), Et_3N (0.70 mL, 5.02 mmol) and DMAP (7.3 mg, 0.060 mmol) in dry CH_2Cl_2 (10 mL), the crude was purified by column chromatography (SiO_2, Hexane/AcOEt 3:1) to afford **75b** as a light-yellow oil (372 mg, 64%).

^{1}H NMR (300 MHz, $CDCl_3$) δ (ppm) = 4.12 (t, $^{3}J_{H,H}$ = 6.7 Hz, 4H; COOCH_2), 3.39 (t, $^{3}J_{H,H}$ = 6.8 Hz, 4H; CH_2Br), 3.35 (s, 2H; COCH_2CO), 1.84 (p, $^{3}J_{H,H}$ = 6.9 Hz, 4H; CH_2), 1.69 – 1.57 (m, 4H; CH_2), 1.46 – 1.29 (m, 16H; CH_2).

^{13}C NMR (75 MHz, $CDCl_3$) δ (ppm) = 166.8 (*C*O), 65.7 (COO*C*H$_2$), 41.8 (CO*C*H$_2$CO), 34.0 (*C*H$_2$Br), 32.8, 29.1, 28.7, 28.5, 28.1, 25.8 (*C*H$_2$).

General procedure for the synthesis of manoadducts 76a-b

DBU (2.5 eq.) was added dropwise to a solution of the corresponding malonate (1 eq.), [60]fullerene (2 eq.) and I_2 (3.5 eq.) in dry toluene (500 mL) under argon at 0 ºC. The reaction mixture was then allowed to warm gradually to room temperature and stirred for 3 hours. After that time, the reaction mixture was washed with sat. $Na_2S_2O_3$ (2 x 100 mL), HCl 0.5 M (2 x 100 mL), water (100 mL) and brine (100 mL). The organic layer was dried over anh. $MgSO_4$, filtered and concentrated under vacuum. The crude was purified by column chromatography under the appropriate conditions.

[199] N. Li, F. Chen, J. Shen, H. Zhang, T. Wang, R. Ye, T. Li, T. Peng Loh, Y. Y. Yang, H. Zeng, *J. Am. Chem. Soc.* **2020**, *142*, 21082.

Compound 76a

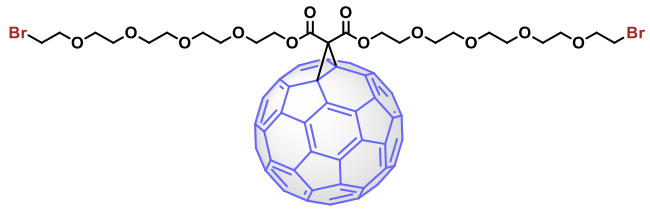

Following the general procedure, using DBU (0.28 mL, 1.90 mmol), **75a** (507 mg, 0.76 mmol), [60]fullerene (1.09 g, 1.51 mmol) and I_2 (675 mg, 2.66 mmol) in dry toluene (500 mL), the crude was purified by column chromatography (SiO_2, CS_2 → Toluene/Acetone 1:1) to afford **76a** as a dark brown solid (293 mg, 28%).

^{1}H NMR (300 MHz, $CDCl_3$) δ (ppm) = 4.69 – 4.60 (m, 4H; COOCH_2CH$_2$O), 3.90 – 3.85 (m, 4H; COOCH$_2$CH_2O), 3.80 (t, $^3J_{H,H}$ = 6.3 Hz, 4H; OCH_2CH$_2$Br), 3.70 – 3.64 (m, 24H; CH_2O), 3.46 (t, $^3J_{H,H}$ = 6.4 Hz, 4H; CH_2Br).

^{13}C NMR (75 MHz, $CDCl_3$) δ (ppm) = 163.6 (*C*O), 145.4, 145.3, 145.0, 144.8, 144.7, 144.0, 143.2, 143.1, 142.3, 142.0, 141.1, 139.2 ($C_{sp2\ fullerene}$), 71.6 ($C_{sp3\ fullerene}$), 71.3 (O*C*H$_2$CH$_2$Br), 70.8, 70.7 (*C*H$_2$O), 68.9 (COOCH$_2$*C*H$_2$O), 66.4 (COO*C*H$_2$CH$_2$O), 52.2 ($C_{q\ bridge}$), 30.5 (*C*H$_2$Br).

FTIR-ATR (ν cm^{-1}): 2868 (C-H), 1745 (C=O).

MALDI-TOF: *m/z* calcd for $C_{73}H_{21}BrO_4$: 1386.0887, found: 1386.0838 $[M]^+$.

Compound 76b

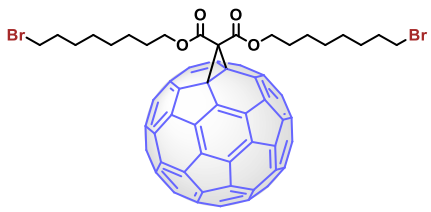

Following the general procedure, using DBU (0.34 mL, 2.28 mmol), **75b** (342 mg, 0.70 mmol), [60]fullerene (1.02 g, 1.41 mmol) and I_2 (622 mg, 2.45 mmol) in dry toluene (500 mL), the crude was purified by column chromatography (SiO_2, CS_2 → Toluene) to afford **76b** as a dark brown solid (416 mg, 49%).

^{1}H NMR (500 MHz, $CDCl_3$) δ (ppm) = 4.49 (t, $^3J_{H,H}$ = 6.6 Hz, 4H; COOCH_2), 3.40 (t, $^3J_{H,H}$ = 6.8 Hz, 4H; CH_2Br), 1.89 – 1.81 (m, 8H; CH_2), 1.51 – 1.32 (m, 16H; CH_2).

^{13}C NMR (75 MHz, $CDCl_3$) δ (ppm) = 163.8 (*C*O), 145.4, 145.3, 145.2, 144.9, 144.7, 144.6, 143.9, 143.1, 143.0, 142.2, 141.9, 141.0, 139.0 ($C_{sp2\ fullerene}$), 71.7 ($C_{sp3\ fullerene}$), 67.4 (COO*C*H$_2$), 52.4 ($C_{q\ bridge}$), 34.0 (*C*H$_2$Br), 32.8, 29.1, 28.8, 28.6, 28.1, 25.9 (*C*H$_2$).

FTIR-ATR (ν cm^{-1}): 2929 (C-H), 1744 (C=O).

MALDI-TOF: *m/z* calcd for $C_{73}H_{21}BrO_4$: 1202.0667, found: 1202.0657 $[M]^+$.

General procedure for the synthesis of hexakis-adducts 77a-b

DBU (20 eq.) was added dropwise to a solution the corresponding monoadduct (1 eq.), compound **6** (10 eq.) and CBr_4 (80 eq.) in dry toluene under argon atmosphere. The mixture was stirred at room temperature for 72 h. After that time, the reaction mixture was washed with sat. $Na_2S_2O_3$ (100 mL), HCl 1 M (2 x 100 mL), water (100 mL) and brine (100 mL). The organic layer was dried over anh. $MgSO_4$, filtered and concentrated under vacuum. The crude was purified by column chromatography under the appropriate conditions.

Compound 77a

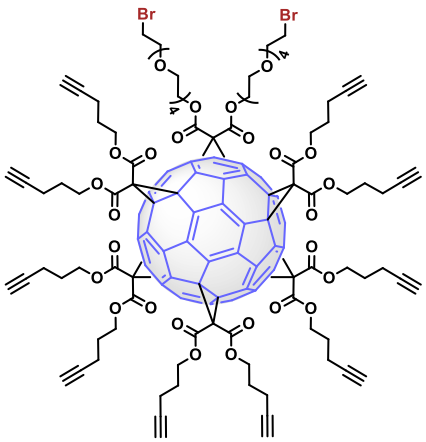

Following the general procedure, using DBU (0.57 mL, 3.80 mmol), **76a** (263 mg, 0.19 mmol), **6** (449 mg, 1.90 mmol) and CBr_4 (5.03 g, 15.17 mmol) in dry toluene (100 mL), the crude was purified by column chromatography (SiO_2, DCM → DCM/Acetone 50:1 → 5:1) to afford **77a** as a red sticky solid (305 mg, 63%).

^{1}H NMR (700 MHz, $CDCl_3$) δ (ppm) = 4.49 – 4.32 (m, 24H; $COOCH_2$), 3.80 (t, $^3J_{H,H}$ = 6.3 Hz, 4H; CH_2CH_2Br), 3.77 – 3.69 (m, 4H; $COOCH_2CH_2O$), 3.66 – 3.61 (m, 24H; CH_2O_{PEG}), 3.47 (t, $^3J_{H,H}$ = 6.3 Hz, 4H; CH_2Br), 2.36 – 2.26 (m, 20H; $COOCH_2CH_2CH_2$), 2.05 – 1.88 (m, 30H; $COOCH_2CH_2CH_2$ and C≡CH).

^{13}C NMR (176 MHz, $CDCl_3$) δ (ppm) = 163.8, 163.7 (CO), 145.9, 141.1 ($C_{sp2\ fullerene}$), 82.6 (C≡CH), 78.5 (C≡CH), 71.3 (CH_2CH_2Br), 70.7, 70.6 (CH_2O_{PEG}), 69.8 (C≡CH), 69.2 ($C_{sp3\ fullerene}$), 68.7 ($COOCH_2CH_2O$), 65.9 ($COOCH_2CH_2O$), 65.5 ($COOCH_2CH_2CH_2$), 45.3, 39.5 ($C_{q\ bridge}$), 30.5 (CH_2Br), 27.2 ($COOCH_2CH_2CH_2$), 16.5, 15.2 ($COOCH_2CH_2CH_2$).

FTIR-ATR (ν cm^{-1}): 3292 (C≡C-H), 2898 (C-H), 1742 (C=O).

Compound 77b

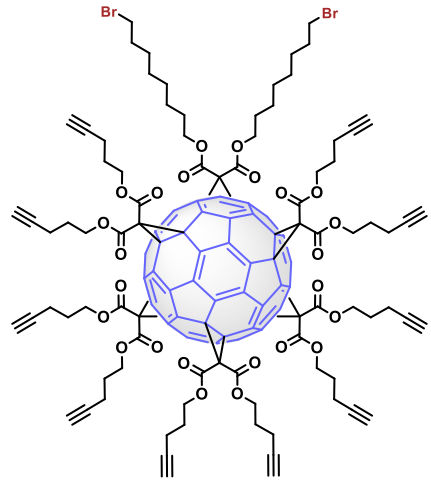

Following the general procedure, using DBU (0.36 mL, 2.40 mmol), **76b** (146 mg, 0.12 mmol), **6** (283 mg, 1.20 mmol) and CBr_4 (3.22 g, 9.71 mmol) in dry toluene (50 mL), the crude was purified by column chromatography (SiO_2, DCM → DCM/Acetone 100:5) to afford **77b** as a red sticky solid (147 mg, 52%).

^{1}H NMR (700 MHz, $CDCl_3$) δ (ppm) = 4.72 – 4.07 (m, 24H; COOC*H*$_2$), 3.42 – 3.38 (m, 4H; C*H*$_2$Br), 2.51 – 2.12 (m, 20H; $COOCH_2CH_2CH_2$); 2.10 – 1.79 (m, 34H; $COOCH_2CH_2CH_2$, C≡C*H* and C*H*$_2$ linker); 1.73 – 1.62 (m, 4H; C*H*$_2$ linker), 1.44 – 1.28 (m, 16H; C*H*$_2$ linker).

^{13}C NMR (176 MHz, $CDCl_3$) δ (ppm) = 163.8 (*C*O), 145.9, 141.2 (*C*$_{sp2\ fullerene}$), 82.6 (*C*≡CH), 78.5, 69.8 (C≡*C*H), 69.2 (*C*$_{sp3\ fullerene}$), 67.1 ($COOCH_2$), 65.5 ($COOCH_2CH_2CH_2$), 45.3, 39.5 (*C*$_{q\ bridge}$), 34.2 (CH_2Br), 32.9, 29.1, 28.8, 28.5, 28.2 ($CH_{2\ linker}$), 27.2 ($COOCH_2CH_2CH_2$), 25.9 ($CH_{2\ linker}$), 16.5, 15.2 ($COOCH_2CH_2CH_2$).

FTIR-ATR (ν cm^{-1}): 3293 (C≡C-H), 2931 (C-H), 1741 (C=O).

General procedure for the synthesis of glycofullerenes 78a-b

A mixture of the corresponding hexakis-adduct (1 eq.), 2-azidoethyl β-D-glucopyranoside (**61**) (18 eq.), $CuBr{\cdot}S(CH_3)_2$ (5 eq.), sodium ascorbate (7.5 eq.) and a piece of copper metal wire in DMSO (1.5 mL) was deoxygenated and kept under argon with vigorous stirring for 72 h. The crude reaction was filtered through a QuadraSil® Mercaptopropyl column. CH_3OH was added to the mixture and the precipitate was centrifuged, extensively washed with CH_3OH and then dried under high vacuum.

Compound 78a

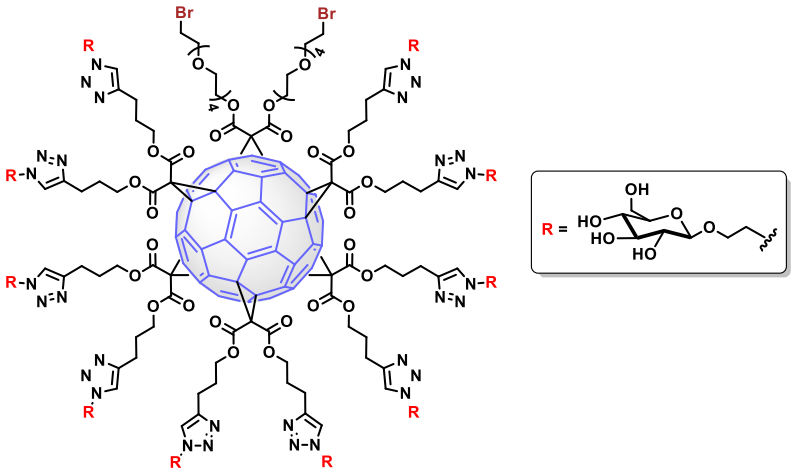

Following the general procedure, using hexakis-adduct **77a** (50 mg, 0.020 mmol), **61** (87 mg, 0.35 mmol), $CuBr{\cdot}S(CH_3)_2$ (21 mg, 0.10 mmol), sodium ascorbate (30 mg, 0.15 mmol) and a piece of copper metal wire in DMSO (1 mL), compound **78a** was obtained as a brown solid (65 mg, 64%).

^{1}H NMR (700 MHz, DMSO-*d*$_6$) δ (ppm) = 8.03 (s, 10H; C*H*$_{triazole}$), 5.12 (s, 10H; O*H*), 5.01 (s, 10H; O*H*), 4.96 (s, 10H; O*H*), 4.59 – 4.48 (m, 30H; OCH$_2$C*H*$_2$N$_{glu}$ and O*H*), 4.43 – 4.26 (m, 24H; COOC*H*$_2$CH$_2$CH$_2$ and COOC*H*$_2$CH$_2$O), 4.24 – 4.19 (m, 10H; C*H*$_{1glu}$), 4.11 – 4.04 (m, 10H; OC*H*$_2$CH$_2$N$_{glu}$), 3.92 – 3.84 (m, 10H; OC*H*$_2$CH$_2$N$_{glu}$), 3.71 – 3.65 (m, 14H; C*H*$_2$OH$_{glu}$ and C*H*$_2$O$_{PEG}$), 3.54 – 3.52 (m, 8H; C*H*$_2$Br and C*H*$_2$O$_{PEG}$), 3.50 – 3.45 (m, 20H; C*H*$_2$O$_{PEG}$), 3.44 – 3.41 (m, 14H; C*H*$_2$OH$_{glu}$ and C*H*$_2$O$_{PEG}$), 3.16 – 3.08 (m, 20H; C*H*$_{glu}$), 3.06 – 3.01 (m, 10H; C*H*$_{glu}$), 2.99 – 2.92 (m, 10H; C*H*$_{glu}$), 2.80 – 2.62 (m, 20H; COOCH$_2$CH$_2$C*H*$_2$), 2.08 – 1.87 (m, 20H; COOCH$_2$C*H*$_2$CH$_2$).

^{13}C NMR (176 MHz, DMSO-*d*$_6$) δ (ppm) = 162.8 (*C*O), 145.8 (*C*$_{triazole}$), 145.0, 140.7 (*C*$_{sp2\ fullerene}$), 123.3 (*C*H$_{triazole}$), 102.8 (*C*H$_{1glu}$), 76.9, 76.5, 73.2 (*C*H$_{glu}$), 70.3 (*C*H$_2$O$_{PEG}$), 70.0 (*C*H$_{glu}$), 69.5 (*C*H$_2$O$_{PEG}$), 68.7 (*C*$_{sp3\ fullerene}$), 67.9 (COO*C*H$_2$CH$_2$O), 67.2 (O*C*H$_2$CH$_2$N$_{glu}$), 66.7 (COO*C*H$_2$CH$_2$CH$_2$), 61.0 (*C*H$_2$OH$_{glu}$), 49.8 (OCH$_2$*C*H$_2$N$_{glu}$), 45.4 (*C*$_{q\ bridge}$), 32.3 (*C*H$_2$Br), 27.6 (COOCH$_2$*C*H$_2$CH$_2$), 21.6 (COOCH$_2$CH$_2$*C*H$_2$).

IR (KBr) (ν cm^{-1}): 3414 (OH), 2883 (C-H), 1741 (C=O).

Compound 78b

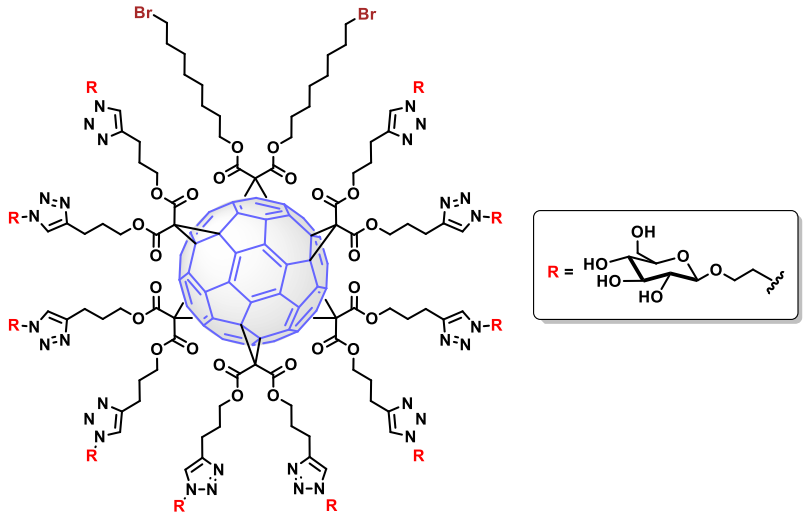

Following the general procedure, using hexakis-adduct **77b** (50 mg, 0.021 mmol), **61** (94 mg, 0.39 mmol), $CuBr{\cdot}S(CH_3)_2$ (23 mg, 0.11 mmol), sodium ascorbate (32 mg, 0.16 mmol) and a piece of copper metal wire in DMSO (1 mL), compound **78b** was obtained as a brown solid (75 mg, 73%).

^{1}H NMR (700 MHz, DMSO-d_6) δ (ppm) = 8.03 (s, 10H; C$H_{triazole}$), 5.12 (s, 10H; OH), 5.00 (s, 10H; OH), 4.95 (s, 10H; OH), 4.59 – 4.48 (m, 30H; $OCH_2CH_2N_{glu}$ and OH), 4.40 – 4.25 (m, 20H; $COOCH_2CH_2CH_2$), 4.24 – 4.17 (m, 14H; CH_{1glu} and $COOCH_2$ $_{linker}$), 4.10 – 4.04 (m, 10H; $OCH_2CH_2N_{glu}$), 3.89 – 3.84 (m, 10H; $OCH_2CH_2N_{glu}$), 3.69 – 3.64 (m, 10H; CH_2OH_{glu}), 3.51 – 3.44 (m, 14H; CH_2OH_{glu} and CH_2Br), 3.15 – 3.08 (m, 20H; CH_{glu}), 3.05 – 3.00 (m, 10H; CH_{glu}), 2.98 – 2.91 (m, 10H; CH_{glu}), 2.78 – 2.62 (m, 20H; $COOCH_2CH_2CH_2$), 2.07 – 1.88 (m, 20H; $COOCH_2CH_2CH_2$), 1.77 – 1.72 (m, 4H; CH_2 $_{linker}$), 1.62 – 1.55 (m, 4H; CH_2 $_{linker}$), 1.31 – 1.19 (m, 16H; CH_2 $_{linker}$).

^{13}C NMR (176 MHz, DMSO-d_6) δ (ppm) = 162.8 (CO), 145.9 ($C_{triazole}$), 144.9, 140.7 (C_{sp2} $_{fullerene}$), 123.3 ($CH_{triazole}$), 102.8 (CH_{1glu}), 76.9, 76.5, 73.2, 70.0 (CH_{glu}), 68.7 (C_{sp3} $_{fullerene}$), 67.2 ($OCH_2CH_2N_{glu}$), 66.6 ($COOCH_2CH_2CH_2$ and $COOCH_2$ $_{linker}$), 61.0 (CH_2OH_{glu}), 49.8 ($OCH_2CH_2N_{glu}$), 45.4 (C_q $_{bridge}$), 35.1 (CH_2Br), 32.1, 28.4, 28.0 (CH_2 $_{linker}$), 27.4 ($COOCH_2CH_2CH_2$ and CH_2 $_{linker}$), 25.3 (CH_2 $_{linker}$), 21.5 ($COOCH_2CH_2CH_2$).

FTIR (KBr) (ν cm^{-1}): 3422 (OH), 2928 (C-H), 1742 (C=O).

General procedure for the synthesis of glycofullerenes 79a-b

A mixture of the corresponding glycofullerene (1 eq.) and NaN_3 (20 eq.) in DMSO-d_6 was heated for 90 min at 55 ºC under microwave irradiation. The crude was purified by size-exclusion chromatography (Sephadex G-25 H_2O/CH_3OH 9:1).

Compound 79a

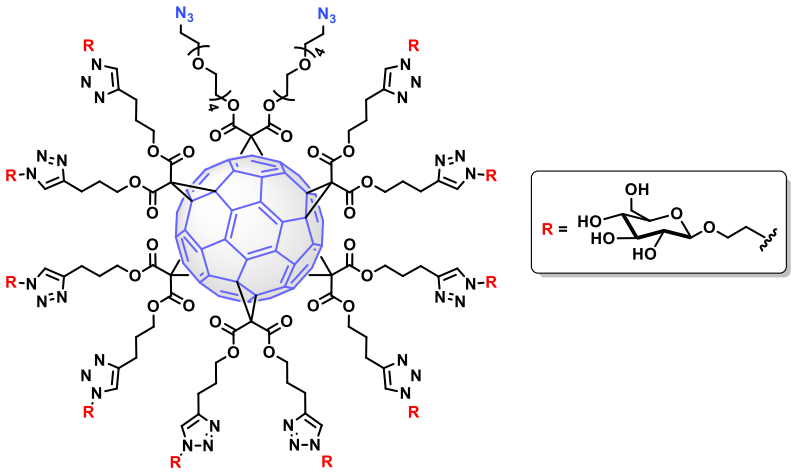

Following the general procedure, using glycofullerene **78a** (42 mg, 8.3 µmol) and NaN_3 (11 mg, 0.17 mmol) in DMSO-*d*$_6$ (0.8 mL), compound **79a** was afforded as a brown glassy solid (30 mg, 73%).

^{1}H NMR (700 MHz, DMSO-*d*$_6$) δ (ppm) = 7.92 (s, 10H; C*H*$_{triazole}$), 5.17 (s, 10H; O*H*), 5.05 (s, 10H; O*H*), 4.99 (s, 10H; O*H*), 4.59 (s, 10H; O*H*), 4.52 – 4.46 (m, 20H; $OCH_2CH_2N_{glu}$), 4.41 – 4.26 (m, 24H; $COOCH_2CH_2CH_2$ and $COOCH_2CH_2O$), 4.22 – 4.19 (m, 10H; C*H*$_{1glu}$), 4.08 – 4.03 (m, 10H; $OCH_2CH_2N_{glu}$), 3.88 – 3.82 (m, 10H; $OCH_2CH_2N_{glu}$), 3.69 – 3.63 (m, 14H; CH_2OH_{glu} and CH_2O_{PEG}), 3.57 – 3.55 (m, 4H; CH_2O_{PEG}), 3.53 – 3.44 (m, 34H; CH_2OH_{glu} and CH_2O_{PEG}), 3.36 – 3.35 (m, 4H; CH_2N_3), 3.15 – 3.09 (m, 20H; C*H*$_{glu}$), 3.05 – 3.01 (m, 10H; C*H*$_{glu}$), 2.98 – 2.93 (m, 10H; C*H*$_{glu}$), 2.71 – 2.59 (m, 20H; $COOCH_2CH_2CH_2$), 2.03 – 1.89 (m, 20H; $COOCH_2CH_2CH_2$).

^{13}C NMR (176 MHz, DMSO-*d*$_6$) δ (ppm) = 162.9 (*C*O), 145.6 (*C*$_{triazole}$), 145.2, 140.6 (*C*$_{sp2\ fullerene}$), 122.9 (*C*H$_{triazole}$), 102.9 (*C*H$_{1glu}$), 77.0, 76.6, 73.4, 70.0 (*C*H$_{glu}$), 69.9, 69.8, 69.4 (*C*H$_2$O$_{PEG}$), 68.8 (*C*$_{sp3\ fullerene}$), 68.0 ($COOCH_2CH_2O$), 67.4 ($OCH_2CH_2N_{glu}$), 66.7 ($COOCH_2CH_2CH_2$), 61.1 (CH_2OH_{glu}), 50.0 (CH_2N_3), 49.5 ($OCH_2CH_2N_{glu}$), 45.6 (*C*$_{q\ bridge}$), 27.8 ($COOCH_2CH_2CH_2$), 21.5 ($COOCH_2CH_2CH_2$).

IR (KBr) (ν cm^{-1}): 3401 (OH), 2879 (C-H), 2105 (N_3), 1740 (C=O).

Compound 79b

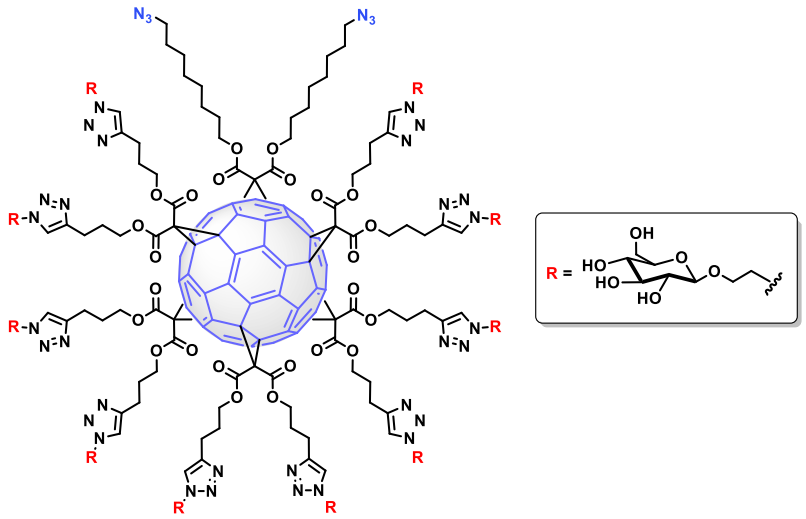

Following the general procedure, using glycofullerene **78b** (50 mg, 0.010 mmol) and NaN_3 (13 mg, 0.21 mmol) in DMSO-d_6 (0.6 mL), compound **79b** was obtained as a brown glassy solid (38 mg, 80%).

^{1}H NMR (700 MHz, DMSO-d_6) δ (ppm) = 7.91 (s, 10H; C$H_{triazole}$), 5.13 (s, 10H; OH), 5.03 (s, 10H; OH), 4.98 (s, 10H; OH), 4.56 (s, 10H; OH), 4.53 – 4.43 (m, 20H; OCH$_2$CH_2N$_{glu}$), 4.42 – 4.25 (m, 20H; COOCH_2CH$_2$CH$_2$), 4.24 – 4.16 (m, 14H; CH_{1glu} and COOC$H_{2\ linker}$), 4.09 – 4.03 (m, 10H; OCH_2CH$_2$N$_{glu}$), 3.88 – 3.83 (m, 10H; OCH_2CH$_2$N$_{glu}$), 3.69 – 3.64 (m, 10H; CH_2OH$_{glu}$), 3.44 – 3.41 (m, 10H; CH_2OH$_{glu}$), 3.30 – 3.25 (m, 4H; CH_2N$_3$), 3.16 – 3.08 (m, 20H; CH_{glu}), 3.06 – 3.01 (m, 10H; CH_{glu}), 2.99 – 2.93 (m, 10H; CH_{glu}), 2.79 – 2.58 (m, 20H; COOCH$_2$CH$_2$CH_2), 2.03 – 1.86 (m, 20H; COOCH$_2$CH_2CH$_2$), 1.63 – 1.56 (m, 4H; C$H_{2\ linker}$), 1.51 – 1.45 (m, 4H; C$H_{2\ linker}$), 1.27 – 1.16 (m, 16H; C$H_{2\ linker}$).

^{13}C NMR (176 MHz, DMSO-d_6) δ (ppm) = 162.9 (*C*O), 145.5 ($C_{triazole}$), 145.1, 140.8 ($C_{sp2\ fullerene}$), 122.8 (*C*H$_{triazole}$), 102.9 (*C*H$_{1glu}$), 77.0, 76.6, 73.3, 70.0 (*C*H$_{glu}$), 68.8 ($C_{sp3\ fullerene}$), 67.4 (O*C*H$_2$CH$_2$N$_{glu}$), 66.7 (COO*C*H$_2$CH$_2$CH$_2$ and COO*C*H$_{2\ linker}$), 61.1 (*C*H$_2$OH$_{glu}$), 50.6 (*C*H$_2$N$_3$), 49.5 (OCH$_2$*C*H$_2$N$_{glu}$), 45.5 ($C_{q\ bridge}$), 28.5, 28.2 (*C*H$_{2\ linker}$), 27.7 (COOCH$_2$*C*H$_2$CH$_2$ and *C*H$_{2\ linker}$), 26.1, 25.3 (*C*H$_{2\ linker}$), 21.5 (COOCH$_2$CH$_2$*C*H$_2$).

FTIR-ATR (ν cm^{-1}): 3392 (OH), 2927 (C-H), 2096 (N_3), 1741 (C=O).

General procedure for the synthesis of glycofullerene-HBC derivatives 80a-b

A mixture of the corresponding glycofullerene (1 eq.), nanographene **74** (2.5 eq.), CuBr·S(CH$_3$)$_2$ (2 eq.) sodium ascorbate (3 eq.) and a piece of copper metal wire in DMSO (0.25 mL) and DCM (0.5 mL) was deoxygenated and kept under argon with vigorous stirring for 72 h. The crude reaction was filtered through a QuadraSil®

Mercaptopropyl column and purified by size-exclusion chromatography (Sephadex G-50 H_2O/CH_3OH 9:1).

Compound 80a

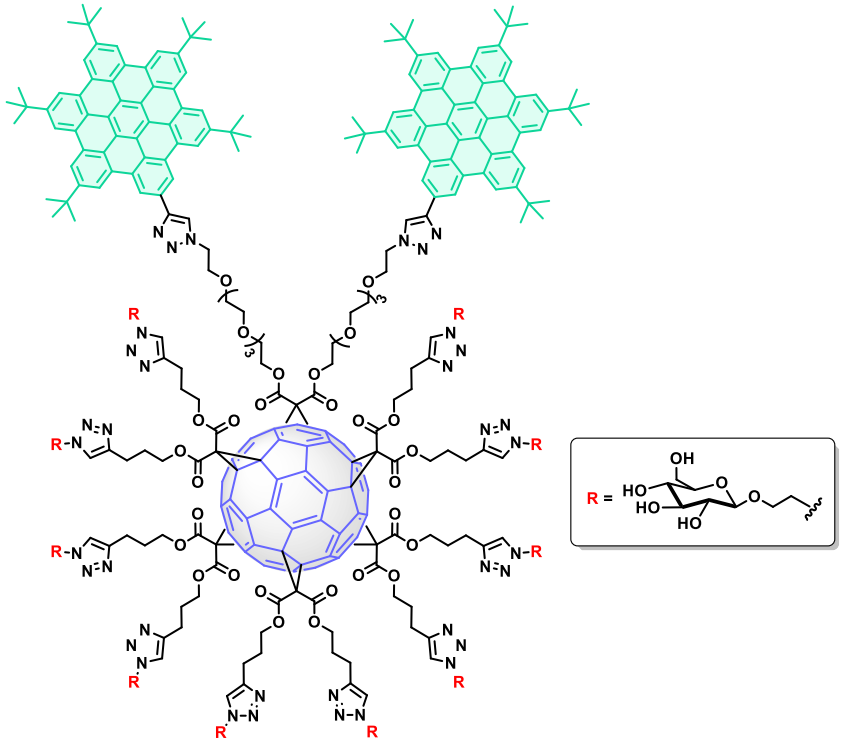

Following the general procedure, using glycofullerene **79a** (12 mg, 2.4 µmol), **74** (5 mg, 6.0 µmol), $CuBr{\cdot}S(CH_3)_2$ (1 mg, 4.8 µmol), sodium ascorbate (1.4 mg, 7.2 µmol) and a piece of copper metal wire in $DMSO/CH_2Cl_2$, compound **80a** was afforded as a brown solid (12 mg, 73%).

^{1}H NMR (700 MHz, DMSO-d_6) δ (ppm) = 9.44 – 8.37 (m, 24H; CH_{HBC}), 7.94 – 7.82 (m, 12H; C$H_{triazole}$), 5.10 (s, 10H; OH), 4.98 (s, 10H; OH), 4.93 (s, 10H; OH), 4.88 – 4.84 (m, 4H; $OCH_2CH_2N_{PEG}$), 4.54 – 4.48 (m, 30H; OH and $OCH_2CH_2N_{glu}$), 4.39 – 4.28 (m, 24H; CH_2CH_3, $COOCH_2CH_2O$ and $COOCH_2CH_2CH_2$), 4.22 – 4.20 (m, 10H; CH_{1glu}), 4.08 – 4.04 (m, 14H; $OCH_2CH_2N_{glu}$ and CH_2O_{PEG}), 3.87 – 3.84 (m, 10H; $OCH_2CH_2N_{glu}$), 3.69 – 3.64 (m, 18H; CH_2OH_{glu} and CH_2O_{PEG}), 3.57 – 3.53 (m, 8H; CH_2O_{PEG}), 3.51 – 3.47 (m, 8H; CH_2O_{PEG}), 3.44 – 3.41 (m, 14H; CH_2OH_{glu} and CH_2O_{PEG}), 3.14 – 3.10 (m, 20H; CH_{glu}), 3.05 – 3.03 (m, 10H; CH_{glu}), 2.98 – 2.95 (m, 10H; CH_{glu}), 2.70 – 2.61 (m, 20H; $COOCH_2CH_2CH_2$), 2.01 – 1.92 (m, 20H; $COOCH_2CH_2CH_2$), 1.84 – 1.75 [m, 90H; $C(CH_3)_3$].

^{13}C NMR (176 MHz, DMSO-d_6) δ (ppm) = 162.9 (*C*O), 147.6 (C_{HBC}), 145.5 ($C_{triazole}$ and $C_{sp2\ fullerene}$), 140.5 ($C_{sp2\ fullerene}$), 129.1 (C_{HBC}), 122.8 ($CH_{triazole}$), 121.8, 118.4 (C_{HBC}), 102.8 (CH_{1glu}), 76.9, 76.6, 73.3, 70.0 (CH_{glu}), 69.8 (CH_2O_{PEG}), 68.8 ($C_{sp3\ fullerene}$), 67.3 ($OCH_2CH_2N_{glu}$ and $COOCH_2CH_2O$), 66.6 ($COOCH_2CH_2CH_2$), 61.1

(CH_2OH_{glu}), 49.5 (OCH_2CH_2N), 45.5 ($C_{q\ bridge}$), 35.5, 35.4, 35.2 [$C(CH_3)_3$], 31.8, 31.7, 31.6 [$C(CH_3)_3$], 27.7 ($COOCH_2CH_2CH_2$), 21.4 ($COOCH_2CH_2CH_2$).

FTIR (KBr) (ν cm^{-1}): 3414 (OH), 2954 (C-H), 1739 (C=O).

Compound 80b

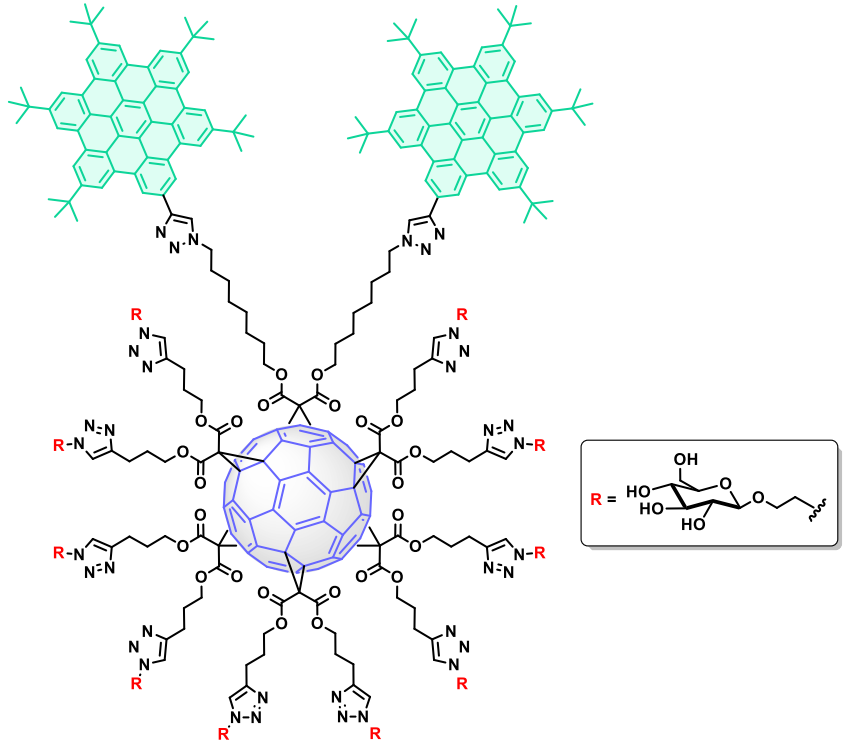

Following the general procedure, using glycofullerene **79b** (14 mg, 2.9 μmol), **74** (6 mg, 7.3 μmol), $CuBr{\cdot}S(CH_3)_2$ (1.2 mg, 5.8 μmol), sodium ascorbate (1.7 mg, 8.7 μmol) and a piece of copper metal wire in $DMSO/CH_2Cl_2$, compound **80b** was obtained as a brown solid (11 mg, 66%).

^{1}H NMR (700 MHz, DMSO-d_6) δ (ppm) = 9.14 – 8.27 (m, 24H; CH_{HBC}), 8.10 – 7.73 (m, 12H; $CH_{triazole}$), 5.14 (s, 10H; OH), 5.07 – 4.96 (m, 20H; OH), 4.59 – 4.46 (m, 34H; OCH_2CH_2N and OH), 4.39 – 4.27 (m, 20H; $COOCH_2CH_2CH_2$), 4.23 – 4.18 (m, 14H; CH_{1glu} and $COOCH_{2\ linker}$), 4.07 – 4.02 (m, 10H; $OCH_2CH_2N_{glu}$), 3.87 – 3.83 (m, 10H; $OCH_2CH_2N_{glu}$), 3.67 – 3.63 (m, 10H; CH_2OH_{glu}), 3.40 (m, 10H; CH_2OH_{glu} overlaps with water), 3.14 – 3.09 (m, 20H; CH_{glu}), 3.05 – 3.02 (m, 10H; CH_{glu}), 2.97 – 2.94 (m, 10H; CH_{glu}), 2.70 – 2.59 (m, 20H; $COOCH_2CH_2CH_2$), 1.85 – 1.77 [m, 134H; $COOCH_2CH_2CH_2$, $C(CH_3)_3$ and $CH_{2\ linker}$].

^{13}C NMR (176 MHz, DMSO-d_6) δ (ppm) = 163.0 (CO), 147.6 (C_{HBC}), 145.6 ($C_{triazole}$ and $C_{sp2\ fullerene}$), 140.7 ($C_{sp2\ fullerene}$), 128.9, 124.3 (CH_{HBC}), 122.9 ($CH_{triazole}$), 121.9, 118.5 (C_{HBC}), 102.9 (CH_{1glu}), 77.0, 76.6, 73.4, 70.0 (CH_{glu}), 68.8 ($C_{sp3\ fullerene}$), 67.4 ($OCH_2CH_2N_{glu}$), 66.5 ($COOCH_2CH_2CH_2$ and $COOCH_{2\ linker}$), 61.1 (CH_2OH_{glu}), 49.5

(OCH_2CH_2N), 45.6 ($C_{q\ bridge}$), 35.5, 35.4 [$C(CH_3)_3$], 31.8, 31.7 [$C(CH_3)_3$], 28.7 ($CH_{2\ linker}$), 27.8 ($COOCH_2CH_2CH_2$ and $CH_{2\ linker}$), 25.4 ($CH_{2\ linker}$), 21.5 ($COOCH_2CH_2CH_2$).

FTIR (KBr) (ν cm^{-1}): 3407 (OH), 2954 (C-H), 1740 (C=O).

Compound 81

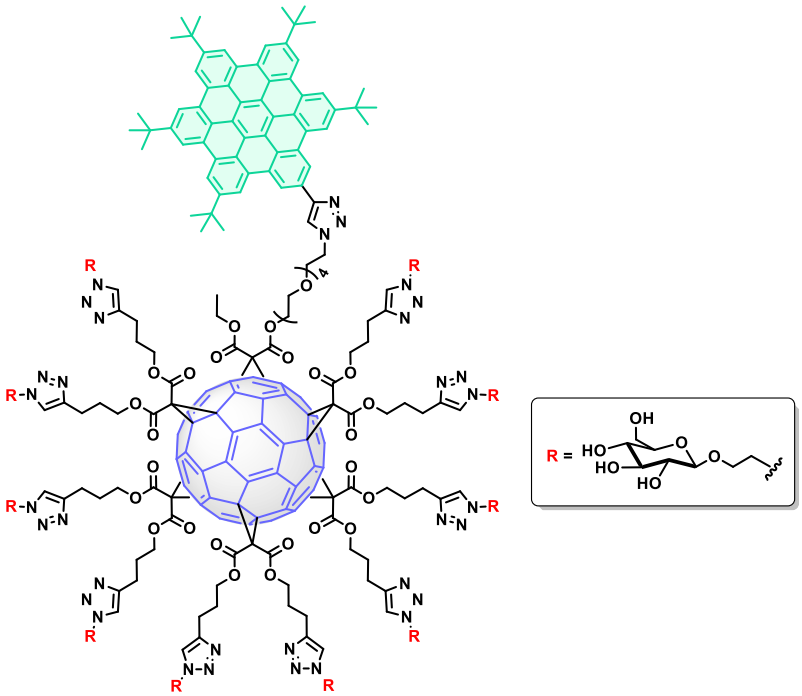

A mixture of **74** (6 mg, 7.2 µmol), **63** (43 mg, 9.0 µmol), $CuBr{\cdot}S(CH_3)_2$ (1.5 mg, 7.2 µmol), sodium ascorbate (2.2 mg, 0.011 mmol) and a piece of copper metal wire in DMSO (0.5 mL) and DCM (1 mL) was deoxygenated and kept under argon with vigorous stirring for 72 h at 40 ºC. The crude reaction was filtered through a QuadraSil® Mercaptopropyl column and purified by size-exclusion chromatography (Sephadex G-50 H_2O/CH_3OH 9:1) to afford **81** as a brown solid (28 mg, 69%).

^{1}H NMR (700 MHz, DMSO-d_6) δ (ppm) = 9.57 – 8.54 (m, 12H; CH_{HBC}), 7.99 – 7.85 (m, 11H; $CH_{triazole}$), 5.11 (s, 10H; OH), 4.99 (s, 10H; OH), 4.95 (s, 10H; OH), 4.88 – 4.85 (m, 2H; $OCH_2CH_2N_{PEG}$), 4.54 (s, 10H; OH), 4.51 – 4.45 (m, 20H; $OCH_2CH_2N_{glu}$), 4.42 – 4.27 (m, 24H; CH_2CH_3, $COOCH_2CH_2O$ and $COOCH_2CH_2CH_2$), 4.22 – 4.20 (m, 10H; CH_{1glu}), 4.12 – 4.10 (m, 2H; CH_2O_{PEG}), 4.08 – 4.03 (m, 10H; $OCH_2CH_2N_{glu}$), 3.88 – 3.83 (m, 10H; $OCH_2CH_2N_{glu}$), 3.74 – 3.71 (m, 2H; CH_2O_{PEG}), 3.68 – 3.63 (m, 12H; CH_2OH_{glu} and CH_2O_{PEG}), 3.55 – 3.52 (m, 4H; CH_2O_{PEG}), 3.50 – 3.47 (m, 4H; CH_2O_{PEG}), 3.44 – 3.42 (m, 12H; CH_2OH_{glu} and CH_2O_{PEG}), 3.15 – 3.10 (m, 20H; CH_{glu}), 3.06 – 3.02 (m, 10H; CH_{glu}), 2.98 – 2.94 (m, 10H; CH_{glu}), 2.72 – 2.59 (m, 20H; $COOCH_2CH_2CH_2$), 2.08 – 1.93 (m, 20H; $COOCH_2CH_2CH_2$), 1.85 – 1.77 [m, 45H; $C(CH_3)_3$], 1.21 – 1.17 (m, 3H; CH_3).

^{13}C NMR (176 MHz, DMSO-d_6) δ (ppm) = 162.9 (*C*O), 148.6 (C_{HBC}), 145.6 ($C_{triazole}$), 145.1, 140.8 ($C_{sp2\ fullerene}$), 129.7, 129.5, 129.3, 129.0, 123.4 (C_{HBC}), 122.8 ($CH_{triazole}$), 122.3, 119.2, 118.9, 118.6 (C_{HBC}), 102.9 (CH_{1glu}), 77.0, 76.6, 73.3, 70.0 (CH_{glu}), 69.8 (CH_2O_{PEG}), 69.2 (CH_2O_{PEG}), 68.8 ($C_{sp3\ fullerene}$), 67.9 (COOCH_2CH_2O), 67.3 (O$CH_2CH_2N_{glu}$), 66.7 (COO$CH_2CH_2CH_2$), 63.3 (CH_2CH_3), 61.1 (CH_2OH_{glu}), 50.0 (O$CH_2CH_2N_{PEG}$), 49.5 (O$CH_2CH_2N_{glu}$), 45.6 ($C_{q\ bridge}$), 35.2 [$C(CH_3)_3$], 31.8 [C(CH_3)$_3$], 27.7 (COOCH$_2$*C*H$_2$CH$_2$), 21.5 (COOCH$_2$CH$_2$*C*H$_2$), 13.7 (*C*H$_3$).

FTIR (KBr) (ν cm^{-1}): 3408 (OH), 2955 (C-H), 1740 (C=O).

Appendix 1

APPENDIX 1. Chapter 1

Liposomes preparation

To enable the cellular delivery of hydrophobic C_{60}-based compounds (**38** and **39**), they were incorporated into the lipid bilayer of liposomes, which serve as biocompatible nanocarriers that enhance solubility, stability and bioavailability.

Lipids used in this study—including 1-palmitoyl-2-oleoyl-*sn*-glycero-3-phosphocholine (POPC), cholesterol (Chol), 1,2-distearoyl-*sn*-glycero-3-phosphoethanolamine-*N*-[carboxy(polyethylene glycol)-2000] (sodium salt) (DSPE-PEG2000), and 1,2-dioleoyl-*sn*-glycero-3-phosphoethanolamine-*N*-(lissamine rhodamine B sulfonyl) (ammonium salt) (RhPE)—were purchased from Avanti Polar Lipids (Merck). Liposomes were prepared using POPC/Chol/DSPE-PEG2000/RhPE in a molar ratio of 85:5:10:0.5 at final lipid concentrations of 3 mg/mL and 2 mg/mL for the preparation of liposomes-**38** and liposomes-**39**, respectively.

The required volumes of lipid stock solutions (in chloroform) were transferred into 1.5 mL Eppendorf tubes. Subsequently, **38** and **39** solutions (in pure ethanol) were added to yield final payload amounts of 350 µg and 750 µg, respectively, in the resulting nanovectors. The mixtures were vortexed to ensure thorough mixing, then subjected to solvent evaporation in a SpeedVac under vacuum for 30 minutes.

Following complete solvent removal, 500 µL of 100 mM HEPES buffer (pH 7.4) was added to each tube containing the dried lipid-drug film. The mixtures were hydrated *via* alternating cycles of vortexing and sonication in a water bath. To ensure complete suspension of the C_{60} compounds within the liposomes, the samples were processed using a probe sonicator (Bioblock Scientific VibraCell 75115) for two cycles of 10 minutes each, with 30-second on/off pulses at 50% amplitude.

Infrared spectra

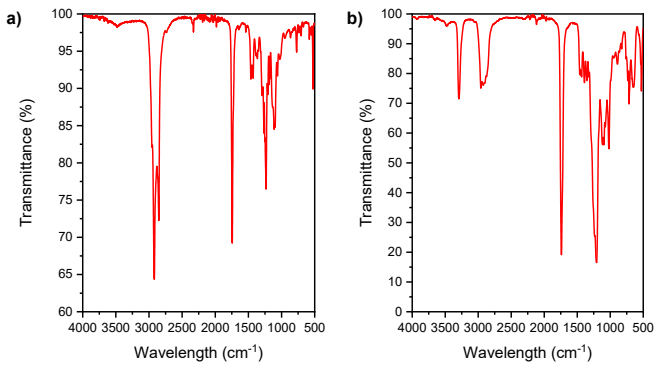

Figure AP1.1. FT-IR spectra of compounds: a) **8** and b) **9**.

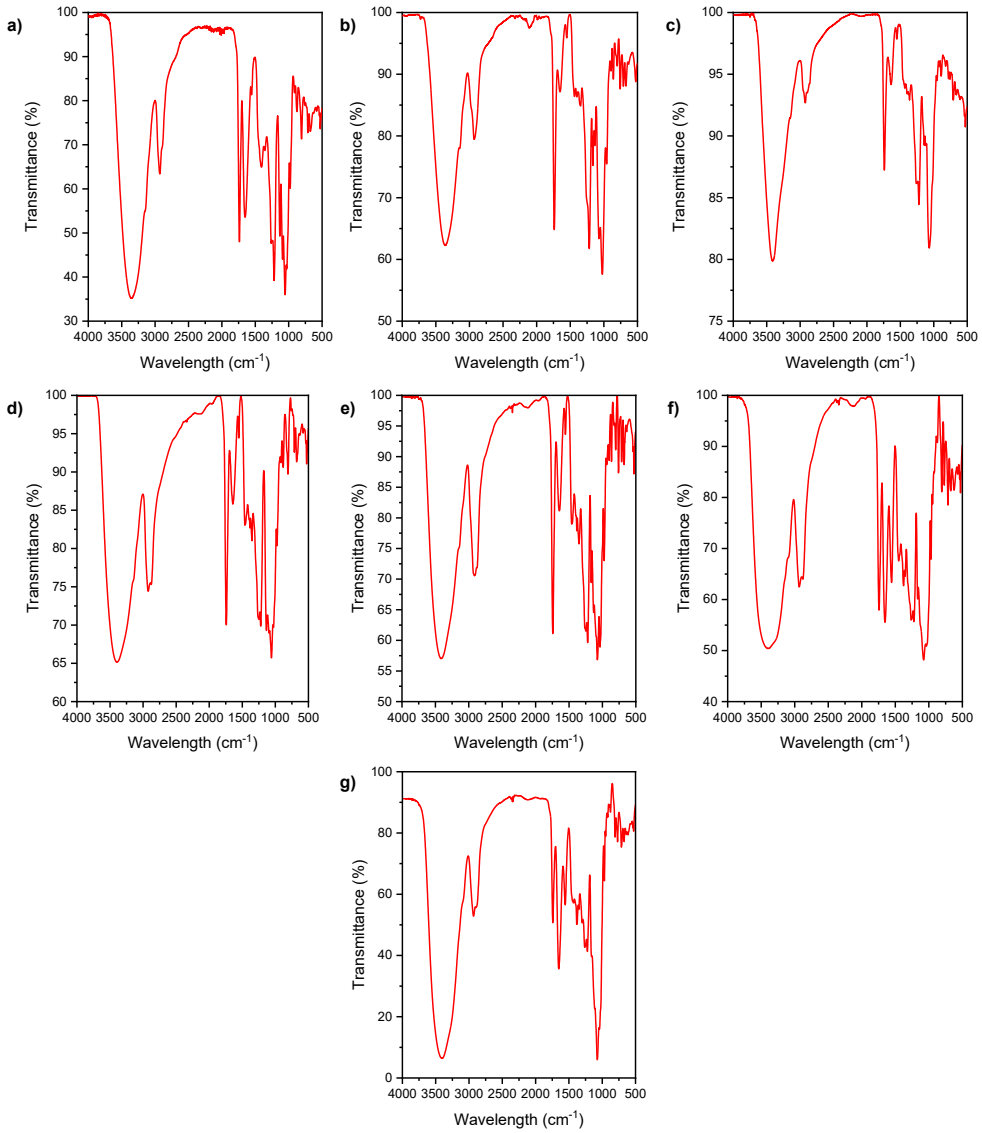

Figure AP1.2. FT-IR spectra of symmetric glycofullerenes: a) **18**, b) **19**, c) **20**, d) **21**, e) **22**, f) **23** and g) **24**.

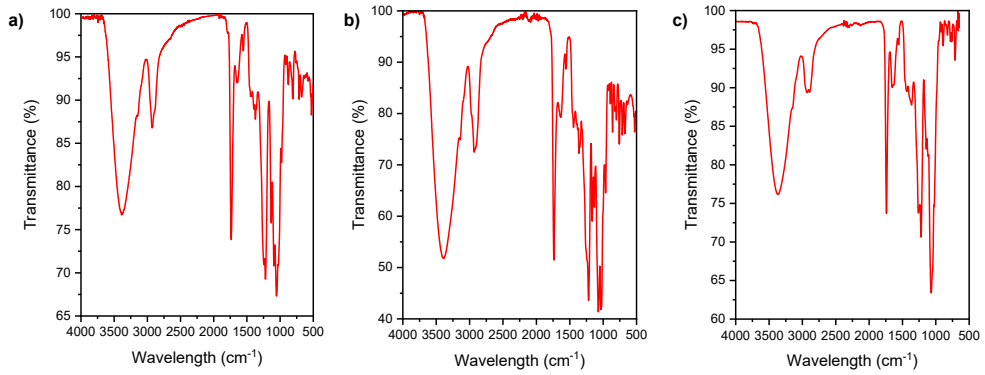

Figure AP1.3. FT-IR spectra of bromo-substituted glycofullerenes: a) **25**, b) **26** and c) **27**.

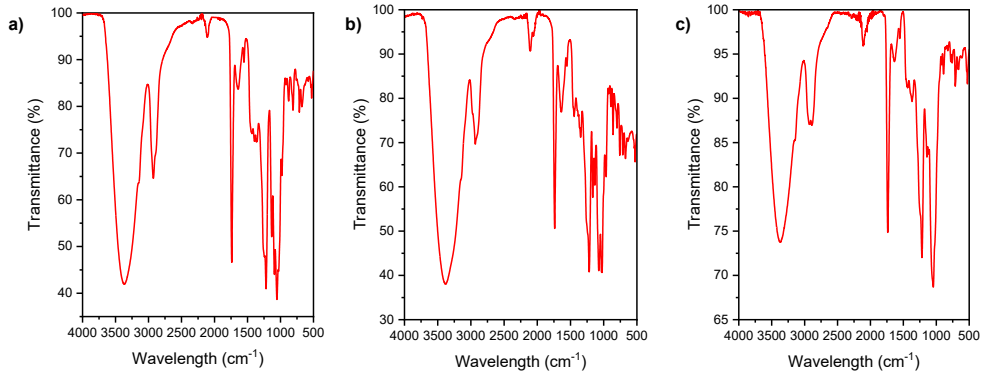

Figure AP1.4. FT-IR spectra of azido-substituted glycofullerenes: a) **28**, b) **29** and c) **30**.

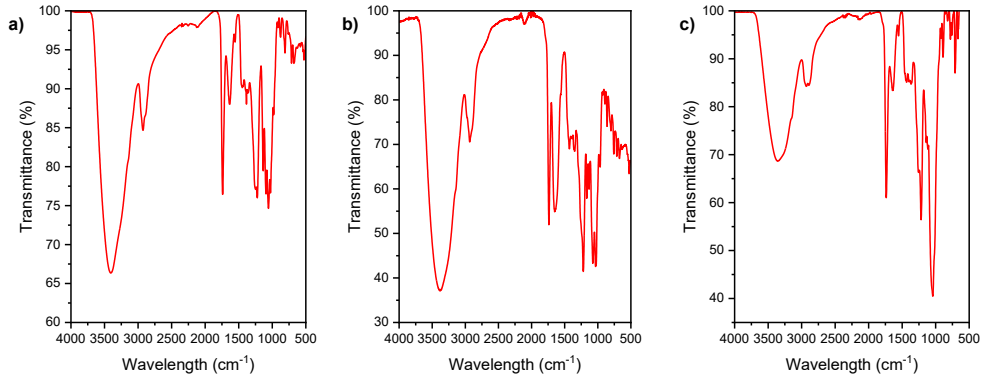

Figure AP1.5. FT-IR spectra of tridecafullerenes: a) **31**, b) **32** and c) **33**.

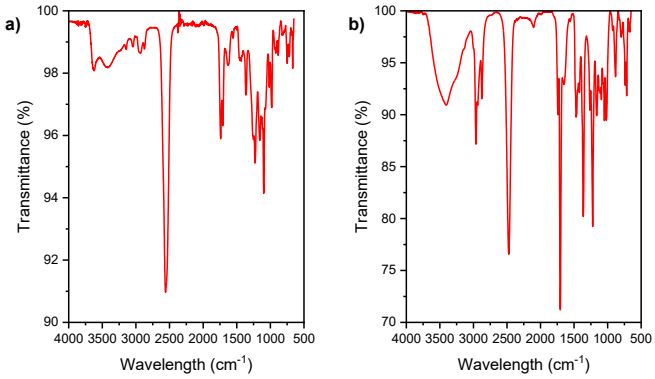

Figure AP1.6. FT-IR spectra of: a) **38** and b) **39**.

Appendix 2

APPENDIX 2. Chapter 2

Infrared spectra

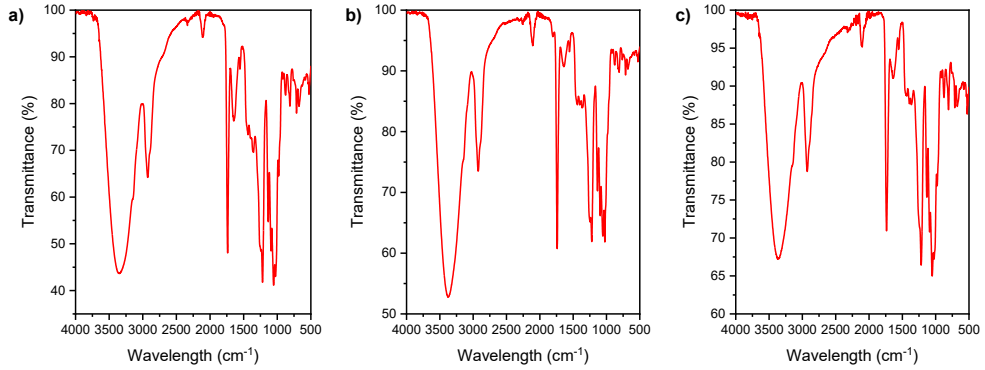

Figure AP2.1. FT-IR spectra of azido-substituted glycofullerenes: a) **49a**, b) **49b** and c) **49c**.

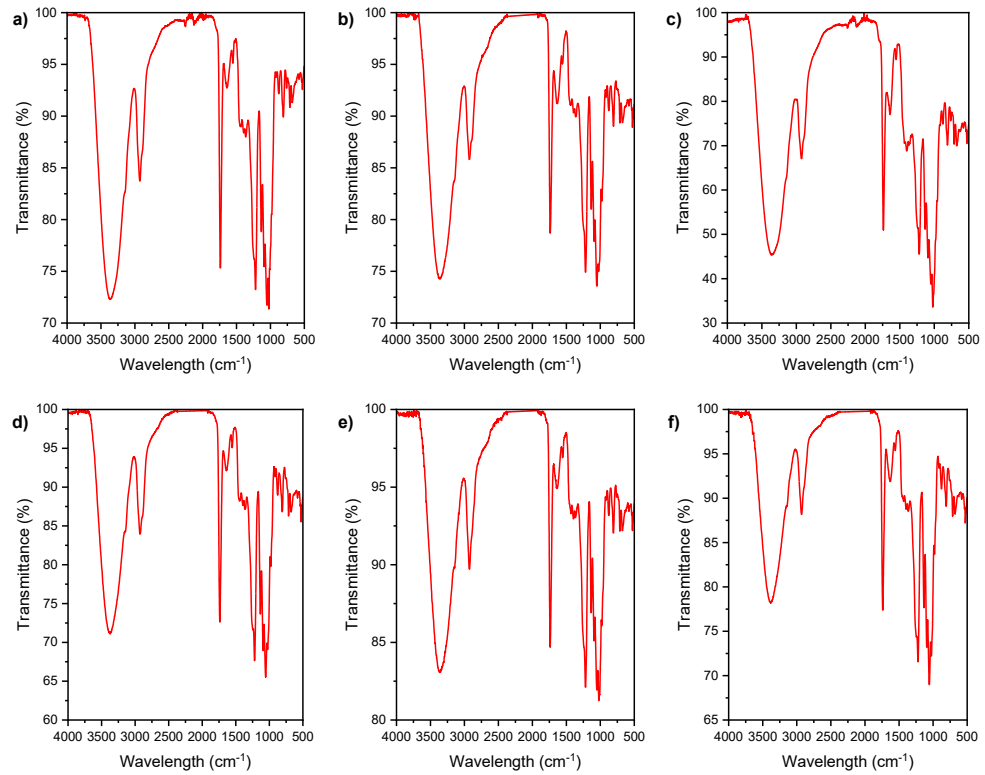

Figure AP2.2. FT-IR spectra of glycoporphyrins: a) **52a**, b) **53a**, c) **52b**, d) **53b**, e) **52c** and f) **53c**.

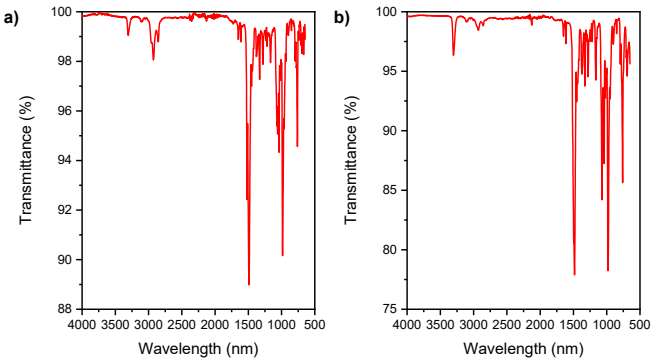

Figure AP2.3. FT-IR spectra of: a) **59** and b) **60**.

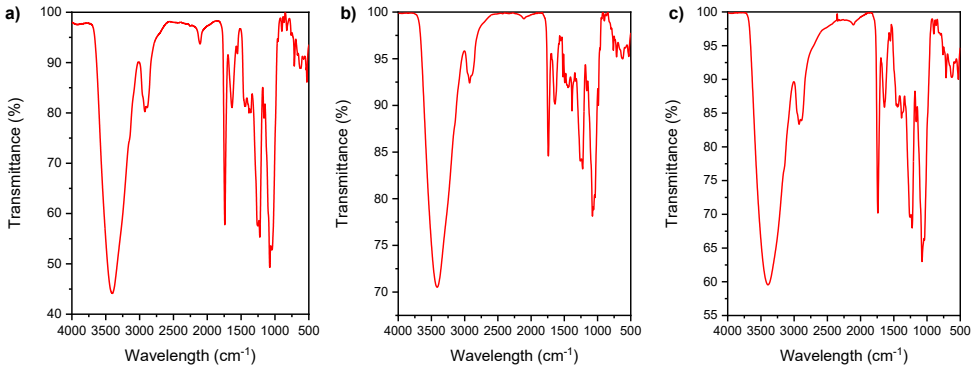

Figure AP2.4. FT-IR spectra of: a) **63**, b) **64** and c) **65**.

Dynamic Light Scattering

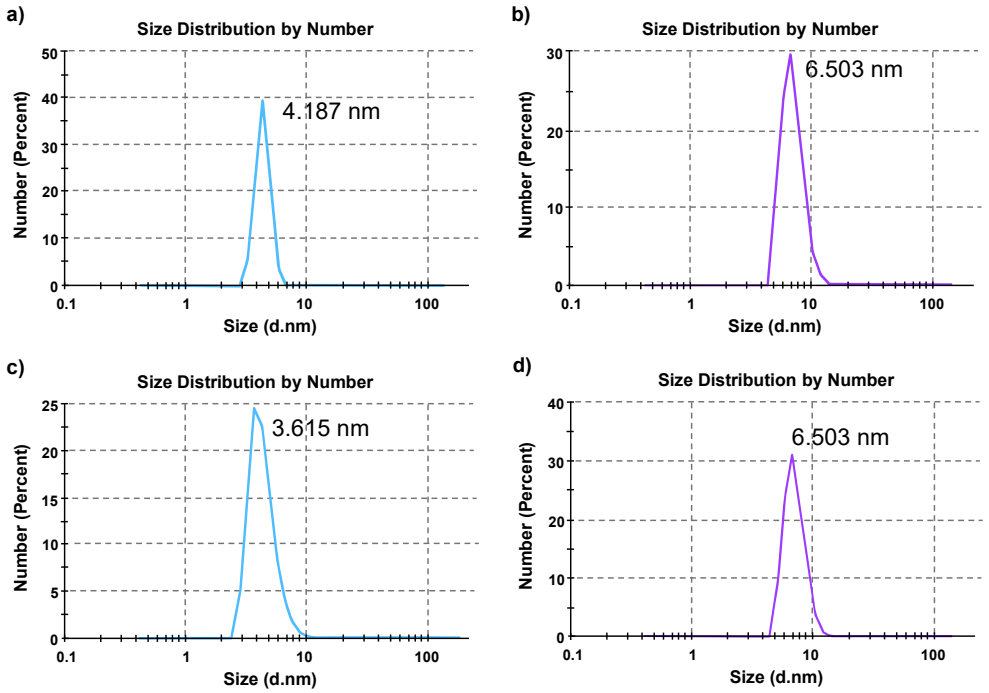

Figure AP2.5. DLS measurements (H_2O, $1 \cdot 10^{-5}$ M) in number % of glycoporphyrins: a) **52a**, b) **53a**, c) **52c** and d) **53c**.

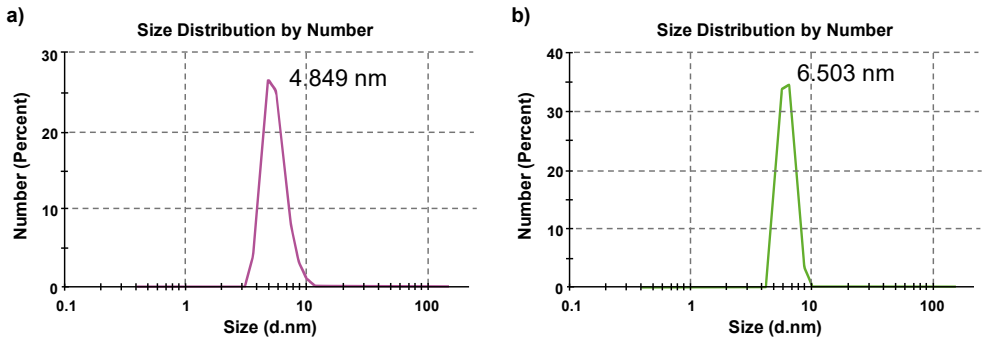

Figure AP2.6. DLS measurements (H_2O, $1 \cdot 10^{-5}$ M) in number % of glycocorroles: a) **64** and b) **65**.

2D-DOSY spectra

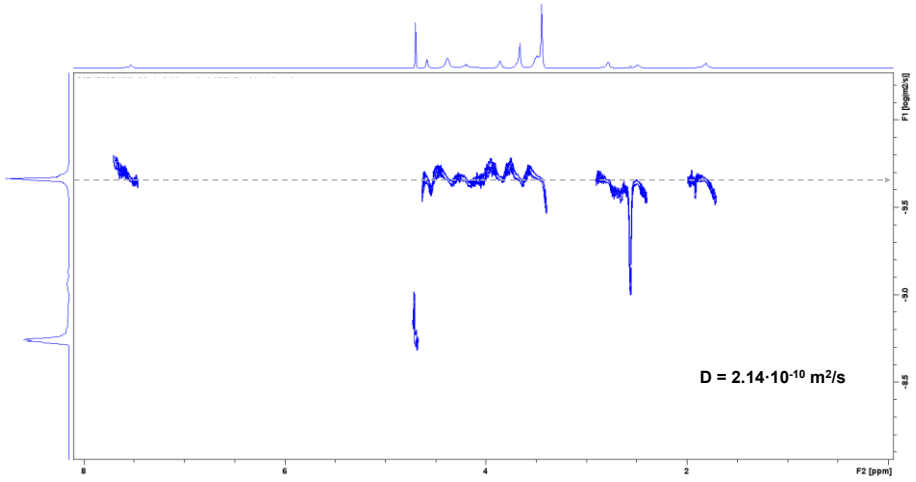

Figure AP2.7. 2D-DOSY NMR spectrum of compound **18** in D_2O.

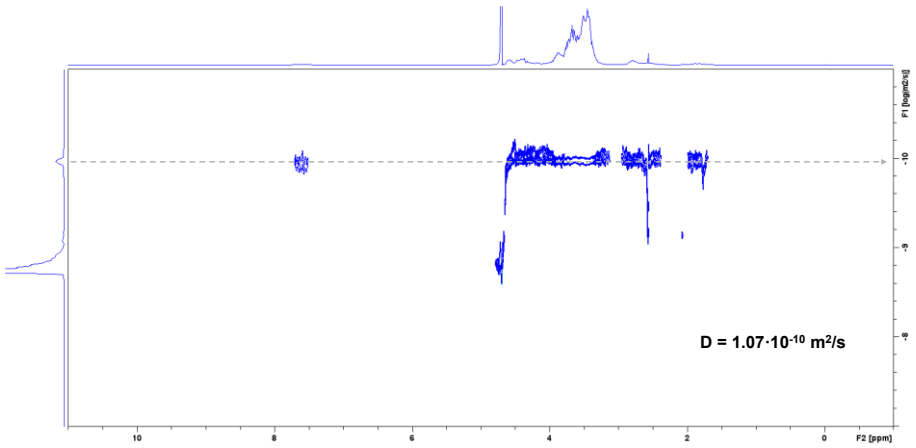

Figure AP2.8. 2D-DOSY NMR spectrum of compound **52b** in D_2O.

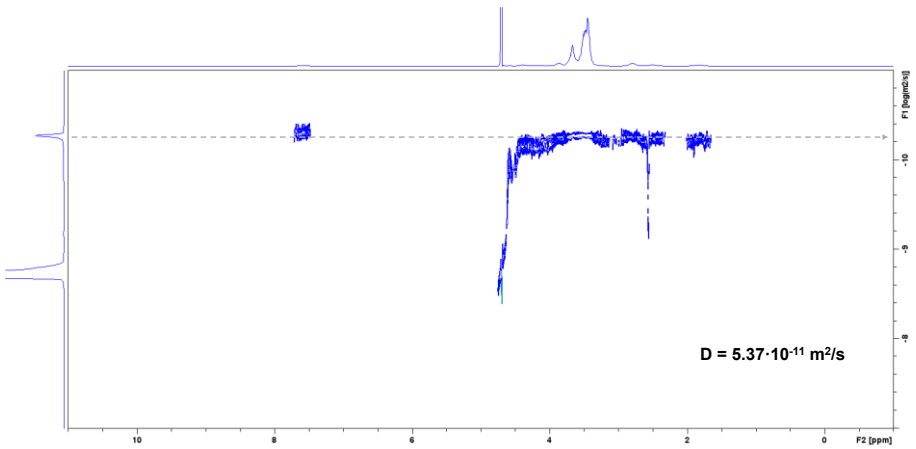

Figure AP2.9. 2D-DOSY NMR spectrum of compound **53b** in D_2O.

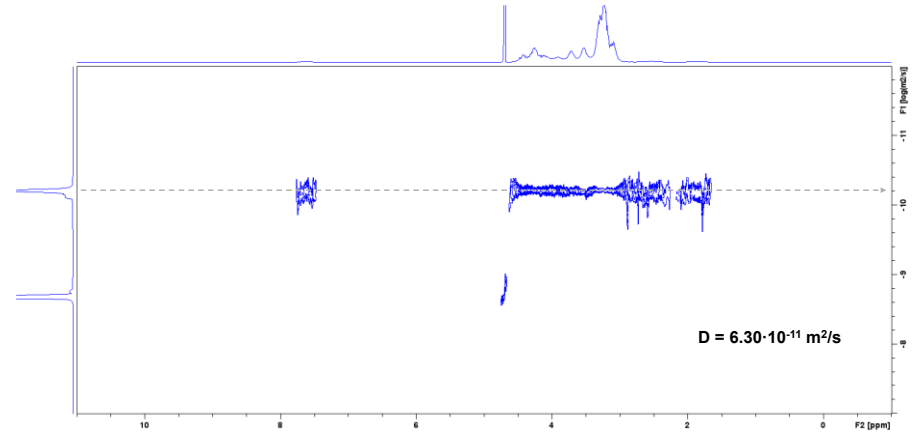

Figure AP2.10. 2D-DOSY NMR spectrum of compound **64** in D_2O.

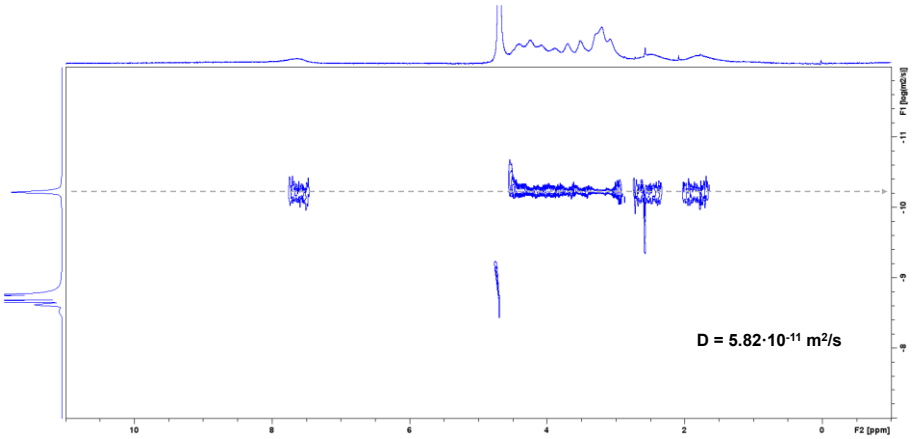

Figure AP2.11. 2D-DOSY NMR spectrum of compound **65** in D_2O.

Photophysical characterization

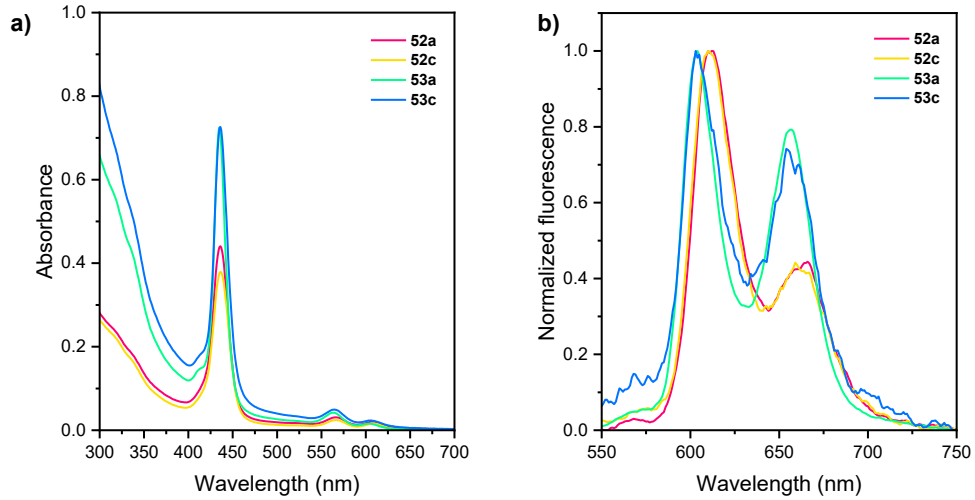

Figure AP2.12. a) Absorption spectra of **52a,c** and **53a,c** (H_2O, $1 \cdot 10^{-6}$ M) and b) emission spectra of **52a,c** and **53a,c** (H_2O, $5 \cdot 10^{-6}$ M, λ_{exc} = 436 nm).

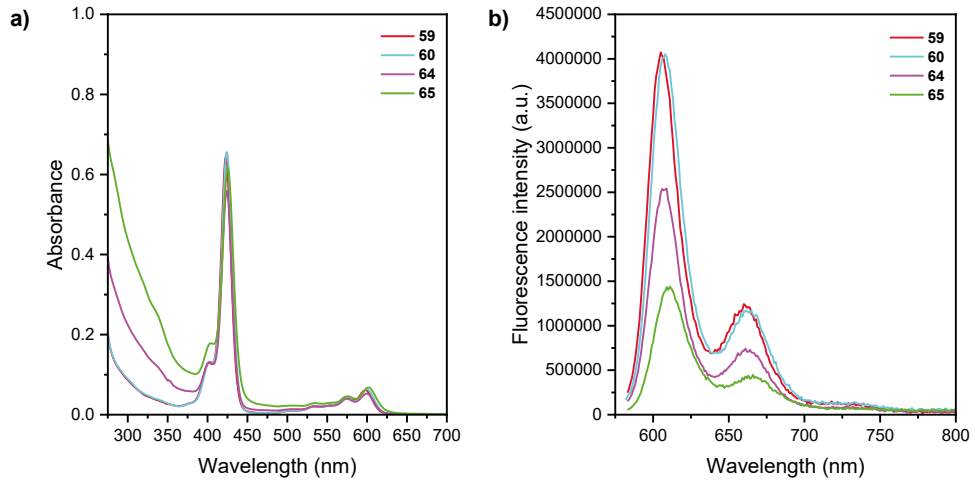

Figure AP2.13. a) Absorption spectra of **59**, **60**, **64** and **65** (DMF, $5 \cdot 10^{-6}$ M) and b) emission spectra of **59**, **60**, **64** and **65** (DMF, $5 \cdot 10^{-6}$ M, λ_{exc} = 575 nm).

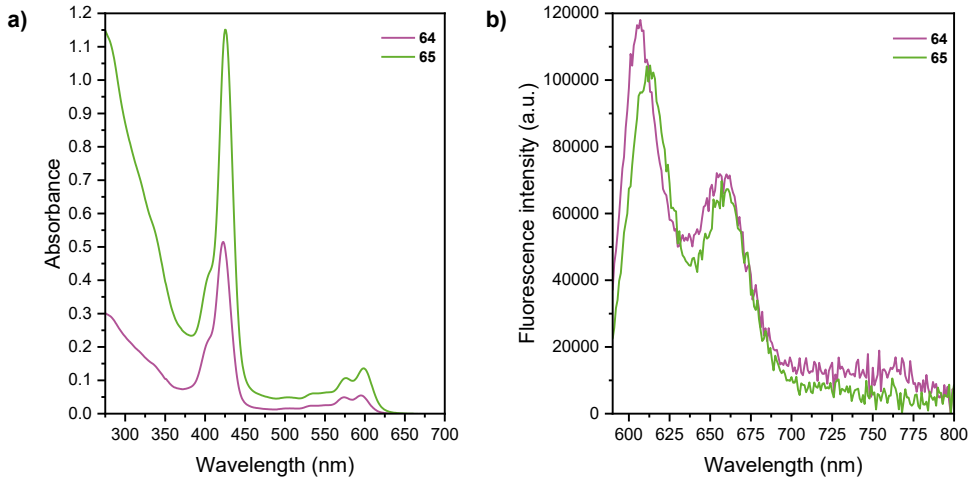

Figure AP2.14. a) Absorption spectra of **64** and **65** (H_2O, $1 \cdot 10^{-5}$ M) and **b)** emission spectra of **64** and **65** (H_2O, $5 \cdot 10^{-5}$ M, λ_{exc} = 575 nm).

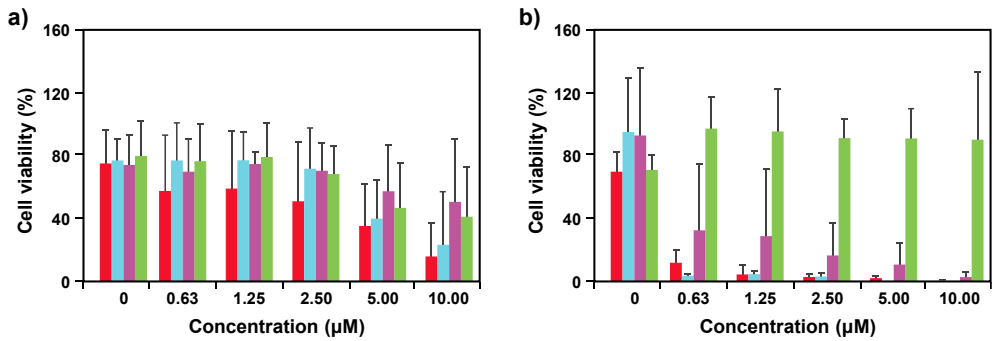

Figure AP2.15. Viability of HeLa cells in the presence of compounds **59**, **60**, **64** and **65** at different concentrations irradiance of 10 mW/cm^2 at 420 nm: a) for 100 s with a fluence of 1 J/cm^2 and b) for 1000 s with a fluence of 10 J/cm^2.

Appendix 3

APPENDIX 3. Chapter 3

Infrared spectra

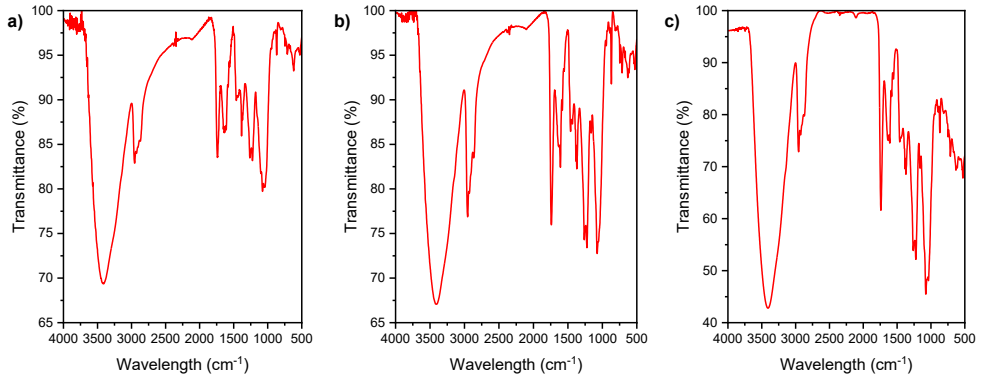

Figure AP3.1. FT-IR spectra of: a) **80a**, b) **80b** and c) **81**.

Electronic microscopy

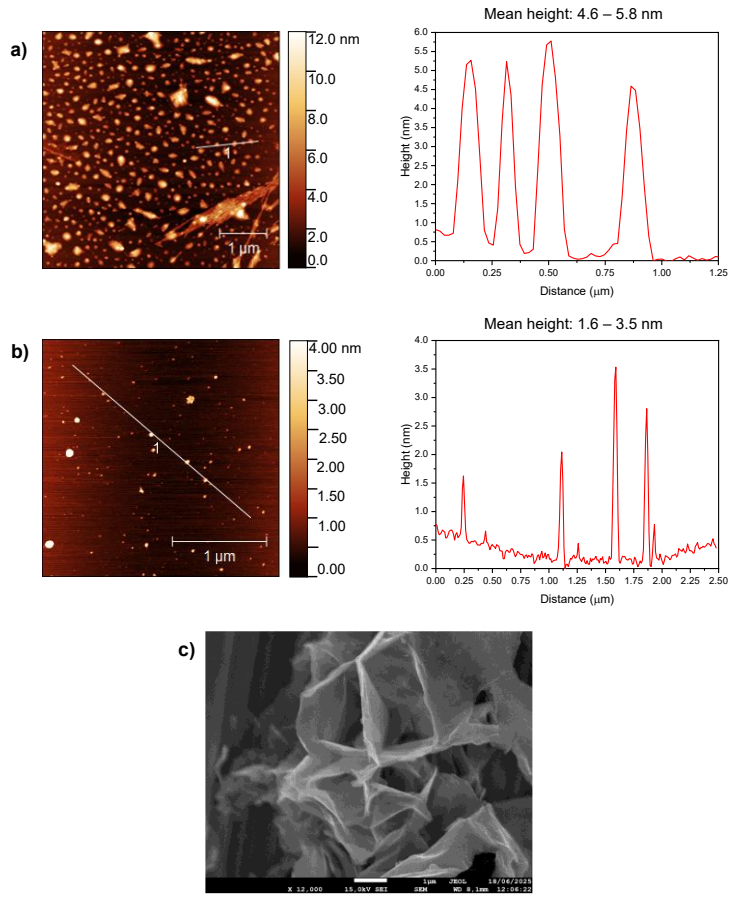

Figure AP3.2. a) AFM image and height profile of of **80a**, b) AFM image and height profile of **81** and c) SEM image of **80b**.

References

REFERENCES

1. a) S. Bayda, M. Adeel, T. Tuccinardi, M. Cordani, F. Rizzolio, The History of Nanoscience and Nanotechnology: From Chemical-Physical Applications to Nanomedicine, *Molecules* **2020**, *25*, 112. b) G. A. Mansoori, T. A. F. Soelaiman, Nanotechnology - An Introduction for the Standards Community, *J. ASTM Int.* **2005**, *2*, 1.

2. R. P. Feynman, There's Plenty of Room at the Bottom, *Eng. Sci.* **1960**, *23*, 22.

3. G. Binnig, H. Rohrer, C. Gerber, E. Weibel, Surface Studies by Scanning Tunneling Microscopy, *Phys. Rev. Lett.* **1982**, *49*, 57.

4. M. J. Mitchell, M. M. Billingsley, R. M. Haley, M. E. Wechsler, N. A. Peppas, R. Langer, Engineering Precision Nanoparticles for Drug Delivery, *Nat. Rev. Drug. Discov.* **2021**, *20*, 101.

5. Z. He, Z. Zhang, S. Bi, Nanoparticles for Organic Electronics Applications, *Mater. Res. Express* **2020**, *7*, 012004.

6. a) A. A. İnada, S. Arman, B. Safaei, A Novel Review on the Efficiency of Nanomaterials for Solar Energy Storage Systems, *J. Energy Storage*, **2022**, *55*, 105661. b) N. Martín, Carbon Nanoforms for Photovoltaics: Myth or Reality? *Adv. Energy Mater.* **2017**, *7*, 1601102.

7. B. Mekuye, B. Abera, Nanomaterials: An Overview of Synthesis, Classification, Characterization, and Applications, *Nano Select* **2023**, *4*, 486.

8. a) C. C. Lee, J. A. MacKay, J. M. J. Fréchet, F. C. Szoka, Designing Dendrimers for Biological Applications, *Nat. Biotechnol*. **2005**, *12*, 1517. b) K. J. Harrington, S. Mohammadtaghi, P. S. Uster, D. Glass, A. M. Peters, R. G. Vile, J. S. Stewart, Effective Targeting of Solid Tumors in Patients with Locally Advanced Cancers by Radiolabeled Pegylated Liposomes, *Clin. Cancer Res.* **2001**, *7*, 243.

9. a) B. Klębowski, J. Depciuch, M. Parlińska-Wojtan, J. Baran, Applications of Noble Metal-Based Nanoparticles in Medicine, *Int. J. Mol. Sci.* **2018**, *19*, 4031. b) G. Singh, J. L. Z. Ddungu, N. Licciardello, R. Bergmann, L. De Cola, H. Stephan, Ultrasmall Silicon Nanoparticles as a Promising Platform for Multimodal Imaging, *Faraday Discuss.* **2020**, *222*, 362.

10. a) A. Muñoz, D. Sigwalt, B. M. Illescas, J. Luczkowiak, L. Rodríguez-Pérez, I. Nierengarten, M. Holler, J. S. Remy, K. Buffet, S. P. Vincent, J. Rojo, R. Delgado, J.-F. Nierengarten, N. Martín, Synthesis of Giant Globular Multivalent Glycofullerenes as Potent Inhibitors in a Model of Ebola Virus Infection, *Nat. Chem.* **2016**, *8*, 50. b) M. Sbacchi, M. Mamone, L. Morbiato, P. Gobbo, G. Filippini, M. Prato, Shining Light on Carbon Dots: New Opportunities in Photocatalysis, *ChemCatChem* **2023**, *15*, e202300667.

11. a) S. Merino, C. Martín, K. Kostarelos, M. Prato, E. Vázquez, Nanocomposite Hydrogels: 3D Polymer-Nanoparticle Synergies for On-Demand Drug Delivery, *ACS Nano* **2015**, *9*, 4686. b) S. Bolisetty, R. Mezzenga, Amyloid-Carbon Hybrid Membranes for Universal Water Purification, *Nat. Nanotechnol.* **2016**, *11*, 365.

12. N. Abid, A. M. Khan, S. Shujait, K. Chaudhary, M. Ikram, M. Imran, J. Haider, M. Khan, Q. Khan, M. Maqbool, Synthesis of Nanomaterials Using Various Top-down and Bottom-up Approaches, Influencing Factors, Advantages, and Disadvantages: A Review, *Adv. Colloid Interface Sci.* **2022**, *300*, 102597.

13. A.-L. de Lavoisier, Ed. *Traité Élémentaire de Chimie*, Chez Cuchet, Paris, **1789**.

14. H. W. Kroto, J. R. Heath, S. C. O'Brien, R. F. Curl, R. E. Smalley, C_{60}: Buckminsterfullerene, *Nature* **1985**, *318*, 162.

15. S. Iijima, Helical Microtubules of Graphitic Carbon, *Nature* **1991**, *354*, 56.

16. X. Xu, R. Ray, Y. Gu, H. J. Ploehn, L. Gearheart, K. Raker, W. A. Scrivens, Electrophoretic Analysis and Purification of Fluorescent Single-Walled Carbon Nanotube Fragments, *J. Am. Chem. Soc.* **2004**, *126*, 12736.

17. K. S. Novoselov, A. K. Geim, S. V. Morozov, D. Jiang, Y. Zhang, S. V. Dubonos, I. V. Grigorieva, A. A. Fisov, Electric Field Effect in Atomically Thin Carbon Films, *Science* **2004**, *306*, 666.

18. G. Speranza, The Role of Functionalization in the Applications of Carbon Materials: An Overview, *Carbon* **2019**, *5*, 84.

19. M. F. L. De Volder, S. H. Tawfick, R. H. Baughman, A. J. Hart, Carbon Nanotubes: Present and Future Commercial Applications, *Science* **2013**, *339*, 535.

20. A. K. Worku, D. W. Ayele, Recent Advances of Graphene-Based Materials for Emerging Technologies, *Results Chem.* **2023**, *5*, 100971.

21. Y. Wang, A. Hu, Carbon Quantum Dots: Synthesis, Properties and Applications, *J. Mater. Chem. C* **2014**, *2*, 6921.

22. H. W. Kroto, The Stability of the Fullerenes C_n, with n = 24, 28, 32, 36, 50, 60 and 70, *Nature* **1987**, *329*, 529.

23. M. Bühl, A. Hirsch, Spherical Aromaticity of Fullerenes, *Chem. Rev.* **2001**, *101*, 1153.

24. A. Hirsch, Principles of Fullerene Reactivity. In *Fullerenes and Related Structures*. Topics in Current Chemistry, vol. 199, A. Hirsch Ed. Springer-Verlag Berlin, Heidelberg, **1999**, pp. 1-65.

25. S. Liu, Y. J. Lu, M. M. Kappes, J. A. Ibers, The Structure of the C_{60} Molecule: X-Ray Crystal Structure Determination of a Twin at 110 K, *Science* **1991**, *254*, 408.

26. W. Krätschmer, L. D. Lamb, K. Fostiropoulos, D. R. Huffman, Solid C_{60}: A New Form of Carbon, *Nature* **1990**, *347*, 354.

27. R. E. Haufler, J. Conceicao, L. P. F. Chibante, Y. Chai, N. E. Byrne, S. Flanagan, M. M. Haley, S. C. O'Brien, C. Pan, Z. Xiao, W. E. Billups, M. A. Ciufolini, R. H. Hauge, J. L. Margrave, L. J. Wilson, R. F. Curl, R. E. Smalley, Efficient Production of C_{60} (Buckminsterfullerene), $C_{60}H_{36}$, and the Solvated Buckide Ion, *J. Phys. Chem.* **1990**, *94*, 8634.

28. a) L. P. F. Chibante, A. Thess, J. M. Alford, M. D. Diener, R. E. Smalley, Solar Generation of the Fullerenes, *J. Phys. Chem.* **1993**, *97*, 8696. b) C. L. Fields, J. R. Pitts, M. J. Hale, C. Bingham, A. Lewandowski, D. E. King, Formation of Fullerenes in Highly Concentrated Solar Flux, *J. Phys. Chem.* **1993**, *97*, 8701.

29. J. B. Howard, J. T. McKinnon, M. E. Johnson, Y. Makarovsky, A. L. Lafleur, Production of C_{60} and C_{70} Fullerenes in Benzene-Oxygen Flames, *J. Phys. Chem.* **1992**, *96*, 6657.

30. R. Taylor, G. J. Langley, H. W. Kroto, D. R. M. Walton, Formation of C_{60} by Pyrolysis of Naphthalene, *Nature* **1993**, *366*, 728.

31. M. Mojica, J. A. Alonso, F. Méndez, Synthesis of Fullerenes, *J. Phys. Org. Chem.* **2013**, *26*, 526.

32. E. Castro, A. Hernández-García, G. Zavala, L. Echegoyen, Fullerenes in Biology and Medicine, *J. Mater. Chem. B* **2017**, *5*, 6523.

33. a) B. M. Illescas, J. Rojo, R. Delgado, N. Martín, Multivalent Glycosylated Nanostructures to Inhibit Ebola Virus Infection, *J. Am. Chem. Soc.* **2017**, *139*, 6018. b) B. M. Illescas, A. Pérez-Sánchez, A. Mallo, A. Martín-Domenech, I. Rodríguez-Crespo, N. Martín, Multivalent Cationic Dendrofullerenes for Gene Transfer: Synthesis and DNA Complexation, *J. Mater. Chem. B* **2020**, *8*, 4505. c) J. Patino-Alonso, J. Cabrera-González, J. Merino, G. Nieto-Ortiz, F. Lasala, J. Katati, C. H. Bezerra da Cruz, A. K. Monnappa, P. Mateos-Gil, A. Canales, I. López-Montero, B. M. Illescas, R. Delgado, N. Martín, C_{60}-based Multivalent Glycoporphyrins Inhibit SARS-CoV-2 Specific Interaction with the DC-SIGN Transmembrane Receptor, *Small* **2024**, *20*, 2307045.

34. a) R. Taylor, D. R. M. Walton, The Chemistry of Fullerenes, *Nature* **1993**, *363*, 685. b) A. Hirsch, M. Brettreich, Eds. *Fullerenes: Chemistry and Reactions*, Wiley-VCH Verlag GmbH & Co. KGaA, Weinheim, **2005**.

35. D. A. Dixon, N. Matsuzawa, T. Fukunaga, F. N. Tebbe, Patterns for Addition to Fullerene (C_{60}), *J. Phys. Chem.* **1992**, *96*, 6107.

36. a) A. Hirsch, Addition Reactions of Buckminsterfullerene (C_{60}), *Synthesis* **1995**, *8*, 895. b) G. Schick, K.-D. Kampe, A. Hirsch, Reaction of [60]Fullerene with Morpholine and Piperidine: Preferred 1,4-Additions and Fullerene Dimer Formation, *J. Chem. Soc. Chem. Commun.* **1995**, *19*, 2023.

37. C. Bingel, Cyclopropylation of Fullerenes, *Chem. Ber.* **1993**, *126*, 1957.

38. X. Camps, A. Hirsch, Efficient Cyclopropanation of C_{60} Starting from Malonates, *J. Chem. Soc. Perkin Trans.* 1 **1997**, *11*, 1595.

39. M. Maggini, G. Scorrano, M. Prato, Addition of Azomethine Ylides to C_{60}: Synthesis, Characterization, and Functionalization of Fullerene Pyrrolidines, *J. Am. Chem. Soc.* **1993**, *115*, 9798.

40. N. Martín, J. L. Segura, F. Wudl, New Concepts in Diels-Alder Cycloadditions to Fullerenes. In *Fullerenes: From Synthesis to Optoelectronic Properties*, D. M. Guldi, N. Martín, Eds. Kluwer Academic Publishers, Dordrecht, **2002**, vol. 4. pp. 81-120.

41. E. Beer, M. Feuerer, A. Knorr, A. Mirlach, J. Daub, Functionalization of C_{60} Buckminsterfullerene by [8 + 2] Cycloaddition: Spectroscopic and Electron-Transfer Properties of a Tetrahydroazulenofullerene, *Angew. Chem. Int. Ed. Engl.* **1994**, *33*, 1087.

42. R. Caballero, P. de la Cruz, F. Langa, Basic Principles of the Chemical Reactivity of Fullerenes, In *Fullerenes: Principles and Applications*, F. Langa, J.-F. Nierengarten, Eds. 2nd ed. The Royal Society of Chemistry, Cambridge, **2011**, ch. 3, pp. 66-124.

43. A. Hirsch, I. Lamparth, T. Grösser, Regiochemistry of Multiple Additions to the Fullerene Core: Synthesis of a T_h-Symmetric Hexakis adduct of C_{60} with Bis(ethoxycarbonyl)methylene, *J. Am. Chem. Soc.* **1994**, *116*, 9385.

44. A. Hirsch, I. Lamparth, H. R. Karfunkel, Fullerene Chemistry in Three Dimensions: Isolation of Seven Regioisomeric Bisadducts and Chiral Trisadducts of C_{60} and Di(ethoxycarbonyl)methylene, *Angew. Chem. Int. Ed. Engl.* **1994**, *33*, 437.

45. L. Isaacs, R. F. Haldimann, F. Diederich, Tether-Directed Remote Functionalization of Buckminsterfullerene: Regiospecific Hexaadduct Formation, *Angew. Chem. Int. Ed. Engl.* **1994**, *33*, 2339.

46. T. M. Figueira-Duarte, V. Lloveras, J. Vidal-Gancedo, B. Delavaux-Nicot, C. Duhayon, J. Veciana, C. Rovira, J.-F. Nierengarten, Ground State Electronic Interactions in Macrocyclic Fullerene Bis-Adducts Functionalized with Bridging Conjugated Oligomers, *Eur. J. Org. Chem.* **2009**, *2009*, 5779.

47. F. Spänig, M. Ruppert, J. Dannhäuser, A. Hirsch, D. M. Guldi, *trans-2* Addition Pattern to Power Charge Transfer in Dendronized Metalloporphyrin C_{60} Conjugates, *J. Am. Chem. Soc.* **2009**, *131*, 9378.

48. a) J.-F. Nierengarten, V. Gramlich, F. Cardullo, F. Diederich, Regio- and Diastereoselective Bisfunctionalization of C_{60} and Enantioselective Synthesis of a C_{60} Derivative with a Chiral Addition Pattern, *Angew. Chem. Int. Ed. Engl.* **1996**, *35*, 2101. b) J.-F. Nierengarten, T. Habicher, R. Kessinger, F. Cardullo, F. Diederich, V. Gramlich, J.-P. Gisselbrecht, C. Boudon, M. Gross, Macrocyclization on the Fullerene Core: Direct Regio- and Diastereoselective Multi-Functionalization of [60]Fullerene, and Synthesis of Fullerene-Dendrimer Derivatives, *Helv. Chim. Acta* **1997**, *80*, 2238.

49. a) J.-P. Bourgeois, L. Echegoyen, M. Fibbioli, E. Pretsch, F. Diederich, Regioselective Synthesis of *trans*-1 Fullerene Bis-Adducts Directed by a Crown Ether Tether: Alkali Metal Cation Modulated Redox Properties of Fullerene-Crown Ether Conjugates, *Angew. Chem. Int. Ed.* **1998**, *37*, 2118. b) J.-P. Bourgeois, P. Seiler, M. Fibbioli, E. Pretsch, F. Diederich, L. Echegoyen, Cyclophane-Type Fullerene-dibenzo[18]crown-6 Conjugates with *trans-1*, *trans-2*, and *trans-3* Addition Patterns: Regioselective Templated Synthesis, X-Ray Crystal Structure, Ionophoric Properties, and Cation-Complexation-Dependent Redox Behavior, *Helv. Chim. Acta* **1999**, *82*, 1572.

50. D. González-Rodríguez, E. Carbonell, G. de Miguel-Rojas, C. Atienza-Castellanos, D. M. Guldi, T. Torres, Activating Multistep Charge-Transfer Processes in Fullerene-Subphthalocyanine-Ferrocene Molecular Hybrids as a Function of π-π Orbital Overlap, *J. Am. Chem. Soc.* **2010**, *132*, 16488.

51. N. Chronakis, A. Hirsch, Regio- and Stereoselective Synthesis of Enantiomerically Pure [60]Fullerene Tris-Adducts with an Inherently Chiral *e*,*e*,*e* Addition Pattern, *Chem. Commun.* **2005**, 3709.

52. A. Kraszewska, P. Rivera-Fuentes, G. Rapenne, J. Crassous, A. G. Petrovic, J. L. Alonso-Gómez, E. Huerta, F. Diederich, C. Thilgen, Regioselectivity in Tether-Directed Remote Functionalization – The Addition of a Cyclotriveratrylene-Based Trimalonate to C_{60} Revisited, *Eur. J. Org. Chem.* **2010**, *2010*, 4402.

53. F. Schillinger, U. Hahn, S. Guerra, T. M. N. Trinh, D. Sigwalt, M. Holler, I. Nierengarten, J.-F. Nierengarten, Si-Tethered Bis- and Tris-Malonates for the Regioselective Preparation of Fullerene Multi-Adducts, *Helv. Chim. Acta* **2023**, *106*, e202300026.

54. F. Beuerle, A. Hirsch, Synthesis of Amphiphilic [60]Fullerene [3:3]Hexakisadducts with Four Spherically Defined Addend Zones, *Chem. Eur. J.* **2009**, *15*, 7447.

55. M. Wachter, L. Jurkiewicz, A. Hirsch, Sequential Tether-Directed Synthesis of New [3 : 2 : 1] Hexakis-Adducts of C_{60} with a Mixed Octahedral Addition Pattern, *Chem. Eur. J.* **2021**, *27*, 7677.

56. I. Lamparth, C. Maichle-Mossmer, A. Hirsch, Reversible Template-Directed Activation of Equatorial Double Bonds of the Fullerene Framework: Regioselective Direct Synthesis, Crystal Structure, and Aromatic Properties of T_h-$C_{66}(COOEt)_{12}$, *Angew. Chem. Int. Ed. Engl.* **1995**, *34*, 1607.

57. a) H. Li, A. Kitaygorodskiy, R. A. Carino, Y.-P. Sun, Simple Modification in Hexakis-Addition for Efficient Synthesis of C_{60}-Centered Dendritic Molecules Bearing Multiple Aromatic Chromophores, *Org. Lett.* **2005**, *7*, 859. b) H. Li, S. A. Haque, A. Kitaygorodskiy, M. J. Meziani, M. Torres-Castillo, Y.-P. Sun, Alternatively Modified Bingel Reaction for Efficient Syntheses of C_{60} Hexakis-Adducts, *Org. Lett.* **2006**, *8*, 5641.

58. T. Andersson, K. Nilsson, M. Sundahl, G. Westman, O. Wennerström, C_{60} Embedded in γ-Cyclodextrin: A Water-Soluble Fullerene, *J. Chem. Soc. Chem. Commun.* **1992**, 604.

59. J. L. Atwood, G. A. Koutsantonis, C. L. Raston, Purification of C_{60} and C_{70} by Selective Complexation with Calixarenes, *Nature* **1994**, *368*, 229.

60. Y. N. Yamakoshi, T. Yagami, K. Fukuhara, S. Sueyoshi, N. Miyata, Solubilization of Fullerenes into Water with Polyvinylpyrrolidone Applicable to Biological Tests, *J. Chem. Soc. Chem. Commun.* **1994**, 517.

61. H. Hungerbuehler, D. M. Guldi, K. D. Asmus, Incorporation of C_{60} into Artificial Lipid Membranes, *J. Am. Chem. Soc.* **1993**, *115*, 3386.

62. N. O. Mchedlov-Petrossyan, V. K. Klochkov, G. V. Andrievsky, Colloidal Dispersions of Fullerene C_{60} in Water: Some Properties and Regularities of Coagulation by Electrolytes, *J. Chem. Soc. Faraday Trans.* **1997**, *93*, 4343.

63. S. A. Jenekhe, X. L. Chen, Self-Assembled Aggregates of Rod-Coil Block Copolymers and their Solubilization and Encapsulation of Fullerenes, *Science* **1998**, *279*, 1903.

64. M. Hetzer, S. Bayerl, X. Camps, O. Vostrowsky, A. Hirsch, T. M. Bayerl, Fullerenes in Membranes: Structural and Dynamic Effects of Lipophilic C_{60} Derivatives in Phospholipid Bilayers, *Adv. Mater.* **1997**, *9*, 913.

65. W. A. Scrivens, J. M. Tour, K. E. Creek, L. Pirisi, Synthesis of ^{14}C-Labeled C_{60}, Its Suspension in Water, and Its Uptake by Human Keratinocytes, *J. Am. Chem. Soc.* **1994**, *116*, 4517.

66. G. V. Andrievsky, M. V. Kosevich, O. M. Vovk, V. S. Shelkovsky, L. A. Vashchenko, On the Production of an Aqueous Colloidal Solution of Fullerenes, *J. Chem. Soc. Chem. Commun.* **1995**, 1281.

67. S. Deguchi, R. G. Alargova, K. Tsujii, Stable Dispersions of Fullerenes, C_{60} and C_{70}, in Water. Preparation and Characterization, *Langmuir* **2001**, *17*, 6013.

68. P.-B. Ancey, C. Contat, E. Meylan, Glucose Transporters in Cancer – From Tumor Cells to the Tumor Microenvironment, *FEBS J* **2018**, *285*, 2926.

69. L. Tanzi, M. Terreni, Y. Zhang, Synthesis and Biological Application of Glyco- and Peptide Derivatives of Fullerene C_{60}, *Eur. J. Med. Chem.* **2022**, *230*, 114104.

70. M. Serda, K. Malarz, A. Mrozek-Wilczkiewicz, M. Wojtyniak, R. Musioł, S. A. Curley, Glycofullerenes as Non-Receptor Tyrosine Kinase Inhibitors- Towards Better Nanotherapeutics for Pancreatic Cancer Treatment, *Sci. Rep.* **2020**, *10*, 260.

71. M. Serda, M. J. Ware, J. M. Newton, S. Sachdeva, M. Krzykawska-Serda, L. Nguyen, J. Law, A. O. Anderson, S. A. Curley, L. J Wilson, S. J. Corr, Development of Photoactive Sweet-C_{60} for Pancreatic Cancer Stellate Cell Therapy, *Nanomedicine* **2018**, *13*, 2981.

72. K. Malarz, J. Korzuch, T. D. Marforio, K. Balin, M. Calvaresi, A. Mrozek-Wilczkiewicz, R. Musiol, M. Serda, Identification and Biological Evaluation of a Water-Soluble Fullerene Nanomaterial as BTK Kinase Inhibitor, *Int. J. Nanomedicine* **2023**, *18*, 1709.

73. F. Rancan, M. Helmreich, A. Mölich, N. Jux, A. Hirsch, B. Röder, F. Böhm, Intracellular Uptake and Phototoxicity of 3^1,3^2-Didehydrophytochlorin-fullerene Hexaadducts, *Photochem. Photobiol.* **2007**, *83*, 1330.

74. R. D. Bolskar, A. F. Benedetto, L. O. Husebo, R. E. Price, E. F. Jackson, S. Wallace, L. J. Wilson, J. M. Alford, First Soluble M@C_{60} Derivatives Provide Enhanced Access to Metallofullerenes and Permit in Vivo Evaluation of Gd@C_{60}[$C(COOH)_2$]$_{10}$ as a MRI Contrast Agent, *J. Am. Chem. Soc.* **2003**, *125*, 5471.

75. a) P. P. Fatouros, F. D. Corwin, Z.-J. Chen, W. C. Broaddus, J. L. Tatum, B. Kettenmann, Z. Ge, H. W. Gibson, J. L. Russ, A. P. Leonard, J. C. Duchamp, H. C. Dorn, In Vitro and in Vivo Imaging Studies of a New Endohedral Metallofullerene Nanoparticle, *Radiology* **2006**, *240*, 756. b) M. Mikawa, H. Kato, M. Okumura, M. Narazaki, Y. Kanazawa, N. Miwa, H. Shinohara,

Paramagnetic Water-Soluble Metallofullerenes Having the Highest Relaxivity for MRI Contrast Agents, *Bioconjugate Chem.* **2001**, *12*, 510.

76. J. B.-K. Kim, Y. Mackeyev, S. Raghuram, S. H. Cho, S. Krishnan, Synthesis and Characterization of Gadolinium-decorated [60]Fullerene for Tumor Imaging and Radiation Sensitization, *Int. J. Radiat. Biol.* **2021**, *97*, 1129.

77. Y. Li, R. Biswas, W. P. Kopcha, T. Dubroca, L. Abella, Y. Sun, R. A. Crichton, C. Rathnam, L. Yang, Y.-W. Yeh, K. Kundu, A. Rodríguez-Fortea, J. M. Poblet, K.-B. Lee, S. Hill, J. Zhang, Structurally Defined Water-Soluble Metallofullerene Derivatives towards Biomedical Applications, *Angew. Chem. Int. Ed.* **2023**, *62*, e202211704.

78. M. Serda, K. Malarz, J. Korzuch, M. Szubka, M. Zubko, R. Musioł, *In Situ* Cellular Localization of Nonfluorescent [60]Fullerene Nanomaterial in MCF-7 Breast Cancer Cells, *ACS Biomater. Sci. Eng.* **2022**, *8*, 3450.

79. T. Y. Zakharian, A. Seryshev, B. Sitharaman, B. E. Gilbert, V. Knight, L. J. Wilson, A Fullerene-Paclitaxel Chemotherapeutic: Synthesis, Characterization, and Study of Biological Activity in Tissue Culture, *J. Am. Chem. Soc.* **2005**, *127*, 12508.

80. F. Lu, A. Haque S.-T. Yang, P. G. Luo, L. Gu, A. Kitaygorodskiy, H. Li, S. Lacher, Y.-P. Sun, Aqueous Compatible Fullerene-Doxorubicin Conjugates, *J. Phys. Chem. C* **2009**, *113*, 17768.

81. M. Brettreich, S. Burghardt, C. Böttcher, T. Bayerl, S. Bayerl, A. Hirsch, Globular Amphiphiles: Membrane-Forming Hexaadducts of C_{60}, *Angew. Chem. Int. Ed.* **2000**, *39*, 1845. b) S. Burghardt, A. Hirsch, B. Schade, K. Ludwig, C. Böttcher, Switchable Supramolecular Organization of Structurally Defined Micelles Based on an Amphiphilic Fullerene, *Angew. Chem. Int. Ed.* **2005**, *44*, 2976.

82. R. Partha, L. R. Mitchell, J. L. Lyon, P. P. Joshi, J. L. Conyers, Buckysomes: Fullerene-Based Nanocarriers for Hydrophobic Molecule Delivery, *ACS Nano* **2008**, *2*, 1950.

83. H. Isobe, W. Nakanishi, N. Tomita, S. Jinno, H. Okayama, E. Nakamura, Gene Delivery by Aminofullerenes: Structural Requirements for Efficient Transfection, *Chem. Asian. J.* **2006**, *1*, 167.

84. E. Nakamura, H. Isobe, N. Tomita, M. Sawamura, S. Jinno, H. Okayama, Functionalized Fullerene as an Artificial Vector for Transfection, *Angew. Chem. Int. Ed.* **2000**, *39*, 4254.

85. D. Sigwalt, M. Holler, J. Iehl, J.-F. Nierengarten, M. Nothisen, E. Morin, J.-S. Remy, Gene Delivery with Polycationic Fullerene Hexakis-adducts, *Chem. Commun.* **2011**, *47*, 4640.

86. T. Feizi, Oligosaccharides that Mediate Mammalian Cell-Cell Adhesion, *Curr. Opin. Struct. Biol.* **1993**, *3*, 701.

87. S. Bhatia, L. Cuellar-Camacho, R. Haag, Pathogen Inhibition by Multivalent Ligand Architectures, *J. Am. Chem. Soc.* **2016**, *138*, 8654.

88. C. S. Mahon, D. A. Fulton, Mimicking Nature with Synthetic Macromolecules Capable of Recognition, *Nat. Chem.* **2014**, *6*, 665.

89. A. K. Bakshi, T. Haider, R. Tiwari, V. Soni, Critical Parameters for Design and Development of Multivalent Nanoconstructs: Recent Trends, *Drug Deliv. and Transl. Res.* **2022**, *12*, 2335.

90. M. Adeli, M. Kalantari, Z. Zarnega, R. Kabiri, Cyclodextrin-based Dendritic Supramolecules; New Multivalent Nanocarriers, *RSC Adv.* **2012**, *2*, 2756.

91. F. Sansone, L. Baldini, A. Casnatia, R. Ungaro, Calixarenes: From Biomimetic Receptors to Multivalent Ligands for Biomolecular Recognition, *New J. Chem.* **2010**, *34*, 2715.

92. J. Khandare, M. Calderón, N. M. Dagia, R. Haag, Multifunctional Dendritic Polymers in Nanomedicine: Opportunities and Challenges, *Chem. Soc. Rev.* **2012**, *41*, 2824.

93. J.-F. Nierengarten, J. P. Schneider, T. M. N. Trinh, A. Joosten, M. Holler, M. L. Lepage, A. Bodlenner, M. I. García-Moreno, C. Ortiz-Mellet, P. Compain, Giant Glycosidase Inhibitors: First- and Second-Generation Fullerodendrimers with a Dense Iminosugar Shell, *Chem. Eur. J.* **2018**, *24*, 2483.

94. M. Durka, K. Buffet, J. Iehl, M. Holler, J.-F. Nierengarten, S. P. Vincent, The Inhibition of Liposaccharide Heptosyltransferase WaaC with Multivalent Glycosylated Fullerenes: A New Mode of Glycosyltransferase Inhibition, *Chem. Eur. J.* **2012**, *18*, 641.

95. A. Tikad, H. Fu, C. M. Sevrain, S. Laurent, J.-F. Nierengarten, S. P. Vincent, Mechanistic Insight into Heptosyltransferase Inhibition by using Kdo Multivalent Glycoclusters, *Chem. Eur. J.* **2016**, *22*, 13147.

96. M. Sánchez-Navarro, A. Muñoz, B. M. Illescas, J. Rojo, N. Martín, [60]Fullerene as Multivalent Scaffold: Efficient Molecular Recognition of Globular Glycofullerenes by Concanavalin A, *Chem. Eur. J.* **2011**, *17*, 766.

97. M. Durka, K. Buffet, J. Iehl, M. Holler, J.-F. Nierengarten, J. Taganna, J. Bouckaert, S. P. Vincent, The Functional Valency of Dodecamannosylated Fullerenes with *Escherichia Coli* FimH—Towards Novel Bacterial Antiadhesives, *Chem. Commun.* **2011**, *47*, 1321.

98. S. Cecioni, V. Oerthel, J. Iehl, M. Holler, D. Goyard, J.-P. Praly, A. Imberty, J.-F. Nierengarten, S. Vidal, Synthesis of Dodecavalent Fullerene-Based

Glycoclusters and Evaluation of their Binding Properties towards a Bacterial Lectin, *Chem. Eur. J.* **2011**, *17*, 3252.

99. K. Buffet, E. Gillon, M. Holler, J.-F. Nierengarten, A. Imberty, S. P. Vincent, Fucofullerenes as Tight Ligands of RSL and LecB, Two Bacterial Lectins, *Org. Biomol. Chem.* **2015**, *13*, 6482.

100. Y. v. Kooyk, T. B. H. Geijtenbeek, DC-SIGN: Escape Mechanism for Pathogens, *Nat. Rev. Immunol.* **2003**, *3*, 697.

101. G. Tabarani, M. Thépaut, D. Stroebel, C. Ebel, C. Vivès, P. Vachette, D. Durand, F. Fieschi, DC-SIGN Neck Domain is a pH-sensor Controlling Oligomerization: SAXS and Hydrodynamic Studies of Extracellular Domain, *J. Biol. Chem.* **2009**, *284*, 21229.

102. J. Ramos-Soriano, J. J. Reina, B. M. Illescas, N. de la Cruz, L. Rodríguez-Pérez, F. Lasala, J. Rojo, R. Delgado, N. Martín, Synthesis of Highly Efficient Multivalent Disaccharide/[60]Fullerene Nanoballs for Emergent Viruses, *J. Am. Chem. Soc.* **2019**, *141*, 15403.

103. M. Ruiz-Santaquiteria, B. M. Illescas, R. Abdelnabi, A. Boonen, A. Mills, O. Martí-Marí, S. Noppen, J. Neyts, D. Schols, F. Gago, A. San-Félix, M.-J. Camarasa, N. Martín, Multivalent Tryptophan- and Tyrosine-Containing [60]Fullerene Hexa-Adducts as Dual HIV and Enterovirus A71 Entry Inhibitors, *Chem. Eur. J.* **2021**, *27*, 10700.

104. J.-F. Nierengarten, Fullerene Hexa-adduct Scaffolding for the Construction of Giant Molecules, *Chem. Commun.* **2017**, *53*, 11855.

105. R. Huisgen, 1,3-Dipolar Cycloadditions. Past and Future**,** *Angew. Chem. Int. Ed.* **1963**, *2*, 565.

106. C. W. Tornøe, C. Christensen, M. Meldal, Peptidotriazoles on Solid Phase: [1,2,3]-Triazoles by Regiospecific Copper(I)-Catalyzed 1,3-Dipolar Cycloadditions of Terminal Alkynes to Azides, *J. Org. Chem.* **2002**, *67*, 3057.

107. V. V. Rostovtsev, L. G. Green, V. V. Fokin, K. B. Sharpless, A Stepwise Huisgen Cycloaddition Process: Copper(I)-Catalyzed Regioselective "Ligation" of Azides and Terminal Alkynes, *Angew. Chem. Int. Ed.* **2002**, *41*, 2596.

108. N. Z. Fantoni, A. H. El-Sagheer, T. Brown, A Hitchhiker's Guide to Click-Chemistry with Nucleic Acids, *Chem. Rev.* **2021**, *121*, 7122.

109. L. Jin, D. R. Tolentino, M. Melaimi, G. Bertrand, Isolation of Bis(copper) Key Intermediates in Cu-catalyzed Azide-alkyne "Click Reaction", *Sci. Adv.* **2015**, *1*, e1500304.

110. a) J. Liu, F. Lu, Y. Chen, E. Plow, J. Qin, Integrin Mediates Cell Entry of the SARS-CoV-2 Virus Independent of Cellular Receptor ACE2, *J. Biol. Chem.*

2022, *298*, 101710. b) M. Thépaut, J. Luczkowiak, C. Vivès, N. Labiod, I. Bally, F. Lasala, Y. Grimoire, D. Fenel, S. Sattin, N. Thielens, G. Schoehn, A. Bernardi, R. Delgado, F. Fieschi, DC/L-SIGN Recognition of Spike Glycoprotein Promotes SARS-CoV-2 Trans-infection and can be Inhibited by a Glycomimetic Antagonist, *PLoS Pathog.* **2021**, *17*, e1009576.

111. Y. Guo, H. Feinberg, E. Conroy, D. A. Mitchell, R. Alvarez, O. Blixt, M. E. Taylor, W. I. Weis, K. Drickamer, Structural Basis for Distinct Ligand-Binding and Targeting Properties of the Receptors DC-SIGN and DC-SIGNR, *Nat. Struct. Mol. Biol.* **2004**, *11*, 591.

112. B. J. Appelmelk, I. v. Die, S. J. v. Vliet, C. M. J. E. Vandenbroucke-Grauls, T. B. H. Geijtenbeek, Y. v. Kooyk, Cutting Edge: Carbohydrate Profiling Identifies New Pathogens that Interact with Dendritic Cell-specific ICAM-3-grabbing Nonintegrin on Dendritic Cells, *J. Immunol.* **2003**, *170*, 1635.

113. G. A. Rabinovich, M. A. Toscano, S. S. Jackson, G. R. Vasta, Functions of Cell Surface Galectin-glycoprotein Lattices, *Curr. Opin. Struct. Biol*. **2007**, *17*, 513.

114. J. Dumic, S. Dabelic, M. Flögel, Galectin-3: An Open-ended Story, *Biochim. Biophys. Acta - Gen. Subj.* **2006**, *1769*, 616.

115. a) R. N. Grimes, Ed. *Carboranes*, 3rd ed. Academic Press, Inc. New York, **2016**. b) N. S. Hosmane, Ed. *Boron Science: New Technologies and Applications*, 1st ed. Taylor & Francis Group, Boca Raton, **2011**.

116. a) J. Poater, M. Solà, C. Viñas, F. Teixidor, π Aromaticity and Three-Dimensional Aromaticity: Two sides of the Same Coin? *Angew. Chem. Int. Ed.* **2014**, *53*, 12191. b) O. El Bakouri, D. W. Szczepanik, K. Jorner, R. Ayub, P. Bultinck, M. Solà, H. Ottosson, Three-Dimensional Fully π-Conjugated Macrocycles: When 3D-Aromatic and When 2D-Aromatic-in-3D? *J. Am. Chem. Soc.* **2022**, *144*, 8560.

117. a) R. Núñez, M. Tarrés, A. Ferrer-Ugalde, F. F. de Biani, F. Teixidor, Electrochemistry and Photoluminescence of Icosahedral Carboranes, Boranes, Metallacarboranes, and their Derivatives, *Chem. Rev.* **2016**, *116*, 14307. b) R. Núñez, I. Romero, F. Teixidor, C. Viñas, Icosahedral Boron Clusters: A Perfect Tool for the Enhancement of Polymer Features, *Chem. Soc. Rev.* **2016**, *45*, 5147.

118. L. Wang, Y. Jiang, S. Duttwyler, F. Lin, Y. Zhang, Chemistry of Three-dimensional Icosahedral Boron Clusters Anions: *Closo*-dodecaborate(2-) $[B_{12}H_{12}]^{2-}$ and Carba-*closo*-dodecaborate(-) $[CB_{11}H_{12}]^{-}$, *Coord. Chem. Rev.* **2024**, *516*, 215974.

119. D. Olid, R. Núñez, C. Viñas, F. Teixidor, Methods to Produce B-C, B-P, B-N and B-S Bonds in Boron Clusters, *Chem. Soc. Rev.* **2013**, *42*, 3318.

120. a) F. Teixidor, R. Núñez, C. Viñas, Towards the Application of Purely Inorganic Icosahedral Boron Clusters in Emerging Nanomedicine, *Molecules* **2023**, *28*, 4449. b) E. Hey-Hawkins, C. Viñas, Eds. *Boron-Based Compounds: Potential and Emerging Applications in Medicine*, 1st ed. John Wiley & Sons Ltd. New Jersey, **2016**.

121. a) A. Marfavi, P. Kavianpour, L. M. Rendina, Carboranes in Drug Discovery, Chemical Biology and Molecular Imaging, *Nat. Rev. Chem.* **2022**, *6*, 486. b) M. Gozzi, B. Schwarze, E. Hey-Hawkins, Preparing (Metalla)carboranes for Nanomedicine, *ChemMedChem* **2021**, *16*, 1533.

122. a) K. Fink, M. Uchman, Boron Cluster Compounds as New Chemical Leads for Antimicrobial Therapy, *Coord. Chem. Rev.* **2021**, *431*, 213684. b) A. Ferrer-Ugalde, S. Sandoval, K. R. Pulagam, A. Muñoz-Juan, A. Laromaine, J. Llop, G. Tobias, R. Núñez, Radiolabeled Cobaltabis(dicarbollide) Anion–Graphene Oxide Nanocomposites for In Vivo Bioimaging and Boron Delivery, *ACS Appl. Nano Mater.* **2021**, *4*, 1613. c) Z. Yinghuai, A. T. Peng, K. Carpenter, J. A. Maguire, N. S. Hosmane, M. Takagaki, Substituted Carborane-Appended Water-Soluble Single-Wall Carbon Nanotubes: New Approach to Boron Neutron Capture Therapy Drug Delivery, *J. Am. Chem. Soc.* **2005**, *127*, 9875.

123. a) M. F. Hawthorne, New Horizons for Therapy Based on the Boron Neutron Capture Reaction, *Mol. Med. Today* **1998**, *4*, 174. b) M. Lamba, A. Goswami, A. Bandyopadhyay, A Periodic Development of BPA and BSH Based Derivatives in Boron Neutron Capture Therapy (BNCT), *Chem. Commun.* **2021**, *57*, 827.

124. R. F. Barth, P. Mi, W. Yang, Boron Delivery Agents for Neutron Capture Therapy of Cancer, *Cancer Commun.* **2018**, *38*, 1.

125. a) A. A. Druzina, A. V. Shmalko, I. B. Sivaev, V. I. Bregadze, Cyclic Oxonium Derivatives of Cobalt and Iron Bis(dicarbollides) and their Use in Organic Synthesis, *Russ. Chem. Rev.* **2021**, *90*, 785. b) A. A. Semioshkin, I. B. Sivaev, V. I. Bregadze, Cyclic Oxonium Derivatives of Polyhedral Boron Hydrides and their Synthetic Applications, *Dalton Trans.* **2008**, 977.

126. a) C. Kim, I. Jung, Preparation of Ethynylsilane Dendrimers, *J. Organomet. Chem.* **2000**, *599*, 208. b) J. Cabrera-González, V. Sánchez-Arderiu, C. Viñas, T. Parella, F. Teixidor, R. Núñez, Redox-Active Metallacarborane-Decorated Octasilsesquioxanes. Electrochemical and Thermal Properties, *Inorg. Chem.* **2016**, *55*, 11630.

127. M. O. Senge, N. N. Sergeeva, K. J. Hale, Classic Highlights in Porphyrin and Porphyrinoid Total Synthesis and Biosynthesis, *Chem. Soc. Rev.* **2021**, *50*, 4730.

128. a) H. Huang, W. Song, J. Rieffel, J. F. Lovell, Emerging Applications of Porphyrins in Photomedicine, *Front. Phys.* **2015**, *3*, 1. b) J. López-Andarias, S.

H. Mejías, T. Sakurai, W. Matsuda, S. Seki, F. Feixas, S. Osuna, C. Atienza, N. Martín, A. L. Cortajarena, Toward Bioelectronic Nanomaterials: Photoconductivity in Protein-Porphyrin Hybrids Wrapped around SWCNT, *Adv. Funct. Mater.* **2018**, *28*, 1704031. c) M. Wolf, C. Villegas, O. Trukhina, J. L. Delgado, T. Torres, N. Martín, T. Clark, D. M. Guldi, Mediating Reductive Charge Shift Reactions in Electron Transport Chains, *J. Am. Chem. Soc.* **2017**, *139*, 17474. d) L. Moreira, J. Calbo, J. Aragó, B. M. Illescas, I. Nierengarten, B. Delavaux-Nicot, E. Ortí, N. Martín, J.-F. Nierengarten, Conjugated Porphyrin Dimers: Cooperative Effects and Electronic Communication in Supramolecular Ensembles with C_{60}, *J. Am. Chem. Soc.* **2016**, *138*, 15359. e) D. Arteaga, R. Cotta, A. Ortíz, B. Insuasty, N. Martín, L. Echegoyen, Zn(II)-porphyrin Dyes with Several Electron Acceptor Groups Linked by Vinyl-fluorene or Vinyl-thiophene Spacers for Dye-sensitized Solar Cells, *Dyes Pigm.* **2015**, *112*, 127. f) G. Bottari, G. de la Torre, D. M. Guldi, T. Torres, An Exciting Twenty-year Journey Exploring Porphyrinoid-based Photo- and Electro-active Systems, *Coord. Chem. Rev.* **2021**, *428*, 213605.

129. W. Küster, Über die Konstitution des Hämins, *Ber. Dtsch. Chem. Ges.* **1912**, *45*, 1935.

130. H. Fischer, K. Zeile, Synthese des Hämatoporphyrins, Protoporphyrins und Hämins, *Justus Liebigs Ann. Chem.* **1929**, *468*, 98.

131. P. J. Brothers, M. O. Senge, Eds. *Fundamentals of Porphyrin Chemistry: A 21st Century Approach*, 1st ed. John Wiley & Sons Ltd. New Jersey, **2022**.

132. a) M. Gouterman, Spectra of Porphyrins, *J. Mol. Spectrosc*. **1961**, *6*, 138. b) A. K. Mandal, M. Taniguchi, J. R. Diers, D. M. Niedzwiedzki, C. Kirmaier, J. S. Lindsey, D. F. Bocian, D. Holten, Photophysical Properties and Electronic Structure of Porphyrins Bearing Zero to Four *meso*-Phenyl Substituents: New Insights into Seemingly Well Understood Tetrapyrroles, *J. Phys. Chem. A* **2016**, *120*, 9719.

133. B. Pucelik, A. Sułek, J. M. Dąbrowski, Bacteriochlorins and their Metal Complexes as NIR-absorbing Photosensitizers: Properties, Mechanisms, and Applications, *Coord. Chem. Rev.* **2020**, *416*, 213340.

134. I. Aviv-Harel, Z. Gross, Aura of Corroles, *Chem. Eur. J.* **2009**, *15*, 8382.

135. a) A. D. Adler, F. R. Longo, W. Shergalis, Mechanistic Investigations of Porphyrin Syntheses. I. Preliminary Studies on *ms*-Tetraphenylporphin, *J. Am. Chem. Soc.* **1964**, *86*, 3145. b) A. D. Adler, F. R. Longo, J. D. Finarelli, J. Goldmacher, J. Assour, L. Korsakoff, A Simplified Synthesis for *meso*-Tetraphenylporphine, *J. Org. Chem*. **1967**, *32*, 476.

136. a) J. S. Lindsey, H. C. Hsu, I. C. Schreiman, Synthesis of Tetraphenylporphyrins Under Very Mild Conditions, *Tetrahedron Lett.* **1986**, *27*, 4969. b) J. S. Lindsey, Synthetic Routes to *meso*-Patterned Porphyrins, *Acc. Chem. Res.* **2010**, *43*, 300.

137. J. W. Buchler, Synthesis and Properties of Metalloporphyrins. In *The Porphyrins: Structure and Synthesis, Part A*, D. Dolphin, Ed. Academic Press, Inc. New York, **1978**, ch. 10, pp. 389-483.

138. C. Gomes, M. Peixoto, M. Pineiro, Modern Methods for the Sustainable Synthesis of Metalloporphyrins, *Molecules* **2021**, *26*, 6652.

139. Z. Gross, N. Galili, I. Saltsman, The First Direct Synthesis of Corroles from Pyrrole, *Angew. Chem. Int. Ed.* **1999**, *38*, 1427.

140. a) D. T. Gryko, B. Koszarna, Refined Methods for the Synthesis of *meso*-Substituted A_3- and *trans*-A_2B-Corroles, *Org. Biomol. Chem.* **2003**, *1*, 350. b) R. Orłowski, D. Gryko, D. T. Gryko, Synthesis of Corroles and their Heteroanalogs, *Chem. Rev.* **2017**, *117*, 3102.

141. J.-W. Ka, W.-S. Cho, C.-H. Lee, Expedient Synthesis of Corroles by Oxidant-mediated, Direct α-α' Coupling of Tetrapyrromethanes, *Tetrahedron Lett.* **2000**, *41*, 8121.

142. a) A. Akbar, S. Khan, T. Chatterjee, M. Ghosh, Unleashing the Power of Porphyrin Photosensitizers: Illuminating Breakthroughs in Photodynamic Therapy, *J. Photochem. Photobiol. B* **2023**, *248*, 112796. b) T. W. Liu, E. Huynh, T. D. MacDonald, G. Zheng. Porphyrins for Imaging, Photodynamic Therapy, and Photothermal Therapy. In *Cancer Theranostics*, X. Chen, S. Wong, Eds. 1st ed. Academic Press, Inc. New York, **2014**, ch. 14, pp. 229-254.

143. X.-T. Yu, S.-Y. Sui, Y.-X. He, C.-H. Yu, Q. Peng, Nanomaterials-based Photosensitizers and Delivery Systems for Photodynamic Cancer Therapy, *Biomater. Adv.* **2022**, *135*, 212725.

144. a) F. Akhtar, L. Misba, A. U Khan, The Dual Role of Photodynamic Therapy to Treat Cancer and Microbial Infection, *Drug Discov. Today* **2024**, *29*, 104099. b) X. Wang, J. Peng, C. Menga, F. Feng, Recent Advances for Enhanced Photodynamic Therapy: From New Mechanisms to Innovative Strategies, *Chem. Sci.* **2024**, *15*, 12234.

145. A. Sahu, K. Min, J. Jeon, H. S. Yang, G. Tae, Catalytic Nanographene Oxide with Hemin for Enhanced Photodynamic Therapy, *J. Control. Release* **2020**, *326*, 442.

146. a) P. Huang, C. Xu, J. Lin, C. Wang, X. Wang, C. Zhang, X. Zhou, S. Guo, D. Cui, Folic Acid-conjugated Graphene Oxide loaded with Photosensitizers for Targeting Photodynamic Therapy, *Theranostics* **2011**, *1*, 240. b) F. Li, S.-J. Park, D. Ling, W. Park, J. Y. Han, K. Nab, K. Char, Hyaluronic Acid-conjugated

Graphene Oxide/Photosensitizer Nanohybrids for Cancer Targeted Photodynamic Therapy, *J. Mater. Chem. B* **2013**, *1*, 1678.

147. a) C. I. M. Santos, M. Cicuéndez, G. Gonçalves, L. Rodríguez-Pérez, M. T. Portolés, M. A. F. Faustino, M. A. Herranz, M. G. P. M. S. Neves, J. M. G. Martinho, E. M. S. Maçôas, N. Martín, Safety Assessment of New Nanodiamonds@corrole Hybrids Addressed by the Response of RAW-264.7 Nacrophages, *J. Mater. Chem. B* **2023**, *11*, 675. b) C. I. M. Santos, L. Rodríguez-Pérez, G. Gonçalves, S. N. Pinto, M. Melle-Franco, P. A. A. P. Marques, M. A. F. Faustino, M. A. Herranz, N. Martín, M. G. P. M. S. Neves, J. M. G. Martinho, E. M. S. Maçôas, Novel Hybrids Based on Graphene Quantum Dots Covalently Linked to Glycol Corroles for Multiphoton Bioimaging, *Carbon* **2020**, *166*, 164. c) C. I. M. Santos, L. Rodríguez-Pérez, G. Gonçalves, C. J. Dias, F. Monteiro, M. A. F. Faustino, S. I. Vieira, L. A. Helguero, M. A. Herranz, N. Martín, M. G. P. M. S. Neves, J. M. G. Martinho, E. M. S. Maçôas, Enhanced Photodynamic Therapy Effects of Graphene Quantum Dots Conjugated with Aminoporphyrins, *ACS Appl. Nano Mater*. **2021**, *4*, 13079.

148. N. B. Magaela, R. Matshitse, B. Babu, M. Managa, E. Prinsloo, T. Nyokong, Sn(IV) Porphyrin-biotin Decorated Nitrogen Doped Graphene Quantum Dots Nanohybrids for Photodynamic Therapy, *Polyhedron* **2022**, *213*, 115624.

149. S. Beack, W. H. Kong, H. S. Jung, I. H. Do, S. Han, H. Kim, K. S. Kim, S. H. Yun, S. K. Hahn, Photodynamic Therapy of Melanoma Skin Cancer Using Carbon Dot – Chlorin e6 – Hyaluronate Conjugate, *Acta Biomater.* **2015**, *26*, 295.

150. R. Youf, M. Müller, A. Balasini, F. Thétiot, M. Müller, A. Hascoët, U. Jonas, H. Schönherr, G. Lemercier, T. Montier, T. Le Gall, Antimicrobial Photodynamic Therapy: Latest Developments with a Focus on Combinatory Strategies, *Pharmaceutics* **2021**, *13*, 1995.

151. U. Sah, K. Sharma, N. Chaudhri, M. Sankar, P. Gopinath, Antimicrobial Photodynamic Therapy: Single-walled Carbon Nanotube (SWCNT)-Porphyrin Conjugate for Visible Light Mediated Inactivation of Staphylococcus Aureus, *Colloids Surf. B Biointerfaces* **2018**, *162*, 108.

152. M. B. Ballatore, M. B. Spesia, M. E. Milanesio, E. N. Durantini, Synthesis, Spectroscopic Properties and Photodynamic Activity of Porphyrin-fullerene C_{60} Dyads with Application in the Photodynamic Inactivation of Staphylococcus Aureus, *Eur. J. Med. Chem.* **2014**, *83*, 685.

153. a) A. R. McDonald, N. Franssen, G. P. M. v. Klink, G. v. Koten, 'Click' Silica Immobilisation of Metallo-porphyrin Complexes and their Application in Epoxidation Catalysis, *J. Organomet. Chem.* **2009**, *694*, 2153. b) S. M. Aly, H. Guernon, B. Guérin, P. D. Harvey, Polyoligopeptides Functionalized

Zinc(II)porphyrins: Step Towards Artificial Hemes, *J. Porphyr. Phthalocyanines* **2011**, *15*, 871.

154. K. F. Morris, C. S. Johnson Jr, Diffusion-ordered Two-dimensional Nuclear Magnetic Resonance Spectroscopy, *J. Am. Chem. Soc.* **1992**, *114*, 3139.

155. O. Engström, A. Muñoz, B. M. Illescas, N. Martín, R. Ribeiro-Viana, J. Rojo, G. Widmalm, Investigation of Glycofullerene Dynamics by NMR Spectroscopy, *Org. Biomol. Chem.* **2015**, *13*, 8750.

156. J. Ramos-Soriano, A. Pérez-Sánchez, S. Ramírez-Barroso, B. M. Illescas, K. Azmani, A. Rodríguez-Fortea, J. M. Poblet, C. Hally, S. Nonell, D. García-Fresnadillo, J. Rojo, N. Martín, An Ultra-Long-Lived Triplet Excited State in Water at Room Temperature: Insights on the Molecular Design of Tridecafullerenes, *Angew. Chem. Int. Ed.* **2021**, *60*, 16109.

157. M. Li, Y. Xu, X. Peng, J. S. Kim, From Low to No O_2-Dependent Hypoxia Photodynamic Therapy (hPDT): A New Perspective, *Acc. Chem. Res.* **2022**, *55*, 3253.

158. a) K. Pederson, D. A. Mitchell, J. H. Prestegard, Structural Characterization of the DC-SIGN–Lewis^X Complex, *Biochemistry* **2014**, *53*, 5700. b) J. Aretz, H. Baukmann, E. Shanina, J. Hanske, R. Wawrzinek, V. A. Zapol'skii, P. H. Seeberger, D. E. Kaufmann, C. Rademacher, Identification of Multiple Druggable Secondary Sites by Fragment Screening against DC-SIGN, *Angew. Chem. Int. Ed.* **2017**, *56*, 7292.

159. M. Thépaut, J. Luczkowiak, C. Vivès, N. Labiod, I. Bally, F. Lasala, Y. Grimoire, D. Fenel, S. Sattin, N. Thielens, G. Schoehn, A. Bernardi, R. Delgado, F. Fieschi, DC/L-SIGN Recognition of Spike Glycoprotein Promotes SARS-CoV-2 Trans-infection and can be Inhibited by a Glycomimetic Antagonist, *PLoS Pathog.* **2021**, *17*, e1009576.

160. J. Bendix, I. J. Dmochowski, H. B. Gray, A. Mahammed, L. Simkhovich, Z. Gross, Structural, Electrochemical, and Photophysical Properties of Gallium(III) 5,10,15-Tris(pentafluorophenyl)corrole, *Angew. Chem. Int. Ed.* **2000**, *39*, 4048.

161. a) C. N. McEwen, R. G. McKay, B. S. Larsen, C_{60} as a Radical Sponge, *J. Am. Chem. Soc.* **1992**, *114*, 4412. b) C.-W. Lee, Y.-H. Su, Y.-C. Chiang, I.-T. Lee, S.-Y. Li, H.-C. Lee, L.-F. Hsu, Y.-L. Yan, H.-Y. Li, M.-C. Chen, K.-T. Peng, C.-H. Lai, Glycofullerenes Inhibit Particulate Matter Induced Inflammation and Loss of Barrier Proteins in HaCaT Human Keratinocytes, *Biomolecules* **2020**, *10*, 514. c) M. R. Hamblin, Fullerenes as Photosensitizers in Photodynamic Therapy: Pros and Cons, *Photochem. Photobiol. Sci.* **2018**, *17*, 1515.

162. a) A. Mahammed, Z. Gross, Bacteriochlorins and their Metal Complexes as NIR-Absorbing Photosensitizers: Properties, Mechanisms, and Applications,

Coord. Chem. Rev. **2019**, *379*, 121. b) H. Saigusa, T. Azumi, M. Sumitani, K. Yoshihara, Internal Heavy Atom Effect on the Triplet Spin Sublevels of the Lowest Triplet State of Naphthalene. II. Intersystem Crossing Processes From the Singlet Excited State to the Individual Spin Sublevels of the Lowest Triplet State, *J. Chem. Phys.* **1980**, *72*, 1713.

163. a) J. M. Englert, C. Dotzer, G. Yang, M. Schmid, C. Papp, J. M. Gottfried, H.-P. Steinrück, E. Spiecker, F. Hauke, A. Hirsch, Covalent Bulk Functionalization of Graphene, *Nat. Chem.* **2011**, *3*, 279. b) A. Criado, M. Melchionna, S. Marchesan, M. Prato, The Covalent Functionalization of Graphene on Substrates, *Angew. Chem. Int. Ed.* 2**015**, *54*, 10734. c) V. Georgakilas, J. N. Tiwari, K. C. Kemp, J. A. Perman, A. B. Bourlinos, K. S. Kim, R. Zboril, Noncovalent Functionalization of Graphene and Graphene Oxide for Energy Materials, Biosensing, Catalytic, and Biomedical Applications, *Chem. Rev.* **2016**, *116*, 5464. d) L. Rodríguez-Pérez, M. A. Herranz, N. Martín, The Chemistry of Pristine Graphene, *Chem. Commun.* **2013**, *49,* 3721. e) K. Dirian, M. A. Herranz, G. Katsukis, J. Malig, L. Rodríguez-Pérez, C. Romero-Nieto, V. Strauss, N. Martín, D. M. Guldi, Low Dimensional Nanocarbons – Chemistry and Energy/Electron Transfer Reactions, *Chem. Sci.* **2013**, *4*, 4335. f) G. Bottari, M. A. Herranz, L. Wibmer, M. Volland, L. Rodríguez-Pérez, D. M. Guldi, A. Hirsch, N. Martín, F. D'Souza, T. Torres, Chemical Functionalization and Characterization of Graphene-based Materials, *Chem. Soc. Rev.* **2017**, *46*, 4464.

164. a) J. Wu, H. Lin, D. J. Moss, K. P. Loh, B. Jia, Graphene Oxide for Photonics, Electronics and Optoelectronics, *Nat. Rev. Chem.* **2023**, *7*, 162. b) F. Bonaccorso, L. Colombo, G. Yu, M. Stoller, V. Tozzini, A. C. Ferrari, R. S. Ruoff, V. Pellegrini, Graphene, Related Two-dimensional Crystals, and Hybrid Systems for Energy Conversion and Storage, *Science* **2015**, *347*, 1246501. c) J. Li, H. Zeng, Z. Zeng, Y. Zeng, T. Xie, Promising Graphene-Based Nanomaterials and their Biomedical Applications and Potential Risks: A Comprehensive Review, *ACS Biomater. Sci. Eng*. **2021**, *7*, 5363.

165. a) P. Izquierdo-García, J. M. Fernández-García, N. Martín, Twenty Years of Graphene: From Pristine to Chemically Engineered Nano-Sized Flakes, *J. Am. Chem. Soc*. **2024**, *146*, 32222. b) N. Martín, C. Nuckolls, Eds. *Molecular Nanographenes: Synthesis, Properties, and Applications*, 1st ed. Wiley-VCH GmbH, Weinheim, **2025**.

166. L. Chen, Y. Hernández, X. Feng, K. Müllen, From Nanographene and Graphene Nanoribbons to Graphene Sheets: Chemical Synthesis, *Angew. Chem. Int. Ed.* **2012**, *51*, 7640.

167. Z. Liu, S. Fu, X. Liu, A. Narita, P. Samori, M. Bonn, H. I. Wang, Small Size, Big Impact: Recent Progress in Bottom-Up Synthesized Nanographenes for Optoelectronic and Energy Applications, *Adv. Sci*. **2022**, *9*, 2106055.

168. A. Halleux, R. H. Martin, G. S. D. King, Synthèses dans la Série des Dérivés Polycycliques Aromatiques Hautement Condensés. L'hexabenzo-1,12; 2,3; 4,5; 6,7; 8,9; 10,11-coronène, le Tétrabenzo-4,5; 6,7; 11,12; 13,14-péropyrène et le Tétrabenzo-1,2; 3,4; 8,9; 10,11-bisanthène, *Helv*. *Chim. Acta* **1958**, *41*, 1177.

169. C. D. Simpson, J. D. Brand, A. J. Berresheim, L. Przybilla, H. J. Räder, K. Müllen, Synthesis of a Giant 222 Carbon Graphite Sheet, *Chem. Eur. J*. **2002**, *8*, 1424.

170. S. Ito, M. Wehmeier, J. D. Brand, C. Kübel, R. Epsch, J. P. Rabe, K. Müllen, Synthesis and Self-Assembly of Functionalized Hexa-*peri*-hexabenzocoronenes, *Chem. Eur. J*. **2000**, *6*, 4327.

171. a) R. Scholl, J. Mansfeld, *meso*-Benzdianthron (Helianthron), *meso*-Naphthodianthron, und ein neuer Weg zum Flavanthren, *Ber. Dtsch. Chem. Ges*. **1910**, *43*, 1734. b) R. Scholl, C. Seer, Abspaltung Aromatisch Gebundenen Wasserstoffs und Verknüpfung aromatischer Kerne durch Aluminiumchlorid, *Justus Liebigs Ann. Chem*. **1912**, *394*, 111.

172. R. S. Jassas, E. U. Mughal, A. Sadiq, R. I. Alsantali, M. M. Al-Rooqi, N. Naeem, Z. Moussa, S. A. Ahmed, Scholl Reaction as a Powerful Tool for the Synthesis of Nanographenes: A Systematic Review, *RSC Adv*. **2021**, *11*, 32158.

173. a) M. Grzybowski, K. Skonieczny, H. Butenschön, D. T. Gryko, Comparison of Oxidative Aromatic Coupling and the Scholl Reaction, *Angew. Chem. Int. Ed*. **2013**, *52*, 9900. b) M. Grzybowski, B. Sadowski, H. Butenschön, D. T. Gryko, Synthetic Applications of Oxidative Aromatic Coupling—From Biphenols to Nanographenes, *Angew. Chem. Int. Ed*. **2020**, *59*, 2998.

174. Y. Zou, Y. Han, S. Wu, X. Hou, C. H. E. Chow, J. Wu, Scholl Reaction of Perylene-Based Polyphenylene Precursors under Different Conditions: Formation of Hexagon or Octagon? *Angew. Chem. Int. Ed.* **2021**, *60*, 17654.

175. X. Yang, M. Hoffmann, F. Rominger, T. Kirschbaum, A. Dreuw, M. Mastalerz, Functionalized Contorted Polycyclic Aromatic Hydrocarbons by a One-Step Cyclopentannulation and Regioselective Triflyloxylation, *Angew. Chem. Int. Ed.* **2019**, *58*, 10650.

176. F. Ko, K. Hirabayashi, T. Shimizu, K.-I. Sugiura, Unexpected Phenyl Group Rearrangement of Thiele's Hydrocarbon Derivative Under Polycyclic Aromatic Hydrocarbon Synthesis, *Tetrahedron* **2018**, *59*, 4251.

177. P. Izquierdo-García, J. M. Fernández-García, J. Perles, I. Fernández, N. Martín, Electronic Control of the Scholl Reaction: Selective Synthesis of Spiro vs Helical Nanographenes, *Angew. Chem. Int. Ed.* **2023**, *61*, e202215655.

178. H.-A. Lin, Y. Sato, Y. Segawa, T. Nishihara, N. Sugimoto, L. T. Scott, T. Higashiyama, K. Itami, A Water-Soluble Warped Nanographene: Synthesis and

Applications for Photoinduced Cell Death, *Angew. Chem. Int. Ed.* **2018**, *57*, 2874.

179. X.-H. Ma, X. Gao, J.-Y. Chen, M. Cao, Q. Dai, Z.-K. Jia, Y.-B. Zhou, X.-J. Zhao, C. Chu, G. Liu, Y.-Z. Tan, Soluble Nanographene C_{222}: Synthesis and Applications for Synergistic Photodynamic/Photothermal Therapy, *J. Am. Chem. Soc.* **2024**, *146*, 2411.

180. R. Li, B. Ma, M. Li, D. Wang, P. Liu, P. An, Multi-heteroatom Doped Nanographenes: Enhancing Photosensitization Capacity by Forming an Electron Donor-acceptor Architecture, *Chem. Sci.* **2024**, *15*, 11408.

181. H. Zhao, L. Guillaud, M. F. Emily, X. Xu, L. Moshniaha, H. Hanayama, R. Kabe, M. Terenzio, A. Narita, Nanographene-Based Polymeric Nanoparticles as Near-Infrared Emissive Neuronal Tracers, *ACS Nano* **2024**, *18*, 34730.

182. C. Zhao, C. Qu, Y. Hu, F. Wu, S. Liu, F. Cai, Y. Chen, Y. Qiu, Z. Shen, Orbicular-Donor-Acceptor System in N-doped Nanographene for Highly Efficient NIR-II Photothermal Therapy, *Adv. Healthcare Mater.* **2024**, *13*, 2402545.

183. D. Lungerich, J. F. Hitzenberger, M. Marcia, F. Hampel, T. Drewello, N. Jux, Superbenzene–Porphyrin Conjugates, *Angew. Chem. Int. Ed.* **2014**, *53*, 12231.

184. F. A. Murphy, S. M. Draper, Superaromatic Terpyridines: Hexa-*peri*-hexabenzocoronenes with Tridentate Functionality, *J. Org. Chem.* **2010**, *75*, 1862.

185. a) E. Arce, P. M. Nieto, V. Díaz, R. G. Castro, A. Bernad, J. Rojo, Glycodendritic Structures Based on Boltorn Hyperbranched Polymers and their Interactions with *Lens culinaris* Lectin, *Bioconjug Chem* **2003**, *14*, 817. b) T. K. Lindhorst, S. Kötter, U. Krallmann-Wenzel, S. Ehlers, Trivalent α-D-Mannoside Clusters as Inhibitors of Type-1 Fimbriae-mediated Adhesion of *Escherichia Coli*: Structural Variation and Biotinylation, *J. Chem. Soc. Perkin Trans. 1* **2001**, 823.

186. J. Geng, G. Mantovani, L. Tao, J. Nicolas, G. Chen, R. Wallis, D. A. Mitchell, B. R. G. Johnson, S. D. Evans, D. M. Haddleton, Site-Directed Conjugation of "Clicked" Glycopolymers to Form Glycoprotein Mimics: Binding to Mammalian Lectin and Induction of Immunological Function, *J. Am. Chem. Soc.* **2007**, *129*, 15156.

187. H. Tamiaki, A. Shinkai, Y. Kataoka, Synthesis of Galactosylated Zinc Bacteriochlorophyll-*d* Analogs and their Self-aggregation in an Aqueous Methanol Solution, *J. Photochem. Photobiol. A Chem.* **2009**, *207*, 115.

188. O. Otman, P. Boullanger, D. Lafont, T. Hamaide, New Amphiphilic Glycopolymers Based on a Polycaprolactone-maleic anhydride Copolymer Backbone: Characterization by ^{15}N NMR and Application to Colloidal Stabilization of Nanoparticles, *Macromol. Chem. Phys.* **2008**, *209*, 2410.

189. V. Yarlagadda, M. M. Konai, G. B. Manjunath, C. Ghosh, J. Haldar, Tackling Vancomycin-resistant Bacteria with 'Lipophilic-vancomycin-carbohydrate Conjugates', *J. Antibiot.* **2015**, *68*, 302.

190. G. Tao, T. Ji, N. Wang, G. Yang, X. Lei, W. Zheng, R. Liu, X. Xu, L. Yang, G.-Q. Yin, X. Liao, X. Li, H.-M. Ding, X. Ding, J. Xu, H.-B. Yang, G. Chen, Self-Assembled Saccharide-Functionalized Amphiphilic Metallacycles as Biofilms Inhibitor *via* "Sweet Talking", *ACS Macro Lett.* **2020**, *9*, 61.

191. T. M. N. Trinh, M. Holler, J. P. Schneider, M. I. García-Moreno, J. M. García-Fernández, A. Bodlenner, P. Compain, C. Ortiz-Mellet, J.-F. Nierengarten, Construction of Giant Glycosidase Inhibitors from Iminosugar-substituted Fullerene Macromonomers, *J. Mater. Chem. B* **2017**, *5*, 6546.

192. J.-F. Nierengarten, J. Iehl, V. Oerthel, M. Holler, B. M. Illescas, A. Muñoz, N. Martín, J. Rojo, M. Sánchez-Navarro, S. Cecioni, S. Vidal, K. Buffet, M. Durka, S. P. Vincent, Fullerene Sugar Balls, *Chem. Commun.* **2010**, *46*, 3860.

193. Y. Min, F. Leng, B. F. Machado, P. Lecante, P. Roblin, H. Martínez, T. Theussl, A. Casu, A. Falqui, M. Barcenilla, S. Coco, B. M. Illescas, N. Martín, M. R. Axet, P. Serp, 2D and 3D Ruthenium Nanoparticle Covalent Assemblies for Phenyl Acetylene Hydrogenation, *Eur. J. Inorg. Chem.* **2020**, *2020*, 4069.

194. B. A. Wojtczak, A. Andrysiak, B. Grüner, Z. J. Lesnikowski, "Chemical Ligation": A Versatile Method for Nucleoside Modification with Boron Clusters, *Chem. Eur. J.* **2008**, *14*, 10675.

195. A. V. Orlova, N. N. Kondakov, B. G. Kimel, L. O. Kononov, E. G. Kononova, I. B. Sivaev, V. I. Bregadze, Synthesis of Novel Derivatives of *Closo*-dodecaborate Anion with Azido Group at the Terminal Position of the Spacer, *Appl. Organometal. Chem.* **2007**, *21*, 98.

196. P.-F. Cao, J. Mangadlao, R. Advincula, A Trefoil Knotted Polymer Produced through Ring Expansion, *Angew. Chem. Int. Ed.* **2015**, *54*, 5127.

197. G. Yang, H. Oh, C. Chanthad, Q. Wang, Dumbbell-Shaped Octasilsesquioxanes Functionalized with Ionic Liquids as Hybrid Electrolytes for Lithium Metal Batteries, *Chem. Mater.* **2017**, *29*, 9275.

198. P. Piotrowski, J. Pawłowska, J. G. Sadło, R. Bilewicz, A. Kaim, TEMPO Functionalized C_{60} Fullerene Deposited on Gold Surface for Catalytic Oxidation of Selected Alcohols, *J. Nanopart. Res.* **2017**, *19*, 161.

199. N. Li, F. Chen, J. Shen, H. Zhang, T. Wang, R. Ye, T. Li, T. Peng Loh, Y. Y. Yang, H. Zeng, Buckyball-Based Spherical Display of Crown Ethers for *De Novo* Custom Design of Ion Transport Selectivity, *J. Am. Chem. Soc.* **2020**, *142*, 21082.